Flight Vehicle Aerodynamics

Mark Drela

Flight Vehicle Aerodynamics

Flight Vehicle Aerodynamics

Mark Drela

Contents

K	Boundary layer kinetic energy defect,	p. 59
K_f	Profile drag form factor,	p. 89
Kn	Knudsen number,	p. 1
ℓ	Body length,	p. 1
ℓ	Coordinate on surface (of $s\ell n$ system),	p. 26
l	Circuit or control volume integration coordinate,	p. 41
L	Lift,	p. 100
L'	Lift per unit span (in 2D),	p. 40
$\mathcal{L}$	Rolling moment,	p. 124
$\mathcal{L}$	Lagrangian function,	p. 118
m	Boundary layer mass defect,	p. 49
m	Aircraft mass,	p. 205
$\dot{m}$	Mass flow,	p. 49
M	Mach number,	p. 10
$\mathbf{M}$	Moment vector,	p. 124
$\mathcal{M}$	Pitching moment,	p. 124
n	Coordinate normal to surface (of $s\ell n$ system),	p. 26
$\hat{\mathbf{n}}$	Unit normal vector,	p. 4
$\tilde{N}$	Laminar instability amplitude exponent,	p. 93
$\mathcal{N}$	Yawing moment,	p. 124
p	Pressure,	p. 1
p'	Dynamic part of pressure field,	p. 20
p	Roll rate,	p. 124
$\bar{p}$	Dimensionless roll rate ($= p b_{\text{ref}}/2V_\infty$),	p. 125
Pr	Prandtl number,	p. 10
P	Boundary layer momentum defect,	p. 59
q	Pitch rate,	p. 124
$\bar{q}$	Dimensionless pitch rate ($= q c_{\text{ref}}/2V_\infty$),	p. 125
$\dot{q}_S$	Heating rate per unit area,	p. 6
$\dot{q}_V$	Heating rate per unit volume,	p. 5
$\dot{\mathbf{q}}$	Heat flux vector,	p. 6
q_∞	Freestream dynamic pressure ($= \frac{1}{2}\rho_\infty V_\infty^2$),	p. 12
Q	Freestream dynamic pressure, for flight dynamics,	p. 209
Q	Coefficient in PP2 equation,	p. 170
$\mathbf{r}$	Cartesian position vector ($= x\,\hat{\mathbf{x}} + y\,\hat{\mathbf{y}} + z\,\hat{\mathbf{z}}$) ,	p. 3
r	Magnitude of Cartesian position vector, ($= \sqrt{x^2 + y^2 + z^2}$),	p. 3
r	Distance to x axis in axisymmetric cases ($= \sqrt{y^2 + z^2}$),	p. 187
r	Yaw rate,	p. 124
$\bar{r}$	Dimensionless yaw rate ($= r b_{\text{ref}}/2V_\infty$),	p. 125
R	Specific gas constant,	p. 2

Preface

Objective

This book is intended as a general reference for the physics, concepts, theories, and models underlying the discipline of aerodynamics. An overarching theme is the technique of velocity field representation and modeling via source and vorticity fields, and via their sheet, filament, or point-singularity idealizations. These models provide an intuitive feel for aerodynamic flow behavior, and are also the basis of aerodynamic force analysis, drag decomposition, flow interference estimation, wind tunnel corrections, computational methods, and many other important applications.

This book covers some topics in depth, while offering introductions or summaries of others. In particular, Chapters 3,4 on Boundary Layers, Chapter 7 on Unsteady Aerodynamics, and Chapter 9 on Flight Dynamics are intended as introductions and overviews of those topics, which deserve to be properly treated in separate dedicated texts. Similarly, there are only glancing mentions of the related topic of Propulsion, which is its own discipline.

Computational Fluid Dynamics (CFD) and computational methods in general are indispensable for today's practicing aerodynamicist. Hence a few computational methods are described here, primarily the vortex lattice and panel methods which are based on the source and vorticity flow-field representation. The main goal is to provide improved understanding of the concepts and physical models which underlie such methods.

Most of this book is based on the lecture notes, handouts, and reference materials which have been developed for the course *Flight Vehicle Aerodynamics* (course number 16.110) taught by the author at MIT's Department of Aeronautics and Astronautics. This course is intended for first-year graduate students, but has also attracted a significant number of advanced undergraduates.

Preparation

This book assumes that the reader is well versed in basic physics and vector calculus, and already has had exposure to basic fluid mechanics and aerodynamics. Hence, little or no space is devoted to introduction or discussion of basic concepts such as fluid velocity, density, pressure, viscosity, stress, etc. Chapter 1 on the Physics of Aerodynamics Flows is intentionally concise, since it is intended primarily as a reference for the underlying physical principles and governing equations of fluid flows rather than as a first introduction to these topics. The author's course at MIT begins with Chapter 2.

Some familiarity with aerodynamics and aeronautics terminology is assumed on the part of the reader. However, a summary of advanced vector calculus notation is given in Appendix A, since this is not commonly seen in basic vector calculus texts.

Acknowledgments

Nomenclature

The page numbers indicate where each symbol is first used.

Roman letters

a Speed of sound,   p. 1

a Boundary layer edge velocity power-law exponent,   p. 71

A Cross-sectional area,   p. 45

$A\!R$ Aspect ratio,   p. 113

A_{ij} Aerodynamic influence coefficient (AIC) matrix,   p. 114

$\mathcal{A}$ G-beta constant for equilibrium turbulent flow,   p. 73

$\mathcal{A}_n$ Fourier coefficients of spanwise circulation distribution,   p. 113

$\mathcal{A}_n$ Fourier coefficients of airfoil's vortex sheet strength distribution,   p. 254

$\bar{\bar{\mathbf{A}}}$ Flight-dynamics system matrix,   p. 207

b Boundary layer lateral width parameter,   p. 75

b Wingspan,   p. 104

b Reference span,   p. 209

B Wind tunnel cross-section aspect ratio,   p. 233

B_{ij} Source-influence matrix for the potential,   p. 151

$\mathcal{B}$ G-beta constant for equilibrium turbulent flow,   p. 73

$\mathcal{B}_n$ Fourier coefficients airfoil thickness distribution,   p. 257

$\bar{\bar{\mathbf{B}}}$ Flight-dynamics control matrix,   p. 207

c Airfoil chord,   p. 9

c Reference chord,   p. 209

c_d 2D section drag coefficient,   p. 40

C_D Drag coefficient,   p. 125

$c_{\mathcal{D}}$ Dissipation coefficient (locally normalized),   p. 66

c_f Skin friction coefficient (locally normalized),   p. 65

C_f Skin friction coefficient,   p. 12

$\bar{C}_f$ Average skin friction coefficient,   p. 88

c_ℓ 2D section lift coefficient,   p. 40

C_L Lift coefficient,   p. 125

C_ℓ Rolling moment coefficient,   p. 125

C_m Pitching moment coefficient,   p. 125

C_n Yawing moment coefficient,   p. 125

C_p	Pressure coefficient,	p. 12
c_p	Specific heat at constant pressure,	p. 2
c_v	Specific heat at constant volume,	p. 2
C_Y	Sideforce coefficient,	p. 125
C	Theodorsen function,	p. 156
d	Body diameter,	p. 115
$\mathcal{D}$	Dissipation integral,	p. 66
D	Drag,	p. 100
D'	Drag per unit span (in 2D),	p. 40
D_i	Induced drag,	p. 105
D_p	Profile drag,	p. 105
D_w	Wave drag,	p. 188
e	Specific energy,	p. 2
e	Span efficiency,	p. 113
$\dot{E}$	Energy rate (power),	p. 59
$\mathbf{f}$	Body force per unit mass field,	p. 4
F	Force,	p. 59
$\mathbf{F}$	Force vector,	p. 124
$\mathcal{F}_\theta$	Momentum thickness growth function,	p. 81
g	Gravitational acceleration magnitude,	p. 19
$\boldsymbol{g}$	Gravitational acceleration vector,	p. 4
g	Gain of control variable on surface deflection,	p. 132
G	Clauser shape parameter,	p. 73
h	Specific enthalpy,	p. 2
h	Unsteady airfoil heave displacement,	p. 152
h	Hyperbolic radius,	p. 185
h	Wind tunnel cross-section height,	p. 239
$\hat{\mathbf{h}}$	Hinge-axis unit vector,	p. 132
$\mathbf{h}$	Angular momentum of onboard rotors,	p. 205
H	Boundary layer shape parameter,	p. 65
H^*	Kinetic energy shape parameter,	p. 66
H^{**}	Density flux thickness shape parameter,	p. 66
$\mathbf{H}$	Total aircraft angular momentum,	p. 205
$\bar{\bar{\mathbf{I}}}$	Unit tensor, identity matrix,	p. 6
$\bar{\bar{\mathbf{I}}}$	Mass moment of inertia tensor,	p. 205
I	Moment of inertia component,	p. 206
k	Heat conductivity,	p. 1
k	Reduced frequency,	p. 156
K	Kernel function for scalar field,	p. 32
$\mathbf{K}$	Kernel function for vector field,	p. 25

R Radius kernel function, p. 38

R Radius of axisymmetric body, p. 139

Re Reynolds number, p. 10

Re_θ Momentum thickness Reynolds number, p. 81

$\mathbf{R}$ Position vector in Earth frame, p. 145

$\mathbf{R}_\mathrm{o}$ Position vector of body-axes origin in Earth frame, p. 149

s Specific entropy, p. 13

s Coordinate on surface (of $s\ell n$ system), p. 26

S Reference area, p. 209

St Strouhal number, p. 11

$\mathcal{S}$ Surface area, p. 7

$\mathcal{S}$ Sonic discriminator ($= 1 - M^2$), p. 196

$\bar{\bar{\mathbf{S}}}$ Stability-axes to body-axes xz rotation matrix, p. 210

t Time, p. 7

t Airfoil thickness, p. 41

T Temperature, p. 1

$\mathcal{T}$ Normalized skin friction function, p. 81

T_S Sutherland's constant for air ($= 110\,\mathrm{K}$), p. 1

$\bar{\bar{\mathbf{T}}}$ Rotation matrix (direction cosine matrix), p. 124

u Cartesian x-velocity component, p. 3

u_1 Streamwise velocity component of 3D boundary layer, p. 76

u_2 Crossflow velocity component of 3D boundary layer, p. 76

U Normalized boundary layer velocity ($= u/u_\mathrm{e}$), p. 60

$\mathbf{U}$ Body velocity vector, p. 4

v Cartesian y-velocity component, p. 3

V Fluid speed, p. 4

$\mathbf{V}$ Fluid velocity, p. 4

V_h Horizontal-tail volume coefficient, p. 218

V_v Vertical-tail volume coefficient, p. 219

$\mathbf{v}$ Flight-dynamics eigenvector, p. 207

$\dot{\mathcal{V}}$ Volume outflow rate, p. 31

$\mathcal{V}$ Volume, p. 7

w Cartesian z-velocity component, p. 3

$\dot{w}_S$ Work rate per unit area, p. 6

$\dot{w}_\mathcal{V}$ Work rate per unit volume, p. 5

x Cartesian coordinate, p. 3

$\hat{\mathbf{x}}$ Cartesian x unit vector, p. 3

$\mathbf{x}$ Flight-dynamics state vector, p. 206

X Axial force, p. 206

X Normalized wind tunnel coordinate, p. 225

Greek letters

θ^* Kinetic energy thickness,   p. 59

Θ Momentum area,   p. 75

Θ^* Kinetic energy area,   p. 75

κ 2D doublet strength,   p. 29

$\mathcal{K}$ 3D doublet strength,   p. 29

λ Molecular mean free path,   p. 1

λ Source sheet strength,   p. 23

λ Thwaites pressure gradient parameter,   p. 81

Λ Scaled pressure gradient parameter,   p. 84

λ Flight-dynamics eigenvalue,   p. 207

λ Wing taper ratio,   p. 216

Λ Source filament strength,   p. 27

Λ Wing sweep angle,   p. 77

Λ Lagrange multiplier,   p. 119

μ Doublet sheet strength,   p. 29

μ Viscosity,   p. 1

μ_t Eddy viscosity,   p. 61

ν Kinematic viscosity $(= \mu/\rho)$,   p. 17

ξ Characteristic variable,   p. 183

ρ Density,   p. 1

σ Real part of flight-dynamics eigenvalue (time constant),   p. 207

σ Source density (dilatation rate $\nabla \cdot \mathbf{V}$),   p. 6

Σ Source point strength,   p. 27

$\bar{\bar{\tau}}$ Viscous stress tensor,   p. 5

$\boldsymbol{\tau}$ Viscous stress vector,   p. 5

Υ Effective wing dihedral angle,   p. 216

φ Perturbation velocity potential,   p. 38

ϕ Velocity potential,   p. 19

ϕ Normalized perturbation potential,   p. 170

ϕ Aircraft roll angle,   p. 202

Φ Wagner function,   p. 154

Φ Full velocity potential,   p. 166

χ Flow curvature from wind tunnel images,   p. 228

ψ Aircraft heading angle,   p. 202

Ψ Küssner function,   p. 154

ω Imaginary part of flight-dynamics eigenvalue (radian frequency),   p. 207

ω Vorticity (in 2D),   p. 28

$\boldsymbol{\omega}$ Vorticity vector (in 3D),   p. 17

$\boldsymbol{\Omega}$ Body angular velocity vector,   p. 4

Operators

$\mathrm{D}(\ )/\mathrm{D}t$ Substantial derivative ($= \frac{\partial(\ )}{\partial t} + \mathbf{V} \cdot \nabla(\ )$),   p. 8

$\nabla(\ )$ Gradient ($= \frac{\partial(\ )}{\partial x}\,\hat{\mathbf{x}} + \frac{\partial(\ )}{\partial y}\,\hat{\mathbf{y}} + \frac{\partial(\ )}{\partial z}\,\hat{\mathbf{z}} = \frac{\partial(\ )}{\partial s}\,\hat{\mathbf{s}} + \frac{\partial(\ )}{\partial \ell}\,\hat{\boldsymbol{\ell}} + \frac{\partial(\ )}{\partial n}\,\hat{\mathbf{n}}$),   p. 6

$\widetilde{\nabla}(\ )$ Surface gradient ($= \frac{\partial(\ )}{\partial s}\,\hat{\mathbf{s}} + \frac{\partial(\ )}{\partial \ell}\,\hat{\boldsymbol{\ell}}$),   p. 28

$\dot{(\ )}$ Time derivative ($= \frac{\partial(\ )}{\partial t}$),   p. 146

Subscripts

$(\ )_0$ Trim-state quantity,   p. 207

$(\ )_\infty$ Freestream,   p. 9

$(\ )_A$ Apparent-mass force or moment,   p. 154

$(\ )_b$ Related to boundary conditions,   p. 25

$(\ )_e$ At edge of boundary layer,   p. 47

$(\ )_{\mathrm{eff}}$ Effective-freestream quantity (excludes near-field contributions),   p. 104

$(\ )_\mathrm{i}$ Equivalent Inviscid Flow,   p. 47

$(\ )_i$ Related to induced drag or downwash,   p. 104

$(\ )_i$ Control-point index in vortex lattice method,   p. 132

$(\ )_j$ Horseshoe vortex index in vortex lattice method,   p. 132

$(\ )_l$ On lower surface,   p. 51

$(\ )_l$ Control variable index in vortex lattice method,   p. 132

$(\ )_{LE}$ At leading edge,   p. 37

$(\ )_o$ Stagnation (total) quantity,   p. 4

$(\ )_Q$ Quasi-steady force or moment,   p. 154

$(\ )_{\mathrm{ref}}$ Reference value,   p. 2

$(\ )_{\mathrm{SL}}$ Sea-level Standard Atmosphere,   p. 1

$(\ )_{TE}$ At trailing edge,   p. 37

$(\ )_{\mathrm{tr}}$ At transition location,   p. 89

$(\ )_u$ On upper surface,   p. 51

$(\ )_\mathrm{u}$ Measured quantity uncorrected for tunnel boundary effects,   p. 223

$(\ )_\mathrm{w}$ At wall,   p. 47

$(\ )_\perp$ Component or quantity perpendicular to wing,   p. 77

$(\ )_\parallel$ Component or quantity parallel to wing,   p. 77

Superscripts

$(\ )'$ Dummy variable of integration,   p. 2

$(\ )^b$ Vector component in body axes,   p. 265

$(\ )^e$ Vector component in Earth axes,   p. 265

$(\ )^\mathrm{s}$ Vector component in stability axes,   p. 124

$(\ )^\mathrm{w}$ Vector component in wind axes,   p. 125

$\overline{(\ )}$ Dimensionless quantity (in Chapters 1, 6),   p. 10

$\bar{(\ )}$ Quantity in Prandtl-Glauert space (in Chapter 8),   p. 173

Chapter 1

Physics of Aerodynamic Flows

This chapter will describe the properties of atmospheric air, summarize key physical relations between these properties, and derive the equations of fluid motion which form the basis of aerodynamics.

1.1 Atmospheric Properties

A typical dimension ℓ of any common aircraft is vastly greater than the molecular mean free path λ of the air at any practical operating altitude, as quantified by the *Knudsen number* $Kn \equiv \lambda/\ell \ll 1$. Consequently the air can be considered to be a continuum fluid having a density ρ, pressure p, temperature T, and speed of sound a at every point in space and time. There are also viscous stresses and heat conduction at each point, which are quantified by the fluid's viscosity μ and heat conductivity k. The US Standard Atmosphere [1] has the following values for these properties for air at sea level.

$$
\begin{aligned}
\text{density:} \quad & \rho_{\mathrm{SL}} &=& \quad 1.225 \ \mathrm{kg/m^3} \\
\text{pressure:} \quad & p_{\mathrm{SL}} &=& \quad 1.0132 \times 10^5 \ \mathrm{Pa} \\
\text{temperature:} \quad & T_{\mathrm{SL}} &=& \quad 288.15 \ \mathrm{K} \\
\text{speed of sound:} \quad & a_{\mathrm{SL}} &=& \quad 340.3 \ \mathrm{m/s} \\
\text{viscosity:} \quad & \mu_{\mathrm{SL}} &=& \quad 1.79 \times 10^{-5} \ \mathrm{kg/m\text{-}s}
\end{aligned}
\tag{1.1}
$$

Reference [1] also gives equations for these quantities at other altitudes, and tabulated values are also available from many sources. Alternatively, the following curve-fit formulas for the pressure and temperature may be more convenient for numerical work, with the altitude z in kilometers and temperatures in Kelvin.

$$
p_{(z)} \;=\; p_{\mathrm{SL}} \, \exp\!\left(-0.118\,z \;-\; \frac{0.0015\,z^2}{1 - 0.018\,z + 0.0011\,z^2}\right)
\tag{1.2}
$$

$$
T_{(z)} \;=\; 216.65 \;+\; 2.0 \, \ln\!\left[\, 1 + \exp\!\left(35.75 - 3.25\,z\right) + \exp\!\left(-3.0 + 0.0003\,z^3\right)\right]
\tag{1.3}
$$

These approximations are accurate for $z < 47\,\mathrm{km}$, and are shown in Figure 1.1 for $z < 26\,\mathrm{km}$.

With $p_{(z)}$ and $T_{(z)}$ known, the atmospheric density $\rho_{(z)}$ can then be obtained from the ideal gas law (1.7), and the speed of sound can be obtained from expression (1.70) given in Section 1.7.3. The viscosity is accurately given by Sutherland's Law with $T_S = 110\,\mathrm{K}$ for air,

$$
\mu_{(z)} \;=\; \mu_{(T_{(z)})} \;=\; \mu_{\mathrm{SL}} \left(\frac{T}{T_{\mathrm{SL}}}\right)^{3/2} \frac{T_{\mathrm{SL}} + T_S}{T + T_S}
\tag{1.4}
$$

which can also be used to relate the local viscosity to the local temperature at any point in a flow-field.

For gases, the heat conductivity k can be most easily obtained from the viscosity via the *Prandtl number*, $Pr \equiv c_p \, \mu/k$, which is very nearly constant across a wide range of temperatures. The specific heat c_p will
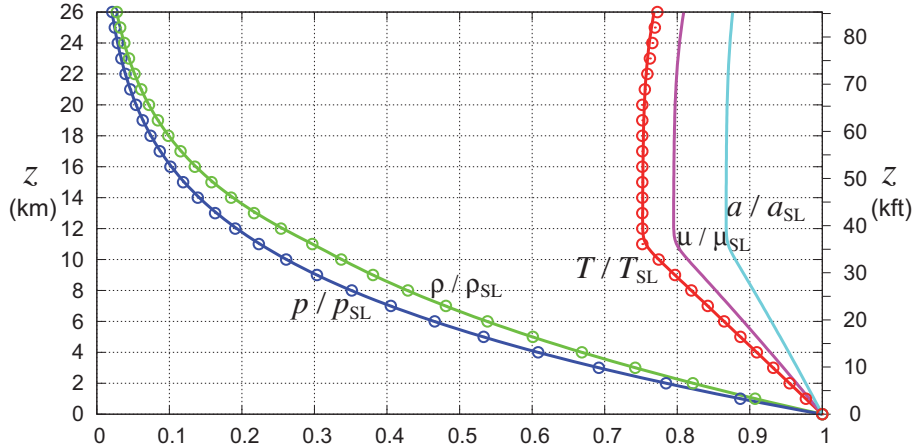
Figure 1.1: Atmospheric properties versus altitude, relative to sea-level values. Symbols are from the US Standard Atmosphere. Lines are curve fits (1.2), (1.3), and gas relations (1.4), (1.7), (1.70).

be defined in the next section.

$$k = c_p\,\mu/Pr \qquad\qquad\qquad\qquad (1.5)$$

$$Pr = 0.72 \qquad\qquad\text{(for air)} \qquad\qquad (1.6)$$

1.2 Ideal-Gas Thermodynamic Relations

The ideal gas law

$$p = \rho RT \qquad\qquad\qquad\qquad (1.7)$$

$$R = 287.04 \text{ J/kg-K} \qquad\qquad\text{(for air)}$$

is an example of an *equation of state*, and is accurate for all common gases over a wide range of temperatures and pressures. The specific gas constant R is inversely proportional to the average molecular weight.

An additional important state variable is the specific internal energy e, which together with p and ρ also defines the specific enthalpy h.

$$h \equiv e + p/\rho \qquad\qquad\qquad\qquad (1.8)$$

$$= e + RT \qquad\qquad\text{(for ideal gas)} \qquad\qquad (1.9)$$

For a *thermally perfect gas*, both e and h depend only on the temperature, and are respectively defined via the specific heat at constant volume $c_v(T)$, and the specific heat at constant pressure $c_p(T)$.

$$\left.\begin{aligned}
e(T) &= e_{\text{ref}} + \int_{T_{\text{ref}}}^{T} c_{v(T')}\,\mathrm{d}T' \\[2mm]
h(T) &= h_{\text{ref}} + \int_{T_{\text{ref}}}^{T} c_{p(T')}\,\mathrm{d}T'
\end{aligned}\right\} \qquad\text{(thermally perfect gas)} \qquad (1.10)$$

The reference values are arbitrary, since only changes in e and h are physically meaningful. The ideal-gas h definition (1.9) implies the following relation between the specific heats and the specific gas constant.

$$c_{p(T)} = c_{v(T)} + R \qquad\qquad\qquad\qquad (1.11)$$

For a *calorically perfect gas*, both c_v and c_p are constant, which makes e and h directly proportional to T,

$$\left.\begin{aligned} e &= c_v T \\ h &= c_p T \end{aligned}\right\} \qquad \text{(calorically perfect gas)} \qquad (1.12)$$

where zero reference values have been chosen. Air at ordinary temperatures is very nearly calorically perfect. Hence, definitions (1.12) are appropriate for external aerodynamic flows, and here it is more natural to work directly with the enthalpy rather than the temperature. A more convenient form of the ideal gas law (1.7) is then given in terms of the enthalpy and the specific heat ratio γ.

$$\gamma p = (\gamma-1)\rho h \qquad (1.13)$$

$$\gamma \equiv c_p/c_v \qquad (1.14)$$

$$= 1.4 \qquad \text{(for air)}$$

$$c_p = \frac{\gamma}{\gamma-1} R = 1004.6 \text{ J/kg-K} \qquad \text{(for air)}$$

In extreme conditions, such as those inside gas turbine hot sections, c_v and c_p can no longer be assumed to be independent of temperature, so the more general $e(T)$ and $h(T)$ definitions (1.10) must be used. Also, γ then depends on temperature and thus has limited applicability. However, R is still nearly constant and the temperature form of the ideal gas law (1.7) still applies.

1.3   Conservation Laws

This section will apply the laws of conservation of mass, momentum, and energy to the fluid instantaneously inside any closed *control volume* which is fixed in space, shown in Figure 1.2.
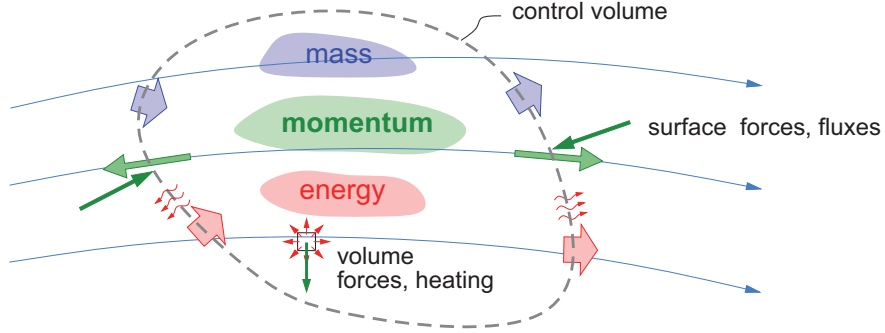
Figure 1.2: Control volume in a flow-field. The time rates of the mass, momentum, and energy inside the control volume are related to the volume and surface forces and fluxes.

All flow-field quantities in general are functions of the spatial position vector $\mathbf{r}$ and of time t. Although the subsequent development uses general vector forms and operations, special cases will typically assume Cartesian axes, in which case the position and velocity vectors have the following Cartesian components.

$$\mathbf{r} = x\,\hat{\mathbf{x}} + y\,\hat{\mathbf{y}} + z\,\hat{\mathbf{z}} \qquad (1.15)$$

$$\mathbf{V} = u\,\hat{\mathbf{x}} + v\,\hat{\mathbf{y}} + w\,\hat{\mathbf{z}} \qquad (1.16)$$

1.3.1 Mass, momentum, energy fluxes

The *mass flux* is the local mass flow rate per unit area moving through the control volume's surface, shown in Figure 1.3. It is equal to the density times the surface-normal component of the velocity.

$$\text{(mass flux)} \;=\; \rho \mathbf{V} \cdot \hat{\mathbf{n}}$$

The mass flux also results in a *momentum flux*, defined as
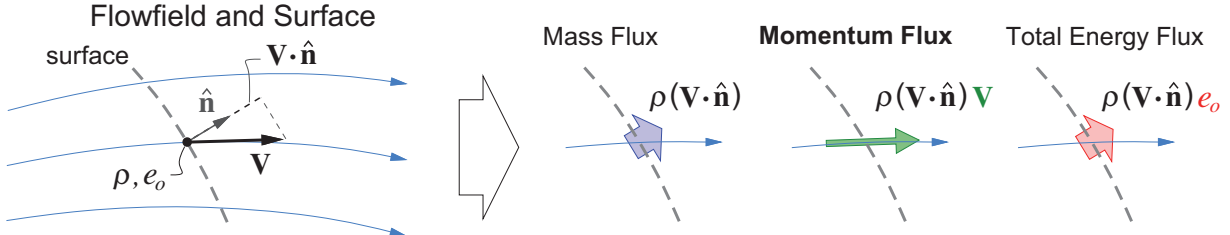
Figure 1.3: Flow-field quantities $\rho, \mathbf{V}, e_o$ together with a surface's normal vector $\hat{\mathbf{n}}$ define mass, momentum, and total internal energy fluxes across each surface point. These are associated with bulk fluid motion.

$$\begin{aligned}
\textbf{momentum flux} &= \text{(mass flux)} \times \textbf{momentum}/\text{mass} \\
&= \rho (\mathbf{V} \cdot \hat{\mathbf{n}}) \, \mathbf{V}
\end{aligned}$$

and which is a vector quantity. In an analogous manner, we can define the *total internal energy flux*,

$$\begin{aligned}
\text{total internal energy flux} &= \text{(mass flux)} \times \text{(total internal energy)}/\text{mass} \\
&= \rho (\mathbf{V} \cdot \hat{\mathbf{n}}) \, e_o
\end{aligned}$$

where e_o is the *specific total energy*, defined as the specific static energy plus the specific kinetic energy.

$$\begin{aligned}
e_o &\equiv e + \tfrac{1}{2} V^2 \\
V^2 &= \mathbf{V} \cdot \mathbf{V} = u^2 + v^2 + w^2
\end{aligned} \tag{1.17}$$

The specific total enthalpy h_o and its flux are defined the same way.

$$\begin{aligned}
h_o &\equiv h + \tfrac{1}{2} V^2 \\
\text{total enthalpy flux} &= \rho (\mathbf{V} \cdot \hat{\mathbf{n}}) \, h_o
\end{aligned} \tag{1.18}$$

1.3.2 Volume forces, work rate, heating

The fluid can be subjected to a force field $\mathbf{f}(\mathbf{r},t)$, the most common example being gravitational acceleration g. In a non-inertial frame this would also include d'Alembert, centrifugal, and Coriolis forces,

$$\mathbf{f}(\mathbf{r},t) \;=\; g \;-\; \dot{\mathbf{U}} \;-\; \dot{\boldsymbol{\Omega}} \times \mathbf{r} \;-\; \boldsymbol{\Omega} \times (\boldsymbol{\Omega} \times \mathbf{r}) \;-\; 2 \boldsymbol{\Omega} \times \mathbf{V} \tag{1.19}$$

where $\mathbf{U}(t)$ is the inertial velocity of the frame's reference point, $\boldsymbol{\Omega}(t)$ is the frame's rotation, $\mathbf{r}$ is the position vector relative to the reference point, and $\mathbf{V}(\mathbf{r},t)$ is the velocity within the non-inertial frame. These quantities are diagrammed in Figure 7.1, in which $\mathbf{V}$ is denoted by $\mathbf{V}_{\text{rel}}$. Flow-Field description in non-inertial frames will not be performed here, so that a constant $\mathbf{f} = g$ will be assumed in the most general case.

For application of $\mathbf{f}$ to the equations of fluid motion, the actual relevant quantity is $\rho\,\mathbf{f}$, which has units of force per unit volume. When acting on fluid moving with local velocity $\mathbf{V}$, this volume force will impart a work rate $\dot{w}_\mathcal{V}(\mathbf{r},t)$ equal to

$$\dot{w}_\mathcal{V} \;=\; \rho\,\mathbf{f}\cdot\mathbf{V} \tag{1.20}$$

which has units of power per unit volume. Possibly adding to this mechanical power is a thermal heating rate, quantified by some imposed body heating source density

$$\dot{q}_\mathcal{V} \;=\; \dot{q}_\mathcal{V}(\mathbf{r},t)$$

which also has units of power per unit volume. This might be from absorbed radiation or combustion. Outside a turbomachine combustor, and for the vast majority of external aerodynamic flows, $\dot{q}_\mathcal{V}$ is zero.

1.3.3 Surface forces, work rate, heating

The fluid is subjected to *stress*, or force per unit area, acting on every area element of the surface of the control volume. This is broken down into the pressure stress $-p\hat{\mathbf{n}}$ along and opposite to the surface-normal $\hat{\mathbf{n}}$, and the viscous stress vector $\boldsymbol{\tau}$ which can have any orientation, as shown in Figure 1.4.
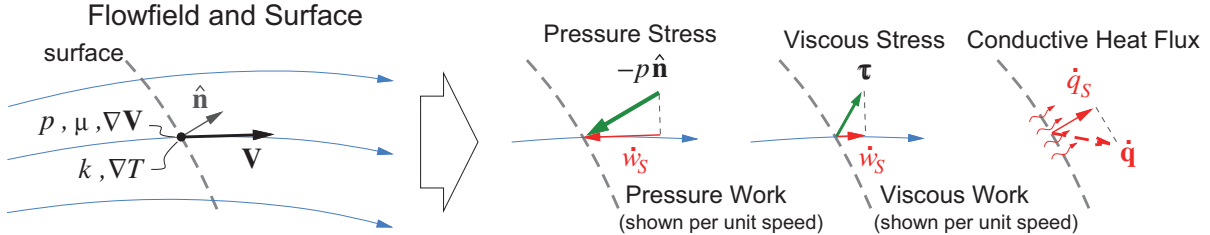
Figure 1.4: Flow-field quantities p, μ, $\nabla\mathbf{V}$ together with a surface normal vector $\hat{\mathbf{n}}$ define pressure and viscous stress forces acting on each surface point, with corresponding work contributions $\dot{w}_S$. Flow-Field quantities k, ∇T define the conductive heat flux vector $\dot{\mathbf{q}}$ at each surface point, with corresponding normal flux component $\dot{q}_S$. These are all associated with molecular motion.

The pressure stress is isotropic (same magnitude for any $\hat{\mathbf{n}}$ direction), and is the only stress which can be present in a fluid which either has a spatially-uniform velocity, or is in solid-body rotation, as shown in Figure 1.5. In contrast, the viscous stress is the result of the fluid's *deformation rate*, or equivalently the *strain rate*, also shown in Figure 1.5. More precisely, the viscous stress vector $\boldsymbol{\tau}$ acting on a surface with unit normal $\hat{\mathbf{n}}$ is given by

$$\boldsymbol{\tau} \;=\; \bar{\bar{\tau}} \cdot \hat{\mathbf{n}} \tag{1.21}$$

where $\bar{\bar{\tau}}$ is the *viscous stress tensor*, which is symmetric and therefore has six independent components.
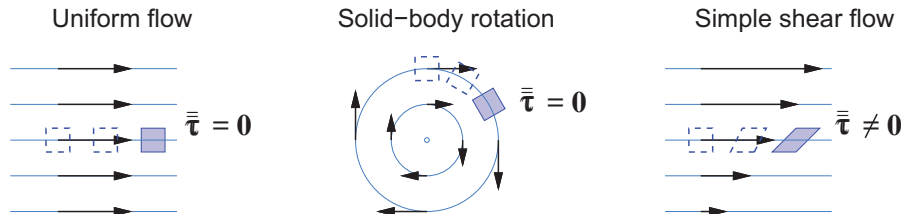
Figure 1.5: Viscous stresses occur in a fluid element which is subjected to a strain rate, as in the simple shear flow case.

Common gases and liquids like air and water are *Newtonian fluids*, for which the $\bar{\bar{\tau}}$ components are proportional (via the viscosity factor) to the corresponding strain rate tensor components, which in turn are

constructed from the nine independent components of the velocity gradient matrix $\nabla \mathbf{V}$ (see Batchelor [2]).

$$
\bar{\bar{\tau}} = \begin{bmatrix} \tau_{xx} & \tau_{xy} & \tau_{xz} \\ \cdot & \tau_{yy} & \tau_{yz} \\ \cdot & \cdot & \tau_{zz} \end{bmatrix} = \mu \left[\nabla \mathbf{V} + (\nabla \mathbf{V})^T - 2\frac{\sigma}{3}\bar{\bar{\mathbf{I}}} \right] = \mu \begin{bmatrix} 2\dfrac{\partial u}{\partial x} - 2\dfrac{\sigma}{3} & \dfrac{\partial u}{\partial y} + \dfrac{\partial v}{\partial x} & \dfrac{\partial u}{\partial z} + \dfrac{\partial w}{\partial x} \\ & 2\dfrac{\partial v}{\partial y} - 2\dfrac{\sigma}{3} & \dfrac{\partial v}{\partial z} + \dfrac{\partial w}{\partial y} \\ \cdot & \cdot & 2\dfrac{\partial w}{\partial z} - 2\dfrac{\sigma}{3} \end{bmatrix} \tag{1.22}
$$

$$
\text{where} \quad \sigma \equiv \nabla \cdot \mathbf{V} = \frac{\partial u}{\partial x} + \frac{\partial v}{\partial y} + \frac{\partial w}{\partial z} \tag{1.23}
$$

The contribution of the velocity divergence σ (also called the *dilatation rate*) is subtracted to make the stress tensor have zero trace, $\tau_{xx} + \tau_{yy} + \tau_{zz} = 0$. This zero-trace assumption is known as *Stokes's Hypothesis* [3].

The pressure and viscous forces will also exert a work rate $\dot{w}_S$ on the moving fluid

$$
\dot{w}_S = (-p\hat{\mathbf{n}} + \bar{\bar{\tau}} \cdot \hat{\mathbf{n}}) \cdot \mathbf{V} = -p\mathbf{V} \cdot \hat{\mathbf{n}} + \mathbf{V} \cdot \bar{\bar{\tau}} \cdot \hat{\mathbf{n}} \tag{1.24}
$$

which has units of power per unit area. Unlike the power per unit volume rate $\dot{w}_V$ given by (1.20), this $\dot{w}_S$ is not an unambiguous field quantity since it is associated with some arbitrary surface whose orientation is specified by its normal vector $\hat{\mathbf{n}}$.

Fourier's Law of heat conduction assumes that the conductive heat flux vector $\dot{\mathbf{q}}$ is proportional to the heat conductivity k and the temperature gradient. This is analogous to the Newtonian viscous stress model, and is valid for most common solids and fluids, including air. For perfect gases the $\dot{\mathbf{q}}$ vector can also be given via the static enthalpy gradient and viscosity via the Prandtl number. Its component $\dot{q}_S$ along the normal of some arbitrary surface is the heat rate per unit area flowing through the surface.

$$
\dot{\mathbf{q}} = -k\,\nabla T = -\frac{\mu}{Pr}\nabla h \tag{1.25}
$$

$$
\dot{q}_S = \dot{\mathbf{q}} \cdot \hat{\mathbf{n}} = -k\,\nabla T \cdot \hat{\mathbf{n}} = -\frac{\mu}{Pr}\nabla h \cdot \hat{\mathbf{n}} \tag{1.26}
$$

1.3.4 Integral conservation laws

A general control volume placed in a flow-field is shown in Figure 1.6, with $d\mathcal{V}$ being an interior volume element, and $d\mathcal{S}$ being a boundary surface area element with outward unit normal $\hat{\mathbf{n}}$.
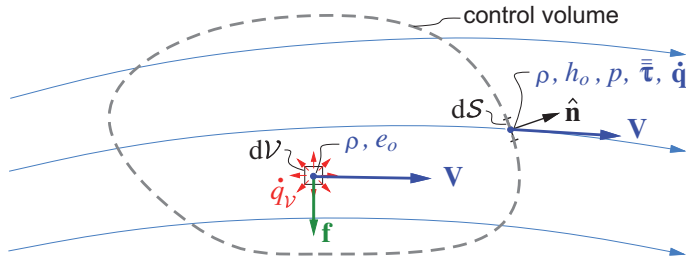
Figure 1.6: Flow variables and geometric quantities involved in control volume analysis.

Integral mass equation

The law of conservation of mass asserts that the time rate of change of the total mass in the volume, plus the net mass outflow rate through the surface of the volume, must sum to zero.

$$
\boxed{\iiint \frac{\partial \rho}{\partial t}\, d\mathcal{V} + \oiint \rho \mathbf{V} \cdot \hat{\mathbf{n}}\, d\mathcal{S} = 0} \tag{1.27}
$$

The second mass outflow term is seen to be the integral of the mass flux over the volume's surface area.

Integral momentum equation

Similarly, the law of conservation of momentum, or equivalently Newton's Third Law, asserts that the time rate of change of the total momentum in the volume, plus the net momentum outflow rate through the surface of the volume, must sum to the total force acting on the interior and the surface of the volume.

$$\iiint \frac{\partial \rho \mathbf{V}}{\partial t} \, \mathrm{d}\mathcal{V} \;+\; \oiint \rho (\mathbf{V} \cdot \hat{\mathbf{n}}) \, \mathbf{V} \, \mathrm{d}\mathcal{S} \;=\; \iiint \rho \mathbf{f} \, \mathrm{d}\mathcal{V} \;+\; \oiint -p\hat{\mathbf{n}} \, \mathrm{d}\mathcal{S} \;+\; \oiint \bar{\bar{\tau}} \cdot \hat{\mathbf{n}} \, \mathrm{d}\mathcal{S} \tag{1.28}$$

Integral energy and enthalpy equations

The law of conservation of energy, or equivalently the First Law of Thermodynamics, asserts that the time rate of change of total energy, plus its net outflow rate, equals the sum of heat and work sources $\dot{q}_\mathcal{V} + \dot{w}_\mathcal{V}$ in the interior, plus heat inflow and work $-\dot{q}_\mathcal{S} + \dot{w}_\mathcal{S}$ at the boundary. The work terms are written out explicitly.

$$\iiint \frac{\partial \rho e_o}{\partial t} \, \mathrm{d}\mathcal{V} + \oiint \rho \mathbf{V} \cdot \hat{\mathbf{n}} \, e_o \, \mathrm{d}\mathcal{S} \;=\; \iiint \dot{q}_\mathcal{V} \, \mathrm{d}\mathcal{V} + \iiint \rho \mathbf{f} \cdot \mathbf{V} \, \mathrm{d}\mathcal{V}$$

$$- \oiint p \mathbf{V} \cdot \hat{\mathbf{n}} \, \mathrm{d}\mathcal{S} + \oiint \mathbf{V} \cdot \bar{\bar{\tau}} \cdot \hat{\mathbf{n}} \, \mathrm{d}\mathcal{S} - \oiint \dot{\mathbf{q}} \cdot \hat{\mathbf{n}} \, \mathrm{d}\mathcal{S} \tag{1.29}$$

We then combine the lefthand energy-flux and righthand pressure-work terms together into an enthalpy flux term on the left, and replace ρe_o with $\rho h_o - p$ in the unsteady term, giving the alternative integral enthalpy equation.

$$\iiint \frac{\partial (\rho h_o - p)}{\partial t} \, \mathrm{d}\mathcal{V} + \oiint \rho \mathbf{V} \cdot \hat{\mathbf{n}} \, h_o \, \mathrm{d}\mathcal{S} \;=\; \iiint \dot{q}_\mathcal{V} \, \mathrm{d}\mathcal{V} + \iiint \rho \mathbf{f} \cdot \mathbf{V} \, \mathrm{d}\mathcal{V}$$

$$+ \oiint \mathbf{V} \cdot \bar{\bar{\tau}} \cdot \hat{\mathbf{n}} \, \mathrm{d}\mathcal{S} - \oiint \dot{\mathbf{q}} \cdot \hat{\mathbf{n}} \, \mathrm{d}\mathcal{S} \tag{1.30}$$

1.4 Differential Conservation Equations

1.4.1 Divergence forms

Using Gauss's Theorem for a general vector field quantity $\mathbf{v}(\mathbf{r})$,

$$\oiint \mathbf{v} \cdot \hat{\mathbf{n}} \, \mathrm{d}\mathcal{S} \;=\; \iiint \nabla \cdot \mathbf{v} \, \mathrm{d}\mathcal{V} \tag{1.31}$$

and setting $\mathbf{v} = \rho \mathbf{V}$, the integral mass equation (1.27) can be restated in terms of only a volume integral.

$$\iiint \left[\frac{\partial \rho}{\partial t} + \nabla \cdot (\rho \mathbf{V}) \right] \mathrm{d}\mathcal{V} \;=\; 0 \tag{1.32}$$

Since this must hold for <u>any</u> control volume, the integrand must necessarily be zero for every point in the flow. The result is the divergence form of the differential mass equation.

$$\frac{\partial \rho}{\partial t} + \nabla \cdot (\rho \mathbf{V}) \;=\; 0 \tag{1.33}$$

The same process applied to the integral momentum and enthalpy equations gives their corresponding divergence differential forms.

$$\frac{\partial(\rho\mathbf{V})}{\partial t} + \nabla\cdot(\rho\mathbf{V}\,\mathbf{V}^T) = \rho\mathbf{f} - \nabla p + \nabla\cdot\bar{\bar{\tau}} \tag{1.34}$$

$$\frac{\partial(\rho h_o - p)}{\partial t} + \nabla\cdot(\rho\mathbf{V}\,h_o) = \dot{q}_v + \rho\mathbf{f}\cdot\mathbf{V} + \nabla\cdot(\bar{\bar{\tau}}\cdot\mathbf{V}) - \nabla\cdot\dot{\mathbf{q}} \tag{1.35}$$

1.4.2 Convective forms

Combining {**momentum** equation (1.34)} − **V**{mass equation (1.33)} and simplifying produces the *convective form* of the momentum equation,

$$\boxed{\rho\frac{\mathrm{D}\mathbf{V}}{\mathrm{D}t} \equiv \rho\frac{\partial\mathbf{V}}{\partial t} + \rho\mathbf{V}\cdot\nabla\mathbf{V} = \rho\mathbf{f} - \nabla p + \nabla\cdot\bar{\bar{\tau}}} \tag{1.36}$$

$$\text{where} \qquad \frac{\mathrm{D}(\,)}{\mathrm{D}t} \equiv \frac{\partial(\,)}{\partial t} + \mathbf{V}\cdot\nabla(\,) \tag{1.37}$$

is the *substantial derivative*, which is the rate of change of any field quantity $(\,)$ as observed by a fluid element moving with velocity $\mathbf{V}$, as shown in Figure 1.7.
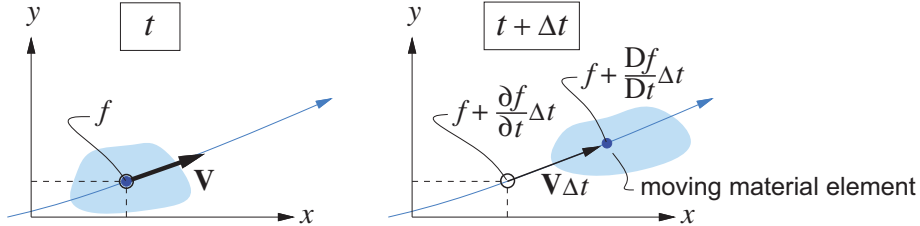
Figure 1.7: The substantial derivative $\mathrm{D}f/\mathrm{D}t$ gives rate of change of field quantity $f_{(\mathbf{r},t)}$ as felt by material element moving at $\mathbf{V}$. The local derivative $\partial f/\partial t$ is rate of change at a fixed point $\mathbf{r}$.

Combining {enthalpy equation (1.35)} − h_o{mass equation (1.33)} and simplifying produces the convective form of the enthalpy equation.

$$\boxed{\rho\frac{\mathrm{D}h_o}{\mathrm{D}t} \equiv \rho\frac{\partial h_o}{\partial t} + \rho\mathbf{V}\cdot\nabla h_o = \frac{\partial p}{\partial t} + \dot{q}_v + \rho\mathbf{f}\cdot\mathbf{V} + \nabla\cdot(\bar{\bar{\tau}}\cdot\mathbf{V}) - \nabla\cdot\dot{\mathbf{q}}} \tag{1.38}$$

The mass, momentum, and enthalpy equations above, either in the divergence or convective forms, are collectively called the *Navier-Stokes equations*, although historically this term was originally first given to only the momentum equation (1.36) in its incompressible form, which will be considered in Section 1.8.

1.4.3 Surface boundary conditions

The appropriate boundary conditions for a viscous flow at a solid surface are the *no-slip condition* on $\mathbf{V}$, and either a temperature condition or a heat-flux condition on h.

$$\mathbf{V} = \mathbf{0} \qquad \text{(on solid fixed surface)} \tag{1.39}$$

$$\text{either} \quad h = c_p\,T_{\text{body}} \quad \text{(on surface with known temperature)} \tag{1.40}$$

$$\text{or} \quad \dot{\mathbf{q}}\cdot\hat{\mathbf{n}} = 0 \quad \text{(on surface at thermal equilibrium with fluid)} \tag{1.41}$$

For the idealization of an inviscid flow, the appropriate solid surface boundary condition is the following *flow-tangency condition* on $\mathbf{V}$. No solid-surface boundary condition required for the temperature.

$$\mathbf{V}\cdot\hat{\mathbf{n}} = 0 \qquad \text{(on solid fixed surface)} \tag{1.42}$$

1.5 Units and Parameters

1.5.1 Unit systems

The quantitative description of any physical system, such as a fluid flow, requires using some set of *units*. Two alternative sets of units, compared in Figure 1.8, can be used to describe any one given situation.

- **Standard Units**. Examples are $\mathrm{m, s, kg}$ (SI), or $\mathrm{ft, s, slug}$ (English). These are universally known, and hence are most convenient for describing a specific physical object, and also for recording raw experimental data.
- **Natural Units (or Scales)**. Generic names are $\ell_{\mathrm{ref}}, V_{\mathrm{ref}}, \rho_{\mathrm{ref}}$, etc. Specific examples are c (chord), V_∞ (freestream speed), ρ_∞ (freestream density). These are most convenient for theoretical work, and for presenting reduced experimental data. Table 1.1 lists the scales which appear in aerodynamic flows.
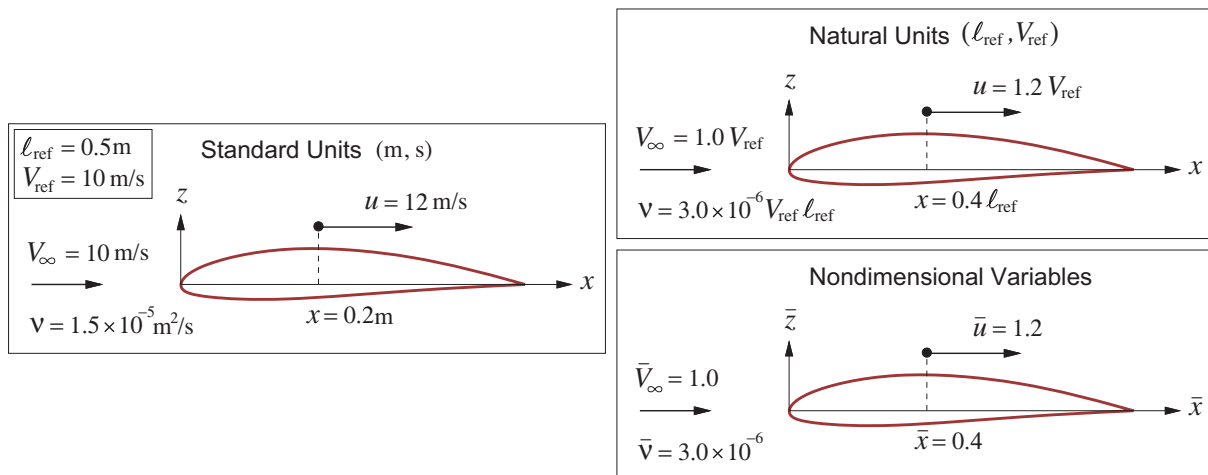
Figure 1.8: Aerodynamic flow-field described in standard units, and alternatively in natural units. The natural units for this case are chosen to be the chord $\ell_{\mathrm{ref}} = c = 0.5\,\mathrm{m}$, and the freestream velocity $V_{\mathrm{ref}} = V_\infty = 10\,\mathrm{m/s}$. Using non-dimensional variables is equivalent to using natural units.

Table 1.1: Physical parameters, or scales, of aerodynamic flows. Scales in bottom block are relevant only for compressible flows. Units are: length l, time t, mass m, temperature θ.

	Scale	Units		Typical specific choice
ℓ_{ref}	length	l	c	airfoil chord
V_{ref}	velocity	l/t	V_∞	freestream speed
ρ_{ref}	density	m/l^3	ρ_∞	freestream density
μ_{ref}	viscosity	m/lt	μ_∞	freestream viscosity
a_{ref}	speed of sound	l/t	a_∞	freestream speed of sound
k_{ref}	heat conductivity	$ml/t^3\theta$	k_∞	freestream value
c_p	heat capacity	$l^2/t^2\theta$	c_p	freestream value ($\sim$ constant)
γ	ratio of specific heats	$-$	γ	freestream value ($\sim$ constant)

The absolute reference pressure and temperature $p_{\mathrm{ref}}, T_{\mathrm{ref}}$ have been omitted from Table 1.1 because for ideal gases these are effectively redundant. Specifically, they can be defined from the other scales via the ideal-gas, speed of sound, and caloric relations.

$$p_{\mathrm{ref}} \equiv \rho_{\mathrm{ref}}\, a_{\mathrm{ref}}^2 \tag{1.43}$$

$$T_{\mathrm{ref}} \equiv a_{\mathrm{ref}}^2 / c_p \tag{1.44}$$

Such derived-scale definitions only need to have the same dimensions. They do not need to be equalities, as in $p = \rho a^2/\gamma$ and $T = a^2/(\gamma - 1)c_p$. This allows the apparently missing γ and $\gamma - 1$ factors to be omitted from the p_{ref} and T_{ref} definitions above.

1.5.2 Non-dimensionalization

Non-dimensionalization can be viewed as the process of converting from standard to natural units. We can define all coordinates and field variables in terms of dimensionless variables $\bar{(\,)}$ and the various natural units or scales listed in Table 1.1.

$$
\begin{aligned}
t &= \bar{t}\,\ell_{\text{ref}}/V_{\text{ref}} & \rho &= \bar{\rho}\,\rho_{\text{ref}} \\
\mathbf{r} &= \bar{\mathbf{r}}\,\ell_{\text{ref}} & p &= \bar{p}\,\rho_{\text{ref}}V_{\text{ref}}^2 \\
\mathbf{V} &= \bar{\mathbf{V}}\,V_{\text{ref}} & \mu &= \bar{\mu}\,\mu_{\text{ref}} \\
h_o &= \bar{h}_o\,a_{\text{ref}}^2 & k &= \bar{k}\,k_{\text{ref}}
\end{aligned}
$$

Substituting these into the compressible mass, momentum, total enthalpy, and ideal-gas state equations (1.33), (1.36), (1.38), (1.13), gives the corresponding dimensionless equations. The body force $\mathbf{f}$ and volume heating $\dot{q}_\mathcal{V}$ are omitted here, since they are not relevant in typical aerodynamic flows.

$$
\frac{\partial \bar{\rho}}{\partial \bar{t}} + \bar{\nabla} \cdot \left(\bar{\rho} \bar{\mathbf{V}} \right) = 0 \tag{1.45}
$$

$$
\bar{\rho}\frac{\partial \bar{\mathbf{V}}}{\partial \bar{t}} + \bar{\rho}\,\bar{\mathbf{V}} \cdot \bar{\nabla}\bar{\mathbf{V}} = -\bar{\nabla}\bar{p} + \frac{1}{Re_{\text{ref}}} \bar{\nabla} \cdot \bar{\bar{\tau}} \tag{1.46}
$$

$$
\bar{\rho}\frac{\partial \bar{h}_o}{\partial \bar{t}} + \bar{\rho}\,\bar{\mathbf{V}} \cdot \bar{\nabla}\bar{h}_o = M_{\text{ref}}^2 \frac{\partial \bar{p}}{\partial \bar{t}} + \frac{M_{\text{ref}}^2}{Re_{\text{ref}}} \bar{\nabla} \cdot \left(\bar{\bar{\tau}} \cdot \bar{\mathbf{V}} \right) - \frac{1}{Re_{\text{ref}}Pr_{\text{ref}}} \bar{\nabla} \cdot \bar{\mathbf{q}} \tag{1.47}
$$

$$
\bar{p} = \frac{\gamma - 1}{\gamma} \bar{\rho} \left(\frac{\bar{h}_o}{M_{\text{ref}}^2} - \frac{1}{2}\left| \bar{\mathbf{V}} \right|^2 \right) \tag{1.48}
$$

Here $\bar{\nabla}(\,) = \ell_{\text{ref}}\nabla(\,)$ is the gradient in terms of $\bar{\mathbf{r}}$ derivatives, and $\bar{\bar{\tau}}, \bar{\mathbf{q}}$ are the non-dimensional viscous stress tensor and heat flux vector, defined using $\bar{\mu}, \bar{k}, \bar{\nabla}\bar{\mathbf{V}}, \bar{\nabla}\bar{h}_o$.

Equations (1.45)–(1.48) have the same form as their dimensional counterparts, except for the appearance of four non-dimensional parameters formed with the reference scales, as summarized in Table 1.2. For incompressible flows, discussed in more detail in Section 1.8, the enthalpy and state equations (1.47), (1.48) are replaced by the simple relation $\bar{\rho} = \text{constant}$. In this case, only (1.45), (1.46) are needed to fully determine the $\bar{\mathbf{V}}, \bar{p}$ fields and the resulting aerodynamic forces. Hence the Reynolds number is the only relevant aerodynamic parameter for steady incompressible flows.

Table 1.2: Non-dimensional parameters of a viscous flow. Parameters in bottom block are relevant only for compressible flows.

Parameter			Common name
Re_{ref}	$\equiv$	$\rho_{\text{ref}}V_{\text{ref}}\ell_{\text{ref}}/\mu_{\text{ref}}$	Reynolds number
M_{ref}	$\equiv$	$V_{\text{ref}}/a_{\text{ref}}$	Mach number
Pr_{ref}	$\equiv$	$c_p\,\mu_{\text{ref}}/k_{\text{ref}}$	Prandtl number
γ			ratio of specific heats

1.5.3 Unsteady-flow parameters

Nonuniform body motion, which will in general result in an unsteady flow, will have some time scale or frequency associated with the motion. The unsteadiness is typically imposed on the flow via the boundary

conditions, in particular the viscous no-slip condition (1.39) which takes on the following more general form for a body which is moving with local velocity $\mathbf{U}_{body}$ in some time-varying manner.

$$\mathbf{V} = \mathbf{U}_{body}(t) \qquad \text{(on solid moving surface)} \qquad (1.49)$$

Consider for example a sinusoidal body motion

$$\mathbf{U}_{body}(t) = \mathbf{U}_1 \sin(\omega t) \qquad (1.50)$$

where ω is the motion frequency and $\mathbf{U}_1$ is some constant. The dimensionless form of (1.49) is

$$\bar{\mathbf{V}} = \bar{\mathbf{U}}_1 \sin(St_{ref}\, \bar{t}) \qquad (1.51)$$

$$St_{ref} \equiv \frac{\omega \ell_{ref}}{V_{ref}} \qquad (1.52)$$

where St_{ref} is the *Strouhal Number*, also called the *reduced frequency*. This is an additional non-dimensional parameter which would need to be added to Table 1.2 for this unsteady flow case. Unsteady flows will be covered partly in Chapter 6, and in more detail in Chapter 7. The other chapters will focus on steady flows where $\mathbf{U}_{body} = \mathbf{0}$.

1.5.4 High Reynolds number flows

Typical aerodynamic flows of interest have very large Reynolds numbers, or $Re_{ref} \gg 1$, when based on a typical body dimension and freestream velocity and viscosity. Because the viscous-stress and heat conduction terms involving $\bar{\bar{\tau}}$ and $\dot{\mathbf{q}}$ in equations (1.46),(1.47) are scaled by $1/Re_{ref}$, these terms must therefore be negligible over most of the flow-field. The exception occurs very close to a body surface where $\mathbf{V} \to \mathbf{0}$ because of the no-slip condition. Here, in the momentum equation (1.46) only $\bar{\nabla}\bar{p}$ remains to balance the viscous term, so the latter must remain significant sufficiently close to a wall. The result is that the action of viscosity and heat conductivity is confined to *boundary layers* and *wakes*, collectively termed the "shear layers" or "viscous regions."

The viscous regions will be examined in much more detail in Chapters 3 and 4. For now, it will suffice to say that at the high Reynolds numbers of typical aerodynamic flows, the viscous regions, distinguished by significant $\bar{\bar{\tau}}$ and $\dot{\mathbf{q}}$, are very thin compared with the body size, as sketched in Figure 1.9. This allows the assumption that the outer flow is inviscid, which is the basis of most aerodynamic models.

Small insect
$Re_{ref} \simeq 10^3$
$\bar{\bar{\tau}} \neq 0$
$\dot{\mathbf{q}} \neq 0$

Model airplane
$Re_{ref} \simeq 10^5$
$\bar{\bar{\tau}} \neq 0$
$\dot{\mathbf{q}} \neq 0$

Full−size airplane
$Re_{ref} \simeq 10^7$
$\bar{\bar{\tau}} \neq 0$
$\dot{\mathbf{q}} \neq 0$
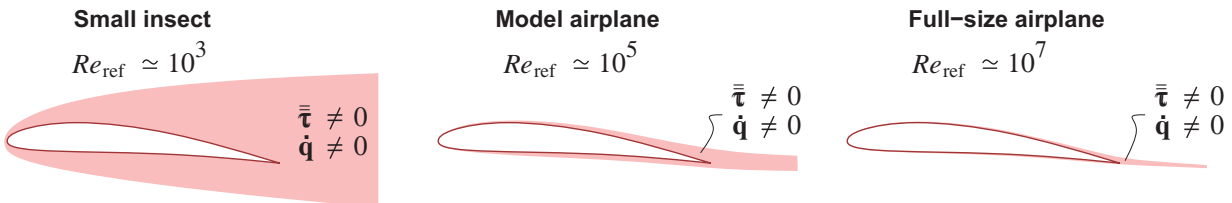
Figure 1.9: Typical aerodynamic flows with large Reynolds numbers have thin boundary layers and wakes (viscous regions) compared to the body dimension. The outer flow is effectively inviscid.

1.5.5 Standard coefficients

For the description of aerodynamic flows, a convenient non-dimensional form of the pressure is the *pressure coefficient C_p*. This is equivalent to the dimensionless pressure variable $\bar{p}$ used in Section 1.5.2, except

that C_p is shifted by some reference pressure p_{ref}, and its normalizing dynamic pressure q_{ref} contains the traditional factor of $\frac{1}{2}$.

$$C_p \equiv \frac{p - p_{\text{ref}}}{q_{\text{ref}}} \quad , \qquad q_{\text{ref}} \equiv \tfrac{1}{2}\rho_{\text{ref}}V_{\text{ref}}^2 \tag{1.53}$$

In external aerodynamics applications, the reference quantities are normally chosen to correspond to freestream flow, $\rho_{\text{ref}} = \rho_\infty$, $V_{\text{ref}} = V_\infty$, $p_{\text{ref}} = p_\infty$,

$$C_p = \frac{p - p_\infty}{q_\infty} \quad , \qquad q_\infty \equiv \tfrac{1}{2}\rho_\infty V_\infty^2 \tag{1.54}$$

so that in the freestream we have $C_p = 0$. Since C_p measures the deviation of the pressure from p_{ref}, it is unaffected by any constant offset in all the pressures.

The *skin friction coefficient*, which is a non-dimensional wall shear stress, is normalized the same way.

$$C_f \equiv \frac{\tau_{\text{w}}}{q_\infty} \tag{1.55}$$

An alternative normalization which uses the local dynamic pressure at a specific surface location gives the local skin friction coefficient c_f, which is more natural in boundary layer theory and will be treated in Chapter 4.

Dimensionless coefficients which quantify aerodynamic forces and moments are also extensively used in aerodynamics. These will be introduced in Chapter 5.

1.6   Adiabatic Flows

For a typical aerodynamic flow we have

- $\partial(\ )/\partial t = 0$, (steady flow)
- $\dot{q}_V = 0$, (no volume heating)
- $\mathbf{f} \cdot \mathbf{V} \simeq 0$, (volume work negligible)
- $\bar{\bar{\tau}} \simeq \mathbf{0}$, (negligible viscous stress outside of viscous layers)
- $\dot{\mathbf{q}} \simeq \mathbf{0}$, (negligible heat conduction outside of viscous layers)

in which case the convective enthalpy equation (1.38) reduces to

$$\frac{\mathrm{D}h_o}{\mathrm{D}t} = 0 \tag{1.56}$$
$$\rightarrow \quad h_o = \text{constant} = h_{o\infty} \tag{1.57}$$

so that wherever the above conditions are met, then h_o is constant and equal to its upstream value.

The requirements $\bar{\bar{\tau}} \simeq \mathbf{0}$ and $\dot{\mathbf{q}} \simeq \mathbf{0}$ seem to preclude viscous regions from having a constant h_o. This is true, but somewhat overly restrictive. Consider applying only the first three adiabatic-flow assumptions above to the integral enthalpy equation (1.30), and retaining the surface viscous and heat conduction terms.

$$\oiint \rho(h_o - h_{o\infty})\mathbf{V} \cdot \hat{\mathbf{n}} \, \mathrm{d}\mathcal{S} = \oiint \mathbf{V} \cdot \bar{\bar{\tau}} \cdot \hat{\mathbf{n}} \, \mathrm{d}\mathcal{S} - \oiint \dot{\mathbf{q}} \cdot \hat{\mathbf{n}} \, \mathrm{d}\mathcal{S} \tag{1.58}$$

In addition, h_o was replaced by $h_o - h_{o\infty}$ as permitted by the steady mass equation $\oiint \rho\mathbf{V} \cdot \hat{\mathbf{n}} \, \mathrm{d}\mathcal{S} = 0$. The first viscous shear integral on the right vanishes if either $\mathbf{V} = \mathbf{0}$ as on a solid wall, or $\bar{\bar{\tau}} = \mathbf{0}$ as on the outer

boundary. The second conduction integral vanishes if $\dot{\mathbf{q}} = \mathbf{0}$ as on an insulated (not heated or cooled) wall, and also on the outer boundaries. These conditions are met in most typical steady aerodynamic flows whose walls have come to temperature equilibrium with the fluid. For these flows we then have:

$$\oiint \rho(h_o - h_{o_\infty})\mathbf{V}\cdot\hat{\mathbf{n}} \ \mathrm{d}\mathcal{S} \ = \ 0 \qquad \text{(steady flows with insulated walls)} \qquad (1.59)$$

Hence, viscous stresses and heat conduction cannot change the net flux of total enthalpy out of the flow-field, but can only <u>redistribute</u> it within the flow, and in particular within the thin viscous layers, as shown in Figure 1.10. Therefore, steady viscous aerodynamic flows with insulated walls and no volume heat or work addition do have $h_o = h_{o_\infty}$ in a mass-flow averaged sense.
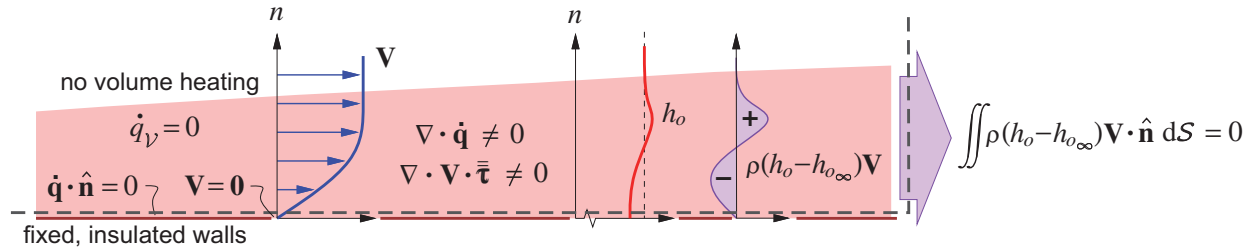
Figure 1.10: Viscous stress work $\mathbf{V}\cdot\bar{\bar{\boldsymbol{\tau}}}$ and heat conduction $\dot{\mathbf{q}}$ can redistribute the total enthalpy within a viscous layer, but they cannot change the net total enthalpy flux. This can only be changed by volume heating $\dot{q}_v$, nonzero wall heat flux $\dot{\mathbf{q}}\cdot\hat{\mathbf{n}}$, or viscous work $\mathbf{V}\cdot\bar{\bar{\boldsymbol{\tau}}}\cdot\hat{\mathbf{n}}$ by a moving wall.

A real aircraft flow-field which includes the propulsive elements will have heat addition via the $\dot{q}_v$ or $\dot{\mathbf{q}}\cdot\hat{\mathbf{n}}$ terms as in a turbine combustor, and will also have work addition via the $\partial p / \partial t$ and $\mathbf{V}\cdot\bar{\bar{\boldsymbol{\tau}}}\cdot\hat{\mathbf{n}}$ terms due to a moving propeller or fan. In that case the mass-averaged h_o leaving any control volume enclosing the aircraft will exceed h_{o_∞}, but this excess is confined to the engine exhaust and propulsive jet.

1.7 Isentropic Flows

1.7.1 Requirements for isentropy

The specific entropy change $\mathrm{d}s$ is defined by the Gibbs relation (1.60), or its equivalent enthalpy form (1.61).

$$T\,\mathrm{d}s \ \equiv \ \mathrm{d}e \ + \ p \ \mathrm{d}(1/\rho) \qquad\qquad (1.60)$$
$$T\,\mathrm{d}s \ = \ \mathrm{d}h \ - \ (1/\rho)\,\mathrm{d}p \qquad\qquad (1.61)$$

Applying these changes $\mathrm{d}(\ )$ to a particular fluid element as it moves during some time interval $\mathrm{d}t$, we have $\mathrm{d}(\ )/\mathrm{d}t = \mathrm{D}(\ )/\mathrm{D}t$. The Gibbs relation (1.61) then becomes a rate equation for the entropy.

$$T\frac{\mathrm{D}s}{\mathrm{D}t} \ = \ \frac{\mathrm{D}h}{\mathrm{D}t} \ - \ \frac{1}{\rho}\frac{\mathrm{D}p}{\mathrm{D}t}$$

$$\text{or} \qquad T\frac{\mathrm{D}s}{\mathrm{D}t} \ = \ \frac{\mathrm{D}h_o}{\mathrm{D}t} \ - \ \frac{\mathrm{D}\frac{1}{2}V^2}{\mathrm{D}t} \ - \ \frac{1}{\rho}\frac{\mathrm{D}p}{\mathrm{D}t} \qquad\qquad (1.62)$$

Combining {enthalpy eq.(1.38)} $-\ \mathbf{V}\cdot$ {**momentum** eq.(1.36)} produces

$$\frac{\mathrm{D}h_o}{\mathrm{D}t} \ - \ \frac{\mathrm{D}\frac{1}{2}V^2}{\mathrm{D}t} \ = \ \frac{1}{\rho}\frac{\mathrm{D}p}{\mathrm{D}t} \ + \ (\bar{\bar{\boldsymbol{\tau}}}\cdot\nabla)\cdot\mathbf{V} \ - \ \nabla\cdot\dot{\mathbf{q}} \ + \ \dot{q}_v \qquad\qquad (1.63)$$

which when added to (1.62) gives an alternative expression for the entropy's material rate of change.

$$T\frac{\mathrm{D}s}{\mathrm{D}t} = (\bar{\bar{\tau}} \cdot \nabla) \cdot \mathbf{V} - \nabla \cdot \dot{\mathbf{q}} + \dot{q}_\nu \tag{1.64}$$

Wherever all three terms on the righthand side are negligible, we have

$$T\frac{\mathrm{D}s}{\mathrm{D}t} = 0 \tag{1.65}$$

$$\rightarrow \quad s = \text{constant} \tag{1.66}$$

so that flow regions which are both inviscid and adiabatic must also be *isentropic*. This is the typical situation outside the viscous layers and without combustion present.

1.7.2   Isentropic relations

Setting $\mathrm{d}s = 0$ in the Gibbs relation (1.61), assuming a calorically-perfect gas with constant c_p, and using the ideal gas law (1.13), gives the following three differential equations.

$$\frac{\mathrm{d}p}{p} = \gamma\frac{\mathrm{d}\rho}{\rho} = \frac{\gamma}{\gamma-1}\frac{\mathrm{d}h}{h} \tag{1.67}$$

These can be integrated to give the three *isentropic relations*,

$$\frac{p_2}{p_1} = \left(\frac{\rho_2}{\rho_1}\right)^\gamma = \left(\frac{h_2}{h_1}\right)^{\gamma/(\gamma-1)} \tag{1.68}$$

where $(\ )_1$ and $(\ )_2$ are any two states along a particle pathline which is unaffected by viscous stress, heat conduction or addition, or shock losses. For regions whose streamlines are isentropic all the way from far-upstream, points 1 and 2 do not need to lie on the same streamline, as indicated in Figure 1.11.
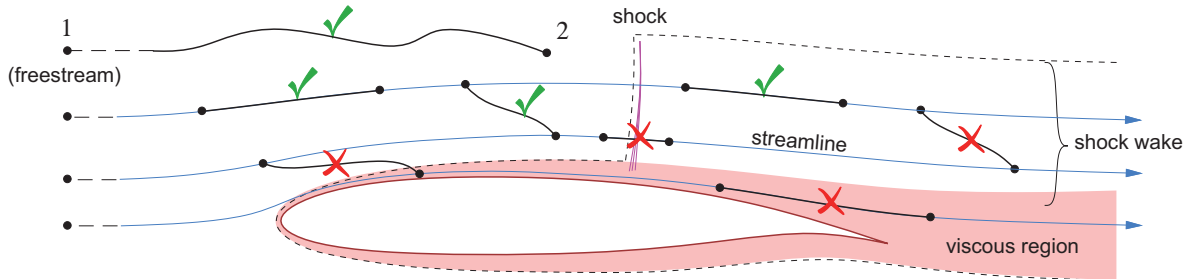
Figure 1.11: Valid and invalid paths for the isentropic relations (1.68) between any two points in an aerodynamic flow. In the the isentropic region outside of shock wake and viscous regions the path is arbitrary, since all points there can be also connected with the single freestream state.

In steady or unsteady external flows, a common choice for state 1 is the freestream state $(\ )_\infty$, and for state 2 is the state at any point $(\mathbf{r}, t)$ in the flow outside of viscous layers or shock wakes, as shown in the upper left of Figure 1.11.

$$\frac{p(\mathbf{r},t)}{p_\infty} = \left(\frac{\rho(\mathbf{r},t)}{\rho_\infty}\right)^\gamma = \left(\frac{h(\mathbf{r},t)}{h_\infty}\right)^{\gamma/(\gamma-1)} \tag{1.69}$$

This uniquely relates all the thermodynamic variable fields. These relations, when applicable, can be used as replacements for the energy equation or the streamwise component of the momentum equation.

1.7.3 Speed of sound

As derived by Batchelor [2], the speed of sound a is given by

$$a^2 = \left.\frac{\partial p}{\partial \rho}\right|_{s=\text{const}}$$

which can be immediately determined from the isentropic differential relation (1.67).

$$a = \sqrt{\frac{\gamma p}{\rho}} = \sqrt{\gamma R T} = \sqrt{(\gamma-1)h} \tag{1.70}$$

1.7.4 Total pressure and density

Consider a hypothetical isentropic stagnation process shown in Figure 1.12, where the flow at any one point is isentropically brought to the *stagnation state* which has $V=0$.
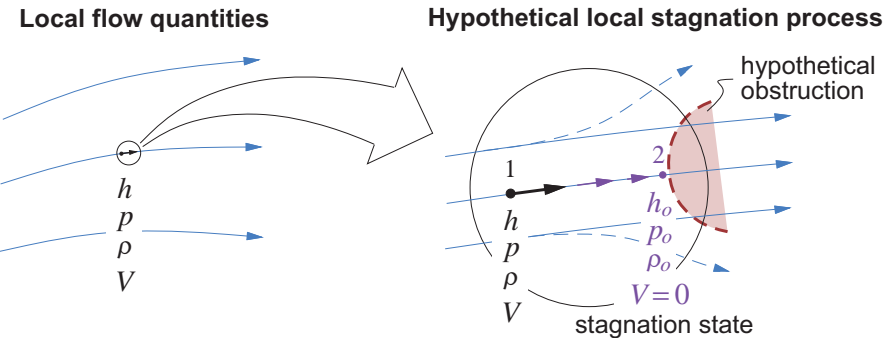
Figure 1.12: Isentropic stagnation process from local state 1, to a hypothetical stagnation state 2 denoted by $(\ )_o$ with $V = 0$. This could actually be done by placing a small obstruction in the flow.

Applying the general isentropic relations (1.68) to this process we set $p_1 = p$ and $h_1 = h$ to be the actual static values at the point, and then set $h_2 = h_o = h + \frac{1}{2}V^2$, which would be the enthalpy at the stagnation state since the total enthalpy cannot change. The corresponding p_2 is then defined as the local *total pressure*,

$$p_o \equiv p\left(\frac{h_o}{h}\right)^{\gamma/(\gamma-1)} = p\left(1 + \frac{1}{2}\frac{V^2}{h}\right)^{\gamma/(\gamma-1)} = p\left(1 + \frac{\gamma-1}{2}M^2\right)^{\gamma/(\gamma-1)} \tag{1.71}$$

where M is the *local Mach number*.

$$M^2 \equiv \frac{V^2}{a^2} = \frac{V^2}{(\gamma-1)h} = \frac{\rho V^2}{\gamma p} \tag{1.72}$$

The *total density* is defined the same way.

$$\rho_o \equiv \rho\left(\frac{h_o}{h}\right)^{1/(\gamma-1)} = \rho\left(1 + \frac{1}{2}\frac{V^2}{h}\right)^{1/(\gamma-1)} = \rho\left(1 + \frac{\gamma-1}{2}M^2\right)^{1/(\gamma-1)} \tag{1.73}$$

These p_o and ρ_o are therefore the hypothetical pressure and density at any flow-field point that <u>would</u> result if the enthalpy at that point was isentropically brought to $h = h_o$, or equivalently to the state with $V = 0$. For this reason p_o and ρ_o are also alternatively called the *stagnation pressure* and *stagnation density*.

In aerodynamic flows where the p_o variation within the flow-field is of particular interest, such as flows with propulsive elements, a convenient non-dimensional form of the total pressure is the *total pressure coefficient*.

$$C_{po} = \frac{p_o - p_{o\infty}}{q_\infty} \tag{1.74}$$

In the clean external flow outside viscous layers or propulsive jets we have $p_o = p_{o\infty}$ and hence $C_{po} = 0$.

1.8   Low Speed and Incompressible Flows

By considering the governing equations and definitions developed earlier, we can estimate the following typical changes $\Delta(\ )$ of various quantities along a streamline, or more precisely along a particle path.

From ideal gas law (1.13): $\qquad\qquad\qquad\qquad \gamma\,\Delta p \;\simeq\; (\gamma{-}1)\,(h\,\Delta\rho + \rho\,\Delta h)$ $\qquad\qquad$ (1.75)

From momentum equation (1.36): $\qquad\qquad\qquad \Delta p \;\simeq\; -\rho V\,\Delta V$ $\qquad\qquad\qquad$ (1.76)

From total enthalpy definition (1.18): $\qquad\qquad\quad \Delta h \;\simeq\; \Delta h_o - V\,\Delta V$ $\qquad\qquad\qquad$ (1.77)

Eliminating Δp between (1.75) and (1.76), eliminating Δh using (1.77), and noting that $V^2/h = (\gamma{-}1)M^2$ gives the fractional density change only in terms of fractional V and h_o changes.

$$\frac{\Delta\rho}{\rho} \;\simeq\; -M^2\frac{\Delta V}{V} - \frac{\Delta h_o}{h} \qquad\qquad (1.78)$$

A *low speed flow* is defined as one with a negligibly small Mach number everywhere.

$$M^2 \;\ll\; 1 \qquad\qquad \text{(low speed flow)} \qquad\qquad (1.79)$$

If in addition the flow is adiabatic so that $h_o \simeq$ constant and hence $\Delta h_o = 0$, then (1.78) implies

$$\frac{\Delta\rho}{\rho} \;\ll\; 1$$

$$\text{or} \qquad \rho \;\simeq\; \text{constant along particle path,} \qquad\qquad (1.80)$$

which constitutes an *incompressible flow*. Figure 1.13 compares typical density variations along a streamline near an airfoil in high speed and low speed flows.
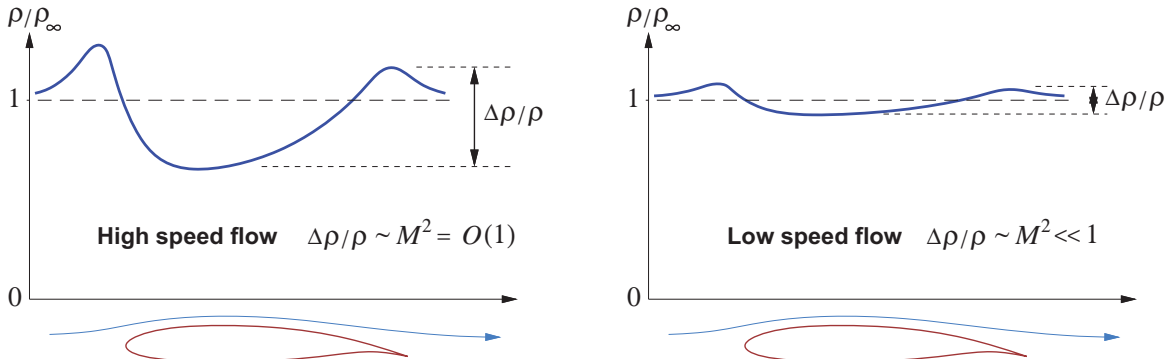
Figure 1.13: In an adiabatic flow, fractional density variations $\Delta\rho/\rho$ scale as M^2. In the low speed flow case $M^2 \ll 1$ this implies a nearly constant ρ equal to the freestream value ρ_∞.

For typical aerodynamic flows where the far-upstream density is uniform, the incompressibility result (1.80) becomes the more general statement that the density is constant everywhere in the flow, and equal to the freestream value.

$$\rho \;\simeq\; \text{constant} \;=\; \rho_\infty \qquad \text{(incompressible aerodynamic flow)} \quad (1.81)$$

For adiabatic low speed flow where $\Delta h_o/h \simeq 0$, relation (1.77) in addition indicates

$$\frac{\Delta h}{h} \;=\; \frac{\Delta h_o}{h} - (\gamma{-}1)M^2\frac{\Delta V}{V} \;\ll\; 1$$

$$\text{or} \qquad h \;\simeq\; \text{constant} \qquad\qquad\qquad (1.82)$$

so such flows are also nearly isothermal, and therefore the viscosity μ is nearly constant everywhere. In this case the vector identity

$$\nabla \cdot \left[\nabla \mathbf{a} + (\nabla \mathbf{a})^T \right] = \nabla^2 \mathbf{a} + \nabla (\nabla \cdot \mathbf{a}) \tag{1.83}$$

together with $\sigma = \nabla \cdot \mathbf{V} = 0$, which is the consequence of mass conservation and $\rho = $ constant, can be used to simplify the viscous momentum term in (1.34) or (1.36) to a Laplacian of the velocity.

$$\nabla \cdot \bar{\bar{\boldsymbol{\tau}}} = \nabla \cdot \left\{ \mu \left[\nabla \mathbf{V} + (\nabla \mathbf{V})^T - 2\frac{\sigma}{3}\bar{\bar{\mathbf{I}}} \right] \right\} = \mu \nabla^2 \mathbf{V} \tag{1.84}$$

Overall, the continuity and momentum equations simplify to the *incompressible Navier Stokes equations*

$$\boxed{\nabla \cdot \mathbf{V} = 0} \tag{1.85}$$

$$\boxed{\frac{\partial \mathbf{V}}{\partial t} + \mathbf{V} \cdot \nabla \mathbf{V} = \mathbf{f} - \frac{\nabla p}{\rho} + \nu \nabla^2 \mathbf{V}} \tag{1.86}$$

where $\nu \equiv \mu/\rho$ is the *kinematic viscosity*. The energy and state equations decouple and are no longer needed.

1.9 Vorticity Transport and Irrotationality

The behavior of vorticity will be examined by formally taking the curl of the momentum equation (1.36). The manipulations will use the following identities, which are valid for any vector fields $\mathbf{a}$ and $\mathbf{b}$.

$$\nabla (\mathbf{a} \cdot \mathbf{b}) = \mathbf{a} \cdot \nabla \mathbf{b} + \mathbf{b} \cdot \nabla \mathbf{a} + \mathbf{a} \times (\nabla \times \mathbf{b}) + \mathbf{b} \times (\nabla \times \mathbf{a}) \tag{1.87}$$

$$\nabla \times (\mathbf{a} \times \mathbf{b}) = \mathbf{a} \nabla \cdot \mathbf{b} - \mathbf{b} \nabla \cdot \mathbf{a} + \mathbf{b} \cdot \nabla \mathbf{a} - \mathbf{a} \cdot \nabla \mathbf{b} \tag{1.88}$$

1.9.1 Helmholtz vorticity transport equation

Setting $\mathbf{a} = \mathbf{b} = \mathbf{V}$ in identity (1.87) gives

$$\frac{1}{2} \nabla (\mathbf{V} \cdot \mathbf{V}) = \mathbf{V} \cdot \nabla \mathbf{V} + \mathbf{V} \times \boldsymbol{\omega} \tag{1.89}$$

$$\boldsymbol{\omega} \equiv \nabla \times \mathbf{V} \tag{1.90}$$

where $\boldsymbol{\omega}$ is the *vorticity*. Using (1.89) to replace the $\mathbf{V} \cdot \nabla \mathbf{V}$ term in the momentum equation (1.36) puts it into the following alternative form.

$$\frac{\partial \mathbf{V}}{\partial t} + \frac{1}{2} \nabla (\mathbf{V} \cdot \mathbf{V}) - \mathbf{V} \times \boldsymbol{\omega} = \mathbf{f} - \frac{\nabla p}{\rho} + \frac{\nabla \cdot \bar{\bar{\boldsymbol{\tau}}}}{\rho} \tag{1.91}$$

We now take the curl $\nabla \times$ [equation (1.91)], use the identity $\nabla \times \nabla() = \mathbf{0}$, and note that the curl commutes with the $\partial()/\partial t$ operation. The body force field $\mathbf{f}$ is also assumed irrotational as is typical, so that $\nabla \times \mathbf{f} = \mathbf{0}$.

$$\frac{\partial \boldsymbol{\omega}}{\partial t} - \nabla \times (\mathbf{V} \times \boldsymbol{\omega}) = -\nabla \left(\frac{1}{\rho}\right) \times \nabla p + \nabla \times \left(\frac{\nabla \cdot \bar{\bar{\boldsymbol{\tau}}}}{\rho}\right) \tag{1.92}$$

Next we set $\mathbf{a} = \mathbf{V}$ and $\mathbf{b} = \boldsymbol{\omega}$ in identity (1.88) which gives

$$\nabla \times (\mathbf{V} \times \boldsymbol{\omega}) = -\rho \boldsymbol{\omega} \frac{\mathrm{D}(1/\rho)}{\mathrm{D}t} + \boldsymbol{\omega} \cdot \nabla \mathbf{V} - \mathbf{V} \cdot \nabla \boldsymbol{\omega} \tag{1.93}$$

where the convective mass equation

$$\frac{1}{\rho}\frac{\mathrm{D}\rho}{\mathrm{D}t} = -\rho\frac{\mathrm{D}(1/\rho)}{\mathrm{D}t} = \nabla\cdot\mathbf{V}$$

and the identity $\nabla\cdot\boldsymbol{\omega} = \nabla\cdot(\nabla\times\mathbf{V}) = 0$, have been used. Substituting (1.93) in (1.92), dividing through by ρ, and combining and rearranging terms finally gives the *Helmholtz vorticity transport equation*, with its simpler incompressible form resulting from ρ and μ being constant.

$$\frac{\mathrm{D}}{\mathrm{D}t}\left(\frac{\boldsymbol{\omega}}{\rho}\right) = \frac{\boldsymbol{\omega}}{\rho}\cdot\nabla\mathbf{V} + \frac{\nabla\rho\times\nabla p}{\rho^3} + \frac{1}{\rho}\nabla\times\left(\frac{\nabla\cdot\bar{\bar{\boldsymbol{\tau}}}}{\rho}\right) \tag{1.94}$$

$$\frac{\mathrm{D}\boldsymbol{\omega}}{\mathrm{D}t} = \boldsymbol{\omega}\cdot\nabla\mathbf{V} + \nu\nabla^2\boldsymbol{\omega} \qquad \text{(incompressible)} \tag{1.95}$$

The *baroclinic* source term $\nabla\rho\times\nabla p$ in the compressible Helmholtz equation (1.94) can cause vorticity to appear wherever there are density and pressure gradients present. However, in isentropic flow where the viscous term is negligible the isentropic $p(\rho)$ relation (1.69) holds, so here the p and ρ gradients are parallel

$$\nabla p = \frac{\mathrm{d}p}{\mathrm{d}\rho}\nabla\rho = \gamma\frac{p}{\rho}\nabla\rho \tag{1.96}$$

and therefore the baroclinic term vanishes since $\nabla\rho\times\nabla p \sim \nabla\rho\times\nabla\rho = \mathbf{0}$.

The term $\boldsymbol{\omega}\cdot\nabla\mathbf{V}$ on the righthand sides represents *vortex tilting* and *vortex stretching*, the latter causing a rotating fluid's vorticity to intensify when the rotating fluid is stretched by the components of the velocity gradient matrix $\nabla\mathbf{V}$ which are parallel to $\boldsymbol{\omega}$ itself. However, if $\boldsymbol{\omega} = \mathbf{0}$ to begin with, then this term is disabled, since there is no vorticity to stretch or tilt.

The Helmholtz vorticity equation (1.94) or (1.95) simplifies greatly for most aerodynamic flows. These typically have uniform flow and hence $\boldsymbol{\omega}=\mathbf{0}$ upstream, and their viscous stresses are negligible outside of viscous layers and outside of shocks. In these circumstances (1.94) gives

$$\frac{\mathrm{D}}{\mathrm{D}t}\left(\frac{\boldsymbol{\omega}}{\rho}\right) = \mathbf{0} \tag{1.97}$$

$$\rightarrow \quad \boldsymbol{\omega} = \mathbf{0} \tag{1.98}$$

with the conclusion being that initial irrotationality persists downstream outside of the viscous layers and shock wakes. These are the same requirements as those for isentropy, discussed earlier and shown in Figure 1.11. Hence we can further conclude that flows which are irrotational are also isentropic, as illustrated in Figure 1.14.

$$s = \text{constant} \qquad \longleftrightarrow \qquad \boldsymbol{\omega} = \mathbf{0}$$
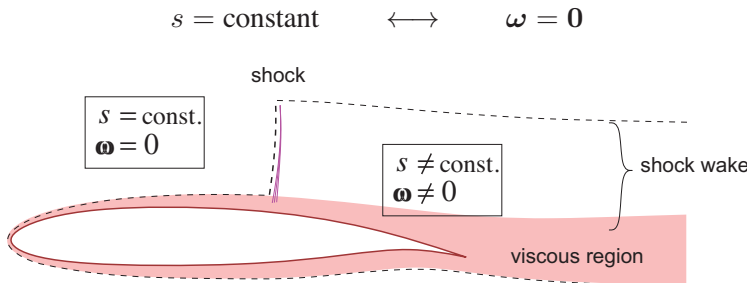
Figure 1.14: Isentropic flow regions are also irrotational, and vice versa.

Irrotationality of the velocity field has great implications for flow-field representation and modeling, which will be treated in Chapter 2. It also enables the various Bernoulli relations for the pressure, considered next.

1.9.2 Crocco relation

The $\mathrm{d}(\ )$ differentials in the Gibbs relation (1.61) can be taken along a $\mathrm{d}x$ interval and then divided by $\mathrm{d}x$ to convert them to partial derivatives.

$$T\frac{\partial s}{\partial x} = \frac{\partial h}{\partial x} - \frac{1}{\rho}\frac{\partial p}{\partial x}$$

Repeating this along $\mathrm{d}y$ and $\mathrm{d}z$ intervals, and adding the three results as vector components, gives the gradient form of the Gibbs relation.

$$\begin{aligned} T\,\nabla s &= \nabla h - \frac{\nabla p}{\rho} \\ &= \nabla h_o - \frac{1}{2}\nabla(\mathbf{V}\cdot\mathbf{V}) - \frac{\nabla p}{\rho} \end{aligned} \tag{1.99}$$

Combining this with the alternative form of the momentum equation (1.91) gives

$$T\,\nabla s = \nabla h_o + \frac{\partial \mathbf{V}}{\partial t} - \mathbf{V}\times\boldsymbol{\omega} - \mathbf{f} - \frac{1}{\rho}\nabla\cdot\bar{\bar{\tau}} \tag{1.100}$$

which for steady inviscid flow without body forces simplifies to the *Crocco relation*.

$$\boxed{T\,\nabla s = \nabla h_o - \mathbf{V}\times\boldsymbol{\omega}} \qquad \text{(steady, inviscid)} \tag{1.101}$$

For the steady adiabatic case this explicitly confirms the equivalence between isentropy and irrotationality deduced in the previous section. It is also useful in many applications in which one of the three terms in (1.101) is known explicitly, which then provides an explicit relation between the two remaining terms.

1.9.3 Bernoulli equation

If the flow is irrotational, then the velocity must be the gradient of a velocity potential $\phi(\mathbf{r},t)$.

$$\mathbf{V} = \nabla\phi \tag{1.102}$$

If $\mathbf{f}$ is the gravitational force per unit mass as is usually case, then we also have

$$\mathbf{f} = -g\,\nabla z \tag{1.103}$$

where g is gravity's acceleration and z is the vertical height. With these assumptions, and also assuming that the flow is effectively inviscid so $\bar{\bar{\tau}}$ can be neglected, the alternative form of the compressible or incompressible momentum equation (1.91) or (1.86) simplifies to

$$\nabla\frac{\partial \phi}{\partial t} + \frac{1}{2}\nabla(V^2) = -g\,\nabla z - \frac{\nabla p}{\rho} \tag{1.104}$$

which can be integrated if we make suitable assumptions about the density ρ.

Incompressible Bernoulli equation

Assuming $\rho =$ constant and integrating (1.104) gives the general *Incompressible Bernoulli equation*

$$\boxed{\frac{\partial \phi}{\partial t} + \frac{1}{2}V^2 + \frac{p}{\rho} + gz = C} \tag{1.105}$$
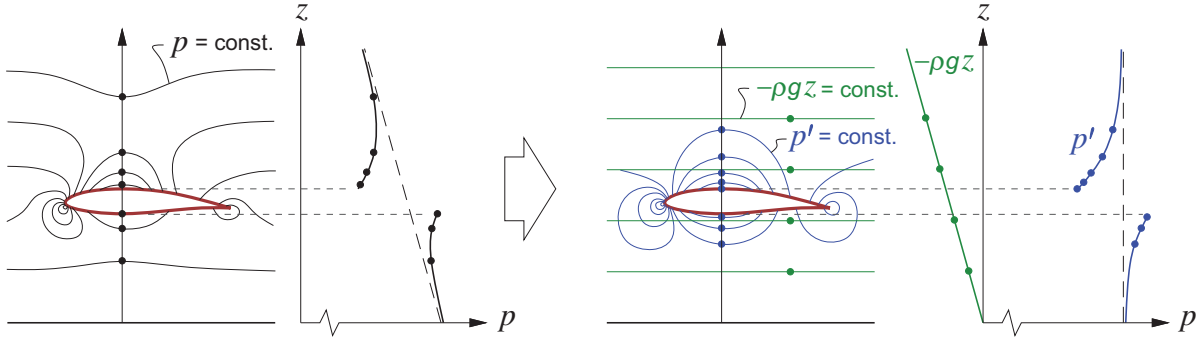
Figure 1.15: Overall pressure p decomposed into hydrostatic and dynamic components $-\rho g z + p'$.

where C is some integration constant. It is convenient to decompose the pressure p into a *hydrostatic* pressure field $-\rho g z$ and a remaining part p' associated with only the fluid motion, as shown in Figure 1.15.

$$p = -\rho g z + p' \tag{1.106}$$

This effectively eliminates the gravity term from the Bernoulli equation (1.105).

$$\frac{\partial \phi}{\partial t} + \frac{1}{2}V^2 + \frac{p'}{\rho} = C \tag{1.107}$$

From now on we will denote p' simply as "p," with the understanding that it really represents the deviation from the known hydrostatic pressure $-\rho g z$. The latter provides a buoyancy force equal to the displaced fluid's weight, which directly adds to the hydrodynamic force from p' and surface viscous stresses.

$$\mathbf{F}_{\text{buoyancy}} = \oiint_{\text{body}} \rho g\, z\, \hat{\mathbf{n}}\, \mathrm{d}\mathcal{S} = \iiint_{\text{body}} \rho g\, \hat{\mathbf{z}}\, \mathrm{d}\mathcal{V} = \rho g\, \mathcal{V}_{\text{body}}\, \hat{\mathbf{z}} \tag{1.108}$$

This buoyancy force is usually ignored, notable exceptions being lighter-than-air and underwater vehicles.

This pressure decomposition is not usable for the free-surface flows about surface water vehicles. Here the overall true pressure $-\rho g z + p'$ is imposed to be constant on the free surface as a boundary condition, which then results in the generation of surface gravity waves with heights z. These waves influence the velocity field, which in turn influences p' and hence the wave shapes. Therefore, the hydrostatic and dynamic parts of the pressure field are two-way coupled and cannot be treated separately.

For low-speed steady aerodynamic flows, the constant C in (1.107) is most conveniently defined from the known freestream total pressure, giving the most familiar form of the Bernoulli equation.

$$\boxed{p + \frac{1}{2}\rho V^2 = p_\infty + \frac{1}{2}\rho V_\infty^2 \equiv p_{o_\infty}} \tag{1.109}$$

In this case, the pressure coefficient definition (1.54) also reduces to a relatively simple form.

$$C_p = 1 - \frac{V^2}{V_\infty^2} \tag{1.110}$$

It must be stressed that the Bernoulli forms (1.109) and (1.110) apply only where the total pressure is equal to the freestream value.

Compressible Bernoulli equation

An alternative assumption for the density is to use the isentropic relation (1.69)

$$\rho = \rho_\infty \left(\frac{p}{p_\infty} \right)^{1/\gamma}$$

in which case (1.104) integrates to the compressible version of the general Bernoulli equation.

$$\frac{\partial \phi}{\partial t} + \frac{1}{2}V^2 + \frac{a_\infty^2}{\gamma-1}\left(\frac{p}{p_\infty} \right)^{(\gamma-1)/\gamma} + gz = C \tag{1.111}$$

Dropping the gravity term as before, and using the freestream to evaluate the integration constant gives the isentropic unsteady pressure formula, with the steady form obtainable by dropping the $\partial\phi/\partial t$ term.

$$\frac{p}{p_\infty} = \left[1 + \frac{\gamma-1}{2}M_\infty^2 \left(1 - \frac{V^2}{V_\infty^2} - \frac{2}{V_\infty^2}\frac{\partial \phi}{\partial t} \right) \right]^{\gamma/(\gamma-1)} \tag{1.112}$$

1.10   Aerodynamic Flow Categories

The various types of high Reynolds number aerodynamic flows can be categorized by the Venn diagram shown in Figure 1.16. All have mostly-irrotational flow with relatively thin boundary layers and wakes. Hence, much of the book will focus on potential flow modeling and prediction. Most aerodynamic bodies are also adiabatic, so the treatment of viscous flows here will focus on adiabatic boundary layers.
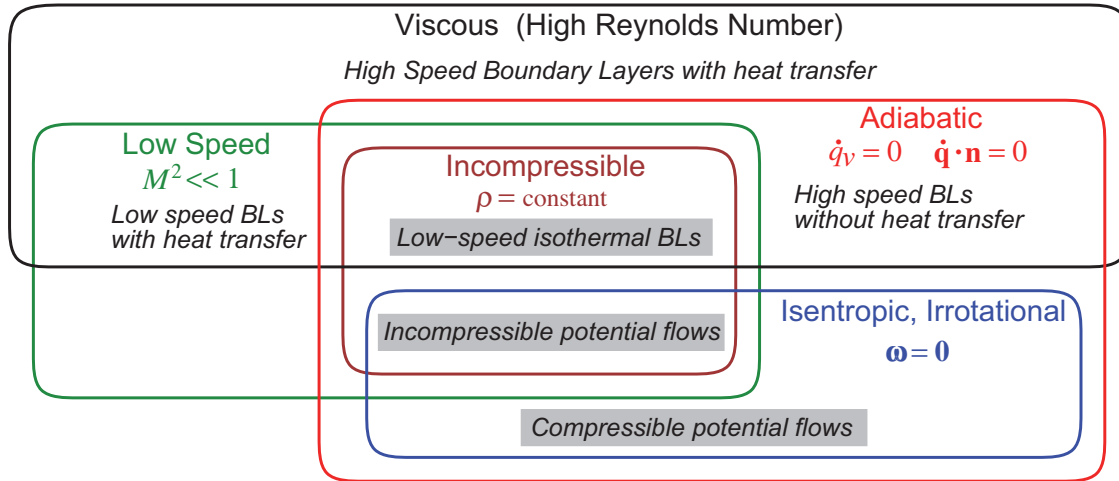
Figure 1.16: Aerodynamic flow categories. This book will focus primarily on potential flows and low speed adiabatic boundary layers, which are shown shaded.

Chapter 2

Flow-Field Modeling

This chapter will address the specification or description of the velocity field of an aerodynamic flow, in terms of its associated source and vorticity fields. Effective simplifications and idealizations of the flow-field will also be developed within this flow description approach.

2.1 Vector Field Representation Methods

The majority of computational methods for fluid flow prediction use one of two different methods to define the velocity field $\mathbf{V}(\mathbf{r})$. These are sketched in Figure 2.1, and described as follows.

1) A *grid method* where discrete values $\mathbf{V}_{ij}$ are defined at the nodes of a grid which fills the entire flow-field. A suitable interpolation scheme is used to interpolate these values to obtain $\mathbf{V}(\mathbf{r})$ at any position vector point $\mathbf{r}$ within the grid. This is the approach used by modern Computational Fluid Dynamics (CFD) methods which solve the Full-Potential equation, the Euler equations, or the Navier-Stokes equations.

2) A *singularity method* which uses the velocity fields of source and vortex sheet strengths $\lambda_i, \boldsymbol{\gamma}_i$ which are defined in limited regions of the flow-field, typically at solid surfaces or other boundaries. Weighted integration or summation over these source and vortex strengths, together with an additional freestream velocity $\mathbf{V}_\infty$, is used to obtain $\mathbf{V}(\mathbf{r})$ at any point in the flow-field. This approach is used by Vortex Lattice and Panel methods for potential flows.
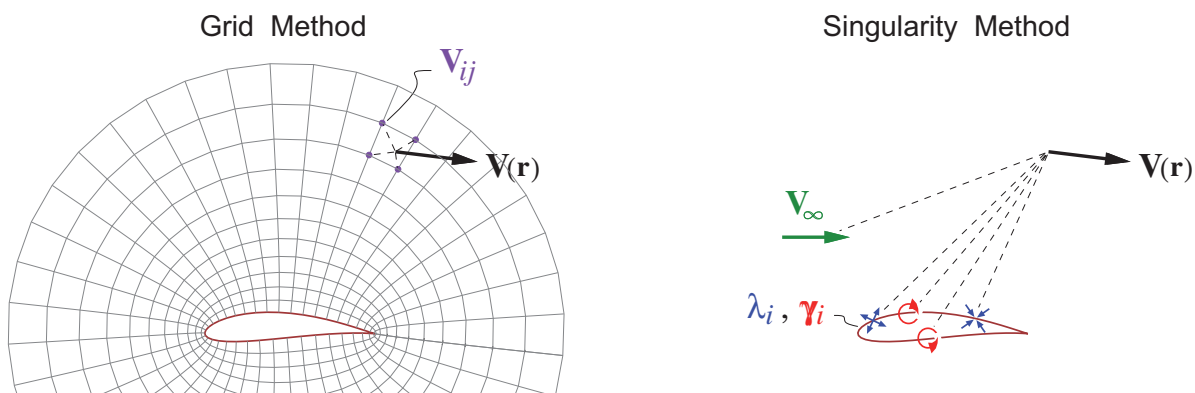
Figure 2.1: Grid and singularity methods used to represent a velocity vector field $\mathbf{V}(\mathbf{r})$.

This chapter will focus on the singularity method 2). In addition to being the basis of Vortex Lattice and Panel flow calculation methods, this flow-field representation is also the basis of many useful engineering approximations, including the formulation of outer boundary conditions in grid-based CFD methods. It also provides an intuitive and physical understanding of aerodynamic flows and general flow behavior, and hence is useful even if the grid-based CFD methods are being employed.

2.2   Velocity / Vorticity-Source Duality

The sheet strengths λ and γ in Figure 2.1 will be shown to be closely related to the source density σ and vorticity ω distributions, which can be obtained from the velocity field by taking its divergence and curl.

$$\sigma(\mathbf{r}) \;=\; \nabla \cdot \mathbf{V} \tag{2.1}$$

$$\boldsymbol{\omega}(\mathbf{r}) \;=\; \nabla \times \mathbf{V} \tag{2.2}$$

Conversely, the velocity field can be obtained from the source and vorticity fields via definite volume integrals over the entire flow-field. This in effect reverses the divergence and curl operations, as discussed by Batchelor [2] in some detail. These reciprocal operations are illustrated in Figure 2.2, and given as follows.

$$\mathbf{V}(\mathbf{r}) \;=\; \mathbf{V}_\sigma + \mathbf{V}_\omega + \mathbf{V}_b \tag{2.3}$$

$$\text{where} \qquad \mathbf{V}_\sigma(\mathbf{r}) \;\equiv\; \frac{1}{4\pi} \iiint \sigma(\mathbf{r}') \, \frac{\mathbf{r}-\mathbf{r}'}{|\mathbf{r}-\mathbf{r}'|^3} \, \mathrm{d}x' \, \mathrm{d}y' \, \mathrm{d}z' \tag{2.4}$$

$$\mathbf{V}_\omega(\mathbf{r}) \;\equiv\; \frac{1}{4\pi} \iiint \boldsymbol{\omega}(\mathbf{r}') \times \frac{\mathbf{r}-\mathbf{r}'}{|\mathbf{r}-\mathbf{r}'|^3} \, \mathrm{d}x' \, \mathrm{d}y' \, \mathrm{d}z' \tag{2.5}$$

$$\mathbf{V}_b \;=\; \mathbf{V}_\infty \qquad \text{(for unbounded external flow)} \tag{2.6}$$
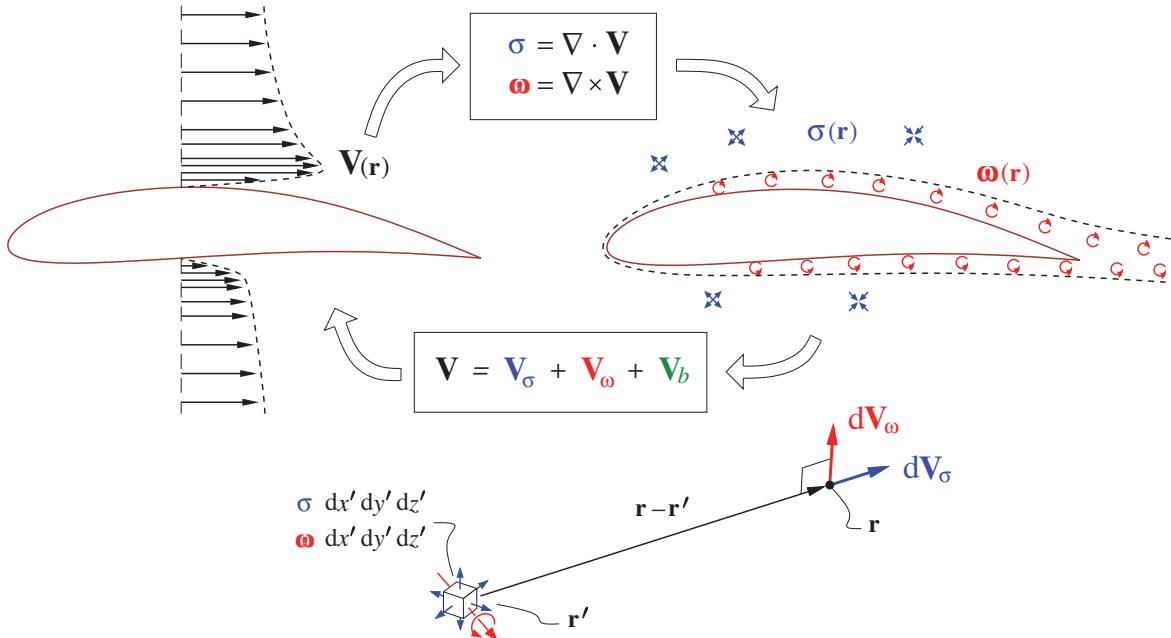
Figure 2.2: A flow velocity field $\mathbf{V}(\mathbf{r})$ shown on the left can be used to define the source and vorticity fields $\sigma(\mathbf{r})$ and $\boldsymbol{\omega}(\mathbf{r})$ shown on the right, and vice versa. Boxes contain reciprocal conversion relations from one description to the other, with $\mathbf{V}_\sigma$ and $\mathbf{V}_\omega$ defined by equations (2.4) and (2.5).

The infinitesimal volume element $\mathrm{d}x'\mathrm{d}y'\mathrm{d}z'$ at the *integration point* location $\mathbf{r}'$ with source density $\sigma(\mathbf{r}')$ and vorticity $\boldsymbol{\omega}(\mathbf{r}')$ has contributions to the total $\mathbf{V}(\mathbf{r})$ at the *field point* at $\mathbf{r}$. The source contribution $\mathrm{d}\mathbf{V}_\sigma$ is parallel to the connecting vector $(\mathbf{r}-\mathbf{r}')$, whose explicit definition and magnitude are as follows.

$$\mathbf{r}-\mathbf{r}' \;=\; (x-x')\,\hat{\mathbf{x}} + (y-y')\,\hat{\mathbf{y}} + (z-z')\,\hat{\mathbf{z}} \tag{2.7}$$

$$|\mathbf{r}-\mathbf{r}'| \;=\; \sqrt{(x-x')^2 + (y-y')^2 + (z-z')^2} \tag{2.8}$$

The vorticity contribution $\mathrm{d}\mathbf{V}_\omega$ is perpendicular to both $(\mathbf{r}-\mathbf{r}')$ and $\boldsymbol{\omega}$.

The last velocity component $\mathbf{V}_b$ in (2.3) is the part of $\mathbf{V}$ which has <u>both</u> zero divergence and zero curl everywhere in the flow-field, and hence cannot be represented by σ or $\boldsymbol{\omega}$ within the flow-field. In the typical external aerodynamic flow extending to infinity, $\mathbf{V}_b$ is a constant field, and equal to the freestream velocity as given by (2.6). In the more general case, such as flow near a wall or inside a wind tunnel, $\mathbf{V}_b$ is not a constant, but it can be uniquely determined as follows.

Since $\nabla \times \mathbf{V}_b = \mathbf{0}$, this velocity must be expressible as a gradient of some scalar potential function $\phi_b(\mathbf{r})$.

$$\mathbf{V}_b = \nabla \phi_b \tag{2.9}$$

Setting the divergence of this $\mathbf{V}_b$ to zero as required by its definition gives

$$\nabla \cdot \mathbf{V}_b = \nabla \cdot (\nabla \phi_b) = 0$$
$$\nabla^2 \phi_b = 0 \tag{2.10}$$

so that ϕ_b must satisfy the Laplace equation (2.10). This will have a solution everywhere inside the flow-field if appropriate *boundary conditions* are specified on all the flow-field boundaries. The boundary conditions are case-dependent, and some typical examples are given below.

$$\phi_b = \mathbf{V}_\infty \cdot \mathbf{r} = u_\infty\, x + v_\infty\, y + w_\infty\, z \quad \text{(at distant boundary)} \tag{2.11}$$
$$\partial \phi_b / \partial n = -(\mathbf{V}_\sigma + \mathbf{V}_\omega) \cdot \hat{\mathbf{n}} \quad \text{(at solid-wall boundary)} \tag{2.12}$$

For simple flat internal-flow boundaries such as wind tunnel walls, $\mathbf{V}_b$ can be alternatively obtained using the method of images. Many examples are given in Chapter 10.

It's useful to note that the $\mathbf{V}_\sigma$ superposition integral (2.4) has the form

$$\mathbf{V}_\sigma(\mathbf{r}) = \iiint \sigma(\mathbf{r}') \, \mathbf{K}(\mathbf{r}-\mathbf{r}') \, \mathrm{d}x' \, \mathrm{d}y' \, \mathrm{d}z' \tag{2.13}$$
$$\mathbf{K}(\mathbf{r},\mathbf{r}') = \mathbf{K}(\mathbf{r}-\mathbf{r}') = \frac{1}{4\pi} \frac{\mathbf{r}-\mathbf{r}'}{|\mathbf{r}-\mathbf{r}'|^3} \tag{2.14}$$

where $\mathbf{K}$ is the *kernel function* which is strictly geometric, in that it depends only on the coordinates of the field point $\mathbf{r}$ and the integration point $\mathbf{r}'$. More specifically, it depends only on the connecting vector $\mathbf{r}-\mathbf{r}'$ between the two points. The specific kernel function (2.14) can be interpreted as the velocity field $\mathbf{V}(\mathbf{r})$ of a unit-strength point source located at $\mathbf{r}'$.

2.3 Aerodynamic Modeling – Vorticity and Source Lumping

The general velocity field representation (2.3) via the source and vorticity fields is primarily conceptual, since the volume integrals for the $\mathbf{V}_\sigma$ and $\mathbf{V}_\omega$ components are impractical to evaluate in numerical applications. However, the representation (2.3) can be approximated and greatly simplified by the process of *lumping*, which is based on the approximation that the kernel function is constant along some small interval of one of the $s\ell n$ coordinates. This allows the source and vorticity volume distributions to be in effect concentrated into surfaces or sheets, and then possibly further concentrated into lines (or filaments), and then possibly even points. This process, illustrated in Figure 2.3, is the basis of aerodynamic modeling.

Note that at each lumping stage the singularity geometry becomes simplified, but the resulting velocity field becomes more singular and less realistic near the sheet, filament, or point (which is the origin of the name *singularity*). However, sufficiently far away the actual and approximated velocity fields become the same.

The lumping operation uses the curvilinear $s\ell n$ coordinates, defined such that $s\ell$ lie on the surface of the sheet, filaments, or points, and n is normal to this surface. For simplicity, the curvatures of the $s\ell n$ coordinate

lines are assumed to be sufficiently small so that they form a local effectively Cartesian system. A volume element is then simply $\mathrm{d}s\,\mathrm{d}\ell\,\mathrm{d}n$, and a surface element is $\mathrm{d}s\,\mathrm{d}\ell$, so that the Jacobian factors which should appear in these elements are assumed to be unity and hence omitted for simplicity. This approximation does not adversely affect the effectiveness of the lumping concept for most aerodynamic applications.
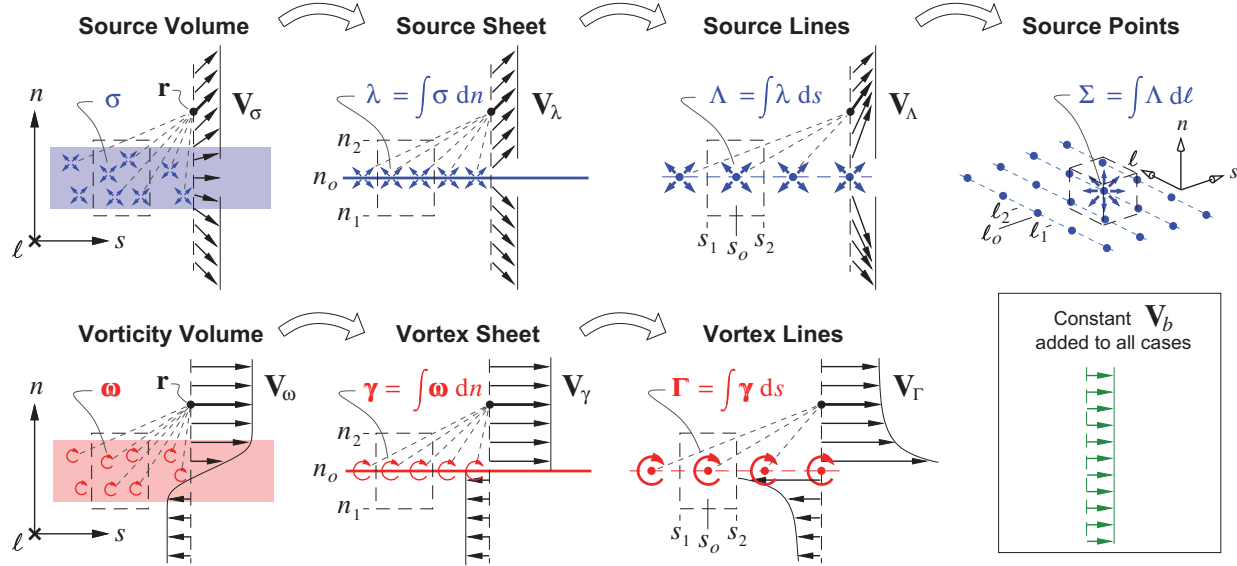
Figure 2.3: Lumping of source and vorticity volume distributions into sheets and then lines. Source lines can be further lumped into source points. The evaluation of the velocity at any field point $\mathbf{r}$ then becomes progressively simplified. Lumping is the basis of aerodynamic modeling.

2.3.1 Sheets

In the first simplification stage we neglect the kernel function's n dependence by assuming a representative integration point $\mathbf{r}'(s,\ell,n) \simeq \mathbf{r}'(s,\ell,n_o)$ at some fixed n_o location, indicated in Figure 2.3. The simplified kernel function can then be removed from the n integral, allowing the σ or $\boldsymbol{\omega}$ distribution to be integrated or lumped in n across the layer thickness from n_1 to n_2, thus defining the sheet strengths $\lambda(s,\ell)$ and $\boldsymbol{\gamma}(s,\ell)$. The volume integrals in the velocity superposition (2.3) then become the simpler surface integrals over the sheet coordinates s and ℓ, with $\mathbf{r}'(s,\ell)$ now denoting the integration points on the sheet.

$$\mathbf{V}_\sigma(\mathbf{r}) \;\simeq\; \mathbf{V}_\lambda(\mathbf{r}) \;\equiv\; \frac{1}{4\pi}\iint \lambda\,\frac{\mathbf{r}-\mathbf{r}'}{|\mathbf{r}-\mathbf{r}'|^3}\,\mathrm{d}s\,\mathrm{d}\ell \quad ; \qquad \lambda(s,\ell) \equiv \int_{n_1}^{n_2}\sigma(s,\ell,n)\,\mathrm{d}n \quad (2.15)$$

$$\mathbf{V}_\omega(\mathbf{r}) \;\simeq\; \mathbf{V}_\gamma(\mathbf{r}) \;\equiv\; \frac{1}{4\pi}\iint \boldsymbol{\gamma}\times\frac{\mathbf{r}-\mathbf{r}'}{|\mathbf{r}-\mathbf{r}'|^3}\,\mathrm{d}s\,\mathrm{d}\ell \quad ; \qquad \boldsymbol{\gamma}(s,\ell) \equiv \int_{n_1}^{n_2}\boldsymbol{\omega}(s,\ell,n)\,\mathrm{d}n \quad (2.16)$$

The resulting velocities $\mathbf{V}_\lambda$ and $\mathbf{V}_\gamma$ are now discontinuous across the sheets, but this does not cause any problems in practice. Note also that outside the original source or vorticity volume, $\mathbf{V}_\lambda$ is very nearly the same as the actual $\mathbf{V}_\sigma$, and $\mathbf{V}_\gamma$ is very nearly the same as the actual $\mathbf{V}_\omega$, as Figure 2.3 suggests. Sheets are extensively used in aerodynamic modeling and computation, and will be discussed in more detail later.

2.3.2 Lines

The second lumping stage consists of dividing the s coordinate into some number of short intervals, and assuming that $\mathbf{r}'(s,\ell) \simeq \mathbf{r}'(s_o,\ell)$ where s_o is some representative s value on each interval. We can then integrate λ or γ across each interval from s_1 to s_2, thus defining the line or filament strengths $\Lambda(\ell)$ or $\boldsymbol{\Gamma}(\ell)$. Each surface integral then becomes a summation over a number of simpler line integrals along the remaining

filament coordinate ℓ, with $\mathbf{r}'(\ell)$ now denoting the integration points on the filament. Here we also assume that ℓ is chosen to be aligned locally with the $\boldsymbol{\gamma}$ vector direction, as indicated in Figure 2.3.

$$\mathbf{V}_\sigma(\mathbf{r}) \;\simeq\; \mathbf{V}_\Lambda(\mathbf{r}) \;\equiv\; \sum_{\text{lines}} \frac{1}{4\pi} \int \Lambda \frac{\mathbf{r}-\mathbf{r}'}{|\mathbf{r}-\mathbf{r}'|^3} \,\mathrm{d}\ell \quad ; \quad \Lambda(\ell) \equiv \int_{s_1}^{s_2} \lambda(s,\ell)\,\mathrm{d}s \qquad (2.17)$$

$$\mathbf{V}_\omega(\mathbf{r}) \;\simeq\; \mathbf{V}_\Gamma(\mathbf{r}) \;\equiv\; \sum_{\text{lines}} \frac{1}{4\pi} \int \boldsymbol{\Gamma} \times \frac{\mathbf{r}-\mathbf{r}'}{|\mathbf{r}-\mathbf{r}'|^3} \,\mathrm{d}\ell \quad ; \quad \boldsymbol{\Gamma}(\ell) \equiv \int_{s_1}^{s_2} \boldsymbol{\gamma}(s,\ell)\,\mathrm{d}s \qquad (2.18)$$

The resulting velocity fields $\mathbf{V}_\Lambda$ and $\mathbf{V}_\Gamma$ defined above are now strongly singular at the filaments, varying as $|\mathbf{V}_\Lambda|, |\mathbf{V}_\Gamma| \sim 1/\Delta r$ where Δr is the nearest distance to a filament. The magnitude of these singularities depends on the width of the s intervals for the lumping integration and the resulting line spacing, which can be chosen arbitrarily. A fine sheet subdivision into many weak filaments proportionally reduces the singularities, giving a smoother velocity field at any given distance from the filament-approximated surface.

The vortex-filament velocity definition (2.18) can be simplified somewhat by applying the Helmholtz vortex law [2] which states that the magnitude of $\boldsymbol{\Gamma}$ cannot change along the filament. In addition, since the ℓ coordinate was chosen to be aligned with $\boldsymbol{\gamma}$, the lumped $\boldsymbol{\Gamma}$ must be parallel to the filament element vector $\mathrm{d}\boldsymbol{\ell}$ at each location. We can then convert the $\mathbf{V}_\Gamma$ definition (2.18) into the familiar Biot-Savart integral.

$$\boldsymbol{\Gamma}\,\mathrm{d}\ell \;=\; \Gamma\,\mathrm{d}\boldsymbol{\ell} \qquad (2.19)$$

$$\mathbf{V}_\Gamma(\mathbf{r}) \;=\; \sum_{\text{lines}} \frac{\Gamma}{4\pi} \int \frac{\mathrm{d}\boldsymbol{\ell} \times (\mathbf{r}-\mathbf{r}')}{|\mathbf{r}-\mathbf{r}'|^3} \qquad (2.20)$$

Note that the integral itself is purely geometric, and can be evaluated without knowing the filament circulation Γ a priori.

2.3.3   Points

The source filaments can be subjected to one more lumping step by dividing the ℓ coordinate into some number of intervals from ℓ_1 to ℓ_2, and lumping $\Lambda(\ell)$ over each interval into a point-source strength Σ. The filament integrals then become a sum of relatively simple algebraic expressions over the point sources.

$$\mathbf{V}_\sigma(\mathbf{r}) \;\simeq\; \mathbf{V}_\Sigma(\mathbf{r}) \;\equiv\; \sum_{\text{points}} \frac{\Sigma}{4\pi} \frac{\mathbf{r}-\mathbf{r}'}{|\mathbf{r}-\mathbf{r}'|^3} \quad ; \quad \Sigma \equiv \int_{\ell_1}^{\ell_2} \Lambda(\ell)\,\mathrm{d}\ell \qquad (2.21)$$

The resulting velocity field is now even more singular than for the filaments, varying as $|\mathbf{V}_\Sigma| \sim 1/\Delta r^2$ where $\Delta r = |\mathbf{r}-\mathbf{r}'|$ is the distance to the point.

Vortex filaments could be lumped into point point vortices or "vortons" in the same manner as the source filaments. However, in addition to having the $|\mathbf{V}| \sim 1/\Delta r^2$ singularity, the resulting velocity field is not exactly irrotational in the vicinity of each vorton. Hence, if perfect irrotationality is required away from the singularities, then equations (2.20) and (2.21) constitute the simplest possible velocity field representation via vortices and sources.

2.3.4   2D forms

This chapter has so far treated only the general three-dimensional case. All the concepts remain largely unchanged in two dimensions. The main simplification in 2D is that the vorticity, vortex sheet strength, and circulation vectors have only one component in the $\hat{\mathbf{y}}$ direction into the x-z plane, and hence can be treated as scalars.

$$\begin{aligned}
\boldsymbol{\omega} &= \omega\,\hat{\mathbf{y}} \\
\boldsymbol{\gamma} &= \gamma\,\hat{\mathbf{y}} \\
\boldsymbol{\Gamma} &= \Gamma\,\hat{\mathbf{y}}
\end{aligned} \qquad (2.22)$$

The velocity superposition integrals then take on the following forms in two dimensions.

$$\mathbf{V}_\sigma(\mathbf{r}) = \frac{1}{2\pi} \iint \sigma(\mathbf{r}') \frac{(\mathbf{r}-\mathbf{r}')}{|\mathbf{r}-\mathbf{r}'|^2} \, \mathrm{d}x' \, \mathrm{d}z' \tag{2.23}$$

$$\mathbf{V}_\omega(\mathbf{r}) = \frac{1}{2\pi} \iint \omega(\mathbf{r}') \frac{\hat{\mathbf{y}}\times(\mathbf{r}-\mathbf{r}')}{|\mathbf{r}-\mathbf{r}'|^2} \, \mathrm{d}x' \, \mathrm{d}z' \tag{2.24}$$

$$\mathbf{r}-\mathbf{r}' = (x-x')\,\hat{\mathbf{x}} + (z-z')\,\hat{\mathbf{z}} \tag{2.25}$$

$$|\mathbf{r}-\mathbf{r}'| = \sqrt{(x-x')^2 + (z-z')^2} \tag{2.26}$$

Their simplified lumped versions follow from the same lumping procedure as in 3D. The sheet coordinates in the x-z plane are now sn, and ℓ is into the plane and parallel to y.

$$\mathbf{V}_\lambda(\mathbf{r}) = \frac{1}{2\pi} \int \lambda \frac{(\mathbf{r}-\mathbf{r}')}{|\mathbf{r}-\mathbf{r}'|^2} \, \mathrm{d}s \quad ; \quad \lambda(s) \equiv \int_{n_1}^{n_2} \sigma(s,n) \, \mathrm{d}n \tag{2.27}$$

$$\mathbf{V}_\gamma(\mathbf{r}) = \frac{1}{2\pi} \int \gamma \frac{\hat{\mathbf{y}}\times(\mathbf{r}-\mathbf{r}')}{|\mathbf{r}-\mathbf{r}'|^2} \, \mathrm{d}s \quad ; \quad \gamma(s) \equiv \int_{n_1}^{n_2} \omega(s,n) \, \mathrm{d}n \tag{2.28}$$

$$\mathbf{V}_\Lambda(\mathbf{r}) = \sum_{\text{points}} \frac{\Lambda}{2\pi} \frac{\mathbf{r}-\mathbf{r}'}{|\mathbf{r}-\mathbf{r}'|^2} = \sum_{\text{points}} \frac{\Lambda}{2\pi} \frac{(x-x')\hat{\mathbf{x}} + (z-z')\hat{\mathbf{z}}}{(x-x')^2 + (z-z')^2} \tag{2.29}$$

$$\mathbf{V}_\Gamma(\mathbf{r}) = \sum_{\text{points}} \frac{\Gamma}{2\pi} \frac{\hat{\mathbf{y}}\times(\mathbf{r}-\mathbf{r}')}{|\mathbf{r}-\mathbf{r}'|^2} = \sum_{\text{points}} \frac{\Gamma}{2\pi} \frac{(z-z')\hat{\mathbf{x}} - (x-x')\hat{\mathbf{z}}}{(x-x')^2 + (z-z')^2} \tag{2.30}$$

2.4   3D Vortex Sheet Strength Divergence Constraint

Although vortex sheets have many attractive properties for representing aerodynamic velocity fields, their main drawback in 3D is that the vortex sheet strength $\boldsymbol{\gamma}$ is a vector whose components are not entirely independent. The complication stems from the vorticity field having identically zero divergence due to its curl definition.

$$\nabla \cdot \boldsymbol{\omega} = \nabla \cdot (\nabla \times \mathbf{V}) = 0 \tag{2.31}$$

Using the locally-cartesian $s\ell n$ sheet coordinates, the resulting divergence of a lumped vortex sheet strength $\boldsymbol{\gamma}$ can then be determined by lumping the divergence of the vorticity.

$$\int_{n_1}^{n_2} \nabla \cdot \boldsymbol{\omega} \, \mathrm{d}n = 0 \tag{2.32}$$

$$\int_{n_1}^{n_2} \left(\frac{\partial \omega_s}{\partial s} + \frac{\partial \omega_\ell}{\partial \ell} + \frac{\partial \omega_n}{\partial n} \right) \mathrm{d}n = 0$$

$$\frac{\partial}{\partial s} \int_{n_1}^{n_2} \omega_s \, \mathrm{d}n + \frac{\partial}{\partial \ell} \int_{n_1}^{n_2} \omega_\ell \, \mathrm{d}n = 0$$

$$\frac{\partial \gamma_s}{\partial s} + \frac{\partial \gamma_\ell}{\partial \ell} = 0 \tag{2.33}$$

$$\text{or} \qquad \widetilde{\nabla} \cdot \boldsymbol{\gamma} = 0 \tag{2.34}$$

$$\text{where} \qquad \widetilde{\nabla} \equiv \hat{\mathbf{s}}\frac{\partial}{\partial s} + \hat{\boldsymbol{\ell}}\frac{\partial}{\partial \ell} \tag{2.35}$$

The surface-gradient operator $\widetilde{\nabla}$ definition simply excludes the $\hat{\mathbf{n}}$ component. The integral $\int \partial \omega_n/\partial n \, \mathrm{d}n$ vanished since the n_1, n_2 endpoints are assumed to be outside the vorticity layer where $\omega_n = 0$.

Equation (2.34) is the key constraint on the $\boldsymbol{\gamma}$ vector. In effect, the $\boldsymbol{\gamma}$ vectors in the vortex sheet must resemble the velocity vectors in 2D incompressible flow which also have zero divergence. Figure 2.4 shows three vortex sheet strength $\boldsymbol{\gamma}(s,\ell)$ distributions. The second case has a nonzero (singular) divergence at one isolated point, which requires a vortex filament to be attached at that point normal to the surface. The third case is nonzero $\boldsymbol{\gamma}$ divergence everywhere which is impossible given the vorticity-lumping assumptions.

$\widetilde{\nabla} \cdot \boldsymbol{\gamma} = 0$ $\boldsymbol{\gamma}(s,\ell)$

$\widetilde{\nabla} \cdot \boldsymbol{\gamma} = 0$ isolated vortex
except at vortex foot

$\widetilde{\nabla} \cdot \boldsymbol{\gamma} \neq 0$ everywhere
(impossible vortex sheet)

branch cut

$\mu(s,\ell)$ isolines $\mu(s,\ell)$ isolines $\mu(s,\ell)$ does not exist
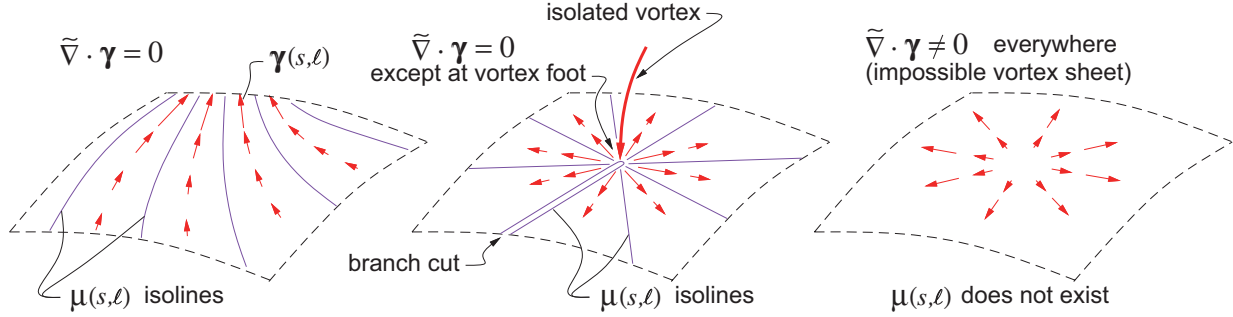
Figure 2.4: Various vortex sheet strength $\boldsymbol{\gamma}(s,\ell)$ distributions. Vortex normal to surface in middle case shows up as branch cut in the μ distribution associated with $\boldsymbol{\gamma}$. Rightmost case is impossible.

An effective way to ensure that $\boldsymbol{\gamma}$ has a zero surface-divergence is to introduce a scalar function $\mu(s,\ell)$, which defines $\boldsymbol{\gamma}$ via μ's surface gradient, rotated $90°$ about the surface unit normal.

$$\boldsymbol{\gamma} = \hat{\mathbf{n}} \times \widetilde{\nabla}\mu \tag{2.36}$$

$$\text{or} \qquad \gamma_s = -\frac{\partial \mu}{\partial \ell} \quad, \quad \gamma_\ell = \frac{\partial \mu}{\partial s}$$

Note that any $\boldsymbol{\gamma}$ defined in this manner automatically has zero surface divergence

$$\widetilde{\nabla} \cdot \boldsymbol{\gamma} = \frac{\partial \gamma_s}{\partial s} + \frac{\partial \gamma_\ell}{\partial \ell} = -\frac{\partial^2 \mu}{\partial s\, \partial \ell} + \frac{\partial^2 \mu}{\partial \ell\, \partial s} = 0$$

so that (2.33) ensures that $\omega_n = 0$. Conversely, if there is a point or line where concentrated vorticity is shed with $\omega_n \neq 0$, such as along the trailing edge of a lifting wing, then $\mu(s,\ell)$ must be discontinuous on a branch cut extending from the point, as shown in Figure 2.4. Such a branch cut must be accounted for in any calculation method which seeks to determine $\mu(s,\ell)$. In a case of a lifting wing, the branch cut is typically placed all along the trailing edge from which vorticity is shed into the otherwise irrotational flow.

One conceptually useful interpretation of $\mu(s,\ell)$ is that it's a streamfunction for $\boldsymbol{\gamma}(s,\ell)$, guaranteeing its zero divergence just like the conventional streamfunction $\psi(x,z)$ guarantees zero divergence of $\mathbf{V}(x,z)$ in two-dimensional flow. And just as streamlines of $\mathbf{V}$ follow constant-ψ lines, the vortex lines parallel to $\boldsymbol{\gamma}$ follow the constant-μ lines on the vortex sheet, as shown in Figure 2.4.

2.5 Equivalence of Vortex and Doublet Sheets

The vorticity streamfunction $\mu(s,\ell)$ can also be interpreted as the *normal-doublet sheet strength*. An area element $\mathrm{d}s\,\mathrm{d}\ell$ of the doublet sheet in effect has an infinitesimal 3D doublet of strength $\mathrm{d}\mathcal{K}_n = \mu\,\mathrm{d}s\,\mathrm{d}\ell$, oriented along the normal direction. In two dimensions, the element $\mathrm{d}s$ of the sheet has an infinitesimal 2D doublet of strength $\mathrm{d}\kappa_n = \mu\,\mathrm{d}s$. The resulting velocity fields in 3D and 2D are

$$\mathbf{V}_\mu(\mathbf{r}) = \frac{1}{4\pi} \iint \mu(s,\ell) \left[\frac{\hat{\mathbf{n}}}{|\mathbf{r}-\mathbf{r}'|^3} - 3\,\hat{\mathbf{n}} \cdot (\mathbf{r}-\mathbf{r}') \frac{\mathbf{r}-\mathbf{r}'}{|\mathbf{r}-\mathbf{r}'|^5} \right] \mathrm{d}s\,\mathrm{d}\ell \qquad \text{(3D)} \qquad (2.37)$$

$$\mathbf{V}_\mu(\mathbf{r}) = \frac{1}{2\pi} \int \mu(s) \left[\frac{\hat{\mathbf{n}}}{|\mathbf{r}-\mathbf{r}'|^2} - 2\,\hat{\mathbf{n}} \cdot (\mathbf{r}-\mathbf{r}') \frac{\mathbf{r}-\mathbf{r}'}{|\mathbf{r}-\mathbf{r}'|^4} \right] \mathrm{d}s \qquad \text{(2D)} \qquad (2.38)$$

which are the same as the $\mathbf{V}_\gamma(\mathbf{r})$ fields of the equivalent vortex sheets given by (2.16) and (2.24). This equivalence can be verified with some effort by substituting $\boldsymbol{\gamma} = \hat{\mathbf{n}} \times \widetilde{\nabla}\mu$ into (2.16) or (2.24) and integrating by parts.

Figure 2.5 illustrates the doublet-sheet/vortex-sheet equivalence for 3D and 2D sheets. In general, a linearly-increasing μ is equivalent to a constant-magnitude $\boldsymbol{\gamma}$, and vice versa. At the edge of the doublet sheet, $\mu(s,\ell)$ in effect has a step change to zero. Here $\widetilde{\nabla}\mu$ and the corresponding $\boldsymbol{\gamma}$ have an impulse, which is equivalent to a vortex filament of strength $\Gamma = \mu$ along the sheet edge. Figure 2.6 shows the constant-strength doublet sheet case.
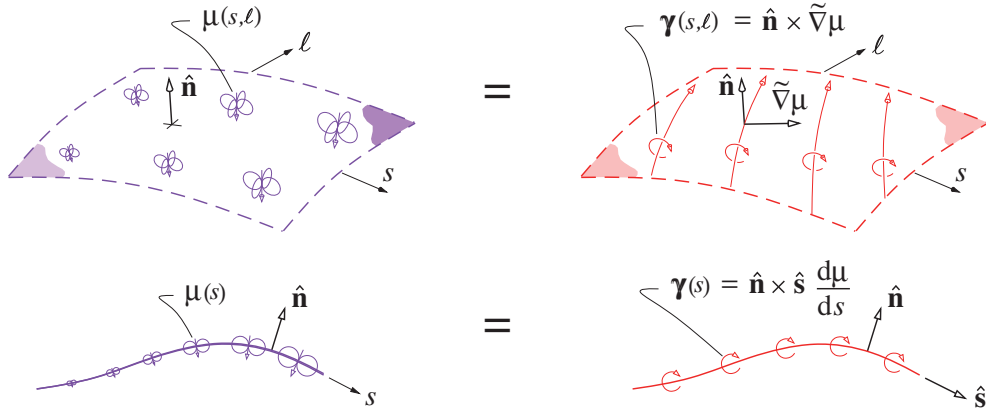
Figure 2.5: Equivalence between normal-doublet sheet and vortex sheet away from edges, for 3D and 2D cases. The doublet and vortex sheets have the same velocity fields.
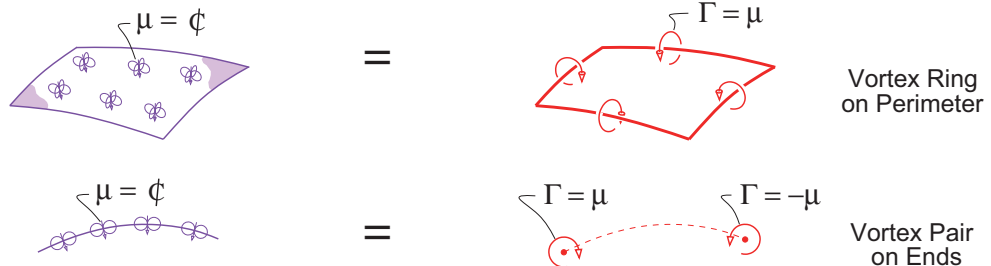
Figure 2.6: Constant-strength normal-doublet sheet with edges, and the equivalent vortex filaments, for 3D and 2D cases.

Because the elimination of the zero-divergence requirement for 3D vorticity is such a great simplification, doublet sheets are heavily favored over vortex sheets in all common 3D panel methods. However, the zero-divergence constraint does not appear in 2D, with the result that vortex sheets tend to be favored over doublet sheets in 2D panel methods. For an extensive review and implementation details of various 2D and 3D panel methods see Katz and Plotkin [4].

In the subsequent discussions and applications here, we will employ either vortex or doublet sheets as most appropriate. In particular, constant-strength doublet panels which are equivalent to vortex rings will be used for 3D configuration analyses in Chapters 5 and 6.

2.6 Integral Velocity / Vorticity-Source Relations

Consider the volume flow rate $\dot{\mathcal{V}}$ outward through a closed surface, defined as the area integral of the normal velocity component over the surface, as shown in Figure 2.7 on the left.

$$\dot{\mathcal{V}} \equiv \oiint \mathbf{V} \cdot \hat{\mathbf{n}} \, d\mathcal{S} \;=\; \iiint_{\text{inside}} \nabla \cdot \mathbf{V} \, d\mathcal{V} \tag{2.39}$$

$$= \iiint_{\text{inside}} \sigma \, dx \, dy \, dz \;+\; \iint_{\text{inside}} \lambda \, ds \, d\ell \;+\; \int_{\text{inside}} \Lambda \, d\ell \;+\; \Sigma \;\equiv\; \Sigma_{\text{inside}} \tag{2.40}$$

The second form in (2.39) follows from Gauss's theorem, for which the volume integral is evaluated over the volume inside the surface. The alternative forms in (2.40) follow from the source density definition (2.1) and the various lumped source sheet, line, and point definitions, and are evaluated over all the source singularities present inside the volume bounded by the surface. The overall result is that $\dot{\mathcal{V}}$ for a closed surface is equal to the sum of all the point sources or integrated volume, sheet, or line source distributions inside.
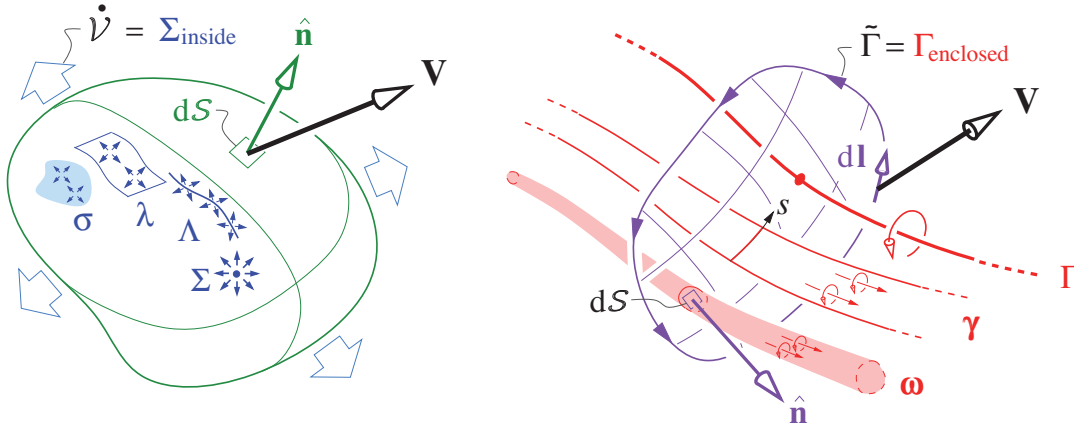
Figure 2.7: Volume outflow $\dot{\mathcal{V}}$ through closed surface (left) is equal to the total integrated source strength of all source density, sheets, filaments, and points inside. Circulation $\tilde{\Gamma}$ over closed circuit (right) is equal to the total circulation of all vorticity, vortex sheets, and vortex filaments enclosed or encircled by the circuit.

Next consider the circulation $\tilde{\Gamma}$ about a closed circuit, defined as the line integral of the tangential velocity component around the circuit, indicated in Figure 2.7 on the right.

$$\tilde{\Gamma} \equiv \oint \mathbf{V} \cdot d\mathbf{l} \;=\; \iint_{\text{enclosed}} (\nabla \times \mathbf{V}) \cdot \hat{\mathbf{n}} \, d\mathcal{S} \tag{2.41}$$

$$= \iint_{\text{enclosed}} \boldsymbol{\omega} \cdot \hat{\mathbf{n}} \, d\mathcal{S} \;+\; \int_{\text{enclosed}} \boldsymbol{\gamma} \cdot \hat{\mathbf{n}} \, ds \;+\; \Gamma \;\equiv\; \Gamma_{\text{enclosed}} \tag{2.42}$$

The second form in (2.41) follows from Stokes's theorem, for which the area integral is understood to be evaluated over any surface bounded by the contour, with $\hat{\mathbf{n}}$ being the unit normal on this surface. The alternative forms in (2.42) follow from the vorticity definition (2.2) and the various lumped vortex sheet and line definitions. The overall result is that the circuit circulation $\tilde{\Gamma}$ is equal to the total strength of all the integrated vorticity, vortex sheets, and vortex filaments enclosed by the circuit. Any vortices outside the circuit have no contribution to $\tilde{\Gamma}$.

2.7 Velocity-Potential Integrals

2.7.1 3D potentials

The velocity fields of the various types of source distributions can be expressed in terms of their velocity potentials, with $\mathbf{V}_\sigma = \nabla \varphi_\sigma$, $\mathbf{V}_\lambda = \nabla \varphi_\lambda$, etc. These are defined by the following superposition integrals.

$$\varphi_\sigma(\mathbf{r}) = \frac{1}{4\pi} \iiint \sigma(\mathbf{r}') \frac{-1}{|\mathbf{r}-\mathbf{r}'|} \, \mathrm{d}x' \, \mathrm{d}y' \, \mathrm{d}z' \tag{2.43}$$

$$\varphi_\lambda(\mathbf{r}) = \frac{1}{4\pi} \iint \lambda(s,\ell) \frac{-1}{|\mathbf{r}-\mathbf{r}'|} \, \mathrm{d}s \, \mathrm{d}\ell \tag{2.44}$$

$$\varphi_\Lambda(\mathbf{r}) = \frac{1}{4\pi} \int \Lambda(\ell) \frac{-1}{|\mathbf{r}-\mathbf{r}'|} \, \mathrm{d}\ell \tag{2.45}$$

$$\varphi_\Sigma(\mathbf{r}) = \frac{\Sigma}{4\pi} \frac{-1}{|\mathbf{r}-\mathbf{r}'|} \tag{2.46}$$

There is no way to explicitly give the potential of 3D vortex sheets, but it is possible to do so for 3D doublet sheets.

$$\varphi_\mu(\mathbf{r}) = \frac{1}{4\pi} \iint \mu(s,\ell) \frac{\hat{\mathbf{n}} \cdot (\mathbf{r}-\mathbf{r}')}{|\mathbf{r}-\mathbf{r}'|^3} \, \mathrm{d}s \, \mathrm{d}\ell \tag{2.47}$$

This is yet another advantage of using doublet sheets in lieu of vortex sheets.

It's again useful to note that as in the general velocity expression (2.13), each potential expression has the same form involving a kernel function. For example, (2.43) can be written as

$$\varphi_\sigma(\mathbf{r}) = \iiint \sigma(\mathbf{r}') \, K(\mathbf{r}-\mathbf{r}') \, \mathrm{d}x' \, \mathrm{d}y' \, \mathrm{d}z' \tag{2.48}$$

$$K(\mathbf{r}-\mathbf{r}') = \frac{1}{4\pi} \frac{-1}{|\mathbf{r}-\mathbf{r}'|} \tag{2.49}$$

where now the scalar kernel function K is the potential field $\varphi(\mathbf{r})$ of a unit point source at $\mathbf{r}'$.

2.7.2 2D potentials

The potentials of source distributions in 2D are given below.

$$\varphi_\sigma(x,z) = \frac{1}{2\pi} \iint \sigma(\mathbf{r}') \ln|\mathbf{r}-\mathbf{r}'| \, \mathrm{d}x' \, \mathrm{d}z' \tag{2.50}$$

$$\varphi_\lambda(x,z) = \frac{1}{2\pi} \int \lambda(s) \ln|\mathbf{r}-\mathbf{r}'| \, \mathrm{d}s \tag{2.51}$$

$$\varphi_\Lambda(x,z) = \frac{\Lambda}{2\pi} \ln|\mathbf{r}-\mathbf{r}'| \tag{2.52}$$

Unlike in 3D, the potentials of vortex sheets and vortex filaments in 2D <u>can</u> be given explicitly:

$$\varphi_\omega(x,z) = \frac{1}{2\pi} \iint -\omega(\mathbf{r}') \arctan\left(\frac{z-z'}{x-x'}\right) \, \mathrm{d}x' \, \mathrm{d}z' \tag{2.53}$$

$$\varphi_\gamma(x,z) = \frac{1}{2\pi} \int -\gamma(s) \arctan\left(\frac{z-z'}{x-x'}\right) \, \mathrm{d}s \tag{2.54}$$

$$\varphi_\Gamma(x,z) = -\frac{\Gamma}{2\pi} \arctan\left(\frac{z-z'}{x-x'}\right) \tag{2.55}$$
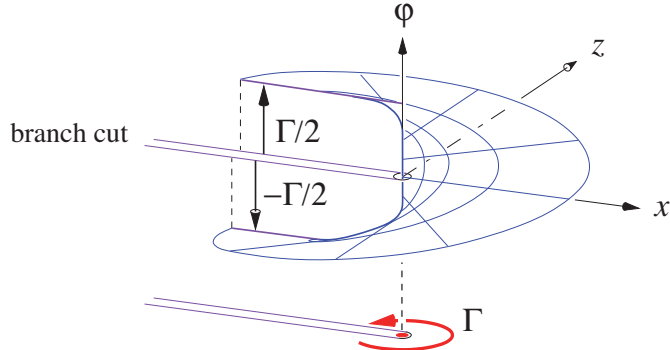
Figure 2.8: Potential of a 2D vortex located at $(x, z) = (0, 0)$. Branch cut accommodates the potential jump of Γ. The sketch corresponds to a negative Γ.

One complication here is that the $\arctan(\ )$ polar angle can contain some arbitrary multiple of 2π. This requires introduction of a *branch cut* extending from the vortex point out to infinity in some direction, as shown in Figure 2.8. The angle jumps by 2π and the potential jumps by Γ across the branch cut.

The branch cut also appears for a doublet sheet, which has the following potential in 2D.

$$\varphi_\mu(x,z) = \frac{1}{2\pi} \int \mu(s) \frac{\hat{\mathbf{n}} \cdot (\mathbf{r} - \mathbf{r}')}{|\mathbf{r} - \mathbf{r}'|^2} \, \mathrm{d}s \tag{2.56}$$

However, the branch cut now is only on the doublet sheet itself. It does not need to extend to infinity like with a vortex, unless the doublet sheet itself extends to infinity. Figure 2.9 compares the branch cuts of a point vortex and a doublet sheet, the latter being equivalent to two point vortices of opposite sign.
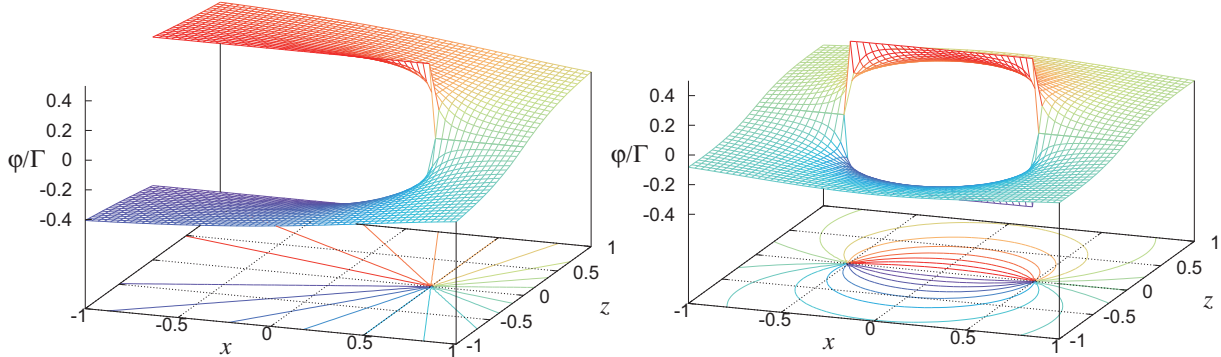
Figure 2.9: Potential of a 2D vortex of strength Γ on the left (same as in Figure 2.8), and of a constant-strength 2D doublet sheet on the right which is equivalent to two equal and opposite vortices $\pm\Gamma$. For the doublet sheet, the branch cut is restricted to the sheet itself.

2.8   Physical Requirements

The velocity field $\mathbf{V}(\mathbf{r})$ description (2.3) via the σ and ω fields is purely mathematical, and in fact can be used to represent <u>any</u> vector field whose divergence and curl are known. In the case of fluid flow, however, physical requirements strongly dictate and frequently simplify the magnitudes and distributions of the σ and ω fields. These physically-dictated simplifications, discussed in this section, are in fact what makes this flow-field representation approach so effective in aerodynamics. Also discussed will be the flow categories where the physical constraints do not provide significant simplification.

2.8.1   Sources in incompressible flow

In the case of effectively-incompressible flow, the low-speed continuity equation (1.85) demands that σ and hence λ, Λ, and Σ are all zero within the flow-field.

$$\nabla \cdot \mathbf{V} = 0$$
$$\rightarrow \quad \sigma = \lambda = \Lambda = \Sigma = 0 \qquad \text{(within flow-field)} \tag{2.57}$$

However, it is perfectly acceptable to have nonzero *fictitious sources* outside the physical flow-field, either within a body or on a flow boundary. Figure 2.10 shows impermissible and permissible uses of sources to represent an incompressible velocity field. The rightmost figure shows the typical use of *image singularities* to represent the effect of a solid wall boundary.
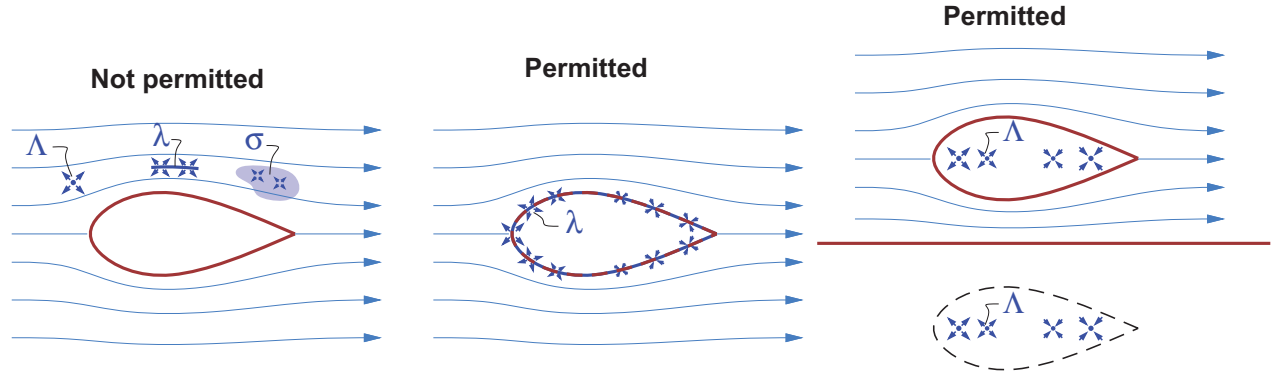
Figure 2.10: Sources within an incompressible flow-field are not permitted by continuity. Fictitious sources inside a body, on a boundary, or outside the physical flow-field are permissible.

2.8.2   Sources in compressible flow

In a compressible flow, with significant density variations, the source distribution σ within the flow-field will in general be nonzero. This can be seen by computing σ using the steady continuity equation (1.33).

$$\nabla \cdot (\rho \mathbf{V}) = 0$$
$$\rho \nabla \cdot \mathbf{V} + \nabla \rho \cdot \mathbf{V} = 0$$
$$\nabla \cdot \mathbf{V} \equiv \sigma = -\frac{1}{\rho} \nabla \rho \cdot \mathbf{V} \tag{2.58}$$

Hence, σ is nonzero wherever the density gradient has a component along the velocity vector. In the irrotational part of the flow outside the viscous layers, the density gradient is uniquely related to the speed gradient via the isentropic $\rho_{(h)}$ relation (1.69), and the adiabatic flow assumption of a constant total enthalpy h_o.

$$\frac{\nabla \rho}{\rho} = \frac{1}{\gamma - 1} \frac{\nabla h}{h} = \frac{\nabla (h_o - \frac{1}{2} V^2)}{a^2} = -\frac{\nabla (\frac{1}{2} V^2)}{a^2} = -V \frac{\nabla V}{a^2} \tag{2.59}$$

Inserting this into (2.58) gives an alternative relation for σ in terms of the streamwise speed gradient and the local Mach number,

$$\sigma = V \frac{\nabla V}{a^2} \cdot \mathbf{V} = V^2 \frac{\nabla V}{a^2} \cdot \hat{\mathbf{s}} = M^2 \frac{\partial V}{\partial s} \tag{2.60}$$

where $\hat{\mathbf{s}}$ was assumed to be parallel to $\mathbf{V}$, with s being the arc length along a streamline. Figure 2.11 shows the typical positive and negative σ field source distributions in the vicinity of a high-speed airfoil.
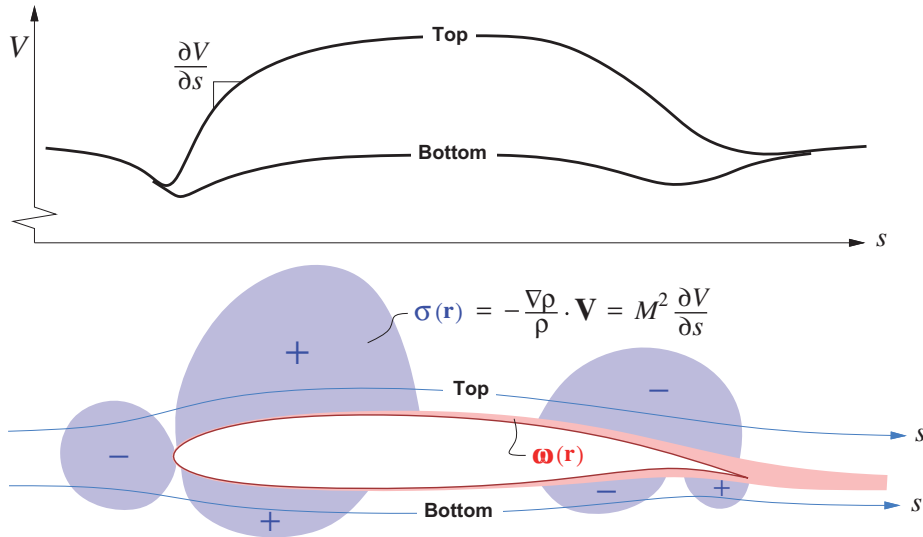
Figure 2.11: Positive and negative source distributions associated with streamwise density gradients, or the related speed gradients, near an airfoil in a compressible flow. The thin viscous vorticity layer is also shown.

The source-superposition integrals (2.4) or (2.23) still correctly define the velocity field from the σ field in this case, and indeed will be used in Chapter 8 to qualitatively investigate and explain compressible-flow behavior. However, because the σ distributions near the airfoil are not necessarily compact and close to the airfoil, they cannot be lumped onto the airfoil surface as source sheets without seriously degrading the accuracy of the resulting velocity field. Hence, σ must be treated as a volume quantity which makes the evaluation of the superposition integrals (2.4) or (2.23) computationally demanding.

A major consequence here is that quantitatively representing a compressible flow-field with sources and vortices is computationally cumbersome and quite impractical, at least in 3D. For this reason, CFD methods used for calculation of compressible flows typically use space-filling grids as shown in Figure 2.1 on which $V(\mathbf{r})$ or $\varphi(\mathbf{r})$ are defined by interpolation, and σ or ω are not explicitly considered.

One exception is the case of *small-disturbance compressible flows* where the velocity everywhere departs only slightly from the freestream. In this case the effects of the nonzero σ field can be captured by the Prandtl-Glauert coordinate transformation, which will be addressed in Chapter 8.

2.8.3 Vorticity in high Reynolds number flows

The Helmholtz vorticity transport equation (1.95) dictates that an aerodynamic flow which is uniform upstream will have zero vorticity everywhere, except in boundary layers and wakes where the action of viscous stress is significant. As sketched in Figure 1.9, at high Reynolds number these vortical regions are thin compared to the body dimensions, which makes them natural candidates for lumping into sheets or filaments with only a small loss of accuracy. Figure 2.12 shows such an approximate representation of an airfoil flow-field via a variable-strength vortex sheet placed on the airfoil surface. In this vortex sheet model, the irrotational inviscid flow extends all the way to the surface. Note also that in the 2D case there is no need to place a vortex sheet on the wake, since the net vorticity integrated across the wake is essentially zero. Chapter 3 will examine this flow-field model in more detail, and improve it for cases where the viscous layer is not particularly thin.
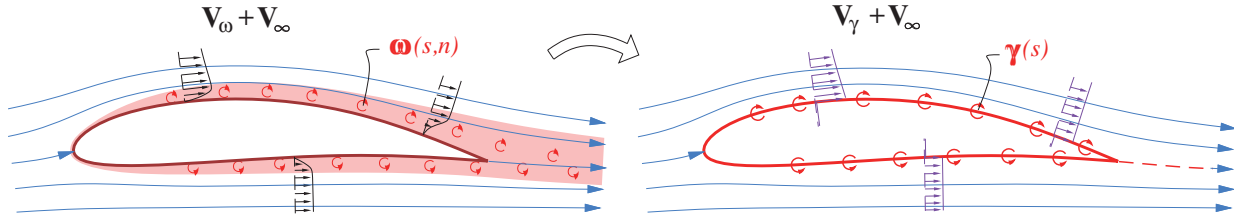
Figure 2.12: Physical vorticity $\boldsymbol{\omega}(s,n)$ in thin boundary layer is lumped into vortex sheet $\boldsymbol{\gamma}(s)$ placed on the airfoil surface. Outside the boundary layer, there is typically very little difference between the actual $\mathbf{V}_\omega(\mathbf{r})$ field and the approximated $\mathbf{V}_\gamma(\mathbf{r})$ field. This model is further examined and improved in Chapter 3.

2.9   Flow-Field Modeling with Source and Vortex Sheets

The representation of low-speed aerodynamic flow-fields using source, vortex, and doublet sheets, when possible, is attractive for a number of reasons.

- In a typical aerodynamic flow with thin viscous layers, very little accuracy is lost when vorticity $\boldsymbol{\omega}$ in the layers is lumped into vortex sheets $\boldsymbol{\gamma}$ placed on the body and wake surfaces. This is equivalent to the usual inviscid-flow approximation. Chapter 3 examines this model's limitations and gives modifications to greatly improve its accuracy for cases where the viscous layers are not very thin.

- Only the body surfaces and possibly trailing wake surfaces need to be geometrically defined. In contrast, directly defining a velocity field $\mathbf{V}(\mathbf{r})$ requires construction of a space-filling grid throughout the flow-field.

- Numerical panel methods, which employ the sheet representation, require roughly $1/100$ fewer unknowns than corresponding grid methods for any given level of accuracy.

- In cases where the velocity jumps $\Delta\mathbf{V}$ or potential jumps $\Delta\varphi$ across the sheets are known, the source, vortex, or doublet sheet strengths can be computed immediately. The defining relations are derived in Appendix B, and restated here:

$$\lambda \;=\; \hat{\mathbf{n}}\cdot\Delta\mathbf{V} \tag{2.61}$$
$$\boldsymbol{\gamma} \;=\; \hat{\mathbf{n}}\times\Delta\mathbf{V} \tag{2.62}$$
$$\mu \;=\; \Delta\varphi \tag{2.63}$$

2.9.1   Source sheet applications

A source sheet can be used to exactly represent the inviscid low speed flow about a non-lifting body, as sketched in the middle of Figure 2.10. The sheet is placed everywhere on the surface, which together with an added freestream defines the total velocity field.

$$\mathbf{V}(\mathbf{r}) \;=\; \frac{1}{4\pi}\iint \lambda(s,\ell)\,\frac{(\mathbf{r}-\mathbf{r}')}{|\mathbf{r}-\mathbf{r}'|^3}\,\mathrm{d}s\,\mathrm{d}\ell \;+\; \mathbf{V}_\infty \tag{2.64}$$

For the usual impermeable body, this velocity must be tangent to the body surface everywhere. Setting the field points just outside the surface at $\mathbf{r} = (s,\ell,0^+)$, this requirement is

$$\mathbf{V}(s,\ell,0^+)\cdot\hat{\mathbf{n}}(s,\ell) \;=\; 0. \tag{2.65}$$

Substitution of (2.64) into (2.65) results in

$$\frac{1}{4\pi} \iint \lambda_{(s,\ell)} \frac{(\mathbf{r}-\mathbf{r}') \cdot \hat{\mathbf{n}}}{|\mathbf{r}-\mathbf{r}'|^3} \, \mathrm{d}s \, \mathrm{d}\ell \;=\; -\mathbf{V}_\infty \cdot \hat{\mathbf{n}}_{(s,\ell)} \quad ; \qquad \mathbf{r} \;=\; \mathbf{r}_{(s,\ell,0^+)} \qquad (2.66)$$

which is an *integral equation* for the unknown sheet strength $\lambda_{(s,\ell)}$. In practice, an approximate numerical solution can be obtained by a panel method, which discretizes the surface into a large number of small panels, and determines a piecewise-constant value of λ over each such panel, such that equation (2.66) is satisfied at one control point on each panel. These λ values can then be substituted into (2.64) which allows numerical calculation of the local $\mathbf{V}$ at any chosen point $\mathbf{r}$, together with the local pressure via Bernoulli's equation (1.109). This thus defines the flow-field. See Katz and Plotkin [4] for the extensive details.

2.9.2 Vortex sheet applications

Source sheets have the disadvantage that they cannot by themselves represent a lifting flow. This problem can be addressed by switching to vortex or doublet sheets, again placed on the body surface, as sketched on the right side of Figure 2.12. In 2D, the velocity of a vortex sheet plus freestream has the following form.

$$\mathbf{V}_{(\mathbf{r})} \;=\; \frac{1}{2\pi} \int \gamma_{(s)} \frac{\hat{\mathbf{y}} \times (\mathbf{r}-\mathbf{r}')}{|\mathbf{r}-\mathbf{r}'|^2} \, \mathrm{d}s \;+\; \mathbf{V}_\infty \qquad (2.67)$$

Like in the source-sheet case, the requirement of flow tangency $\mathbf{V} \cdot \hat{\mathbf{n}} = 0$ gives an integral equation for the vortex sheet strength.

$$\frac{1}{2\pi} \int \gamma_{(s)} \frac{\hat{\mathbf{y}} \times (\mathbf{r}-\mathbf{r}') \cdot \hat{\mathbf{n}}}{|\mathbf{r}-\mathbf{r}'|^2} \, \mathrm{d}s \;=\; -\mathbf{V}_\infty \cdot \hat{\mathbf{n}} \qquad (2.68)$$

In addition, it is also necessary to impose a *Kutta Condition* to model the smooth flow off the trailing edge, which is what's seen in a real viscous flow. In the vortex sheet model this requires that the summed sheet strength of the upper and lower surfaces be zero at the trailing edge.

$$\gamma_{TE_{\mathrm{upper}}} \;+\; \gamma_{TE_{\mathrm{lower}}} \;=\; 0 \qquad (2.69)$$

The solution for the unknown $\gamma_{(s)}$ can be again obtained by a panel method.

2.10 Modeling Non-uniqueness

In any given practical application, the flow-field representation via sources or vortices is non-unique, in that different source, vortex, and freestream combinations can give the same velocity field. For example, the source sheet superposition (2.64) and the vortex sheet superposition (2.67) can both represent exactly the same (non-lifting) flow-field about the body. There will be a different velocity within the body, but that is physically irrelevant.

The non-uniqueness extends even to the freestream component of the flow-field. For example, in the general velocity superposition (2.3) the freestream can be represented either as a specified constant, or via infinite source sheets or vortex sheets, as sketched in Figure 2.13. Using a constant added $\mathbf{V}_b$ to represent a uniform flow is of course the simplest and the preferred approach in applications.

This representation non-uniqueness gives rise to many different possible types of panel methods, based either on source sheets, or vortex/doublet sheets, or both. Katz and Plotkin [4] give an overview of many such alternative formulations.
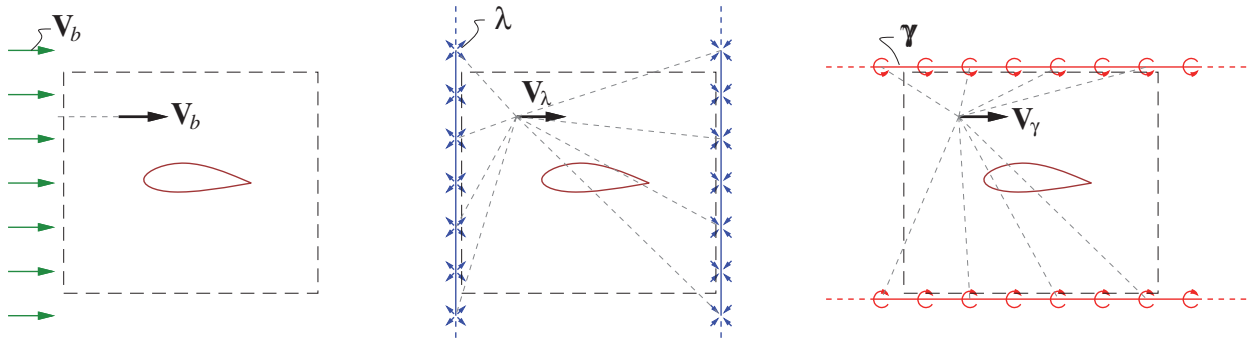
Figure 2.13: Three methods for imposing a uniform velocity (e.g. to represent a freestream $\mathbf{V}_\infty$) on the region of interest inside the dashed box: via the uniform added velocity $\mathbf{V}_b$, via two infinite source sheets, and via two infinite vortex sheets. All are valid, but using $\mathbf{V}_b$ is simplest. The three representations also have different velocities outside the dashed box.

2.11   2D Far-Field Approximations

The lumping process described in Section (2.3) made ad-hoc simplifications to the kernel functions, which introduced some unknown amount of error in the resulting simplified velocity fields. In this section the kernel function approximation will be made more precise by using a Taylor series. This will give the option of increasing the accuracy of the lumped model, and will also give insight into the behavior of the *far-field*, or flow-field far from the body. The detailed derivation will be performed for the velocity potential in the 2D case for simplicity. The corresponding 3D results will be summarily presented in the next section.

2.11.1   2D source and vortex distribution far-field

By combining and recasting (2.50) and (2.53), arbitrary distributions of source and vorticity in 2D are seen to have the following perturbation potential field φ, as sketched in Figure 2.14. The $\ln R$ and Θ kernel functions are defined for convenience.

$$\varphi(x,z) \;=\; \frac{1}{2\pi} \iint (\sigma \, \ln R \,-\, \omega \, \Theta) \; \mathrm{d}x' \, \mathrm{d}z' \tag{2.70}$$

$$\ln R_{(x,z\,;\,x',z')} \;\equiv\; \ln \sqrt{(x-x')^2 + (z-z')^2} \tag{2.71}$$

$$\Theta_{(x,z\,;\,x',z')} \;\equiv\; \arctan \frac{z-z'}{x-x'} \tag{2.72}$$

We now consider the case where the field point distance r is large compared to the extent of the source and vorticity distributions, and we choose the origin to be located somewhere near these distributions. In these circumstances, the kernel functions $\ln R$ and Θ will not change very much with respect to x' and z' within the integration region, as indicated in Figure 2.14. Hence, they can be approximated well by their Taylor series in x' and z' about the local origin $(x', z') = (0,0)$,

$$
\begin{aligned}
\ln R \;&=\; \ln R \Big|_{0,0} \;+\; \frac{\partial \ln R}{\partial x'}\Big|_{0,0} x' \;+\; \frac{\partial \ln R}{\partial z'}\Big|_{0,0} z' \;+\; \text{H.O.T.} \\[2mm]
&=\; \ln r \;-\; \frac{x}{r^2}\, x' \;-\; \frac{z}{r^2}\, z' \;+\; \text{H.O.T.} \quad ; \quad r \equiv \sqrt{x^2 + z^2} \\[4mm]
\Theta \;&=\; \Theta \Big|_{0,0} \;+\; \frac{\partial \Theta}{\partial x'}\Big|_{0,0} x' \;+\; \frac{\partial \Theta}{\partial z'}\Big|_{0,0} z' \;+\; \text{H.O.T.} \\[2mm]
&=\; \theta \;+\; \frac{z}{r^2}\, x' \;-\; \frac{x}{r^2}\, z' \;+\; \text{H.O.T.} \quad ; \quad \theta \equiv \arctan \frac{z}{x}
\end{aligned}
$$
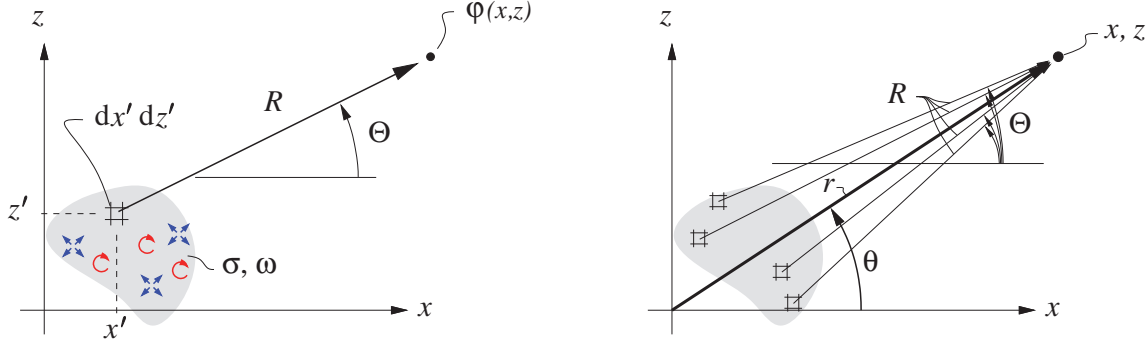
Figure 2.14: Potential superposition of 2D source and vorticity distributions. If the distributions are compact compared to the field-point distance r, the kernel functions $\ln R$ and Θ will vary only slightly, and hence can be well-approximated by Taylor series about their origin values $\ln r$ and θ.

where H.O.T. denotes higher-order terms with $x'^2, z'^2, x'z', x'^3$, etc. Substituting these Taylor series into the $\varphi_{(x,z)}$ integral (2.70) above, and rearranging gives

$$
\begin{aligned}
2\pi\,\varphi_{(x,z)} \;=\;& \iint \left\{ \sigma\left(\ln r - \frac{x}{r^2}x' - \frac{z}{r^2}z' \right) + \omega\left(-\theta - \frac{z}{r^2}x' + \frac{x}{r^2}z' \right) + \text{H.O.T.} \right\} \mathrm{d}x'\,\mathrm{d}z' \\
=\;& \left[\iint \sigma\,\mathrm{d}x'\,\mathrm{d}z' \right] \ln r - \left[\iint \omega\,\mathrm{d}x'\,\mathrm{d}z' \right] \theta \\
&+ \left[\iint \left(-\sigma x' + \omega z' \right) \mathrm{d}x'\,\mathrm{d}z' \right] \frac{x}{r^2} + \left[\iint \left(-\sigma z' - \omega x' \right) \mathrm{d}x'\,\mathrm{d}z' \right] \frac{z}{r^2} + \text{H.O.T.} \quad (2.73)
\end{aligned}
$$

with (2.73) being the result after the powers of x and z are collected and taken outside the $x'z'$ integrals. In terms of the convenient shorthand definitions

$$
\Lambda \;\equiv\; \iint \sigma\,\mathrm{d}x'\,\mathrm{d}z' \tag{2.74}
$$

$$
\Gamma \;\equiv\; \iint \omega\,\mathrm{d}x'\,\mathrm{d}z' \tag{2.75}
$$

$$
\kappa_x \;\equiv\; \iint \left(-\sigma x' + \omega z' \right) \mathrm{d}x'\,\mathrm{d}z' \tag{2.76}
$$

$$
\kappa_z \;\equiv\; \iint \left(-\sigma z' - \omega x' \right) \mathrm{d}x'\,\mathrm{d}z' \tag{2.77}
$$

equation (2.73) is a *far-field expansion* for the perturbation potential

$$
\varphi_{(x,z)} \;\simeq\; \varphi_{\text{ff}(x,z)} \;\equiv\; \frac{\Lambda}{2\pi}\ln r - \frac{\Gamma}{2\pi}\theta + \frac{\kappa_x}{2\pi}\frac{x}{r^2} + \frac{\kappa_z}{2\pi}\frac{z}{r^2} \tag{2.78}
$$

which is approximate because the higher-order terms have been dropped from the Taylor series. Taking the gradient and adding the freestream part gives the corresponding far-field expansion for the total velocity.

$$
\begin{aligned}
\mathbf{V}_{(x,z)} \;\simeq\; \mathbf{V}_{\text{ff}(x,z)} \;\equiv\;& \mathbf{V}_\infty + \nabla\varphi_{\text{ff}} \\
=\;& \mathbf{V}_\infty + \frac{\Lambda}{2\pi}\frac{x\,\hat{\mathbf{x}} + z\,\hat{\mathbf{z}}}{r^2} + \frac{\Gamma}{2\pi}\frac{z\,\hat{\mathbf{x}} - x\,\hat{\mathbf{z}}}{r^2} \\
&+ \frac{\kappa_x}{2\pi}\frac{(z^2 - x^2)\,\hat{\mathbf{x}} - 2xz\,\hat{\mathbf{z}}}{r^4} + \frac{\kappa_z}{2\pi}\frac{-2xz\,\hat{\mathbf{x}} + (x^2 - z^2)\,\hat{\mathbf{z}}}{r^4} \tag{2.79}
\end{aligned}
$$

Replacing the exact velocity $\mathbf{V}_{(x,z)}$ with the approximate $\mathbf{V}_{\text{ff}(x,z)}$ is equivalent to replacing the σ and ω distributions with the corresponding $\Lambda, \Gamma, \kappa_x, \kappa_z$, filaments as indicated by Figure 2.15. These Λ and Γ are

equivalent to those obtained by the lumping procedure described in the previous sections. However, the added doublet κ_x and κ_z terms are new, and can be considered as corrections for the errors due to lumping in cases where the the chosen lumped source and vortex location is offset from the centroids of the σ and ω distributions.
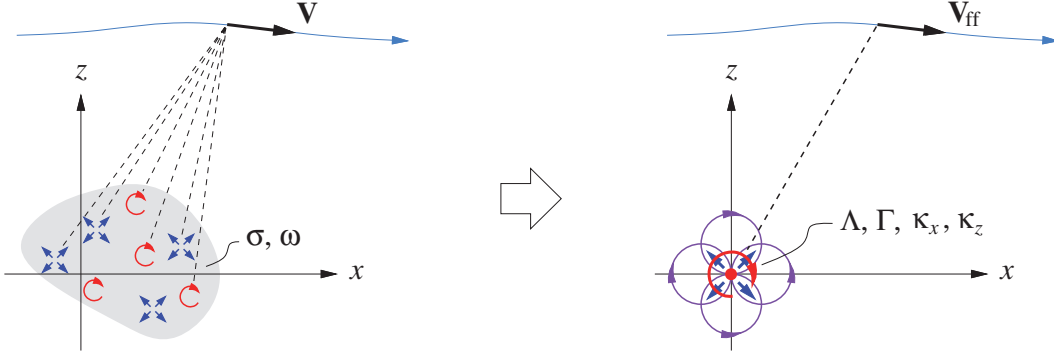
Figure 2.15: Far-field approximation obtained by replacing $\sigma(x,z)$ and $\omega(x,z)$ distributions or sheet $\lambda(s)$ and $\gamma(s)$ configurations with the much simpler filament singularities.

For cases where the starting distributions are source and vortex <u>sheets</u> with strengths $\lambda(s)$ and $\gamma(s)$, the far-field coefficients would be defined as

$$\Lambda \equiv \int \lambda \; \mathrm{d}s \tag{2.80}$$

$$\Gamma \equiv \int \gamma \; \mathrm{d}s \tag{2.81}$$

$$\kappa_x \equiv \int \left(-\lambda x' + \gamma z'\right) \; \mathrm{d}s \tag{2.82}$$

$$\kappa_z \equiv \int \left(-\lambda z' - \gamma x'\right) \; \mathrm{d}s \tag{2.83}$$

where the parametric functions $x'(s)$, $z'(s)$ specify the sheet geometry or geometries. The integrals are evaluated over all the sheets present.

Application of the far-field potential or velocity expressions (2.78) or (2.79) requires knowing the values of the coefficients $\Lambda, \Gamma, \kappa_x, \kappa_z$. However, obtaining these from their definitions (2.80)–(2.83) is not possible in the typical situation where the field stregths σ, ω or sheet strengths λ, γ are not known without additional information or modeling. The subsequent sections will describe alternative means for computing the coefficients from other relevant properties of the aerodynamic body.

2.11.2 Far-field effect of lift and drag

As derived in detail in Appendix C, the far-field vortex and source are related to the airfoil lift/span L' and drag/span D', or equivalently to the 2D lift and drag coefficients c_ℓ and c_d based on the airfoil chord c.

$$\Gamma = \frac{L'}{\rho V_\infty} = \frac{1}{2}V_\infty \, c \, c_\ell \tag{2.84}$$

$$\Lambda = \frac{D'}{\rho V_\infty} = \frac{1}{2}V_\infty \, c \, c_d \tag{2.85}$$

Relation (2.84) is the well-known Kutta-Joukowsky lift theorem. Relation (2.85) is perhaps less familiar, but can be considered as the complementing theorem for the drag. Note that unstalled 2D airfoils typically

have $c_d \ll c_\ell$ and thus $\Lambda \ll \Gamma$, and hence the vortex term dominates the source term in typical airfoil far-fields. In contrast, the source term is dominant for 2D bluff-body flows which typically have large drag and comparatively little or no lift.

2.11.3 Far-field effect of thickness

Using a simplification of the models presented in Appendix D, the flow about a non-lifting thin airfoil of thickness distribution $t(x)$ can be represented by superimposing the freestream with a source sheet on the chord line, as shown in Figure 2.16. The required sheet strength $\lambda(x)$ is determined by mass conservation applied to the local control volume.
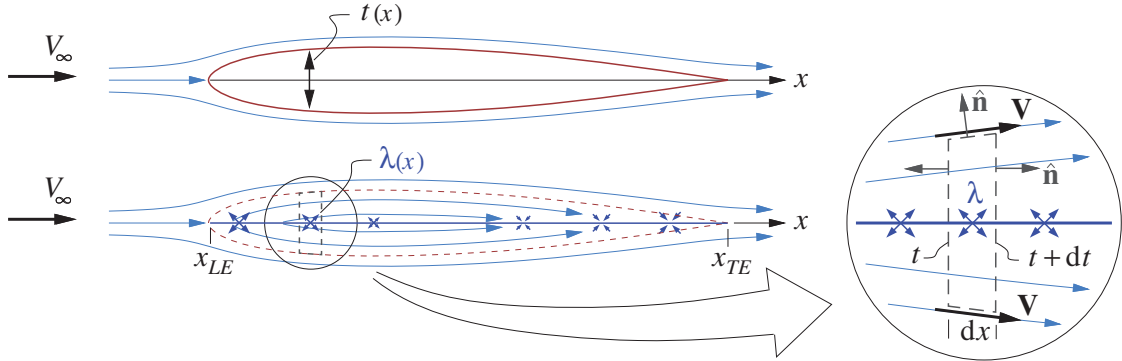
Figure 2.16: Flow about slender 2D airfoil represented by a source sheet of variable strength $\lambda(x)$.

The total velocity is required to be tangent to the top and bottom of the control volume, since that lies on the airfoil surface. Using the 2D version of result (2.39), the net outflow from the source sheet inside the control volume is therefore equal to the volume flow difference between the left and right faces of height t and $t+\mathrm{d}t$. This gives the required source sheet strength distribution.

$$\lambda\,\mathrm{d}x \;=\; \oint \mathbf{V}\cdot\hat{\mathbf{n}}\;\mathrm{d}l \;=\; V_\infty(t+\mathrm{d}t) \,-\, V_\infty t \;=\; V_\infty\,\mathrm{d}t$$

$$\lambda(x) \;=\; V_\infty \frac{\mathrm{d}t}{\mathrm{d}x} \tag{2.86}$$

This is the same as result D.17) obtained for the general airfoil case, so the assumption of a non-lifting airfoil is justified here. The source sheet extends over $x_{LE}\dots x_{TE}$ (rather than say $0\dots c$) since $x=0$ is the chosen location where the far-field singularities are to be placed, as indicated in Figure 2.15. This is not necessarily the leading edge.

From the κ_x definition (2.82), with $\gamma = 0$ for this case, we have

$$\kappa_x \;=\; \int_{x_{LE}}^{x_{TE}} -\lambda\,x\;\mathrm{d}x \;=\; V_\infty\int_{x_{LE}}^{x_{TE}} -\frac{\mathrm{d}t}{\mathrm{d}x}\,x\;\mathrm{d}x \tag{2.87}$$

where x has been used for both the sheet geometry x' and the integration coordinate s. The last integral above can be integrated by parts.

$$\kappa_x \;=\; V_\infty\int_{x_{LE}}^{x_{TE}} -\frac{\mathrm{d}t}{\mathrm{d}x}\,x\;\mathrm{d}x \;=\; -V_\infty\,t\,x\,\Big|_{x_{LE}}^{x_{TE}} \,+\, V_\infty\int_{x_{LE}}^{x_{TE}} t\;\mathrm{d}x$$

The first term on the right vanishes since $t(x_{LE}) = t(x_{TE}) = 0$ at the leading and trailing edges, and the rightmost integral is the airfoil area $A=\int_{x_{LE}}^{x_{TE}} t\;\mathrm{d}x$. This gives a simple result for the x doublet strength.

$$\kappa_x \;=\; V_\infty\,A \tag{2.88}$$

This result is strictly valid only if the airfoil is thin, which is required for accuracy of the source sheet model. For airfoils of moderate thickness, a better empirical estimate is

$$\kappa_x = V_\infty A \left(1 + \frac{t_{\max}}{c} \right) \tag{2.89}$$

where $t_{\max}$ is the maximum airfoil thickness and $c = x_{TE} - x_{LE}$ is the airfoil chord.

2.11.4   Far-field effect of lift's pitching moment

Again following the thin airfoil theory model of Appendix D, the lift distribution on a thin cambered airfoil can be represented by superimposing the freestream with a vortex sheet placed along the chord line. As shown in Figure 2.17, this results in a jump in tangential velocity equal to the local sheet strength.

$$\Delta u(x) = \gamma(x)$$
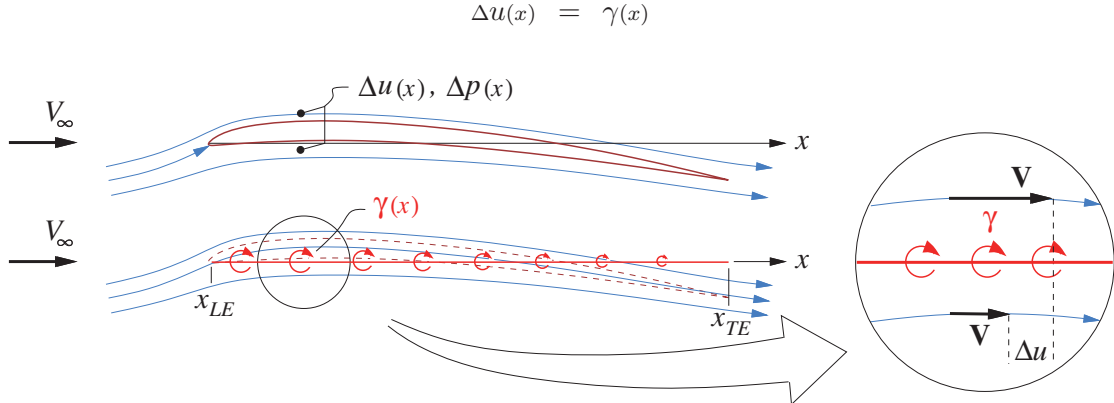
Figure 2.17: Tangential velocity jump $\Delta u(x)$ across thin lifting airfoil, and corresponding pressure load distribution $\Delta p(x)$, represented by a vortex sheet of variable strength $\gamma(x)$.

The corresponding pressure jump from Bernoulli's equation is

$$\begin{aligned} \Delta p(x) &= \frac{1}{2}\rho \left[(V_\infty + \Delta u/2)^2 - (V_\infty - \Delta u/2)^2 \right] \\ &= \rho V_\infty \Delta u \\ &= \rho V_\infty \gamma \end{aligned} \tag{2.90}$$

which is in effect a local Kutta-Joukowsky relation. The pitching moment/span of the airfoil about the origin, defined positive nose up, is then obtained by integrating this loading with the moment arm $-x$.

$$M'_0 = \int_{x_{LE}}^{x_{TE}} -\Delta p\, x\, \mathrm{d}x = \rho V_\infty \int_{x_{LE}}^{x_{TE}} -\gamma\, x\, \mathrm{d}x \tag{2.91}$$

From the κ_z definition (2.83), with $\lambda=0$ for this case, we also have

$$\kappa_z = \int_{x_{LE}}^{x_{TE}} -\gamma\, x\, \mathrm{d}x \tag{2.92}$$

where again x has been used for both x' and s. Comparing (2.91) and (2.92) gives the z-doublet in terms of the pitching moment/span, or equivalently in terms of the pitching moment coefficient c_{m_0} about the origin.

$$\kappa_z = \frac{M'_0}{\rho V_\infty} = \frac{1}{2}c^2 V_\infty c_{m_0} \tag{2.93}$$

It's important to note that M_0' is defined about the origin of the far-field coefficient integrals (2.74)–(2.77). This is also the same location that is used to place the far-field singularities, and in particular the vortex. If a moment M_{ref}' about some other location x_{ref} is to be used to calculate κ_z, it's necessary to derive the equivalent M_0' from it by using the moment-reference shift relation.

$$M_0' = M_{\text{ref}}' - x_{\text{ref}} L' \tag{2.94}$$

$$\text{or} \quad c_{m_0} = c_{m_{\text{ref}}} - \frac{x_{\text{ref}}}{c} c_\ell \tag{2.95}$$

This M_0' or c_{m_0} can then be used to obtain κ_z from (2.93) as before.

2.11.5 Doublet orientation

The x and z doublet expressions (2.89) and (2.93) have been derived for the case where the freestream is along the x axis. For the more general case where $\mathbf{V}_\infty$ has an angle α relative to the x axis, these doublet expressions actually give the streamwise and normal doublets relative to the freestream direction.

$$\kappa_s = V_\infty A \left(1 + \frac{t_{\max}}{c} \right) \tag{2.96}$$

$$\kappa_n = \frac{1}{2} c^2 V_\infty c_{m_0} \tag{2.97}$$

The corresponding cartesian κ_x and κ_z are then obtained from these by a rotation transformation.

$$\kappa_x = \kappa_s \cos\alpha - \kappa_n \sin\alpha = \kappa_s \frac{u_\infty}{V_\infty} - \kappa_n \frac{w_\infty}{V_\infty} \tag{2.98}$$

$$\kappa_z = \kappa_s \sin\alpha + \kappa_n \cos\alpha = \kappa_s \frac{w_\infty}{V_\infty} + \kappa_n \frac{u_\infty}{V_\infty} \tag{2.99}$$

In general, a doublet strength is a vector $\boldsymbol{\kappa}$ whose components depend on the orientation of the chosen coordinate axes. These components also obey the usual transformation relations due to axes rotation.

2.11.6 2D far-field observations

A number of observations about the 2D far-field expansion can be made.

- It is rather fortuitous that the airfoil quantities which are of the most interest for engineering — lift, drag, moment, area and thickness — are also the quantities which are needed to estimate the velocity field far from the airfoil.

- All the $\mathbf{V}_{\text{ff}}$ terms in (2.79) after $\mathbf{V}_\infty$ decay to zero with increasing distance r, so very far away we have $\mathbf{V}_{\text{ff}} \simeq \mathbf{V}_\infty$ as expected. However, for moderate distances from the airfoil, the far-field terms give a much better approximation to the actual $\mathbf{V}$.

- The various far-field terms in (2.79) after $\mathbf{V}_\infty$ have different rates of decay with distance. The Λ and Γ terms decay as $1/r$, while the κ_x and κ_z doublet terms decay as $1/r^2$. In practice this means that at sufficiently large distances, the doublet terms can be dropped from the expansion with little loss in accuracy. Conversely, when sufficiently close to the airfoil the doublet terms may very well dominate.

- If only one type of singularity is present (e.g. only vorticity but no source density), and if in addition the overall lumped vortex strength Γ is nonzero, then the far-field doublets can be made to vanish by a suitable choice of the vortex location, which is then defined as the vorticity centroid. In the case of the thin airfoil, this location is also the center of lift, defined as the point about which the pitching moment is zero.

2.12   3D Far-Fields

The 3D potential of a source distribution is given by (2.43), with the kernel's distance function R again defined for convenience.

$$\varphi(\mathbf{r}) = \frac{1}{4\pi} \iiint \sigma(\mathbf{r}') \frac{-1}{R} \, \mathrm{d}x' \, \mathrm{d}y' \, \mathrm{d}z' \tag{2.100}$$

$$R \equiv |\mathbf{r} - \mathbf{r}'| = \sqrt{(x-x')^2 + (y-y')^2 + (z-z')^2} \tag{2.101}$$

As in the 2D case, the kernel function $1/R$ is now expanded as a Taylor series about the origin $\mathbf{r}' = \mathbf{0}$, this time using compact vector notation.

$$
\begin{aligned}
\frac{1}{R} &= \left.\frac{1}{R}\right|_{\mathbf{0}} + \left.\nabla\left(\frac{1}{R}\right)\right|_{\mathbf{0}} \cdot \mathbf{r}' + \text{H.O.T.} \\
&= \frac{1}{r} - \frac{\mathbf{r} \cdot \mathbf{r}'}{r^3} + \text{H.O.T.} \\
r &\equiv |\mathbf{r}| = \sqrt{x^2 + y^2 + z^2}
\end{aligned}
\tag{2.102}
$$

Substituting (2.102) into (2.100) and dropping the higher order terms gives the corresponding 3D source-far-field approximation.

$$
\begin{aligned}
\varphi(\mathbf{r}) \simeq \varphi_{\text{ff}}(\mathbf{r}) &\equiv \frac{\Sigma}{4\pi}\frac{-1}{r} + \frac{\boldsymbol{\mathcal{K}} \cdot \mathbf{r}}{4\pi}\frac{1}{r^3} \\
&= \frac{\Sigma}{4\pi}\frac{-1}{r} + \frac{\mathcal{K}_x}{4\pi}\frac{x}{r^3} + \frac{\mathcal{K}_y}{4\pi}\frac{y}{r^3} + \frac{\mathcal{K}_z}{4\pi}\frac{z}{r^3}
\end{aligned}
\tag{2.103}
$$

$$\Sigma = \iiint \sigma \, \mathrm{d}x' \, \mathrm{d}y' \, \mathrm{d}z' = \int \Lambda \, \mathrm{d}\ell \tag{2.104}$$

$$\mathcal{K}_x = \iiint -\sigma \, x' \, \mathrm{d}x' \, \mathrm{d}y' \, \mathrm{d}z' = \int -\Lambda \, x' \, \mathrm{d}\ell \tag{2.105}$$

$$\mathcal{K}_y = \iiint -\sigma \, y' \, \mathrm{d}x' \, \mathrm{d}y' \, \mathrm{d}z' = \int -\Lambda \, y' \, \mathrm{d}\ell \tag{2.106}$$

$$\mathcal{K}_z = \iiint -\sigma \, z' \, \mathrm{d}x' \, \mathrm{d}y' \, \mathrm{d}z' = \int -\Lambda \, z' \, \mathrm{d}\ell \tag{2.107}$$

The second integrals in (2.104)–(2.107) would be used for the case where the starting source distribution is a filament $\Lambda(\ell)$ rather than a volume source density. Like in the 2D case, a 3D doublet strength $\boldsymbol{\mathcal{K}}$ is a vector whose three components depend on the chosen axes. Its being a vector is also what allows (2.103) to have its coordinate-independent form.

2.12.1   3D far-field effect of drag

A 3D body with profile drag will have a viscous wake with some velocity defect $\Delta u_{\text{wake}}(y,z) \equiv u - V_\infty$, shown in Figure 2.18. Following the 2D airfoil analysis of Appendix C, the far-field source strength is the integrated volume flow rate of the wake velocity defect, and the profile drag is the associated integrated momentum defect.

$$\Sigma = \iint -\Delta u_{\text{wake}} \, \mathrm{d}y \, \mathrm{d}z \tag{2.108}$$

$$D_p = \iint (V_\infty + \Delta u_{\text{wake}})(-\Delta u_{\text{wake}}) \, \mathrm{d}y \, \mathrm{d}z \tag{2.109}$$

The drag derivation will also be given later in Section 5.6.

In the far wake we also have $\Delta u_{\text{wake}} \to 0$, so that the two relations above can be combined to give the far-field source strength in terms of the profile drag D_p of the body, or equivalently in terms of its profile drag coefficient C_{D_p} based on some reference area S_{ref}.

$$\Sigma = \frac{D_p}{\rho V_\infty} = \frac{1}{2} V_\infty S_{\text{ref}} C_{D_p} \tag{2.110}$$
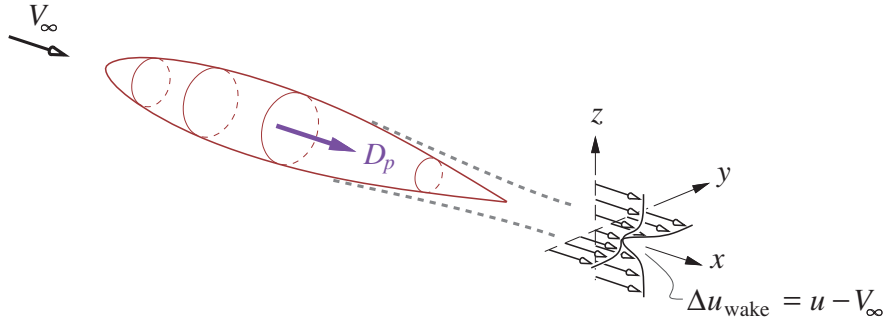
Figure 2.18: Viscous wake behind 3D body, with wake velocity defect Δu_{wake}.

2.12.2 3D far-field effect of volume

The inviscid flow about a slender body of revolution, such as an airplane fuselage, can be accurately represented by a variable-strength source filament placed along the body centerline, superimposed with a freestream. This model is shown in Figure 2.19.
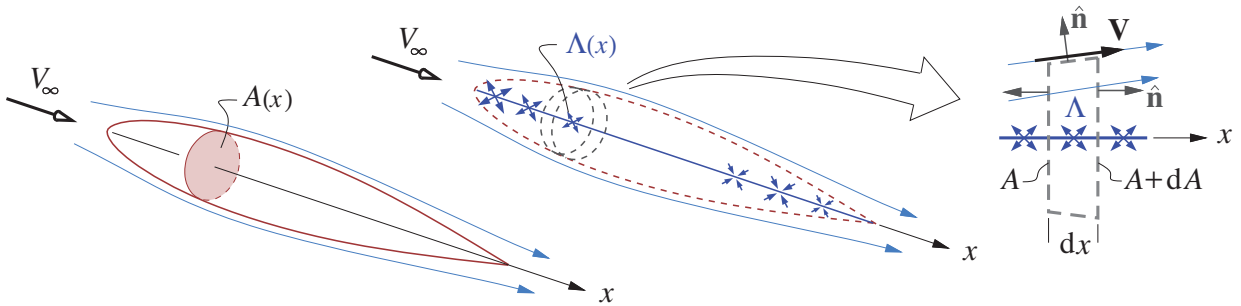
Figure 2.19: Flow about slender body represented by a source filament of variable strength $\Lambda_{(x)}$.

Following the 2D airfoil thickness analysis, the source filament strength $\Lambda_{(x)}$ can be determined by mass conservation applied to the local control volume which has the body's cross sectional area $A_{(x)}$ and is $\mathrm{d}x$ thick in the axial direction. The flow is required to be tangent to the outside perimeter surface of the control volume, so the net outflow from the source filament inside is equal to the volume flow difference between the front and rear faces of area A and $A + \mathrm{d}A$, as given by (2.39). This gives the required source filament strength.

$$\Lambda\,\mathrm{d}x = \oiint \mathbf{V}\cdot\hat{\mathbf{n}}\,\mathrm{d}\mathcal{S} = V_\infty(A+\mathrm{d}A) - V_\infty A = V_\infty\,\mathrm{d}A$$

$$\Lambda_{(x)} = V_\infty \frac{\mathrm{d}A}{\mathrm{d}x} \tag{2.111}$$

The far-field x-doublet for this source filament is then determined from the $\mathcal{K}_x$ definition (2.105).

$$\mathcal{K}_x \;\; = \;\; \int_{x_{LE}}^{x_{TE}} -\Lambda\, x \;\mathrm{d}x \;\; = \;\; V_\infty \int_{x_{LE}}^{x_{TE}} -\frac{\mathrm{d}A}{\mathrm{d}x}\, x \;\mathrm{d}x \tag{2.112}$$

The last integral above can be integrated by parts as in the 2D case, giving a rather simple expression for $\mathcal{K}_x$ in terms of the body volume $\mathcal{V} = \int_{x_{LE}}^{x_{TE}} A\,\mathrm{d}x$.

$$\mathcal{K}_x \;\; = \;\; V_\infty \mathcal{V} \tag{2.113}$$

The above analysis is strictly valid only if the body is slender, which is a prerequisite for accuracy of the source filament model. For non-slender bodies (2.113) tends to somewhat underpredict the actual far-field doublet strength. For bodies of revolution, an improved empirical estimate is

$$\mathcal{K}_x \;\; = \;\; V_\infty \mathcal{V} \left(1 \,+\, \frac{1.25\,(d_{\max}/\ell)^{3/2}}{1.5 + d_{\max}/\ell} \right) \tag{2.114}$$

where $d_{\max}$ is the maximum cross-section diameter and $\ell = x_{TE} - x_{LE}$ is the body length. For more general body shapes, $d_{\max}$ can be replaced by $\sqrt{4A_{\max}/\pi}$, where $A_{\max}$ is the maximum cross-sectional area.

Chapter 3

Viscous Effects in Aerodynamic Flows

This chapter will examine the changes in an aerodynamic flow caused by the presence of viscous wall boundary layers and trailing wakes. The objective is to model and quantify these changes and to explain their associated phenomena such as loss of lift at stall.

3.1 Inviscid Flow Model

Lumping of the vorticity in the viscous layers into vortex sheets, as illustrated in Figure 2.12 in Chapter 2, produces a fictitious strictly-potential *Equivalent Inviscid Flow* (EIF) velocity field $u_i, v_{i(s,n)}$. The EIF also has a pressure field $p_{i(s,n)}$ related to u_i, v_i by the Bernoulli equation (1.109).

$$p_{i(s,n)} \;=\; p_\infty + \frac{1}{2}\rho V_\infty^2 \;-\; \frac{1}{2}\rho(u_i^2 + v_i^2) \tag{3.1}$$

Here u, v will denote velocity components along the local orthogonal sheet coordinates s, n.

Figure 3.1 compares the EIF to the real flow in more detail, for the case where the lumped vortex sheet is placed on the real surface. It is labeled "Simple" to distinguish it from the more advanced and accurate models considered later, which mostly eliminate the modeling discrepancies in the velocity and pressure in the Simple model.
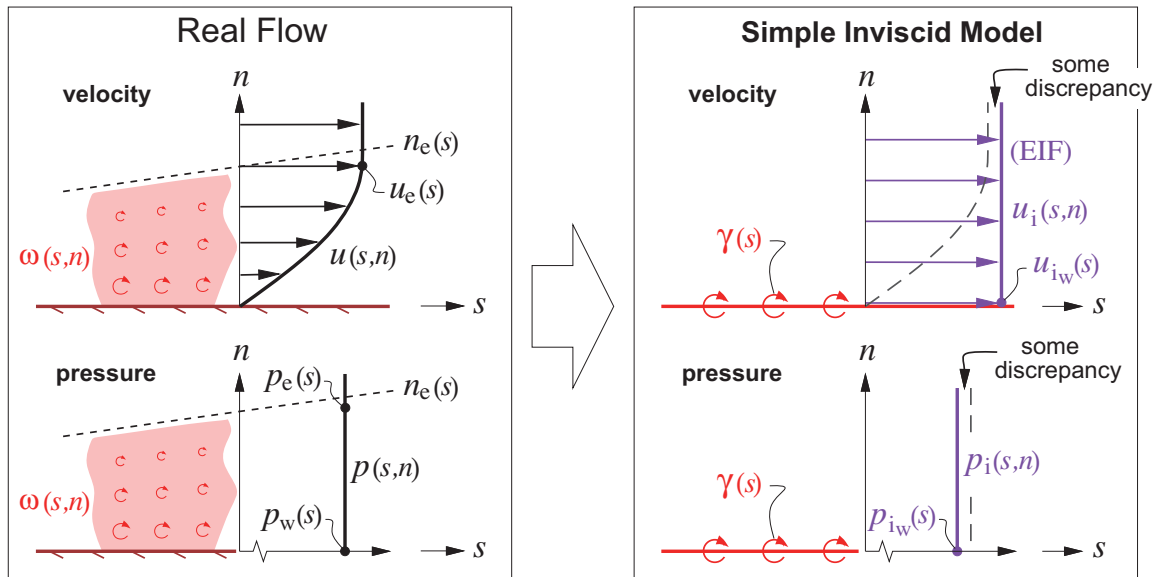
Figure 3.1: Real viscous flow approximated by Simple Inviscid Model. The v and v_i wall-normal velocity components are small and are not shown. This is a zoom-in of Figure 2.12.

Since the real flow in the boundary layer has almost parallel streamlines, the static pressure across it must be almost constant regardless of the velocity distribution. Hence the wall pressure $p_w(s)$ is nearly equal to the edge pressure $p_e(s)$, which in turn is related to the edge velocity via the Bernoulli equation. The negligibly small wall-normal velocity contribution $v_e^2 \ll u_e^2$ is omitted.

$$p_w(s) \simeq p_e(s) = p_\infty + \frac{1}{2}\rho V_\infty^2 - \frac{1}{2}\rho u_e^2 \tag{3.2}$$

The subscript $(\ )_e$ will in general denote an "edge" quantity in the irrotational flow just outside the edge of viscous layer, which is demarked by the $n_e(s)$ curve shown in Figure 3.1. The subscript $(\ )_w$ will denote a wall quantity at $n=0$.

If the boundary layer is thin the vorticity-lumping procedure will incur little error, in which case the wall velocity of the EIF closely approximates the edge velocity of the real flow.

$$u_{i_w}(s) \simeq u_e(s) \tag{3.3}$$

Combining (3.1),(3.2),(3.3) we have

$$p_{i_w}(s) \simeq p_w(s) \tag{3.4}$$

so that the EIF captures the real surface pressures, and hence should produce reasonably accurate lift forces and moments. Of course the EIF cannot represent the viscous skin friction in the real flow, so that it cannot correctly predict the drag. This will be addressed in Chapter 4.

Although the above discussion assumed incompressible flows, the EIF concept and flow models can be applied to compressible flows. The only differences are that the compressible Bernoulli relation (1.112) would be used in lieu of (3.1), and a grid method would be used in lieu of the vortex-sheet EIF model shown in Figure 3.1.

3.2   Displacement Effect

3.2.1   Normal mass flux matching

The major shortcoming of the simple inviscid model shown in Figure 3.1 is that it does not account for the *displacement effect* of the slower-moving fluid inside the boundary layer. This acts as a wedge, tilting and displacing the outer streamlines away from the wall, as shown in Figure 3.2.
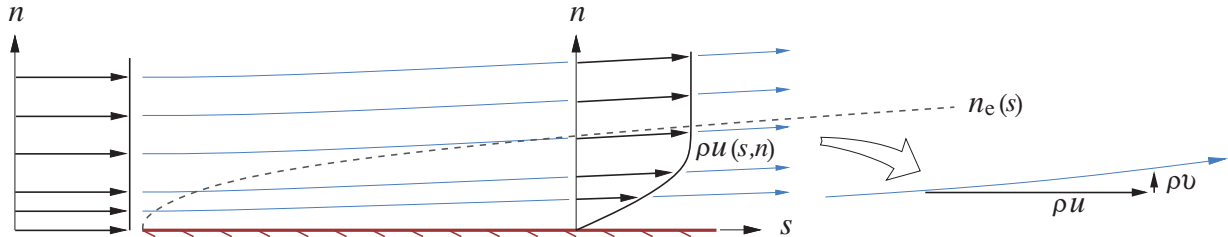
Figure 3.2: Actual viscous flow with displaced streamlines and corresponding vertical mass flux ρv, caused by piling up of the slower-moving fluid in the boundary layer.

This displacement changes the apparent flow tangency seen by the bulk flow, and thus modifies the overall flow-field. In the simple inviscid model this effect is ignored, which is the main reason for the discrepancies between the EIF's and real flow's edge velocity, wall pressure, and lift, shown in Figure 3.1. If the boundary layers are thin, then these discrepancies are small and are often ignored. But if the boundary layers are thick,

perhaps due to a low Reynolds number or the airfoil being close to or beyond stall, then the discrepancies between the real flow and the Simple Inviscid Model's EIF may be unacceptably large.

To mostly eliminate these modeling errors, the EIF must be constructed so that its vertical mass flux equals that of the real flow outside the real boundary layer.

$$\rho v_{(s,n)} \;=\; \rho_{\mathrm{i}} v_{\mathrm{i}(s,n)} \qquad (\text{ for } n > n_{\mathrm{e}(s)}) \tag{3.5}$$

3.2.2 Normal mass flux in real flow

Consider the real viscous flow shown in Figure 3.2. The wall-normal mass flux ρv at some location $n > n_{\mathrm{e}}$ outside the shear layer is computed by integrating its n-gradient from the wall. After also invoking mass continuity, the result is more concisely given in terms of the shear layer's mass defect $m_{(s)}$, or the related displacement thickness $\delta^*_{(s)}$.

$$\rho v_{(s,n)} \;=\; \rho v_{(s,0)} + \int_0^n \frac{\partial \,\rho v}{\partial n}\, \mathrm{d}n \;=\; 0 + \int_0^n -\frac{\partial \,\rho u}{\partial s}\, \mathrm{d}n$$

$$=\; \int_0^n \frac{\partial}{\partial s}\left(\rho_{\mathrm{e}} u_{\mathrm{e}} - \rho u\right)\, \mathrm{d}n \;-\; n\,\frac{\mathrm{d}\,\rho_{\mathrm{e}} u_{\mathrm{e}}}{\mathrm{d}s}$$

$$=\; \frac{\mathrm{d}}{\mathrm{d}s}\left[\rho_{\mathrm{e}} u_{\mathrm{e}} \int_0^{n_{\mathrm{e}}}\left(1 - \frac{\rho u}{\rho_{\mathrm{e}} u_{\mathrm{e}}}\right) \mathrm{d}n\right] \;-\; n\,\frac{\mathrm{d}\,\rho_{\mathrm{e}} u_{\mathrm{e}}}{\mathrm{d}s}$$

$$\text{or} \qquad \rho v_{(s,n)} \;=\; \frac{\mathrm{d}m}{\mathrm{d}s} \;-\; n\,\frac{\mathrm{d}\,\rho_{\mathrm{e}} u_{\mathrm{e}}}{\mathrm{d}s} \qquad\qquad (\text{actual flow, for } n > n_{\mathrm{e}}) \tag{3.6}$$

$$\text{where} \qquad m_{(s)} \;\equiv\; \int_0^{n_{\mathrm{e}}} (\rho_{\mathrm{e}} u_{\mathrm{e}} - \rho u)\, \mathrm{d}n \;=\; \rho_{\mathrm{e}} u_{\mathrm{e}} \delta^*$$

$$\delta^*_{(s)} \;\equiv\; \int_0^{n_{\mathrm{e}}}\left(1 - \frac{\rho u}{\rho_{\mathrm{e}} u_{\mathrm{e}}}\right) \mathrm{d}n$$

Taking the $\mathrm{d}/\mathrm{d}s$ derivative outside the integral is allowed provided the integrand is zero at the upper limit, which is the reason for the $n > n_{\mathrm{e}}$ requirement for the final relation (3.6). The mass defect is the difference in the mass flow between the EIF and the real flow, integrated across the shear layer, and the displacement thickness is the resulting physical displacement of the potential flow away from the wall.

It must be stressed here that calculation of $m_{(s)}$ and $\delta^*_{(s)}$ requires an analysis of the boundary layer itself, which will be treated in Chapter 4. Here they are assumed to be known properties of the boundary layer.

3.3 Improved Inviscid Flow Models

Two improved EIF models considered next are sketched in Figure 3.3. They define the EIF such that it satisfies the normal mass flux matching requirement (3.5), and thus they capture the displacement effect. The result is much better flow-field prediction accuracy, especially for flows with thick boundary layers.

3.3.1 Displacement Body model

This model employs the concept of a fictitious *displacement body*, which is offset from the actual body by some distance $\Delta n_{(s)}$. The EIF is defined to be tangent to the displacement body, and hence can be constructed by a vortex sheet placed on this displacement body, as shown in Figure 3.3, rather than on the
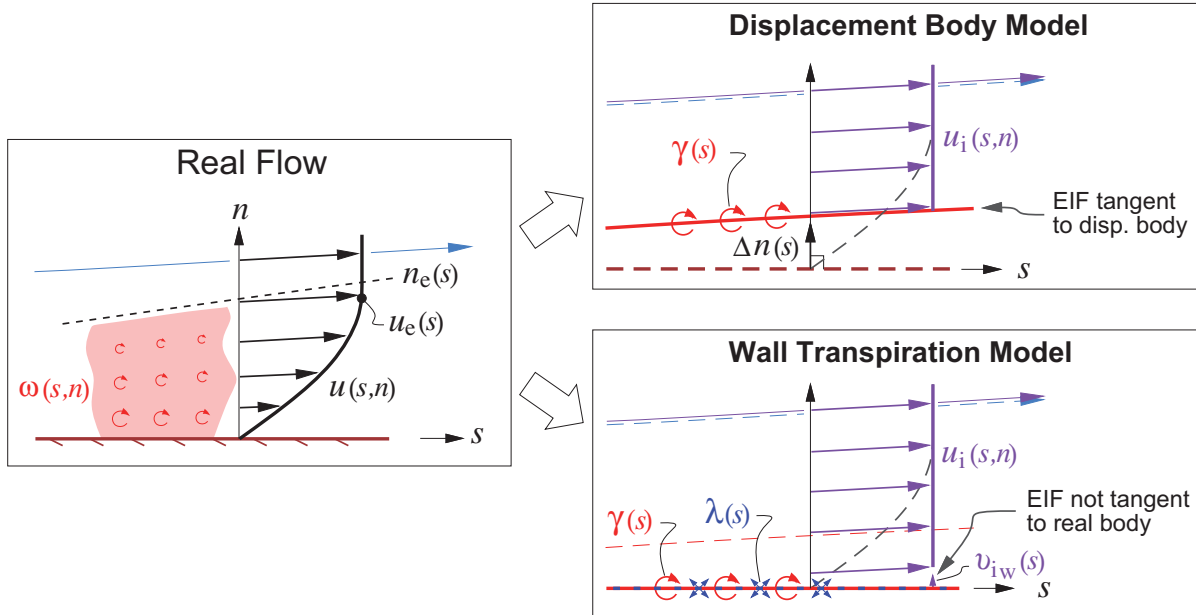
Figure 3.3: Real viscous flow approximated by two improved EIF models which capture the real flow's displacement effect. This mostly eliminates the modeling discrepancies shown in Figure 3.1.

wall as in Figure 3.1. The objective here is to determine what $\Delta n(s)$ has to be so that the vertical mass flux matching condition (3.5) is satisfied.

The EIF's $\rho_i v_i$ in this situation is computed using the continuity equation, as for the real-flow case. Note that $\rho_i v_i$ is not zero at the displacement body, since displacement body's normal vector is tilted away from the n axis by the slope $\mathrm{d}\,\Delta n/\mathrm{d}s$. The model is also assumed a priori to give the correct EIF which matches the real flow, so that we can set $u_i = u_e$.

$$\rho_i v_{i(s,n)} = \rho_e u_e \frac{\mathrm{d}\,\Delta n}{\mathrm{d}s} + \int_{\Delta n}^{n} \frac{\partial\,\rho_i v_i}{\partial n}\,\mathrm{d}n = \rho_e u_e \frac{\mathrm{d}\,\Delta n}{\mathrm{d}s} - \int_{\Delta n}^{n} \frac{\partial\,\rho_i u_i}{\partial s}\,\mathrm{d}n$$

$$= \rho_e u_e \frac{\mathrm{d}\,\Delta n}{\mathrm{d}s} - (n - \Delta n) \frac{\mathrm{d}\,\rho_e u_e}{\mathrm{d}s}$$

$$\text{or} \qquad \rho_i v_{i(s,n)} = \frac{\mathrm{d}(\rho_e u_e \,\Delta n)}{\mathrm{d}s} - n \frac{\mathrm{d}\,\rho_e u_e}{\mathrm{d}s} \qquad \text{(displacement-body model)} \qquad (3.7)$$

Requiring this $\rho_i v_i$ to be equal to the real flow's ρv as defined by (3.6), gives

$$\boxed{\Delta n(s) = \delta^*(s)} \qquad\qquad (3.8)$$

so that the necessary offset for the displacement body is just the displacement thickness (hence the name).

3.3.2   Wall Transpiration model

This model places the vortex sheet on the actual body as in the Simple Inviscid Model shown in Figure 3.1. But now a source sheet of some strength $\lambda(s)$ is also added, as shown in Figure 3.3. This generates a fictitious *wall transpiration* or mass flux distribution $(\rho_i v_i)_w(s)$. The resulting EIF is thus intentionally <u>not</u> made tangent to the real body, which enables simulating the displacement effect.

The resulting $\rho_i v_i$ at some distance n above the wall again follows from continuity.

$$\rho_i v_{i(s,n)} = (\rho_i v_i)_w + \int_0^n \frac{\partial \rho_i v_i}{\partial n} \, dn = (\rho_i v_i)_w - \int_0^n \frac{\partial \rho_i u_i}{\partial s} \, dn$$

$$\text{or} \qquad \rho_i v_{i(s,n)} = (\rho_i v_i)_w - n \frac{d \rho_e u_e}{ds} \qquad \text{(wall-transpiration model)} \qquad (3.9)$$

Again requiring this to be equal to ρv of the actual flow (3.6) gives the the required wall mass flux.

$$\boxed{(\rho_i v_i)_w = \frac{dm}{ds}} \qquad (3.10)$$

In a low-speed flow the normal velocity can be imposed using a source sheet, as indicated in Figure 3.3. In this case the airfoil's interior velocity can still be set to zero when the vortex sheet strength $\gamma_{(s)}$ is calculated by the panel method. The required source sheet strength is then equal to the transpiration velocity, and related to the mass defect as follows.

$$\lambda_{(s)} = (v_i)_w = \frac{1}{\rho} \frac{dm}{ds} \qquad (3.11)$$

3.3.3 Wake modeling

The boundary layers on a body merge together at the trailing edge or rear point and trail downstream as a wake. A wake has two edges — upper and lower — where the potential-flow quantities will now be denoted by $()_u$ and $()_l$, respectively. The particular vertical location of the s-axis, or equivalently the $n=0$ point, is not significant, and it can lie anywhere in or near the wake.

If the wake is thin compared to the streamwise radius of curvature, then it has a nearly uniform static pressure across it like a boundary layer. Also, the lower and upper potential flows have the same freestream total pressure, so that the two edge velocities must also be the same, and so both can be denoted by u_e.

$$p_{u(s)} = p_{l(s)} \qquad \rightarrow \qquad u_{u(s)} = u_{l(s)} = u_{e(s)} \qquad (3.12)$$

The 2D wake has a nonzero mass defect and in general nonzero normal mass fluxes at n_u and n_l. Repeating the previous mass flux analysis for the wake, the real-flow edge mass flux relation (3.6) becomes a *jump* condition across the wake.

$$\Delta(\rho v) \equiv \rho v_{(s,n_u)} - \rho v_{(s,n_l)} = \frac{dm}{ds} - (n_u - n_l) \frac{d \rho_e u_e}{ds} \qquad \text{(actual wake)} \qquad (3.13)$$

$$\text{where} \qquad m_{(s)} \equiv \int_{n_l}^{n_u} (\rho_e u_e - \rho u) \, dn = \rho_e u_e \delta^*$$

$$\delta^*_{(s)} \equiv \int_{n_l}^{n_u} \left(1 - \frac{\rho u}{\rho_e u_e}\right) dn$$

Note that the m and δ^* definitions are the same as for the wall case, aside from the different edge limits.

Repeating the mass flux analysis for the Displacement-Body and Wall-Transpiration models, and requiring that the resulting $\Delta(\rho v)$ matches the real-flow result (3.13), gives the required displacement body thickness, and the required source sheet strength.

$$\Delta n_{(s)} = \delta^*_{(s)} \qquad \text{(2D-wake Displacement Body model)} \qquad (3.14)$$

$$\lambda_{(s)} = \frac{1}{\rho} \frac{dm}{ds} \qquad \text{(2D-wake Wall Transpiration model)} \qquad (3.15)$$

These are the same as (3.8) and (3.11) for the boundary layer, except that $\triangle n$ now only gives the thickness of the wake displacement body. The camber shape of the wake displacement body must be implicitly determined from the zero pressure jump or velocity jump requirement, such that the wake displacement body carries no lift.
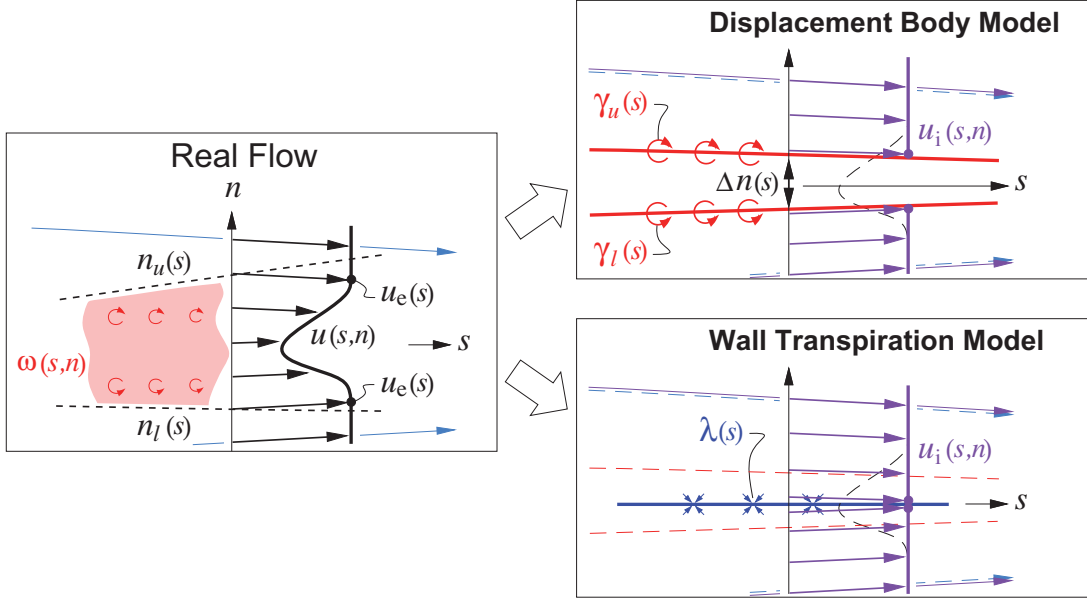
Figure 3.4: Real viscous flow of wake approximated by two EIF models which capture the wake's displacement effect.

The EIF models resulting from the above matching relations are shown in Figure 3.4. Note that the Displacement Body model requires the use of two vortex sheets, which must have equal and opposite strengths as required by zero velocity jump requirement across the whole wake.

$$\gamma_u(s) + \gamma_l(s) = 0 \tag{3.16}$$

3.3.4   Improved flow model advantages

Both the Displacement Body and the Wall Transpiration models quantitatively give very nearly the same results when incorporated into potential flow calculation methods, and both are great improvements over the Simple Inviscid model when separation is present. An example comparison is shown in Figure 3.5 for an airfoil from zero lift to beyond stall. At small lift coefficients where the displacement effects are weak, the three models give comparable results, as shown in Figure 3.6 for $\alpha = 0°$. At a large lift coefficient with trailing edge separation, the differences are quite significant, as shown in Figure 3.7 for $\alpha = 16°$.

3.4   Viscous Decambering Stall Mechanism

The Displacement Body model combined with Glauert's thin airfoil theory [8], sections D.2 and D.3, provides an intuitive explanation for the loss of lift at stall. This theory gives the general lift result

$$c_\ell(\alpha) = 2\pi\alpha + c_{\ell_0} \tag{3.17}$$

for any thin airfoil. The lift intercept c_{ℓ_0} depends only on the airfoil's camberline shape, and is most sensitive to the deflection angle of the camberline over the rear portion of the airfoil. These results also apply to more general airfoils, except with finite thickness the slope $dc_\ell/d\alpha = 2\pi$ will be somewhat larger.
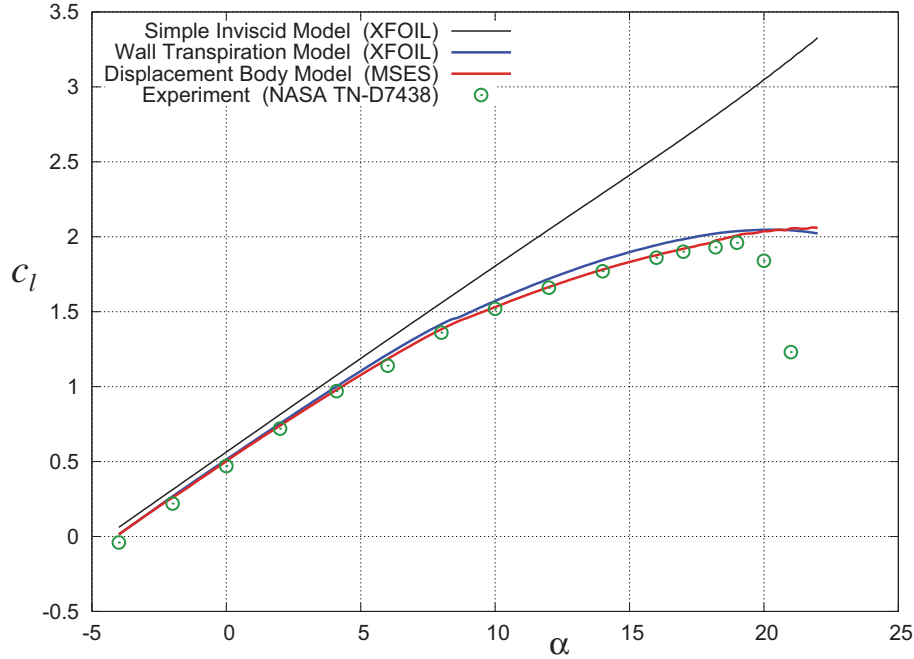
Figure 3.5: Comparison of $c_\ell(\alpha)$ lift curves for GAW(1) airfoil at $Re_c = 6$ million, $M_\infty = 0.15$, calculated by XFOIL [5] and MSES [6]. Experimental data is from McGhee et al [7].

In light of this result we examine the camberlines of the displacement bodies of the GAW(1) airfoil at the $\alpha = 0°$ and $\alpha = 16°$ operating points, shown in Figure 3.8. The large separation region over the upper rear of the airfoil at high α increases the displacement body offset Δn there, creating an upward deflection in its camberline which then causes the downward shift in the lift curve for that shape. This upward deflection of the effective camberline is called the *viscous flap*. The two resulting fixed-camberline $c_\ell(\alpha)$ functions intersect the actual $c_\ell(\alpha)$ curve for the airfoil, which in effect goes through a progression of ever-increasing upward viscous flap deflections which gradually reduce the lift from its strictly inviscid value. Maximum lift and subsequent stall occurs when this viscous flap decambering progression overpowers the inviscid lift coefficient gradient $\mathrm{d}c_\ell/\mathrm{d}\alpha$.

3.5 Considerations in Flow Model Selection

The Simple Inviscid model shown is Figure 3.1 is attractive because it requires only the body geometry and the freestream velocity as inputs. Hence, it's relatively simple to apply via any inviscid-flow theory or calculation method. For this reason it is often used as a first estimate, and whenever the viscous effects can be considered negligible, as for the small angles of attack in the GAW(1) airfoil example above.

Although the Displacement Body or Wall Transpiration models are clearly superior for all cases, they are considerably more complex to implement and to use. The major complication in their implementation is that they require knowledge of the boundary layer's mass defect $m(s)$ or displacement thickness $\delta^*(s)$ distributions. These quantities not known a priori, but must come from an analysis of the boundary layer itself (as treated in Chapter 4). Furthermore, the inviscid flow calculation and the boundary layer calculation are also coupled, in that the output of one is the input to the other. For this reason they must be solved in a coupled manner, as for example in the XFOIL 2D airfoil code [5]. This treatment is considerably more complex than the straightforward use of only an inviscid method, such as a panel method, in the Simple Inviscid model, especially for 3D flows. Section 4.12 gives further discussion of the coupling of inviscid and boundary layer flows.
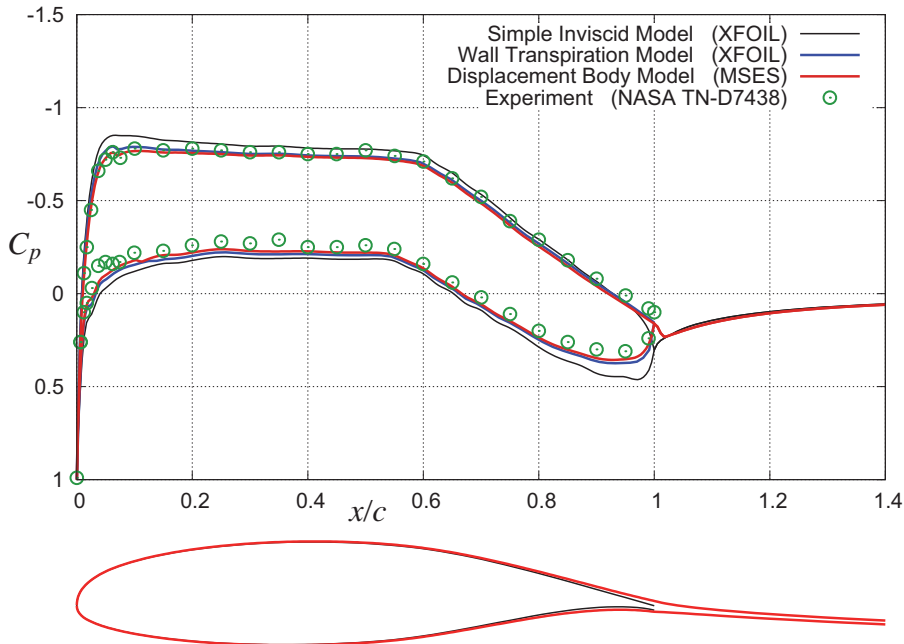
Figure 3.6: Comparison of GAW(1) airfoil surface C_p distributions for the $\alpha = 0°$ point. The airfoil is shown with the displacement body superimposed. The flow is well attached, so that the displacement effects are weak and the displacement body differs only slightly from the actual airfoil.
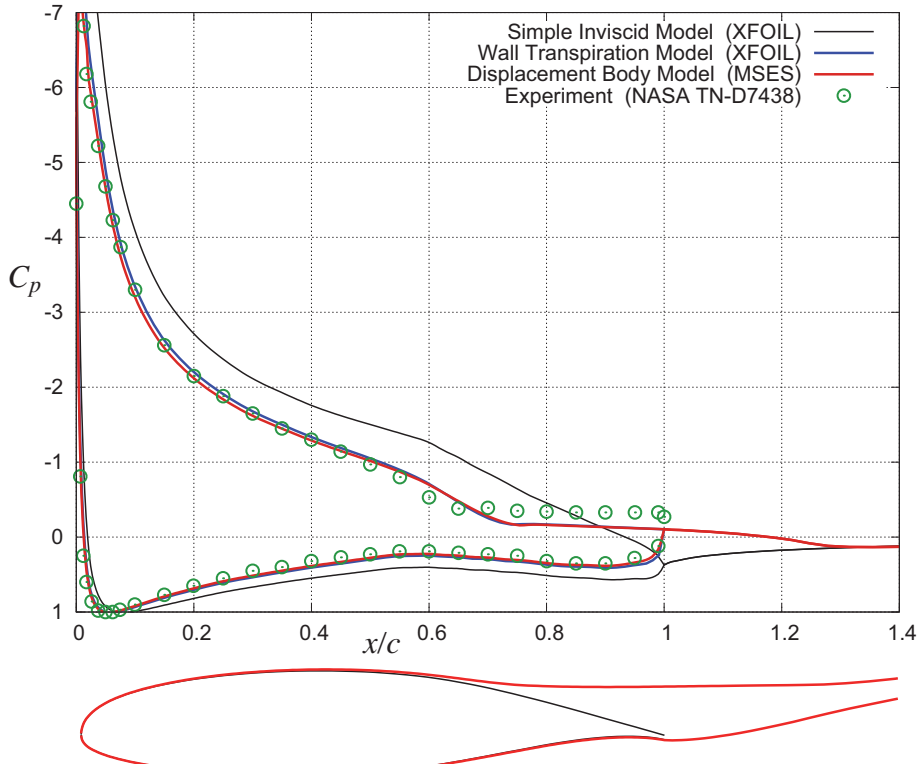
Figure 3.7: Comparison of GAW(1) airfoil surface C_p distributions for the $\alpha = 16°$ point. The displacement body is now very different from the actual body, due to trailing edge boundary layer separation which also extends into the wake.
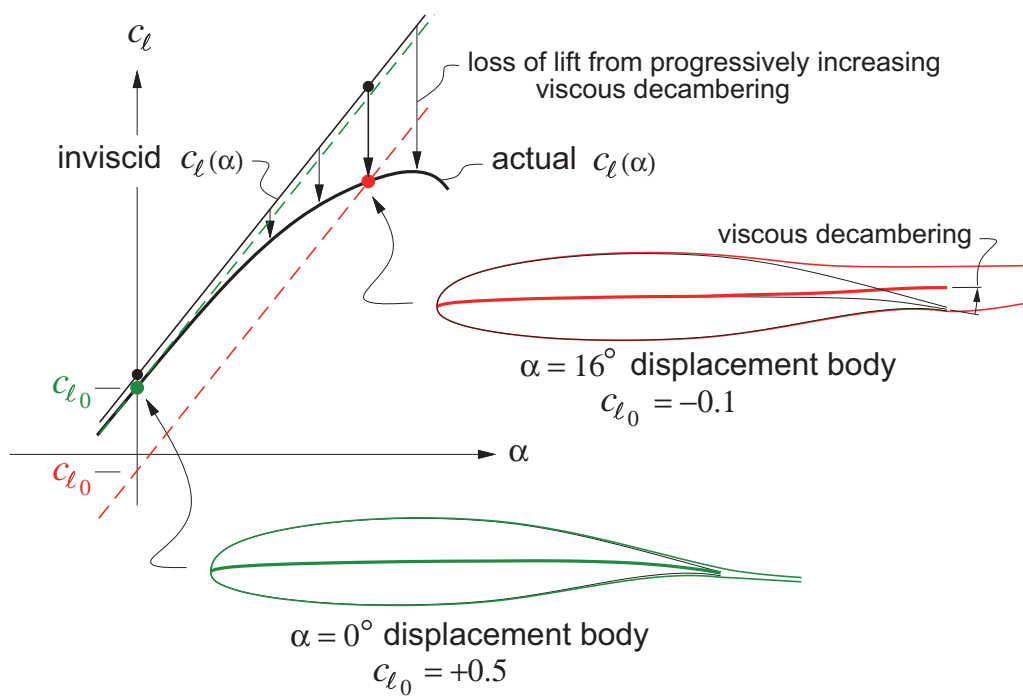
Figure 3.8: Lift curves (dashed) of two GAW(1) displacement bodies with different camberline rear deflections. Viscous decambering correctly models the loss of lift and stall at high angles of attack.

Chapter 4

Boundary Layer Analysis

This chapter will treat the physics of aerodynamic boundary layers flows. The objectives include identification of relevant boundary layer parameters, derivation of their governing equations, and formulation of solution methods. Additional objectives are to obtain insight into boundary layer behavior and how it determines overall viscous losses and profile drag.

4.1 Boundary Layer Flow Features and Overview

In general, a boundary layer flow is either *laminar* with smooth and nearly parallel streamlines, or *turbulent* with chaotic motion and significant fluid mixing. Most aerodynamic flows over streamline shapes, such as the airfoil flow shown in Figure 4.1, have laminar boundary layers on each side starting from the leading edge stagnation point, which eventually undergo *transition* and become turbulent. The two boundary layers then merge at the trailing edge into a *wake* which is almost invariably turbulent. The airfoil's profile drag is related to the properties of the far-downstream wake, as derived in Appendix C.
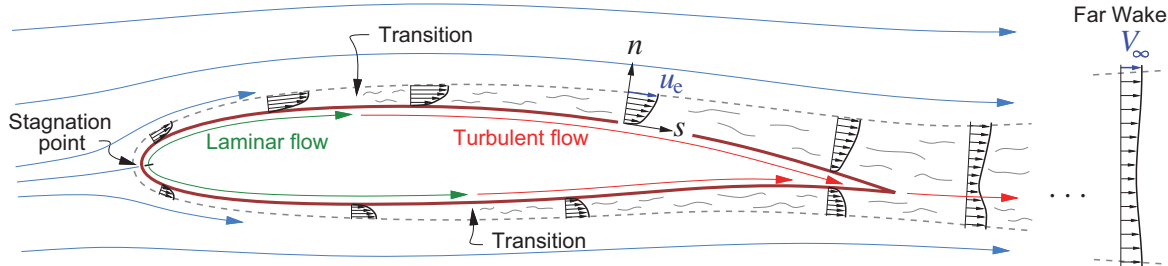
Figure 4.1: Boundary layer and wake development on a typical airfoil, shown by the $u(n)$ velocity profiles. The layer thicknesses are shown exaggerated.

The goals of this chapter are description and prediction of the important aspects and parameters of the boundary layer flow shown in Figure 4.1. Examples are quantities such as the mass defect $m(s)$ and displacement thickness $\delta^*(s)$ distributions, already identified in Chapter 3 as being required to model the boundary layer's effects on the overall potential flow. Both laminar and turbulent boundary layers as well as the transition locations will be considered.

Other goals of this chapter include prediction of profile drag, and prediction of boundary layer behavior in general, in particular its response to pressure gradients. A major motivation is the fact that much of aerodynamic design can be viewed as "boundary layer management," in that boundary layers determine profile drag, and their separation also determines the maximum attainable lift, as discussed in Chapter 3. Hence, boundary layer behavior ultimately sets fundamental limits on most aspects of aerodynamic performance.

The focus here will be on 2D flows, which is sufficient to investigate the majority of the important features of boundary layer behavior. Basic 3D effects will also be briefly considered.

4.2   Defect Integrals and Thicknesses

As a first step, it's useful to identify important overall properties of the boundary layer at any streamwise location s. As in Chapter 3, u, v will denote the s, n axis velocity components, which for a turbulent boundary layer represent the *mean flow* (e.g. time-averaged flow). The Equivalent Inviscid Flow (EIF) concept, first introduced in Section 3.1, will also be invoked here. Here we will assume that the EIF exactly matches the actual flow outside the boundary layer, and that it's constant through the boundary layer thickness, so that

$$u_i(s,n) \;=\; u_e(s) \qquad , \qquad \rho_i(s,n) \;=\; \rho_e(s) \tag{4.1}$$

at every streamwise station s. The assumption is equivalent to assuming that the boundary layer is very thin compared to the streamwise radius of curvature. This curvature is accounted for in *higher-order boundary layer theory*, as for example by Lock and Williams [9]. It will not be addressed here.

4.2.1   Mass flow comparison

Figure 4.2 shows the mass flow per unit span passing through the streamtube of height n_e, for the real flow and the corresponding EIF. These mass flows might be needed for a control-volume analysis for example.

$$\dot{m} \;=\; \int \mathrm{d}\dot{m} \;=\; \int_0^{n_e} \rho u \, \mathrm{d}n \;=\; \int_0^{n_e} \rho_e u_e \, \mathrm{d}n \;-\; \int_0^{n_e} (\rho_e u_e - \rho u) \, \mathrm{d}n$$

$$\text{or} \qquad \boxed{\dot{m} \;=\; \dot{m}_i - m} \tag{4.2}$$

$$\text{where} \qquad \dot{m}_i \;\equiv\; \int_0^{n_e} \rho_e u_e \, \mathrm{d}n \;=\; \rho_e u_e \, n_e$$

$$m \;\equiv\; \int_0^{n_e} (\rho_e u_e - \rho u) \, \mathrm{d}n \;=\; \rho_e u_e \, \delta^* \tag{4.3}$$

$$\text{and} \qquad \delta^* \;\equiv\; \int_0^{n_e} \left(1 - \frac{\rho u}{\rho_e u_e} \right) \mathrm{d}n \tag{4.4}$$

The EIF mass flow is greater than the actual mass flow, the difference being the mass defect m. This is seen to be the fictitious mass flow between the real and displacement bodies locally spaced a distance $\Delta n = \delta^*$ apart. This result is closely related to the viscous displacement models shown in Figure 3.3. Those were also based on mass conservation, and hence also depended on the $m(s)$ and $\delta^*(s)$ of the boundary layer.
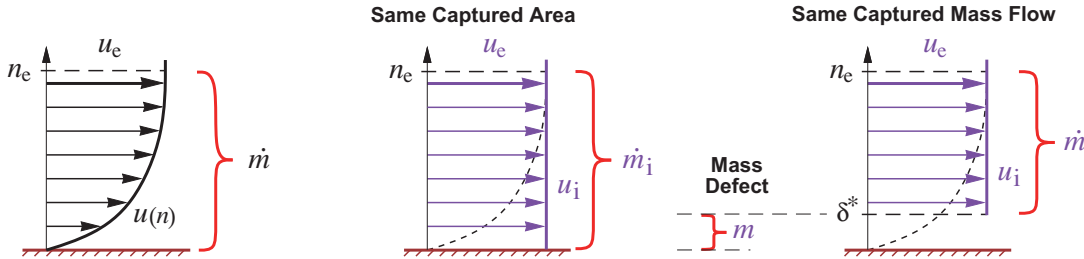
Figure 4.2: Comparison of actual and EIF mass flows.

4.2.2   Momentum and kinetic energy flow comparisons

Momentum flow is carried by mass flow, and was already treated in the momentum control volume flow analysis in Section 1.3. Here it will be viewed as the force which acts on a hypothetical barrier which captures the mass flow and brings the fluid's velocity to zero. Similarly, the kinetic energy flow carried by a mass flow will be viewed as the power obtained from an ideal turbine array which brings the fluid to rest
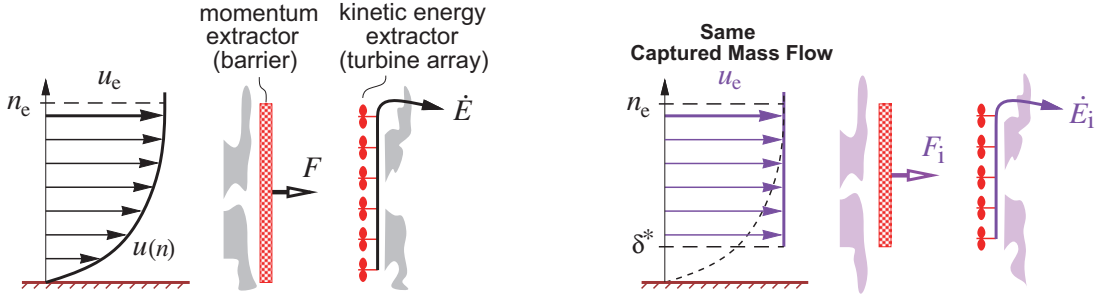
Figure 4.3: Comparison of actual and EIF's momentum flow and kinetic energy flow, for the same mass flow. Momentum flow is equal to the force on a hypothetical barrier which brings the fluid stream's s-velocity to zero. Kinetic energy flow is equal to the power from an ideal turbine array which brings the fluid stream's velocity to zero reversibly.

reversibly. Figure 4.3 compares the barriers and turbine arrays between the actual flow and the EIF. The comparison is done at the same mass flow for all cases, which requires the EIF's barrier and turbine array to be shorter by the displacement thickness height δ^*.

The force and power are obtained by integrating the momentum and kinetic energy fluxes across the profile. The EIF flow case in Figure 4.3 on the right gives the following.

$$F_\mathrm{i} \;=\; \int u_\mathrm{i}\,\mathrm{d}\dot{m}_\mathrm{i} \;=\; \int_{\delta^*}^{n_\mathrm{e}} \rho_\mathrm{i} u_\mathrm{i}^2 \,\mathrm{d}n \;=\; \rho_\mathrm{e} u_\mathrm{e}^2 (n_\mathrm{e}-\delta^*) \tag{4.5}$$

$$\dot{E}_\mathrm{i} \;=\; \int \tfrac{1}{2} u_\mathrm{i}^2 \,\mathrm{d}\dot{m}_\mathrm{i} \;=\; \int_{\delta^*}^{n_\mathrm{e}} \tfrac{1}{2}\rho_\mathrm{i} u_\mathrm{i}^3 \,\mathrm{d}n \;=\; \tfrac{1}{2}\rho_\mathrm{e} u_\mathrm{e}^3 (n_\mathrm{e}-\delta^*) \tag{4.6}$$

For the real flow case shown in Figure 4.3 on the left we have

$$F \;=\; \int u\,\mathrm{d}\dot{m} \;=\; \int_0^{n_\mathrm{e}} \rho u^2 \,\mathrm{d}n \;=\; \int_0^{n_\mathrm{e}} \rho_\mathrm{e} u_\mathrm{e}^2 \,\mathrm{d}n \;-\; u_\mathrm{e}\int_0^{n_\mathrm{e}} (\rho_\mathrm{e} u_\mathrm{e}-\rho u)\,\mathrm{d}n \;-\; \int_0^{n_\mathrm{e}} (u_\mathrm{e}-u)\,\rho u \,\mathrm{d}n$$

$$= \; \rho_\mathrm{e} u_\mathrm{e}^2 \, n_\mathrm{e} \;-\; u_\mathrm{e}(\rho_\mathrm{e} u_\mathrm{e}\delta^*) \;-\; \rho_\mathrm{e} u_\mathrm{e}^2 \theta$$

$$\boxed{F \;=\; F_\mathrm{i} - P} \tag{4.7}$$

$$\dot{E} \;=\; \int \tfrac{1}{2} u^2 \,\mathrm{d}\dot{m} \;=\; \int_0^{n_\mathrm{e}} \tfrac{1}{2}\rho u^3 \,\mathrm{d}n \;=\; \int_0^{n_\mathrm{e}} \tfrac{1}{2}\rho_\mathrm{e} u_\mathrm{e}^3 \,\mathrm{d}n \;-\; \tfrac{1}{2}u_\mathrm{e}^2\int_0^{n_\mathrm{e}} (\rho_\mathrm{e} u_\mathrm{e}-\rho u)\,\mathrm{d}n \;-\; \int_0^{n_\mathrm{e}} \tfrac{1}{2}(u_\mathrm{e}^2-u^2)\,\rho u \,\mathrm{d}n$$

$$= \; \tfrac{1}{2}\rho_\mathrm{e} u_\mathrm{e}^3 \, n_\mathrm{e} \;-\; \tfrac{1}{2}u_\mathrm{e}^2(\rho_\mathrm{e} u_\mathrm{e}\delta^*) \;-\; \tfrac{1}{2}\rho_\mathrm{e} u_\mathrm{e}^3 \theta^*$$

$$\boxed{\dot{E} \;=\; \dot{E}_\mathrm{i} - K} \tag{4.8}$$

where the following new defect quantities and associated thicknesses have appeared.

$$P \;\equiv\; \int_0^{n_\mathrm{e}} (u_\mathrm{e}-u)\,\rho u \,\mathrm{d}n \;=\; \rho_\mathrm{e} u_\mathrm{e}^2 \theta \qquad \text{(momentum defect)} \tag{4.9}$$

$$K \;\equiv\; \int_0^{n_\mathrm{e}} \tfrac{1}{2}(u_\mathrm{e}^2-u^2)\,\rho u \,\mathrm{d}n \;=\; \tfrac{1}{2}\rho_\mathrm{e} u_\mathrm{e}^3 \theta^* \qquad \text{(kinetic energy defect)} \tag{4.10}$$

$$\theta \;\equiv\; \int_0^{n_\mathrm{e}} \left(1 - \frac{u}{u_\mathrm{e}}\right) \frac{\rho u}{\rho_\mathrm{e} u_\mathrm{e}} \,\mathrm{d}n \qquad \text{(momentum thickness)} \tag{4.11}$$

$$\theta^* \;\equiv\; \int_0^{n_\mathrm{e}} \left(1 - \frac{u^2}{u_\mathrm{e}^2}\right) \frac{\rho u}{\rho_\mathrm{e} u_\mathrm{e}} \,\mathrm{d}n \qquad \text{(kinetic energy thickness)} \tag{4.12}$$

From the final results (4.7) and (4.8) we see that the actual flow has momentum and kinetic energy flows which are less than the EIF's values by the corresponding defects P and K.

The momentum defect P has also appeared in the airfoil far-field profile drag analysis in Appendix C. The kinetic energy defect K will be seen to be related to the viscous dissipation in the boundary layer, and to the profile drag as well. The associated thicknesses θ and θ^* will also appear in the formulation of integral boundary layer calculation methods considered later in this chapter.

4.2.3   Other integral thickness interpretations

In incompressible flow where $\rho = \rho_e = $ constant, the displacement, momentum, and kinetic energy thicknesses have additional interpretations in terms of the geometry of the normalized velocity profile U. By setting $\rho/\rho_e = 1$, the thickness definitions (4.4),(4.11),(4.12) simplify as follows.

$$U \equiv \frac{u}{u_e} \tag{4.13}$$

$$\delta^* = \int_0^{n_e} (1 - U)\,\mathrm{d}n \quad , \qquad \theta = \int_0^{n_e} (U - U^2)\,\mathrm{d}n \quad , \qquad \theta^* = \int_0^{n_e} (U - U^3)\,\mathrm{d}n \tag{4.14}$$

These incompressible thickness definitions can be interpreted as the geometric areas defined by the U, U^2, U^3 profiles as shown in Figure 4.4 on the left. The displacement thickness has another interpretation as the height of the line which splits the profile into two equal areas. This is shown in the middle sketch of Figure 4.4.

In a separated flow region, such as would occur on the upper rear surface of the nearly-stalled airfoil shown in Figure 3.7, most of the vortical fluid of the boundary layer has lifted off the wall. A typical velocity profile for this type of flow is shown in Figure 4.4 on the right. It is more correct to call this a *free shear layer* which lies between two distinct flow regions. One is the potential flow region outside the shear layer, and the other is the nearly-stagnant recirculating flow region between the wall and the shear layer. In this case we can interpret θ as being a measure of the thickness this shear layer (numerically its thickness is approximately 8θ). In contrast, δ^* is a measure of the distance from the wall to the shear layer centerline.
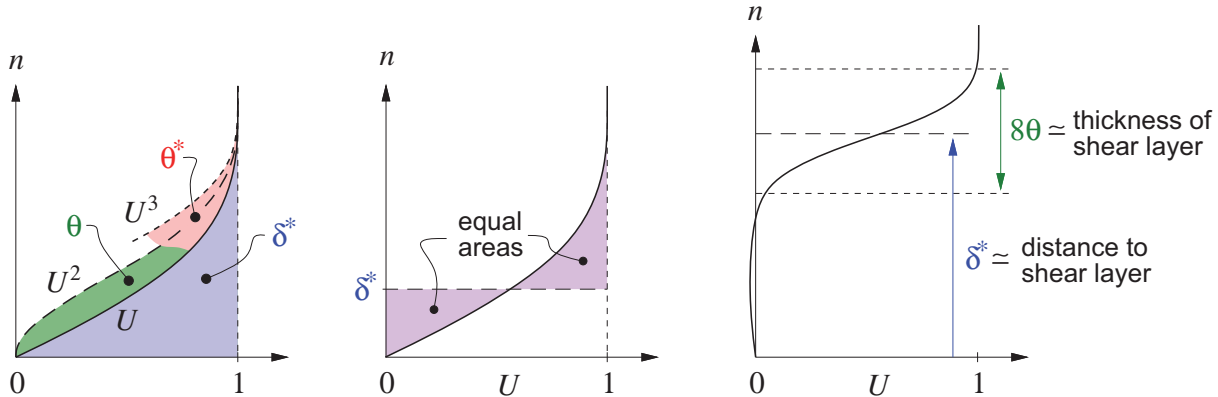
Figure 4.4: Interpretation of the integral thicknesses for incompressible flow, in terms of the geometry of the normalized velocity profile $U = u/u_e$, and also U^2 and U^3. Since the horizontal scale is dimensionless, the areas have the same length unit as the vertical n axis.

4.3 Boundary Layer Governing Equations

4.3.1 Thin Shear Layer approximations

As discussed in Section 1.5.4, at high Reynolds number the viscous layers are thin compared to their streamwise length. This allows making the following Thin Shear Layer (TSL) approximations in the locally-cartesian s, n surface coordinates (see Figure 3.2).

$$v \ll u \tag{4.15}$$

$$\frac{\partial u}{\partial s} \ll \frac{\partial u}{\partial n} \tag{4.16}$$

$$\frac{\partial p}{\partial n} \simeq 0 \tag{4.17}$$

Approximation (4.15) is a geometric consequence of the streamlines having only a small angle away from the wall and the s axis, as shown in Figure 3.2. Approximation (4.16) follows from the relatively rapid variation of the velocity across the layer. Together with (4.15) this allows dropping all but the $\partial u / \partial n$ term in the 2D version of the full viscous stress tensor (1.22), so that only the off-diagonal shear-stress terms $\tau_{sn} = \tau_{ns} = \tau$ are significant.

$$\bar{\bar{\tau}} = \begin{bmatrix} \tau_{ss} & \tau_{sn} \\ \tau_{ns} & \tau_{nn} \end{bmatrix} \simeq \begin{bmatrix} 0 & \tau \\ \tau & 0 \end{bmatrix} \tag{4.18}$$

Approximation (4.17) follows from the streamlines being almost parallel within the layer. This was already used in Chapter 3 to give the wall pressure result (3.2), shown in Figure 3.1. Here this approximation allows replacing the n-momentum equation with the simple statement that the pressure across the boundary layer at any s location is constant, and equal to the inviscid flow's edge pressure at that same s location.

$$p(s,n) \simeq p_e(s) \tag{4.19}$$

Consequently, the streamwise pressure gradient in the remaining s-momentum equation can be replaced by the edge velocity gradient using the inviscid streamwise momentum equation.

$$-\frac{\partial p}{\partial s} = -\frac{\mathrm{d} p_e}{\mathrm{d} s} = \rho_e u_e \frac{\partial u_e}{\partial s} + \rho_e v_e \frac{\partial u_e}{\partial n} \simeq \rho_e u_e \frac{\mathrm{d} u_e}{\mathrm{d} s} \tag{4.20}$$

4.3.2 Boundary layer equations

Applying all the TSL approximations above to the full Navier-Stokes momentum equation (1.36), and using the unmodified mass equation (1.33), produces the following simpler *boundary layer equations*.

$$\boxed{\begin{aligned} \frac{\partial \, \rho u}{\partial s} + \frac{\partial \, \rho v}{\partial n} &= 0 \\ \rho u \frac{\partial u}{\partial s} + \rho v \frac{\partial u}{\partial n} &= \rho_e u_e \frac{\mathrm{d} u_e}{\mathrm{d} s} + \frac{\partial \tau}{\partial n} \\ \tau &= (\mu + \mu_t) \frac{\partial u}{\partial n} \end{aligned}} \tag{4.21}$$

In the shear τ definition above, $\mu_t(s,n)$ is the *Boussinesq eddy viscosity*. This captures the effects of turbulence, as will be discussed in the next section.

Appropriate boundary conditions at every s location for a wall boundary layer are

$$\boxed{\begin{aligned} \text{at wall}, \quad n = 0 : \quad & u = 0, \ v = 0 \\ \text{at edge}, \quad n = n_e : \quad & u = u_e \end{aligned}} \tag{4.22}$$

where the boundary condition "at infinity" is now imposed as a specified u_e at the edge location n_e just outside the boundary layer. The boundary layer equations (4.21) also apply for other shear layer flows such as jets, wakes, and mixing layers. But for these flows different boundary conditions would be used.

If the outer potential flow is incompressible, and in addition there is no significant wall heating or cooling, then the boundary layer is also incompressible and the viscosity is constant, as discussed in Section 1.8. Specifically, in the boundary layer equations (4.21) we have $\rho = \rho_e = $ constant and $\mu = $ constant. If μ_t is also known via some *turbulence model*, these equations are then *closed*, meaning that they are solvable for the $u, v_{(s,n)}$ velocity fields.

If significant wall cooling or heating is present, or if the edge Mach number is sufficiently large for significant frictional heating to occur, then the density and viscosity variation across the boundary layer need to be accounted for via the temperature variation. These compressibility corrections are somewhat beyond scope and will not be treated here in any theoretical detail.

4.3.3   Characteristics of turbulent boundary layers

A turbulent boundary layer features small-scale, rapid, chaotic velocity fluctuations, which result in *turbulent mixing* which transports momentum across the boundary layer. This momentum transport is an apparent *Reynolds shear stress*, also called *turbulent shear stress*, and is given by $\tau_t = \mu_t \, \partial u / \partial n$. This adds to the molecular-motion transport which constitutes the usual laminar viscous shear stress $\tau_\ell = \mu \, \partial u / \partial n$, so that the *total shear stress* in equations (4.21) is the sum of the laminar and turbulent contributions.

$$\tau_{(s,n)} \;=\; \tau_\ell + \tau_t \;=\; \left(\mu + \mu_{t(s,n)} \right) \frac{\partial u}{\partial n} \tag{4.23}$$

In contrast to the laminar viscosity μ which is nearly constant, the eddy viscosity $\mu_{t(n)}$ varies strongly across the boundary layer at any given location s, with the result that the turbulent $\partial u / \partial n$ profile and hence the u profile are markedly different from the laminar case. The various relevant laminar and turbulent profiles are sketched and compared in Figure 4.5.
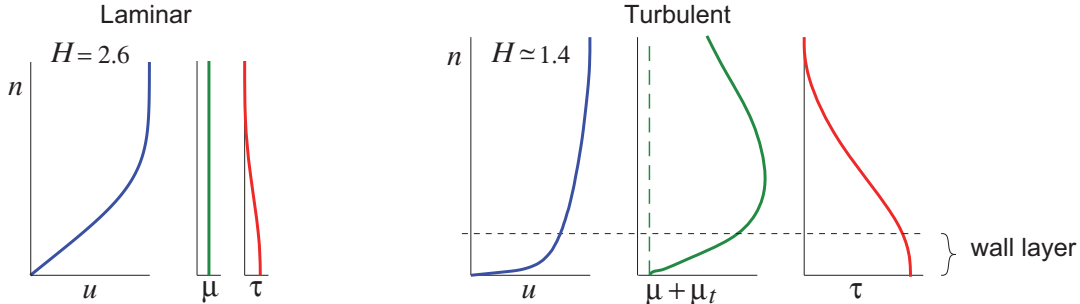
Figure 4.5: Comparison of laminar and turbulent flat-plate velocity, viscosity, and shear profiles. The shape parameter H is introduced in Section 4.5.

The key feature which makes turbulent boundary layers so different is that μ_t is large relative to μ over most of the turbulent boundary layer, but falls linearly to zero over roughly the bottom 20% portion called the *wall layer*. Here the total stress τ is approximately constant and equal to the wall shear stress τ_w. Hence in the wall layer $\partial u / \partial n$ varies roughly as $1/n$, and therefore $u_{(n)} \sim \ln n$. The variation of all the quantities in the wall layer can be summarized as follows.

$$\begin{aligned}
\tau_{(n)} \;&\simeq\; \tau_w \;\;&\sim\;\; &\text{const.} \\
\mu_{t(n)} \;&&\sim\;\; &n \\
\partial u / \partial n \;=\; \tau_{(n)} / \mu_{t(n)} \;&&\sim\;\; &1/n \qquad (\text{assuming } \mu \ll \mu_t) \\
u_{(n)} \;&&\sim\;\; &\ln n
\end{aligned}$$

The logarithmic profile in the wall layer gives the overall turbulent profile its distinctive "knee." Its greater velocities near the wall greatly increase the turbulent boundary layer's resistance to adverse pressure gradients by a factor of five or more over laminar flow, which is crucial for the lift generation capability of typical airfoils. The main drawback is that turbulent flow results in increased skin friction and profile drag compared to laminar flow, and this discrepancy increases with increasing Reynolds number. For this reason, turbulent flow is generally undesirable wherever its adverse pressure gradient resistance is not needed.

To solve the boundary layer equations (4.21) for turbulent flow, we must also simultaneously determine the entire eddy viscosity $\mu_{t(s,n)}$ field, inside and outside the wall layer. This is one of the central goals addressed by *turbulence modeling*, which is an enormous field (see Reynolds [10]). Covering any such models is beyond scope here. Instead, we will only discuss the general features of turbulence on boundary layer behavior, and consider only relatively simple integral turbulent calculation methods which do not need detailed turbulence models for the eddy viscosity.

4.4 Boundary Layer Response to Pressure and Shear Gradients

If we temporarily redefine s, n to be parallel and normal to some particular streamline, then locally $v = 0$ in these coordinates, and the s-momentum equation becomes

$$\rho u \frac{\partial u}{\partial s} \;=\; \rho_{\mathrm{e}} u_{\mathrm{e}} \frac{\mathrm{d} u_{\mathrm{e}}}{\mathrm{d}s} \;+\; \frac{\partial \tau}{\partial n}$$

which provides an estimate of the change in a fluid element's velocity Δu over some small distance Δs.

$$\Delta u \;\simeq\; \frac{\partial u}{\partial s}\Delta s \;=\; \frac{\rho_{\mathrm{e}} u_{\mathrm{e}}}{\rho u}\Delta u_{\mathrm{e}} \;+\; \frac{1}{\rho u}\frac{\partial \tau}{\partial n}\Delta s \tag{4.24}$$

The first term on the right in (4.24) represents the effect of a streamwise pressure gradient $\mathrm{d}p/\mathrm{d}s$. Of particular importance is the factor $\rho_{\mathrm{e}} u_{\mathrm{e}}/\rho u$ which "magnifies" any edge velocity change Δu_{e} into a larger change Δu inside the boundary layer, as shown in Figure 4.6.
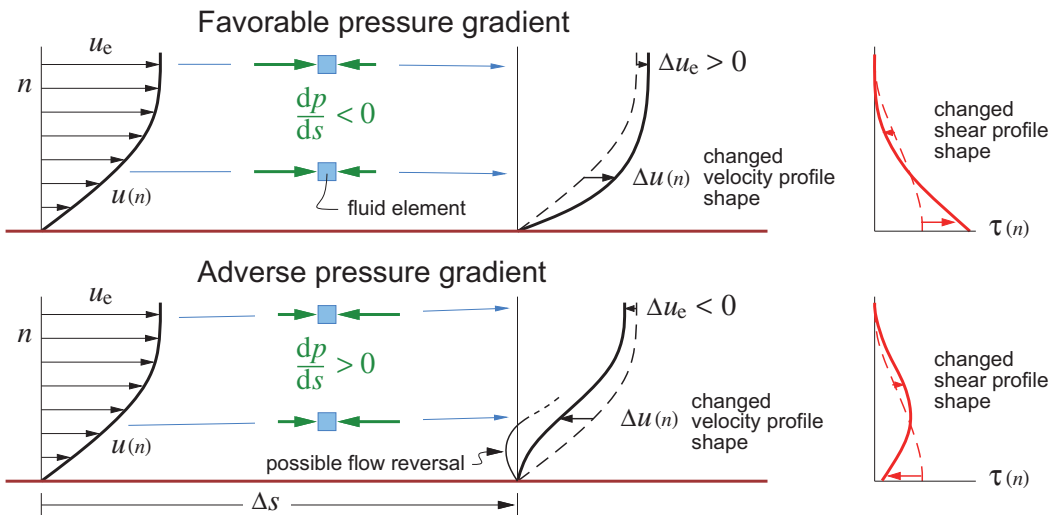
Figure 4.6: Velocity changes Δu along streamlines resulting from a favorable or adverse pressure gradient which applies the same accelerating or decelerating net force per unit volume to all fluid elements. Slower-moving elements have a larger Δu, resulting a distortion of the velocity profile. A sufficiently strong adverse pressure gradient will cause a flow reversal and boundary layer separation.

When $\mathrm{d}p/\mathrm{d}s < 0$ we have a *favorable pressure gradient*. This corresponds to $\mathrm{d}u_\mathrm{e}/\mathrm{d}s > 0$, so this is also called an *accelerating boundary layer*. As pictured at the top of Figure 4.6, the pressure gradient applies the same accelerating force per unit volume to all the fluid elements in the boundary layer, but the slower element responds more strongly due to its larger $\rho_\mathrm{e}u_\mathrm{e}/\rho u$ factor in (4.24).

When $\mathrm{d}p/\mathrm{d}s > 0$ we have an *adverse pressure gradient*. This corresponds to $\mathrm{d}u_\mathrm{e}/\mathrm{d}s < 0$, so this is also called a *decelerating boundary layer*, pictured at the bottom of Figure 4.6. In this case we have the possibility of *flow reversal* near the wall, which results in *flow separation* where the bulk of the shear layer lifts off the wall as shown in Figure 4.4 on the right. This also results in rapid increases in the mass defect, and thus produces strong viscous displacement effects on the outer potential flow.

Unlike the streamwise pressure gradient which is uniform across the boundary layer thickness, the transverse shear gradient $\partial\tau/\partial n$ varies strongly across the layer and applies different streamwise forces to different fluid elements, as shown in Figure 4.7. These variations in the shear forces persistently tend to "flatten" the velocity profile, and their cumulative effect is to cause the overall boundary layer to thicken downstream. The shear gradient also provides a negative feedback in the streamwise momentum equation, in that it acts to partially counter the possibly rapid $u(n)$ profile shape distortions caused by streamwise pressure gradients.
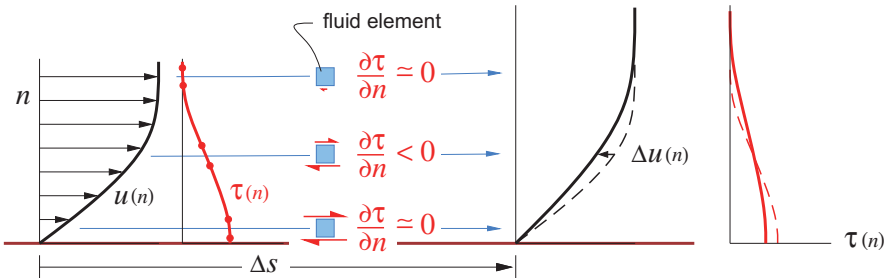
Figure 4.7: A transverse shear gradient produces a net streamwise force per unit volume which tends to "flatten" the velocity profile, and results in an overall growth of the boundary layer.

4.5   Integral Boundary Layer Relations

4.5.1   Integral momentum equation

The integral momentum analysis begins by combining the continuity and s-momentum equations as follows.

$$(u_\mathrm{e}-u)\left[\ \frac{\partial\,\rho u}{\partial s}\ +\ \frac{\partial\,\rho v}{\partial n}\ =\ 0\ \right]$$

$$-\ \left[\ \rho u\frac{\partial u}{\partial s}\ +\ \rho v\frac{\partial u}{\partial n}\ =\ \rho_\mathrm{e}u_\mathrm{e}\frac{\mathrm{d}u_\mathrm{e}}{\mathrm{d}s}\ +\ \frac{\partial\tau}{\partial n}\ \right]$$

$$\frac{\partial}{\partial s}\left[(u_\mathrm{e}-u)\rho u\right]\ +\ \frac{\partial}{\partial n}\left[(u_\mathrm{e}-u)\rho v\right]\ =\ -(\rho_\mathrm{e}u_\mathrm{e}-\rho u)\frac{\mathrm{d}u_\mathrm{e}}{\mathrm{d}s}\ -\ \frac{\partial\tau}{\partial n} \tag{4.25}$$

Integrating $\int_0^{n_\mathrm{e}}[$ equation (4.25)$]\,\mathrm{d}n$ term by term then gives the dimensional form of the *von Karman integral momentum equation*,

$$\boxed{\ \frac{\mathrm{d}}{\mathrm{d}s}\left(\rho_\mathrm{e}u_\mathrm{e}^2\theta\right)\ =\ \tau_\mathrm{w}\ -\ \rho_\mathrm{e}u_\mathrm{e}\delta^*\frac{\mathrm{d}u_\mathrm{e}}{\mathrm{d}s}\ } \tag{4.26}$$

or equivalently $$\frac{\mathrm{d}P}{\mathrm{d}s}\ =\ \tau_\mathrm{w}\ +\ \delta^*\frac{\mathrm{d}p}{\mathrm{d}s} \tag{4.27}$$

where we see the reappearance of the mass defect $m = \rho_e u_e \delta^*$ and momentum defect $P = \rho_e u_e^2 \theta$ which previously appeared in Section 4.2.2 in the mass and momentum flow comparisons between viscous and inviscid flows.

Dividing equation (4.26) by $\rho_e u_e^2$ produces the exactly equivalent dimensionless form,

$$\frac{d\theta}{ds} = \frac{c_f}{2} - (H + 2 - M_e^2) \frac{\theta}{u_e} \frac{du_e}{ds} \qquad (4.28)$$

where the following new dimensionless parameters have been defined.

$$H \equiv \frac{\delta^*}{\theta} \qquad \text{shape parameter}$$

$$c_f \equiv \frac{\tau_w}{\frac{1}{2}\rho_e u_e^2} \qquad \text{skin friction coefficient}$$

$$M_e \equiv \frac{u_e}{a_e} \qquad \text{edge Mach number}$$

The edge Mach number appears in (4.28) via the isentropic relation (1.78) between density and velocity differentials, which is valid for the edge quantities since these are in the inviscid flow.

$$\frac{d\rho_e}{\rho_e} = -M_e^2 \frac{du_e}{u_e} \qquad (4.29)$$

The dimensional von Karman equation (4.26) is seen to govern the evolution of the momentum defect P, while the dimensionless form (4.28) governs the evolution of the related momentum thickness θ. The solution of (4.28) to determine $\theta_{(s)}$ will be addressed in later sections.

4.5.2 Integral kinetic energy equation

An equation for the kinetic energy is obtained by multiplying the momentum equation by the velocity u. The mass equation is also incorporated to put the result into divergence form as follows.

$$\frac{1}{2}(u_e^2 - u^2) \left[\frac{\partial \rho u}{\partial s} + \frac{\partial \rho v}{\partial n} = 0 \right]$$

$$- u \left[\rho u \frac{\partial u}{\partial s} + \rho v \frac{\partial u}{\partial n} = \rho_e u_e \frac{du_e}{ds} + \frac{\partial \tau}{\partial n} \right]$$

$$\overline{\frac{\partial}{\partial s} \left[\frac{1}{2}(u_e^2 - u^2) \rho u \right] + \frac{\partial}{\partial n} \left[\frac{1}{2}(u_e^2 - u^2) \rho v \right] = -u(\rho_e - \rho) u_e \frac{du_e}{ds} - u \frac{\partial \tau}{\partial n}} \qquad (4.30)$$

Integrating $\int_0^{n_e} [$ equation (4.30)$]$ dn term by term gives the dimensional *integral kinetic energy equation*,

$$\frac{d}{ds} \left(\frac{1}{2}\rho_e u_e^3 \theta^* \right) = \mathcal{D} - \rho_e u_e^2 \delta^{**} \frac{du_e}{ds} \qquad (4.31)$$

or equivalently $\qquad \frac{dK}{ds} = \mathcal{D} + u_e \delta^{**} \frac{dp}{ds} \qquad (4.32)$

where the kinetic energy defect $K = \frac{1}{2}\rho_e u_e^3 \theta^*$ appeared previously in Section 4.2.2 in the kinetic energy flow comparisons between viscous and inviscid flows. New quantities which appear here are

$$\delta^{**} \equiv \int_0^{n_e} \left(1 - \frac{\rho}{\rho_e} \right) \frac{u}{u_e} \, dn \qquad (4.33)$$

$$\mathcal{D} \equiv \int_0^{n_e} \tau \frac{\partial u}{\partial n} \, dn = \int_0^{n_e} (\mu + \mu_t) \left(\frac{\partial u}{\partial n} \right)^2 \, dn \qquad (4.34)$$

where δ^{**} is the *density flux thickness* which measures the work done (positive or negative) by the pressure gradient in conjunction with density variations across the boundary layer, and $\mathcal{D}$ is the *dissipation integral* which measures the local rate of flow kinetic energy dissipation into heat by the shear stress τ acting on the fluid which is deforming at the shear strain rate $\partial u / \partial n$. Note that $\delta^{**} = 0$ in incompressible flow where $\rho/\rho_e = 1$, while $\mathcal{D}$ is always present and is virtually always positive ($\mu_t < 0$ is very unlikely).

Dividing equation (4.31) by $\frac{1}{2}\rho_e u_e^3$ produces its exactly equivalent dimensionless form,

$$\boxed{\frac{\mathrm{d}\theta^*}{\mathrm{d}s} = 2\,c_{\mathcal{D}} - \left(\frac{2H^{**}}{H^*} + 3 - M_e^2\right)\frac{\theta^*}{u_e}\frac{\mathrm{d}u_e}{\mathrm{d}s}} \qquad (4.35)$$

where the following new dimensionless parameters have been defined.

$$H^* \equiv \frac{\theta^*}{\theta} \qquad \text{kinetic energy shape parameter}$$

$$H^{**} \equiv \frac{\delta^{**}}{\theta} \qquad \text{density flux shape parameter}$$

$$c_{\mathcal{D}} \equiv \frac{\mathcal{D}}{\rho_e u_e^3} \qquad \text{dissipation coefficient}$$

The dimensional kinetic energy equation (4.31) is seen to govern the evolution of the kinetic energy defect K, while the dimensionless form (4.35) governs the evolution of the related kinetic energy thickness θ^*. The dimensionless kinetic energy equation (4.35) is used in some advanced integral calculation methods. See Rosenhead [11], Schlichting [12], and Drela et al. [6] for examples.

4.5.3 Integral defect evolution

To gain insight into how the integral defects evolve along a boundary layer, and how they relate to 2D profile drag, we integrate the dimensional von Karman equation (4.26) on each airfoil side and in the wake. On the airfoil surfaces the integration runs from the stagnation point $s = 0$ to some surface location s, while in the wake it runs from the trailing edge s_{TE} to some wake location s, as sketched in Figure 4.8.

$$\int_0^s \left\{\frac{\mathrm{d}P}{\mathrm{d}s'} = \tau_w - m\frac{\mathrm{d}u_e}{\mathrm{d}s'}\right\}\mathrm{d}s'$$

$$P_{(s)} = \int_0^s \tau_w\,\mathrm{d}s' + \int_0^s -m\frac{\mathrm{d}u_e}{\mathrm{d}s'}\,\mathrm{d}s' \qquad \text{(on airfoil surface)} \qquad (4.36)$$

$$P_{(s)} = P_{TE} + \int_{s_{TE}}^s -m\frac{\mathrm{d}u_e}{\mathrm{d}s'}\,\mathrm{d}s' \qquad \text{(in wake)} \qquad (4.37)$$

Since the stagnation point momentum defect $P_{(0)}$ is zero, it was dropped from (4.36). And since the wall shear is zero in the wake, the τ_w term was dropped from (4.37). The initial wake defect P_{TE} in (4.37) is the sum of the upper and lower surface defects at the trailing edge.

The same integration can be applied to the dimensional kinetic energy equation (4.31).

$$\int_0^s \left\{\frac{\mathrm{d}K}{\mathrm{d}s'} = \mathcal{D}\right\}\mathrm{d}s'$$

$$K_{(s)} = \int_0^s \mathcal{D}\,\mathrm{d}s' \qquad \text{(on airfoil surface)} \qquad (4.38)$$

$$K_{(s)} = K_{TE} + \int_{s_{TE}}^s \mathcal{D}\,\mathrm{d}s' \qquad \text{(in wake)} \qquad (4.39)$$

The δ^{**} term in (4.31) has been neglected since it vanishes in incompressible flow, and is usually small in any case. For adiabatic compressible flows Sato [13] has incorporated the δ^{**} term into a modified dissipation integral $\mathcal{D}$, so the forms of the integrated $K(s)$ expressions (4.38) and (4.39) are generally valid.
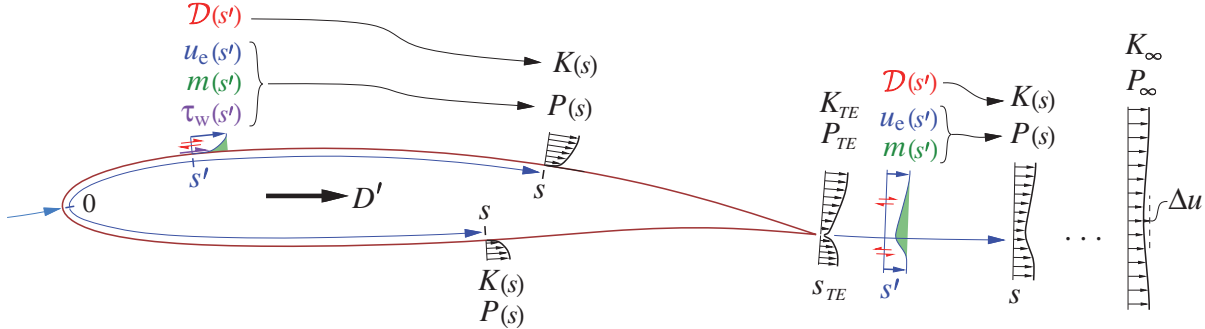
Figure 4.8: Momentum defect $P(s)$ at any location s, including in the wake, obtained as an integral over upstream $\tau_{\mathrm{w}}, m, u_{\mathrm{e}}(s')$ distributions. Kinetic energy defect $K(s)$ is obtained from upstream $\mathcal{D}(s')$ distribution. Far-downstream wake's P_∞, K_∞ are related to the airfoil's profile drag/span D'.

We now examine the $P(s)$ and $K(s)$ distributions on the GAW-1 airfoil. Figure 4.9 shows its C_p distributions at $\alpha = 5°$. Figure 4.10 shows the $\tau_{\mathrm{w}}(s)$ and $\mathcal{D}(s)$ distributions on the upper surface and wake, and also the corresponding defects $P(s)$ and $K(s)$. Also shown is the friction-only defect $P_{\mathrm{friction}}(s)$, which then also indicates the remaining pressure defect $P_{\mathrm{pressure}}(s)$ as the difference from the total $P(s)$.

$$P_{\mathrm{friction}}(s) \;=\; \int_0^s \tau_{\mathrm{w}}\,\mathrm{d}s' \qquad\qquad P_{\mathrm{pressure}}(s) \;=\; \int_0^s -m\,\frac{\mathrm{d}u_{\mathrm{e}}}{\mathrm{d}s'}\,\mathrm{d}s' \;=\; P - P_{\mathrm{friction}}$$

We see that τ_{w} dominates the $P(s)$ development over the front of the airfoil, but $-m\,\mathrm{d}u_{\mathrm{e}}/\mathrm{d}s$ dominates over the back of the airfoil. In the wake, the latter term decreases $P(s)$ due to the wake's favorable pressure gradient, or $\mathrm{d}u_{\mathrm{e}}/\mathrm{d}s > 0$. In contrast, $K(s)$ is strictly monotonic since its only source term $\mathcal{D}(s)$ is everywhere positive, including in the wake. In particular, the evolution of $K(s)$ does not depend on the pressure gradient, except indirectly via the pressure gradient's relatively weak influence on $\mathcal{D}$.
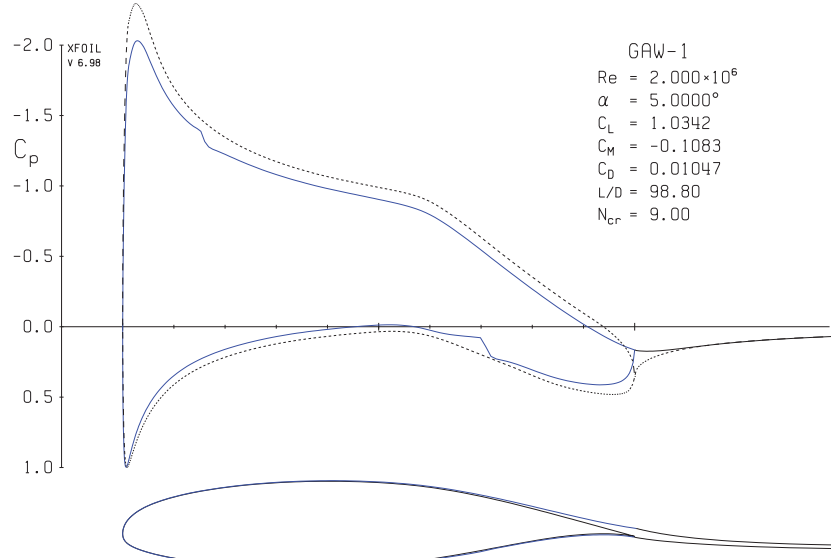
Figure 4.9: Computed pressure distributions on GAW-1 airfoil at $\alpha = 5°$, $Re = 2 \times 10^6$. Dotted line is the Simple Inviscid model. Solid line is the more realistic Wall Transpiration model. Bumps in the solid line are due to separation bubbles and transition, discussed in Section 4.14.4.
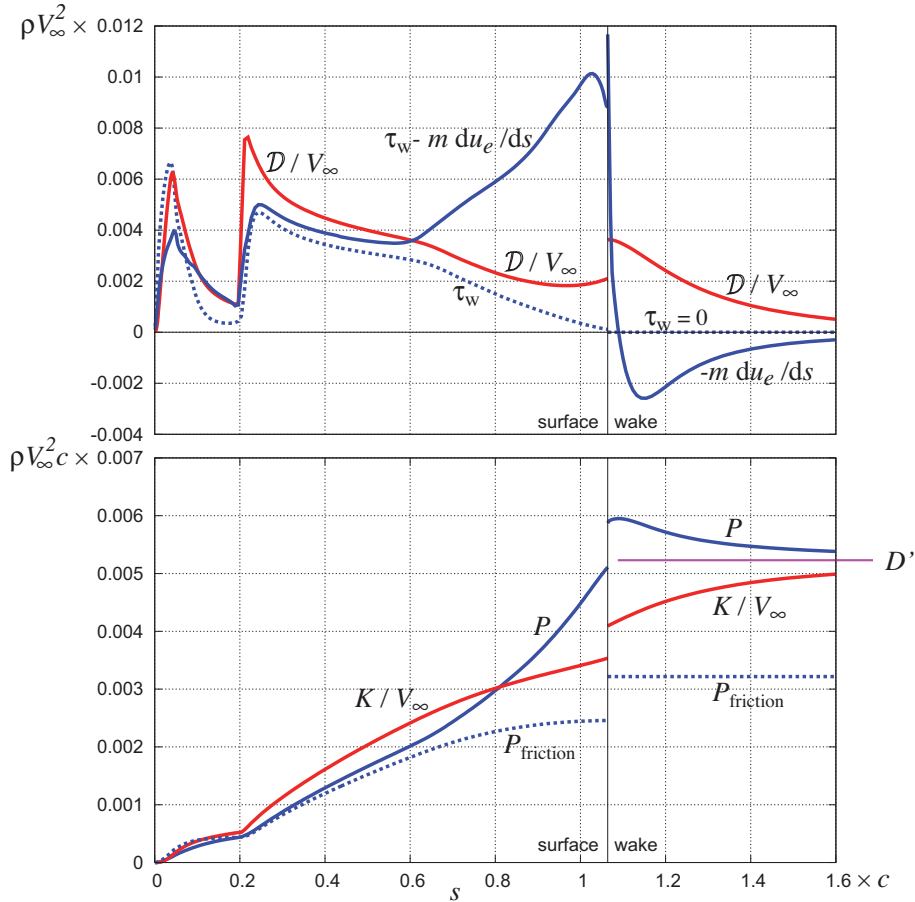
Figure 4.10: Distributions of boundary layer parameters for upper surface and wake of GAW-1 airfoil at $\alpha = 5°$, $Re = 2 \times 10^6$. Transition occurs at $s \simeq 0.2c$, where τ_w and $\mathcal{D}$ increase sharply. P and K/V_∞ in the far wake asymptote towards the profile drag/span D'. The jumps in P and K at the trailing edge are from the bottom surface's P and K (not shown) adding to the wake.

4.5.4   Integral defect / profile drag relations

As derived in Appendix C, the airfoil's profile drag is equal to the far-downstream wake momentum defect P_∞. Noting that P_{TE} in (4.37) is the sum of the upper and lower surfaces' $P(s)$ given by (4.36) at the trailing edge, we then have the following result from (4.37). The D' limit is indicated in the bottom of Figure 4.10.

$$
D' \;=\; P_\infty \;=\; \int_{\mathrm{airfoil}} \tau_\mathrm{w} \, \mathrm{d}s \;+\; \int_{\mathrm{airfoil+wake}} -m\,\frac{\mathrm{d}u_e}{\mathrm{d}s}\,\mathrm{d}s \tag{4.40}
$$

It is useful to compare the two terms in (4.40) with the friction+pressure drag components, both of which will be further addressed in Chapter 5. Choosing the x-axis to be parallel to $\mathbf{V}_\infty$ we have

$$
D' \;=\; D'_\mathrm{friction} \;+\; D'_\mathrm{pressure}
$$

$$
D'_\mathrm{friction} \;\equiv\; \oint_{\mathrm{airfoil}} \boldsymbol{\tau}_\mathrm{w} \cdot \hat{\mathbf{x}} \, \mathrm{d}s \qquad , \qquad D'_\mathrm{pressure} \;\equiv\; \oint_{\mathrm{airfoil}} -p_\mathrm{w}\,\hat{\mathbf{n}} \cdot \hat{\mathbf{x}} \, \mathrm{d}s \tag{4.41}
$$

where $\hat{\mathbf{n}}$ is the airfoil-surface outward unit normal, and $\boldsymbol{\tau}_\mathrm{w}$ is the surface viscous stress vector. Evidently, the first integral in (4.40) can be interpreted as the friction drag, while the second integral must then be the

remaining pressure drag part.

$$D'_{\text{friction}} \simeq \int_{\text{airfoil}} \tau_{\text{w}} \, ds \tag{4.42}$$

$$D'_{\text{pressure}} = D' - D'_{\text{friction}} \simeq \int_{\text{airfoil+wake}} -m \frac{du_{\text{e}}}{ds} \, ds = \int_{\text{airfoil+wake}} \delta^* \frac{dp}{ds} \, ds \tag{4.43}$$

The friction drag estimate (4.42) is only approximate because the viscous surface force vector τ_{w} is very nearly parallel to the surface, while an exact match with the friction drag definition (4.41) would require τ_{w} to be parallel to the freestream $\mathbf{V}_\infty$ along $\hat{\mathbf{x}}$. However, the angle between τ_{w} and $\mathbf{V}_\infty$ is small over most of the surface, especially for thin airfoils, so the friction and pressure drag component estimates (4.42) and (4.43) are still useful conceptually. In particular, the integrals in (4.43) indicate that most of the pressure drag is produced where there is an adverse pressure gradient in the presence of a large mass defect m or displacement thickness δ^*. This combination typically occurs over the rear portion of the airfoil at high lift, and can be clearly seen in the top of Figure 4.10 for $s > 0.6c$.

To relate the kinetic energy defect result (4.38) and (4.39) to profile drag, we first write P and K in terms of the velocity defect Δu.

$$\Delta u \equiv u - u_{\text{e}} \tag{4.44}$$

$$P = \int (u_{\text{e}} - u) \, \rho u \, dn = \int -\Delta u \, \rho u \, dn \tag{4.45}$$

$$K = \int \tfrac{1}{2}(u_{\text{e}}^2 - u^2) \, \rho u \, dn = \int -\Delta u \left(u_{\text{e}} + \tfrac{1}{2}\Delta u\right) \rho u \, dn \tag{4.46}$$

If Δu is very small compared to u_{e}, then K and P become simply related to a good approximation.

$$K \simeq \int -\Delta u \, u_{\text{e}} \, \rho u \, dn = P \, u_{\text{e}} \qquad (\text{if } \Delta u \ll u_{\text{e}}) \tag{4.47}$$

This occurs in the far-downstream wake where Δu goes to zero as the wake spreads and mixes out. And in the far wake u_{e} also approaches V_∞, so that the two defects become exactly related far downstream.

$$\boxed{K_\infty = P_\infty V_\infty} \tag{4.48}$$

Combining this with (4.40) then gives an alternative expression for the overall profile drag in terms of the far-downstream wake kinetic energy defect, and also the dissipation everywhere.

$$\boxed{D' V_\infty = K_\infty = \int_{\text{airfoil+wake}} \mathcal{D} \, ds} \tag{4.49}$$

This rather simple result has a power balance interpretation: The drag D' must be balanced by an external thrust force which moves at speed V_∞ relative to the airmass, and thus exerts a power of $D'V_\infty$ which is all dissipated in the viscous layers. The conclusion is that profile drag is uniquely related to viscous stresses as quantified by the distribution of the dissipation integral $\mathcal{D}(s)$, and this dissipation contributes positively to the drag everywhere since $\mathcal{D} \geq 0$ always. This strictly-positive dependence of drag on viscous forces isn't immediately obvious from the alternative momentum-based profile drag expression (4.40). Its second pressure term always has some locally negative contributions to the total drag, and its first friction term also has locally negative contributions in separated regions which exhibit reversed flow and hence $\tau_{\text{w}} < 0$.

Invoking the friction and pressure drag definitions (4.41), the power-balance relation (4.49) gives an alternative relation for the friction plus pressure drag.

$$D'_{\text{friction}} + D'_{\text{pressure}} = \frac{1}{V_\infty} \int_{\text{airfoil+wake}} \mathcal{D} \; \mathrm{d}s \tag{4.50}$$

Since the $\mathcal{D}$ and D'_{friction} terms both depend only on the viscous stresses $\tau_{(s,n)}$ via their definitions (4.34) and (4.41), the remaining pressure drag D'_{pressure} term then also depends only on the viscous stresses. In this power balance view, we can then conclude that the pressure field is not the <u>cause</u> of pressure drag, but rather it's a necessary additional power-transmission mechanism (the surface friction forces alone are insufficient) from the body surface to the flow-field interior where the viscous power dissipation takes place. This has implications for aerodynamic design as will be discussed in Section 4.11.4.

4.6   Self-Similar Laminar Boundary Layers

Most finite-difference methods for solving the boundary layer equations (4.21), to be summarized in Section 4.10.2, actually solve transformed versions of these equations. One example is the following transformation $n, u \rightarrow \eta, U$ using the local normal-length and streamwise-velocity scales $\delta(s)$ and $u_e(s)$.

$$\eta(s,n) \equiv \frac{n}{\delta(s)} \quad , \quad U(s,\eta) \equiv \frac{u(s,n)}{u_e(s)} \tag{4.51}$$

The local length scale $\delta(s)$ can be chosen arbitrarily. However, it is advantageous to define it such that it is roughly proportional to the physical thickness of the boundary layer, so that the s–η computational grid grows along with the layer, as shown in Figure 4.11 on the left. This makes the $U(s,\eta)$ velocity profiles stay within the s–η grid, which considerably simplifies the finite-difference solution procedure when it is applied on this grid, instead of on the physical s–n grid.

One practical complication of the length scale choice $\delta = n_e$ shown in Figure 4.11 is that the boundary layer's edge location is somewhat subjective, since u approaches u_e only asymptotically. Alternative choices for δ are δ^*, θ, etc., which have the advantage of being unambiguously defined.
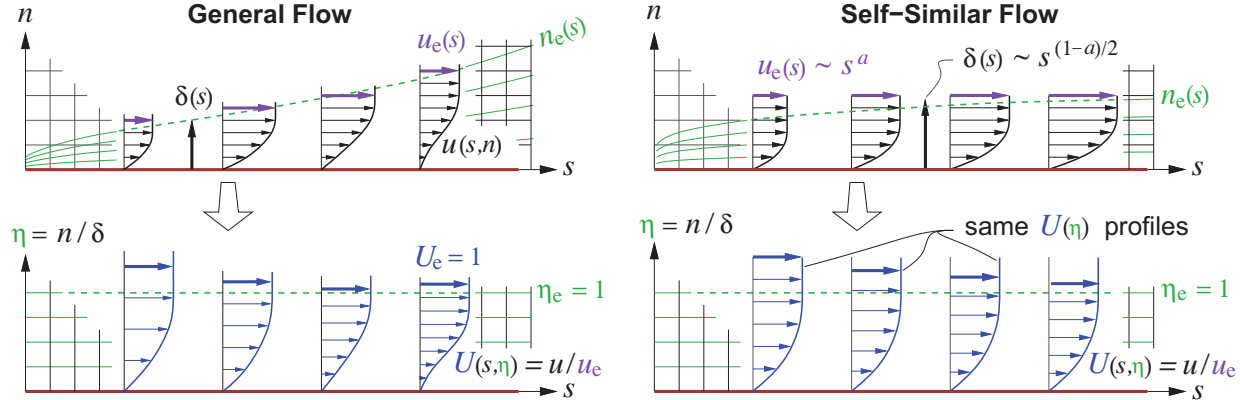
Figure 4.11:   Local scaling transformation using $\delta(s)$ and $u_e(s)$ makes the s–η grid grow with the boundary layer, so $U(\eta)$ stays within this grid (left). The special case of power-law $u_e(s)$ (right) makes all the $U(\eta)$ profiles the same for each s location, which constitutes a self-similar flow.

Another feature of the transformation (4.51) is that it fundamentally simplifies the problem for a special class of incompressible laminar boundary layer flows where $u_e(s)$ has a *power-law* form,

$$u_e(s) = C \, s^a \tag{4.52}$$

and C and a are specified constants. If for $\delta(s)$ we now make the specific choice

$$\delta(s) \;=\; \sqrt{\frac{\nu s}{u_{\mathrm{e}}(s)}} \;=\; \sqrt{\frac{\nu}{C}}\, s^{(1-a)/2} \;\equiv\; \delta_{\mathrm{FS}}(s) \tag{4.53}$$

we have the *Falkner-Skan Transformation* [12], [11]. The resulting transformed boundary layer equations no longer have any dependence on s, so their solution has the form $U = U(\eta\,;a)$. This is called a *self-similar boundary layer flow*, in that all the velocity profiles are "similar," or more precisely they have the same normalized $U(\eta)$ at each streamwise location s. The situation is pictured in Figure 4.11 on the right. The $U(\eta)$ shape does depend on the power-law exponent, however, so we get a different flow for each value of a.

The Falkner-Skan solution velocity profiles are shown in Figure 4.12 for several values of a. Their numerical parameter values of interest are listed in Table 4.1. Note that because δ_{FS} is significantly smaller than the boundary layer thickness n_{e}, the η values are considerably greater than unity.
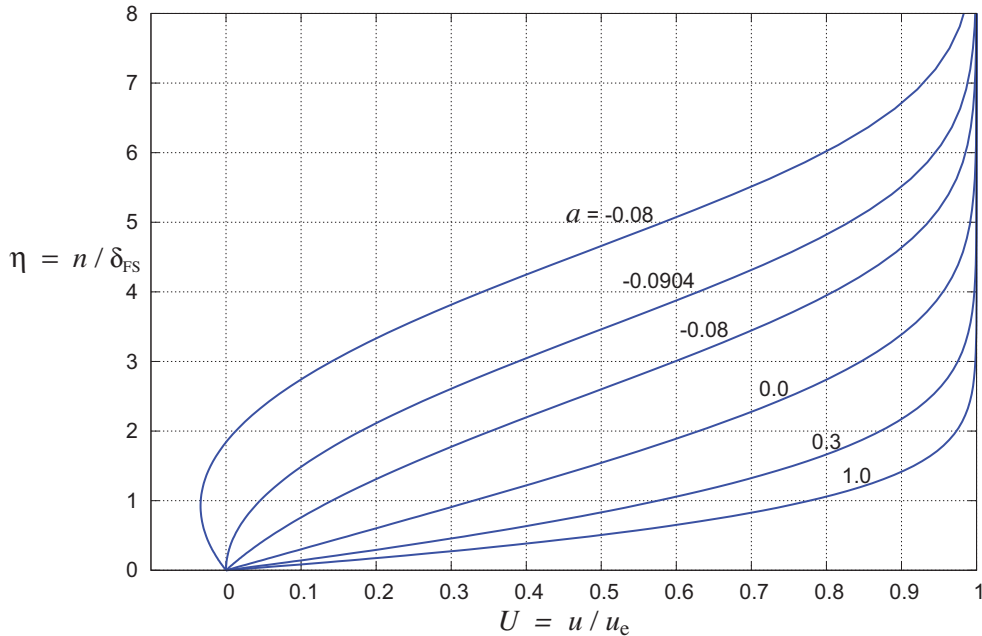
Figure 4.12: Falkner-Skan velocity profiles, for several values of $u_{\mathrm{e}} \sim s^a$ power-law exponent a. Each $U(\eta)$ profile describes the entire self-similar velocity field $u(s,n\,;a)$, via (4.51), (4.52), (4.53). Numerical parameter values of interest for these profiles are listed in Table 4.1.

Although these solutions apply only to self-similar (power-law) laminar boundary layer flows, they reveal a number of important characteristics which apply to more general laminar boundary layer flows. They also confirm the general effects of pressure gradients which were qualitatively examined in Section 4.4.

- For favorable pressure gradients $a > 0$, the velocity profile is "full" near the wall, with a monotonic curvature, relatively large skin friction coefficient c_f values, and small shape parameter H values.

- For adverse pressure gradients $a < 0$, the velocity profile is inflected, with a smaller skin friction and large shape parameters H.

- There is a minimum value $a \simeq -0.0904$, which is the incipient-separation case, with $c_f = 0$ and $H \simeq 4.029$. For a less than this minimum, no physical self-similar solution of the boundary layer equations (4.21) exists.

- Separated-flow solutions with $c_f < 0$ and $H > 4.029$ do exist, but their a parameter is less negative than the minimum value. They also exhibit reversed flow $U < 0$ near the wall.

- The small minimum achievable negative value of $a_{\min} = -0.0904$ indicates that laminar flows cannot tolerate significant adverse pressure gradients, or equivalently, significant decreases in $u_e(s)$. For example, over a doubled laminar run distance, $s_2/s_1 = 2$, the minimum tolerable velocity decrease is $u_{e_2}/u_{e_1} = (s_2/s_1)^{a_{\min}} = 0.939$ which is only a 6.1% deceleration.

Table 4.1: Falkner-Skan solution parameters for self-similar boundary flows with $u_e(s) = Cs^a$. The local Reynolds number is $Re_x = u_e(s)\, s/\nu$. Parameters $\lambda, \mathcal{T}, \mathcal{F}_\theta$ will be defined in Section 4.11.1.

a	$\dfrac{\delta^*}{\delta_{\mathrm{FS}}}$	$\dfrac{\theta}{\delta_{\mathrm{FS}}}$	H	H^*	$Re_x^{1/2}\dfrac{c_f}{2}$	$Re_x^{1/2} c_{\mathcal{D}}$	λ	$\mathcal{T}$	$\mathcal{F}_\theta$
2.00000	0.47648	0.21775	2.18820	1.63101	1.71507	0.97666	0.09483	0.37345	-0.04742
1.00000	0.64790	0.29235	2.21622	1.62575	1.23259	0.71291	0.08547	0.36034	0.00000
0.60000	0.79760	0.35483	2.24783	1.62006	0.97532	0.57484	0.07554	0.34608	0.05036
0.30000	1.01961	0.44196	2.30702	1.61009	0.72574	0.44474	0.05860	0.32075	0.13672
0.10000	1.34787	0.55660	2.42161	1.59308	0.49657	0.33251	0.03098	0.27639	0.27882
0.00000	1.72080	0.66412	2.59109	1.57259	0.33206	0.26109	0.00000	0.22053	0.44105
-0.05000	2.11777	0.75148	2.81815	1.55196	0.21348	0.21867	-0.02824	0.16043	0.59294
-0.08000	2.67173	0.82973	3.22000	1.52916	0.10155	0.19031	-0.05508	0.08426	0.74351
-0.09043	3.49786	0.86814	4.02916	1.51509	0.00000	0.18014	-0.06815	0.00022	0.82179
-0.08700	4.14726	0.84989	4.87975	1.52470	-0.04678	0.18303	-0.06284	-0.03976	0.78515
-0.08000	4.75540	0.80734	5.89021	1.55216	-0.07361	0.18800	-0.05214	-0.05943	0.70399

4.6.1 Wedge flows

The Falkner-Skan solutions are strictly valid only for flows with the power-law edge velocity distribution. It is fortuitous that such potential flows do indeed occur over simple geometries, the so-called *wedge flows*. Three particular wedge flows are shown in Figure 4.13, and their boundary layer solution parameters are also listed in Table 4.1. The case of $a = 1$, called *stagnation point flow*, occurs in practically every aerodynamic flow which has a body with a blunt leading edge, such as a common airfoil. For this flow we have $\delta_{\mathrm{FS}} = \sqrt{\nu/C}$, so that the boundary layer thickness near a stagnation point is locally constant.
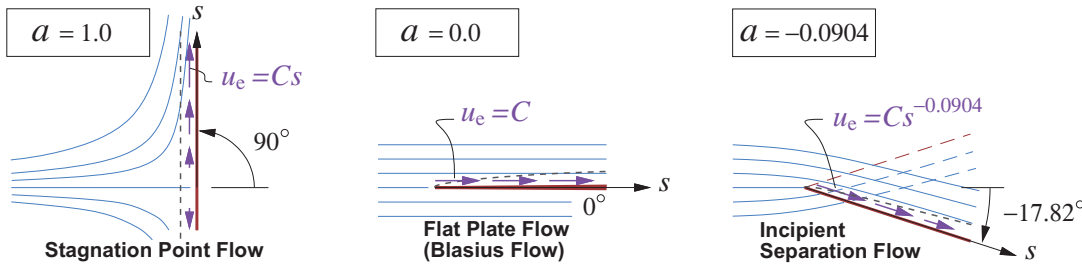
Figure 4.13: Three particular wedge flows. Displacement effect not shown.

The case $a = 0$, corresponding to a constant pressure and edge velocity, is commonly called *flat plate flow* or *Blasius flow*. For this case we have $\delta_{\mathrm{FS}} = \sqrt{\nu s/C}$, so that the boundary layer thickness grows as $\sqrt{s}$. A Blasius boundary layer is commonly used as a first approximation to laminar boundary layer flows which have nearly-constant pressure or edge velocity over most of their extent.

The last case $a = -0.0904$ shown in Figure 4.13 is called *incipient separation flow*, which has zero skin friction everywhere. This wedge flow is mainly a mathematical curiosity, since the top and bottom flows occupy the same space above the plate which is physically impossible. A more plausible example is a thin airfoil whose camber shape is such that it has the $u_e(s) \sim s^{-0.0904}$ edge velocity distribution on one side. However, since the incipient-separation boundary layer is theoretically infinitely sensitive to any $u_e(s)$

perturbations and hence to geometric irregularities, such an airfoil flow would still be virtually impossible to realize in practice. Incipient separation flow is also very susceptible to transition to turbulent flow, as will be discussed in Section 4.14, and therefore can exist only at relatively low Reynolds numbers. In this case it will have large viscous displacement effects, which will further complicate the realization of such a flow.

Besides providing physical insight and quantitative results for the special case of wedge power-law flows, the Falkner Skan solutions are also very useful for "calibrating" approximate integral solution methods for general boundary layer flows. These will be treated in Section 4.11.

4.7 Self-Similar Turbulent Boundary Layers

For the laminar case we saw that the $n, u \rightarrow \eta, U$ variable rescaling (4.51) led to a self-similar boundary layer flow for a power-law edge velocity. A suitable corresponding rescaling for the outer layer of a turbulent boundary layer is

$$\eta(s,n) \equiv \frac{n}{\delta(s)} \quad , \qquad \Delta u^+(s,\eta) \equiv \frac{\Delta u(s,n)}{u_\tau(s)} = \frac{u(s,n) - u_e(s)}{u_\tau(s)} \tag{4.54}$$

where the normalizing velocity is now the *shear velocity* u_τ, defined in terms of the wall shear stress.

$$u_\tau \equiv \sqrt{\frac{\tau_w}{\rho}} = u_e\sqrt{c_f/2} \tag{4.55}$$

Note also that this transformation addresses the *defect velocity* $\Delta u = u - u_e$, rather than u itself.

Turbulent self-similar boundary layers, also known as *equilibrium flows*, are theoretically possible when plotted in terms of the $\eta, \Delta u^+$ variables, and were first demonstrated experimentally by Clauser[14]. They are characterized by streamwise-constant values of the *Clauser parameters* G and β.

$$G \equiv \frac{\int (\Delta u^+)^2 \, dn}{\int -\Delta u^+ \, dn} = \frac{1}{\sqrt{c_f/2}} \frac{H-1}{H} \tag{4.56}$$

$$\beta \equiv \frac{\delta^* \, dp}{\tau_w \, ds} = -\frac{H}{c_f/2} \frac{\theta}{u_e} \frac{du_e}{ds} = -\frac{H}{c_f/2} \frac{\lambda}{Re_\theta} \tag{4.57}$$

An empirical relation between G and β for equilibrium flows is known as the *G-beta locus*.

$$\tilde{G}_{(\beta)} \simeq \mathcal{A}(1+\mathcal{B}\beta)^{1/2} \quad , \qquad \mathcal{A} \simeq 6.7 \ , \quad \mathcal{B} \simeq 0.75 \tag{4.58}$$

This can be considered to be the turbulent-flow equivalent of the $H_{(\lambda)}$ laminar self-similar flow relation implied by Table 4.1. The form of (4.58) is based on theoretical physical models of the turbulent boundary layer (see Coles [15]), and the values of its two constants $\mathcal{A}, \mathcal{B}$ are obtained from measurements of equilibrium boundary layers from Clauser [14], Simpson et al [16], and others. Figure 4.14 shows three turbulent equilibrium flows for three values of β.

Note that $\beta > 0$ is an adverse pressure gradient which results in a rapid thickening of the boundary layer, while $\beta < 0$ is a favorable pressure gradient with much slower growth. All the velocity profiles for each flow all collapse to the same $\Delta u^+(\eta)$ curve for that flow. This is directly analogous to the self-similar laminar wedge flows sketched in Figures 4.11 and 4.13, whose profiles all collapse to the normalized profiles shown in Figure 4.12. The good fit to the experimental data validates the turbulent equilibrium flow concept.

The special case of a very large G corresponds to a turbulent incipient-separation boundary layer flow, analogous to the laminar $H = 4.0$ Falkner-Skan flow. Flows of this type have been used by Liebeck [17] to design airfoils with the fastest-possible pressure recovery without separation, which results in extraordinarily high maximum lift. A distinctive feature of Liebeck's airfoils is a "concave" $u_e(s)$ distribution on the upper surface, comparable to the $G = 14.17$ case shown in Figure 4.14.
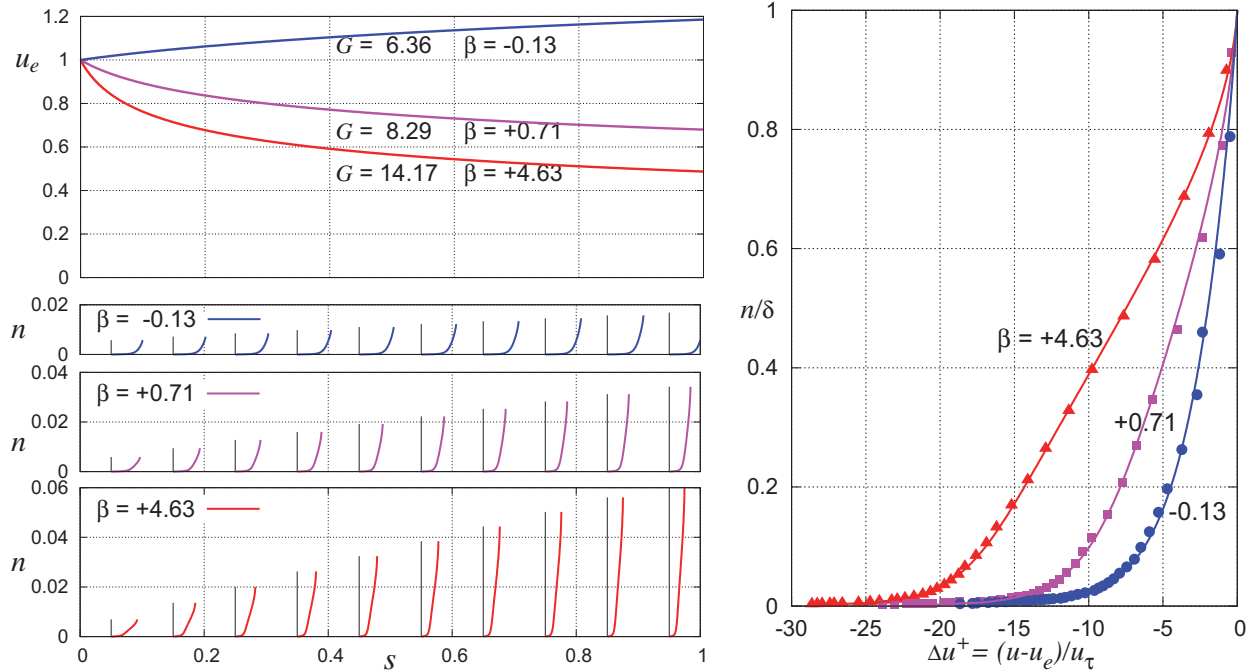
Figure 4.14: Three turbulent self-similar (equilibrium) flows, each with a constant Clauser pressure gradient parameter β, and corresponding constant G given by the G-beta locus (4.58). Each flow has an initial momentum-thickness Reynolds number $u_e\theta/\nu = 1500$ at $s = 0$. All the velocity profiles of each flow collapse to a single normalized defect profile on the right plot. Experimental data (symbols) is from Simpson et al [16].

4.8 Axisymmetric Boundary Layers

Boundary layer analysis readily applies to axisymmetric flows, such as the one shown in Figure 4.15. Extending the 2D profile drag analysis in Appendix C to the 3D case, or following the analysis in Section 5.6, we obtain the 3D profile drag in terms of the far-downstream *momentum area* Θ_∞.

$$D_p = \iint (V_\infty - u)\,\rho u\,\mathrm{d}\mathcal{S} = \rho_\infty V_\infty^2\,\Theta_\infty \tag{4.59}$$

$$\Theta_\infty \equiv \iint \left(1 - \frac{u}{V_\infty}\right)\frac{\rho u}{\rho_\infty V_\infty}\,\mathrm{d}\mathcal{S} \tag{4.60}$$
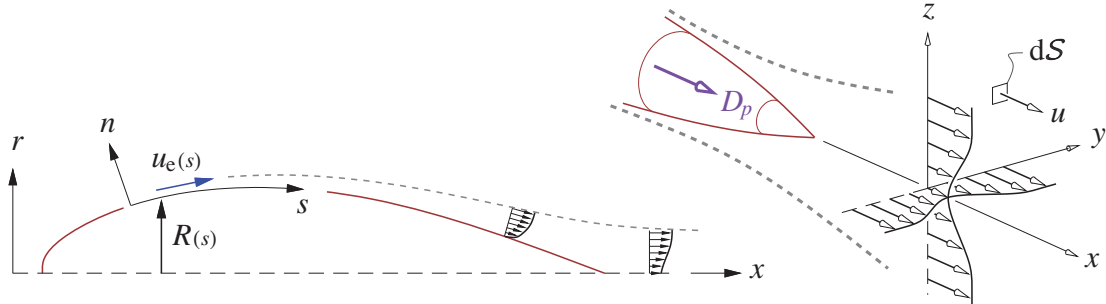
Figure 4.15: Boundary layer and wake of axisymmetric body.

For the axisymmetric 3D boundary layer and wake case, the integral (4.60) is best put into axisymmetric form using the local width parameter

$$b_{(s,n)} = 2\pi\left(R + n\sqrt{1 - (\mathrm{d}R/\mathrm{d}s)^2}\right) \simeq 2\pi\left(R + n\right) \tag{4.61}$$

as shown in Figure 4.16. The body shape is given by the local radius function $R_{(s)}$, with $R = 0$ in the wake. The second approximate form above makes the assumption that $\mathrm{d}R/\mathrm{d}s \ll 1$, which is reasonable for slender bodies, although the exact form can be used with little complication.
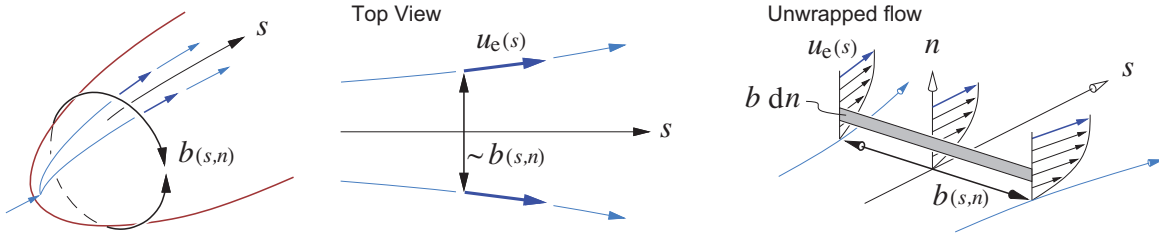
Figure 4.16: Transverse area element $b\,\mathrm{d}n$ inside boundary layer with lateral divergence, which is quantified by lateral width parameter $b_{(s,n)}$.

The transverse area element now becomes $\mathrm{d}\mathcal{S} = b\,\mathrm{d}n$, so that at any body location the momentum area, and also the displacement and kinetic energy areas, can now be defined using the usual transverse coordinate n.

$$\Delta^*_{(s)} \equiv \int_0^{n_e} \left(1 - \frac{\rho u}{\rho_e u_e}\right) b \; \mathrm{d}n \tag{4.62}$$

$$\Theta_{(s)} \equiv \int_0^{n_e} \left(1 - \frac{u}{u_e}\right) \frac{\rho u}{\rho_e u_e} b \; \mathrm{d}n \tag{4.63}$$

$$\Theta^*_{(s)} \equiv \int_0^{n_e} \left(1 - \frac{u^2}{u_e^2}\right) \frac{\rho u}{\rho_e u_e} b \; \mathrm{d}n \tag{4.64}$$

The integral equations which govern these integral areas have nearly the same form as in 2D,

$$\frac{\mathrm{d}\Theta}{\mathrm{d}s} = \frac{c_f}{2} b_{\mathrm{w}} - \left(H + 2 - M_e^2\right) \frac{\Theta}{u_e} \frac{\mathrm{d}u_e}{\mathrm{d}s} \tag{4.65}$$

$$\frac{\mathrm{d}\Theta^*}{\mathrm{d}s} = 2c_{\mathcal{D}}\, b_{\mathrm{avg}} - \left(\frac{2H^{**}}{H^*} + 3 - M_e^2\right) \frac{\Theta^*}{u_e} \frac{\mathrm{d}u_e}{\mathrm{d}s} \tag{4.66}$$

except for the lateral width friction factor $b_{\mathrm{w}} = b_{(n=0)} = 2\pi R$, and the b_{avg} dissipation factor which is a local dissipation-weighted average over the boundary layer thickness. The shape parameters have the same definitions as in 2D. For example, $H = \Delta^*/\Theta$, etc.

A significant simplification results if we replace n in the $b_{(s,n)}$ definition (4.61) with a representative height in the shear layer, the rational choice being the usual 2D displacement thickness (see Figure 4.4).

$$b_{(s)} \simeq 2\pi \left(R + \delta^* \sqrt{1 - (\mathrm{d}R/\mathrm{d}s)^2}\right) \simeq 2\pi \left(R + \delta^*\right) \tag{4.67}$$

This approximate $b_{(s)}$ can now be taken outside of the integral area definition integrals (4.62)–(4.64), making them simply related to the usual 2D thicknesses.

$$\Delta^* = \delta^* b \quad , \qquad \Theta = \theta\, b \quad , \qquad \Theta^* = \theta^* b \tag{4.68}$$

The assumptions

$$b_{\mathrm{w}} \simeq b_{\mathrm{avg}} \simeq b \tag{4.69}$$

can also be made if we assume $\delta^* \ll R$ on the body, and $b_{\mathrm{avg}} \simeq \delta^*$ in the wake.

Substitution of $\Theta = \theta\, b$ etc. into (4.65) and (4.66) gives essentially the 2D integral equations,

$$\frac{\mathrm{d}\theta}{\mathrm{d}s} = \frac{c_f}{2} - (H + 2 - M_\mathrm{e}^2)\frac{\theta}{u_\mathrm{e}}\frac{\mathrm{d}u_\mathrm{e}}{\mathrm{d}s} - \frac{\theta}{b}\frac{\mathrm{d}b}{\mathrm{d}s} \tag{4.70}$$

$$\frac{\mathrm{d}\theta^*}{\mathrm{d}s} = 2c_\mathcal{D} - \left(\frac{2H^{**}}{H^*} + 3 - M_\mathrm{e}^2\right)\frac{\theta^*}{u_\mathrm{e}}\frac{\mathrm{d}u_\mathrm{e}}{\mathrm{d}s} - \frac{\theta^*}{b}\frac{\mathrm{d}b}{\mathrm{d}s} \tag{4.71}$$

except for the appearance of the lateral divergence terms involving $\mathrm{d}b/\mathrm{d}s$. The streamwise changes in the thicknesses θ, θ^* resulting from these terms can be seen to be the result of a given amount of boundary layer fluid being spread over a varying perimeter $b(s)$. However, the perimeter changes do not affect the overall amount of viscous fluid at any streamwise location, and hence cannot directly affect the overall momentum and kinetic energy areas Θ, Θ^*. This can also be seen by the absence of explicit $\mathrm{d}b/\mathrm{d}s$ terms in equations (4.65), (4.66). An important consequence is that the predicted far-downstream Θ_∞ and hence the drag will be insensitive to the details of the $b(s)$ approximation (4.67) used here.
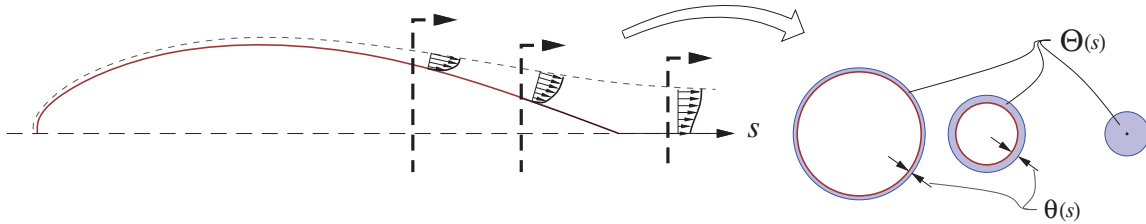
Figure 4.17: Momentum area $\Theta(s)$ evolution along axisymmetric body and wake. Over the rear of the body, the momentum thickness $\theta(s)$ increases faster than in 2D, due to the viscous fluid flowing onto a progressively smaller perimeter.

4.9 3D Boundary Layers

Three dimensional boundary layer flows can be quite complex, and a complete treatment of 3D boundary layer theory is far out of scope here. Only a general overview of the key new effects will be given here. See McLean [18] for a much more comprehensive discussion.

4.9.1 Streamwise and crossflow profiles

A 3D boundary layer features non-planar velocity profiles $\mathbf{V}(n)$, such as the one shown in Figure 4.18. Traditional notation uses s_1, s_2, n as the local cartesian coordinates (instead of s, ℓ, n), with s_1 parallel to the edge velocity vector $\mathbf{V}_\mathrm{e}$, and s_2 perpendicular to it. Within the boundary layer we then have

$$\mathbf{V}(n) = u_1\,\hat{\mathbf{s}}_1 + u_2\,\hat{\mathbf{s}}_2 \tag{4.72}$$

where $u_1(n)$ is the *streamwise* profile, and $u_2(n)$ is the *crossflow* profile which appears only in 3D boundary layers. The presence of crossflow means that the wall shear stress vector τ_w is in general not parallel to the local edge velocity. The lines parallel to τ_w are called *wall streamlines*, which differ from the usual potential-flow streamlines which are parallel to $\mathbf{V}_\mathrm{e}$.

Crossflow is typically generated by a transverse pressure gradient $\partial p/\partial s_2$ which is felt by the fluid over the entire boundary layer thickness. The slower-moving fluid within the boundary layer curves in response more strongly than does the outer potential flow, and thus forms the crossflow profile some distance downstream, as shown in Figure 4.18 on the right. This is essentially the same mechanism as the one shown in Figure 4.6, but here it occurs in the transverse direction.
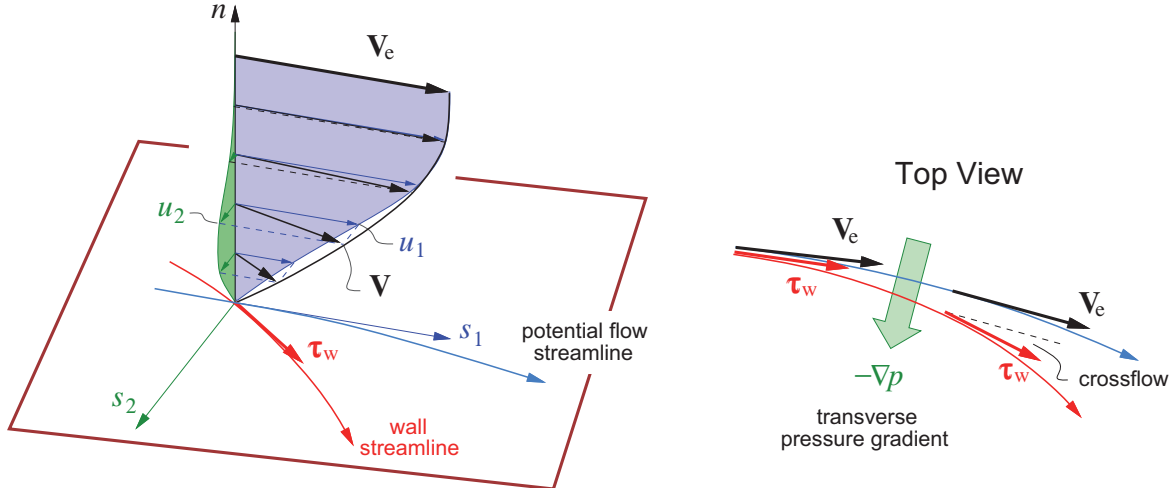
Figure 4.18: 3D Boundary layer at one surface location, with streamwise and crossflow profile components u_1, u_2. Crossflow is primarily the result of a transverse pressure gradient.

4.9.2   Infinite swept wing

Swept-wing potential flow

An infinite swept cylindrical body, such as a wing for example, is shown in Figure 4.19. The perpendicular and parallel freestream velocity components are

$$
\begin{aligned}
V_\perp &= V_\infty \cos \Lambda \\
V_\| &= V_\infty \sin \Lambda
\end{aligned}
$$

where Λ is the sweep angle. The x, z surface coordinates are chosen such that z runs spanwise, with x being the usual 2D-like chordwise coordinate.
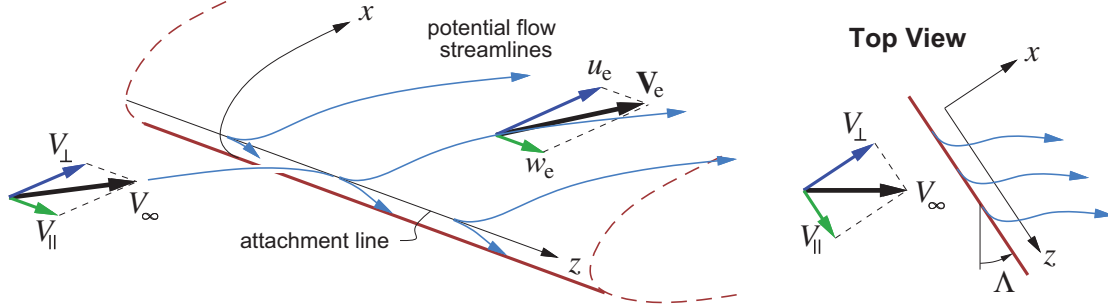
Figure 4.19: Potential flow over infinite swept cylinder or wing, with x, z surface coordinates.

Since there is no special z location on the wing, we must have

$$
\frac{\partial ()}{\partial z} = 0
$$

for all flow quantities. In the potential flow, the z-momentum equation which governs w_e then simplifies to

$$
\rho_e \mathbf{V}_e \cdot \nabla w_e = -\frac{\partial p}{\partial z} = 0 \tag{4.73}
$$

so that w_e is constant everywhere in the flow-field, and must be equal to its freestream value.

$$
w_e = V_\| \tag{4.74}
$$

The local pressure is given by the isentropic relation (1.112), or by the Bernoulli equation (1.112) for the case of low speed flow.

$$p_e(x) = p_\infty \left(\frac{h_e}{h_\infty}\right)^{\gamma/(\gamma-1)} = p_\infty \left[1 + \frac{\gamma-1}{2}M_\perp^2\left(1 - \frac{u_e^2}{V_\perp^2}\right)\right]^{\gamma/(\gamma-1)} \tag{4.75}$$

$$p_e(x) = p_\infty + \frac{1}{2}\rho\left(V_\perp^2 - u_e^2\right) \qquad \text{(low speed flow)} \tag{4.76}$$

In either case, the spanwise velocity w_e has no influence on the pressure, and hence no influence on the lift. It is therefore appropriate and useful to define "perpendicular" pressure and lift coefficients referenced to the perpendicular dynamic pressure,

$$C_{p_\perp} = \frac{p_e - p_\infty}{\frac{1}{2}\rho_\infty V_\perp^2}$$

$$c_{\ell_\perp} = \int_0^1 \Delta C_{p_\perp} \, \mathrm{d}\left(\frac{x}{c_\perp}\right)$$

where $\Delta C_{p_\perp}$ is the pressure coefficient difference between the lower and upper surface of the airfoil, and $c_\perp$ is the perpendicular chord. These quantities correspond to those of a 2D flow in which the spanwise velocity $V_\parallel$ is absent. So for example, $C_{p_\perp}(x;\alpha_\perp)$ and $c_{\ell_\perp}(\alpha_\perp)$ on a high aspect ratio swept wing can be obtained from 2D calculations or 2D experimental data, with

$$\alpha_\perp = \arcsin\frac{V_\mathrm{vert}}{V_\perp}$$

being the angle of attack seen in the perpendicular plane, and V_vert is net vertical freestream velocity reduced by the local 3D induced downwash velocity.

Swept-wing boundary layer flow

With the $\partial()/\partial z = 0$ condition, the 3D boundary layer equations for low speed flow, with the kinematic eddy viscosity $\nu_t = \mu_t/\rho$ invoked, simplify as follows.

$$\frac{\partial u}{\partial x} + \frac{\partial v}{\partial y} = 0 \tag{4.77}$$

$$u\frac{\partial u}{\partial x} + v\frac{\partial u}{\partial y} = \frac{\partial}{\partial y}\left((\nu + \nu_t)\frac{\partial u}{\partial y}\right) + u_e\frac{\mathrm{d}u_e}{\mathrm{d}x} \tag{4.78}$$

$$u\frac{\partial w}{\partial x} + v\frac{\partial w}{\partial y} = \frac{\partial}{\partial y}\left((\nu + \nu_t)\frac{\partial w}{\partial y}\right) \tag{4.79}$$

Evidently (4.77) and (4.78) are the 2D boundary layer equations in x, y, decoupled from the z-momentum equation (4.79) and the spanwise w velocity. As pointed out in the previous section, $u_e(x)$ and the pressure are the same as in a 2D flow with w_e absent. Hence, the chordwise velocities u, v governed by (4.77),(4.78) are also the same as in 2D flow, and are unaffected by the spanwise flow component.

Because neither the local potential flow nor the boundary layer flow are affected by the $V_\parallel$ spanwise velocity component, the overall conclusion is that the relevant airfoil shape which determines the aerodynamic characteristics of a swept high aspect ratio wing is perpendicular to the wing, not parallel to the freestream direction. In particular, adding a spanwise freestream velocity component to a given wing does not affect its surface pressures and lift, and also does not affect its boundary layer its separation resistance or chordwise separation location for the same perpendicular-plane angle of attack. This is shown in Figure 4.20.
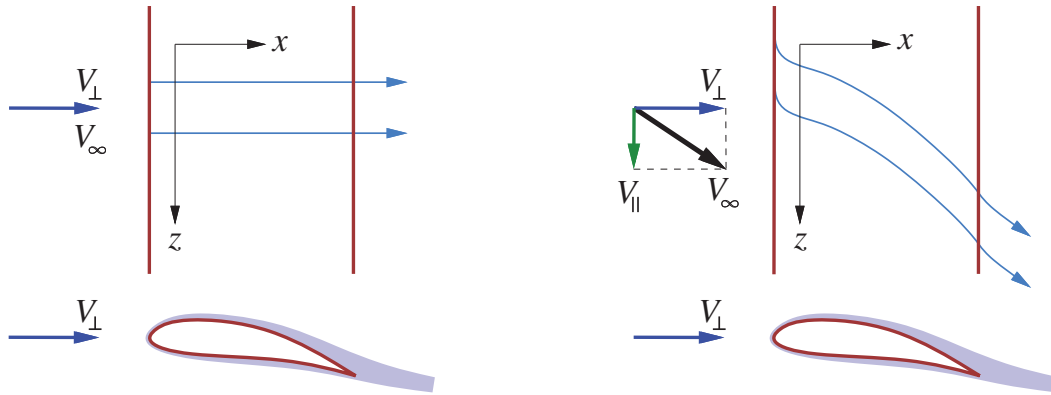
Figure 4.20: Adding a spanwise freestream velocity component $V_\parallel$ does not affect a wing's lift, or the characteristics of a laminar boundary layer projected onto the perpendicular plane. A turbulent boundary layer will change somewhat from the larger Reynolds number's effect on the turbulence.

The independence of the chordwise $u(x,y)$ velocity from the spanwise $w(x,y)$ velocity is strictly valid only for laminar flow. For turbulent flow, the spanwise velocity will increase the effective Reynolds number of the turbulence, and hence will have some effect on ν_t, so the decoupling isn't perfect. Nevertheless, since Reynolds number effects on turbulence are weak, the conclusions are very nearly correct also for turbulent flow. McLean [18] discusses the effects of wing sweep on boundary layers in much more detail.

4.9.3 Crossflow gradient effects

Although the infinite swept wing has a 3D boundary layer with crossflow, one simple explanation why the crossflow is immaterial to the boundary layer development is that there is no crossflow gradient, in the spanwise z direction in that case. In contrast, in more general 3D boundary layers with nonzero crossflow gradients, such as the one sketched in Figure 4.21, the presence of the crossflow will certainly have an effect.

In general, any lateral gradient in the crossflow will cause lateral convergence/divergence effects as in the axisymmetric case, except here the convergence or divergence occurs only near the wall rather than over the whole boundary layer thickness. However, the overall effect is the same, with the boundary layer growth being increased or decreased relative to the 2D case without crossflow. Figure 4.21 shows a case with crossflow convergence, causing an additional boundary layer thickening. Crossflow divergence would have the opposite effect.
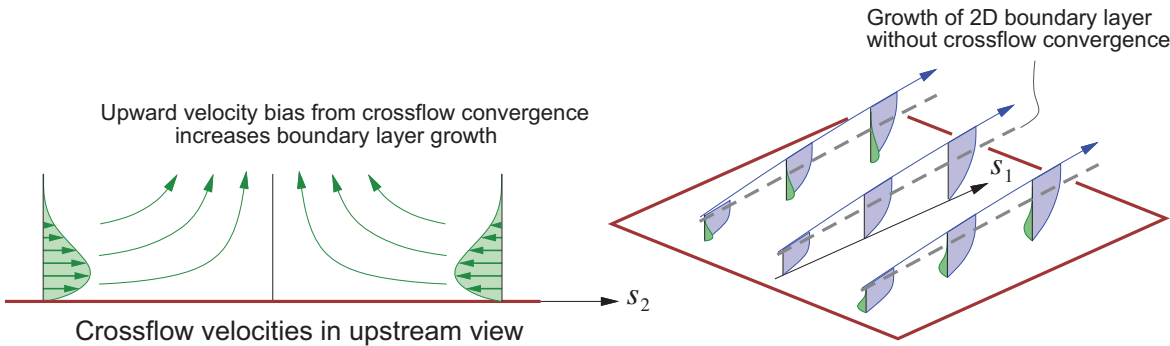
Figure 4.21: Crossflow convergence increases boundary layer growth compared to a 2D boundary layer with the same streamwise profile. Crossflow divergence would have the opposite effect.

4.10   2D Boundary Layer Solution Methods – Overview

4.10.1   Classical boundary layer problem

The classical incompressible 2D wall boundary layer problem has the following inputs and outputs.

Inputs:		Outputs:	
ν or Re_{ref}	viscosity or Reynolds number	$u(s,n), v(s,n)$	velocity field
$u_{\mathrm{e}}(s)$	edge velocity distribution	$\delta^*(s), \theta(s) \dots$	thicknesses, from $u(s,n)$
$u_0(n), v_0(n)$	initial velocities at s_0	$H(s), c_f(s)$	shape parameter, skin friction

The inputs are quantities which appear in the boundary layer equations (4.21) and boundary conditions (4.22). The outputs are the unknowns in these equations, or functions of these unknowns.

The initial velocities u_0, v_0 at the first location s_0 (shown in Figure 4.22) are not needed if this is a leading edge or stagnation point, which is the most common situation. In this case they can be taken from one of the self-similar solutions treated earlier.

4.10.2   Finite-difference solution methods

The most general solution approach is the grid-based *finite-difference method*, sketched in Figure 4.22. The solution procedure solves for all the u, v unknowns at one s station at a time, starting at the first s_0 station. This solution procedure is known as *space marching*. For details, see Cebeci and Smith [19], Cebeci and Bradshaw [20].
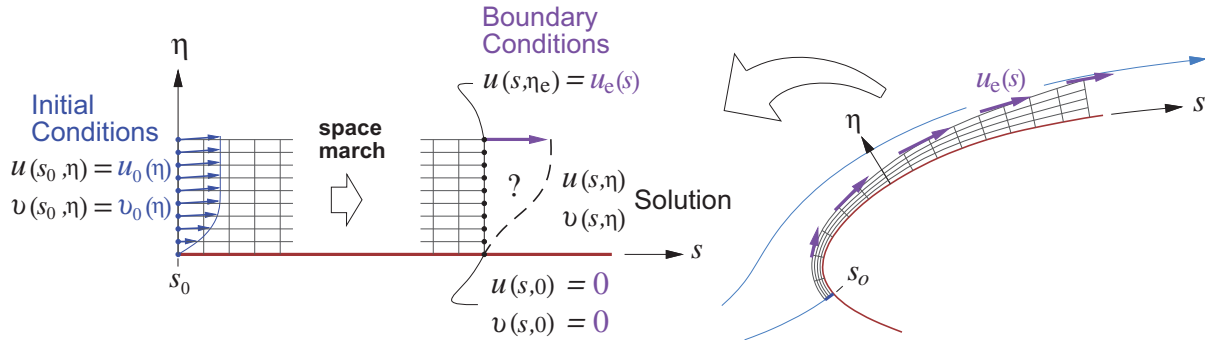
Figure 4.22: Solution of boundary layer equations on a finite-difference grid.

For the general boundary layer problem, the space-marching finite-difference solution procedure is accurate and effective, but requires considerable computational effort. For acceptable accuracy for laminar flows, it requires at least 20 or more grid nodes across the layer at each surface point, with the three u, v, τ unknowns per grid node. Turbulent flows may require 80 or more grid nodes per surface point. A typical $u_{\mathrm{e}}(s)$ distribution, over an airfoil surface say, might require over 100 surface points, resulting in many thousands of unknowns for the entire 2D boundary layer. When the boundary layer is to be solved simultaneously with the potential flow, as will be described in Section 4.12.2, this large total number of unknowns is prohibitive. Another drawback of the finite-difference method is that it is purely numerical, and gives no direct insight into boundary layer behavior. An alternative approach is taken by the *integral methods*, described next.

4.10.3   Integral solution methods

Instead of computing the detailed $u, v, \tau(s,n)$ fields, integral methods determine only the integral thicknesses and key shear quantities, namely $\delta^*, \theta, c_f, c_{\mathcal{D}}(s)$, etc. This relatively small number of unknowns makes the integral methods very economical, but a drawback is that their solutions must always be approximate, in

that they cannot produce theoretically exact solutions of the laminar boundary layer equations (4.21). For turbulent flows this is not really an issue, since even nominally "exact" solutions of equations (4.21) still require turbulence models for μ_t which are inherently approximate. In practice, the simpler and much more economical integral methods are sufficiently accurate for a large majority of aerodynamic flow prediction applications, for both laminar and turbulent flows.

To compute the integral thicknesses $\delta^*, \theta, \theta^*(s)$, integral methods solve either the von Karman equation (4.28) or the kinetic energy equation (4.35), or both as in some advanced methods. In effect, they seek to evaluate the integrals in (4.36) and/or (4.38) in some manner. Here we will focus on solving only the von Karman equation (4.28). This equation is not integrable as written, because it contains the terms c_f and H which are additional unknowns, and therefore require two additional *closure relations* or functions to relate them to the primary variables θ, u_e, ν. How these additional unknowns are determined is primarily what distinguishes the many different integral calculation methods which have been developed to date.

4.11 Integral Boundary Layer Solution

4.11.1 Thwaites method

Assumptions and formulation

The Thwaites method [21], [11], [12] solves the classical low-speed laminar boundary layer problem by assuming specific functional forms for c_f, H, and the entire righthand side of the von Karman equation (4.28). This is first manipulated by multiplying $2Re_\theta \times$ [equation (4.28)], where

$$Re_{\theta(s)} \equiv \frac{\rho_e u_e \theta}{\mu_e} = \frac{u_e \theta}{\nu} \tag{4.80}$$

is the local *momentum thickness Reynolds number*. We also set $M_e^2 = 0$ for low speed flow. The result is

$$\frac{u_e}{\nu} \frac{\mathrm{d}(\theta^2)}{\mathrm{d}s} = 2\left[\mathcal{T} - (H+2)\lambda\right] \equiv \mathcal{F}_\theta \tag{4.81}$$

$$\mathcal{T} \equiv Re_\theta \frac{c_f}{2} \quad , \quad \lambda \equiv \frac{\theta^2}{\nu} \frac{\mathrm{d}u_e}{\mathrm{d}s} \tag{4.82}$$

where $\mathcal{T}$ is a normalized wall shear, and λ is a normalized edge velocity gradient or equivalently a normalized pressure gradient. For the power-law flow case $u_e = Cs^a$ these are also products of Falkner-Skan solution parameters, and also of the normalized velocity profile derivatives at the wall.

$$\mathcal{T} = \frac{\theta}{\delta_{\mathrm{FS}}} Re_x^{1/2} \frac{c_f}{2} = \left.\frac{\mathrm{d}U}{\mathrm{d}(n/\theta)}\right|_{\mathrm{w}} \quad , \quad \lambda = \frac{\theta^2 u_e}{\nu s} \frac{s}{u_e} \frac{\mathrm{d}u_e}{\mathrm{d}s} = \frac{\theta^2}{\delta_{\mathrm{FS}}^2} a = \left.\frac{\mathrm{d}^2 U}{\mathrm{d}(n/\theta)^2}\right|_{\mathrm{w}} \tag{4.83}$$

Their numerical values are listed in Table 4.1. Also listed is the entire righthand side parameter combination $\mathcal{F}_\theta$ in the manipulated von Karman equation (4.81).

For power-law flows, all the Falkner-Skan parameters (columns of Table 4.1) are functions of the exponent a, or more generally functions of each other. The key assumption of Thwaites's method is that the $H(\lambda), \mathcal{T}(\lambda), \mathcal{F}_\theta(\lambda)$ relations are valid for <u>any</u> boundary layer flow, not just a power-law flow. In effect this assumes that the boundary layer profile $\overline{U}(\eta; s)$ at each s location has the same shape as one of the Falkner-Skan profiles. That is, if λ is known at a location s in a general flow, then $H, \mathcal{T}, \mathcal{F}_\theta$ at that location are also immediately known from the corresponding row in Table 4.1.

Explicit integration

Rather than use the Falkner-Skan solutions in Table 4.1, Thwaites examined a number of other theoretical flows to quantify these functions. For $\mathcal{F}_\theta$ he chose

$$\tilde{\mathcal{F}}_{\theta(\lambda)} = 0.45 - 6\lambda \qquad (4.84)$$

which doesn't quite match the values in Table 4.1, but it is close. His H and $\mathcal{T}$ were provided in tabulated form. They are shown in Figure 4.23, and are closely approximated by the following convenient curve fits.

$$\tilde{H}_{(\lambda)} = 2.61 - 4.1\lambda + 14\lambda^3 + \frac{0.56\lambda^2}{(\lambda + 0.18)^2} \qquad (4.85)$$

$$\tilde{\mathcal{T}}_{(\lambda)} = 0.220 + 1.52\lambda - 5\lambda^3 - \frac{0.072\lambda^2}{(\lambda + 0.18)^2} \qquad (4.86)$$
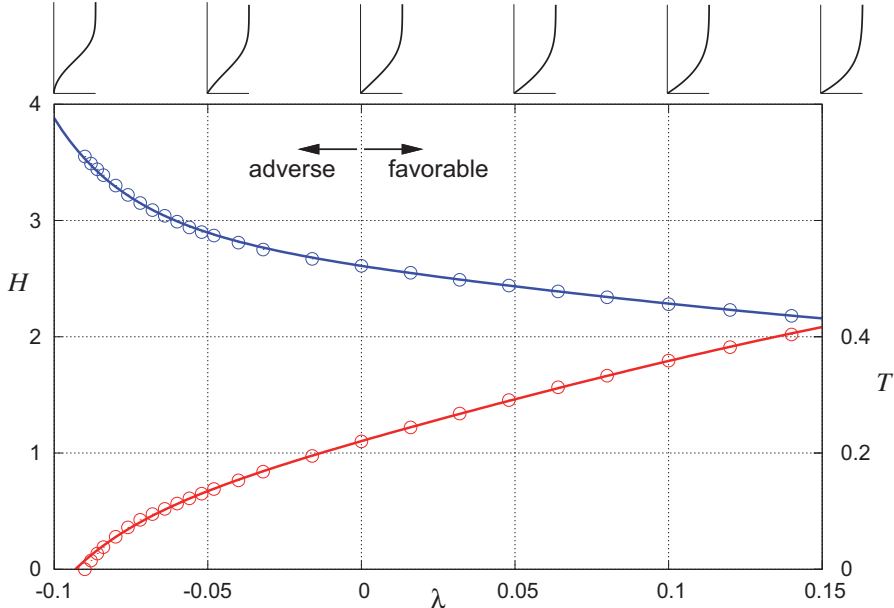
Figure 4.23: Thwaites's values for parameters H and $\mathcal{T}$ versus λ, plotted as symbols. Curve-fit functions $\tilde{H}_{(\lambda)}$ and $\tilde{\mathcal{T}}_{(\lambda)}$ given by (4.85) and (4.86) are plotted as solid lines. Falkner-Skan $U_{(\eta)}$ profile shapes corresponding to the H values are drawn on top.

Strictly speaking, equation (4.81) could be numerically integrated using only the $\tilde{\mathcal{T}}_{(\lambda)}$ and $\tilde{H}_{(\lambda)}$ functions inserted in its righthand side. However, the fact that their combination $\mathcal{F}_{\theta(\lambda)}$ is very nearly linear allows a simpler explicit solution. When the approximate $\tilde{\mathcal{F}}_{\theta(\lambda)}$ given by (4.84) is inserted for the entire righthand side of equation (4.81), and the entire equation is then multiplied by νu_e^5, its lefthand side becomes a perfect differential which can then be explicitly integrated.

$$\left\{ \frac{u_e}{\nu} \frac{d(\theta^2)}{ds} = 0.45 - 6\lambda \right\} \nu u_e^5$$

$$\frac{d(u_e^6 \theta^2)}{ds} = 0.45 \nu u_e^5$$

$$\theta^2_{(s)} = \frac{1}{u_e^6{}_{(s)}} \left[u_e^6{}_{(s_0)} \theta^2{}_{(s_0)} + 0.45\nu \int_{s_0}^{s} u_e^5{}_{(s')} \, ds' \right] \qquad (4.87)$$

If $u_e(s)$ and ν are provided, the corresponding $\theta(s)$ can be immediately obtained by evaluation of the integral in (4.87), numerically if necessary. This $\theta(s)$ is then used in the closure relations to obtain the remaining quantities of interest.

$$\lambda(s) = \frac{\theta^2(s)}{\nu} \frac{\mathrm{d}u_e(s)}{\mathrm{d}s} \tag{4.88}$$

$$Re_\theta(s) = \frac{u_e(s)\,\theta(s)}{\nu} \tag{4.89}$$

$$H(s) = \tilde{H}(\lambda(s)) \tag{4.90}$$

$$c_f(s) = \frac{2}{Re_\theta(s)} \tilde{\mathcal{T}}(\lambda(s)) \tag{4.91}$$

In general, the integral in (4.87) is evaluated from some initial location s_0 where $\theta(s_0)$ must be specified. But if this s_0 is the sharp leading edge of a Blasius flow, then $\theta(s_0)=0$. Alternatively, if s_0 is at a blunt leading edge stagnation point, then $u_e(s_0)=0$, in which case $\theta(s_0)$ in (4.87) is immaterial. Hence, in both of these typical situations no initial data is required.

Reynolds number independence

It is interesting to note that the boundary evolution predicted by the Thwaites formula (4.87) with zero initial values at s_0 obeys the simple scalings

$$\theta(s) \sim \sqrt{\nu} \sim 1/\sqrt{Re} \quad , \quad c_f(s) \sim \sqrt{\nu} \sim 1/\sqrt{Re} \tag{4.92}$$

with $\lambda(s)$ and $H(s)$ completely unaffected by the viscosity, or more generally by the Reynolds number. The conclusion is that aside from the simple $\sqrt{Re}$ scalings, boundary layer evolution and in particular the separation location is independent of Reynolds number, as sketched in Figure 4.24. Only the shape (but not the magnitude) of the input $u_e(s)$ distribution matters. This conclusion also holds for effectively exact finite-difference solution methods.
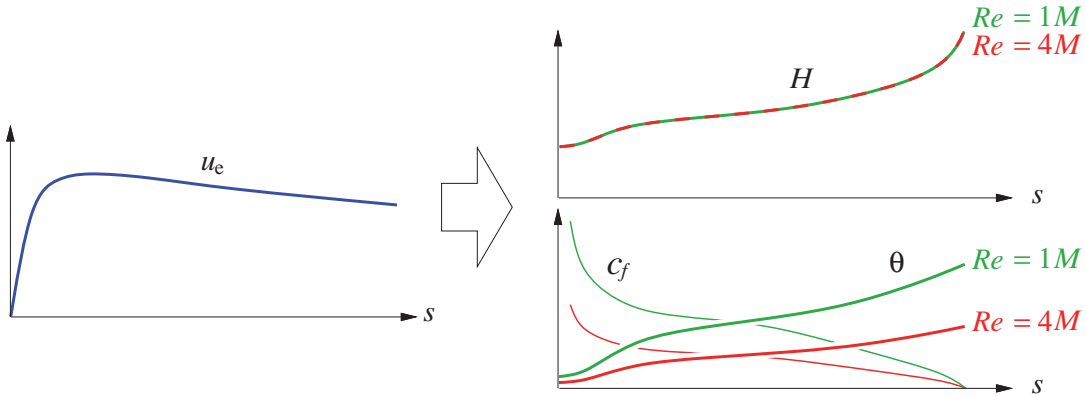
Figure 4.24: For a prescribed $u_e(s)$, the resulting shape parameter $H(s)$ distribution of a laminar boundary layer is independent of Reynolds number. The skin friction and momentum thickness distributions are also unaffected except for simple $c_f(s), \theta(s) \sim 1/\sqrt{Re}$ scalings.

However, the assumption that $u_e(s)$ is fixed and independent of Reynolds number is not exactly correct for a fixed body geometry. As examined in Chapter 3, the overall potential flow-field and hence $u_e(s)$ are affected by the viscous displacement mechanism. The resulting changes to $u_e(s)$ themselves scale as $\delta^* \sim 1/\sqrt{Re}$ and hence are very small, but only if the flow is attached. So in actual applications the Reynolds number independence of laminar flow is only approximately correct, and only in the absence of flow separation.

4.11.2   White's equilibrium method

The Thwaites method's functions $\mathcal{F}_\theta(\lambda)$, $\tilde{\mathcal{T}}(\lambda)$, and $\tilde{H}(\lambda)$ are valid only for laminar flow. To integrate the von Karman momentum equation (4.28) for a turbulent boundary layer, it is necessary to provide <u>turbulent</u> closure relations for c_f and H, ultimately in terms of the primary unknown θ and the inputs ν and u_{e}. Such an approach is described by White [22], mainly for illustrative purposes. It is summarized below.

A suitable turbulent skin-friction relation is the Coles formula, which is a fit to equilibrium flow data.

$$\tilde{c}_{f(H, Re_\theta)} \;\; = \;\; \frac{0.3\, e^{-1.33H}}{(\log_{10} Re_\theta)^{1.74+0.31H}} \tag{4.93}$$

A suitable turbulent shape parameter relation is the G-beta locus (4.58), after replacement of G and β by their definitions (4.56), (4.57). Squaring both sides and further multiplying through by $c_f/2\mathcal{A}^2$ gives the more convenient form

$$\left(\frac{H-1}{\mathcal{A}H}\right)^2 \;\; = \;\; \frac{c_f}{2} - \mathcal{B}H\,\Lambda \tag{4.94}$$

$$\Lambda \;\; \equiv \;\; \frac{\theta}{u_{\mathrm{e}}} \frac{\mathrm{d}u_{\mathrm{e}}}{\mathrm{d}s} \;\; = \;\; \frac{\lambda}{Re_\theta} \;\; = \;\; -\frac{c_f}{2}\frac{\beta}{H} \tag{4.95}$$

where Λ is a new pressure-gradient parameter. This is a scaled version of Thwaites's λ, and is more relevant for turbulent flows.

Equations (4.93) and (4.94) are two constraints between the four parameters $H, c_f, \Lambda, Re_\theta$. If Λ and Re_θ are specified, these equations can be numerically solved (e.g. by Newton iteration) for the corresponding H and c_f values. Hence, we in effect have

$$\Lambda, Re_\theta \;\rightarrow\; \left\{ \begin{array}{c} \text{eq.(4.93)} \\ \text{eq.(4.94)} \end{array} \right\} \;\rightarrow\; \left\{ \begin{array}{c} \tilde{c}_{f(\Lambda, Re_\theta)} \\ \tilde{H}_{(\Lambda, Re_\theta)} \end{array} \right. \tag{4.96}$$

which are the direct replacements of Thwaites's $\tilde{\mathcal{T}}(\lambda)$ and $\tilde{H}(\lambda)$ closure functions.

We can now insert the $\tilde{c}_f$ and $\tilde{H}$ functions (4.96) into the von Karman equation (4.28), putting it into the following functional form.

$$\frac{\mathrm{d}\theta}{\mathrm{d}s} \;\; = \;\; \frac{1}{2}\tilde{c}_{f(\Lambda, Re_\theta)} - \left(\tilde{H}_{(\Lambda, Re_\theta)} + 2\right)\Lambda \;\; = \;\; f(\theta, u_{\mathrm{e}}, \nu) \tag{4.97}$$

If ν and $u_{\mathrm{e}}(s)$ are provided, then this can be numerically integrated for the $\theta(s)$ distribution, usually starting from the transition location s_{tr}. The initial value $\theta(s_{\mathrm{tr}})$ is also required, and typically would be obtained from the last laminar θ value at s_{tr}.

In contrast to the laminar boundary layer Reynolds number independence discussed earlier, turbulent boundary layer evolution is affected by Reynolds number. This can be seen from the explicit appearance of the Reynolds number in the $\tilde{H}_{(\Lambda, Re_\theta)}$ function (4.96). In general, increasing Re_θ tends to decrease H slightly, giving slightly greater resistance to adverse pressure gradients. Consequently, increasing the overall Reynolds number of a turbulent flow tends to delay separation and increase maximum lift.

4.11.3   Two-equation methods

Thwaites's method and White's equilibrium method are examples of *one-equation integral methods*, meaning that they integrate one differential equation to obtain the solution. One of their main drawbacks is that they cannot correctly represent the behavior of a separated boundary layer. For Thwaites's method this can be seen by examining the H and λ column values in Table 4.1. For adverse pressure gradients ($\lambda < 0$) this

true $H(\lambda)$ function is actually two-valued, with one $H < 4$ value which is the attached solution, and another $H > 4$ value which is the separated solution. Even if the curve-fit $\tilde{H}(\lambda)$ expression (4.85) were somehow modified to have this two-value form, it would be impossible to use in the H evaluation step (4.90), since there's no way to know whether to choose the attached or the separated $\tilde{H}$ value for any given negative λ value.

This problem is eliminated by the so-called *two-equation integral methods*, such as those of LeBalleur [23], Whitfield et al [24], and Drela et al [6]. These methods integrate <u>both</u> the von Karman equation (4.28) for $\theta(s)$, and also the kinetic energy equation (4.35) for θ^*, or equivalently for $H^* = \theta^*/\theta$. The latter is actually obtained more conveniently from the combination [equation (4.35)]$/\theta^*$ − [equation (4.28)]$/\theta$ which produces the kinetic energy shape parameter equation.

$$\frac{1}{H^*}\frac{\mathrm{d}H^*}{\mathrm{d}s} = \frac{2c_\mathcal{D}}{H^*} - \frac{c_f}{2} + \left(H - 1 - \frac{2H^{**}}{H^*}\right)\frac{\theta}{u_\mathrm{e}}\frac{\mathrm{d}u_\mathrm{e}}{\mathrm{d}s} \qquad (4.98)$$

Two equation methods assume that H and H^* are uniquely related via a $\tilde{H}^*(H)$ correlation function, so that equation (4.98) above is in effect an ODE for $H(s)$. For laminar flow, the $\tilde{H}^*(H)$ function is implied by Table 4.1. For turbulent flow, a $\tilde{H}^*(H, Re_\theta)$ function is obtained from the self-similar turbulent profiles shown in Figure 4.14, but actually differs very little from the laminar version. Since H is calculated directly in the two-equation methods, there is no ambiguity as to whether the flow is attached or separated at any given location. In these methods λ or Λ is not needed and is not used explicitly.

Another type of two-equation method is developed by Head [25] and Green et al [26], and is based on the *entrainment equation*, which is an integral form of the mass equation. The behavior of entrainment-based methods is similar to those of the kinetic energy-based methods, and the details are not important here.

Besides enabling the representation of a separated boundary layer, two-equation methods are considerably more accurate than the one-equation methods, especially for turbulent flow. Since their derivation makes the same basic correlation assumptions as the one-equation methods, i.e. the Falkner-Skan solutions for laminar flow and the equilibrium profiles and G-beta locus for turbulent flow, presenting them in detail here would add little besides complexity. The reader is referred to references for the derivation details.

4.11.4 Viscous dissipation relations

In Section 4.5.4, viscous dissipation was shown to be ultimately responsible for total profile drag, including the pressure drag component. Since dissipation is therefore a key quantity to be minimized, it's useful to examine how the dissipation coefficient $c_\mathcal{D}$ depends on the other boundary layer parameters. For self-similar laminar flow, this dependence is given by Table 4.1. For self-similar turbulent flow, it can be obtained from the kinetic energy shape parameter equation (4.98) together with the G-beta locus (4.58) as follows.

Since turbulent equilibrium flows have a streamwise-constant G, they must have a very nearly constant H and hence also a constant H^* if we neglect the slight streamwise variation of the turbulent $\sqrt{c_f/2}$ factor in the G definition (4.56).

$$\frac{\mathrm{d}H^*}{\mathrm{d}s} \simeq 0 \qquad \text{(equilibrium flow)} \qquad (4.99)$$

We can now obtain an expression for equilibrium-flow $c_\mathcal{D}$ from (4.98) by dropping the $\mathrm{d}H^*/\mathrm{d}s$ term and eliminating $\theta/u_\mathrm{e}\,\mathrm{d}u_\mathrm{e}/\mathrm{d}s$ using the G-beta locus (4.94). The H^{**} term is also dropped since this is typically small, and is exactly zero in incompressible flow.

$$\tilde{c}_\mathcal{D}(H, Re_\theta) = \frac{H^*}{2}\left[\frac{c_f}{2}\left(1 - \frac{H-1}{\mathcal{B}H}\right) + \frac{1}{\mathcal{A}^2\mathcal{B}}\left(\frac{H-1}{H}\right)^3\right] \qquad \text{(equilibrium flow)} \quad (4.100)$$

Aside from additional minor non-equilibrium corrections, expression (4.100) is in fact used in two-equation methods as a closure function for c_D in the ODE (4.98) to enable its integration. It is shown in Figure 4.25 for several momentum thickness Reynolds numbers. Also overlaid is the laminar $\tilde{c}_D(H, Re_\theta)$ function for the laminar Falkner-Skan flows, tabulated in Table 4.1. The turbulent c_D is seen to have a fairly weak dependence on Re_θ, while the laminar $c_D \sim 1/Re_\theta$ dependence is much stronger.
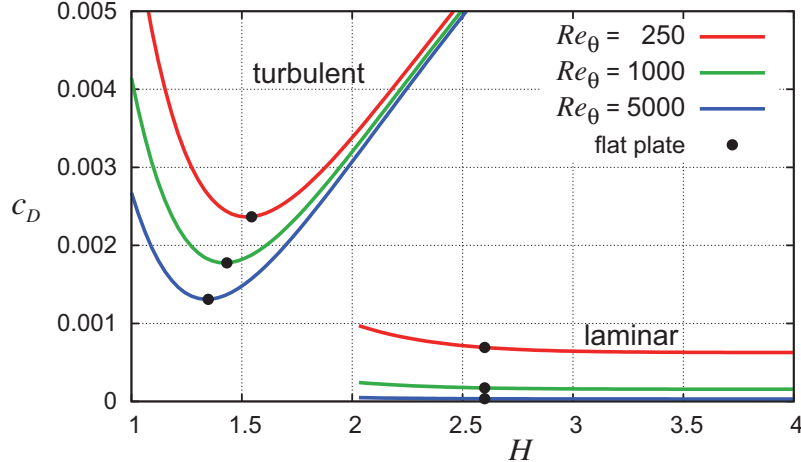
Figure 4.25: Dissipation coefficient for self-similar flows. Laminar values are listed in Table 4.1. Turbulent values are given by equation (4.100). Weak pressure gradients which displace H slightly from the flat plate value have little effect on c_D.

For any given local Re_θ, the minimum dissipation occurs very close to the zero pressure gradient (flat-plate) H value, so that the dissipation is relatively insensitive to small changes in H, i.e. to weak favorable or adverse pressure gradients. The laminar c_D is also very nearly independent of pressure gradient.

The weak dependence of c_D on pressure gradients (assuming fixed transition locations) indicates that the dissipation $\mathcal{D}(s) = \rho_e u_e^3 c_D$ is primarily determined by the <u>cube</u> of the edge velocity u_e. And since the integrated $\mathcal{D}(s)$ distribution gives the profile drag via expression (4.49), airfoils which have strong "overspeeds" or regions of high velocity are expected to have large integrated dissipation and high drag. Conversely, low drag is likely to be achieved by airfoils which have more uniform velocity distributions.

Note that since expression (4.49) captures the sum of friction and pressure drags, this argument applies to both the friction and pressure drag components. Attempting to reduce the pressure drag "directly," for example by reducing pressures on front-facing surfaces and increasing pressures on aft-facing surfaces, is bound to be futile if viscous dissipation is not reduced in the process.

Another important role of the dissipation coefficient is that it controls the maximum tolerable adverse pressure gradient which a boundary layer can sustain with a constant margin from separation, or equivalently with a nearly constant H and H^*. In this situation the shape parameter equation (4.98) with $dH^*/ds = 0$ can be viewed as an equation for the most negative tolerable velocity gradient.

$$\Lambda_{min} = \left(\frac{\theta}{u_e}\frac{du_e}{ds}\right)_{min} = \frac{1}{H-1}\left(\frac{c_f}{2} - \frac{2c_D}{H^*}\right) \simeq -0.65\,c_D \qquad (4.101)$$

The second approximate value in (4.101) is valid for turbulent flow in very strong adverse pressure gradients near separation where $H \simeq 3$, $H^* \simeq 1.5$, and c_f is relatively negligible.

One implication of (4.101) is that the adverse pressure gradient capability of the boundary layer can be increased by increasing its dissipation, preferably away from the surface so that the offsetting c_f term in (4.101) is not increased as much. One common technique is by the use of *vortex generators* [27], which

increase dissipation by introducing streamwise vortices into the boundary layer at some distance from the wall.

4.12 Coupling of Potential Flow and Boundary Layers

4.12.1 Classical solution

The classical boundary layer problem is schematically shown in Figure 4.26. An inviscid (potential) flow problem is first solved with the displacement effect ignored. This then provides the edge velocity $u_e(s)$ distribution which is the input to one of the boundary layer solution methods presented in this chapter. The outputs are the various viscous variables of interest, $\theta(s), \delta^*(s), c_f(s)$, etc.
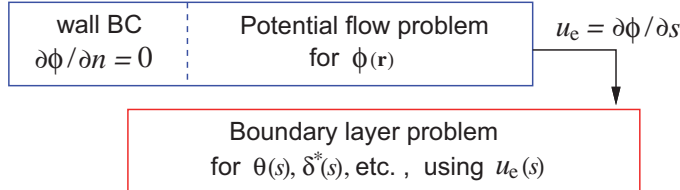
Figure 4.26: One-way coupling from the potential flow problem to the classical boundary layer problem. The boundary layer solution fails if separation is encountered.

Although conceptually simple, this solution approach has two shortcomings:

1. The potential flow solution ignores the viscous displacement effect. Hence it cannot predict the gradual loss of lift as stall is approached, which is illustrated in Figure 3.8. Also, if the displacement effects are large, then the specified $u_e(s)$ is inaccurate and the resulting boundary layer solution and predicted profile drag are suspect.

2. If the specified $u_e(s)$ leads to separation, the boundary layer solution will fail at that point, and subsequent downstream integration is impossible. This behavior was already observed for self-similar laminar flows, which have no solution for $a < -0.0904$ which is the incipient-separation case. For a general (not power-law) flow, there is also no solution at the first streamwise location where separation is encountered. This occurs with finite-difference and two-equation integral methods, and is known as the *Goldstein separation singularity* [28]. The consequence is that the boundary layer solution cannot proceed downstream into the separated flow region. Ironically, the simpler one-equation methods do not have this singularity, essentially because their physics modeling is too inadequate to represent it. This is not really an advantage, since they become wildly inaccurate or problematic in other ways once separation is indicated. For example, if $\lambda < -0.09$ in Thwaites's method, which roughly indicates separation, its closure functions become undefined.

4.12.2 Viscous/inviscid coupling

The solution failure at separation is traceable to the neglect of the viscous displacement mechanism. In brief, there is one unique value of du_e/ds which is admissible by the boundary layer at the separation point, so this value cannot be imposed via the input $u_e(s)$. The problem is eliminated if the displacement effect is incorporated into the potential flow problem, which is termed *viscous/inviscid coupling*. The boundary layer flow can now influence the potential flow's $u_e(s)$ distribution, and can thus enforce the requirement of the unique du_e/ds value at the separation point.

A practical consequence of incorporating a viscous displacement model into a potential flow calculation is that now the potential and the boundary layer flow problems are two-way coupled, as diagrammed in

Figure 4.27. Specifically, the potential and boundary layer problems now depend on each other and cannot be solved in the simple sequential manner of the classical case diagrammed in Figure 4.26.

A possible solution approach is to iterate between the potential and boundary layer equations, as suggested by the dotted arrows in Figure 4.27, which is known as *direct viscous/inviscid iteration*. This is not satisfactory since it tends to be unstable, as analyzed by Wigton and Holt [29]. The boundary layer problem will also fail outright if separation is encountered. Other iteration schemes have been proposed, such as the one by Veldman [30] and LeBalleur [23], with various degrees of success. The most reliable approach has been to solve the inviscid and viscous equations simultaneously by the Newton method. The XFOIL [5] and MSES [6] codes are two 2D implementations of this approach. Example results have been shown in Figures 3.6, 3.7, 4.9, 4.10. An example of simultaneously-coupled 2D viscous and 3D inviscid methods is the TRANAIR code, as reported by Bieterman et al [31].
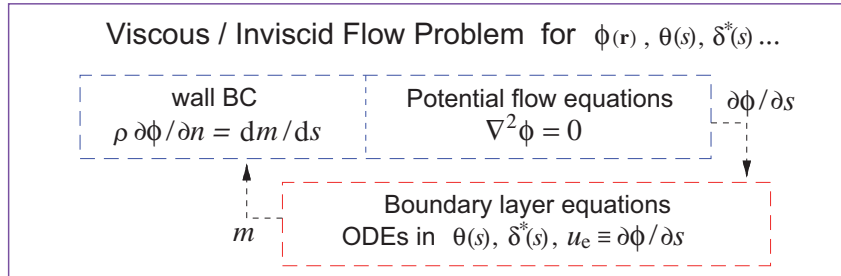
Figure 4.27: Two-way coupling between potential-flow equations and boundary layer equations occurs if a displacement model is incorporated into the potential flow problem. The direct viscous/inviscid iteration suggested by the dotted arrows will fail if separation is present. A simultaneous solution of all the equations is most effective at avoiding this solution failure.

4.13   Profile Drag Prediction

The prediction of profile drag D_p can be performed using a number of different approaches. These are presented in the subsequent sections in order of increasing accuracy and also increasing cost and complexity.

4.13.1   Wetted-area methods

The so-called *wetted-area methods* are based on the drag of a zero-thickness flat plate with a constant freestream edge velocity, $u_e = V_\infty$. In this case there is no pressure drag, so that the profile drag consists entirely of friction drag which can be conveniently given in terms of an average skin friction coefficient $\bar{C}_f$ based on the freestream dynamic pressure q_∞.

$$D_p = \iint \tau_w \, dS = q_\infty S_{\text{wet}} \bar{C}_f \qquad \text{(flat plate)} \qquad (4.102)$$

$$q_\infty \equiv \frac{1}{2} \rho_\infty V_\infty^2 \qquad (4.103)$$

$$\bar{C}_f(Re_\ell) \equiv \frac{1}{\ell} \int_0^\ell C_f(x) \, dx \qquad (4.104)$$

Here, ℓ is the streamwise length of the boundary layer flow, which also defines the streamwise-length Reynolds number Re_ℓ. The wetted area S_{wet} is defined as the surface area in contact with the moving fluid, which for the flat plate is twice the planform area. The average skin friction coefficient is obtained

from Blasius flow and experimental data for the laminar and turbulent cases.

$$\bar{C}_{f_l} = \frac{1.328}{Re_\ell^{1/2}} \qquad \text{(fully laminar)} \tag{4.105}$$

$$\bar{C}_{f_t} = \frac{0.455}{(\log_{10} Re_\ell)^{2.58}} \qquad \text{(fully turbulent)} \tag{4.106}$$

$$\bar{C}_f = \max\left(\bar{C}_{f_l}, \bar{C}_{f_t} - \frac{Re_{x_{\mathrm{tr}}}/320 - 39}{Re_\ell}\right) \qquad \text{(transition at } s_{\mathrm{tr}}) \tag{4.107}$$

$$Re_\ell = \frac{\rho_\infty V_\infty \ell}{\mu_\infty} \quad , \qquad Re_{x_{\mathrm{tr}}} = \frac{\rho_\infty V_\infty s_{\mathrm{tr}}}{\mu_\infty} \tag{4.108}$$

These $\bar{C}_f$ functions are shown in Figure 4.28. The added transition-location term in (4.107) is based on the formulation of Schlichting [12], and depends on the transition-length Reynolds number $Re_{x_{\mathrm{tr}}}$.
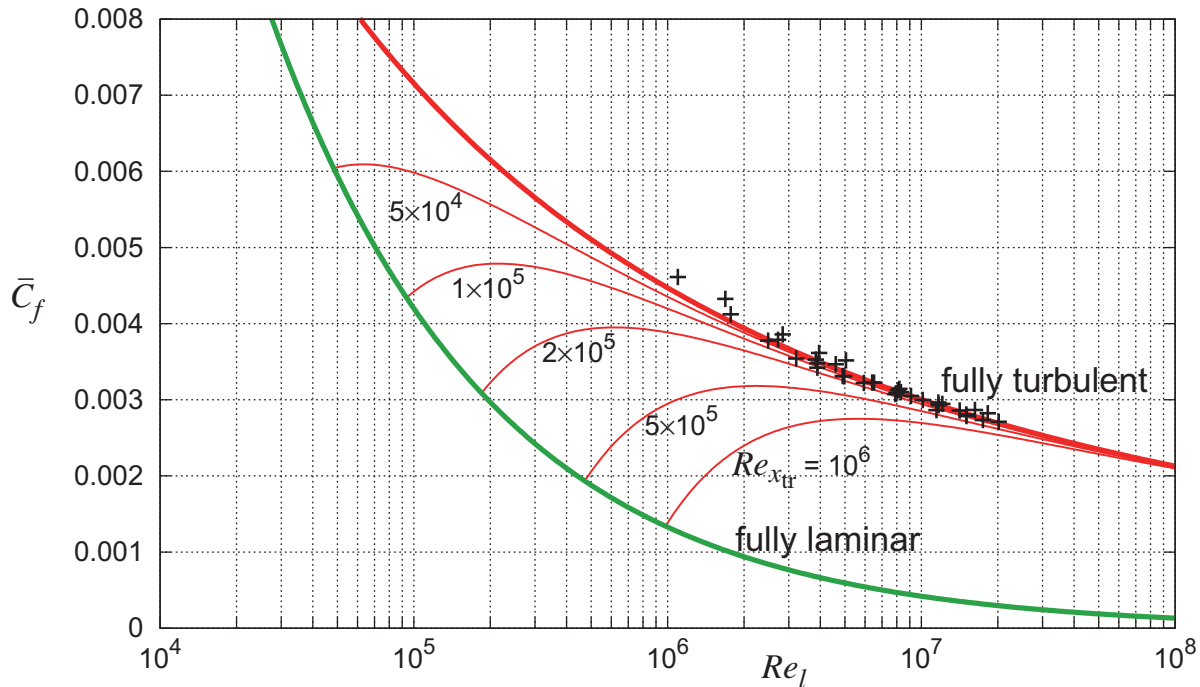
Figure 4.28: Average skin friction coefficient for constant-pressure boundary layers versus flow-length Reynolds number Re_ℓ. Thin turbulent lines correspond to different transition-location Reynolds numbers $Re_{x_{\mathrm{tr}}}$. Symbols are fully-turbulent experimental data from Osterlund [32].

For bodies other than flat plates, the profile drag is assumed to be given by

$$D_p = q_\infty S_{\mathrm{wet}} \bar{C}_f K_f \tag{4.109}$$

$$\text{or} \qquad C_{D_p} \equiv \frac{D_p}{q_\infty S_{\mathrm{ref}}} = \frac{S_{\mathrm{wet}}}{S_{\mathrm{ref}}} \bar{C}_f K_f \tag{4.110}$$

where $K_f \geq 1$ is an empirical *form factor* which depends on the shape of the body, and possibly also on the angle of attack and Mach number. Hoerner [33] gives extensive data for form factor values for a variety of 2D and 3D body shapes.

The main shortcoming of the wetted-area profile drag estimate (4.109) is that it's not really predictive, but is in effect a means of experimental drag interpolation or extrapolation via the assumption that the form factor K_f does not change much over the range of body shapes being considered. If modifications in the

body shape change K_f in some unknown way which is not accounted for, then the resulting profile drag predictions for the modified body shapes will be inaccurate. In other situations where novel or unusual body shapes are being examined and drag data is not available, then the necessary K_f values must be guessed and the resulting drag estimates become uncertain.

4.13.2   Local-friction and local-dissipation methods

To determine the physical basis of the form factor, we can compare the wetted-area drag formula (4.110) with the exact profile drag formula (4.40) based on the integral momentum equation.

$$S_{\text{ref}} C_{D_p} = S_{\text{wet}} \bar{C}_f K_f \tag{4.111}$$

$$S_{\text{ref}} C_{D_p} = \iint \frac{q_e}{q_\infty} C_f \, dS_{\text{wet}} + \iint \delta^* \frac{dC_p}{ds} \, dS_{\text{wet}} + \iint \delta^* \frac{dC_p}{ds} \, dS_{\text{wake}} \tag{4.112}$$

Evidently the form factor K_f accounts for the larger local dynamic pressures via the ratio q_e/q_∞ inside the first friction integral in (4.112), and also accounts for the remaining two surface and wake integrals which represent roughly the pressure drag. Clearly, K_f represents fairly complex flow physics, and consequently has been resistant to being reliably estimated from only potential-flow quantities via first principles. For example, one might attempt including a local dynamic pressure in the wetted area integral

$$S_{\text{ref}} C_{D_p} \stackrel{?}{=} \bar{C}_f \iint \frac{q_e}{q_\infty} \, dS_{\text{wet}} \tag{4.113}$$

but this will significantly under-predict the drag for most bodies of finite thickness.

Sato [13] has made some progress in simple profile drag estimation by employing the profile drag formula as related to the kinetic energy equation (4.49), which can be written as follows.

$$S_{\text{ref}} C_{D_p} = \iint \frac{\rho_e u_e^3}{q_\infty V_\infty} c_{\mathcal{D}} \, dS_{\text{wet}} + \iint \frac{\rho_e u_e^3}{q_\infty V_\infty} c_{\mathcal{D}} \, dS_{\text{wake}} \tag{4.114}$$

Noting that the dissipation coefficient $c_{\mathcal{D}}$ is very insensitive to pressure gradients (much less so than C_f), we can interpret K_f as a measure of the average $\rho_e u_e^3/\rho_\infty V_\infty^3$ ratio over the surface and the wake. This leads to a fairly reliable profile drag estimation formula

$$S_{\text{ref}} C_{D_p} = \bar{C}_f \iint \frac{\rho_e u_e^3}{\rho_\infty V_\infty^3} \, dS_{\text{wet}} \tag{4.115}$$

which has the same form as (4.113), but with a local $\rho_e u_e^3$ weighting rather than $\rho_e u_e^2$. This still has the great simplicity of requiring only potential-flow velocities to be integrated over the surface. The ratio between $c_{\mathcal{D}}$ and C_f, and the additional contribution of the wake dissipation, have all been lumped into the $\bar{C}_f$ factor, by the requirement that the formula give the correct result for the flat plate. Additional refinements can be made by splitting the integral between the laminar and turbulent portions as appropriate.

Sato [13] has shown that the profile drag predictions of formula (4.115) are reliable to within a few percent for flows which do not have trailing edge separation. He has also introduced modifications for wall roughness, and also for compressibility which gives good results up to weakly transonic flow.

4.13.3   Boundary layer calculation methods

The next most reliable method of profile drag prediction is to actually perform the boundary layer calculations to obtain the far-downstream P_∞ or K_∞. However, this can run into difficulties if a simple classical boundary layer calculation is used, since the $u_e(s)$ distribution from a potential solution typically has a very

steep adverse pressure gradient immediately ahead of the trailing edge stagnation point. Consequently the classical boundary layer calculation will fail there due to the Goldstein separation singularity, as discussed in Section 4.12.1. The fully-coupled viscous/inviscid XFOIL and MSES methods avoid these pitfalls by allowing $u_e(s)$ to adjust in response to the viscous displacement, which removes the Goldstein singularity.

The boundary layer calculation can be stopped at the trailing edge, or continued into the wake if $u_e(s)$ is known along the wake. This raises the practical problem of how to determine P_∞ or θ_∞ from $\theta(\bar{x})$ at the last calculated point $\bar{x}$, which may be either at the trailing edge or at the end of a wake of finite length. A suitable method is to use the von Karman equation (4.28) which in the wake simplifies as follows.

$$\frac{1}{\theta}\frac{d\theta}{ds} = -(H+2)\frac{1}{u_e}\frac{du_e}{ds}$$
$$d(\ln\theta) = -(H+2)\,d(\ln u_e) \qquad \text{(in wake)} \qquad (4.116)$$

This can be approximately integrated from the last known location $s = \bar{s}$ to far downstream $s \to \infty$ if we assume an average value of H_{avg} over this interval. Since $H \to 1$ far downstream in an incompressible wake, a reasonable approximation is

$$H_{\text{avg}} \simeq \frac{H(\bar{s})+1}{2} \qquad (4.117)$$

so that equation (4.116) then explicitly gives θ_∞ in terms of the known quantities at $\bar{s}$.

$$\ln\theta(s)\Big|_{\bar{s}}^{\infty} = -(H_{\text{avg}}+2)\,\ln u_e(s)\Big|_{\bar{s}}^{\infty}$$
$$\theta_\infty = \theta(\bar{s})\left(\frac{u_e(\bar{s})}{V_\infty}\right)^{(H_{\text{avg}}+2)} \qquad (4.118)$$

The relations are diagrammed in Figure 4.29. Equation (4.118) is known as the *Squire-Young formula* [34], and was originally developed for cases where $\bar{s}$ is at the trailing edge, so that the extrapolation is over the entire wake. However, it can be used if $\bar{s}$ is some distance downstream in the wake, and in fact it then becomes more accurate because the $H \simeq H_{\text{avg}}$ assumption then gets better.
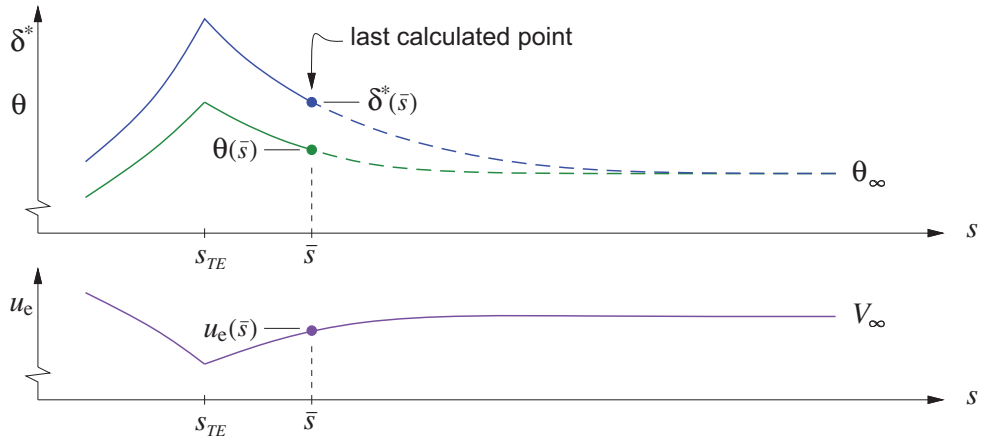

Figure 4.29: Extrapolation of last-calculated θ at $s = \bar{s}$ to far-downstream value θ_∞.

The Squire-Young formula is also useful in experiments, where it can be used to extrapolate a measured wake momentum defect near the airfoil to downstream infinity, so that the actual profile drag can be determined from the measurements. This is described in Section 10.4.2.

4.14   Transition

The average skin friction chart in Figure 4.28 indicates that the transition location has considerable influence on the profile drag of an airfoil or body, and often affects maximum lift as well. For boundary layer calculation purposes, the transition point is where a switch is made from a laminar to a turbulent calculation method. It is therefore necessary to determine the transition point in terms of laminar boundary layer quantities and other relevant parameters. Since transition prediction is a large field, only a few key results can be given here. See Reed et al [35] for an overview.

4.14.1   Transition types

Transition is in most cases initiated by some sort of unsteady external freestream disturbances, or by surface vibration which oscillates the entire flow. How the outside disturbances enter the boundary layer is known as the *receptivity problem* (see Saric et al [36]). The subsequent mechanisms which make these initial disturbances trigger transition can be grouped into three broad types, shown in Figure 4.30.
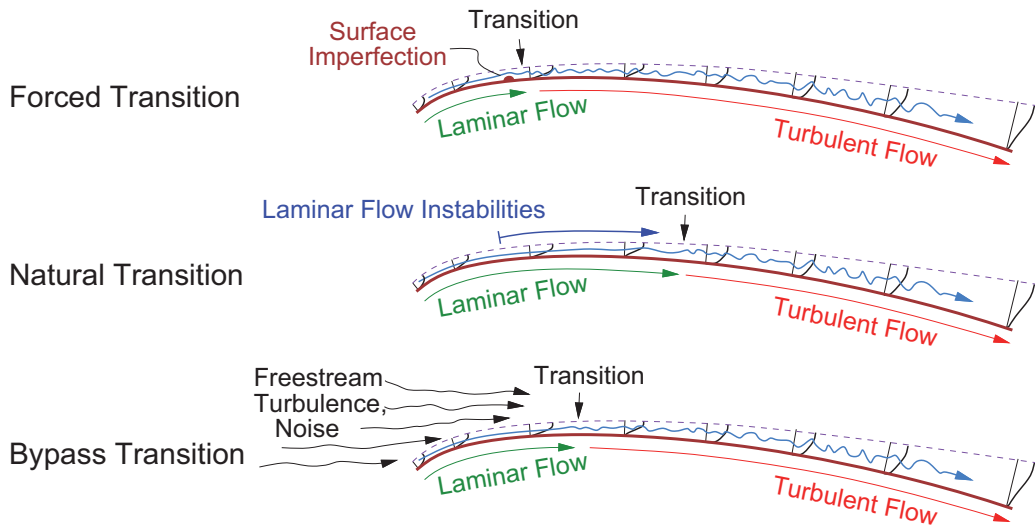
Figure 4.30: Main types of transition.

1. **Forced transition**.
   This is caused by a geometric feature on the surface, such as a panel edge, rivet line, or an intentionally-placed "trip strip." If the feature's size is comparable to the height of the local boundary layer, as measured by the displacement thickness for example, then it is a strong receptivity site where the external disturbances can enter the boundary layer. These are usually sufficiently strong to trigger transition to turbulence a short distance downstream.

2. **Natural transition**.
   This occurs on relatively smooth surfaces in quiet flow, when the external disturbances are extremely weak and the resulting initial disturbances or oscillations in the boundary layer are very weak as well. Examples are external flows in flight or in a quiet wind tunnel. The initial disturbances are amplified by natural *flow instabilities* and increase exponentially in amplitude downstream, and eventually become strongly chaotic. The changeover to chaotic turbulent flow defines the transition location. Transition of this type can be predicted by the so-called e^N methods [37], [38]. One example of such a method is summarized in the next section.

3. **Bypass transition**.
   This occurs only in very noisy environments, where the disturbances in the outer inviscid flow are

sufficiently strong to enter the boundary layer almost everywhere. Examples are flows found inside turbomachinery. Chaotic turbulent flow in a boundary layer on a turbomachine blade airfoil will begin where the local Reynolds number Re_θ becomes sufficiently large to allow the turbulence to be sustained. This minimum value is in the range $Re_\theta \geq 150 \ldots 250$, depending on the local shape parameter H. The method of Abu-Ghannam and Shaw [39] has been popular for predicting bypass transition, especially in turbomachinery flow applications.

4.14.2 TS-wave natural transition prediction

Many types of exponentially-growing instabilities can precipitate natural transition. The most common types in 2D-like flows are called *Tollmien-Schlichting (TS) waves*, which are sinusoidally-oscillating pressure and velocity perturbations within the boundary layer (see Schlichting [12] and Cebeci and Bradshaw [20]). The TS wave perturbations initially have very small amplitudes near the leading edge, usually orders of magnitude smaller than u_e. For unstable waves these amplitudes grow exponentially downstream to levels sufficient to trigger transition, roughly a few percent of u_e. The ratio of the local to initial TS wave amplitudes is defined as $e^{\tilde{N}}$, where the exponent $\tilde{N}(s)$ is the so-called "N-factor" which quantifies the instability growth. In the "envelope e^N" transition prediction method, the N-factor is computed by an accumulating integral over the upstream surface, much like the $P(s)$ and $K(s)$ defects are accumulated as indicated in Figure 4.8.

$$\text{local / initial TS wave amplitude ratio} \;=\; \exp\left(\tilde{N}(s)\right) \tag{4.119}$$

$$\tilde{N}(s) \;=\; \int_0^s \frac{d\tilde{N}}{ds'}\, ds' \tag{4.120}$$

$$\text{where} \quad \frac{d\tilde{N}}{ds} \;=\; \begin{cases} 0 & , \quad Re_\theta < Re_{\theta_o}(H) \quad \text{(stable)} \\ \dfrac{1}{\theta}\, f_{\mathrm{TS}}(H) & , \quad Re_\theta > Re_{\theta_o}(H) \quad \text{(unstable)} \end{cases} \tag{4.121}$$

The empirical functions $f_{\mathrm{TS}}(H)$ and $Re_{\theta_o}(H)$ which determine the $\tilde{N}(s)$ growth are shown in Figure 4.31. Curve fits are provided by Drela [6]. Transition is assumed to occur at the s location where the $\tilde{N}(s)$ variable reaches a specified critical value N_{crit}, which is a measure of the ambient noise or disturbance level.

4.14.3 Influence of shape parameter

For self-similar (power-law) flows, the TS growth rate functions can be used to explicitly determine the Re_θ value at the transition location, and also the corresponding Re_x value.

$$\left(\frac{u_e\,\theta}{\nu}\right)_{\mathrm{tr}} \;\equiv\; Re_{\theta_{\mathrm{tr}}}(H, N_{\mathrm{crit}}) \;=\; Re_{\theta_o}(H) \;+\; \frac{N_{\mathrm{crit}}}{d\tilde{N}/dRe_\theta\,(H)} \tag{4.122}$$

$$\left(\frac{u_e\,s}{\nu}\right)_{\mathrm{tr}} \;\equiv\; Re_{x_{\mathrm{tr}}}(H, N_{\mathrm{crit}}) \;=\; \left(Re_{\theta_{\mathrm{tr}}}\,\frac{\delta_{\mathrm{FS}}}{\theta}\right)^2 \tag{4.123}$$

Figure 4.32 shows this $Re_{x_{\mathrm{tr}}}$ versus the H value of the self-similar flow, for two typical N_{crit} values. Note the dramatic sensitivity of the transition location on the shape parameter H. Between the Blasius and incipient-separation flows, $H = 2.6$ and 4.0, the transition distance is reduced by roughly a factor of 100.

The transition location also depends on the specified parameter N_{crit}, which is a measure of the initial TS wave amplitude, or in effect the ambient disturbance level together with some degree of receptivity. Since the initial disturbances must be amplified by a factor of $e^{N_{\mathrm{crit}}}$ to precipitate transition, a large N_{crit} value corresponds to a clean flow, and vice versa. $N_{\mathrm{crit}} = 11$ or 12 is a typical value in a very clean flow like a sailplane in flight, $N_{\mathrm{crit}} = 9$ is appropriate for the flow in a very quiet wind tunnel, while $N_{\mathrm{crit}} = 4$ corresponds to a fairly turbulent environment such as in a noisy wind tunnel. Note that $e^9 \simeq 8100$ and $e^{12} \simeq 163\,000$, so enormous amplifications are required for TS waves to trigger transition in clean flows.
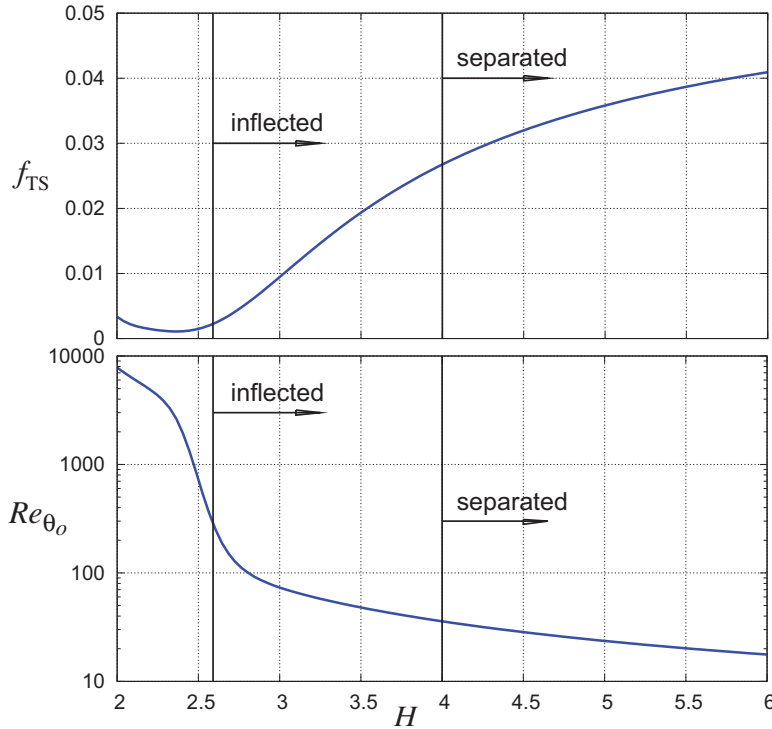
Figure 4.31: TS-wave growth rate $f_{\mathrm{TS}} = \theta \, \mathrm{d}\tilde{N}/\mathrm{d}s$ and threshold Re_{θ_o} for start of growth, versus shape parameter H.
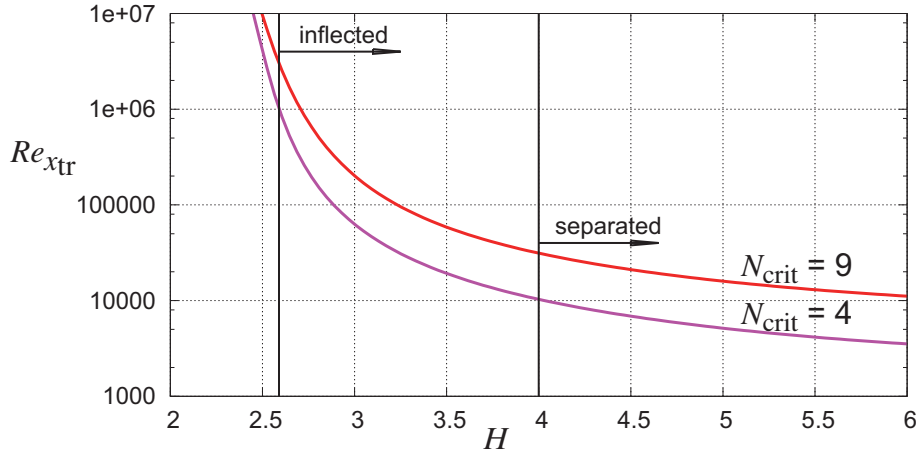
Figure 4.32: Transition Reynolds number versus shape parameter H for self-similar flows, as predicted by the envelope e^N method for two N_{crit} values. Transition Reynolds number for incipient-separation flow ($H = 4.0$) is about 100 times smaller than for Blasius flow ($H = 2.6$).

Influence of freestream Reynolds number

It's useful to examine the effect of <u>freestream</u> Reynolds number on the transition location as indicated by relation (4.123). Laminar boundary layer theory indicates that the momentum thickness (or any other integral thickness) scales as $\theta \sim 1/\sqrt{Re_\infty}$. For example, Thwaites method for a constant $u_{\mathrm{e}} = V_\infty$ gives

$$\theta_{(s)} = \sqrt{\frac{0.45\nu \, s}{V_\infty}} = 0.664\, c \sqrt{\frac{s/c}{Re_\infty}} \tag{4.124}$$

$$\text{where} \qquad Re_\infty \equiv \frac{V_\infty c}{\nu} \tag{4.125}$$

and c is a global reference length such as the chord. Therefore, the N-factor growth rate scales as $\sqrt{Re_\infty}$ via the $1/\theta$ factor which multiplies f_{TS} in (4.121). In addition, the local momentum-thickness Reynolds number in this case is

$$Re_\theta \;\equiv\; \frac{u_e\theta}{\nu} \;=\; 0.664\,\sqrt{s/c}\sqrt{Re_\infty} \qquad\text{(Blasius flow)}\qquad (4.126)$$

which affects where the growth begins via the $Re_{\theta_o}(H)$ threshold function. The effects are illustrated in Figure 4.33 for two Blasius flows with different freestream Reynolds numbers. As Re_∞ increases, $\tilde{N}(s)$ starts growing sooner because the larger Re_θ reaches $Re_{\theta_o}(2.6)$ sooner, and also grows faster because of the smaller $\theta(s)$. Both effects contribute to moving transition upstream with increasing Re_∞.
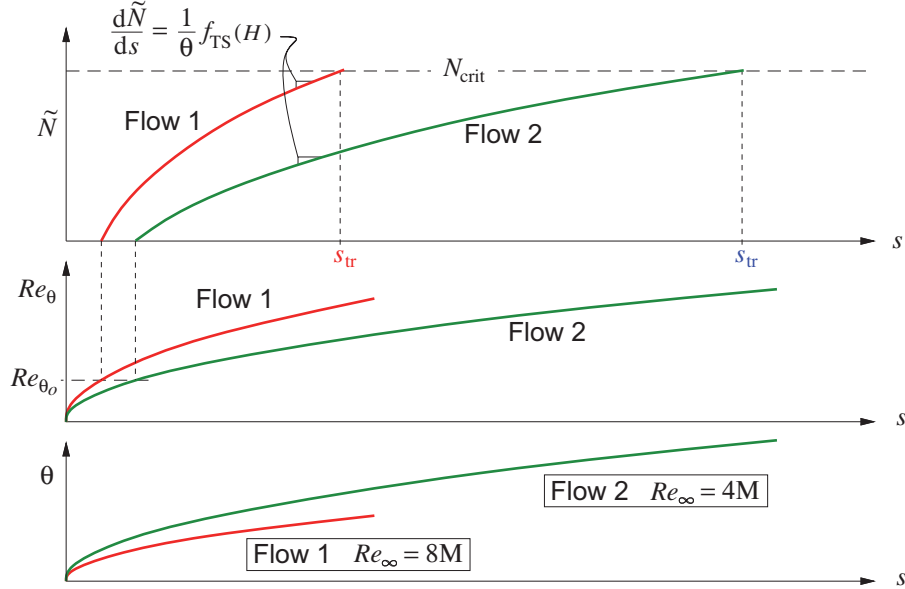
Figure 4.33: Envelope e^N transition prediction for two flat-plate flows with the same constant $H = 2.6$, but different freestream Reynolds number. Flow 1 starts growing earlier due to its larger $Re_\theta(s) \sim \sqrt{Re_\infty}$, and also has a faster growth rate due to its smaller $\theta(s) \sim 1/\sqrt{Re_\infty}$. Both effects move transition forward as Re_∞ is increased.

4.14.4 Transitional separation bubbles

In a sufficiently clean flow and at a sufficiently low Reynolds number, natural transition will occur after laminar separation takes place. Past transition, the now-turbulent separated shear layer is able to reattach, forming a *transitional separation bubble* (also called a *laminar separation bubble*), originally investigated by Tani [40] and Gaster [41]. An example of such a flow is shown in Figure 4.34, in which a separation bubble is revealed by the *pressure plateau* over its laminar portion, followed by a rapid pressure rise over the turbulent portion after transition. The plateau is a consequence of the nearly-still fluid inside the laminar part of the bubble being unable to sustain any significant pressure gradients. In contrast, the strong turbulent mixing in the turbulent portion can support the strong adverse pressure gradient.

Figure 4.35 diagrams the overall separation bubble flow, together with its associated edge velocity $u_e(s)$, shape parameter $H(s)$, and momentum defect $P(s)$ distributions. The steep velocity decrease from u_{e_1} to u_{e_2} over the turbulent portion results in an associated steep momentum defect increase from P_1 to P_2. Since skin friction is largely negligible in a separation bubble, these changes are related by the wake form of the
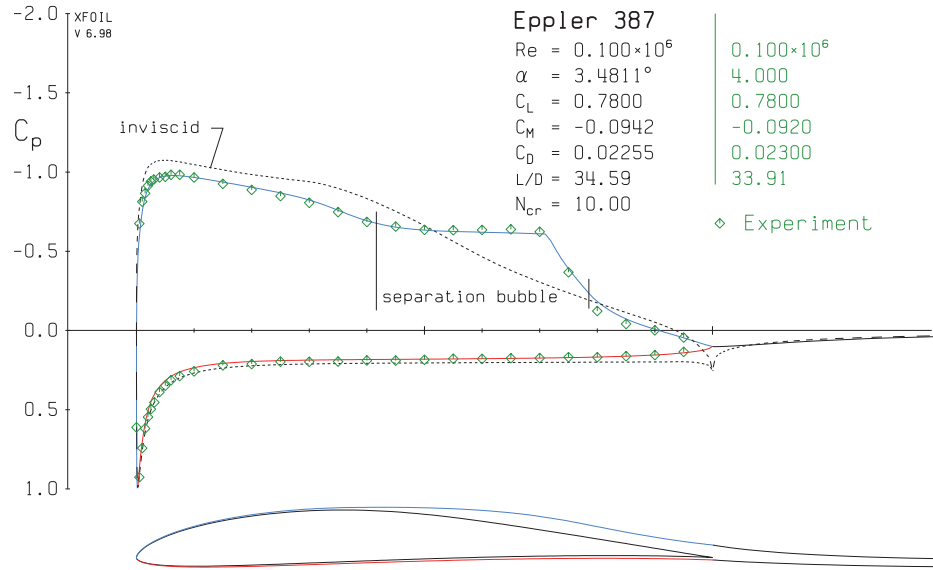
Figure 4.34: XFOIL [5] pressure distributions on Eppler 387 airfoil at $Re = 100\,000$ reveal a transitional separation bubble on the upper surface. Experimental data is from McGhee at al [42].

von Karman momentum equation (4.116).

$$P_2 \;\simeq\; P_1 \left(\frac{u_{e_1}}{u_{e_2}} \right)^{H_{avg}} \tag{4.127}$$

where $H_{avg} \simeq \frac{1}{2}(H_{max} + H_{turb})$ is an average shape parameter over the velocity change interval. Large H_{max} values in the bubble will therefore increase H_{avg} and increase the downstream defect P_2.

The smallest-possible downstream defect, denoted by P_2' in Figure 4.35, is obtained when transition occurs close to laminar separation so that the bubble does not form and H_{avg} stays very low at its turbulent value. The difference

$$\Delta P_{bubble} \;=\; P_2 - P_2' \tag{4.128}$$

can be considered to be "bubble drag," or the drag penalty of the bubble being present.

The excess ΔP_{bubble} from large H_{max} values persists into the far wake and implies a corresponding increase in the overall profile drag D', referred to as *bubble drag*. This is the mechanism responsible for the inordinate drag increases experienced by most airfoils which are operated well below their intended Reynolds numbers, which results in strong separation bubble formation.

Reducing separation bubble loss ΔP_{bubble} is one of the major design goals for airfoils at low Reynolds numbers, below $250\,000$ or so. A specific objective is to make H_{max} as small as possible and also u_{e_1}/u_{e_2} as close to unity as possible, while still maintaining the transition point at the ideal location. This is achieved via a suitable *transition ramp*, which is a region of weak adverse pressure gradient in the inviscid velocity $u_{e_{INV}}(s)$ ahead and over the bubble, which encourages instabilities but is too weak to produce early laminar separation. Once separation does occur, the weak inviscid adverse pressure gradient also gives a modest $H(s)$ growth in the bubble, so H_{max} at transition is modest as well. Furthermore, the longer weak adverse gradient reduces the velocity u_{e_1} at transition, so that the velocity ratio u_{e_1}/u_{e_2} is smaller as well. Both effects are seen to decrease the downstream defect P_2 in equation (4.127).

Figure 4.36 shows the SD7037 airfoil with features a transition ramp starting at 5% chord. The result is a 32% drag reduction compared to the Eppler 387 airfoil in Figure 4.34 which has a shorter and steeper
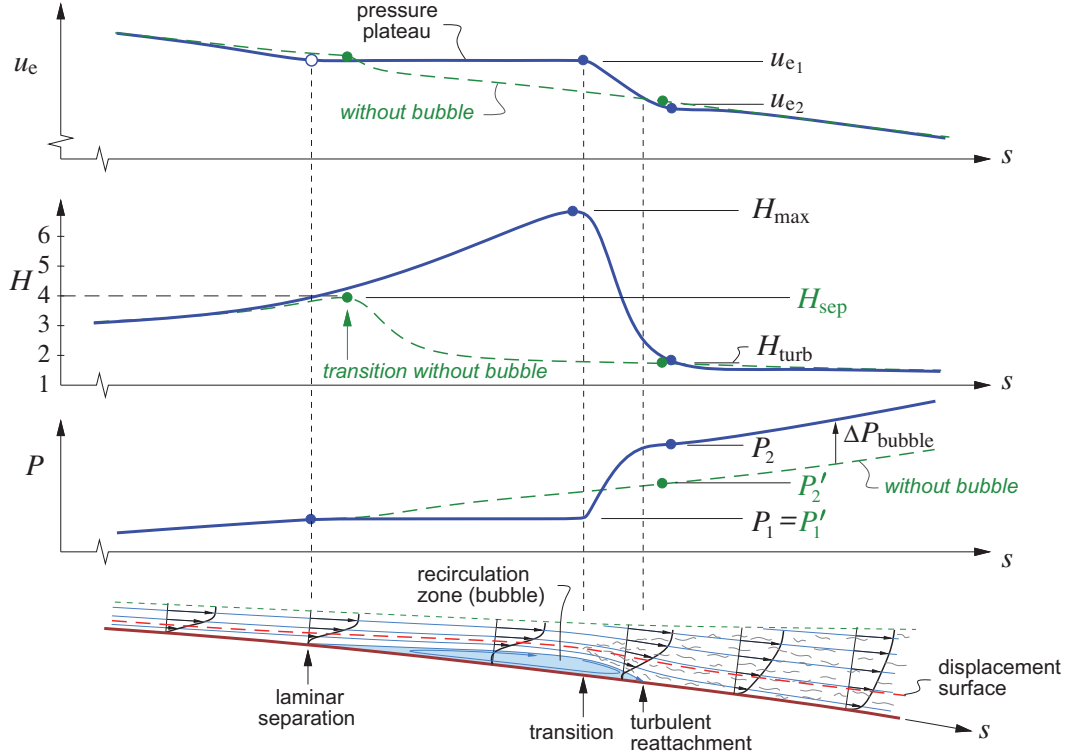
Figure 4.35: Transitional separation bubble is produced when laminar separation is followed by transition and subsequent reattachment. The excess momentum defect increase ΔP_{bubble} due to a large $H_{\max}$ is a bubble drag penalty.

transition ramp starting at 35% chord. The relevant boundary layer parameter distributions for the two airfoils are compared in Figure 4.37. The $H_{\max}$ value is seen to be smaller for the SD7037. Comparing the $C_p(x)$ distributions between Figures 4.34 and 4.36 reveals that the SD7037 has a noticeably smaller C_p jump between transition and reattachment, so its u_{e_1}/u_{e_2} ratio is smaller as well.
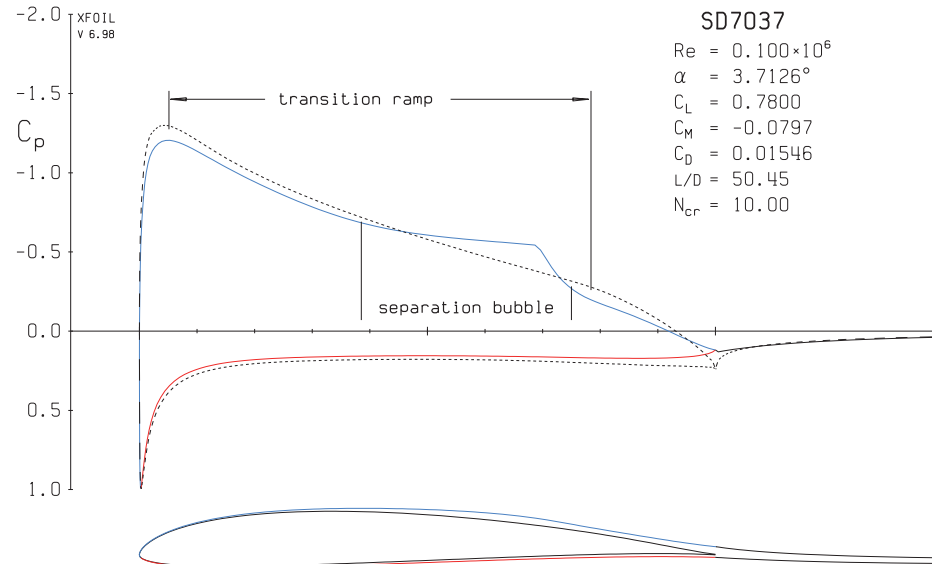
Figure 4.36: XFOIL [5] pressure distributions on SD7037 airfoil at $Re = 100\,000$, which features a long transition ramp (weak adverse pressure gradient) starting at $x/c \simeq 0.05$ to reduce bubble loss.

A long bubble ramp requires a reduction in the overall airfoil thickness, which influences the structural merit (maximum spar thickness) and other properties such as c_m and off-design performance, making the overall airfoil design problem quite complex. These various design considerations are discussed in more detail in the low Reynolds number airfoil design studies by Drela [43], Liebeck [44], and Selig [45]. Control of separation bubbles using intentional boundary layer trips is discussed by Gopalarathnam et al [46].
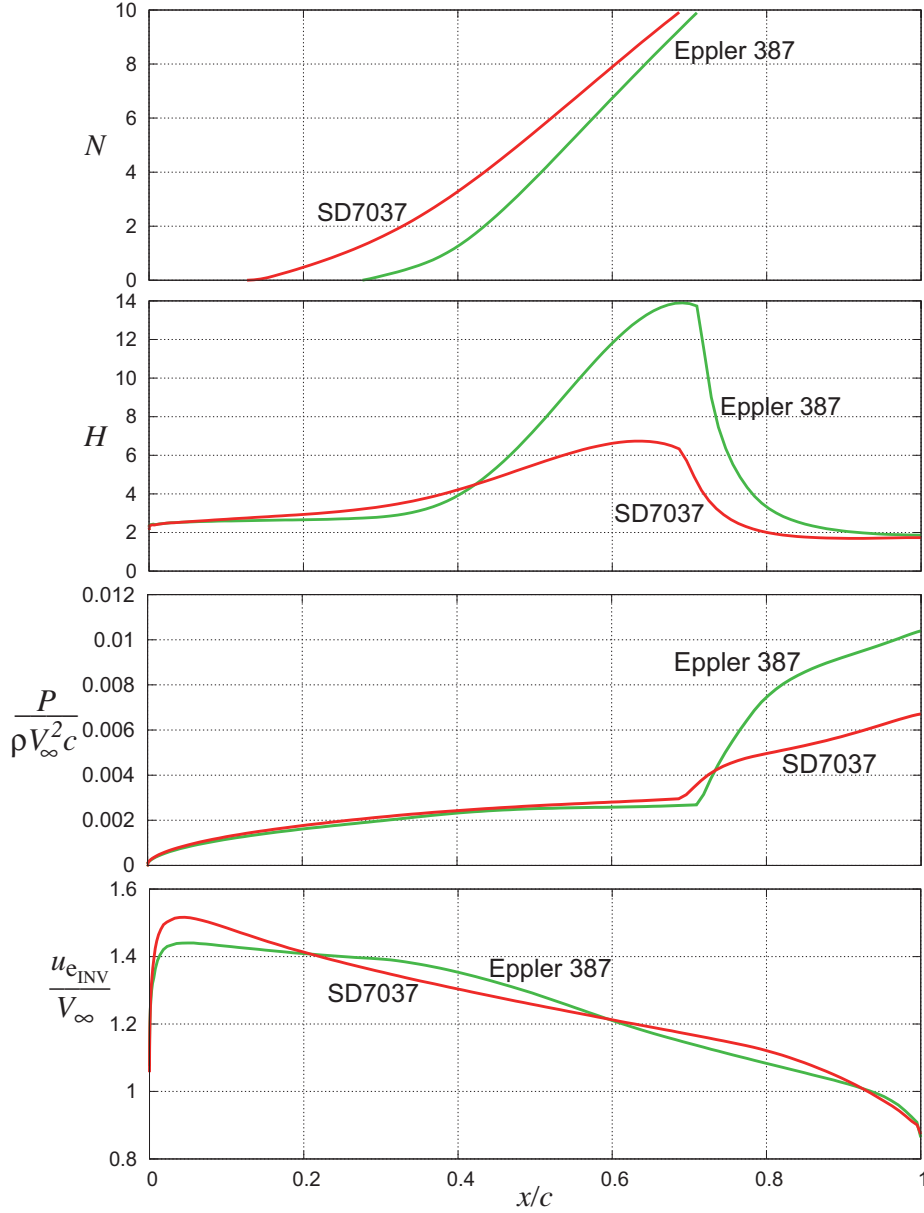
Figure 4.37: Upper surface inviscid edge velocity distributions and resulting shape parameter and TS-wave envelope distributions for SD7037 and Eppler387 airfoils. Long and shallow transition ramp in the $u_e(x)$ distribution of the SD7037 airfoil produces a smaller maximum H value and a smaller u_e decrease over the bubble. The result is a much smaller rise in the momentum defect P past transition at $x/c \simeq 0.7$ for the SD7037 compared to the Eppler387. The SD7037 has 32% less drag as a consequence.

Chapter 5

Aerodynamic Force Analysis

This chapter will examine aerodynamic forces acting on a body, and how they are related to the properties of the flow-field. A major goal is to rigorously relate the lift, drag, and sideforce components to the flow-field on a closed bounding surface which is either on the body surface itself (near-field force), or arbitrarily far from the body (far-field force).

Another major goal is to simplify the far-field forces using suitable simplifications and idealizations of the flow-field, in particular the trailing vortex wake. This will produce expressions for the lift, drag, and sideforce which involve the trailing vortex wake alone. It will also allow the decomposition of the drag force into profile-drag and induced-drag constituents, and thus enable the optimization of aerodynamic configurations for minimum induced drag.

5.1 Near-Field Forces

5.1.1 Force definitions

The *near-field* aerodynamic force $\mathbf{F}$ on a body is the total force that the fluid exerts on its surface S_{body}, as shown in Figure 5.1. This can be decomposed into pressure normal forces and viscous stress forces,

$$\mathbf{F} = \mathbf{F}_{\text{pressure}} + \mathbf{F}_{\text{friction}} \tag{5.1}$$

$$\mathbf{F}_{\text{pressure}} \equiv \oiint -p_{\text{w}}\,\hat{\mathbf{n}}\,\mathrm{d}\mathcal{S} = \oiint (p_{\infty} - p_{\text{w}})\,\hat{\mathbf{n}}\,\mathrm{d}\mathcal{S} \tag{5.2}$$

$$\mathbf{F}_{\text{friction}} \equiv \oiint \boldsymbol{\tau}_{\text{w}}\,\mathrm{d}\mathcal{S} \quad , \quad \boldsymbol{\tau}_{\text{w}} \equiv \bar{\bar{\boldsymbol{\tau}}}_{\text{w}} \cdot \hat{\mathbf{n}} \tag{5.3}$$

where $p_{\text{w}}, \boldsymbol{\tau}_{\text{w}}$ are the pressure and viscous stress vector acting on area element $\mathrm{d}\mathcal{S}$, with unit normal $\hat{\mathbf{n}}$. Replacing $-p_{\text{w}}$ with $p_{\infty} - p_{\text{w}}$ in the second pressure integral is allowed because the uniform pressure p_{∞} does not exert a net force on a body. This follows from the identity $\oiint \hat{\mathbf{n}}\,\mathrm{d}\mathcal{S} = \mathbf{0}$, valid for any volume.

Choosing the x-axis to be aligned with the freestream, $\mathbf{V}_{\infty} = V_{\infty}\,\hat{\mathbf{x}}$, the streamwise drag force component is then $D = \mathbf{F} \cdot \hat{\mathbf{x}}$, which has pressure and friction contributions, as shown in Figure 5.1.

$$D = \mathbf{F} \cdot \hat{\mathbf{x}} = D_{\text{pressure}} + D_{\text{friction}} \tag{5.4}$$

$$D_{\text{pressure}} \equiv \oiint (p_{\infty} - p_{\text{w}})\,\hat{\mathbf{n}} \cdot \hat{\mathbf{x}}\,\mathrm{d}\mathcal{S} \tag{5.5}$$

$$D_{\text{friction}} \equiv \oiint \boldsymbol{\tau}_{\text{w}} \cdot \hat{\mathbf{x}}\,\mathrm{d}\mathcal{S} \tag{5.6}$$
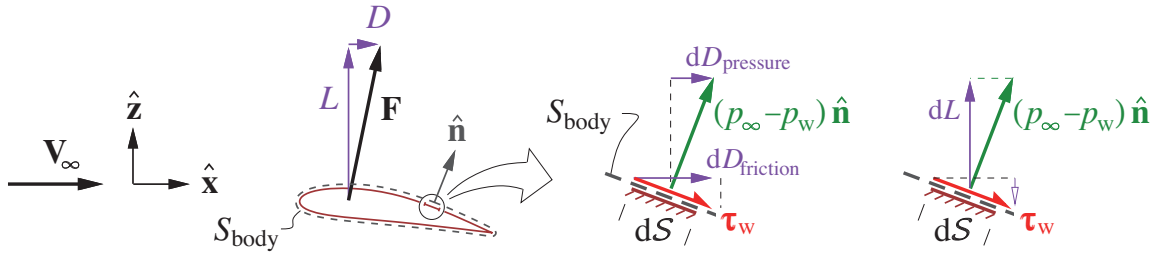
Figure 5.1: Surface pressure and viscous stress forces resolved into drag and lift components. Third dimension y and sideforce Y are not shown. The viscous stress contribution to lift and sideforce is typically negligible.

The transverse-horizontal and transverse-vertical components are the sideforce Y and the lift L.

$$Y \;=\; \mathbf{F} \cdot \hat{\mathbf{y}} \;\simeq\; \oiint (p_\infty - p_\mathrm{w})\,\hat{\mathbf{n}} \cdot \hat{\mathbf{y}} \; \mathrm{d}\mathcal{S} \tag{5.7}$$

$$L \;=\; \mathbf{F} \cdot \hat{\mathbf{z}} \;\simeq\; \oiint (p_\infty - p_\mathrm{w})\,\hat{\mathbf{n}} \cdot \hat{\mathbf{z}} \; \mathrm{d}\mathcal{S} \tag{5.8}$$

The viscous stress contributions to Y, L will be neglected in the subsequent discussion, since at high Reynolds numbers they are typically negligible compared to the pressure contributions.

5.1.2   Near-field force calculation

In grid-based CFD solutions of the Navier-Stokes equations, the D, Y, L force components are calculated directly from the above definitions via numerical integration over the surface. But in simplified flow models, such as inviscid panel methods with or without viscous displacement models, this approach works only for the transverse Y, L components. If the streamwise D component were computed in this manner, it would be simply incorrect or very inaccurate. The main reason is that the D_pressure integral has relatively large positive and negative integrand contributions over the surface which mostly cancel, as shown in Figure 5.2.

Signs of local $\mathrm{d}D_\mathrm{pressure} \sim (p_\infty - p_\mathrm{w})\,\hat{\mathbf{n}} \cdot \hat{\mathbf{x}}$ Signs of local $\mathrm{d}L \sim (p_\infty - p_\mathrm{w})\,\hat{\mathbf{n}} \cdot \hat{\mathbf{z}}$
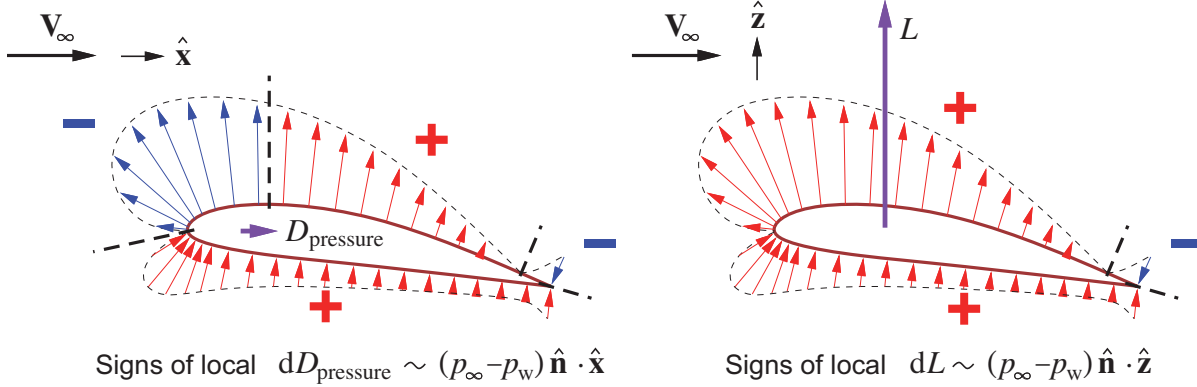
Figure 5.2: Streamwise components of the surface pressure forces on a streamlined shape almost entirely cancel, with the small net residual being the pressure drag. There is no such cancellation of the transverse components which form the much larger lift.

In fact, for 2D inviscid flow the cancellation is theoretically perfect, which constitutes d'Alembert's paradox.

$$D \;=\; D_\mathrm{pressure} \;=\; 0 \qquad \text{(2D inviscid flow)} \tag{5.9}$$

For 3D inviscid lifting flows the cancellation is not total, but is still extensive so that the pressure drag force is small. Even small errors in the surface pressures, or in the discrete integration method, then become very large when compared against the small (but crucial) remaining pressure drag.

The pressure-drag calculation difficulties remain for viscous flow simulations which employ the displacement effect. Such methods were discussed in Chapters 3 and 4, and two computed examples are shown in Figures 3.6 and 3.7. The modification of p_w by the viscous displacement has the following effects:

- The modified lift L is now much more accurate than what's predicted by the simple inviscid model. In particular, it can capture the effects of flow separation and stall as was shown in Figure 3.5.

- The modified D_{pressure} is now correctly nonzero in 2D flow. However, its accuracy is still relatively poor due to the streamwise-component pressure force cancellation shown in Figure 5.2. One reason is that errors associated with numerical integration over the discretized surface are still present. This is most severe for simple panel methods with relatively coarse paneling. Another reason is that even with the displacement effect corrections, the computed wall pressures p_w still have residual errors. These may be small relative to lift, but are very significant relative to the much smaller pressure drag. These errors in p_w are caused by the neglect of streamwise flow curvature in the viscous displacement-effect models, and are not easily removed.

5.2 Far-Field Forces

Consider the indented control volume shown in Figure 5.3, which has the body outside of it topologically. Since the volume is empty, the integral momentum equation (1.28) can be applied to it. Assuming steady flow, and eliminating the gravity force $\rho \mathbf{f}$ by re-defining p to exclude the hydrostatic pressure, we have

$$\oiint \left[\rho(\mathbf{V} \cdot \hat{\mathbf{n}})\mathbf{V} + p\hat{\mathbf{n}} - \bar{\bar{\tau}} \cdot \hat{\mathbf{n}} \right] \mathrm{d}\mathcal{S} = \mathbf{0} \tag{5.10}$$

where the contour integral can be broken up into three S_{body}, S_{outer}, and S_{cut} pieces indicated in Figure 5.3.

$$\oiint [\ ]\,\mathrm{d}\mathcal{S} = \oiint_{\text{body}} [\ ]\,\mathrm{d}\mathcal{S} + \oiint_{\text{outer}} [\ ]\,\mathrm{d}\mathcal{S} + \iint_{\text{cut}} [\ ]\,\mathrm{d}\mathcal{S} = \mathbf{0}$$

Since the two parts of S_{cut} have equal and opposite $\hat{\mathbf{n}}$ vectors its contribution vanishes.

$$\iint_{\text{cut}} [\ ]\,\mathrm{d}\mathcal{S} = \mathbf{0} \tag{5.11}$$

Furthermore, S_{body} is defined to lie on the body's solid surface where $\mathbf{V} \cdot \hat{\mathbf{n}} = 0$, so that the S_{body} integral upon comparison with (5.1)–(5.3) is seen to be the body force $\mathbf{F}$.

$$\oiint_{\text{body}} \left[\rho(\mathbf{V} \cdot \hat{\mathbf{n}})\mathbf{V} + p\hat{\mathbf{n}} - \bar{\bar{\tau}} \cdot \hat{\mathbf{n}} \right] \mathrm{d}\mathcal{S} = \oiint_{\text{body}} \left[p_w\hat{\mathbf{n}} - \tau_w \right] \mathrm{d}\mathcal{S} = \mathbf{F} \tag{5.12}$$

The integrand above differs in sign from (5.1)–(5.3) because here $\hat{\mathbf{n}}$ is in the opposite direction, as can be seen by comparing Figures 5.1 and 5.3.

Combining (5.11) and (5.12) with (5.10) then gives an expression for the body force which involves only the S_{outer} contour. This is known as the *Integral momentum theorem*.

$$\boxed{\mathbf{F} = \oiint_{\text{outer}} \left[(p_\infty - p)\,\hat{\mathbf{n}} - \rho(\mathbf{V} \cdot \hat{\mathbf{n}})(\mathbf{V} - \mathbf{V}_\infty) \right] \mathrm{d}\mathcal{S}} \tag{5.13}$$
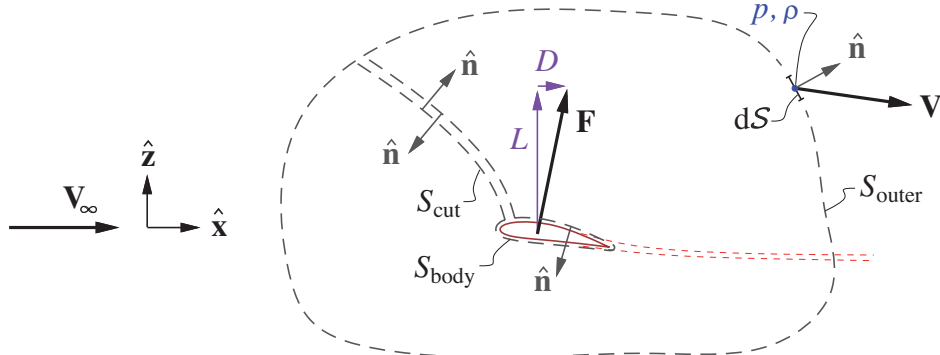
Figure 5.3: Body force $\mathbf{F}$ is related to quantities on any contour S_{outer} enclosing the body. Third dimension y and sideforce Y are not shown.

The viscous stress $\bar{\bar{\boldsymbol{\tau}}} \cdot \hat{\mathbf{n}}$ was assumed to be negligible on S_{outer} and has been left out of (5.13), although it could be retained if appropriate. As before, $-p$ was replaced with $p_\infty - p$ in (5.13) with no effect. Also, $\mathbf{V}$ was replaced with $\mathbf{V} - \mathbf{V}_\infty$ which is allowed because of the mass conservation integral for the volume.

$$\oiint_{\text{outer}} \rho(\mathbf{V} \cdot \hat{\mathbf{n}}) \, \mathrm{d}\mathcal{S} \;=\; 0 \tag{5.14}$$

The integral (5.13) gives an alternative way to calculate the force $\mathbf{F}$ on the body, using flow quantities on any surface S_{outer} surrounding the body. Although it's called the "far-field force," the integral is valid for any distance of the S_{outer} contour, provided only that $\bar{\bar{\boldsymbol{\tau}}} \cdot \hat{\mathbf{n}}$ on it is negligible as assumed. A distant placement is required only if far-field models are used to estimate the p and $\mathbf{V}$ needed to evaluate the integral.

5.3 Flow-Field Idealization

The objective now will be to simplify the lift, drag, and sideforce components of the far-field force expression (5.13) into forms which involve only the wake trailing from the lifting body. This will provide physical insight into the links between forces and flow-field properties, and will also result in practical calculation methods for the forces which will enhance aerodynamic configuration design and optimization procedures.

Consider the rather complicated but typical vortex wake shed by an aerodynamic body, sketched in Figure 5.4. The following simplifications and idealizations of the wake vortex sheet will be made:

- The wake vortex sheet is assumed to trail straight back from the trailing edge where it is shed, along the freestream direction (i.e. along the x-axis). The yz cross-sectional shapes of the sheet will therefore be the yz-shape of the wing trailing edge. In effect this neglects the *roll-up* of the vortex sheet which typically begins at the sheet edges and eventually involves the entire sheet. The straight-wake assumption will be modified slightly in Section 5.9 where a fuselage affects the wake trajectory.

- Only the streamwise vorticity ω_x is assumed to have a nonzero lumped vortex sheet strength γ. This will be used to construct the perturbation velocity field $\nabla \varphi$ outside of the sheet, which is associated with the lift, sideforce, and induced drag. The transverse vorticity ω_s is associated with the viscous velocity defect within the sheet which determines the remaining profile drag component.

5.4 Wake Potential Jump

The idealized far-field force components will be seen to depend on the potential jump $\Delta\varphi(s)$ across the idealized wake sheet in the far-downstream *Trefftz plane*. The objective here is to relate $\Delta\varphi(s)$ to the aerodynamic parameters of the lifting body which generated the sheet.
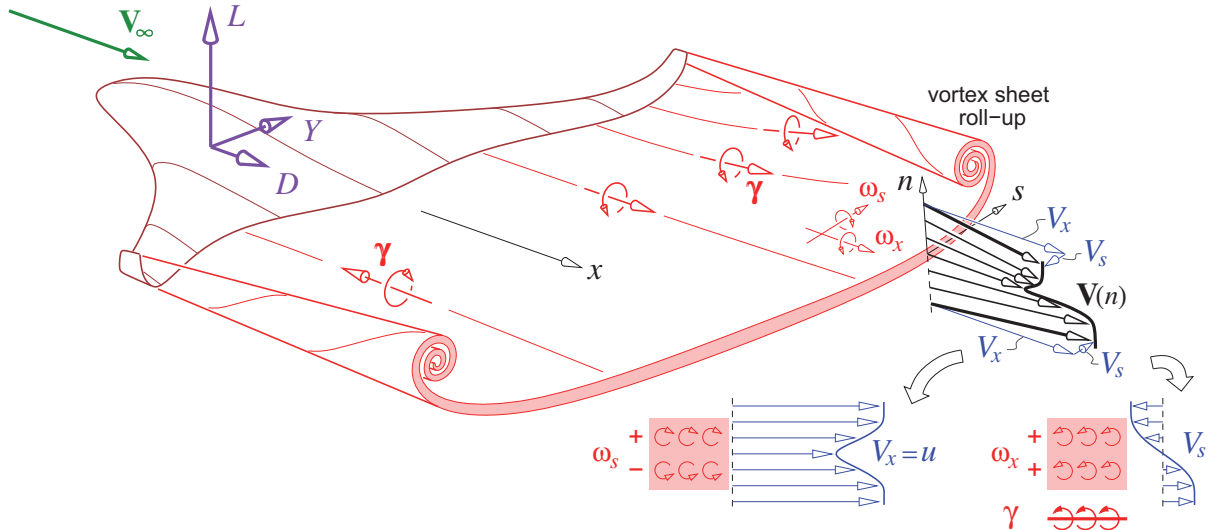
Figure 5.4: A body with lift, drag and sideforce, trailing a thin sheet of vorticity with components ω_x, ω_s. It will be assumed that the sheet trails straight back, and the equivalent lumped vortex sheet strength γ is in the streamwise direction. In effect this neglects the vortex sheet roll-up.

A thin wake layer must have a zero static pressure jump $\Delta p \equiv p_l - p_u$ across it. Assuming the total pressure is the same on the upper and lower sides of the wake vortex sheet, the compressible or incompressible steady Bernoulli equation then implies a zero jump in the velocity magnitude. We then have,

$$
\begin{aligned}
\Delta p = 0 \qquad \rightarrow \qquad \mathbf{V}_u \cdot \mathbf{V}_u - \mathbf{V}_l \cdot \mathbf{V}_l &= 0 \\
\tfrac{1}{2} \left(\mathbf{V}_u + \mathbf{V}_l \right) \cdot \left(\mathbf{V}_u - \mathbf{V}_l \right) &= 0 \\
\mathbf{V}_a \cdot \Delta \mathbf{V} &= 0 \\
\mathbf{V}_a \cdot \widetilde{\nabla}(\Delta\varphi) &= 0
\end{aligned} \qquad (5.15)
$$

$$
\begin{aligned}
\mathbf{V}_a &\equiv \tfrac{1}{2} \left(\mathbf{V}_u + \mathbf{V}_l \right) \\
\Delta \mathbf{V} &\equiv \mathbf{V}_u - \mathbf{V}_l
\end{aligned}
$$

where $\mathbf{V}_a$ denotes the *average sheet velocity*, shown in Figure 5.5. In the final relation (5.15), the velocity jump $\Delta \mathbf{V}$ was replaced by the equivalent surface gradient of the potential jump $\Delta\varphi$.

Equation (5.15) states that the gradient of the sheet potential jump $\Delta\varphi(s,\ell)$ is perpendicular to $\mathbf{V}_a$, or equivalently that $\Delta\varphi(s,\ell)$ is constant along the *average sheet streamlines* which are everywhere parallel to $\mathbf{V}_a$, as shown in Figure 5.5. Hence, the $\Delta\varphi_{TE}$ value at the body's trailing edge where the sheet is shed persists downstream along the average streamline into the Trefftz plane. This $\Delta\varphi_{TE}$ is also the circulation $\tilde{\Gamma}$ about a contour around the wing or body section which contains that trailing edge point.

In principle one could trace the average wake streamlines from the wing trailing edge to determine its shape $y(s), z(s)$ and loading $\Delta\varphi(s)$ in the far-downstream Trefftz plane. This would require tracking the roll-up process in detail which for most cases is impractical. A more common and much simpler approach is to trace the wake streamlines straight back along the freestream direction. This is equivalent to assuming

$$
\mathbf{V}_a \simeq \mathbf{V}_\infty \qquad \text{(straight-wake assumption)} \qquad (5.16)
$$

which is the model shown in Figures 5.6 and 5.7 in the following sections.
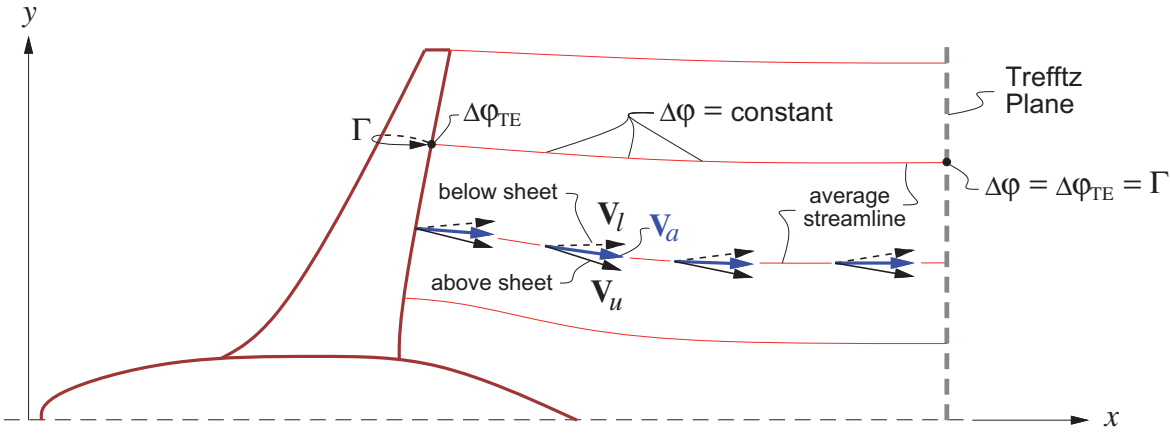
Figure 5.5: Wake sheet potential jump $\Delta\varphi$ is constant along average streamlines which are parallel to average sheet velocity $\mathbf{V}_a$. This defines $\Delta\varphi(s)$ in the Trefftz plane from the body's circulations Γ.

5.5   Lifting-Line Analysis

A practical approach to lift and drag calculation for high aspect ratio 3D wings is based on the *lifting line approximation*. This is actually a hybrid far-field/near-field model which uses the idealized straight-wake approximation together with specified spanwise wing chord and twist distributions $c(y)$ and $\alpha_{\mathrm{aero}}(y)$. The lifting-line model hinges on the following assumptions, illustrated in Figure 5.6.

- The near-field flow is 2D, but with an effective freestream velocity $\mathbf{V}_{\mathrm{eff}}$. This is the freestream plus the velocity of wake, so that it contains all contributions <u>except</u> those of the vortices and sources representing the local 2D wing section. These are intentionally not shown in Figure 5.6, since they do not contribute to $\mathbf{V}_{\mathrm{eff}}$. The wake vorticity lies mostly along the freestream, so its *downwash* velocity w_{wake} at the wing is in the vertical $\hat{\mathbf{z}}$ direction, and therefore acts primarily to tilt the freestream by the *induced angle* α_i.

$$\mathbf{V}_{\mathrm{eff}} \;=\; V_\infty\,\hat{\mathbf{x}} \;+\; w_{\mathrm{wake}}\,\hat{\mathbf{z}} \tag{5.17}$$

$$\alpha_i \;=\; \arctan\frac{-w_{\mathrm{wake}}}{V_\infty} \;\simeq\; \frac{-w_{\mathrm{wake}}}{V_\infty} \tag{5.18}$$

For a positive (upward) lift, the downwash is typically negative and hence α_i is positive.

- At each spanwise location, w_{wake} is assumed to be nearly uniform over the chordwise extent of the wing's airfoil, so that α_i acts to modify the airfoil's angle of attack at that location.

- At each spanwise location y, $w_{\mathrm{wake}}(y)$ is related to the wake vortex sheet strength γ at all spanwise locations y' by considering the wake to be a row of semi-infinite vortex filaments of strength $\gamma(y')\,dy'$. The vertical velocity at y, of a filament at y', is then $dw_{\mathrm{wake}} = \gamma\,dy'/4\pi(y-y')$. Integrating this over the span $y = -b/2\ldots b/2$ gives the overall local downwash.

$$\frac{\partial\varphi}{\partial z}(0,y,0) \;\equiv\; w_{\mathrm{wake}}(y) \;=\; \frac{1}{4\pi}\int_{-b/2}^{b/2}\frac{\gamma(y')}{y-y'}\,dy' \tag{5.19}$$

The physical lifting-line model described here does not require that the wing be unswept. However, classical wing analysis methods based on the lifting-line model, like the one given in Appendix E, do assume zero sweep. For simplicity, the rest of this section will also assume zero sweep.
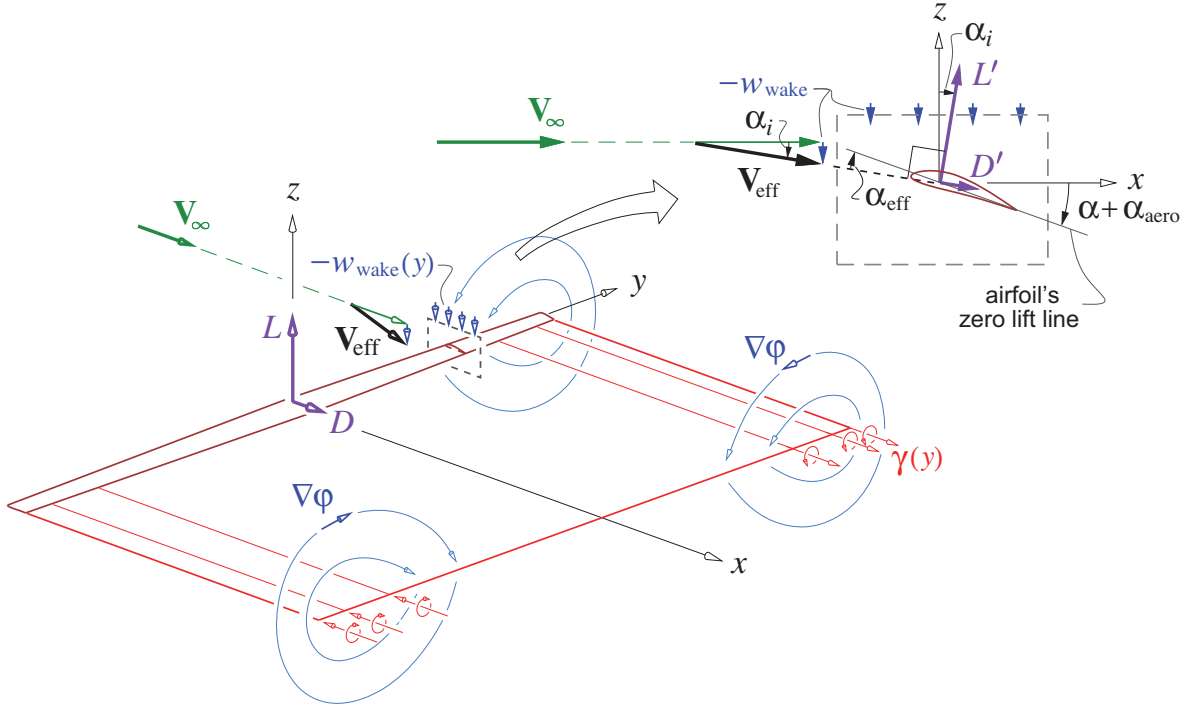
Figure 5.6: Vortex wake with vertical "downwash" velocity w_{wake} (defined positive up, but is typically negative for a positive lift). Lifting-line approximation assumes w_{wake} is nearly constant over extent of the airfoil's 2D near-field, producing a modified effective local freestream $\mathbf{V}_{\text{eff}}$ at each spanwise location y which is rotated from $\mathbf{V}_\infty$ by the induced angle α_i.

A very attractive feature of the lifting-line approximation is its ability to exploit known airfoil characteristics. Because the near-field flow is effectively 2D, its lift/span and drag/span are described by the usual 2D airfoil coefficients c_ℓ, c_d corresponding to the wing-section airfoil shape at that location.

$$L'(y) = \tfrac{1}{2}\rho_\infty V_\infty^2\, c\; c_\ell(\alpha_{\text{eff}}) \tag{5.20}$$

$$D'(y) = \tfrac{1}{2}\rho_\infty V_\infty^2\, c\; c_d(\alpha_{\text{eff}}) \tag{5.21}$$

$$\alpha_{\text{eff}}(y) = \alpha + \alpha_{\text{aero}} - \alpha_i \tag{5.22}$$

Here α_{eff} is the effective local angle of attack, which is less than the overall aerodynamic angle $\alpha + \alpha_{\text{aero}}(y)$ because of the induced angle $\alpha_i(y)$. The induced angle also rotates the local lift and drag forces L', D' as indicated in Figure 5.6. Projecting L', D' onto the global freestream-aligned z, x axes and integrating over the span gives the overall lift and drag L, D.

$$L = \int \left(L' \cos \alpha_i - D' \sin \alpha_i\right) \mathrm{d}y \simeq \int L'\, \mathrm{d}y \tag{5.23}$$

$$D = \int \left(D' \cos \alpha_i + L' \sin \alpha_i\right) \mathrm{d}y \simeq D_p + D_i \tag{5.24}$$

$$D_p = \int D'\, \mathrm{d}y \quad , \qquad D_i = \int L'\, \alpha_i\, \mathrm{d}y \tag{5.25}$$

The rightmost (approximate) forms of the L, D expressions assume

$$\alpha_i \ll 1 \quad , \qquad c_d \ll c_\ell$$

which is valid for high aspect ratio wings with unstalled airfoils.

Although the above lifting-line analysis has defined the overall wing lift and the wing drag components in terms of the relevant quantities, it is not fully predictive as given. Actual calculation of the forces would require knowledge of the vortex sheet strength distribution $\gamma(y)$ as a starting point. This is determined from the wing geometry using the classical procedures given in Appendix E.

The lifting-line force analysis summarized by equations (5.23) and (5.24) is seen to naturally produce a breakdown of the total drag D into *profile drag* and *induced drag* components D_p and D_i, and gives them in terms of the sectional D', L' forces and the induced angle α_i by relations (5.25). The main limitation of this analysis is that it assumes a high aspect ratio wing. For low aspect ratio wings, or more general lifting body shapes like the one shown in Figure 5.4, the vertical velocity w_{wake} of the vortex wake cannot be assumed to be uniform across the chord. In this case a locally-constant induced angle α_i and hence a local effective angle of attack $\alpha_{\mathrm{eff}}(y)$ cannot be defined, so that the lift and drag coefficient c_ℓ and c_d in (5.20) and (5.21) cannot be uniquely determined. Furthermore, with low aspect ratios the locally-2D flow assumption becomes invalid, so that the 2D coefficients c_ℓ and c_d would become questionable even if some suitable chord-averaged α_{eff} could be assumed. The overall consequence is that lift and drag expressions (5.23), (5.24) become inapplicable for general body geometries. These limitations will be avoided with the more general far-field force analyses considered in the subsequent sections.

5.6   Idealized Far-Field Drag

The exact far-field drag is defined as the streamwise component of the total far-field force (5.13).

$$D \;=\; \mathbf{F}\cdot\hat{\mathbf{x}} \;=\; \oiint_{\mathrm{outer}} \left[\, (p_\infty - p)\,\hat{\mathbf{n}}\cdot\hat{\mathbf{x}} \;-\; \rho(\mathbf{V}\cdot\hat{\mathbf{n}})(u-V_\infty) \,\right]\, \mathrm{d}\mathcal{S} \tag{5.26}$$

Appendix C evaluates the 2D form of this relation by integrating around a circular contour far from the airfoil, using potential 2D far-field approximations for p and $\mathbf{V}$, with a special treatment of the viscous wake velocity defect. For a lifting 3D body, the integrand in (5.26) is negligible everywhere except in the downstream Trefftz-plane part of S_{outer}, where the trailing wake exits. Hence, for 3D cases the drag integral above can be conveniently restricted to only this yz Trefftz plane, which has $\hat{\mathbf{n}} = \hat{\mathbf{x}}$.

$$D \;=\; \iint_{TP} \left[\, p_\infty - p \;-\; \rho u(u-V_\infty) \,\right]\, \mathrm{d}y\,\mathrm{d}z \tag{5.27}$$

We will now decompose the effectively-exact far-field drag expression (5.27) into profile and induced components. This requires an idealization of the flow in the Trefftz plane, as sketched in Figure 5.7. Specifically, the vortex sheet thickness is assumed to be small compared to its span, and its net strength $\gamma(s)$ is assumed to be in the x direction. The wake roll-up will also be neglected to simplify the sheet's yz shape. The roll-up issue in drag calculations is discussed in more detail by Kroo [47].

As shown in Figure 5.7, the total velocity at the Trefftz plane is broken down into the freestream $V_\infty\hat{\mathbf{x}}$, a potential perturbation velocity $\nabla\varphi$ associated with the streamwise vorticity $\gamma(s)$, and a streamwise viscous defect Δu associated with the transverse vorticity (shown in Figure 5.4) inside the viscous wake.

$$\mathbf{V} \;=\; (V_\infty + \Delta u)\hat{\mathbf{x}} \;+\; \nabla\varphi \tag{5.28}$$

The pressure is related to the potential part of the velocity (excludes Δu) by the incompressible Bernoulli equation (1.109). This is valid since Trefftz-plane velocities are typically low even for high-speed vehicles.

$$\begin{aligned} p &= p_\infty + \tfrac{1}{2}\rho_\infty V_\infty^2 - \tfrac{1}{2}\rho_\infty |V_\infty\hat{\mathbf{x}} + \nabla\varphi|^2 \\ &= p_\infty - \rho_\infty V_\infty\,\varphi_x - \tfrac{1}{2}\rho_\infty \left(\varphi_x^2 + \varphi_y^2 + \varphi_z^2\right) \end{aligned} \tag{5.29}$$
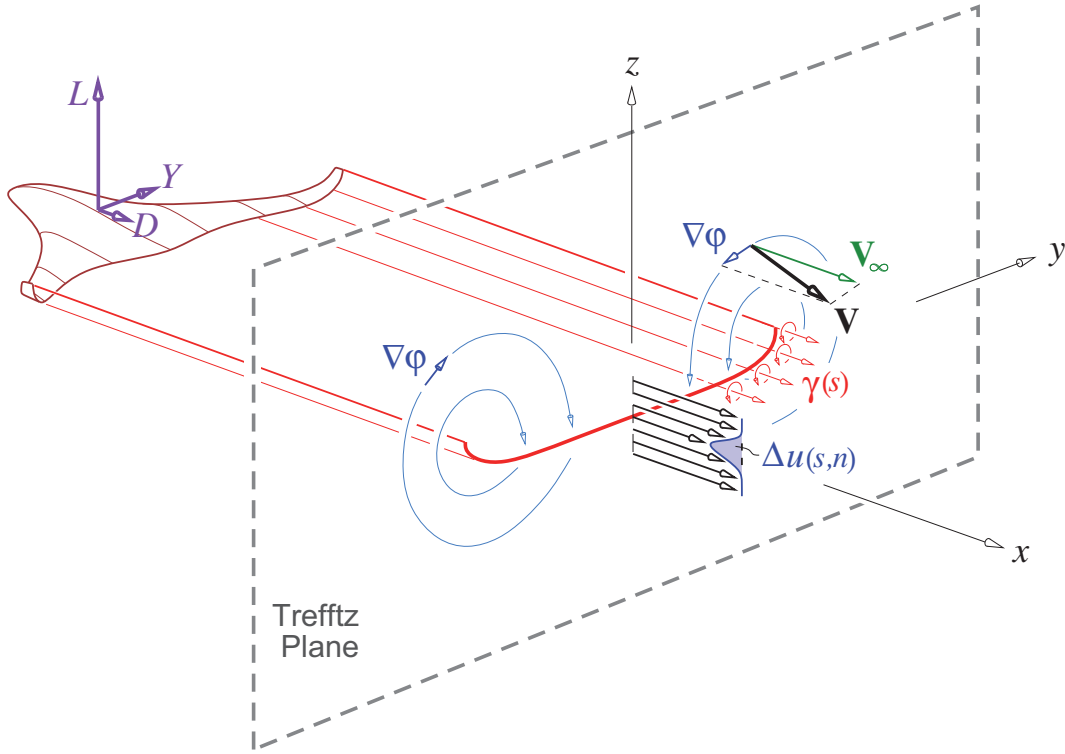
Figure 5.7: Flow in Trefftz plane behind a lifting 3D object, idealized from the actual flow shown in Figure 5.4. Trailing vortex sheet of strength $\gamma_{(s)}$ generates crossflow perturbation velocity $\nabla\varphi$ which defines induced drag, and far-field lift and sideforce. Viscous axial velocity defect $\Delta u_{(s,n)}$ within wake sheet defines profile drag.

Substituting the velocity (5.28) and pressure (5.29) expressions into the drag integral (5.27) and simplifying the result produces a natural decomposition of the drag into its induced-drag and profile-drag components.

$$D \;=\; D_i \;+\; D_p \tag{5.30}$$

$$D_i \;\equiv\; \iint \tfrac{1}{2}\rho_\infty \left(\varphi_y^2 + \varphi_z^2 - \varphi_x^2\right)\,\mathrm{d}\mathcal{S} \;\simeq\; \iint \tfrac{1}{2}\rho_\infty \left(\varphi_y^2 + \varphi_z^2\right)\,\mathrm{d}\mathcal{S} \tag{5.31}$$

$$D_p \;\equiv\; \iint \rho\left(V_\infty + 2\varphi_x + \Delta u\right)\left(-\Delta u\right)\,\mathrm{d}\mathcal{S} \;\simeq\; \iint \rho\left(V_\infty + \Delta u\right)\left(-\Delta u\right)\,\mathrm{d}\mathcal{S} \tag{5.32}$$

The approximations reasonably assume that the perturbation velocity $\nabla\varphi$ is mostly parallel to the yz Trefftz plane, as indicated by Figure 5.7. Specifically, the following assumptions are made.

$$\begin{aligned}
\varphi_x^2 &\;\ll\; \varphi_y^2 + \varphi_z^2 \\
\varphi_x &\;\ll\; V_\infty + \Delta u
\end{aligned} \tag{5.33}$$

The induced drag expression (5.31) is seen to be the crossflow kinetic energy (per unit distance) deposited by the body. This energy is provided by part of the body's propelling force working against the induced drag. The remaining part works against the profile drag, considered next.

5.6.1 Profile drag relations

The profile drag (5.32) can be rewritten as

$$\boxed{D_p \;=\; \iint \rho u \left(V_\infty - u\right)\,\mathrm{d}\mathcal{S}} \tag{5.34}$$

which has the same integrand as the 2D momentum defect P defined by (4.9), with $u_e = V_\infty$ in the downstream wake. Assuming the wake sheet is thin compared to its spanwise extent, the area element can be expressed in the sheet coordinates as $dS = dn\, ds$, and the profile drag is then the spanwise integral of the wake's momentum defect along the whole transverse length of the wake sheet.

$$D_p = \int_0^{s_{\max}} P\, ds \tag{5.35}$$

$$P(s) = \int \rho u\, (V_\infty - u)\, dn = \left(\rho u_e^2 \theta\right)_{\text{wake}} = \rho_\infty V_\infty^2\, \theta_\infty(s) \tag{5.36}$$

5.6.2 Trefftz-plane velocities

As stated earlier, the perturbation potential velocity $\nabla\varphi$ is associated with the wake vortex sheet strength $\boldsymbol{\gamma} = \gamma\,\hat{\mathbf{x}}$. Based on the equivalence between vortex and doublet sheets presented in Section 2.5, this $\boldsymbol{\gamma}(s)$ is related to the sheet's potential jump $\Delta\varphi(s)$ as follows.

$$\boldsymbol{\gamma}(s) = \hat{\mathbf{n}} \times \widetilde{\nabla}(\Delta\varphi) = -\frac{d(\Delta\varphi)}{ds}\,\hat{\mathbf{x}}$$

$$\gamma(s) = \boldsymbol{\gamma} \cdot \hat{\mathbf{x}} = -\frac{d(\Delta\varphi)}{ds} \tag{5.37}$$

Referring to Figure 5.8, this vortex sheet defines the 2D perturbation velocity field $\nabla\varphi$ in the Trefftz plane, via the usual 2D superposition integral,

$$\boxed{\nabla\varphi(\mathbf{r}) = \frac{1}{2\pi} \int_0^{s_{\max}} \gamma(s)\, \frac{\hat{\mathbf{x}} \times (\mathbf{r} - \mathbf{r}')}{|\mathbf{r} - \mathbf{r}'|^2}\, ds \quad , \quad \mathbf{r} = y\,\hat{\mathbf{y}} + z\,\hat{\mathbf{z}}} \tag{5.38}$$

where $\mathbf{r}$ is the yz field point, and $\mathbf{r}'(s) = y'(s)\,\hat{\mathbf{y}} + z'(s)\,\hat{\mathbf{z}}$ parametrically defines the shape of the sheet.
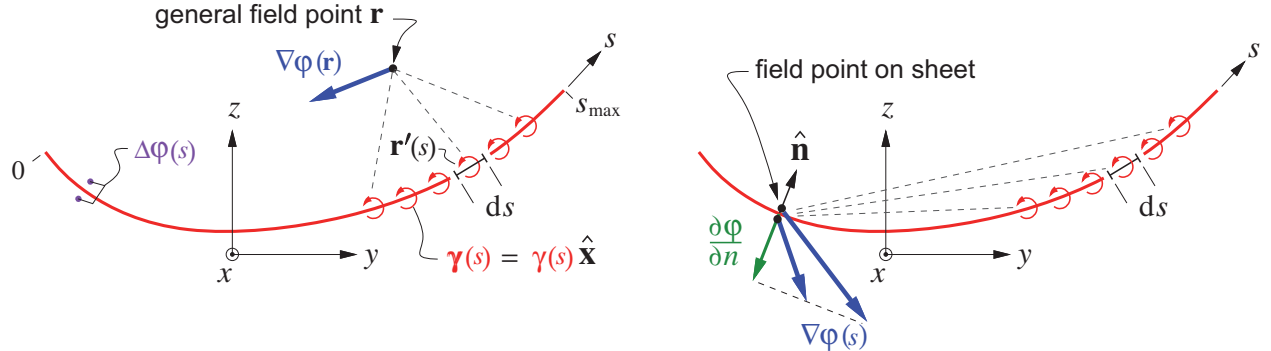

Figure 5.8: Vortex sheet in Trefftz plane, with associated perturbation velocity field $\nabla\varphi$, which has normal velocity component $\partial\varphi/\partial n$ on the sheet itself.

For the particular field point locations on the sheet itself, we can also define the normal component of this velocity.

$$\frac{\partial\varphi}{\partial n} = \nabla\varphi \cdot \hat{\mathbf{n}} \tag{5.39}$$

One of the two velocities (or their average) on either side of the sheet can be used here, since they have the same normal component, which is continuous across any vortex sheet.

Many applications consider the simpler situation of a flat wing of span b, where the vortex sheet is also flat and lies on the y axis from $-b/2$ to $b/2$. The above relations then simplify as follows.

$$\gamma_{(y)} = -\frac{\mathrm{d}(\Delta\varphi)}{\mathrm{d}y} \tag{5.40}$$

$$\frac{\partial\varphi}{\partial n} = \frac{\partial\varphi}{\partial z} = \frac{1}{2\pi}\int_{-b/2}^{b/2}\frac{\gamma_{(y')}}{y-y'}\,\mathrm{d}y' \qquad \text{(flat wake)} \tag{5.41}$$

The potential field $\varphi_{(y,z)}$ for this flat-wake case, with an elliptic potential jump $\Delta\varphi = \sqrt{1-(2y/b)^2}$, is shown in Figure 5.9. The corresponding streamfunction shows the crossflow streamlines.
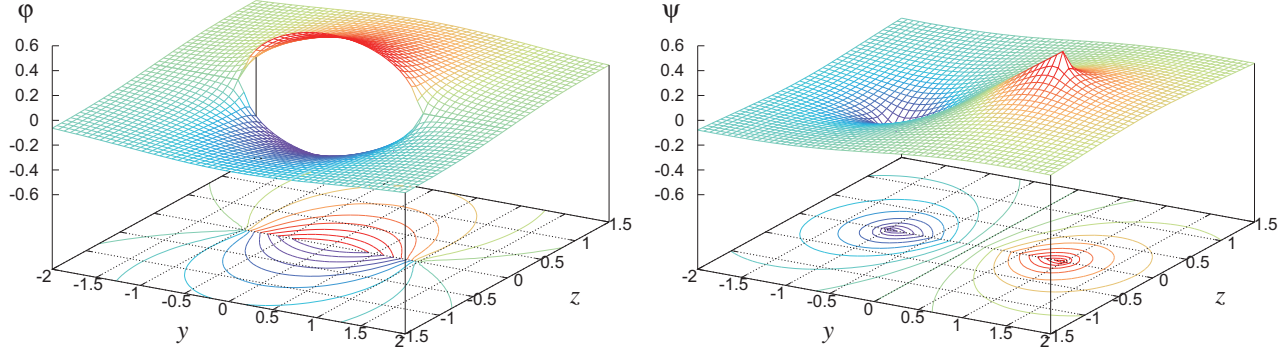

Figure 5.9: Trefftz-plane potential $\varphi_{(y,z)}$ for an elliptic potential jump on a flat wake. The isolines of the corresponding streamfunction $\psi_{(y,z)}$ show the actual crossflow streamlines, also sketched in Figure 5.7.

5.6.3 Induced drag relations

The induced drag definition (5.31) is awkward or impractical to evaluate as written because of the infinite double integral. It can be simplified considerably by using the identity

$$\nabla f \cdot \nabla f = \nabla \cdot (f\,\nabla f) - f\,\nabla^2 f \tag{5.42}$$

which is valid for any differentiable function f. Choosing $f = \varphi$, which satisfies the continuity requirement $\nabla^2\varphi = 0$, simplifies the identity to the following form.

$$\nabla\varphi \cdot \nabla\varphi = \nabla \cdot (\varphi\,\nabla\varphi) \tag{5.43}$$

Referring to Figure 5.10, the induced drag integral (5.31) then becomes

$$\begin{aligned}
D_i &= \iint \frac{1}{2}\rho_\infty \nabla\varphi \cdot \nabla\varphi\,\mathrm{d}\mathcal{S} \\
&= \iint \frac{1}{2}\rho_\infty \nabla \cdot (\varphi\,\nabla\varphi)\,\mathrm{d}\mathcal{S} \\
&= \oint \frac{1}{2}\rho_\infty\,\varphi\,\nabla\varphi \cdot \hat{\mathbf{n}}\,\mathrm{d}l
\end{aligned} \tag{5.44}$$

where the last step (5.44) was obtained via the Gauss Theorem. This integral is over the outer contour with arc length l, and its unit normal vector $\hat{\mathbf{n}}$ points out of the domain.

The outer contour must have φ continuous inside, otherwise Gauss's Theorem or identity (5.43) would not be valid. This requires placing the vortex sheet (and its $\Delta\varphi$ jump) topologically outside the contour, as shown in
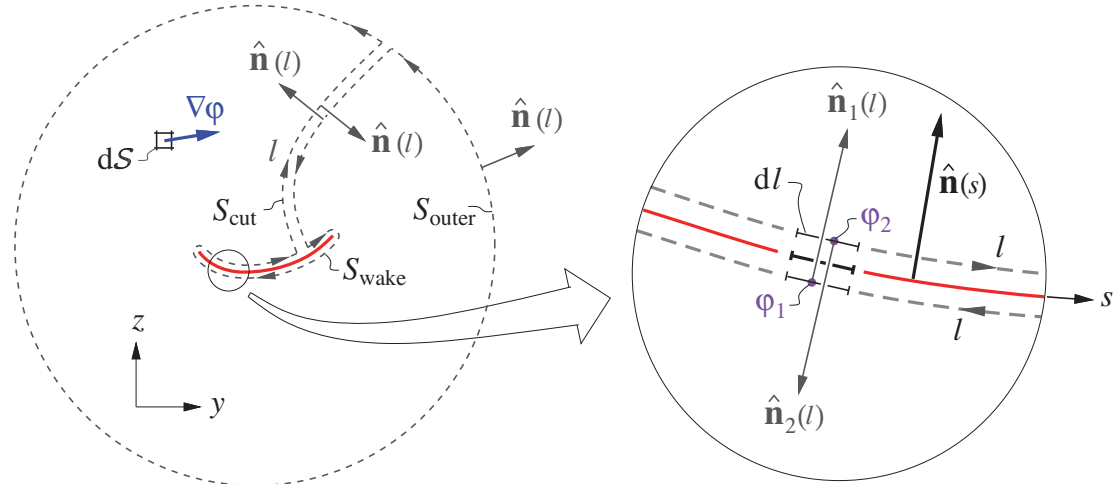
Figure 5.10: Induced drag line integral over l on entire contour perimeter is reduced to only a single integral over s on the vortex wake sheet.

Figure 5.10. For the three contour pieces $S_{\text{wake}}, S_{\text{cut}}, S_{\text{outer}}$, the contribution of S_{outer} to integral (5.44) will vanish when it's taken out to infinity, and the contribution of piece S_{cut} is always zero by antisymmetry of its two $\hat{\mathbf{n}}$ vectors. For the only remaining piece S_{wake} wrapped around the wake vortex sheet, the following relations hold for the two opposing points 1,2:

$$\hat{\mathbf{n}}_1(l) = -\hat{\mathbf{n}}_2(l) = \hat{\mathbf{n}}(s) \tag{5.45}$$

$$dl = ds \tag{5.46}$$

The S_{wake} surface integral around the wake can now be replaced by an integral along the wake, and further simplified using the potential jump definition $\Delta\varphi = \varphi_2 - \varphi_1$.

$$
\begin{aligned}
D_i &= \frac{1}{2}\,\rho_\infty \oint_{\text{wake}} \varphi\,\nabla\varphi \cdot \hat{\mathbf{n}}\,dl \\
&= \frac{1}{2}\,\rho_\infty \int \left[\,\varphi_1 \nabla\varphi_1 \cdot \hat{\mathbf{n}}_1 + \varphi_2 \nabla\varphi_2 \cdot \hat{\mathbf{n}}_2\,\right]\,ds \\
&= \frac{1}{2}\,\rho_\infty \int \left[\,\varphi_1 \nabla\varphi_1 \cdot \hat{\mathbf{n}} - \varphi_2 \nabla\varphi_2 \cdot \hat{\mathbf{n}}\,\right]\,ds
\end{aligned}
$$

$$\boxed{D_i = -\frac{1}{2}\,\rho_\infty \int_0^{s_{\max}} \Delta\varphi\,\frac{\partial\varphi}{\partial n}\,ds} \tag{5.47}$$

For the common case of a flat wake of span b, relation (5.47) can be alternatively given as follows.

$$D_i = -\frac{1}{2}\,\rho_\infty \int_{-b/2}^{b/2} \Delta\varphi\,\frac{\partial\varphi}{\partial z}\,dy \qquad \text{(flat wake)} \tag{5.48}$$

The profile drag expression (5.34) or (5.36) based on the momentum defect, together with the induced drag expression (5.47) based on the crossflow kinetic energy, provide a relatively simple and quite accurate means of calculating or estimating the overall drag of a general 3D configuration.

The required input for the profile drag expression is the spanwise momentum defect distribution $P(s)$. The input for the induced drag expression is the wake sheet potential jump distribution $\Delta\varphi(s)$. Both of these can be obtained with a suitable combination of inviscid and boundary layer calculation methods, preferably coupled via one of the displacement-effect models. The overall far-field drag is relatively accurate, since it does not suffer from pressure drag cancellation errors which make near-field pressure drag calculation unreliable.

The first righthand side term in the identity (5.57) vanished inside the contour integrals via Gauss's Theorem and the $\mathrm{div}(\mathrm{curl}) = 0$ identity.

$$\oiint [\nabla \times (a\mathbf{v})] \cdot \hat{\mathbf{n}} \, \mathrm{d}\mathcal{S} \;=\; \iiint \nabla \cdot [\nabla \times (a\mathbf{v})] \, \mathrm{d}\mathcal{V} \;=\; \iiint 0 \, \mathrm{d}\mathcal{V} \;=\; 0$$

For the final step in simplifying the sideforce and lift expressions (5.58), (5.59) we note that their integrands are nonzero only on the Trefftz plane where the trailing vorticity $\boldsymbol{\omega}$ exits the control volume. Here we have $\hat{\mathbf{n}} = \hat{\mathbf{x}}$, so that $\boldsymbol{\omega} \cdot \hat{\mathbf{n}} = \omega_x$ where the scalar ω_x is the streamwise vorticity component along x. As in the drag derivations, we now also make the assumption that the viscous wake is thin, so that the area element can be recast using the sheet's coordinates, $\mathrm{d}\mathcal{S} = \mathrm{d}n \, \mathrm{d}s$, which permits lumping of the vorticity ω_x into the equivalent vortex sheet strength $\gamma = \int \omega_x \, \mathrm{d}n$.

$$Y \;=\; \rho_\infty V_\infty \iint_{TP} -z \, \omega_x \, \mathrm{d}n \, \mathrm{d}s \;=\; \rho_\infty V_\infty \int_0^{s_{\max}} -z \, \gamma \, \mathrm{d}s \tag{5.60}$$

$$L \;=\; \rho_\infty V_\infty \iint_{TP} y \, \omega_x \, \mathrm{d}n \, \mathrm{d}s \;=\; \rho_\infty V_\infty \int_0^{s_{\max}} y \, \gamma \, \mathrm{d}s \tag{5.61}$$

Next, using relation (5.37), the vortex sheet strength is replaced by the potential-jump derivative, and the resulting expressions are integrated by parts.

$$Y \;=\; \rho_\infty V_\infty \int_0^{s_{\max}} z \, \frac{\mathrm{d}(\Delta\varphi)}{\mathrm{d}s} \, \mathrm{d}s \;=\; \rho_\infty V_\infty \, z \, \Delta\varphi \Big|_0^{s_{\max}} - \rho_\infty V_\infty \int_0^{s_{\max}} \Delta\varphi \, \frac{\mathrm{d}z}{\mathrm{d}s} \, \mathrm{d}s \tag{5.62}$$

$$L \;=\; \rho_\infty V_\infty \int_0^{s_{\max}} -y \, \frac{\mathrm{d}(\Delta\varphi)}{\mathrm{d}s} \, \mathrm{d}s \;=\; -\rho_\infty V_\infty \, y \, \Delta\varphi \Big|_0^{s_{\max}} + \rho_\infty V_\infty \int_0^{s_{\max}} \Delta\varphi \, \frac{\mathrm{d}y}{\mathrm{d}s} \, \mathrm{d}s \tag{5.63}$$

Since the potential jump is zero at each end of the sheet, the first term in (5.62) and (5.63) disappears. The final expressions for the far-field sideforce and lift are then simple integrals of the potential jump or jumps over the $-z$ and y projections of the vortex sheet, as shown in Figure 5.11.

$$\boxed{\; Y \;=\; \rho_\infty V_\infty \int_{z_{\min}}^{z_{\max}} -\Delta\varphi \; \mathrm{d}z \;} \tag{5.64}$$

$$\boxed{\; L \;=\; \rho_\infty V_\infty \int_{y_{\min}}^{y_{\max}} \Delta\varphi \; \mathrm{d}y \;} \tag{5.65}$$

For this reason, the wake potential jump $\Delta\varphi$ is frequently called "the loading," since the quantity $\rho_\infty V_\infty \Delta\varphi$ is in effect the load/span acting on the body which is shedding the wake, and acts normal to the wake.

5.8   Trefftz Plane Integral Evaluation

5.8.1   Fourier series method for flat wake

The mathematical technique used in the lifting-line wing analysis described in Appendix E also provides a convenient means of computing lift and induced drag for the flat-wake case if we make the substitution $\Gamma \to \Delta\varphi$. The potential jump is first expanded as a Fourier sine series in the angle coordinate ϑ.

$$s(\vartheta) \;=\; y(\vartheta) \;=\; \frac{b}{2} \cos\vartheta \qquad , \qquad \mathrm{d}y \;=\; -\frac{b}{2} \sin\vartheta \, \mathrm{d}\vartheta \tag{5.66}$$

$$\Delta\varphi(\vartheta) \;=\; \Delta\varphi(y(\vartheta)) \;=\; 2bV_\infty \sum_{n=1}^{\infty} A_n \sin(n\vartheta) \tag{5.67}$$
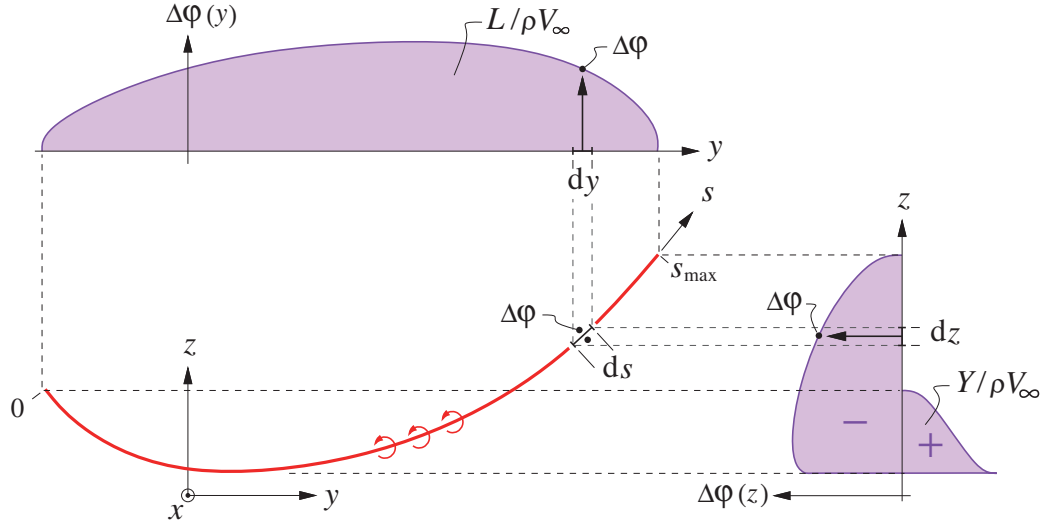
Figure 5.11: Far-field lift and sideforce are areas under projected $\Delta\varphi_{(y)}$ and $-\Delta\varphi_{(z)}$ distributions.

If $\Delta\varphi_{(y)}$ is known, then its coefficients $\mathcal{A}_n$ can be obtained by Fourier analysis of the above expansion.

$$\mathcal{A}_n = \frac{1}{\pi b V_\infty} \int_0^\pi \Delta\varphi_{(\vartheta)} \, \sin(n\vartheta) \, \mathrm{d}\vartheta \tag{5.68}$$

The Trefftz-plane lift integral (5.65) is seen to be the same as the lifting-line result (E.19), and depends only on the first coefficient $\mathcal{A}_1$.

$$L = \rho_\infty V_\infty \int_{-b/2}^{b/2} \Delta\varphi \, \mathrm{d}y = \frac{1}{2}\rho_\infty V_\infty^2 \, b^2 \, \pi \, \mathcal{A}_1 \tag{5.69}$$

The flat-wake normal velocity $\partial\varphi/\partial z$ defined by (5.41) is seen to be twice the lifting-line downwash w_{wake} definition (E.2). This is evaluated in terms of the Fourier coefficients by result (E.10).

$$\frac{\partial\varphi}{\partial z}(y) = \frac{1}{2\pi} \int_{-b/2}^{b/2} \frac{\mathrm{d}\,\Delta\varphi}{\mathrm{d}y'} \frac{\mathrm{d}y'}{y'-y} = -2V_\infty \sum_{n=1}^\infty n\mathcal{A}_n \frac{\sin(n\vartheta)}{\sin\vartheta} \tag{5.70}$$

The flat-wake induced drag integral (5.48) can now be expressed in terms of the Fourier coefficients, by the lifting-line result (E.20).

$$D_i = \pi b^2 \frac{1}{2}\rho_\infty V_\infty^2 \sum_{n=1}^\infty n\mathcal{A}_n^2 = \frac{(L/b)^2}{\frac{1}{2}\rho_\infty V_\infty^2 \, \pi}(1+\delta) = \frac{(L/b)^2}{\frac{1}{2}\rho_\infty V_\infty^2 \, \pi \, e} \tag{5.71}$$

$$\delta \equiv 2\left(\frac{\mathcal{A}_2}{\mathcal{A}_1}\right)^2 + 3\left(\frac{\mathcal{A}_3}{\mathcal{A}_1}\right)^2 + \ldots = \sum_{n=2}^\infty n\left(\frac{\mathcal{A}_n}{\mathcal{A}_1}\right)^2 \tag{5.72}$$

The factor $1+\delta$ in (5.71) is sometimes replaced by the inverse of the *span efficiency*, $1/e$.

By choosing some suitable reference area S_{ref}, with corresponding aspect ratio $A\!R \equiv b^2/S_{\text{ref}}$, the above lift and induced drag can be put into convenient dimensionless forms.

$$C_L \equiv \frac{L}{\frac{1}{2}\rho_\infty V_\infty^2 \, S_{\text{ref}}} = \mathcal{A}_1 \, \pi A\!R \tag{5.73}$$

$$C_{D_i} \equiv \frac{D_i}{\frac{1}{2}\rho_\infty V_\infty^2 \, S_{\text{ref}}} = \frac{\pi}{A\!R} \sum_{n=1}^\infty n\mathcal{A}_n^2 = \frac{C_L^2}{\pi \, A\!R \, e} \tag{5.74}$$

For a given specified lift and span, the above results show that the minimum induced drag is obtained if $\delta = 0$, or $e = 1$, or equivalently $\mathcal{A}_2 = \mathcal{A}_3 \ldots = 0$, and the potential jump has an elliptical distribution on the wake. For this case the normal velocity is also constant everywhere across the wake.

$$\Delta\varphi(y) \;=\; 2bV_\infty \mathcal{A}_1 \sin\vartheta \;=\; 2bV_\infty \frac{C_L}{\pi \, A\!R} \sqrt{1 - (2y/b)^2} \tag{5.75}$$

$$\frac{\partial\varphi}{\partial n}(y) \;=\; -2V_\infty \mathcal{A}_1 \;=\; -2V_\infty \frac{C_L}{\pi \, A\!R} \tag{5.76}$$

5.8.2   Discrete panel method for a general wake

For a general wake shape, the force integrals must be evaluated using numerical integration. A relatively simple method is to discretize the wake into $i = 1 \ldots N$ panels as shown in Figure 5.12, with each panel i having a length Δs_i, and a piecewise-constant potential jump $\Delta\varphi_i$. The sideforce and lift integrals (5.64),(5.65) then become sums over all the panels. The convenient panel inclination angle θ_i is also introduced, so that $\Delta y_i = \cos\theta_i \, \Delta s_i$ and $\Delta z_i = \sin\theta_i \, \Delta s_i$.

$$Y \;=\; \sum_{i=1}^{N} -\Delta\varphi_i \, \sin\theta_i \, \Delta s_i \tag{5.77}$$

$$L \;=\; \sum_{i=1}^{N} \Delta\varphi_i \, \cos\theta_i \, \Delta s_i \tag{5.78}$$
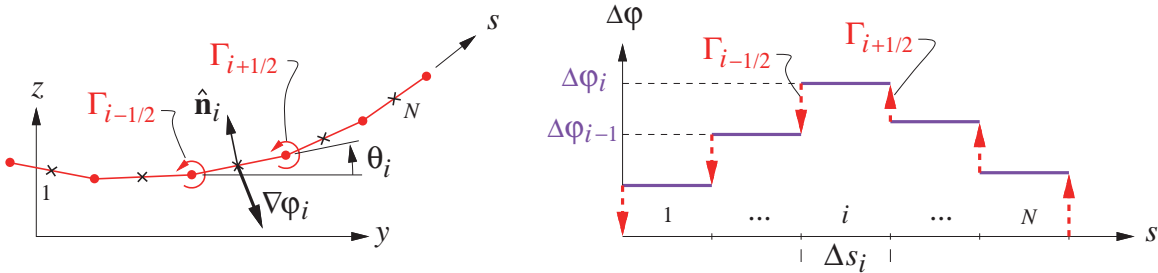
Figure 5.12: Wake paneling for evaluation of Trefftz-plane forces.

To evaluate the induced drag integral (5.47) it is necessary to first determine the normal velocity $\nabla\varphi_i \cdot \hat{\mathbf{n}}_i$ at each panel midpoint. This is the velocity of all the trailing vortices resulting from the discrete steps in the potential jump. Referring to Figure 5.12, each trailing vortex strength is

$$\Gamma_{i-1/2} \;=\; \Delta\varphi_{i-1} - \Delta\varphi_i \tag{5.79}$$

defined positive about the x axis, or counterclockwise in the yz plane. The velocity at each panel midpoint is then the discrete counterpart of the 2D velocity superposition (5.38).

$$\nabla\varphi_i \;=\; \frac{1}{2\pi} \sum_{j=1}^{N+1} \Gamma_{j-1/2} \frac{\hat{\mathbf{x}} \times (\mathbf{r}_i - \mathbf{r}_{j-1/2})}{|\mathbf{r}_i - \mathbf{r}_{j-1/2}|^2} \;=\; \frac{1}{2\pi} \sum_{j=1}^{N+1} \Gamma_{j-1/2} \frac{-(z_i - z_{j-1/2})\hat{\mathbf{y}} + (y_i - y_{j-1/2})\hat{\mathbf{z}}}{(y_i - y_{j-1/2})^2 + (z_i - z_{j-1/2})^2} \tag{5.80}$$

Its normal component can then be condensed into a convenient *Aerodynamic Influence Coefficient* (AIC) matrix A_{ij} which depends only on the wake geometry,

$$\nabla\varphi_i \cdot \hat{\mathbf{n}}_i \;\equiv\; \frac{\partial\varphi}{\partial n_i} \;=\; \sum_{j=1}^{N} A_{ij} \, \Delta\varphi_j \tag{5.81}$$

and allows calculation of $\partial\varphi/\partial n_i$ for any panel $\Delta\varphi_i$ distribution by the simple summation. The induced drag integral (5.47) is then approximated by a second sum over the panels.

$$D_i = -\frac{1}{2}\rho_\infty \sum_{i=1}^{N} \Delta\varphi_i \frac{\partial\varphi}{\partial n_i} \Delta s_i \tag{5.82}$$

5.9 Fuselage wake contraction effect

For a configuration with a fuselage of significant size, such as the one shown in Figure 5.5, the average sheet velocity $\mathbf{V}_a$ can no longer be assumed to be parallel to the freestream, so the wake does not trail straight back from the wing trailing edge. The actual velocities and streamline trajectories can be determined from a panel or slender-body model of the fuselage (see Section 6.6). Nikolski [48] used instead a simple axisymmetric fuselage flow model shown in Figure 5.13, where $\mathbf{V}_a$ is assumed to be parallel to axisymmetric streamtubes. Conservation of mass between the streamtube cross-section at the wing and in the Trefftz Plane gives

$$\dot{m}_{(y)} = \rho_\infty V_\infty \pi \left(y^2 - (d/2)^2\right) = \rho_\infty V_\infty \pi \tilde{y}^2 \tag{5.83}$$

$$y_{(\tilde{y})} = \sqrt{\tilde{y}^2 + (d/2)^2} \tag{5.84}$$

which assumes that the mass flux ρV magnitudes adjacent to the fuselage of maximum diameter d are nearly the same as in the freestream.
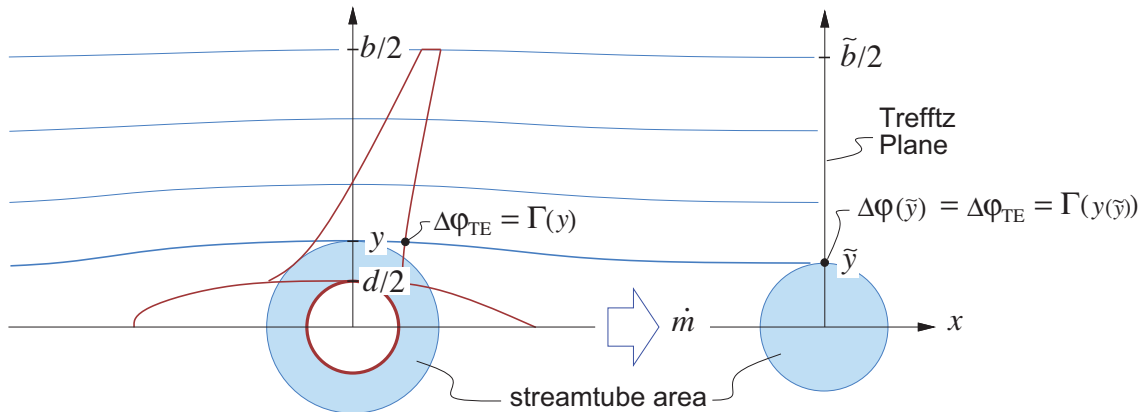
Figure 5.13: Axisymmetric streamtube flow around fuselage determines wake contraction from wing to the Trefftz plane.

Equation (5.84) is the *correspondence function* which specifies the wing location y which is connected to wake location $\tilde{y}$ by an average streamline. For a given wing circulation distribution $\Gamma(y)$, the potential jump in the wake is then given in terms of the correspondence function.

$$\Delta\varphi_{(\tilde{y})} = \Gamma_{(y(\tilde{y}))} \tag{5.85}$$

As an example, consider the case of an elliptical spanwise loading <u>in the wake</u>.

$$\Delta\varphi_{(\tilde{y})} = \Delta\varphi_0 \sqrt{1 - (2\tilde{y}/\tilde{b})^2} = \Delta\varphi_0 \sin\vartheta \tag{5.86}$$

$$\tilde{b}^2 = b^2 - d^2 \tag{5.87}$$

The span $\tilde{b}$ of the wake in the Trefftz plane is given by (5.84) applied at the wing tip and wake tip. The flat-wake Trefftz plane results give the following lift and induced drag.

$$\mathcal{A}_1 = \frac{\Delta\varphi_0}{2\tilde{b}V_\infty} \tag{5.88}$$

$$L = \frac{1}{2}\rho_\infty V_\infty^2 \, \tilde{b}^2 \, \pi \, \mathcal{A}_1 = \frac{\pi}{4}\rho_\infty V_\infty \, \tilde{b} \, \Delta\varphi_0 \tag{5.89}$$

$$D_i = \frac{(L/\tilde{b})^2}{\frac{1}{2}\rho_\infty V_\infty^2 \, \pi} = \frac{(L/b)^2}{\frac{1}{2}\rho_\infty V_\infty^2 \, \pi} \frac{1}{(\tilde{b}/b)^2} \tag{5.90}$$

Comparing (5.90) with (5.71) shows that the wake contraction due to the fuselage gives an effective span efficiency of

$$(\tilde{b}/b)^2 = 1 - (d/b)^2 \tag{5.91}$$

which for example is 0.99 for a fuselage diameter ratio of $d/b = 0.1$.

5.10   Minimum Induced Drag

The minimum induced drag results (5.75),(5.76) from the Fourier series method applied only to a flat wake. This section will consider the more general case of a non-planar wake, and will also consider other constraints being imposed in addition to the lift.

5.10.1   Minimum induced drag problem statement

The minimum induced drag problem for a fixed lift is stated as follows.

Given: ρ_∞ freestream density
V_∞ freestream speed
$\mathbf{r}'(s)$ wake shape
L_{spec} specified lift

Find: $\partial\varphi/\partial n\,(s)$ particular normal velocity which results in the minimum D_i
$\Delta\varphi(s)$ wake potential jump which gives this particular $\partial\varphi/\partial n\,(s)$

The lift and induced drag are given by (5.47) and (5.65), restated here for convenience.

$$L = \rho_\infty V_\infty \int \Delta\varphi \, \cos\theta \, \mathrm{d}s \tag{5.92}$$

$$D_i = -\frac{1}{2}\rho_\infty \int \Delta\varphi \, \frac{\partial\varphi}{\partial n} \, \mathrm{d}s \tag{5.93}$$

The implied integration limits $0 \dots s_{\max}$ over the entire wake will be omitted here for clarity.

The specified-lift constraint in the problem statement above is necessary to rule out the trivial solution $\partial\varphi/\partial n = 0$, $\Delta\varphi = 0$. Other constraints can also be used in addition to the lift. One example is a specified root bending moment, which strongly affects a wing's structural weight and hence may need to be constrained in some applications. For the typical y-symmetric wake shape, this moment about the yz origin is defined as follows.

$$M_0 = \frac{1}{2}\rho_\infty V_\infty \int \Delta\varphi \left| y \cos\theta + z \sin\theta \right| \, \mathrm{d}s \tag{5.94}$$

Only the lift constraint will be assumed first to simplify the initial discussion of the concepts. Adding other constraints will then be considered.

which holds for any two fields f, g which satisfy $\nabla^2 f = 0$ and $\nabla^2 g = 0$. For our case we choose $f = \varphi$ and $g = \delta\varphi$, in which case the identity shows that the two terms in the equation (5.96) integrand are actually equal. Hence, omitting the second term and doubling the first term will not change the result.

$$\delta D_i = -\rho_\infty \int \Delta \, \delta\varphi \, \frac{\partial\varphi}{\partial n} \, \mathrm{d}s \qquad (5.97)$$

If D_i is to be a minimum it's necessary that it be *stationary*, specifically that $\delta D_i = 0$, for any admissible $\Delta \, \delta\varphi_{(s)}$ distribution along the sheet. This is satisfied by a normal velocity distribution which is everywhere proportional to the local $\cos\theta$,

$$\frac{\partial\varphi}{\partial n}_{(s)} = \Lambda \, \cos\theta_{(s)} \qquad (5.98)$$

where Λ is some constant. This solution can be verified by putting it into the δD_i expression (5.97), to give

$$\delta D_i = -\rho_\infty \int \Delta \, \delta\varphi \, \Lambda \, \cos\theta \, \mathrm{d}s = -\frac{\Lambda}{V_\infty} \delta L = 0 \qquad (5.99)$$

as required. The conclusion is that a normal velocity which is given by (5.98) results in the smallest possible induced drag for a given lift and a given wake shape. This result is exactly consistent with the result (5.76) obtained via the Fourier series approach for the flat wake case. The great advantage of (5.98) is that it applies to a wake of any shape.

5.10.3 Optimum potential jump calculation

The above application of Calculus of Variations produced the optimum normal velocity distribution $\partial\varphi/\partial n_{(s)}$. The one remaining step is to determine the corresponding $\Delta\varphi_{(s)}$. A suitable numerical approach is to use the 2D panel method sketched in Figure 5.12. Using the AIC matrix A_{ij} defined by (5.81), condition (5.98) is imposed at each panel control point.

$$\sum_{j=1}^{N} A_{ij} \, \Delta\varphi_j - \Lambda \, \cos\theta_i = 0 \qquad (i = 1\dots N) \qquad (5.100)$$

The constant Λ is one additional unknown in the problem. The appropriate additional equation is the specified-lift constraint, written by using the discrete lift expression (5.78).

$$\rho_\infty V_\infty \sum_{i=1}^{N} \Delta\varphi_i \, \cos\theta_i \, \Delta s_i = L_{\mathrm{spec}} \qquad (5.101)$$

Equations (5.100) and (5.101) together constitute a $(N{+}1)\times(N{+}1)$ linear system for the unknowns $\Delta\varphi_i$, Λ. The corresponding induced drag can then be computed by re-using the AIC matrix A_{ij} to obtain $\partial\varphi/\partial n_i$, and then using this in the discrete induced drag expression (5.82).

5.10.4 Additional constraints

Any number of other constraints can be added in addition to the lift, such as the root bending moment mentioned earlier. An effective general solution technique here is define a Lagrangian function $\mathcal{L}$, which is the objective function plus all the constraints,

$$\mathcal{L}_{(\Delta\varphi_{(s)}, \Lambda_1, \Lambda_2 \dots)} \equiv D_i + \Lambda_1(L - L_{\mathrm{spec}}) + \Lambda_2(M_0 - M_{0\mathrm{spec}}) + \dots \qquad (5.102)$$

where the $\Lambda_{1,2...}$ coefficients are *Lagrange multipliers* associated with the constraints, and are solved as part of the problem. The constant Λ in the previous section was in fact the same as Λ_1 here.

The constrained-optimum solution $\Delta\varphi_{(s)}, \Lambda_1, \Lambda_2$ is defined by the requirement that $\mathcal{L}$ is stationary.

$$\delta\mathcal{L} \equiv \delta D_i + \delta\Lambda_1 \left(L - L_{\text{spec}}\right) + \delta\Lambda_2 \left(M_0 - M_{0\text{spec}}\right) + \Lambda_1 \delta L + \Lambda_2 \delta M_0 = 0 \quad (5.103)$$

Substituting for $\delta D_i, \delta L, \delta M_0, L, M_0$, and collecting terms having the same $\Delta\,\delta\varphi, \delta\Lambda_1, \delta\Lambda_2$ factors gives

$$\rho_\infty \int \Delta\,\delta\varphi \left[-\frac{\partial\varphi}{\partial n} + \Lambda_1 V_\infty \cos\theta + \Lambda_2 \frac{1}{2} V_\infty \left| y\cos\theta + z\sin\theta \right| \right] \mathrm{d}s$$

$$+ \delta\Lambda_1 \left[\rho_\infty V_\infty \int \Delta\varphi \, \cos\theta \, \mathrm{d}s - L_{\text{spec}} \right]$$

$$+ \delta\Lambda_2 \left[\frac{1}{2}\rho_\infty V_\infty \int \Delta\varphi \left| y\cos\theta + z\sin\theta \right| \mathrm{d}s - M_{0\text{spec}} \right] = 0 \quad (5.104)$$

which for optimality must be zero for <u>any</u> $\Delta\,\delta\varphi_{(s)}, \delta\Lambda_1, \delta\Lambda_2$. This requirement is met by setting all the quantities in the brackets to zero, using the wake panel method to discretize the integrals. Since the first bracket is inside the integral (and inside the equivalent discrete sum), it must be set to zero at each of the N discrete panel points. In contrast, the second and third brackets set to zero are single equations. The result is the following $(N+2) \times (N+2)$ linear system for $\Delta\varphi_i, \Lambda_1, \Lambda_2$.

$$\sum_{j=1}^{N} A_{ij}\,\Delta\varphi_j - \Lambda_1 V_\infty \cos\theta_i - \Lambda_2 \frac{1}{2}V_\infty \left| y_i\cos\theta_i + z_i\sin\theta_i \right| = 0 \qquad (i = 1\ldots N) \quad (5.105)$$

$$\rho_\infty V_\infty \sum_{i=1}^{N} \Delta\varphi_i \, \cos\theta_i \, \Delta s_i = L_{\text{spec}} \quad (5.106)$$

$$\frac{1}{2}\rho_\infty V_\infty \sum_{i=1}^{N} \Delta\varphi_i \left| y_i\cos\theta_i + z_i\sin\theta_i \right| \Delta s_i = M_{0\text{spec}} \quad (5.107)$$

After solution, the AIC matrix A_{ij} is re-used to obtain $\partial\varphi/\partial n_i$ via (5.81), and the induced drag D_i can then be computed from (5.82).

5.10.5 Example optimum load distributions

Planar wake

As shown in Section 5.8.1, the elliptical load distribution is optimum for the case of a planar wake with a fixed span. However, in many aircraft applications a more relevant constraint is not on the span but on the root bending moment, since this dominates the wing's structural weight which offsets induced drag reductions.

To illustrate this tradeoff, Figure 5.16 shows three load distributions for three different specified spans, each having the same lift and root bending moment. Increasing the span reduces D_i significantly, even though the resulting load distributions are very "sub-optimal" in a fixed-span sense. Referring to the Fourier D_i expression (5.71), the increase in the span b more than overcomes the increased parameter δ which measures how much the loading deviates from elliptical.

Figure 5.17 shows the relative D_i for a continuous range of spans for the flat-wing case with constrained bending moment. With no bending moment constraint, the optimum loading is elliptical for any span, and the induced drag then scales simply as $D_i \sim 1/b^2$, indicated by the thin line in Figure 5.17.
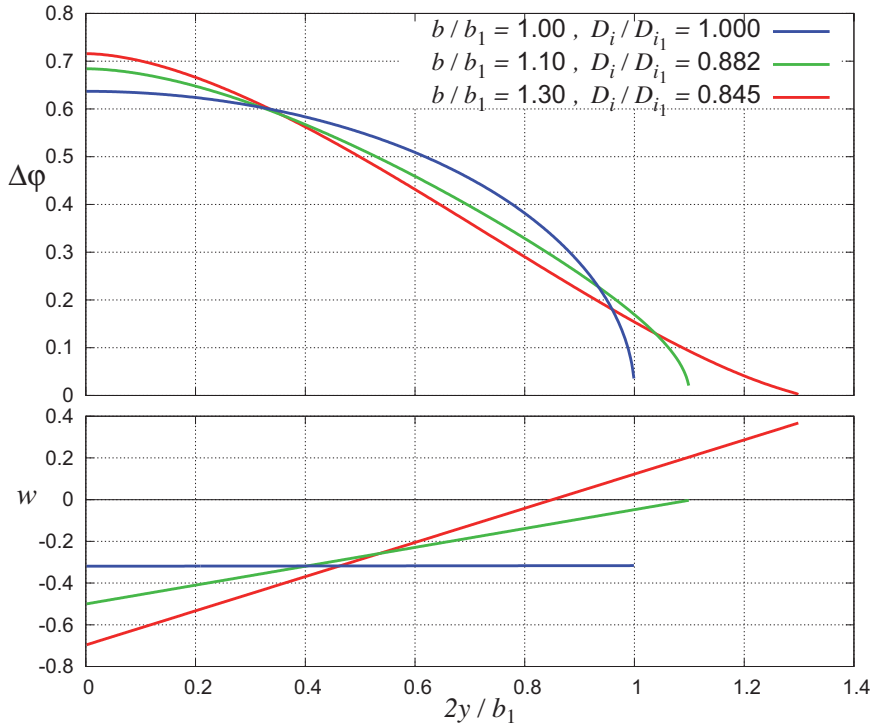
Figure 5.16: Optimum $\Delta\varphi(y)$ load distributions and corresponding $w(y)$ normal velocity distributions for three specified spans, all with the same specified lift and root bending moment. The baseline elliptic-loading case has span b_1 and induced drag D_{i_1}.
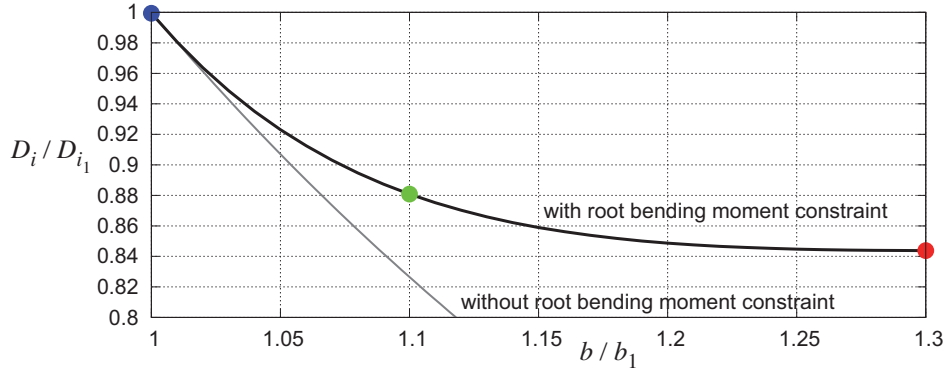

Figure 5.17: Induced drag versus span, with fixed lift and root bending moment, relative to baseline case. The three symbols correspond to the three cases in Figure 5.16. Thin line is the result $D_i/D_{i_1} = (b/b_1)^{-2}$ for elliptical loading for all spans, which is optimal in the absence of a bending moment constraint.

Non-planar wake

Another interesting case is a non-planar wake, such as that produced by a wing with winglets, which were originally developed by Whitcomb [49]. A winglet acts much like a span extension in that both spread out the shed vorticity, which reduces the velocities and kinetic energy in the Trefftz plane, and thus reduce D_i. A span increase does this more effectively than a winglet, but on the other hand a winglet produces a smaller increase in the root bending moment.

Figures 5.18 and 5.19 show two possible ways to parameterize the geometry of the wing+winglet combination, and the resulting D_i relative to the no-winglet case value D_{i_1}. Results both without and with the root bending moment constraint are shown. The bending moment constraint is seen to put a floor on the

D_i/D_{i_1} ratio at about 0.84, which is comparable to the minimum value of the best flat-wing case shown in Figures 5.16 and 5.17. The only apparent advantage of the winglet is that much of this benefit can be obtained with a smaller overall span. The conclusion is that winglets are effective mainly in cases where the overall span is limited by other than structural constraints. The relative merits of winglets and various other types of non-planar lifting surface systems is discussed by Kroo [47].
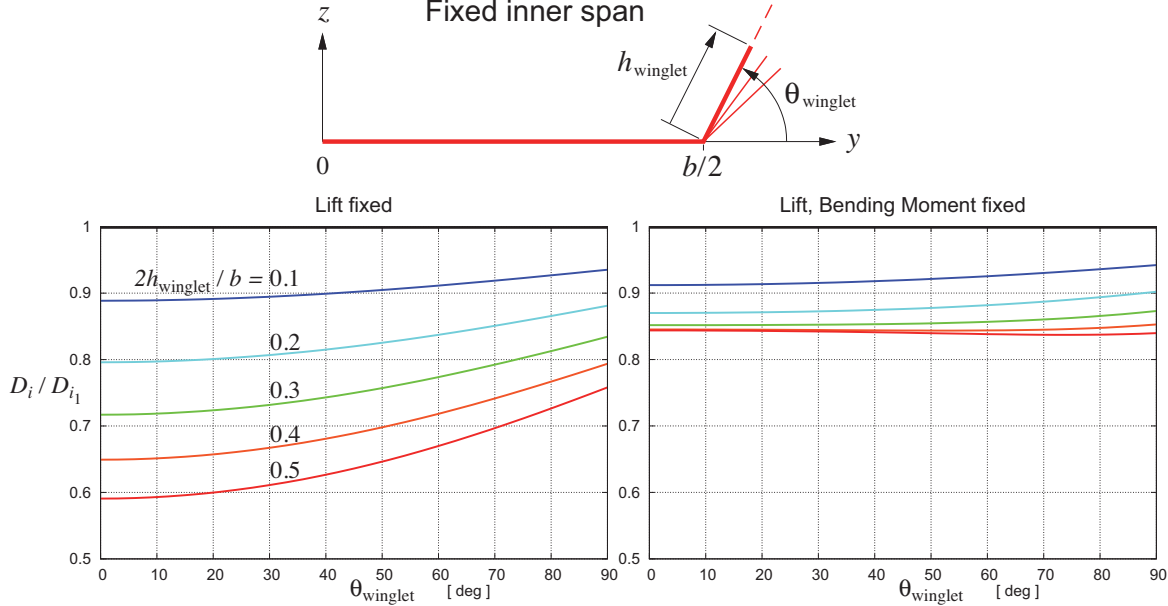
Figure 5.18: Induced drag of wing + winglet with fixed inner span, versus winglet height and angle above horizontal. Lift is the same for all cases. Plot on right in addition has a fixed root bending moment. The no-winglet case with elliptical loading provides the reference value D_{i_1}, and also the fixed lift and bending moment values.
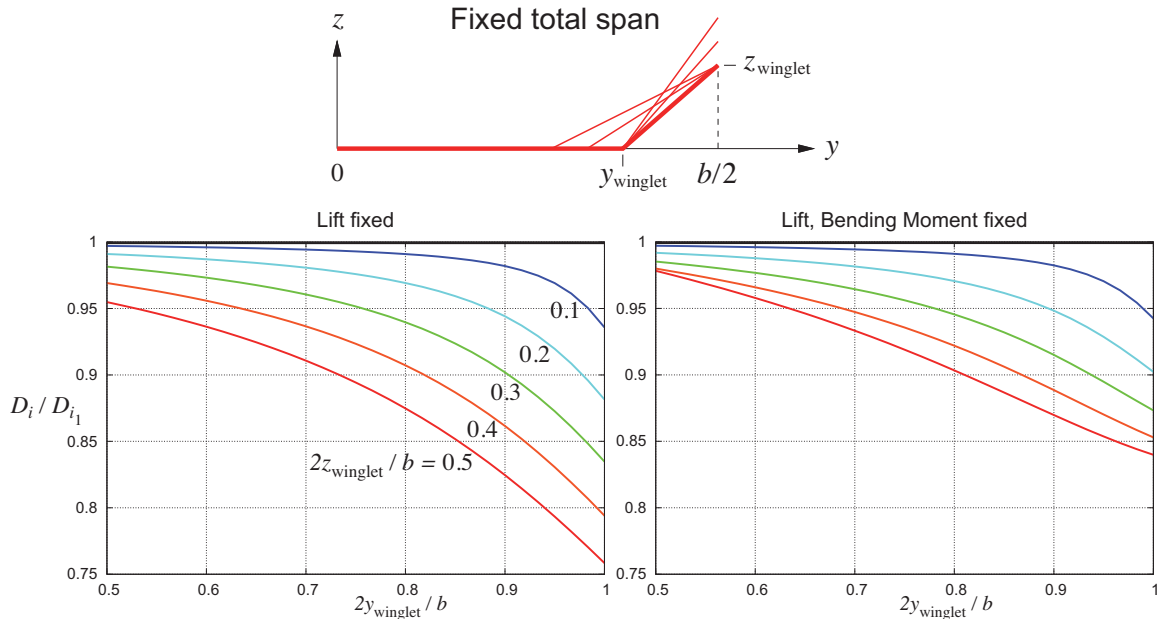
Figure 5.19: Induced drag of wing + winglet with fixed total span, versus winglet z and y endpoints. Lift is the same for all cases. Plot on the right in addition has a fixed root bending moment.

Chapter 6

Aerodynamics of Aircraft in Maneuver

This chapter will examine the aerodynamics of thin wings of arbitrary planform and of slender bodies in arbitrary translation and rotation. Quasi-steady flow will be assumed.

6.1 Aircraft Motion Definition

Chapter 9 will derive in detail the Earth and body axis systems used for describing aircraft motion. Here, a few of those key relations will be simply stated without derivation. Unless otherwise indicated, all vector components will be assumed to be in the *geometry axes* shown in Figure 6.1, which have x and z reversed from the body axes given in Chapter 9. The other axis systems will be discussed where appropriate.

6.1.1 Aircraft velocity and rotation

The aircraft motion is defined by the velocity $\mathbf{U}$ of its axis-origin point, and by its rotation rate $\mathbf{\Omega}$. Both are shown in Figure 6.1. These are defined relative to the Earth frame, and hence they are also the velocity and rotation rate of the aircraft relative to a still airmass.

Angles of Attack and Sideslip   **Aircraft Velocity and Rotation Rate**
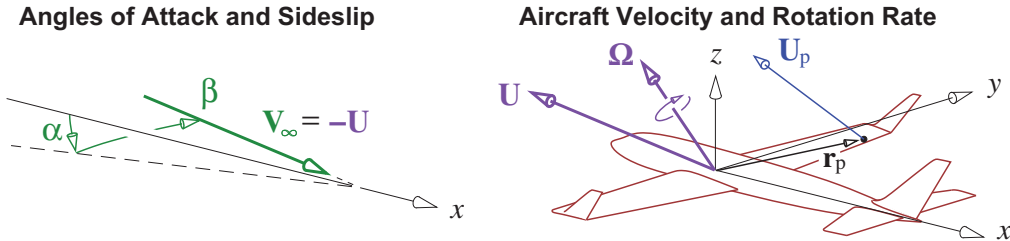
Figure 6.1: Aircraft velocity and rotation rate $\mathbf{U}, \mathbf{\Omega}$, and resulting velocity $\mathbf{U}_\mathrm{p}$ of body point $\mathbf{r}_\mathrm{p}$. Normalized velocity $\mathbf{U}/V_\infty$ is specified by the angles of attack and sideslip α, β. For computation, all vectors are specified via their components along the aircraft's xyz geometry axes.

The aerodynamic "freestream" velocity $\mathbf{V}_\infty$ is directly opposite to $\mathbf{U}$, and is conventionally specified by the two aerodynamic flow angles α and β, applied in that order as shown in Figure 6.1.

$$\mathbf{U} = \begin{Bmatrix} U_x \\ U_y \\ U_z \end{Bmatrix} = -\mathbf{V}_\infty = V_\infty \begin{Bmatrix} -\cos\alpha\,\cos\beta \\ \sin\beta \\ -\sin\alpha\,\cos\beta \end{Bmatrix} \tag{6.1}$$

$$V_\infty = \sqrt{U_x^2 + U_y^2 + U_z^2} \quad , \qquad \alpha = \arctan\frac{-U_z}{-U_x} \quad , \qquad \beta = \arctan\frac{U_y}{\sqrt{U_x^2 + U_z^2}} \tag{6.2}$$

Given these reciprocal relations, $\{V_\infty, \alpha, \beta\}$ and $\{U_x, U_y, U_z\}$ are equivalent alternative parameter sets. In practice, α, β are chosen as the independent parameters. These define the three components of the normalized aircraft velocity $\mathbf{U}/V_\infty$ via (6.1), which are needed to compute the aerodynamic forces and moments.

6.1.2 Body-point velocity

The Earth-frame velocity of any point $\mathbf{r}_\mathrm{p}$ fixed on the body is given by

$$\mathbf{U}_\mathrm{p} \;=\; \mathbf{U} + \boldsymbol{\Omega}{\times}\mathbf{r}_\mathrm{p} \tag{6.3}$$

as shown in Figure 6.1. If the airmass is still (without wind or gusts), then the apparent airmass velocity seen by this point is $-\mathbf{U}_\mathrm{p}$, which is in effect a "local freestream." This will be used to formulate flow-tangency boundary conditions in computational methods.

6.2 Axis Systems

In computational methods, the aircraft motion vectors $\mathbf{U}, \boldsymbol{\Omega}$, and the aerodynamic force and moment vectors $\mathbf{F}, \mathbf{M}$ are most easily specified or calculated in the same xyz axes which are used to specify the geometry itself, shown in Figure 6.1. To apply the results to aircraft performance, stability and control, and other related disciplines it is necessary to provide these vector quantities in other more relevant axes.

6.2.1 Stability axes

The drag, sideforce, and lift force components are most commonly defined in the *stability axes*, which are rotated from the geometry axes by only the angle of attack α (not by sideslip β), as shown in Figure 6.2.
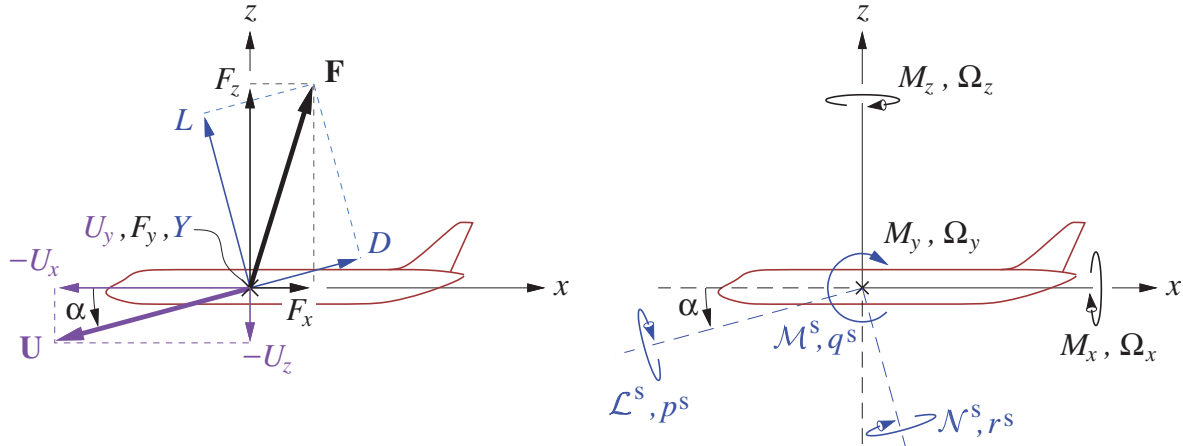
Figure 6.2: Orientation of stability-axis (freestream-aligned) aerodynamic force components $D, Y, L,$ moment components $\mathcal{L}^\mathrm{s}, \mathcal{M}^\mathrm{s}, \mathcal{N}^\mathrm{s},$ and rotation rate components $p^\mathrm{s}, q^\mathrm{s}, r^\mathrm{s}$.

All the standard vector components in stability axes are defined from their components in geometry axes using the $\bar{\bar{\mathbf{T}}}^\mathrm{s}$ rotation matrix.

$$\bar{\bar{\mathbf{T}}}^\mathrm{s} \;=\; \begin{bmatrix} \cos\alpha & 0 & \sin\alpha \\ 0 & 1 & 0 \\ -\sin\alpha & 0 & \cos\alpha \end{bmatrix} \tag{6.4}$$

$$\begin{Bmatrix} D \\ Y \\ L \end{Bmatrix} = \begin{bmatrix} \bar{\bar{\mathbf{T}}}^\mathrm{s} \end{bmatrix} \begin{Bmatrix} F_x \\ F_y \\ F_z \end{Bmatrix} \;,\quad \begin{Bmatrix} \mathcal{L}^\mathrm{s} \\ \mathcal{M}^\mathrm{s} \\ \mathcal{N}^\mathrm{s} \end{Bmatrix} = \begin{bmatrix} \bar{\bar{\mathbf{T}}}^\mathrm{s} \end{bmatrix} \begin{Bmatrix} -M_x \\ M_y \\ -M_z \end{Bmatrix} \;,\quad \begin{Bmatrix} p^\mathrm{s} \\ q^\mathrm{s} \\ r^\mathrm{s} \end{Bmatrix} = \begin{bmatrix} \bar{\bar{\mathbf{T}}}^\mathrm{s} \end{bmatrix} \begin{Bmatrix} -\Omega_x \\ \Omega_y \\ -\Omega_z \end{Bmatrix} \tag{6.5}$$

Note that the moment and rotation-rate components, $\mathcal{L}^\mathrm{s}, \mathcal{N}^\mathrm{s}$ and $p^\mathrm{s}, r^\mathrm{s}$, have reverse signs compared to the force components D, L. In effect, the stability axes used for the moments and rates are rotated by $180°$ about the y axis relative to the stability axes used for the forces. Note also that the $\bar{\bar{\mathbf{T}}}^\mathrm{s}$ matrix leaves all the vector y components unchanged. Hence we have $Y = F_y$, $\mathcal{M}^\mathrm{s} = M_y$, $q^\mathrm{s} = \Omega_y$.

6.2.2 Wind axes

The stability axes are not quite appropriate when examining the drag of an aircraft in sideslipping flight with $\beta \neq 0$, since the drag D as defined by the $\bar{\bar{\mathbf{T}}}^{\mathrm{s}}$ matrix in (6.5) is <u>not</u> the true streamwise drag force. In this situation we can invoke the *wind axes*, which are implemented by the rotation matrix $\bar{\bar{\mathbf{T}}}^{\mathrm{w}}$, which consists of α and β rotations, applied in that order as shown in Figure 6.1.

$$\begin{Bmatrix} D \\ Y \\ L \end{Bmatrix} = \begin{bmatrix} & \bar{\bar{\mathbf{T}}}^{\mathrm{w}} & \end{bmatrix} \begin{Bmatrix} F_x \\ F_y \\ F_z \end{Bmatrix} \tag{6.6}$$

$$\bar{\bar{\mathbf{T}}}^{\mathrm{w}} = \begin{bmatrix} \cos\beta & -\sin\beta & 0 \\ \sin\beta & \cos\beta & 0 \\ 0 & 0 & 1 \end{bmatrix} \begin{bmatrix} \cos\alpha & 0 & \sin\alpha \\ 0 & 1 & 0 \\ -\sin\alpha & 0 & \cos\alpha \end{bmatrix} = \begin{bmatrix} \cos\beta\cos\alpha & -\sin\beta & \cos\beta\sin\alpha \\ \sin\beta\cos\alpha & \cos\beta & \sin\beta\sin\alpha \\ -\sin\alpha & 0 & \cos\alpha \end{bmatrix} \tag{6.7}$$

Note that the drag as defined by the $\bar{\bar{\mathbf{T}}}^{\mathrm{w}}$ matrix in (6.6) is exactly equivalent to the dot product of the total force and the unit freestream.

$$D = \mathbf{F} \cdot \mathbf{V}_\infty / V_\infty \tag{6.8}$$

Furthermore, the sideforce Y produced by $\bar{\bar{\mathbf{T}}}^{\mathrm{w}}$ in (6.6) is almost the same as that produced by $\bar{\bar{\mathbf{T}}}^{\mathrm{s}}$ in (6.5), and the lift L is identical. Because the simple relation (6.8) is available to define the exact D when needed, and the exact Y is of relatively little importance, wind axes see little use in practice.

6.3 Non-Dimensionalization and Parameterization

6.3.1 Dimensionless variables

Aerodynamic characteristics are almost invariably defined, described, or provided in terms of the following dimensionless force coefficients, moment coefficients, and rotation rates. The latter two are commonly used in either the body or the stability axes.

$$\begin{aligned} C_D &= \frac{D}{q_\infty S_{\mathrm{ref}}} & C_\ell &= \frac{\mathcal{L}}{q_\infty S_{\mathrm{ref}} b_{\mathrm{ref}}} & \bar{p} &= \frac{p\, b_{\mathrm{ref}}}{2V_\infty} \\ C_Y &= \frac{Y}{q_\infty S_{\mathrm{ref}}} & C_m &= \frac{\mathcal{M}}{q_\infty S_{\mathrm{ref}} c_{\mathrm{ref}}} & \bar{q} &= \frac{q\, c_{\mathrm{ref}}}{2V_\infty} \\ C_L &= \frac{L}{q_\infty S_{\mathrm{ref}}} & C_n &= \frac{\mathcal{N}}{q_\infty S_{\mathrm{ref}} b_{\mathrm{ref}}} & \bar{r} &= \frac{r\, b_{\mathrm{ref}}}{2V_\infty} \end{aligned} \tag{6.9}$$

All the reference quantities are arbitrary. The traditional choice for the reference area S_{ref} is the projected wing area S. This typically includes any hidden "carry-through" wing area inside a fuselage, but may exclude root fairings or fillets. The choice for b_{ref} is the actual projected wingspan, which may or may not include tip devices such as winglets. The traditional choice for c_{ref} is the wing's *mean aerodynamic chord*,

$$c_{\mathrm{ref}} = c_{\mathrm{mac}} \equiv \frac{1}{S} \int_{-b/2}^{b/2} c_{(y)}^2 \, \mathrm{d}y \tag{6.10}$$

which is in effect a root-mean-square chord. Workable alternatives are the average chord $c_{\mathrm{ref}} = S/b$, or simply the root chord $c_{\mathrm{ref}} = c_{(0)}$.

Theoretically, additional important parameters are the dimensionless flow-angle rates.

$$\bar{\alpha} = \frac{\dot{\alpha} c_{\mathrm{ref}}}{2V_\infty} \qquad\qquad \bar{\beta} = \frac{\dot{\beta} b_{\mathrm{ref}}}{2V_\infty} \tag{6.11}$$

This $\bar{\alpha}$ quantifies the strength and influence of the wing's *shed vorticity*, which is present in unsteady airfoil flows and is discussed in more detail in Section 7.4.2. In brief, $\bar{\alpha}$ determines the time delay in the wing's downwash seen by the horizontal tail, and therefore during pitching maneuvers it influences the time evolution of the overall C_m, and to a lesser extent of the C_L also. In most aircraft $\bar{\bar{\beta}}$ has relatively little influence and is usually ignored, although it may be significant for unusual aircraft configurations.

6.3.2 Quasi-steady force and moment parameterization

Dimensional analysis indicates that all the force and moment coefficients have the following parametric dependence for steady flows. The same dependencies also approximately hold for quasi-steady flows such as an aircraft in slow maneuver.

$$C_D = C_D(\alpha, \beta, \bar{p}, \bar{q}, \bar{r}, \bar{\alpha}, \bar{\bar{\beta}}, \delta_T, \delta_a, \delta_e, \delta_r, M_\infty, Re_\infty)$$
$$C_Y = C_Y(\alpha, \beta, \bar{p}, \bar{q}, \bar{r}, \bar{\alpha}, \bar{\bar{\beta}}, \delta_T, \delta_a, \delta_e, \delta_r, M_\infty, Re_\infty)$$
$$\vdots$$
$$C_n = C_n(\alpha, \beta, \bar{p}, \bar{q}, \bar{r}, \bar{\alpha}, \bar{\bar{\beta}}, \delta_T, \delta_a, \delta_e, \delta_r, M_\infty, Re_\infty)$$

The parameters $\delta_T, \delta_a, \delta_e, \delta_r$ are throttle, aileron, elevator, rudder *control parameters* (there may be more). These represent thrust settings or control-surface deflection angles, which influence the overall force and moment on the aircraft.

Figure 6.3 shows typical flows over the entire possible α, β range, most of which involve large-scale separation and flow reversal. The result is that the force and moment coefficients have complicated dependencies on the operating parameters, as indicated in the sample $C_L(\alpha)$ and $C_n(\beta)$ line plots in Figure 6.3.
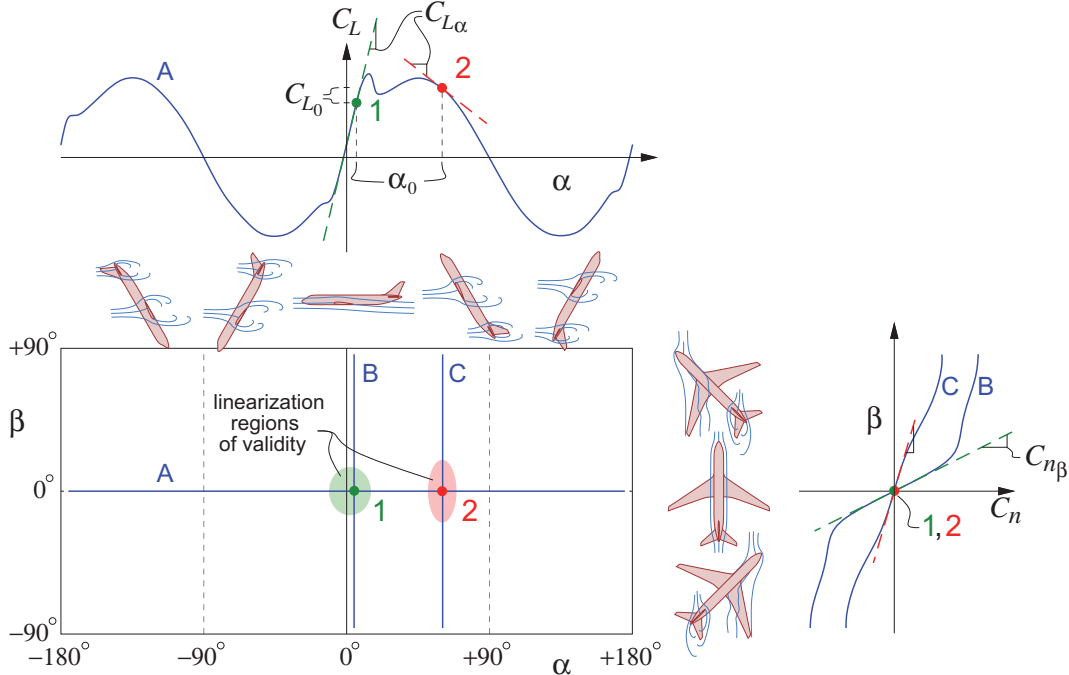
Figure 6.3: Aircraft α, β flow parameter space (remaining parameters $\bar{p}, \bar{q}, \bar{r}\ldots$ not shown). $C_L(\alpha)$ variation is shown for parameter slice A, and $C_n(\beta)$ variation is shown for slices B, C. The linearized force or moment representations, indicated by dashed lines, are valid in a sufficiently small region near the chosen baseline operating point. Two baseline points 1, 2 at two different α_0 values are indicated, with the stability derivative $C_{L\alpha}$ changing dramatically between the two points.

The overall parameter space is enormously larger than the two-axis slice shown in Figure 6.3, since there are additional axes for $\bar{p}, \bar{q}, \bar{r}, \dot{\bar{\alpha}}, \dot{\bar{\beta}}, \delta_T \ldots, M_\infty, Re_\infty$. For many applications, such as mission performance estimates, stability and control analysis and design, etc., the force and moment coefficients only need to be defined within a small region of the parameter space, described by small deviations about some *operating point* or *trim state*, denoted by the $()_0$ subscript. Here the force and moment coefficient functions can be approximated by their <u>linearized</u> forms, or equivalently their first-order Taylor series approximations.

$$C_L \simeq C_{L_0} + C_{L_\alpha}\,\Delta\alpha + C_{L_q}\,\Delta\bar{q} + C_{L_{\dot{\alpha}}}\,\Delta\dot{\bar{\alpha}} + C_{L_{\delta_e}}\,\Delta\delta_e \tag{6.12}$$

$$C_n \simeq C_{n_0} + C_{n_\beta}\,\Delta\beta + C_{n_p}\,\Delta\bar{p} + C_{n_r}\,\Delta\bar{r} + C_{n_{\delta_r}}\,\Delta\delta_r \tag{6.13}$$

$$\vdots$$

where

$$
\begin{array}{llll}
C_{L_0} = C_L{}_{(\alpha_0,\beta_0,\ldots)} & C_{L_\alpha} = \partial C_L/\partial\alpha\,{}_{(\alpha_0,\beta_0,\ldots)} & C_{L_q} = \partial C_L/\partial\bar{q}\,{}_{(\alpha_0,\beta_0,\ldots)} & \cdots \\
C_{n_0} = C_n{}_{(\alpha_0,\beta_0,\ldots)} & C_{n_\beta} = \partial C_n/\partial\beta\,{}_{(\alpha_0,\beta_0,\ldots)} & C_{n_p} = \partial C_n/\partial\bar{p}\,{}_{(\alpha_0,\beta_0,\ldots)} & \cdots \\
\vdots & \vdots & \vdots &
\end{array}
\tag{6.14}
$$

The series variables are the aerodynamic parameter perturbations from the trim state.

$$\Delta\alpha = \alpha - \alpha_0 \qquad \Delta\beta = \beta - \beta_0 \qquad \Delta\bar{p} = \bar{p} - \bar{p}_0 \qquad \ldots \tag{6.15}$$

The series coefficients $C_{L_\alpha}, C_{L_q} \ldots$ are *stability derivatives*, and $C_{L_{\delta_e}}, C_{n_{\delta_r}} \ldots$ are *control derivatives*. These play a crucial role in aircraft flight dynamics and stability and control, as outlined in Chapter 9. Note that these coefficients can substantially depend on the baseline trim state values, and some may have their signs reversed between different trim states, as for example C_{L_α} shown in Figure 6.3.

6.4 Lifting Surface Theory

Lifting surface theory is an extension of thin airfoil theory to 3D. It models the flow about the wings and tails of a general 3D aircraft configuration using vortex sheets $\boldsymbol{\gamma}_{(s,\ell)}$, or the equivalent normal-doublet sheets $\mu_{(s,\ell)}$. The objective is to represent the lift, sideforce, moments, and induced drag of the configuration using only the camber surface shapes, with the volume effects of the various components being ignored.

6.4.1 Vortex/doublet sheet geometry

The assumed geometry of the vortex or doublet sheets is shown in Figure 6.4. The sheets are assumed to be everywhere parallel to the x axis, with the camber-surface shapes of the actual geometry represented only by their normal vector distribution $\hat{\mathbf{n}}_{(s,\ell)}$. The sheet strengths $\boldsymbol{\gamma}_{(s,\ell)}$ or $\mu_{(s,\ell)}$ are unknown only over the extent of the actual surface. On the trailing wake portions of the sheets, the strengths are constant in x, and equal to their trailing-edge values.

$$
\begin{array}{rlll}
& \gamma_{(s)} &=\ \boldsymbol{\gamma}_{(s,\ell_{TE})}\cdot\hat{\mathbf{x}} & \text{(on wake)} \\
\text{or} & \mu_{(s)} &=\ \mu_{(s,\ell_{TE})} & \text{(on wake)}
\end{array}
\tag{6.16}
$$

These are also the sheet strengths in the Trefftz plane, as shown in Figure 6.4.

6.4.2 Lifting-surface problem formulation

The perturbation velocity field of the vortex sheet distribution is given by the superposition integral (2.16),

$$\mathbf{V}_\gamma(\mathbf{r}) = \frac{1}{4\pi}\iint \boldsymbol{\gamma}_{(s,\ell)}\times\frac{\mathbf{r}-\mathbf{r}'}{|\mathbf{r}-\mathbf{r}'|^3}\,\mathrm{d}s\,\mathrm{d}\ell \tag{6.17}$$
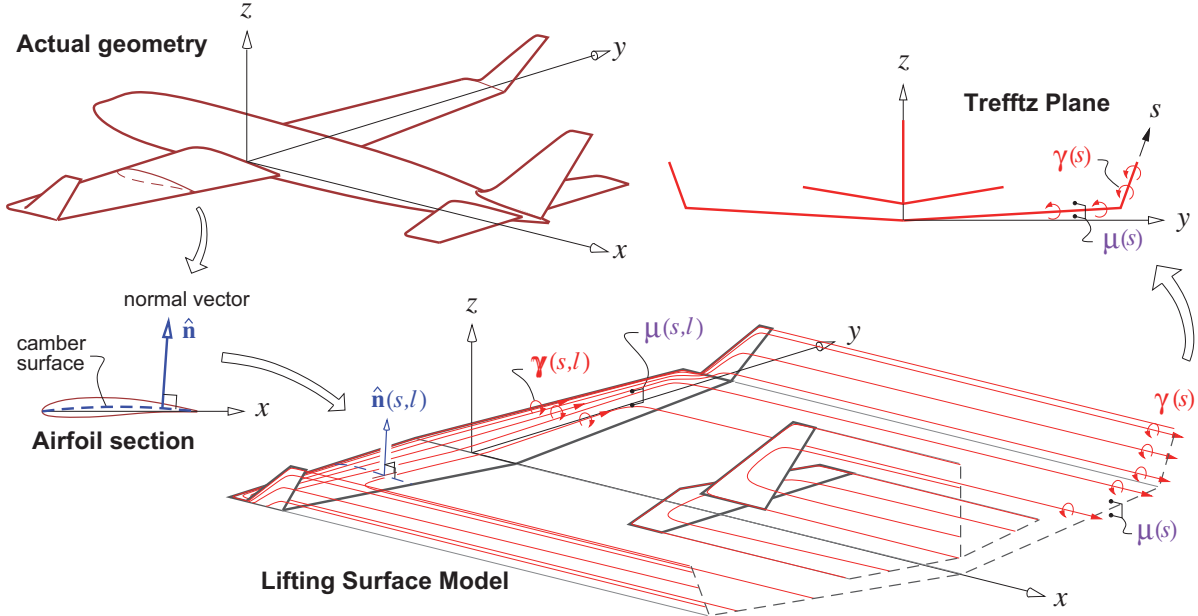
Figure 6.4: 3D configuration represented using a lifting-surface model. The model consists of vortex sheets with strength $\boldsymbol{\gamma}(s,\ell)$ on the surfaces, and $\gamma(s)\,\hat{\mathbf{x}}$ on the trailing wakes and in the Trefftz plane.

where $\mathbf{r}'(s,\ell)$ is the assumed vortex sheet geometry. The integral is over both the surface and wake vortex sheets. With an airmass which is still in the Earth frame, the total fluid velocity observed by a point $\mathbf{r}$ fixed in the body frame is then obtained by subtracting that point's velocity $\mathbf{U}_{\mathrm{p}}$ as given by (6.3).

$$\mathbf{V}(\mathbf{r}) \;=\; \mathbf{V}_\gamma \;-\; (\mathbf{U} + \boldsymbol{\Omega} \times \mathbf{r}) \tag{6.18}$$

The flow-tangency boundary condition is then

$$\mathbf{V}(\mathbf{r}) \cdot \hat{\mathbf{n}} \;=\; \Big[\, \mathbf{V}_\gamma - (\mathbf{U} + \boldsymbol{\Omega} \times \mathbf{r}) \Big] \cdot \hat{\mathbf{n}} \;=\; 0 \tag{6.19}$$

for each $\mathbf{r}(s,\ell)$ surface point. The Kutta condition

$$\boldsymbol{\gamma}(s,\ell_{TE}) \times \hat{\mathbf{x}} \;=\; \mathbf{0} \tag{6.20}$$

is also applied all along the trailing edge of each surface. Equations (6.17), (6.19), (6.20) together constitute an integral-equation problem for the unknown $\boldsymbol{\gamma}(s,\ell)$ distribution. If instead $\mu(s,\ell)$ is chosen as the unknown variable, then $\boldsymbol{\gamma} = \hat{\mathbf{n}} \times \widetilde{\nabla}\mu$ would be substituted into all the above expressions. This lifting-surface problem can be solved by the Vortex Lattice Method, described later in Section 6.5.

6.4.3   Near-field loads

Once the surface vortex sheet strength $\boldsymbol{\gamma}(s,\ell)$ distribution is known from the solution of the lifting-surface problem as described above, the resulting pressure jump or equivalently the loading can be determined using the Bernoulli equation as follows.

$$\Delta p \;\equiv\; p_l \;-\; p_u \;=\; \tfrac{1}{2}\rho\,\Delta(\mathbf{V}\!\cdot\!\mathbf{V}) \;=\; \rho\,\mathbf{V}_a \cdot \Delta\mathbf{V} \tag{6.21}$$

$$\Delta\mathbf{V} \;\equiv\; \mathbf{V}_u - \mathbf{V}_l \;=\; \boldsymbol{\gamma} \times \hat{\mathbf{n}}$$
$$\mathbf{V}_a \;\equiv\; \tfrac{1}{2}(\mathbf{V}_u + \mathbf{V}_l) \;=\; (\mathbf{V}_\gamma)_a - (\mathbf{U} + \boldsymbol{\Omega} \times \mathbf{r})$$

The $()_u$ and $()_l$ subscripts denote the upper and lower sides of the surface, as also used in Section 5.4 for a wake. Here $(\mathbf{V}_\gamma)_a$ is the velocity of the entire vortex sheet configuration, averaged between two field points on the two sides of the sheet. An equivalent version of the loading expression (6.21) is

$$\Delta p\,\hat{\mathbf{n}} \;=\; \rho\,\mathbf{V}_a\times\boldsymbol{\gamma} \tag{6.22}$$

which in effect is a local Kutta-Joukowsky relation.

The lifting surface approximation largely neglects the details of the flow in the leading edge region, which consequently requires a special treatment in the force calculations. Figure 6.5 shows the actual $(p_\infty - p)\,\hat{\mathbf{n}}$ surface load vectors on 2D inviscid airfoils of different thicknesses. The strongly negative pressure distribution acting on the small leading radius is known as *leading edge suction*, and is the mechanism by which the pressure drag of the aft-pointing pressure forces over the rest of the airfoil are canceled. In 2D the cancellation is theoretically perfect, while in 3D the cancellation is partial but still very significant. This problem of properly capturing pressure drag was raised previously in the near-field force analysis in Section 5.1.2.
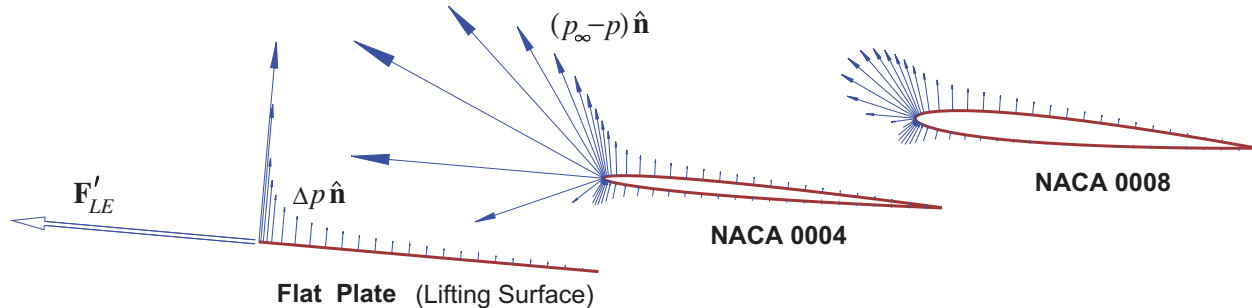
Figure 6.5: Surface pressure vectors on inviscid NACA 0008 and NACA 0004 airfoils at $\alpha = 5°$ computed with a panel method. In the zero thickness limit the leading edge suction becomes a tangential force $\mathbf{F}'_{S_{LE}}$, and the remaining pressure loads are represented by the $\Delta p\,\hat{\mathbf{n}}$ distribution.

The leading edge suction force can be determined by applying the integral momentum theorem to a control volume enclosing the leading edge point, and assuming that the local vortex sheet strength varies as

$$\gamma(x) \;\simeq\; \frac{C}{\sqrt{x}}$$

where x is the distance from the leading edge and C is some constant. The resulting suction force per leading edge arc length is

$$\begin{aligned}
\mathbf{F}'_{S_{LE}} &= \frac{\pi}{4}\,\rho C^2\,\hat{\mathbf{t}} \\
C &= \lim_{x\to 0}\left(\gamma\sqrt{x}\right)
\end{aligned} \tag{6.23}$$

where C is now determined from the actual sheet strength $\gamma(s,\ell)$ of the solution, and $\hat{\mathbf{t}}$ is the unit tangential vector pointing ahead of the leading edge, and normal to both $\hat{\mathbf{n}}$ and the leading edge line.

The overall force and moment on the configuration from the normal forces are finally obtained by integration of the pressure loading distribution and also the leading edge suction forces over all the surfaces.

$$\mathbf{F} \;=\; \sum_{\text{surfaces}} \iint_{\text{surface}} \Delta p\,\hat{\mathbf{n}}\,\mathrm{d}s\,\mathrm{d}\ell \;+\; \int_{\text{L.E.}} \mathbf{F}'_{S_{LE}}\,\mathrm{d}s \tag{6.24}$$

$$\mathbf{M} \;=\; \sum_{\text{surfaces}} \iint_{\text{surface}} \Delta p\,\mathbf{r}\times\hat{\mathbf{n}}\,\mathrm{d}s\,\mathrm{d}\ell \;+\; \int_{\text{L.E.}} \mathbf{r}\times\mathbf{F}'_{S_{LE}}\,\mathrm{d}s \tag{6.25}$$

The integration over the wakes is not performed. The rationale is that a real wake must have $\Delta p = 0$ anyway, even if this isn't quite true in the simplified lifting-surface model in which the wake γ is assumed to be aligned with $\hat{\mathbf{x}}$. To get a truly force-free wake in the model would require aligning the wake geometry and its strength γ with the local $\mathbf{V}_a$ direction. This would make the lifting surface problem nonlinear, since the geometry of the vortex sheets would then depend on the flow solution itself. All these complications are sidestepped by assuming the fixed $\hat{\mathbf{x}}$ wake direction and simply ignoring the resulting implied wake loads.

6.4.4   Trefftz-plane loads

An alternative to the above near-field force calculation is to use the far-field or Trefftz-plane approach. In general, this is a more reliable approach especially for the D_i component, since it avoids the usual pressure-drag cancellation errors discussed in Chapter 5, these being especially problematic with the simple leading edge suction model.

Referring to Figure 5.7, the first step here is to compute the Trefftz-plane perturbation velocity

$$\nabla\varphi(s) \;=\; \sum_{\text{sheets}} \frac{1}{2\pi} \int_0^{s_{\max}} \gamma(s') \, \frac{\hat{\mathbf{x}} \times (\mathbf{r}-\mathbf{r}')}{|\mathbf{r}-\mathbf{r}'|^2} \, \mathrm{d}s' \tag{6.26}$$

at each sheet location $\mathbf{r}(s)$, where the integral is taken along all sheet traces shown in Figure 6.4. The wake sheet potential jump is also required.

$$\Delta\varphi(s) \;=\; \int_0^s \gamma(s') \, \mathrm{d}s' \tag{6.27}$$

$$\text{or} \qquad \Delta\varphi(s) \;=\; \mu(s) \tag{6.28}$$

The induced drag is then computed directly via expression (5.47).

$$D_i \;=\; \sum_{\text{sheets}} -\frac{1}{2}\rho \int_0^{s_{\max}} \Delta\varphi \; \nabla\varphi \cdot \hat{\mathbf{n}} \; \mathrm{d}s \tag{6.29}$$

The Trefftz plane also provides alternative means of computing the total lift and sideforce via expressions (5.64) and (5.65).

$$Y \;=\; \sum_{\text{sheets}} \rho V_\infty \int_0^{s_{\max}} -\Delta\varphi \; n_y \; \mathrm{d}s \tag{6.30}$$

$$L \;=\; \sum_{\text{sheets}} \rho V_\infty \int_0^{s_{\max}} \Delta\varphi \; n_z \; \mathrm{d}s \tag{6.31}$$

Note however, that this Trefftz plane force calculation method gives only the <u>total</u> forces. Equations (6.24) and (6.25) must be used for moments, and also for forces on the individual surfaces.

6.5   Vortex Lattice Method

The Vortex Lattice (VL) method is a numerical solution implementation of the general 3D lifting surface problem described above. It is also the simplest general 3D potential flow calculation method. It is commonly used in initial aircraft configuration development, where its simplicity and speed allow a large number of configurations to be examined. It is also used for initial structural load estimation, and to provide the trim state values and stability and control derivatives for the linearized force and moment equations (6.12), (6.13).

6.5.1 Vortex lattice discretization

The VL method discretizes the vortex-sheet strength distribution on each lifting surface and its wake by lumping it into a collection of *horseshoe vortices*, as shown in Figure 6.6. Each horseshoe vortex (h.v.) consists of three straight legs, or segments: a *bound leg* which lies on the surface, and two *trailing legs* extending from the bound leg's endpoints to downstream infinity and parallel to the x axis. All three legs of the i'th h.v. have the same constant circulation strength Γ_i.
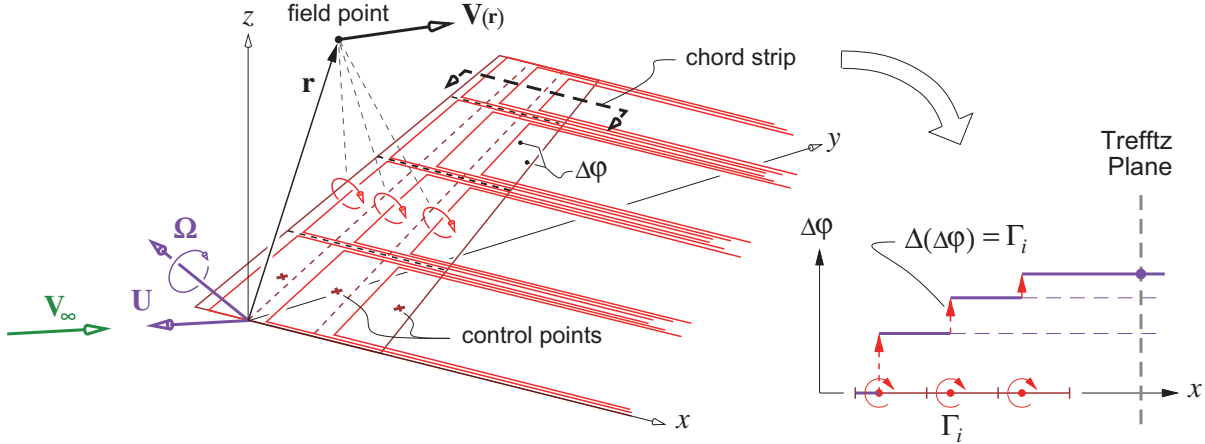
Figure 6.6: 3D lifting surface discretized by a Vortex Lattice of horseshoe vortices, which all contribute to the velocity $\mathbf{V}$ at any field point $\mathbf{r}$. Setting $\mathbf{r}$ at each control point allows imposition of flow tangency there. Each horseshoe vortex i also adds a contribution of Γ_i to the total potential jump $\triangle\varphi$ within its perimeter. Total accumulated $\triangle\varphi$ along a chord strip is the Trefftz-plane value shown in Figure 5.12.

In a discrete sense, this configuration of vortices satisfies the zero-divergence requirement on the vortex sheet strength $\boldsymbol{\gamma}_{(s,\ell)}$ which is discussed in Section 2.4, since any circuit drawn on the surface will have a filament with a fixed circulation both entering and leaving it. Note also that each h.v. adds zero net circulation in the Trefftz plane, where its two trailing legs have equal and opposite circulations.

An equivalent interpretation of the h.v. configuration is a piecewise-constant potential jump or normal-doublet distribution. Each h.v. contributes $\Delta(\triangle\varphi) = \Gamma_i$ to the total potential jump $\triangle\varphi$ within its perimeter. The total circulation of all the h.v.'s in a chord strip then gives the $\triangle\varphi$ in the Trefftz plane, as shown in Figure 6.6. This $\triangle\varphi$ is also shown in Figure 5.12, where it's used to construct the Trefftz-plane velocity and evaluate the Trefftz-plane forces.

6.5.2 Velocity field representation

The overall velocity field relative to the VL configuration at any point $\mathbf{r}$ is given by relation (6.18), where the $\boldsymbol{\gamma}_{(s,\ell)}$ vortex-sheet strength is now lumped into the collection of h.v. filaments, with each filament having a constant strength Γ_i. The surface integral in (6.17) is therefore replaced with a collection of Biot-Savart line integrals, one for each h.v.

$$
\begin{aligned}
\mathbf{V}_{(\mathbf{r})} &= \sum_{\text{h.v.'s}} \frac{\Gamma}{4\pi} \int \frac{\mathrm{d}\boldsymbol{\ell}' \times (\mathbf{r}-\mathbf{r}')}{|\mathbf{r}-\mathbf{r}'|^3} - (\mathbf{U} + \boldsymbol{\Omega}\times\mathbf{r}) \\
&= \sum_{i=1}^{N} \Gamma_i\, \hat{\mathbf{V}}_{i(\mathbf{r})} - (\mathbf{U} + \boldsymbol{\Omega}\times\mathbf{r})
\end{aligned}
\tag{6.32}
$$

Evaluation of the Biot-Savart integral of the i'th h.v. has produced the $\hat{\mathbf{V}}_i$ kernel function, given by the following expression. The $\mathbf{a}$ and $\mathbf{b}$ vectors are shown in Figure 6.7.

$$\hat{\mathbf{V}}_{i(\mathbf{r})} = \frac{1}{4\pi}\left\{\frac{\mathbf{a}\times\mathbf{b}}{|\mathbf{a}||\mathbf{b}|+\mathbf{a}\cdot\mathbf{b}}\left(\frac{1}{|\mathbf{a}|}+\frac{1}{|\mathbf{b}|}\right) + \frac{\mathbf{a}\times\hat{\mathbf{x}}}{|\mathbf{a}|-\mathbf{a}\cdot\hat{\mathbf{x}}}\frac{1}{|\mathbf{a}|} - \frac{\mathbf{b}\times\hat{\mathbf{x}}}{|\mathbf{b}|-\mathbf{b}\cdot\hat{\mathbf{x}}}\frac{1}{|\mathbf{b}|}\right\} \quad (6.33)$$

The three terms in (6.33) correspond to the bound leg, the $\mathbf{r}_a$-point trailing leg, and the $\mathbf{r}_b$-point trailing leg, respectively. Note that $\hat{\mathbf{V}}_i$ has units of $1/\text{length}$.
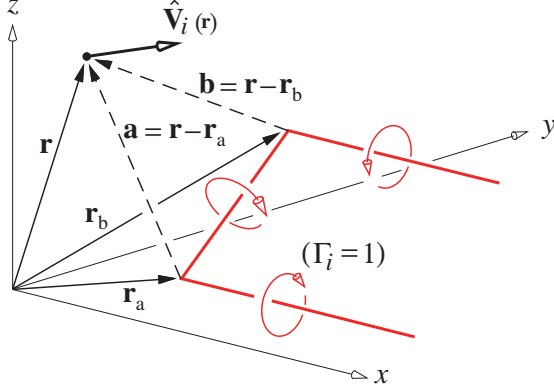
Figure 6.7: Geometry of one horseshoe vortex, producing a unit-strength velocity $\hat{\mathbf{V}}_{i(\mathbf{r})}$ at some field point $\mathbf{r}$.

6.5.3 Flow tangency condition

The flow tangency condition (6.19) is imposed at the N control points by choosing $\mathbf{r}$ in (6.32) to be the control point $\mathbf{r}_i^c$ of each h.v. in turn, and setting the resulting normal velocity component to zero.

$$\mathbf{V}(\mathbf{r}_i^c)\cdot\mathbf{n}_{i(\delta_l)} = \left(\sum_{j=1}^N \Gamma_j\,\hat{\mathbf{V}}_{j(\mathbf{r}_i^c)} - (\mathbf{U}+\mathbf{\Omega}\times\mathbf{r}_i^c)\right)\cdot\mathbf{n}_{i(\delta_l)} = 0 \quad (i=1\dots N) \quad (6.34)$$

To avoid conflict with the control point index i, the summation index over the h.v.'s has been changed to j.

The normal vector $\mathbf{n}_i$ depends on δ_l, which are control variables which define the deflections of some number of control surfaces. The control index $l=1,2\dots N_l$ is more practical for computation than the earlier $\delta_a,\delta_e\dots$ notation introduced in Section 6.3.2.

The deflections are modeled by rotating each $\mathbf{n}_i$ on that control surface about a specified hinge axis. In keeping with the small-angle approximations used throughout lifting surface theory and the VL method in particular, each normal vector's dependence on δ_l is linearized. Referring to Figure 6.8 we have

$$\mathbf{n}_{i(\delta_l)} \simeq \mathbf{n}_{0_i} + \sum_{l=1}^{N_l}\mathbf{n}_{l_i}\,\delta_l \quad (6.35)$$

$$\mathbf{n}_{l_i} \equiv \frac{\partial\mathbf{n}_i}{\partial\delta_l} = g_l\,\hat{\mathbf{h}}_{l_i}\times\mathbf{n}_{0_i} \quad (6.36)$$

where $\hat{\mathbf{h}}_l$ is the hinge-axis unit vector about which $\mathbf{n}$ rotates in response to the δ_l control deflection, and g_l is the "control gain," included so that the δ_l control variable doesn't have to be the actual local deflection angle in radians. To linearize the control influence we will assume that $-U_x\hat{\mathbf{x}}\simeq V_\infty\hat{\mathbf{x}}$ which is equivalent to

$\alpha, \beta \ll 1$, and that the normal-vector control deflections $\mathbf{n}_{l_i} \delta_l$ are small compared to the undeflected normal vector $\mathbf{n}_{0_i}$. Thus the flow-tangency equations (6.34) are approximated by

$$\left(\sum_{j=1}^{N} \Gamma_j \, \hat{\mathbf{V}}_{j(\mathbf{r}_i^c)} \;-\; (\mathbf{U} + \mathbf{\Omega} \times \mathbf{r}_i^c) \right) \cdot \mathbf{n}_{0_i} \;+\; \sum_{l=1}^{N_l} V_\infty \, \hat{\mathbf{x}} \cdot \mathbf{n}_{l_i} \, \delta_l \;=\; 0 \qquad (i = 1 \dots N) \quad (6.37)$$

where all products of two small quantities have been dropped.
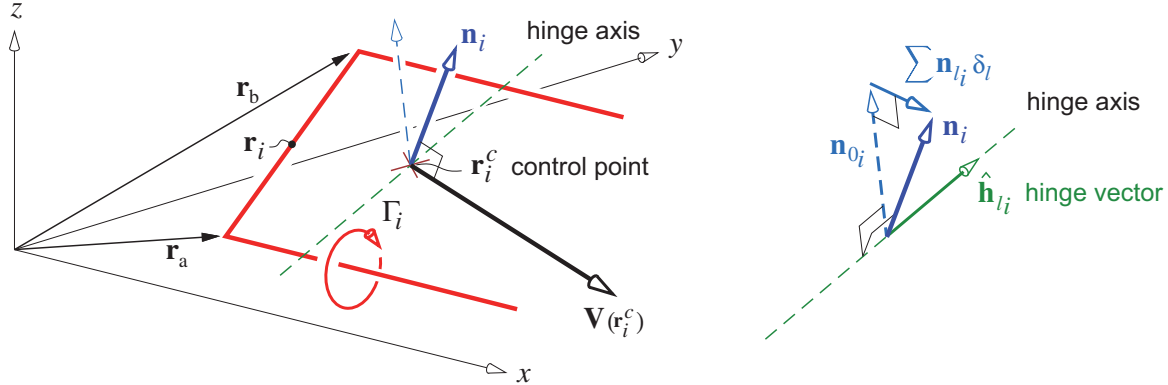
Figure 6.8: Flow tangency imposed at control point of i'th horseshoe vortex, biased by rotation of the normal vector $\mathbf{n}_i$ via the control variables δ_l.

6.5.4 Linear system setup and solution

The subsequent numerical implementation of equations (6.37) will be done in terms of the following variables normalized with V_∞, denoted by the overbar $\bar{(\;)}$. Note that $\bar{\mathbf{U}}$ is then dimensionless, while $\bar{\Gamma}$ and $\bar{\mathbf{\Omega}}$ have units of length and $1/\text{length}$, respectively.

$$\bar{\Gamma}_i \equiv \frac{\Gamma_i}{V_\infty} \quad , \quad \bar{\mathbf{U}} \equiv \frac{\mathbf{U}}{V_\infty} = \left\{ \begin{matrix} \bar{U}_x \\ \bar{U}_y \\ \bar{U}_z \end{matrix} \right\} = \left\{ \begin{matrix} -\cos\alpha \cos\beta \\ \sin\beta \\ -\sin\alpha \cos\beta \end{matrix} \right\} \quad , \quad \bar{\mathbf{\Omega}} \equiv \frac{\mathbf{\Omega}}{V_\infty} = \left\{ \begin{matrix} \bar{\Omega}_x \\ \bar{\Omega}_y \\ \bar{\Omega}_z \end{matrix} \right\} \quad (6.38)$$

The linearized flow tangency conditions (6.37) constitute an $N \times N$ linear system for the $\bar{\Gamma}_i$ normalized vortex strengths when the $\bar{\mathbf{U}}, \bar{\mathbf{\Omega}}, \delta_l$ terms are placed on the righthand side.

$$\left[A_{ij} \right] \left\{ \bar{\Gamma}_j \right\} = \bar{U}_x \left\{ \; \hat{\mathbf{x}} \cdot \mathbf{n}_{0_i} \; \right\} + \bar{U}_y \left\{ \; \hat{\mathbf{y}} \cdot \mathbf{n}_{0_i} \; \right\} + \bar{U}_z \left\{ \; \hat{\mathbf{z}} \cdot \mathbf{n}_{0_i} \; \right\}$$

$$+ \; \bar{\Omega}_x \left\{ \hat{\mathbf{x}} \times \mathbf{r}_i^c \cdot \mathbf{n}_{0_i} \right\} + \bar{\Omega}_y \left\{ \hat{\mathbf{y}} \times \mathbf{r}_i^c \cdot \mathbf{n}_{0_i} \right\} + \bar{\Omega}_z \left\{ \hat{\mathbf{z}} \times \mathbf{r}_i^c \cdot \mathbf{n}_{0_i} \right\}$$

$$+ \; \delta_1 \left\{ -\hat{\mathbf{x}} \cdot \mathbf{n}_{1_i} \right\} + \delta_2 \left\{ -\hat{\mathbf{x}} \cdot \mathbf{n}_{2_i} \right\} + \dots + \delta_{N_l} \left\{ -\hat{\mathbf{x}} \cdot \mathbf{n}_{N l_i} \right\} \qquad (6.39)$$

$$A_{ij} \equiv \hat{\mathbf{V}}_{j(\mathbf{r}_i^c)} \cdot \mathbf{n}_{0_i} \qquad (6.40)$$

The Aerodynamic Influence Coefficient matrix A_{ij} and the righthand side vectors in braces are functions of the vortex lattice geometry only, and hence are known a priori.

Multiplying (6.39) through by A_{ij}^{-1} using LU-factorization and back-substitution gives the solution vector $\bar{\Gamma}_i$ as a sum of known $6 + N_l$ independent vectors, whose coefficients (arbitrary at this point) are the operating

parameters $\bar{U}_x, \bar{U}_y \ldots \delta_{N_l}$. When these parameters are specified, $\bar{\Gamma}_i$ is determined by summing all $6+N_l$ vectors.

$$\left\{\bar{\Gamma}_i\right\} = \bar{U}_x\left\{\bar{\Gamma}_{1_i}\right\} + \bar{U}_y\left\{\bar{\Gamma}_{2_i}\right\} + \bar{U}_z\left\{\bar{\Gamma}_{3_i}\right\} + \bar{\Omega}_x\left\{\bar{\Gamma}_{4_i}\right\} + \bar{\Omega}_y\left\{\bar{\Gamma}_{5_i}\right\} + \bar{\Omega}_z\left\{\bar{\Gamma}_{6_i}\right\} + \sum_{l=1}^{N_l}\delta_l\left\{\bar{\Gamma}_{6+l_i}\right\} \quad (6.41)$$

6.5.5 Near-field force and moment calculation

Once the $\bar{\Gamma}_i$ strengths are known, the normalized velocity relative to the midpoint $\mathbf{r}_i$ of the i'th h.v. is calculated, as shown in Figure 6.9. This uses the same form as (6.32),

$$\frac{\mathbf{V}_i}{V_\infty} \equiv \bar{\mathbf{V}}_i = \left\{\begin{array}{c}\bar{V}_{xi}\\\bar{V}_{yi}\\\bar{V}_{zi}\end{array}\right\} = \sum_{j=1}^{N}\bar{\Gamma}_j\,\hat{\mathbf{V}}_{j(\mathbf{r}_i)} - \left\{\begin{array}{c}\bar{U}_x\\\bar{U}_y\\\bar{U}_z\end{array}\right\} - \left\{\begin{array}{c}\bar{\Omega}_x\\\bar{\Omega}_y\\\bar{\Omega}_z\end{array}\right\} \times \mathbf{r}_i \quad (6.42)$$

$$\mathbf{r}_i = \tfrac{1}{2}(\mathbf{r}_{\mathrm{a}} + \mathbf{r}_{\mathrm{b}}) \quad (6.43)$$

except the h.v. kernel functions $\hat{\mathbf{V}}_j$ here are different than those in the flow-tangency condition (6.34), since the bound-leg midpoint locations $\mathbf{r}_i$ are different from the control-point locations $\mathbf{r}_i^c$. In the $\hat{\mathbf{V}}_j$ function in (6.42) it is also necessary to omit the bound leg's contribution on itself, which is the first term in (6.33), since this is singular at $\mathbf{r}_i$.

The normalized force $\bar{\mathbf{F}}_i$ on each h.v. is computed by the integrated form of the local pressure loading relation (6.22).

$$\mathbf{F}_i = \iint_{\mathrm{element}}\Delta p\,\hat{\mathbf{n}}\;\mathrm{d}\mathcal{S} = \iint_{\mathrm{element}}\rho\,\mathbf{V}_a\times\boldsymbol{\gamma}\;\mathrm{d}\mathcal{S} = \rho\mathbf{V}_i\times\boldsymbol{\ell}_i\,\Gamma_i \quad (6.44)$$

$$\text{where}\qquad \boldsymbol{\ell}_i = \mathbf{r}_{\mathrm{b}} - \mathbf{r}_{\mathrm{a}}$$

$$\bar{\mathbf{F}}_i \equiv \frac{\mathbf{F}_i}{\tfrac{1}{2}\rho_\infty V_\infty^2 S_{\mathrm{ref}}} \simeq \frac{2}{S_{\mathrm{ref}}}\bar{\mathbf{V}}_i\times\boldsymbol{\ell}_i\,\bar{\Gamma}_i \quad (6.45)$$

The last step in (6.44) consists of lumping the vortex sheet on the element into the element h.v.'s bound leg vortex segment, $\iint\boldsymbol{\gamma}\,\mathrm{d}\mathcal{S} \simeq \boldsymbol{\ell}_i\Gamma_i$. The relevant quantities are shown in Figure 6.9.

Interestingly enough, the Kutta-Joukowsky force calculation form (6.45) gives exactly zero drag in the 2D case where there are no trailing h.v. legs. Therefore it implicitly accounts for the leading edge suction force, which then does not need to be added explicitly.

The total normalized force and moment on the whole configuration are obtained by summation of all the individual h.v. contributions. The moment is defined about a specified point $\mathbf{r}_{\mathrm{ref}}$.

$$\bar{\mathbf{F}} = \sum_{i=1}^{N}\bar{\mathbf{F}}_i \quad (6.46)$$

$$\bar{\mathbf{M}} = \sum_{i=1}^{N}(\mathbf{r}_i - \mathbf{r}_{\mathrm{ref}})\times\bar{\mathbf{F}}_i \quad (6.47)$$

The standard dimensionless force and moment coefficients in stability axes, shown in Figure 6.2, are obtained by rotating $\bar{\mathbf{F}}$ and $\bar{\mathbf{M}}$ using the $\bar{\bar{\mathbf{T}}}^{\mathrm{s}}$ matrix given by (6.5). The reference span and chord $b_{\mathrm{ref}}, c_{\mathrm{ref}}$ are
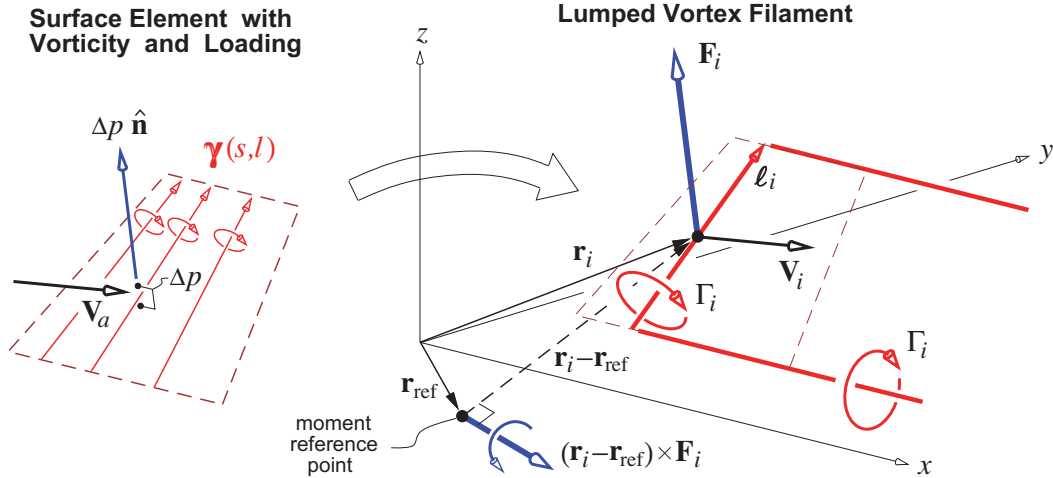
Figure 6.9: Net pressure loading on a surface element approximated by the Kutta-Joukowsky force on the element's horseshoe vortex bound leg ℓ_i.

also used here to non-dimensionalize the moments.

$$\begin{Bmatrix} C_{D_i} \\ C_Y \\ C_L \end{Bmatrix} = \begin{bmatrix} \bar{\bar{\mathbf{T}}}^{\mathrm{s}} \end{bmatrix} \begin{Bmatrix} \bar{F}_x \\ \bar{F}_y \\ \bar{F}_z \end{Bmatrix} \tag{6.48}$$

$$\begin{Bmatrix} C'_\ell \\ C'_m \\ C'_n \end{Bmatrix} = \begin{bmatrix} \bar{\bar{\mathbf{T}}}^{\mathrm{s}} \end{bmatrix} \begin{Bmatrix} -\bar{M}_x/b_{\mathrm{ref}} \\ \bar{M}_y/c_{\mathrm{ref}} \\ -\bar{M}_z/b_{\mathrm{ref}} \end{Bmatrix} \tag{6.49}$$

If there is a nonzero sideslip, $\beta \neq 0$, then the physically correct expression for the induced drag coefficient is given by the wind-axis relation (6.8).

$$C_{D_i} = -\bar{\mathbf{F}} \cdot \bar{\mathbf{U}} \tag{6.50}$$

6.5.6 Trefftz-plane force calculation

As discussed in Section 6.4.4, the Trefftz-plane provides an alternative to the near-field result (6.6) for calculating the wind-axes forces. A suitable discrete formulation of the Trefftz-plane integrals which is applicable to the VL method here was already given in Section 5.8.2. To apply those results it is first necessary to define the piecewise-constant wake potential jump distribution $\Delta\varphi_i$ for each h.v. "chord strip," shown in Figure 6.6, whose h.v.'s have their trailing legs superimposed in the Trefftz-plane.

$$\Delta\bar{\varphi}_i = \sum_{\mathrm{strip}} \bar{\Gamma}_i \tag{6.51}$$

The summation is only over the h.v.'s within that chord strip, indicated in Figure 6.6. The normalized version of expression (5.81) for the wake-normal velocity $\partial\bar{\varphi}/\partial n_i$ and expressions (5.77), (5.78), (5.82) for the forces Y, L, D_i can then be used as written.

6.5.7   Stability and control derivative calculation

The VL method is well suited to rapid calculation of stability and control derivatives in the small-angle operating range $\alpha, \beta, \bar{p}, \bar{q}, \bar{r} \ll 1$. The calculation can be performed by finite-differencing slightly perturbed flow solutions, e.g.

$$C_{L_\alpha} \simeq \frac{C_L(\alpha_0 + \Delta\alpha, \beta_0) - C_L(\alpha_0, \beta_0)}{\Delta\alpha} \quad , \quad C_{n_\beta} \simeq \frac{C_n(\alpha_0, \beta_0 + \Delta\beta) - C_n(\alpha_0, \beta_0)}{\Delta\beta} \tag{6.52}$$

A more economical alternative is to implicitly differentiate the overall force and moment summations with respect to each parameter via the chain rule, noting that $\bar{\Gamma}_i$ as given by (6.41) and $\bar{\mathbf{V}}_i$ as given by (6.42) have relatively simple dependencies on the parameters. For example, the α-derivatives of the following quantities can be evaluated in parallel with each quantity itself.

$$\frac{\partial \bar{\mathbf{U}}}{\partial \alpha} = \left\{ \begin{matrix} \sin\alpha \cos\beta \\ 0 \\ -\cos\alpha \cos\beta \end{matrix} \right\} \tag{6.53}$$

$$\frac{\partial \bar{\Gamma}_i}{\partial \alpha} = \frac{\partial \bar{U}_x}{\partial \alpha} \bar{\Gamma}_{1_i} + \frac{\partial \bar{U}_z}{\partial \alpha} \bar{\Gamma}_{3_i} \tag{6.54}$$

$$\frac{\partial \bar{\mathbf{V}}_i}{\partial \alpha} = \sum_{j=1}^{N} \frac{\partial \bar{\Gamma}_j}{\partial \alpha} \hat{\mathbf{V}}_{j(\mathbf{r}_i)} - \frac{\partial \bar{\mathbf{U}}}{\partial \alpha} \tag{6.55}$$

$$\frac{\partial \bar{\mathbf{F}}_i}{\partial \alpha} = \frac{2}{S_{\text{ref}}} \left(\frac{\partial \bar{\mathbf{V}}_i}{\partial \alpha} \times \boldsymbol{\ell}_i \, \bar{\Gamma}_i + \bar{\mathbf{V}}_i \times \boldsymbol{\ell}_i \, \frac{\partial \bar{\Gamma}_i}{\partial \alpha} \right) \tag{6.56}$$

$$\frac{\partial \bar{\mathbf{F}}}{\partial \alpha} = \sum_{i=1}^{N} \frac{\partial \bar{\mathbf{F}}_i}{\partial \alpha} \tag{6.57}$$

$$\frac{\partial}{\partial \alpha} \left\{ \begin{matrix} C_{D_i} \\ C_Y \\ C_L \end{matrix} \right\} = \frac{\mathrm{d}\bar{\bar{\mathbf{T}}}^{\text{s}}}{\mathrm{d}\alpha} \bar{\mathbf{F}} + \bar{\bar{\mathbf{T}}}^{\text{s}} \frac{\partial \bar{\mathbf{F}}}{\partial \alpha} \tag{6.58}$$

Note how each derivative calculation uses the derivatives calculated earlier. The final result (6.58) is the sought-after force stability derivatives with respect to α. The same procedure is used for the moment derivative vector. The procedure is also repeated for all the remaining parameters $\beta, \bar{p}, \bar{q}, \bar{r}, \delta_l$. The advantage of this direct differentiation method over the finite-difference approach (6.52) is that it is economical and effectively exact.

6.6   Slender Body Theory

Slender Body Theory is applicable to bodies such as slender fuselages and nacelles, and also to very slender delta wings with $A\!R \ll 1$. The key simplifying assumption, and the definition of "slender," is that the yz-plane cross sections of the body and the flow vary slowly in the streamwise x direction relative to the y, z directions. This implies that the streamwise component φ_x of the perturbation velocity $\nabla\varphi$ is negligible compared to the transverse components φ_y, φ_z.

$$\varphi_x \ll \varphi_y, \varphi_z \tag{6.59}$$

It's useful to note the similarities with the Trefftz plane, introduced in Section 5.6.

6.6.1   Slender body geometry

The geometry of the body is specified by its surface position vector

$$\tilde{\mathbf{r}}_{(x,s)} = x\,\hat{\mathbf{x}} + \left[\tilde{y}_{(s;x)}\right]\hat{\mathbf{y}} + \left[\tilde{z}_{(s;x)}\right]\hat{\mathbf{z}} \tag{6.60}$$

where s is some parameter, such as the arc length in the yz plane. This defines the $\tilde{y}, \tilde{z}$ cross-section shape of the body at some x location, as shown in Figure 6.10. Since the vectors $\partial\tilde{\mathbf{r}}/\partial s$ and $\partial\tilde{\mathbf{r}}/\partial x$ are both tangent to the body surface, the unit normal vector can be determined via their cross product.

$$\mathbf{n}_{(x,s)} = \frac{\partial\tilde{\mathbf{r}}}{\partial s}\times\frac{\partial\tilde{\mathbf{r}}}{\partial x} = \left[\frac{\partial\tilde{y}}{\partial s}\frac{\partial\tilde{z}}{\partial x} - \frac{\partial\tilde{z}}{\partial s}\frac{\partial\tilde{y}}{\partial x}\right]\hat{\mathbf{x}} + \frac{\partial\tilde{z}}{\partial s}\hat{\mathbf{y}} - \frac{\partial\tilde{y}}{\partial s}\hat{\mathbf{z}} \quad , \qquad \hat{\mathbf{n}} = \frac{\mathbf{n}}{|\mathbf{n}|} \qquad (6.61)$$

In practice, the dimensional normal vector $\mathbf{n}$ is simpler and is adequate for the construction of flow tangency boundary conditions.
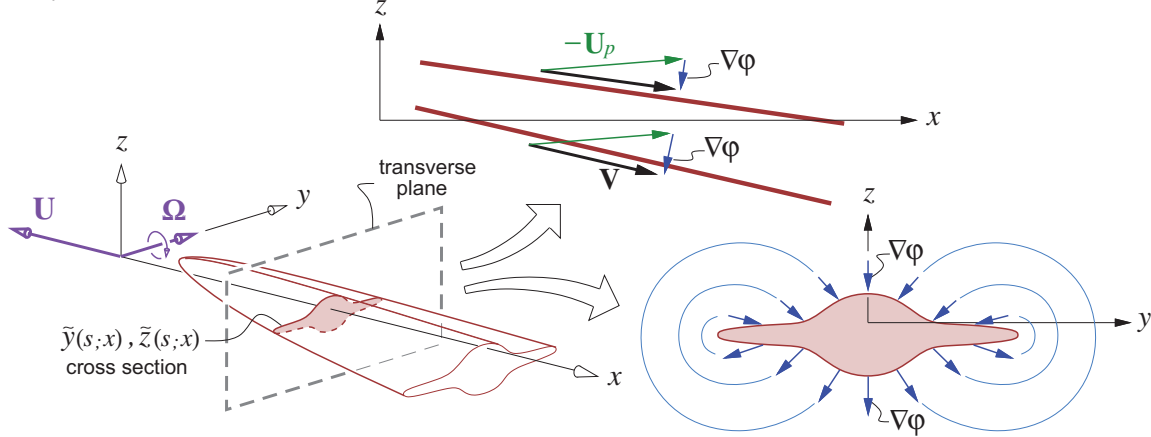
Figure 6.10: Slender body's perturbation velocity $\nabla\varphi$ is nearly two-dimensional in the transverse yz plane. Body cross section at each station x is given by the $\tilde{y}(s\,;x), \tilde{z}(s\,;x)$ coordinate functions.

6.6.2 Slender body flow-field

The body is assumed to move at steady velocity $\mathbf{U} = -V_\infty\,\hat{\mathbf{x}}$ and pitch rate $\mathbf{\Omega} = q\,\hat{\mathbf{y}}$, so the local apparent freestream is $-\mathbf{U}_p = -(\mathbf{U} + \mathbf{\Omega}\times\mathbf{r}) = V_\infty\,\hat{\mathbf{x}} + qx\,\hat{\mathbf{z}}$. Any angle of attack or sideslip is assumed to be included in the $\tilde{\mathbf{r}}$ geometry definition. The perturbation potential $\varphi_{(x,y,z)}$ of the flow about the slender body is assumed to locally satisfy the <u>two-dimensional</u> crossflow Laplace's equation

$$\varphi_{yy} + \varphi_{zz} = 0 \qquad (\text{ for } y^2 + z^2 \ll \ell^2) \qquad (6.62)$$

where ℓ is the length of the body. Dropping the φ_{xx} term has been justified by the slender-flow assumption (6.59). The appropriate boundary conditions are flow tangency of the total velocity on the body surface, and asymptotically zero perturbation flow far away.

$$[(V_\infty + \varphi_x)\,\hat{\mathbf{x}} + \varphi_y\,\hat{\mathbf{y}} + (qx + \varphi_z)\,\hat{\mathbf{z}}]\cdot\mathbf{n} = 0$$

$$\text{or} \qquad \varphi_y\, n_y + \varphi_z\, n_z \simeq -(V_\infty\, n_x + qx\, n_z) \qquad (\text{ on body }) \qquad (6.63)$$

$$\text{and} \qquad \varphi \rightarrow 0 \qquad (\text{for } y^2 + z^2 \gg \ell^2) \qquad (6.64)$$

The $\varphi_x n_x$ term has been dropped from the right side of (6.63) since it is negligible relative to the other terms.

Laplace's equation (6.62) and boundary conditions (6.63),(6.64) define a 2D incompressible potential flow with a known nonzero normal velocity $-(V_\infty\, n_x + qx\, n_z)$ which is due to the pitch rate and also the inclination of the body surface relative to the freestream x direction. Such a flow is sketched in Figure 6.10 on bottom right. It can be computed for a given arbitrary cross-section using any standard 2D panel method, but with a different righthand side than usual. To compute the overall 3D flow, some sufficiently large number of individual 2D problems would actually have to be solved, one for each discrete x location.

Once the potential $\varphi_{(x,y,z)}$ is computed, the pressure is determined using the Bernoulli equation.

$$p + \tfrac{1}{2}\rho \left[(V_\infty + \varphi_x)^2 + \varphi_y^2 + \varphi_z^2 \right] = p_\infty + \tfrac{1}{2}\rho V_\infty^2$$

$$p - p_\infty = -\rho V_\infty \varphi_x - \tfrac{1}{2}\rho \left(\varphi_y^2 + \varphi_z^2 \right) \tag{6.65}$$

Even though the streamwise perturbation velocity φ_x was neglected in the local 2D problem defined by Laplace's equation (6.62) and boundary condition (6.63), it is required for the pressure calculation. The reason is that $V_\infty \varphi_x$ is not necessarily negligible compared to $\varphi_y^2 + \varphi_z^2$ and hence must be retained here.

6.6.3   2D unsteady flow interpretation

The sequence of solutions along x can be interpreted as a 2D unsteady flow $\varphi_{(t,y,z)}$ if we make the Galilean transformation

$$x = V_\infty t \quad, \qquad \frac{\partial}{\partial x} = \frac{1}{V_\infty}\frac{\partial}{\partial t}$$

where the new observer is traveling along the x axis at the freestream speed V_∞. The $\tilde{y}_{(s\,;t)}, \tilde{z}_{(s\,;t)}$ cross-sectional shape in the transverse plane and the resulting transverse flow then appear to change in time. In this unsteady interpretation the streamwise perturbation velocity transforms as $\varphi_x \to \varphi_t/V_\infty$, which converts the steady 3D Bernoulli equation (6.65) into its 2D unsteady form which gives the same pressure.

$$p - p_\infty = -\rho\,\varphi_t - \tfrac{1}{2}\rho \left(\varphi_y^2 + \varphi_z^2 \right)$$

In practice, when solving the 2D Laplace problem (6.62)–(6.64), the spatial sequence in x or the time sequence in t are computationally equivalent. And for computing the pressure, the 3D steady or the 2D un-steady Bernoulli equations are equivalent as well. Therefore, this transformation and unsteady interpretation does not provide any computational advantages, but it does give some additional insight into the problem.

6.6.4   Local 2D far-field

At intermediate distances which are large compared to the local body y, z dimension but small compared to the body length ℓ, the perturbation potential must have a local 2D far-field form as given by (2.78).

$$\varphi_{(r,\theta\,;x)} = \frac{\Lambda_{(x)}}{2\pi}\ln r + \frac{\kappa_{z(x)}}{2\pi}\frac{\sin\theta}{r} \tag{6.66}$$

$$\text{where} \qquad r_{(x,y,z)} \equiv \sqrt{y^2 + (z - z_{0(x)})^2}$$

$$\theta_{(x,y,z)} \equiv \arctan\frac{z - z_{0(x)}}{y}$$

The vortex term was omitted since there cannot be an overall circulation about this 3D body. The y doublet was omitted by the assumption of left/right symmetry about $y = 0$, and it can always be eliminated in any case by rotating the axes so that the z axis aligns with the doublet-vector axis. Also, for generality the singularities are placed at some location $z = z_{0(x)}$ rather than at $z = 0$.

The source strength is related to the body's cross-sectional area $A_{(x)}$ as derived in Section 2.12.

$$\Lambda_{(x)} = V_\infty \frac{\mathrm{d}A}{\mathrm{d}x} \tag{6.67}$$

The z-doublet is related to the lift via the the far-field lift integral (5.50). This requires the pressure, which is obtained from the Bernoulli equation (6.65),

$$p_\infty - p = \rho V_\infty \varphi_x = \rho V_\infty \frac{\mathrm{d}\kappa_z}{\mathrm{d}x}\frac{\sin\theta}{2\pi r} \tag{6.68}$$

The quadratic terms in (6.65) have been omitted here, since they become negligible at a sufficiently large control volume. Following the procedure in Section C.4, integral (5.50) is now evaluated on a dx–long circular control volume of some radius r, whose arc length element is $dl = r\, d\theta$.

$$\frac{dL}{dx} = \oint \left[(p_\infty - p)\, n_z - \rho\, \varphi_z\, \varphi_r \right]\, dl = \rho V_\infty \frac{d\kappa_z}{dx} \int_0^{2\pi} \frac{\sin^2\theta}{2\pi r}\, r\, d\theta$$

$$= \frac{1}{2}\rho V_\infty \frac{d\kappa_z}{dx} \tag{6.69}$$

Using (6.69) to calculate the overall lift of the body still requires relating κ_z to the body geometry, which in general is case-dependent. A simple geometry is considered next as an example.

6.6.5 Cambered body of revolution

A cambered body with circular cross sections is shown in Figure 6.11. Its surface geometry is defined by

$$\tilde{\mathbf{r}}_{(x,\theta)} = x\,\hat{\mathbf{x}} + \left[R\cos\theta \right]\hat{\mathbf{y}} + \left[R\sin\theta + Z - \alpha x \right]\hat{\mathbf{z}} \tag{6.70}$$

where $Z_{(x)}$ is the camber of the centerline, α is the overall body angle of attack, and $R_{(x)}$ is the radius of the local circular cross-section which is centered on $z = z_0(x) = Z_{(x)} - \alpha x$.

The local normal vector is computed from (6.70) using the cross-product relation (6.61), with $\theta = s/R$.

$$\mathbf{n}_{(x,\theta)} = \left[-R\frac{dR}{dx} + \left(\alpha - \frac{dZ}{dx} \right) R\sin\theta \right]\hat{\mathbf{x}} + \left[R\cos\theta \right]\hat{\mathbf{y}} + \left[R\sin\theta \right]\hat{\mathbf{z}} \tag{6.71}$$
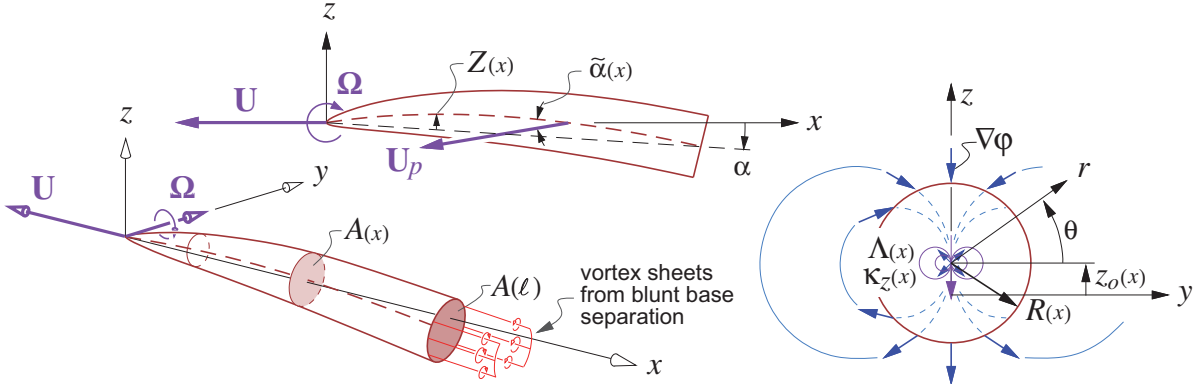
Figure 6.11: Slender body of revolution with overall angle of attack α, local added camber $Z_{(x)}$, and resulting local angle of attack $\tilde{\alpha}_{(x)}$. Local transverse flow is represented by source strength $\Lambda_{(x)}$ and z-doublet strength $\kappa_z(x)$, both located at the body center at $z_0(x)$. Vortex sheets are shed if a blunt base is present.

In terms of the cross-sectional area $A_{(x)} = \pi R^2$, the far-field source and doublet strengths are

$$\Lambda_{(x)} = 2\pi V_\infty R \frac{dR}{dx} = V_\infty \frac{dA}{dx} \tag{6.72}$$

$$\kappa_z(x) = 2\pi V_\infty R^2\,\tilde{\alpha} = 2V_\infty A\,\tilde{\alpha} \tag{6.73}$$

$$\tilde{\alpha}(x) \equiv \alpha - \frac{dZ}{dx} + \frac{qx}{V_\infty} \tag{6.74}$$

where $\tilde{\alpha}$ is the <u>local</u> angle of attack of the body centerline relative to the local body velocity $\mathbf{U}_p$. The potential expression (6.66) with the strengths (6.72),(6.73), and the geometry given by (6.70) all together

exactly satisfy the 2D Laplace's equation (6.62) and boundary conditions (6.63), (6.64). Therefore this far-field flow happens to be an exact solution of the transverse-flow equations for this geometry.

With the z-doublet strength known, the overall lift can be obtained by integration of the lift gradient (6.69).

$$L \;=\; \int_0^\ell \frac{\mathrm{d}L}{\mathrm{d}x}\,\mathrm{d}x \;=\; \rho V_\infty^2 \int_0^\ell \frac{\mathrm{d}(A\tilde{\alpha})}{\mathrm{d}x}\,\mathrm{d}x \;=\; \rho V_\infty^2\, A(\ell)\,\tilde{\alpha}(\ell) \tag{6.75}$$

This final result shows that within the assumptions of potential flow, the lift of a slender body of revolution depends only on its base area $A(\ell)$ and the local angle of attack $\tilde{\alpha}(\ell)$ at the base location. Trefftz-plane analysis requires that any lifting body must generate trailing vorticity, and indeed the blunt base will shed the necessary vortex sheets as sketched in Figure 6.11. A related conclusion is that bodies which come to a sharp point at the rear cannot generate lift, since they cannot shed vorticity in the absence of flow separation.

The lift distribution $\mathrm{d}L/\mathrm{d}x$ will also produce the following overall pitching moment (positive about the y axis) about the $x=0$ reference point.

$$\mathcal{M}_0 \;=\; \int_0^\ell -x\,\frac{\mathrm{d}L}{\mathrm{d}x}\,\mathrm{d}x \;=\; \rho V_\infty^2 \int_0^\ell -x\,\frac{\mathrm{d}(A\tilde{\alpha})}{\mathrm{d}x}\,\mathrm{d}x \;=\; -\rho V_\infty^2\, \ell\, A(\ell)\,\tilde{\alpha}(\ell) \;+\; \rho V_\infty^2 \int_0^\ell A\tilde{\alpha}\,\mathrm{d}x \tag{6.76}$$

With zero base area and zero camber the lift is zero, and the pitching moment simplifies to

$$\mathcal{M} \;=\; \rho V_\infty^2\, \alpha \int_0^\ell A\,\mathrm{d}x \;=\; \rho V_\infty^2\, \mathcal{V}\,\alpha \tag{6.77}$$

about any reference point x location, where $\mathcal{V} = \int_0^\ell A\,\mathrm{d}x$ is the body's volume. An important result is $\mathrm{d}\mathcal{M}/\mathrm{d}\alpha = \rho V_\infty^2 \mathcal{V} > 0$. An angle of attack change $\Delta\alpha$ will therefore produce a pitching moment change $\Delta\mathcal{M}$ of the same sign, which will tend to increase $\Delta\alpha$ even more. A body of revolution therefore exhibits an inherent *pitch instability*, which must be stabilized using fins as on a blimp or submarine, or gyroscopically via axial spin as on a finless projectile or a football thrown with a "spiral."

The results above have also been obtained by Ashley and Landahl [50] who used complex mapping to define the transverse flow. They also assumed a more general "finned" body of revolution with local span $b(x)$ whose cross-section is shown in Figure 6.12. The local z–doublet for this case can be given in terms of an effective area A',

$$\kappa_z(x) \;=\; 2V_\infty\, A'\, \tilde{\alpha} \tag{6.78}$$

$$A'(x) \;=\; \pi\left[\frac{R^4}{(b/2)^2} + (b/2)^2 - R^2\right] \tag{6.79}$$

while the local lift relation (6.69) remains the same. The total lift and moment is therefore given by expressions (6.75) and (6.76) if the area A is replaced by the effective area A' defined above. For the case $b/2 = R$ where the fins have zero width, we have $A' = A$, and the finned-body results reduce to the circular cross-section body results as expected.
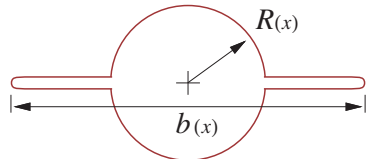
Figure 6.12: Cross section of body of revolution with fins of local span $b(x)$.

6.6.6 Limits of slender-body theory

The conclusion that a rear-pointed body generates no lift assumes strictly potential flow. In reality, slender bodies will have some amount of flow separation if the rear taper is sufficiently rapid or if the local angle of attack is sufficiently large. Fuselages with large rear upsweep angles exhibit such rear separation, and slender delta wings at large angles of attack exhibit *leading edge vortices*. Figure 6.13 shows these flows, and compares them with their strictly-potential flow versions. Although the slender-body approximations and the 2D local far-field expansion (6.66) still remain reasonably valid with such separations, the strengths $\Lambda(x)$ and $\kappa_z(x)$ will become significantly modified. In particular, the free vorticity which is antisymmetric in y will significantly modify the doublet strength κ_z, as can be seen from its definition (2.83). It will therefore modify the local and total lift, and also the moment. Specifically, the separation from the upswept rear body produces a downward bias in the local lift contribution, while the leading edge vortices on a delta wing significantly increase the upward lift, which is known as the *vortex lift* phenomenon. The effect is shown in Figure 6.14 for delta wings of two different aspect ratios.
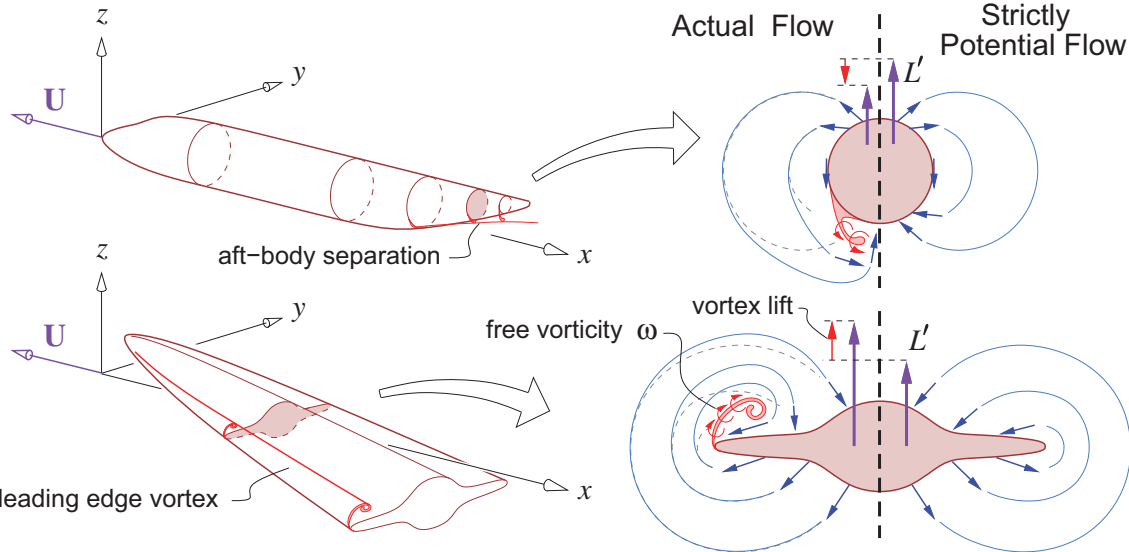
Figure 6.13: Viscous separation from an upswept rear fuselage, and leading edge vortices on a delta wing at high angle of attack. The free vorticity modifies the strictly-potential flow pattern, and also modifies the 2D strengths $\Lambda(x)$ and $\kappa_z(x)$, and the associated aerodynamic loads.

6.6.7 Vortex lift models

Polhamus [51] has developed a method for estimating vortex lift based on the leading-edge suction concept. In this formulation the leading edge suction force magnitude is obtained from the slender-body flow solution for a flat plate, corresponding to the geometry in Figure 6.12 with $R=0$. This force is then applied normal to the surface rather than tangential to the surface, which in effect rotates it by $90°$ about the leading edge line. The equivalent formulation for general lifting surface geometries uses the leading edge suction force defined by equation (6.23), but applied in the normal direction.

$$\mathbf{F}'_{S_{LE}} \;=\; \frac{\pi}{4}\,\rho C^2\,\hat{\mathbf{n}} \qquad\qquad \text{(at sharp leading edge)} \qquad (6.80)$$

This rotation of the leading edge suction force from $\hat{\mathbf{t}}$ to $\hat{\mathbf{n}}$ models the boundary layer vorticity lifting off the surface and forming a free vortex sheet above the surface, as sketched in Figure 6.13 on the bottom right. The force rotation clearly increases the lift, and thus captures the vortex lift contribution. The lift increase reported by Polhamus matches experimental data fairly well.

The rotation of the leading edge suction force changes its direction from partly forward to partly aft, which significantly increases the drag. This effect on drag was also examined by Polhamus [52], with the conclusion that the added drag behaves much like induced drag from the added lift.
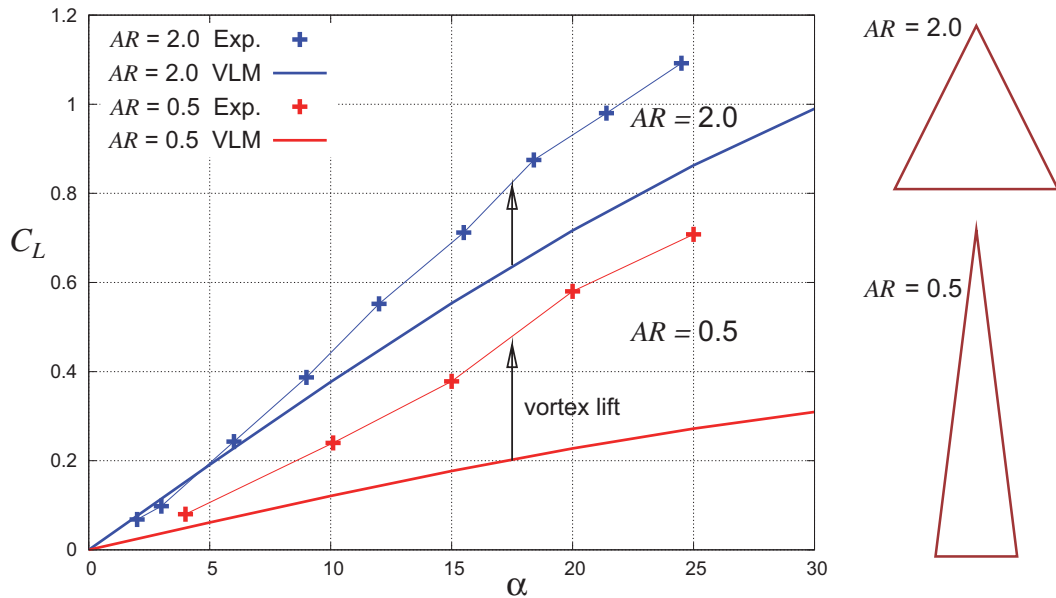
Figure 6.14: Experimental $C_L(\alpha)$ for two delta wings from Polhamus [51], compared to Vortex Lattice Method calculations. Excess lift in the experiment at large angles of attack demonstrates the effect of vortex lift resulting from the formation of leading edge vortices, which the standard VLM does not capture. The effect is captured by Polhamus's vortex lift model.

Chapter 7

Unsteady Aerodynamic Flows

This chapter will examine the general low-speed unsteady potential flow problem. Specifically, we will revisit flow-field modeling in the unsteady case, and also the unsteady Bernoulli equation for the unsteady pressure. The special case of unsteady airfoil flows will be examined in more detail.

7.1 Unsteady Flow-Field Representation

Chapter 2 defined the source density and vorticity as the divergence and curl of the velocity field.

$$\sigma = \nabla \cdot \mathbf{V}$$
$$\boldsymbol{\omega} = \nabla \times \mathbf{V}$$

These involve only spatial derivatives and hence apply instantaneously even if $\mathbf{V}$ is changing in time. Similarly, representation of the velocity field via its source, vorticity, and boundary contributions

$$\mathbf{V}_{(\mathbf{r},t)} = \mathbf{V}_\sigma + \mathbf{V}_\omega + \mathbf{V}_b$$

involves only spatial integrations, and likewise applies instantaneously. An unsteady flow can therefore be represented in the same manner as a steady flow, but all the relevant quantities will now depend on time as well as space.

$$\mathbf{V}_{\sigma(\mathbf{r},t)} \equiv \frac{1}{4\pi} \iiint \sigma(\mathbf{r}',t) \frac{(\mathbf{r}-\mathbf{r}')}{|\mathbf{r}-\mathbf{r}'|^3} \, dx' \, dy' \, dz' \tag{7.1}$$

$$\mathbf{V}_{\omega(\mathbf{r},t)} \equiv \frac{1}{4\pi} \iiint \boldsymbol{\omega}(\mathbf{r}',t) \times \frac{(\mathbf{r}-\mathbf{r}')}{|\mathbf{r}-\mathbf{r}'|^3} \, dx' \, dy' \, dz' \tag{7.2}$$

$$\mathbf{V}_b = \mathbf{V}_\infty \qquad \text{(observer moving steadily in airmass)} \tag{7.3}$$

$$\mathbf{V}_b = \mathbf{0} \qquad \text{(observer fixed in airmass)} \tag{7.4}$$

We see that the unsteadiness of the velocity field is captured entirely by the time dependence of the source and vorticity fields $\sigma(\mathbf{r},t), \boldsymbol{\omega}(\mathbf{r},t)$. Furthermore, since the lumping process is strictly spatial, as in the steady case the integrals above can be simplified using the lumped unsteady sheet strengths $\lambda(s,\ell,t), \boldsymbol{\gamma}(s,\ell,t)$, line strengths $\Lambda(\ell,t), \boldsymbol{\Gamma}(\ell,t)$, or point strengths $\Sigma(t)$. For *free vorticity* such as in trailing wakes, an alternative approach is to move the vortex points rather than change the singularity strengths. In that case (7.2) is still valid, but now the integration points $\mathbf{r}'$ are functions of time.

In typical steady flow applications so far we have assumed that the body is fixed, so that the last boundary-condition component $\mathbf{V}_b$ is the freestream velocity $\mathbf{V}_\infty$. In unsteady flow applications it is often more convenient to represent the body motion explicitly via its velocity $\mathbf{U}(t)$ and rotation rate $\boldsymbol{\Omega}(t)$. In this case we choose $\mathbf{V}_b = \mathbf{0}$, and $\mathbf{V}$ then represents the "perturbation velocity," which is what's seen by an observer stationary with respect to the airmass.

7.2   Unsteady Potential Flow

The Helmholtz vorticity transport equation (1.95) dictates that aerodynamic flows have zero vorticity everywhere except in thin viscous layers adjacent to a solid body and in its trailing wakes. This conclusion remains valid for unsteady flows.

$$\boldsymbol{\omega} \;\equiv\; \nabla \times \mathbf{V} \;=\; \mathbf{0} \qquad \text{(outside viscous layers)} \tag{7.5}$$

Furthermore, the low-speed continuity equation is unchanged in the unsteady case,

$$\sigma \;\equiv\; \nabla \cdot \mathbf{V} \;=\; 0 \tag{7.6}$$

so that the velocity field still has zero divergence everywhere in the flow interior. The overall conclusion is that the physical constraints on the vorticity and source distributions are the same in both steady and unsteady low speed flows. The instantaneous velocity field outside the viscous layers (or the entire Equivalent Inviscid Flow, introduced in Chapter 3) can still be represented by the perturbation potential $\varphi_{(\mathbf{r},t)}$.

$$\mathbf{V}_{(\mathbf{r},t)} \;=\; \nabla\varphi \tag{7.7}$$

If source sheets and doublet sheets are used as in most panel methods, then the unsteady potential can be expressed explicitly via the usual superposition integrals, which now have unsteady sheet strength distributions.

$$\varphi_{(\mathbf{r},t)} \;=\; \varphi_\lambda \;+\; \varphi_\mu \tag{7.8}$$

$$\varphi_\lambda{}_{(\mathbf{r},t)} \;=\; \frac{1}{4\pi} \iint \lambda_{(s,\ell,t)} \frac{-1}{|\mathbf{r}-\mathbf{r}'|} \, ds \, d\ell \tag{7.9}$$

$$\varphi_\mu{}_{(\mathbf{r},t)} \;=\; \frac{1}{4\pi} \iint \mu_{(s,\ell,t)} \frac{\hat{\mathbf{n}} \cdot (\mathbf{r}-\mathbf{r}')}{|\mathbf{r}-\mathbf{r}'|^3} \, ds \, d\ell \tag{7.10}$$

7.3   Governing Equations for Unsteady Potential Flow

Figure 7.1 shows a rigid body moving through the fluid, seen in two different frames.
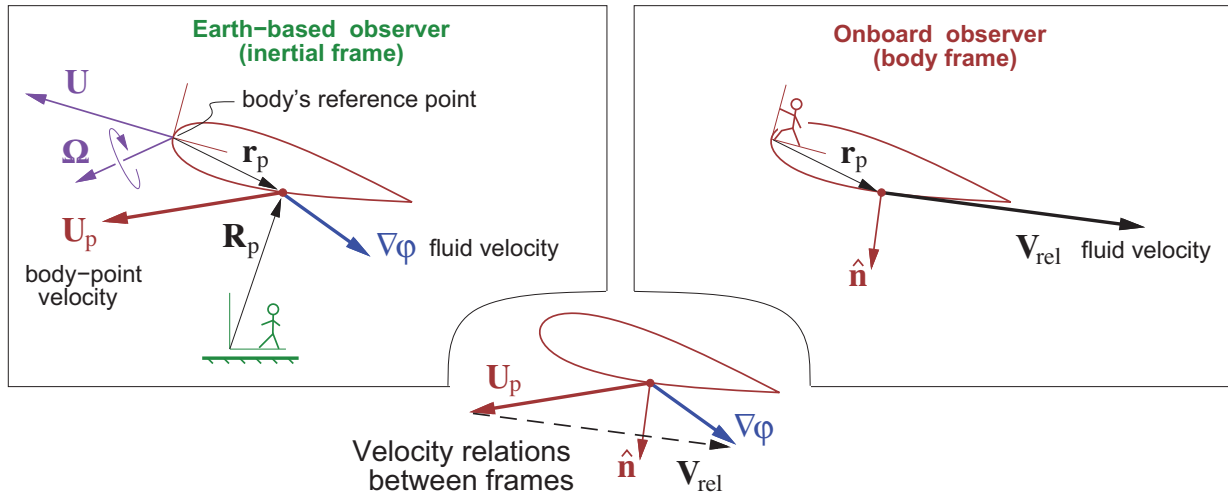
Figure 7.1: Positions and velocities seen by an Earth-based observer, and by an onboard observer.

The body's motion is defined by the velocity $\mathbf{U}(t)$ of some chosen reference point on the body, and by the body's rotation rate $\mathbf{\Omega}(t)$. An arbitrary point P on the body has location $\mathbf{r}_\mathrm{p}$ relative to the reference point, and $\mathbf{R}_\mathrm{p}$ relative to the ground observer. This point's velocity relative to the ground observer is then

$$\mathbf{U}_\mathrm{p} \;=\; \frac{\mathrm{d}\mathbf{R}_\mathrm{p}}{\mathrm{d}t} \;=\; \mathbf{U} \;+\; \mathbf{\Omega}\times\mathbf{r}_\mathrm{p} \tag{7.11}$$

which is the same as equation (6.3) considered earlier. The fluid velocity as seen by the ground observer is $\nabla\varphi$ as defined previously. The local fluid velocity seen in the local body frame at point $\mathbf{r}$ is then obtained by subtracting the body frame's local velocity.

$$\mathbf{V}_\mathrm{rel}(\mathbf{r},t) \;=\; \nabla\varphi \;-\; (\mathbf{U} + \mathbf{\Omega}\times\mathbf{r}) \tag{7.12}$$

The field equation and boundary conditions for the perturbation potential $\varphi(\mathbf{r},t)$ are

$$
\begin{aligned}
\frac{\partial^2\varphi}{\partial x^2} + \frac{\partial^2\varphi}{\partial y^2} + \frac{\partial^2\varphi}{\partial z^2} \;\equiv\; \nabla^2\varphi \;&=\; 0 \\[4pt]
\text{Solid-body BC:}\quad \mathbf{V}_\mathrm{rel}\cdot\hat{\mathbf{n}} \;&=\; 0 \\[2pt]
\text{or equivalently:}\quad \nabla\varphi\cdot\hat{\mathbf{n}} \;&=\; (\mathbf{U}+\mathbf{\Omega}\times\mathbf{r})\cdot\hat{\mathbf{n}} \\[2pt]
\text{Freestream BC:}\quad \varphi \;&\to\; 0
\end{aligned}
\tag{7.13}
$$

which must all instantaneously hold for each instant in time. The time dependence arises through the body motion $\mathbf{U}(t)$ and $\mathbf{\Omega}(t)$, and possibly also through atmospheric motion and body deformation as will be described later.

7.3.1   Pressure calculation

Chapter 1 gave the derivation if the unsteady Bernoulli equation (1.105) for incompressible flow:

$$\frac{\partial\varphi}{\partial t} \;+\; \frac{1}{2}V^2 \;+\; \frac{p}{\rho} \;+\; gz \;=\; C \tag{7.14}$$

Here we have $V^2 = |\nabla\varphi|^2$, and we will also absorb the hydrostatic term gz into p/ρ, as described in Section 1.9.3. The integration constant C can be evaluated at any point where the pressure and velocity are known, such as at infinity where $p = p_\infty$, and where the fluid is at rest so that all φ derivatives vanish.

$$p \;+\; \frac{1}{2}\rho\,|\nabla\varphi|^2 \;+\; \rho\frac{\partial\varphi}{\partial t} \;=\; p_\infty \tag{7.15}$$

It's essential to note that (7.15) as written applies only in an inertial frame of reference, since it was ultimately derived from the momentum equation (1.86) for which we set $\mathbf{f}$ to be gravity, omitting any non-inertial forces. This is why we chose $V^2 = |\nabla\varphi|^2$, and <u>not</u> $V^2 = |\mathbf{V}_\mathrm{rel}|^2$. Furthermore, the time derivative $\partial\varphi/\partial t$ must be performed at a spatial point which is inertial, meaning that this point is either stationary ($V_\infty = 0$) or at most translating with uniform speed ($V_\infty \neq 0$) relative to Earth. Specifically, the time derivative must <u>not</u> be performed at a point fixed on an accelerating or rotating body.

A practical complication here is that because the solution to the potential-flow problem as formulated above is given in the body coordinates in the form $\varphi(\mathbf{r},t)$, its explicit time derivative is at fixed $\mathbf{r}$ which is not an inertial point. However, we require a time derivative at fixed $\mathbf{R}$ which is inertial. The distinction between the time derivatives in the two frames is shown in Figure 7.2.
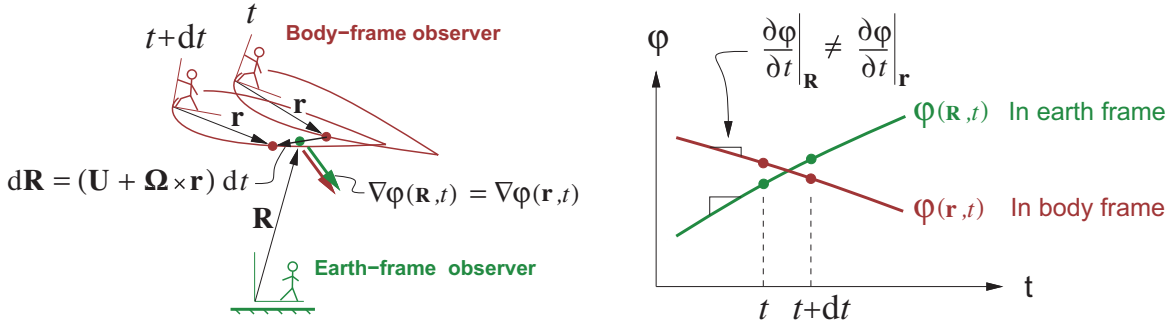
Figure 7.2: Potential-field time variation at a point $\mathbf{R}$ fixed in the Earth frame, and another point $\mathbf{r}$ fixed in the body frame. At the moment when the points coincide, the φ and $\nabla\varphi$ values in the two frames are equal, but the time derivatives $\partial\varphi/\partial t$ are not.

To perform the frame conversion, we first note from Figure 7.1 that positions in the two frames are related by the correspondence function $\mathbf{R}(\mathbf{r},t)$ which obeys

$$\left.\frac{\partial\mathbf{R}}{\partial t}\right|_{\mathbf{r}} = \mathbf{U} + \mathbf{\Omega}\times\mathbf{r}$$

which can then be used to relate time derivatives in the two frames. Considering the potential to be in the form $\varphi(\mathbf{R}(\mathbf{r},t),t)$, we obtain its time rate in the body frame via the chain rule,

$$\dot{\varphi} \equiv \left.\frac{\partial\varphi}{\partial t}\right|_{\mathbf{r}} = \left.\frac{\partial\varphi}{\partial t}\right|_{\mathbf{R}} + \left.\frac{\partial\varphi}{\partial\mathbf{R}}\right|_{t}\cdot\left.\frac{\partial\mathbf{R}}{\partial t}\right|_{\mathbf{r}} = \left.\frac{\partial\varphi}{\partial t}\right|_{\mathbf{R}} + \nabla\varphi\cdot(\mathbf{U}+\mathbf{\Omega}\times\mathbf{r}) \tag{7.16}$$

where $\partial\varphi/\partial\mathbf{R}$ is just a more intuitive way to write the spatial gradient $\nabla\varphi$ in this context. Relation (7.16) then gives the potential's time-rate in the Earth frame entirely in terms of quantities in the body frame.

$$\left.\frac{\partial\varphi}{\partial t}\right|_{\mathbf{R}} = \dot{\varphi} - \nabla\varphi\cdot(\mathbf{U}+\mathbf{\Omega}\times\mathbf{r}) \tag{7.17}$$

The pressure can now be expressed using the unsteady Bernoulli equation (7.15) applied in the frame of the Earth-based observer in Figure 7.2:

$$p(\mathbf{r},t) = p_\infty - \tfrac{1}{2}\rho\,|\nabla\varphi|^2 - \rho\left.\frac{\partial\varphi}{\partial t}\right|_{\mathbf{R}} \tag{7.18}$$

$$\boxed{p(\mathbf{r},t) = p_\infty - \tfrac{1}{2}\rho\,|\nabla\varphi|^2 + \rho\,\nabla\varphi\cdot(\mathbf{U}+\mathbf{\Omega}\times\mathbf{r}) - \rho\,\dot{\varphi}} \tag{7.19}$$

An equivalent alternative form is in terms of the body-relative velocity $\mathbf{V}_{\text{rel}}$ given by (7.12).

$$p(\mathbf{r},t) = p_\infty + \tfrac{1}{2}\rho\,|\mathbf{U}+\mathbf{\Omega}\times\mathbf{r}|^2 - \tfrac{1}{2}\rho\,|\mathbf{V}_{\text{rel}}|^2 - \rho\,\dot{\varphi} \tag{7.20}$$

It's useful to note that in a steady flow situation we have

$$\mathbf{U} = -\mathbf{V}_\infty$$
$$\mathbf{\Omega} = \mathbf{0}$$
$$\dot{\varphi} = 0$$

in which case (7.20) reduces to the familiar steady Bernoulli equation.

$$p(\mathbf{r},t) = p_\infty + \tfrac{1}{2}\rho V_\infty^2 - \tfrac{1}{2}\rho\,|\mathbf{V}_{\text{rel}}|^2$$

7.4   Potential Jump of Unsteady Vortex Sheet

The physical zero pressure jump requirement across a vortex sheet was combined with the steady Bernoulli equation in Section 5.4 to obtain the convection condition (5.15) for the potential jump. For the unsteady case this needs to be re-examined because of the additional term in the unsteady Bernoulli equation (7.19). We therefore consider an unsteady vortex sheet shown in Figure 7.3 which has separate potentials and velocities on its upper and lower sides. The vortex sheet can represent either a thin lifting surface or a wake.
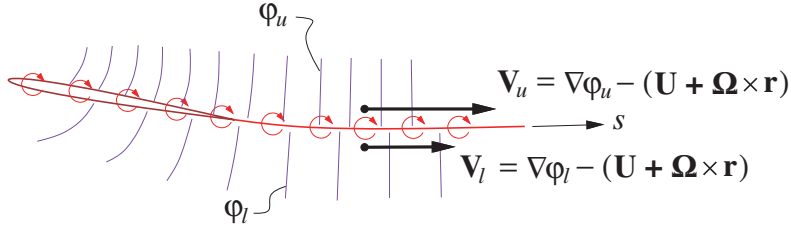
Figure 7.3: Perturbation potential isolines and airfoil-frame velocities above and below an unsteady vortex sheet, on the airfoil and on the wake.

As in the steady case, a thin unsteady wake has the same physical requirement of a zero static pressure jump $\Delta p \equiv p_l - p_u$ across it. Taking the difference of the unsteady pressure expression (7.20) between a lower and upper point across the sheet, and setting the result to zero gives

$$\Delta p = 0 \qquad \rightarrow \qquad \tfrac{1}{2}\left(\mathbf{V}_u \cdot \mathbf{V}_u - \mathbf{V}_l \cdot \mathbf{V}_l\right) + \left(\dot{\varphi}_u - \dot{\varphi}_l\right) \;=\; 0$$

$$\tfrac{1}{2}\left(\mathbf{V}_u + \mathbf{V}_l\right) \cdot \left(\mathbf{V}_u - \mathbf{V}_l\right) + \left(\dot{\varphi}_u - \dot{\varphi}_l\right) \;=\; 0$$

$$\mathbf{V}_a \cdot \widetilde{\nabla}(\Delta\varphi) + (\dot{\overline{\Delta\varphi}}) \;=\; 0 \qquad\qquad (7.21)$$

where $\mathbf{V}_u, \mathbf{V}_l$ are the upper and lower $\mathbf{V}_{\mathrm{rel}}$ velocities, $\mathbf{V}_a$ is the average *sheet velocity*

$$\mathbf{V}_a = \tfrac{1}{2}\left(\mathbf{V}_u + \mathbf{V}_l\right)$$

and $\widetilde{\nabla}()$ is the surface gradient within the sheet. Note that (7.21) reduces to the earlier steady-flow potential jump result (5.15) if we set $(\dot{\overline{\Delta\varphi}}) = 0$.

7.4.1   Potential-jump convection

The unsteady wake zero pressure jump condition (7.21) can be rewritten as a substantial derivative.

$$\frac{\partial(\Delta\varphi)}{\partial t} + \mathbf{V}_a \cdot \widetilde{\nabla}(\Delta\varphi) \;=\; 0$$

$$\text{or} \qquad \frac{\mathrm{D}(\Delta\varphi)}{\mathrm{D}t} \;=\; 0 \qquad \text{(on wake)} \qquad (7.22)$$

Equation (7.22) implies that the wake potential jump $\Delta\varphi(s,\ell,t) \equiv \varphi_u - \varphi_l$, set initially at the trailing edge by the Kutta condition, convects unchanged at the sheet velocity $\mathbf{V}_a$, as sketched in Figure 7.4.

7.4.2   Shed vorticity

From Figure 7.3 we see that the wake sheet has a tangential velocity jump $\mathbf{V}_u - \mathbf{V}_l = \widetilde{\nabla}(\Delta\varphi)$, which corresponds to a vortex sheet of the following strength.

$$\boldsymbol{\gamma} \;=\; \hat{\mathbf{n}} \times (\mathbf{V}_u - \mathbf{V}_l) \;=\; \hat{\mathbf{n}} \times \widetilde{\nabla}(\Delta\varphi) \qquad\qquad (7.23)$$
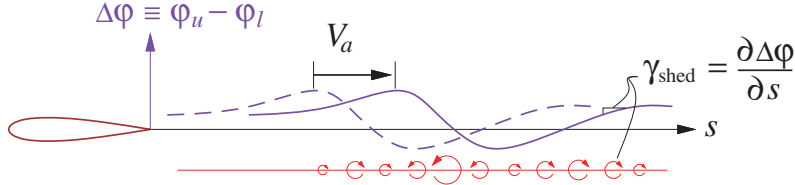
Figure 7.4: Potential jump $\Delta\varphi$ across a wake convects without change at the average sheet velocity. If the flow is unsteady, the resulting streamwise gradients in $\Delta\varphi$ imply the presence of shed vorticity perpendicular to $\mathbf{V}_a$.

The *trailing vorticity* is the streamwise component of this $\boldsymbol{\gamma}$ vector, and the *shed vorticity* is the transverse component. Choosing the s coordinate to be parallel to $\mathbf{V}_a$,

$$\hat{\mathbf{s}} \equiv \frac{\mathbf{V}_a}{|\mathbf{V}_a|} \tag{7.24}$$

gives the following explicit definitions of the trailing and shed vorticity components.

$$\gamma_{\text{trail}} \equiv \hat{\mathbf{s}} \cdot \boldsymbol{\gamma} \tag{7.25}$$

$$\gamma_{\text{shed}} \equiv (\hat{\mathbf{s}} \times \boldsymbol{\gamma}) \cdot \hat{\mathbf{n}} = \hat{\mathbf{s}} \cdot \widetilde{\nabla}(\Delta\varphi) = \frac{\partial \Delta\varphi}{\partial s} \tag{7.26}$$

Comparing equation (7.26) with (7.21) together with the $\hat{\mathbf{s}}$ definition shows that γ_{shed} can be alternatively given by the time rate of $\Delta\varphi$.

$$\gamma_{\text{shed}} = -\frac{(\dot{\Delta\varphi})}{|\mathbf{V}_a|} \begin{cases} = 0 & , \quad \text{steady flow} \\ \neq 0 & , \quad \text{unsteady flow} \end{cases} \tag{7.27}$$

Shed vorticity is therefore present only in unsteady flows, and is a major complication in the formulation of unsteady potential flow calculation methods.

7.5 Unsteady Flow Categories

As derived above, unsteady potential flow introduces three basic new effects not present in steady flow: unsteady $\nabla\varphi \cdot \hat{\mathbf{n}}$ due to body motion $\mathbf{U}(t), \boldsymbol{\Omega}(t)$, the additional $\rho\,\partial\varphi/\partial t$ term in the Bernoulli equation for the pressure, and the generation of shed vorticity γ_{shed}. Only some of these effects may be important in any given situation, giving a natural categorization of unsteady flows summarized in Table 7.1.

Table 7.1: Unsteady flow regimes and retained or discarded effects

	$\partial(\nabla\varphi \cdot \hat{\mathbf{n}})/\partial t$	$\rho\,\partial\varphi/\partial t$	γ_{shed}
Steady	0	0	0
Quasi-steady I	$\checkmark$	neglected	neglected
Quasi-steady II	$\checkmark$	neglected	estimated
Unsteady	$\checkmark$	$\checkmark$	$\checkmark$

The quasi-steady approximation is employed for defining the aerodynamic loads in flight in Chapter 6, where the unsteady forces on a maneuvering aircraft are assumed to be the same as those in steady flight at the same instantaneous flight condition defined by the parameters $\alpha, \beta, \bar{p}, \bar{q}, \bar{r}$. In the "Quasi-steady II" case a slight refinement is made by estimating the shed vorticity effects via the additional $\dot{\bar{\alpha}}$ parameter.

7.6 Unsteady Panel Method

Standard panel methods which solve the steady potential flow problem can be extended to the unsteady case. The source+doublet panel method will be used here to illustrate these necessary modifications.

7.6.1 Sources of unsteadiness

Figure 7.5 shows the possible origins of flow unsteadiness in an aerodynamic flow which must be captured by any general unsteady flow solution method. These are further described below.
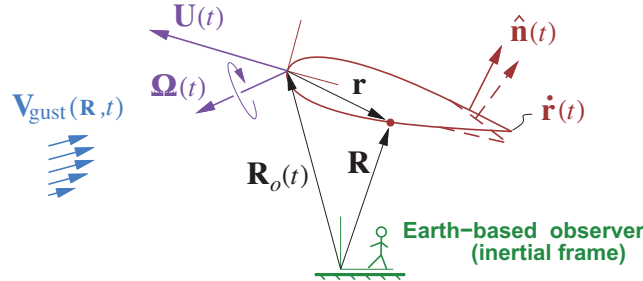
Figure 7.5: Typical sources of unsteadiness in an aerodynamic flow are unsteady body motion $\mathbf{U}(t), \mathbf{\Omega}(t)$, unsteady body deformation $\hat{\mathbf{n}}(t), \dot{\mathbf{r}}(t)$, and a spatially-varying or unsteady atmospheric velocity field $\mathbf{V}_{\text{gust}}(\mathbf{R},t)$.

Body motion

One possible source of unsteadiness is unsteady rigid-body motion. This is defined by the specified velocity and rotation rate $\mathbf{U}(t)$ and $\mathbf{\Omega}(t)$ introduced in the body-point velocity definition (7.11).

Gust field

Unsteady flow can also be caused by a nonuniform atmospheric motion or "gust" velocity field $\mathbf{V}_{\text{gust}}(\mathbf{R},t)$ which is specified. The instantaneous Earth position of any body point $\mathbf{r}$ on the aircraft is

$$\mathbf{R}(\mathbf{r},t) = \mathbf{R}_{\text{o}}(t) + \mathbf{r}$$

where $\mathbf{R}_{\text{o}}$ is obtained by integrating $\mathbf{U}$ in time, as described in Chapter 9. The gust velocity at the body point $\mathbf{r}$ is then

$$\mathbf{V}_{\text{gust}}(\mathbf{r},t) = \mathbf{V}_{\text{gust}}(\mathbf{R}(\mathbf{r},t),t)$$

where Earth/body axis conversions using the body Euler angles would be used, as described in Section 9.4. These are obtained by integration of the aircraft rotation rate $\mathbf{\Omega}(t)$. In reality, any such gust field will be modified by the presence of the body, but for the typical gust field which has long variations relative to the body size this effect will be small and is generally neglected. This is consistent with classical thin airfoil approximations.

Body deformation

The third cause of flow unsteadiness is a time-dependent body geometry with local velocity $\dot{\mathbf{r}}$, such as an oscillating flap or a flapping wing. If the deformation of the motion is small, its effects can be approximated by holding the geometry fixed, but still using the actual surface velocity $\dot{\mathbf{r}}$ and normal vectors $\hat{\mathbf{n}}$ when forming the flow-tangency condition.

7.6.2 Wake convection

A major complication in calculation of unsteady flows is the evolution of the wake, both its doublet strength as well as its geometry. The physically correct wake shape is the streakline (in 2D) or streaksurface (in 3D) attached to the trailing edge. An example is shown in Figure 7.6 for a heaving airfoil. In the most physically accurate free wake case the wake shape's evolution in time depends on the history of the velocity field of the airfoil+wake combination, and hence depends on the flow solution itself. This renders the problem nonlinear, since the kernel functions for the wake doublet sheet, in particular the $\mathbf{r}'$ values in the φ_μ integral (7.10), will now depend on the solution.
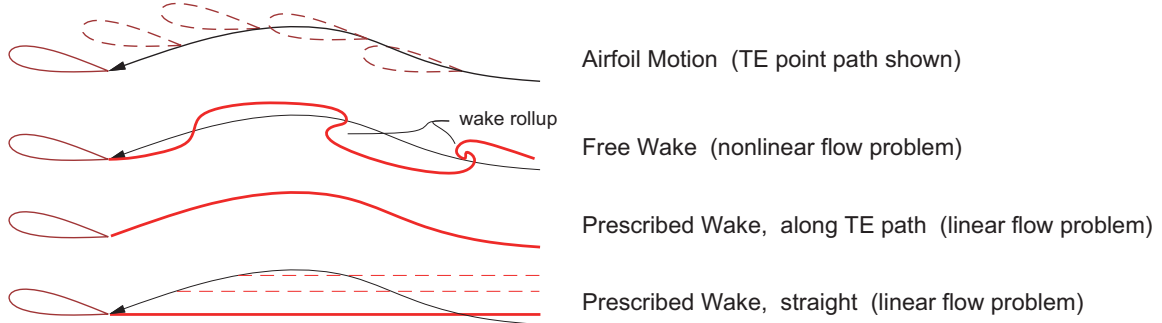
Figure 7.6: Three different wake geometry models. In free wake model, spanwise wake roll-up typically occurs at locations of strong shed vorticity.

A further complication is that a free vortex sheet will in general undergo *roll-up* wherever the vorticity is concentrated. Steady flow problems which only have trailing vorticity typically have wake roll-up at the wake sheet's wingtip edges, as sketched in Figure 5.4. Unsteady flow problems in addition also have roll-up caused by shed vorticity. The extreme deformation of the wake shape undergoing roll-up makes accurate tracking of this shape difficult and computationally expensive.

These complications associated with a free wake can be mostly eliminated by using the *prescribed-wake assumption*. Here the convection of the wake by the velocity field is ignored, and instead the wake geometry is prescribed explicitly. Two possible choices are shown in Figure 7.6. The simplest straight-wake assumption is quite adequate for modest airfoil motions, and is almost invariably used by Vortex-Lattice methods. The great advantage of a prescribed wake is that it renders the potential flow problem linear, since the kernel functions then become independent of the flow solution. Unless the rolled-up wake closely interacts with a downstream surface, the neglect of roll-up generally results in very minor errors in a potential flow solution.

7.6.3 Panel method formulation

Figure 7.7 shows the velocity field relative to the body, both on the exterior and the interior. These are defined as

$$\mathbf{V}_{(\mathbf{r},t)} \;=\; -\mathbf{U} - \mathbf{\Omega}\times\mathbf{r} - \dot{\mathbf{r}} + \mathbf{V}_{\text{gust}} + \nabla\varphi \qquad \text{(physical exterior velocity)} \qquad (7.28)$$

$$\mathbf{V}_{\text{int}(\mathbf{r},t)} \;=\; -\mathbf{U} - \mathbf{\Omega}\times\mathbf{r} - \dot{\mathbf{r}} + \mathbf{V}_{\text{gust}} \qquad\qquad \text{(nonphysical interior velocity)} \qquad (7.29)$$

where only $\nabla\varphi$ is unknown a priori. The physical flow-tangency requirement on the exterior is

$$\mathbf{V} \cdot \hat{\mathbf{n}} \;=\; 0 \qquad (7.30)$$

so that the source sheet strength is

$$\lambda \;\equiv\; (\mathbf{V} - \mathbf{V}_{\text{int}}) \cdot \hat{\mathbf{n}} \;=\; -\mathbf{V}_{\text{int}} \cdot \hat{\mathbf{n}} \qquad (7.31)$$

which is known and thus can be explicitly specified for each point on the body surface.

If we now specify a zero interior potential, $\varphi_{\text{int}} = 0$, the doublet sheet strength then becomes the physical external perturbation potential φ, while on the wake it represents the physical jump $\Delta\varphi$.

$$\mu \equiv \varphi - \varphi_{\text{int}} = \varphi \tag{7.32}$$

$$\mu_{\text{w}} = \Delta\varphi \tag{7.33}$$
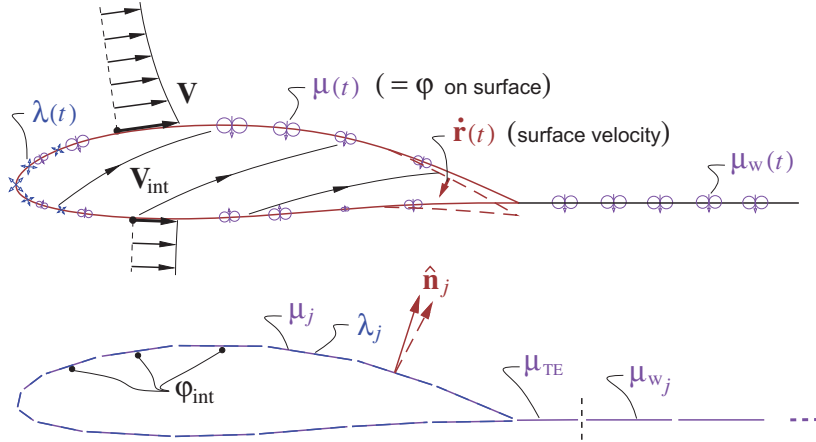
Figure 7.7: Body-relative exterior and interior velocities represented by body motion, gust field, and surface source and doublet sheets, shown in top figure. Panel discretization of the sheet strengths is shown in the bottom figure.

The zero interior potential is imposed via Green's identity

$$\varphi_{\text{int}} = -\frac{1}{2}\mu + \frac{1}{4\pi}\iint \mu \nabla\left(\frac{1}{r}\right)\cdot\hat{\mathbf{n}}\ \mathrm{d}\mathcal{S} + \frac{1}{4\pi}\iint \lambda\frac{-1}{r}\ \mathrm{d}\mathcal{S} + \frac{1}{4\pi}\iint \mu_{\text{w}} \nabla\left(\frac{1}{r}\right)\cdot\hat{\mathbf{n}}\ \mathrm{d}\mathcal{S}_{\text{w}} = 0 \tag{7.34}$$

which after evaluation on the paneled geometry becomes the following matrix equation for the unknown surface-panel doublet strengths μ_j.

$$A_{ij}\,\mu_j = -A_{ij}^{\text{w}}\,\mu_{\text{w}_j} - B_{ij}\lambda_j \tag{7.35}$$

The trailing edge wake panel strength at each spanwise location is an unknown, but is related to the two top and bottom surface strengths at the trailing edge at that same location.

$$\mu_{\text{w}_{TE}} = (\mu_{j_{TE}})_u + (\mu_{j_{TE}})_l \tag{7.36}$$

This is equivalent to a Kutta condition.

The unsteady solution proceeds in a sequence of time steps, with the following operations performed at each time step:

1. Set the source panel strengths λ_j from the known $\mathbf{V}_{\text{int}}(\mathbf{r},t)$.

2. Set all the wake-panel doublet strengths μ_{w_j} from the previous time step, by convecting μ_{w} without change along $\mathbf{V}_a$, according to the zero wake-load condition.

$$\frac{\mathrm{D}\mu_{\text{w}}}{\mathrm{D}t} = 0$$

A common approximation made here is to assume

$$\mathbf{V}_a \simeq -(\mathbf{U} + \boldsymbol{\Omega}\times\mathbf{r})$$

which is computationally simpler and much less expensive to evaluate.

3. Evaluate the righthand side in (7.35) using the known λ_j and μ_{w_j}

4. Solve linear system (7.35) for μ_j, using the same LU-factored A_{ij} matrix for all time steps.

5. Using $\mu_j, \mu_{w_j}, \lambda_j$, evaluate $\dot{\varphi}, \nabla\varphi, \mathbf{V}$ on surface, compute pressure and airloads.

For a much more detailed description of the necessary calculations see Katz and Plotkin [4].

The 3D unsteady panel method described above is quite general, but provides little insight into unsteady flow behavior except via numerical experimentation. Hence we will next consider simplified models of several specific unsteady flows of interest. Suitable approximations will be used as needed to obtain more concise semi-analytical results for unsteady aerodynamic forces and moments.

7.7 Unsteady 2D Airfoil

The unsteady 2D airfoil problem is important in many applications, such as prediction of gust loads on wings, cyclic loads on rotor blades, and the onset of flutter. See Bisplinghoff et al [53] for an overview. Here we will consider the case of a rigid airfoil moving at a uniform horizontal speed U, while undergoing unsteady heaving $h(t)$ and pitching $\theta(t)$ displacements about a baseline position and angle of attack α_0, as shown in Figure 7.8. Note that the heave displacement h is defined positive down.
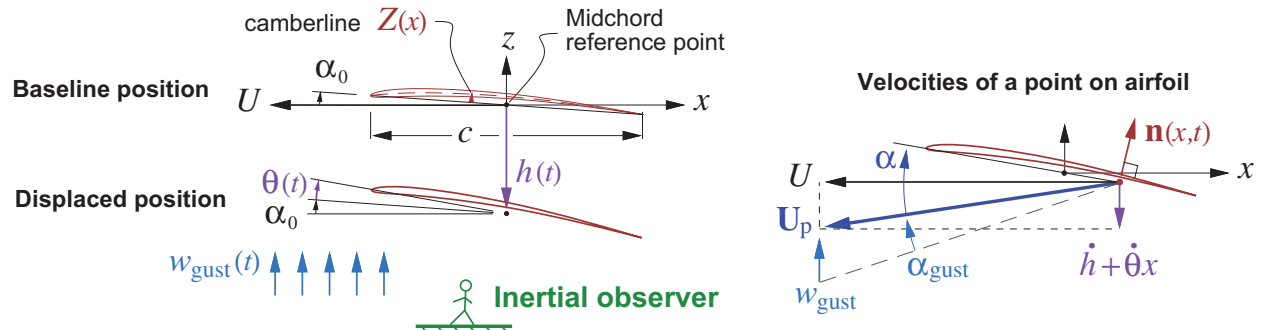
Figure 7.8: Airfoil moving at uniform horizontal baseline velocity U. Heave and pitch displacements $h(t), \theta(t)$ from baseline position give net resultant vertical velocity $\dot{h} + \dot{\theta}x$ at a some point x, which then define the local angle of attack $\alpha_{(x,t)}$. Some vertical gust velocity $w_{\text{gust}}(t)$ produces an additional angle of attack α_{gust}.

7.7.1 Geometric relations

The assumptions of first-order thin airfoil theory will be employed here. The airfoil camberline shape is $Z(x)$, with a negligibly small thickness. The geometric and flow angles are assumed to be small.

$$Z' \ll 1 \quad , \quad \alpha_0, \theta \ll 1 \quad , \quad \dot{h}, \dot{\theta}c, w_{\text{gust}} \ll U$$

Following historical convention for unsteady airfoil analysis, the airfoil extends over $-c/2 \le x \le c/2$, so the reference point $x=0$ is at midchord, as shown in Figure 7.8.

7.7.2 Problem formulation

The problem will be formulated in the frame and the axes of the inertial Earth-based observer. The camberline's normal vector therefore rotates with the airfoil.

$$\mathbf{n}(x,t) = (\alpha_0 + \theta - Z')\hat{\mathbf{x}} + \hat{\mathbf{z}} \tag{7.37}$$

The small-angle assumptions give the following total velocity of a point on the airfoil.

$$\mathbf{U}_{\mathrm{p}(x,t)} = -U\hat{\mathbf{x}} - (\dot{h} + \dot{\theta}x)\hat{\mathbf{z}} \tag{7.38}$$

The perturbation velocity field is represented by a vortex sheet of strength $\gamma(x)$ on the airfoil and wake. The wake portion is absent in steady thin airfoil theory (Appendix D), but is needed here to represent shed vorticity. In the Earth frame, the total vortex sheet strength gives the following instantaneous vertical fluid velocity w at any given location on the x-axis, which adds to any w_{gust} already present.

$$w(x,t) = \frac{1}{2\pi} \int_{-c/2}^{\infty} -\gamma(x',t) \frac{\mathrm{d}x'}{x-x'} \tag{7.39}$$

In the airfoil frame, the corresponding fluid velocity at location x is then

$$\mathbf{V}_{\mathrm{rel}} = (w + w_{\mathrm{gust}})\,\hat{\mathbf{z}} - \mathbf{U}_{\mathrm{p}} = U\hat{\mathbf{x}} + \left(\dot{h} + \dot{\theta}x + w + w_{\mathrm{gust}}\right)\hat{\mathbf{z}} \tag{7.40}$$

which is then used in the usual flow tangency condition on the camberline.

$$\mathbf{V}_{\mathrm{rel}} \cdot \mathbf{n} = 0 \qquad\qquad (-c/2 \le x \le c/2) \tag{7.41}$$

This applies only on the airfoil. In the wake, we must instead impose the zero pressure jump condition, by taking the x-derivative of the $\Delta\varphi$ convection equation (7.22), which then becomes the γ convection equation. The governing equations over the entire vortex sheet $-c/2 \le x < \infty$ are then stated as follows.

$$\frac{1}{2\pi} \int_{-c/2}^{\infty} \gamma(x',t) \frac{\mathrm{d}x'}{x-x'} = U\alpha_0 - UZ' + \dot{h} + (U\theta + \dot{\theta}x) + w_{\mathrm{gust}} \qquad (-c/2 \le x \le c/2) \tag{7.42}$$

$$\frac{\partial\gamma}{\partial t} + U\frac{\partial\gamma}{\partial x} = 0 \qquad\qquad (c/2 \le x < \infty) \tag{7.43}$$

The pressure loading required to calculate the lift and moment is obtained from equation (7.21). This in turn requires the time rate of the potential jump, which is defined in terms of the vortex sheet strength time rate.

$$\Delta p(x,t) = \rho\left(\dot{\overline{\Delta\varphi}}\right) + \rho U\gamma \tag{7.44}$$

$$(\dot{\overline{\Delta\varphi}})(x,t) = \int_{-c/2}^{x} \dot{\gamma}(x',t)\,\mathrm{d}x' \tag{7.45}$$

Because equations (7.42) and (7.43) are both linear in γ, their solution $\gamma(x,t)$ and corresponding $\Delta\varphi(x,t)$ and $\Delta p(x,t)$ can be decomposed into five independent components, with each component determined entirely by one of the five righthand side source terms in (7.42).

$$\gamma(x,t) = \gamma_\alpha(x) + \gamma_Z(x) + \gamma_h(x,t) + \gamma_\theta(x,t) + \gamma_{\mathrm{gust}}(x,t) \tag{7.46}$$

The first two contributions γ_α, γ_Z are steady since they depend only on the fixed baseline angle of attack α_0 and camberline shape $Z(x)$, respectively. These are treated by standard steady first-order thin airfoil theory, as derived in Appendix D. This result for the steady case is

$$\left.\begin{aligned} c_\ell &= c_{\ell_0} + 2\pi\alpha_0 \\ c_{m_{c/4}} &= c_{m_0} \end{aligned}\right\} \qquad \text{(steady baseline)}$$

where c_{ℓ_0} and c_{m_0} depend only on the camberline shape. In the subsequent sections we will ignore these steady contributions and focus only on the three remaining unsteady parts driven by $h(t), \theta(t), w_{\mathrm{gust}}(t)$ which determine $\gamma_h, \gamma_\theta, \gamma_{\mathrm{gust}}$, respectively, and also their corresponding unsteady lift and moment.

7.7.3   Canonical impulse solutions

A solution to equations (7.42) and (7.43) have been obtained by Wagner [54] based on a unit step in $\dot{h}, \theta, \dot{\theta}$ corresponding to a sudden change of airfoil motion in heave rate, pitch, and pitch rate. Küssner [55] obtained a solution for the case of a unit step of w_{gust}, corresponding to the airfoil flying into a uniform vertical gust field with a sharp boundary.

In the Wagner case an important quantity is the angle of attack relative to the camber line at the $\frac{3}{4}$-chord location, or $x = c/4$.

$$\alpha_{3c/4} = \frac{\dot{h}}{U} + \theta + \frac{\dot{\theta}c}{4U} \tag{7.47}$$

In the Küssner case the relevant quantity is the apparent angle of attack resulting from the vertical gust velocity shown in Figure 7.8, which is assumed to act everywhere on the chord.

$$\alpha_{\text{gust}} = \frac{w_{\text{gust}}}{U} \tag{7.48}$$

If these quantities have step jumps of $\Delta\alpha_{3c/4}$ and/or $\Delta\alpha_{\text{gust}}$ at $t=0$, then the lift is

$$\frac{L'}{\frac{1}{2}\rho U^2 c} \equiv c_\ell(\bar{t}) = c_{\ell_Q} + c_{\ell_A} \tag{7.49}$$

$$c_{\ell_Q}(\bar{t}) = 2\pi \, \Delta\alpha_{3c/4} \, \Phi(\bar{t}) + 2\pi \, \Delta\alpha_{\text{gust}} \, \Psi(\bar{t}) \tag{7.50}$$

$$c_{\ell_A}(\bar{t}) = 2\pi \left[\frac{1}{2}\frac{\Delta\dot{h}}{U} + \frac{1}{2}\Delta\theta \right] \delta(\bar{t}) \tag{7.51}$$

$$\bar{t} \equiv \frac{U\,t}{c/2} \tag{7.52}$$

where $\Phi(\bar{t})$ is the *Wagner function*, $\Psi(\bar{t})$ is the *Küssner function*, and $\delta(\bar{t})$ is the unit impulse function. Their argument $\bar{t}$ is a non-dimensionalized time, which can also be interpreted as the distance that the airfoil has moved, in units of half-chord.

The lift is seen to be the sum of two parts:

1) c_{ℓ_Q} is the "quasi-steady" or "circulatory" part associated with vorticity shedding and circulation, and evolves in time according to the Wagner and Küssner functions shown in Figure 7.9.

2) c_{ℓ_A} is an "apparent-mass" or "impulsive" part associated with the instantaneous acceleration of the fluid immediately adjacent to the airfoil. A step change in velocity or angle produces an infinite acceleration, resulting in the impulsive lift.

Both the Wagner and Küssner functions asymptote to unity in the limit $t \to \infty$. Therefore, the general solution (7.50) asymptotes to the value $c_{\ell_\infty} = 2\pi(\Delta\alpha_{3c/4} + \Delta\alpha_{\text{gust}})$, as expected from steady thin airfoil theory.

The exact Wagner and Küssner functions cannot be expressed in terms of elementary functions, but are available in tabulated form. For calculations, the following curve-fit expressions are fairly accurate and convenient.

$$\Phi(\bar{t}) = 1 - 0.165 \exp(-0.045\bar{t}) - 0.335 \exp(-0.3\bar{t}) \tag{7.53}$$
$$\Psi(\bar{t}) = 1 - 0.5 \exp(-0.13\bar{t}) - 0.5 \exp(-1.0\bar{t}) \tag{7.54}$$
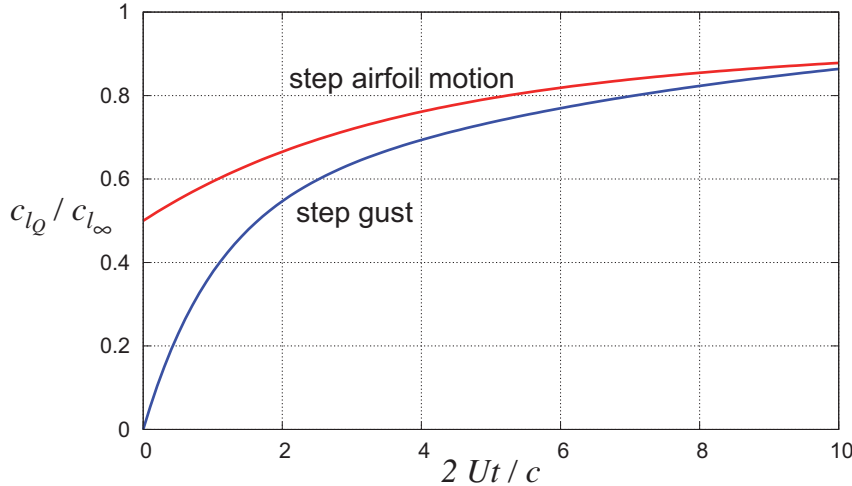
Figure 7.9: Circulatory part of lift coefficient versus time for a step increase in $\alpha_{3c/4}$ due to airfoil motion (Wagner solution), and a step increase in α_{gust} due to a gust velocity (Küssner solution). Total lift for the airfoil motion case contains an additional impulsive component, not shown.

7.7.4 General motion solution

The airfoil lift for a general motion can be obtained by Duhamel's (convolution) integral, which is a super-position of the infinitesimal step solutions over the motion history.

$$
\begin{aligned}
c_{\ell_Q}(\bar{t}) \;=\;& 2\pi\,\alpha_{3c/4}(0)\,\Phi(\bar{t}) \;+\; 2\pi \int_{0^+}^{\bar{t}} \frac{\mathrm{d}\alpha_{3c/4}}{\mathrm{d}\bar{t}'}\,\Phi(\bar{t}-\bar{t}')\,\mathrm{d}\bar{t}' \\
&+\; 2\pi\,\alpha_{\text{gust}}(0)\,\Psi(\bar{t}) \;+\; 2\pi \int_{0^+}^{\bar{t}} \frac{\mathrm{d}\alpha_{\text{gust}}}{\mathrm{d}\bar{t}'}\,\Psi(\bar{t}-\bar{t}')\,\mathrm{d}\bar{t}'
\end{aligned}
\tag{7.55}
$$

$$
c_{\ell_A}(\bar{t}) \;=\; 2\pi \left[\frac{c}{4}\frac{\ddot{h}}{U^2} + \frac{c}{4}\frac{\dot{\theta}}{U} \right]
\tag{7.56}
$$

The inputs are the airfoil motion given by $h(t)$ and $\theta(t)$, and the atmospheric gust motion given by $w_{\text{gust}}(t)$. These quantities define $\alpha_{3c/4}(t)$ and $\alpha_{\text{gust}}(t)$ which are then used in the convolution integrals for c_{ℓ_Q} above, and are also used directly for c_{ℓ_A}.

7.7.5 Apparent mass

It is useful to note that the dimensional lift/span corresponding to c_{ℓ_A} given by (7.56) is

$$
L'_A \;=\; \tfrac{1}{2}\rho U^2\, c\, c_{\ell_A} \;=\; m'_A\,(\ddot{h} + U\dot{\theta})
\tag{7.57}
$$
$$
m'_A \;\equiv\; \rho\,\pi\,(c/2)^2
\tag{7.58}
$$

where m'_A is the *apparent mass* (per unit span), which is the mass of a unit-span cylinder of fluid whose diameter is airfoil chord. Hence, subjecting an airfoil to a normal acceleration results in an additional reaction force as though this cylindrical mass of the air was attached to the airfoil and also accelerated. The effective normal acceleration, in addition to $\ddot{h}$, also includes a Coriolis-like term $U\dot{\theta}$ due to airfoil rotation.

7.7.6 Sinusoidal motion solution

Theodorsen [56] derived solutions for the case of small-magnitude sinusoidal motion at some frequency ω, specifically for use in predicting wing flutter. This situation is most conveniently treated by the introduction

of complex variables,

$$h(t) = h_0 \cos(\omega t + \varphi_h) = \mathrm{Re}\{\bar{h}\,\mathrm{e}^{\mathrm{i}\omega t}\} \quad ; \quad \bar{h} = h_0\,\mathrm{e}^{\mathrm{i}\varphi_h} \tag{7.59}$$

$$\theta(t) = \theta_0 \cos(\omega t + \varphi_\theta) = \mathrm{Re}\{\bar{\theta}\,\mathrm{e}^{\mathrm{i}\omega t}\} \quad ; \quad \bar{\theta} = \theta_0\,\mathrm{e}^{\mathrm{i}\varphi_\theta} \tag{7.60}$$

where the convenient complex amplitudes $\bar{h}, \bar{\theta}$ incorporate both the heave and pitch amplitudes h_0, θ_0, and also the heave and pitch phase angles $\varphi_h, \varphi_\theta$. The notation $\mathrm{Re}\{\ \}$ denotes the real part of a complex quantity.

Substitution of the sinusoidal $h(t)$ and $\theta(t)$ expressions above into the general-motion Wagner solutions (7.55) and (7.56), gives the following solution for the lift coefficient, again as a sum of quasi-steady and apparent-mass contributions. The pitching moment coefficient can also be obtained.

$$\frac{L'}{\frac{1}{2}\rho U^2 c} \equiv c_\ell = \mathrm{Re}\left\{C_{(k)}\,c_{\ell_Q} + c_{\ell_A}\right\} \tag{7.61}$$

$$c_{\ell_Q} = 2\pi\left[\theta + \frac{\dot{h}}{U} + \frac{c}{4}\frac{\dot{\theta}}{U}\right] = 2\pi\left[\bar{\theta} + \mathrm{i}k\frac{2\bar{h}}{c} + \mathrm{i}k\frac{\bar{\theta}}{2}\right]\mathrm{e}^{\mathrm{i}\omega t} = 2\pi\,\alpha_{3c/4} \tag{7.62}$$

$$c_{\ell_A} = 2\pi\left[\frac{c}{4}\frac{\dot{\theta}}{U} + \frac{c}{4}\frac{\ddot{h}}{U^2}\right] = 2\pi\left[\mathrm{i}k\frac{\bar{\theta}}{2} - k^2\frac{\bar{h}}{c}\right]\mathrm{e}^{\mathrm{i}\omega t} \tag{7.63}$$

$$\frac{M'}{\frac{1}{2}\rho U^2 c^2} \equiv c_{m_{c/2}} = \mathrm{Re}\left\{C_{(k)}\,c_{m_Q} + c_{m_A}\right\} \tag{7.64}$$

$$c_{m_Q} = \frac{1}{4}c_{\ell_Q} \tag{7.65}$$

$$c_{m_A} = 2\pi\left[-\frac{c}{16}\frac{\dot{\theta}}{U} - \frac{c^2}{128}\frac{\ddot{\theta}}{U^2}\right] = 2\pi\left[-\mathrm{i}k\frac{\bar{\theta}}{8} + k^2\frac{\bar{\theta}}{32}\right]\mathrm{e}^{\mathrm{i}\omega t} \tag{7.66}$$

$$k \equiv \frac{\omega c}{2U} = \pi\,\frac{\text{chord}}{\text{distance traveled in one period}} \tag{7.67}$$

The dimensionless parameter k which appears in this Theodorsen solution is the *reduced frequency*, which was previously mentioned in Section 1.5.3. It affects the strength of the shed vorticity, and also is a measure of the relative importance of the $\dot{\varphi}$ term in the unsteady Bernoulli equation (7.19). The other relevant parameters which appear are the maximum heave/chord ratio h_0/c, the maximum pitch displacement θ_0, and the relative phase $\varphi_h - \varphi_\theta$ between the heave and pitch motions.

For finite values of k, the circulatory parts of the lift and moment in (7.61) and (7.64) are modified by the *Theodorsen Lag Function* $C_{(k)}$ factor. This is a complex quantity, and is explicitly defined in terms of standard and modified Bessel functions J_0, J_1 and Y_0, Y_1, respectively.

$$H_{0(k)} = J_{0(k)} - \mathrm{i}\,Y_{0(k)} \quad , \quad H_{1(k)} = J_{1(k)} - \mathrm{i}\,Y_{1(k)}$$

$$C_{(k)} = \frac{H_{1(k)}}{H_{1(k)} + \mathrm{i}H_{0(k)}} \tag{7.68}$$

Its real and imaginary components and its magnitude and phase angle are plotted in Figure 7.10.

In the quasi-steady limit $k \to 0$ the lag function becomes unity, $C_{(0)} = 1 + 0\mathrm{i}$, and also all the time-rate terms in the unsteady lift and moment expressions become negligible. The resulting lift and moment coefficients then reduce to $c_\ell = 2\pi\alpha$, $c_{m_{c/2}} = c_\ell/4$, which matches thin airfoil theory.

For $k > 0$ we have $|C_{(k)}| < 1$ and $\angle C_{(k)} < 0$, so the lift contribution of c_{ℓ_Q} will now be reduced in magnitude and will also have a phase lag. The main origin of these effects is the convection of shed vorticity into the wake. This contributes a vertical velocity w at the airfoil which tends to oppose the current angle of attack,

and thus reduces the lift magnitude. But this vertical velocity contribution is delayed by the vorticity's convection time into the wake, which results in the phase lag.

As in the general-motion result (7.56), the remaining c_{ℓ_A} and c_{m_A} "apparent-mass" parts act instantaneously. Because of their extra time derivatives these introduce phase leads into the lift and moment, but become significant only at larger k values. Figure 7.11 shows the relative magnitudes of these various contributions to the lift for sinusoidally-heaving airfoils at two different reduced frequencies.
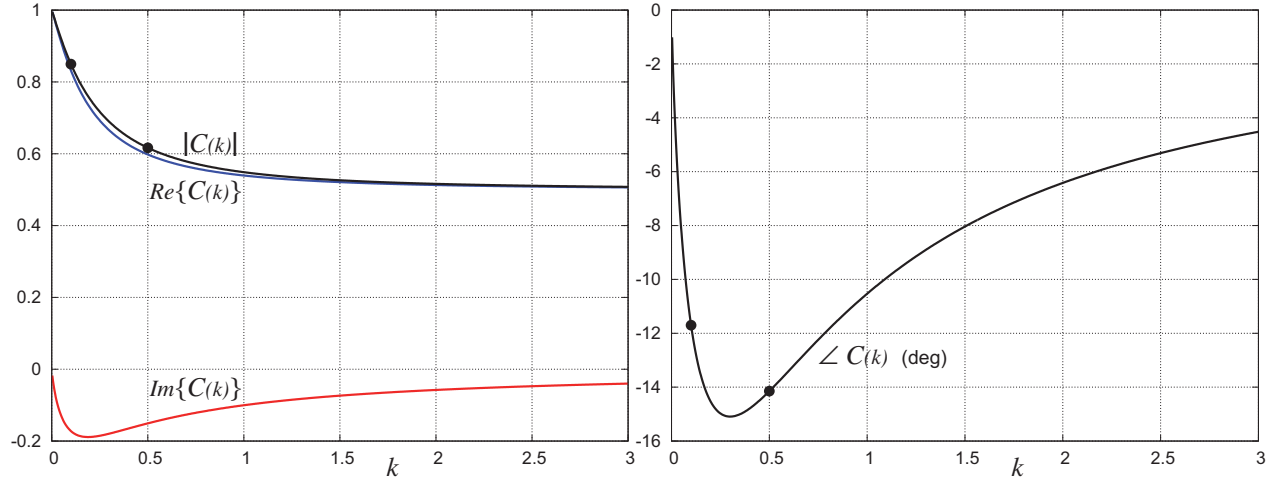
Figure 7.10: Real and imaginary parts, and magnitude and phase of the Theodorsen lag function. Magnitude and phase lag values at $k = 0.1$ and $k = 0.5$ are used in the example in Figure 7.11.
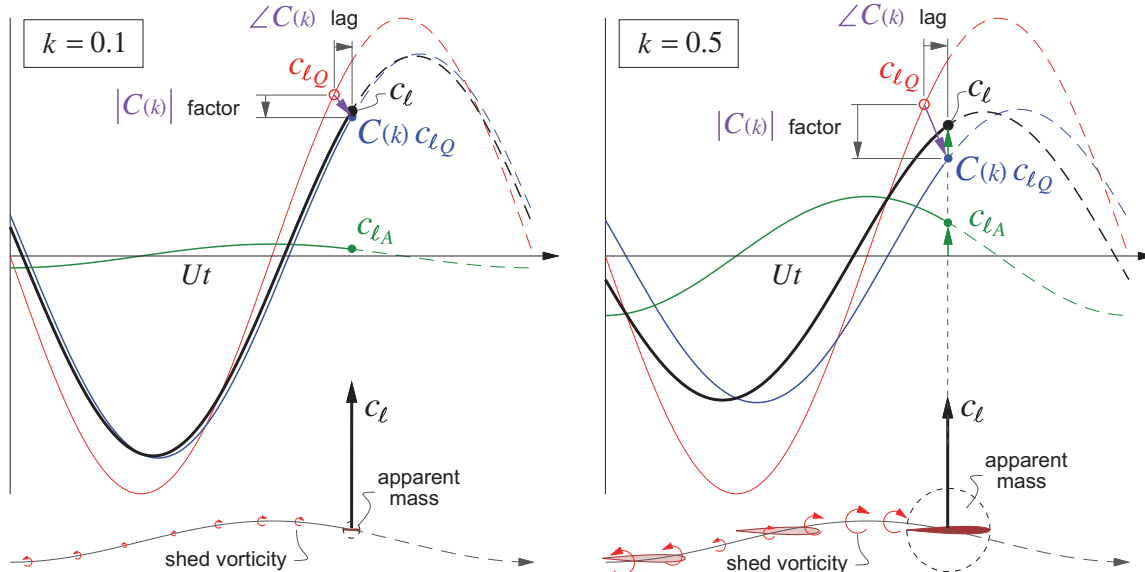
Figure 7.11: Unsteady lift coefficient components of airfoils undergoing sinusoidal heaving at zero pitch angle. Only the physical (real) parts are shown. The two airfoils have the same heave amplitude and wavelength, but different chords and hence different reduced frequencies $k = \pi \times \text{chord/wavelength}$. The quasi-steady lift $c_{\ell_Q} = 2\pi\alpha_{3c/4}$ is lagged and reduced in magnitude by the $C(k)$ Theodorsen function associated with shed vorticity. The impulsive lift contribution c_{ℓ_A} is the inertial reaction of the fluid's apparent mass subjected to vertical acceleration, and leads the quasi-steady lift by $90°$.

Chapter 8

Compressible Aerodynamic Flows

This chapter will examine the aerodynamics of airfoils, wings, and bodies in compressible flow. Modeling techniques, approximations, and associated solution methods will also be examined, particularly for the important class of small-disturbance flows. Subsonic, transonic, and supersonic flows will be addressed.

8.1 Effects of Compressibility

8.1.1 Compressibility definition

A *compressible flow* is defined as one with significant density ρ variations along particle pathlines. The resulting complications for flow-field representation were briefly discussed in Chapter 2. To summarize, a compressible flow has a nonzero *field source* distribution $\sigma(\mathbf{r})$, which can be related to the density-gradient and velocity fields via the continuity equation and the isentropic density-speed relation.

$$\sigma(\mathbf{r}) \; \equiv \; \nabla \cdot \mathbf{V} \; = \; -\frac{1}{\rho}\nabla\rho \cdot \mathbf{V} \; = \; \frac{1}{2}\frac{\nabla(V^2) \cdot \mathbf{V}}{a^2} \; = \; M^2\frac{\partial V}{\partial s} \; \neq \; 0 \tag{8.1}$$

This field source must be accounted for if source+vorticity superposition is employed to represent the velocity field. However, because this $\sigma(\mathbf{r})$ is typically extensive, it cannot be effectively lumped into source sheets, lines, or points, so that actually performing the velocity superposition calculation numerically, or constructing its AIC matrices, becomes impractical for the general case, especially in 3D. Resorting to CFD methods which used grid-based flow-field representation then becomes necessary.

One exception is the case of *small-disturbance flows*, for which the field source distribution can be approximately accounted for via the Prandtl-Glauert coordinate transformation. The superposition approach then becomes effective again for such compressible flows. These will be treated later in this chapter.

8.1.2 Flow-field changes

The field source distribution in a typical compressible flow-field over a 2D airfoil is shown in Figure 8.1. The acceleration over the front half of the airfoil produces a positive source area, while the deceleration over the rear half produces a negative source (sink) area. This has two major effects:

1. Increase in the overall velocity over the airfoil, as sketched on the left in Figure 8.2, and also quantitatively plotted in Figure 8.3.

2. Relative to the streamtubes of the incompressible case where $\sigma = 0$, the compressible case shows a divergence of the streamtubes in the front where $\sigma > 0$, and a convergence of the streamtubes in the rear where $\sigma < 0$. This results in a thickening of the streamtubes over most of the airfoil, which is quantitatively shown in Figure 8.4.

3. Since the airfoil surface is fixed, the streamtubes can only thicken outward, which results in a *lateral dilation* of the overall velocity and pressure field isolines, which is quantitatively shown in Figure 8.5.
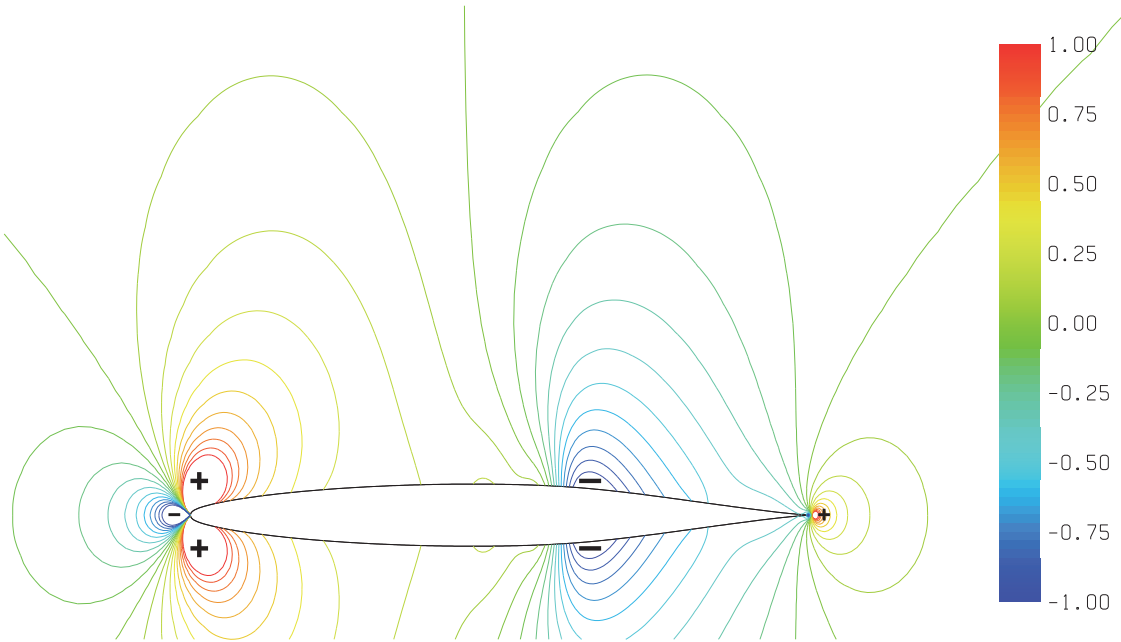
Figure 8.1: Contours of constant $\sigma(\mathbf{r})\,c/V_\infty$ with increment 0.1, near NACA N66-010 airfoil at $\alpha = 0°$, $M_\infty = 0.77$. Region over most of airfoil's front half has $\sigma > 0$ (sources), and region over rear half has $\sigma < 0$ (sinks).
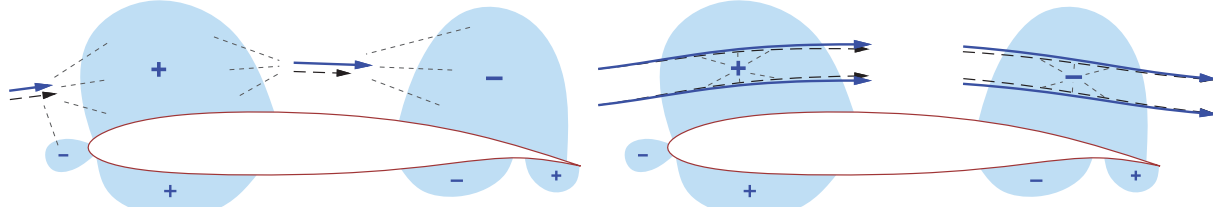
Figure 8.2: Comparison of velocity vectors and streamlines between incompressible (dashed) and compressible (solid) flows. Source and sink regions in the compressible case increase the velocity adjacent to the airfoil (left), and also cause streamtube thickening (right).

8.1.3   Transonic flow and shock waves

In flows with a subsonic freestream, or $M_\infty < 1$, the maximum <u>local</u> Mach number can become supersonic, or $M > 1$. Such a flow with both subsonic and supersonic regions present is called a *transonic flow*. An example is shown in Figure 8.6. Transonic flows will be treated in more detail later in this chapter.

8.1.4   Flow-field representation

As mentioned above, the presence of field sources creates difficulties for a calculation method using the freestream+source+vorticity superposition to represent the flow. Consider a non-lifting case which can be represented by fictitious source sheets $\lambda(s,\ell)$ to represent the airfoil, and a source density $\sigma(\mathbf{r})$ as defined
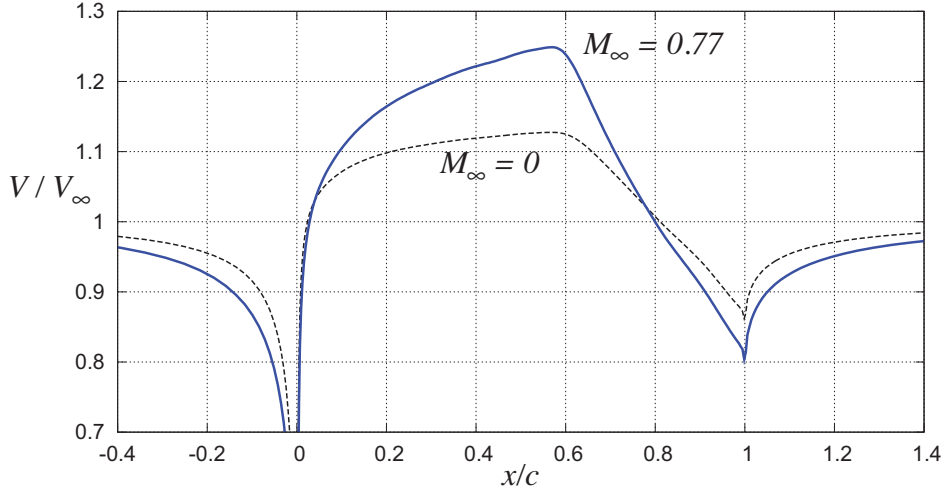
Figure 8.3: Comparison of surface speed distributions $V(x)$ on NACA N66-010 airfoil at $\alpha = 0°$ at $M_\infty = 0$ and $M_\infty = 0.77$. Field sources and sinks increase the speed over most of the airfoil, and decrease the speed ahead and behind the airfoil.
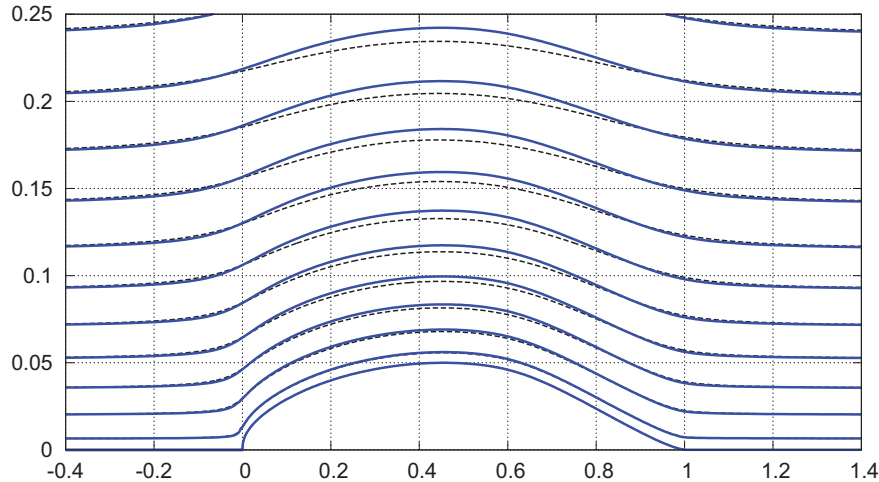
Figure 8.4: Comparison of computed streamlines at $M_\infty = 0$ and $M_\infty = 0.77$, above NACA N66-010 airfoil at $\alpha = 0°$. Vertical scale is exaggerated $4\times$, clearly showing the streamtube thickening effect in the compressible case.

by (8.1) above to represent the field sources. The overall velocity field is then given as follows.

$$\mathbf{V}_{(\mathbf{r})} = \mathbf{V}_\infty + \frac{1}{4\pi} \iint \lambda(s',\ell') \frac{(\mathbf{r}-\mathbf{r}')}{|\mathbf{r}-\mathbf{r}'|^3} \, \mathrm{d}s' \, \mathrm{d}\ell' + \frac{1}{4\pi} \iiint \frac{1}{2} \frac{\nabla(V^2) \cdot \mathbf{V}}{a^2} \frac{(\mathbf{r}-\mathbf{r}')}{|\mathbf{r}-\mathbf{r}'|^3} \, \mathrm{d}x' \, \mathrm{d}y' \, \mathrm{d}z' \quad (8.2)$$

One difficulty is due to the integrand in the second superposition integral in (8.2) being nonlinear, since V^2 and a^2 both depend on the local $\mathbf{V}_{(\mathbf{r}')}$. This is a relatively minor complication which could be handled with a suitable iterative solution method. The real difficulty arises from this being a volume integral, which requires a space-filling grid to enable its numerical evaluation. Such a method would then offer no advantage in the number of flow unknowns over a method which uses a grid-based flow-field representation approach. Furthermore, each unknown field source directly influences all field points, so the associated AIC matrix is large, dense, and would be dramatically expensive to solve. In contrast, in a grid-based method each flow unknown influences only its few grid neighbors, so the AIC matrices of grid methods are always very sparse and thus more economical to solve.
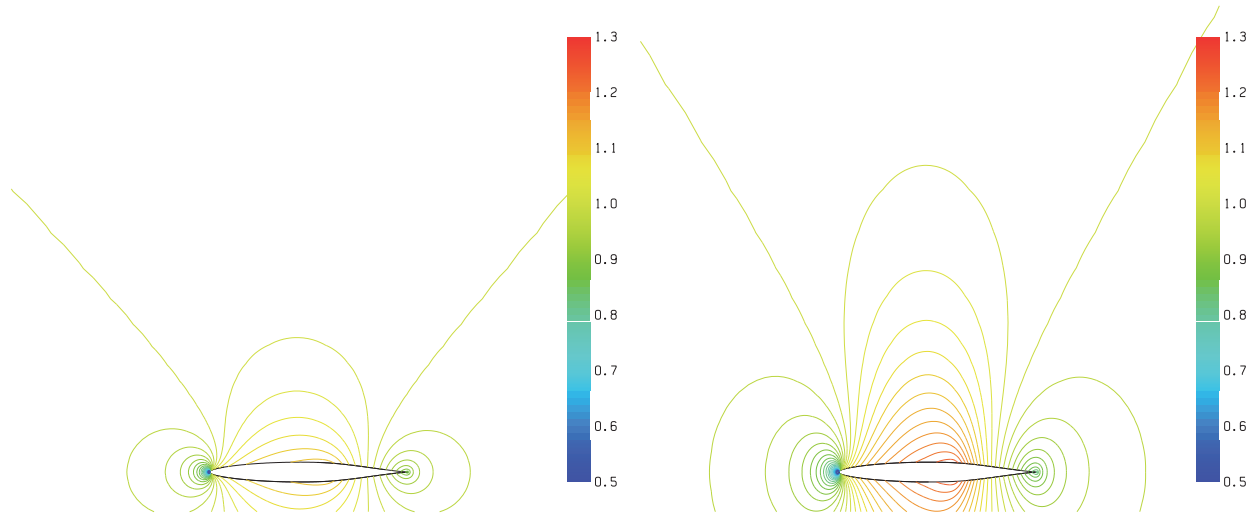
Figure 8.5: Contours of constant $V_{(\mathbf{r})}/V_\infty$ with increment 0.02, over NACA N66-010 airfoil at $\alpha = 0°$, for $M_\infty = 0$ (left) and $M_\infty = 0.77$ (right). High speed flow on right exhibits lateral dilation of the flow pattern due to streamtube thickening.
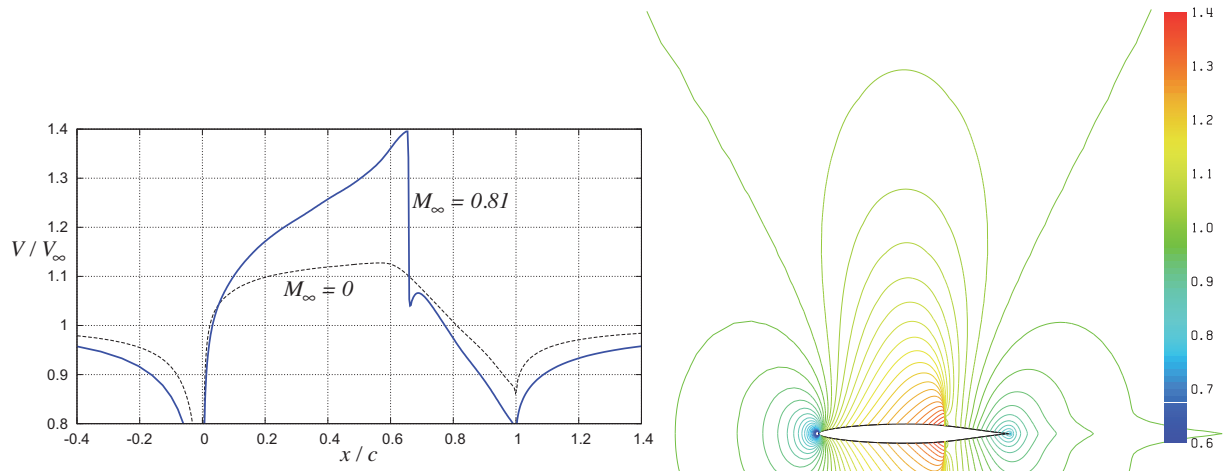
Figure 8.6: Surface and contour $V_{(\mathbf{r})}/V_\infty$ distributions in transonic flow over NACA N66-010 airfoil at $\alpha = 0°$, $M_\infty = 0.81$. Local $M > 1$ region ends in a normal shock wave.

8.2   Compressible Flow Quantities

The various thermodynamic definitions and relations derived in Chapter 1 will now be recast into forms suitable for compressible aerodynamic analysis.

8.2.1   Stagnation quantities

The *stagnation enthalpy* or equivalently the *total enthalpy*, which was defined and treated in Chapter 1, is constant in an adiabatic flow and is therefore equal to its freestream value.

$$h_o \equiv h + \frac{V^2}{2} = \frac{a^2}{\gamma-1} + \frac{V^2}{2} = h\left(1 + \frac{\gamma-1}{2}M^2\right) \tag{8.3}$$

$$h_o = h_{o\infty} = \frac{a_\infty^2}{\gamma-1} + \frac{V_\infty^2}{2} = h_\infty\left(1 + \frac{\gamma-1}{2}M_\infty^2\right) \tag{8.4}$$

In (8.4) the freestream quantities have been used to define the constant h_o value. The stagnation enthalpy (8.3) together with the isentropic relations (1.69) define the stagnation density and pressure.

$$\rho_o = \rho \left(\frac{h_o}{h}\right)^{1/(\gamma-1)} = \rho \left(1 + \frac{\gamma-1}{2}M^2\right)^{1/(\gamma-1)} \tag{8.5}$$

$$p_o = p \left(\frac{h_o}{h}\right)^{\gamma/(\gamma-1)} = p \left(1 + \frac{\gamma-1}{2}M^2\right)^{\gamma/(\gamma-1)} \tag{8.6}$$

These must also be constant and equal to their freestream values, but only in isentropic regions of the flow.

The known freestream total enthalpy in (8.3) also gives convenient alternative expressions for the local speed of sound and Mach number in terms of their freestream values and the local normalized speed V/V_∞.

$$a^2 = a_\infty^2 \left(1 + \tfrac{\gamma-1}{2}M_\infty^2 \left[1 - (V/V_\infty)^2\right]\right) \tag{8.7}$$

$$M^2 = M_\infty^2 \frac{(V/V_\infty)^2}{1 + \tfrac{\gamma-1}{2}M_\infty^2 \left[1 - (V/V_\infty)^2\right]} \tag{8.8}$$

8.2.2 Isentropic static density and pressure

Wherever ρ_o and p_o are equal to the known freestream values, i.e. in isentropic regions of the flow, there we can express the static density and pressure only in terms of the Mach number or the velocity.

$$\frac{\rho}{\rho_\infty} = \left[\frac{1 + \frac{\gamma-1}{2}M_\infty^2}{1 + \frac{\gamma-1}{2}M^2}\right]^{1/(\gamma-1)} = \left[1 + \frac{\gamma-1}{2}M_\infty^2\left(1 - \frac{V^2}{V_\infty^2}\right)\right]^{1/(\gamma-1)} \tag{8.9}$$

$$\frac{p}{p_\infty} = \left[\frac{1 + \frac{\gamma-1}{2}M_\infty^2}{1 + \frac{\gamma-1}{2}M^2}\right]^{\gamma/(\gamma-1)} = \left[1 + \frac{\gamma-1}{2}M_\infty^2\left(1 - \frac{V^2}{V_\infty^2}\right)\right]^{\gamma/(\gamma-1)} \tag{8.10}$$

Since external aerodynamic analyses frequently employ the velocity potential, the velocity forms above will be the more useful ones here. Note that relation (8.10) is the same as the steady version of the compressible Bernoulli equation (1.112).

The definition of the pressure coefficient remains unchanged from the incompressible case, but its dependence on the Mach number or velocity is now different.

$$C_p \equiv \frac{p - p_\infty}{\frac{1}{2}\rho_\infty V_\infty^2} = \frac{2}{\gamma M_\infty^2}\left(\frac{p}{p_\infty} - 1\right)$$

$$= \frac{2}{\gamma M_\infty^2}\left\{\left[\frac{1 + \frac{\gamma-1}{2}M_\infty^2}{1 + \frac{\gamma-1}{2}M^2}\right]^{\gamma/(\gamma-1)} - 1\right\} \tag{8.11}$$

$$\boxed{C_p = \frac{2}{\gamma M_\infty^2}\left\{\left[1 + \frac{\gamma-1}{2}M_\infty^2\left(1 - \frac{V^2}{V_\infty^2}\right)\right]^{\gamma/(\gamma-1)} - 1\right\}} \tag{8.12}$$

8.3 Shock Waves and Wave Drag

The normal shock wave shown in Figure 8.6 will typically result in *shock losses* and associated *wave drag* which are important in transonic flows. From conservation of mass, momentum, and total enthalpy across a normal shock wave, the total pressure ratio across the shock is calculated to be

$$\frac{p_{o_2}}{p_{o_1}} = \left(\frac{(\gamma+1)M_1^2}{2 + (\gamma-1)M_1^2}\right)^{\gamma/(\gamma-1)} \left(\frac{\gamma+1}{1 - \gamma + 2\gamma M_1^2}\right)^{1/(\gamma-1)} \simeq 1 - \frac{\gamma\,(M_1-1)^3}{1 + 2\gamma\,(M_1-1)} \tag{8.13}$$

where M_1 and p_{o_1} are just upstream of the shock, and p_{o_2} is just downstream. This ratio is plotted in Figure 8.7. The second approximate form in (8.13) is based on an asymptotic analysis of the exact form for $M_1 \to 1$. It shows that the total pressure loss is cubic in $M_1 - 1$, with the "knee" roughly at $M_1 \simeq 1.15$ beyond which the loss increases rapidly.
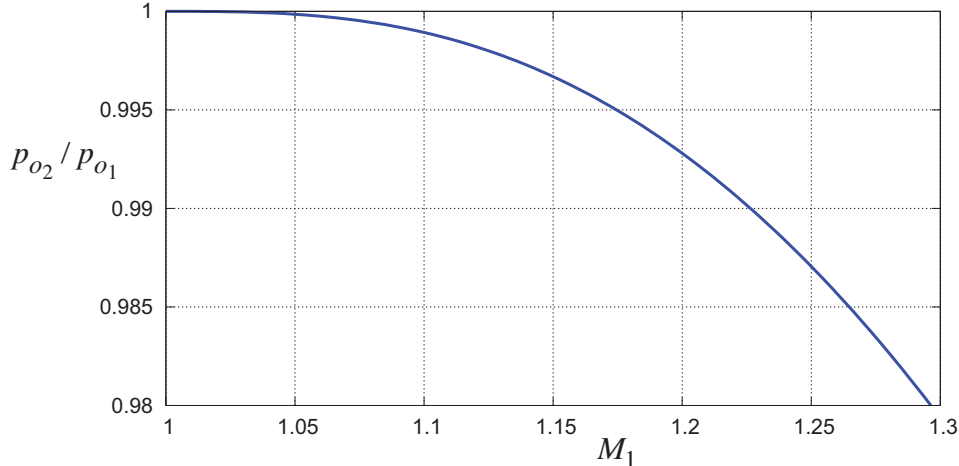
Figure 8.7: Total pressure ratio across a normal shock wave with $\gamma = 1.4$.

The streamlines passing through the shock suffer a reduction in total pressure, from $p_{o_1} = p_{o_\infty}$ down to $p_{o_2} = p_{o_\text{wake}}$ which persists downstream, as shown in Figure 8.8. When they reach ambient pressure p_∞ downstream, they will therefore have a velocity below freestream $V_\text{wake} < V_\infty$, and thus form a *shock wake*.
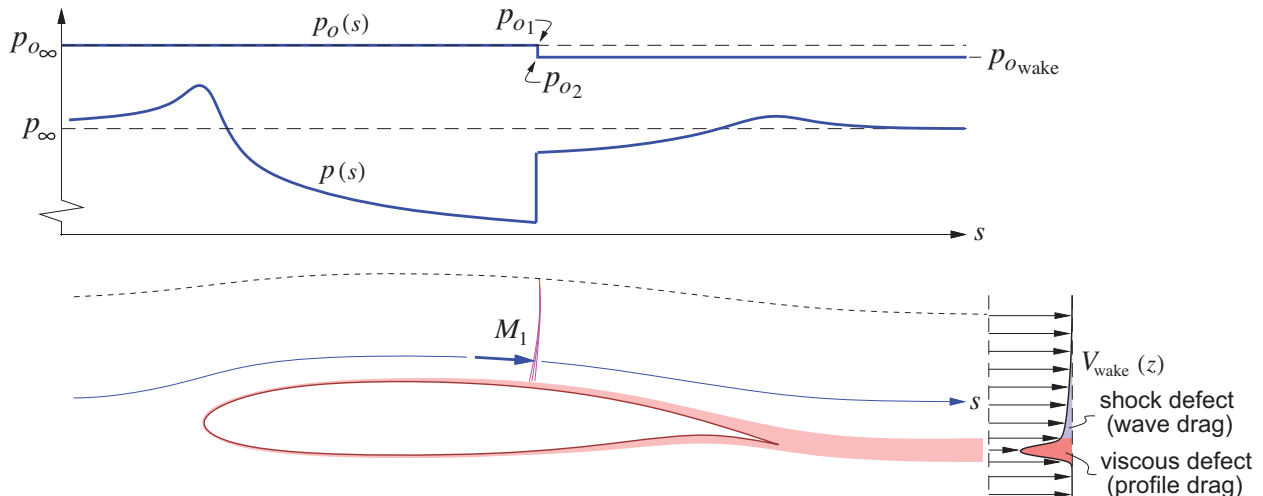
Figure 8.8: Total pressure drop across a normal shock on the airfoil results in a shock wake downstream. The shock wake's momentum defect is the wave drag.

To quantify the magnitude of this shock wake defect we first write the total pressure in terms of the static pressure and the velocity.

$$p_o \equiv p\left(1 + \frac{\gamma-1}{2}M^2\right)^{\gamma/(\gamma-1)} = p\left(1 + \frac{\gamma-1}{2}M_\infty^2\right)^{\gamma/(\gamma-1)}\left[1 + \frac{\gamma-1}{2}M_\infty^2\left(1 - \frac{V^2}{V_\infty^2}\right)\right]^{-\gamma/(\gamma-1)} \tag{8.14}$$

Applying this to the shock wake we set $p = p_\infty$ and $p_o = p_{o_\text{wake}} = p_{o_\infty}(p_{o_2}/p_{o_1})$, which then gives the

shock-wake velocity for any given streamline.

$$p_{o_\text{wake}} = p_{o\infty}(p_{o_2}/p_{o_1}) = p_\infty \left(1 + \frac{\gamma-1}{2}M_\infty^2\right)^{\gamma/(\gamma-1)} \left[1 + \frac{\gamma-1}{2}M_\infty^2\left(1 - \frac{V_\text{wake}^2}{V_\infty^2}\right)\right]^{-\gamma/(\gamma-1)} \tag{8.15}$$

$$\frac{V_\text{wake}}{V_\infty} = \left\{1 - \frac{2}{(\gamma-1)M_\infty^2}\left[\left(\frac{p_{o_2}}{p_{o_1}}\right)^{-(\gamma-1)/\gamma} - 1\right]\right\}^{1/2} \tag{8.16}$$

$$\frac{V_\text{wake}}{V_\infty} \simeq 1 - \frac{1}{M_\infty^2}\frac{(M_1-1)^3}{1+2\gamma(M_1-1)} \tag{8.17}$$

Here M_1 is the shock-wave Mach number which that streamline had just before passing though the shock, as shown in Figure 8.8. The final simplified form (8.17) assumes $1-V_\text{wake}/V_\infty \ll 1$ which holds for any practical transonic flow. This wake velocity ratio is plotted in Figure 8.9 for two freestream Mach numbers.
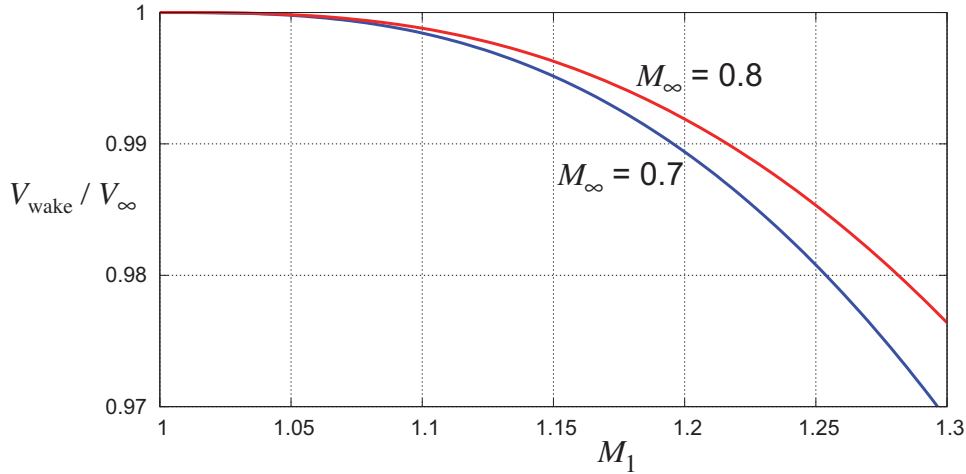
Figure 8.9: Wake velocity versus shock-wave Mach number M_1 for that streamline.

Total section drag/span is the total momentum defect of the wake shown in Figure 8.8. The wave drag is the part corresponding to the mass flow which passed through the shock, with the remainder being the usual viscous defect.

$$D' = D'_\text{viscous} + D'_\text{wave} \tag{8.18}$$

$$D'_\text{wave} = \int (V_\infty - V_\text{wake})\,\mathrm{d}\dot{m}_\text{shock}$$

$$\simeq \int (V_\infty - V_\text{wake})\,\rho_\infty V_\infty\,\mathrm{d}z \tag{8.19}$$

$$c_{d\text{wave}} \equiv \frac{D'_\text{wave}}{\frac{1}{2}\rho_\infty V_\infty^2 c} \simeq 2\int\left(1 - \frac{V_\text{wake}}{V_\infty}\right)\frac{\mathrm{d}z}{c} \tag{8.20}$$

The approximations above assume that the wake defect is small compared to unity, which is quite reasonable.

Since typical transonic airfoils have $c_d \simeq 0.01$ or less, and the shock height and corresponding shock wake height is a significant fraction of the chord length, it is clear that the fractional defect $1 - V_\text{wake}/V_\infty$ must be kept well below roughly 0.01 to keep $c_{d\text{wave}}$ from adding significantly to the total drag. Hence, a relatively weak shock of $M_1 < 1.2$ or less is required for acceptably low wave drag of transonic airfoils.

8.4   Compressible Potential Flows

Since shock waves in practical transonic flows are weak, such flows are nearly isentropic outside the viscous layers, so that their velocity field is nearly irrotational and hence can be represented by the *full potential* Φ.

$$\mathbf{V} \;=\; \nabla\Phi \tag{8.21}$$

Since this $\mathbf{V}$ is irrotational it cannot exactly represent the slightly rotational flow in a shock wake. Specifically, defining $\mathbf{V}$ via the full potential will always result in exactly $V_{\text{wake}}/V_\infty = 1$ in the far-downstream shock wake. But as can be seen in Figure 8.9, in typical aerodynamic flows which have weak shock waves this error in the shock's wake velocity is very small, and the effects on the surface pressures and hence on the lift are small as well. For this reason the slight error in the velocities will be neglected in most of the subsequent compressible potential flow analyses.

An exception is the wave drag, which by definition (8.19) is exactly zero when $V_{\text{wake}}/V_\infty = 1$. This shortcoming will be resolved in Section 8.4.3 where the wave drag is defined in an alternative manner.

8.4.1   Full potential equation – problem formulation

A general compressible potential flow is described by the full potential (FP) equation which governs the full potential field $\Phi(\mathbf{r}\,;M_\infty,\alpha,\beta)$. The overall FP analysis problem is stated as follows.

$$\text{FP flow equation:} \quad \nabla \cdot (\rho\,\nabla\Phi) \;=\; 0 \tag{8.22}$$

$$\text{where} \quad \rho \;=\; \rho_\infty \left[1 + \frac{\gamma-1}{2} M_\infty^2 \left(1 - \frac{\nabla\Phi \cdot \nabla\Phi}{V_\infty^2} \right) \right]^{1/(\gamma-1)} \tag{8.23}$$

$$\text{BCs:} \quad \nabla\Phi \cdot \hat{\mathbf{n}} \;=\; 0 \qquad \text{(on solid body)} \tag{8.24}$$

$$\Delta\Phi \;=\; \Gamma \qquad \text{(on wake branch cut)} \tag{8.25}$$

$$\Phi \;\to\; \Phi_\infty(\alpha,\beta,\Gamma) \qquad \text{(as } r \to \infty\text{)} \tag{8.26}$$

The circulation variables Γ along the span are additional unknowns, and are constrained with matching Kutta conditions along the span. Only one Γ and one Kutta condition is present in 2D.

8.4.2   Full potential solution

Because the isentropic density as given by (8.23) has a complicated nonlinear dependence on $\nabla\Phi$, analytic solutions to the FP analysis problem are not possible even for very simple geometries. Instead, solutions must be obtained numerically by using either a finite-volume or finite-element discretization method formulated on a space-filling grid. Such a method is commonly called a *Full Potential Solver*. If transonic flows are to be computed, some type of modification is also needed in order to capture shock waves. The most common approach is to modify the density in the FP equation (8.22) by an *upwinding* term proportional to the streamwise gradient of the density. One example of such a modification due to Hafez et al. [57] is

$$\rho \;\to\; \rho - \nu\,\Delta\ell\,\nabla\rho \cdot \nabla\Phi/|\nabla\Phi| \tag{8.27}$$

where ν is the upwinding parameter (comparable to unity in magnitude), and $\Delta\ell$ is the local grid cell size. Note that in the limit of a very fine grid we have $\Delta\ell \to 0$ and the density modification term disappears, so that the equation actually solved is consistent with the analytical FP equation.

Besides the body geometry, the required input parameters to the overall problem are the freestream Mach number M_∞ and the freestream flow angles α, β. The resulting pressure field then has the same functional form as the potential,

$$\frac{p(\mathbf{r}\,;M_\infty,\alpha,\beta)}{p_\infty} \;=\; \left[1 + \frac{\gamma-1}{2} M_\infty^2 \left(1 - \frac{\nabla\Phi \cdot \nabla\Phi}{V_\infty^2} \right) \right]^{\gamma/(\gamma-1)}$$

so that the integrated force and moment coefficients will then also depend on M_∞, α, β (or M_∞, α in 2D).

8.4.3 Limitations of full potential solutions

One limitation of the FP equation is that it applies only to inviscid flows. This can be mostly remedied by using the Wall-Transpiration boundary layer model described in Chapter 3. For example, in the 2D case the flow-tangency BC (8.24) would be modified to

$$\rho \nabla \Phi \cdot \hat{\mathbf{n}} = \frac{\mathrm{d}m}{\mathrm{d}s} \tag{8.28}$$

where $m = \rho_e u_e \delta^*$ is the viscous mass defect. This is governed by a suitable form of the boundary layer equations which would need to be solved together with the FP equation.

Another limitation of the FP equation is that its resulting velocity field $\mathbf{V} = \nabla \Phi$ is irrotational, and hence its solution will not have a shock wake like the one shown in Figure 8.8, even if the solution has a shock present on the airfoil. The wave drag as calculated by far-field integral (8.19) over the shock wake will then incorrectly be zero. The correct calculation of wave drag therefore appears to require the direct pressure force integration over the airfoil surface via (5.5). However, this was shown to be very sensitive to cancellation errors in Section 5.1.2, so the following more accurate approach is needed.

Consider the control volume surface shown in Figure 8.10, consisting of the four pieces $\mathcal{S}_{\text{outer}}, \mathcal{S}_{\text{cut}}, \mathcal{S}_{\text{body}}, \mathcal{S}_{\text{shock}}$. The integral momentum theorem in the freestream $\hat{\mathbf{x}}$ direction summed over all four pieces can be assumed to be zero, since the overall contour is topologically empty and contains only smooth potential flow which satisfies the momentum equation.

$$\oint [\, p\hat{\mathbf{n}} + \rho(\mathbf{V} \cdot \hat{\mathbf{n}})\mathbf{V} \,] \cdot \hat{\mathbf{x}} \ \mathrm{d}\mathcal{S} = 0$$

or $\qquad \oint_{\text{outer}} [\ ] \, \mathrm{d}\mathcal{S} + \oint_{\text{cut}} [\ ] \, \mathrm{d}\mathcal{S} + \oint_{\text{body}} [\ ] \, \mathrm{d}\mathcal{S} + \oint_{\text{shock}} [\ ] \, \mathrm{d}\mathcal{S} = 0$

In addition, in 2D flow the $\mathcal{S}_{\text{outer}}$ piece can also assumed to be zero since the outer flow is potential and has no momentum defect, and the $\mathcal{S}_{\text{cut}}$ piece is also zero since its two $\hat{\mathbf{n}}$ vectors are opposite. Hence the two remaining pieces must be equal and opposite, so we have

$$
\begin{aligned}
D'_{\text{wave}} &= \oint_{\text{body}} [\ ] \, \mathrm{d}\mathcal{S} \\
&= -\oint_{\text{shock}} [\, p\hat{\mathbf{n}} + \rho(\mathbf{V} \cdot \hat{\mathbf{n}})\mathbf{V} \,] \cdot \hat{\mathbf{x}} \ \mathrm{d}\mathcal{S}
\end{aligned} \tag{8.29}
$$

and therefore the wave drag can be computed by evaluating integral (8.29) only on the contour surrounding the shock, noting that $\hat{\mathbf{n}}$ points into this contour. This avoids the cancellation errors which would occur with evaluating the $\mathcal{S}_{\text{body}}$ integral directly.

Similar arguments can be made for wave drag in 3D potential flows. In this case the $\mathcal{S}_{\text{outer}}$ integral is only the induced drag D_i, which can be evaluated by Trefftz-plane integration over the wake cut as discussed previously. The $\mathcal{S}_{\text{body}}$ integral is then $D_i + D_{\text{wave}}$, so that the integral over the shock-enclosing contour isolates the wave drag component.

$$D_{\text{wave}} = -\oiint_{\text{shock}} [\, p\hat{\mathbf{n}} + \rho(\mathbf{V} \cdot \hat{\mathbf{n}})\mathbf{V} \,] \cdot \hat{\mathbf{x}} \ \mathrm{d}\mathcal{S} \tag{8.30}$$
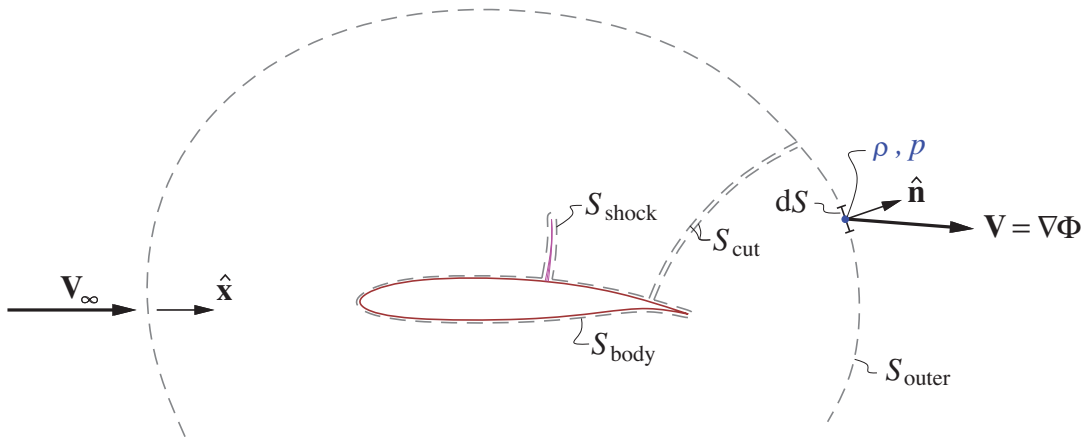
Figure 8.10: Control volume surface for wave drag calculation from a potential-flow solution.

8.5   Small-Disturbance Compressible Flows

The full potential equation is very general, but it requires grid-based CFD solution methods which offer little insight into compressible flow behavior. For this reason we will now consider the more restricted class of *Small-Disturbance Flows*, which in many circumstances can be treated by superposition-based solution methods.

8.5.1   Perturbation velocities

The perturbation velocity is defined in the usual way, as the difference between the local velocity $\mathbf{V}$ and the freestream velocity $\mathbf{V}_\infty$. To minimize equation complexity, we will from now on assume that the freestream is along the x axis, so that the angles of attack or sideslip are in the geometry definition. Furthermore, u, v, w will here denote the perturbation velocity components, which are also assumed to be normalized by the freestream speed V_∞. The local total velocity $\mathbf{V}$ and its magnitude V are then expressed as follows.

$$\mathbf{V}_\infty = V_\infty\,\hat{\mathbf{x}} \tag{8.31}$$

$$\mathbf{V} = V_\infty\left[(1+u)\,\hat{\mathbf{x}} + v\,\hat{\mathbf{y}} + w\,\hat{\mathbf{z}}\right] \tag{8.32}$$

$$V^2 \equiv \mathbf{V}\cdot\mathbf{V} = V_\infty^2\left[1 + 2u + u^2+v^2+w^2\right] \tag{8.33}$$

The local adiabatic speed of sound, the local Mach number, and the isentropic density and pressure expressions can also be expressed in terms of the perturbation velocities as follows.

$$a^2 = a_\infty^2 - \tfrac{\gamma-1}{2}\left(V^2 - V_\infty^2\right) = a_\infty^2\left\{1 - (\gamma-1)M_\infty^2\left[u + \tfrac{1}{2}(u^2+v^2+w^2)\right]\right\} \tag{8.34}$$

$$M^2 \equiv \frac{V^2}{a^2} = M_\infty^2\left[1 + 2u + u^2+v^2+w^2\right]\left\{1 - (\gamma-1)M_\infty^2\left[u + \tfrac{1}{2}(u^2+v^2+w^2)\right]\right\}^{-1} \tag{8.35}$$

$$\frac{\rho}{\rho_\infty} = \left(\frac{a^2}{a_\infty^2}\right)^{1/(\gamma-1)} = \left\{1 - (\gamma-1)M_\infty^2\left[u + \tfrac{1}{2}(u^2+v^2+w^2)\right]\right\}^{1/(\gamma-1)} \tag{8.36}$$

$$\frac{p}{p_\infty} = \left(\frac{a^2}{a_\infty^2}\right)^{\gamma/(\gamma-1)} = \left\{1 - (\gamma-1)M_\infty^2\left[u + \tfrac{1}{2}(u^2+v^2+w^2)\right]\right\}^{\gamma/(\gamma-1)} \tag{8.37}$$

8.5.2 Small-disturbance approximation

The above restatement of the various flow quantities in terms of perturbation velocities has so far been exact, with no new approximations introduced. We now consider *Small-Disturbance Flows*, where the condition

$$u, v, w \ll 1 \tag{8.38}$$

is assumed to hold. This is generally valid if

- The geometry is slender: $t/c \ll 1$ for an airfoil, or $d/\ell \ll 1$ for a fuselage.

- The aerodynamic angles are small: $\alpha \ll 1$ and $\beta \ll 1$

Under normal circumstances it is tempting to drop all higher powers of the perturbation velocities like u^2, uv, etc. and retain only the linear terms to greatly simplify the flow equations. However, this will be seen to be premature for transonic flows, where some of the nonlinear terms always remain crucial. Hence we will perform the simplification in three steps:

1. First only the cubic and higher terms will be dropped.

2. Next, all the quadratic terms be dropped except the ones which remain indispensable.

3. Next, all the quadratic terms will be dropped, finally giving a linear problem.

8.5.3 Second-order approximations

Using the Taylor series expansion in a small parameter ϵ

$$(1-\epsilon)^{-1} = 1 + \epsilon + \epsilon^2 + \dots \tag{8.39}$$

the local Mach number expression (8.35) is converted from a rational form to a polynomial form,

$$M^2 = M_\infty^2 \left\{ 1 + \left(1 + \tfrac{\gamma-1}{2} M_\infty^2\right)\left[2u + u^2 + v^2 + w^2\right] + \tfrac{\gamma-1}{2} M_\infty^2 \left(1 + \tfrac{\gamma-1}{2} M_\infty^2\right) 4u^2 + \dots \right\} \tag{8.40}$$

where "..." denotes cubic terms $\mathcal{O}\left(M_\infty^4 |u, v, w|^3\right)$ and higher. Using the more general Taylor series expansion

$$(1-\epsilon)^b = 1 - b\epsilon + \tfrac{1}{2} b(b-1)\epsilon^2 + \dots \tag{8.41}$$

the isentropic density and pressure (8.36), (8.37) likewise convert from power-law forms to the following polynomial forms.

$$\frac{\rho}{\rho_\infty} = 1 - M_\infty^2 \left[u + \left(\tfrac{1}{2} - \tfrac{2-\gamma}{2} M_\infty^2\right) u^2 + \tfrac{1}{2}(v^2 + w^2)\right] + \dots \tag{8.42}$$

$$\frac{p}{p_\infty} = 1 - \gamma M_\infty^2 \left[u + \tfrac{1}{2}(1 - M_\infty^2)u^2 + \tfrac{1}{2}(v^2 + w^2)\right] + \dots \tag{8.43}$$

Again, the "..." denotes cubic terms and higher.

To put the continuity equation into a polynomial form, we first need to expand the components of the normalized mass flux $\rho\mathbf{V}/\rho_\infty V_\infty$. These are obtained by multiplying the ρ/ρ_∞ expression (8.42) in turn

with each component of $\mathbf{V}/V_\infty$, and then collecting the various powers and products of u, v, w.

$$\frac{\rho}{\rho_\infty}(1+u) = \left\{ 1 - M_\infty^2 \left[u + \left(\tfrac{1}{2} - \tfrac{2-\gamma}{2} M_\infty^2 \right) u^2 + \tfrac{1}{2}(v^2+w^2) \right] + \ldots \right\}(1+u)$$

$$= 1 + (1-M_\infty^2)u - M_\infty^2 \left[\left(\tfrac{3}{2} - \tfrac{2-\gamma}{2} M_\infty^2 \right) u^2 + \tfrac{1}{2}(v^2+w^2) \right] + \ldots \qquad (8.44)$$

$$\frac{\rho}{\rho_\infty}v = \left\{ 1 - M_\infty^2 \left[u + \left(\tfrac{1}{2} - \tfrac{2-\gamma}{2} M_\infty^2 \right) u^2 + \tfrac{1}{2}(v^2+w^2) \right] + \ldots \right\} v$$

$$= v - M_\infty^2\, uv + \ldots \qquad (8.45)$$

$$\frac{\rho}{\rho_\infty}w = \left\{ 1 - M_\infty^2 \left[u + \left(\tfrac{1}{2} - \tfrac{2-\gamma}{2} M_\infty^2 \right) u^2 + \tfrac{1}{2}(v^2+w^2) \right] + \ldots \right\} w$$

$$= w - M_\infty^2\, uw + \ldots \qquad (8.46)$$

We next insert these mass flux component expressions into the compressible continuity equation, and also put the flow-tangency boundary condition in perturbation-velocity form.

$$\frac{1}{\rho_\infty V_\infty}\nabla \cdot (\rho \mathbf{V}) = 0 \qquad (8.47)$$

$$\frac{1}{V_\infty}\mathbf{V} \cdot \hat{\mathbf{n}} = 0 \qquad \text{(Body BC)} \qquad (8.48)$$

This gives the second-order continuity equation and corresponding flow-tangency BC.

$$\left\{ (1-M_\infty^2)u - \tfrac{1}{2}M_\infty^2 \left[Qu^2 + v^2 + w^2 \right] \right\}_x + \left\{ v - M_\infty^2 uv \right\}_y + \left\{ w - M_\infty^2 uw \right\}_z = 0 \qquad (8.49)$$

$$\text{where} \qquad Q \equiv 3 - (2-\gamma)M_\infty^2 \qquad (8.50)$$

$$(1+u)\,n_x + v\,n_y + w\,n_z = 0 \qquad \text{(Body BC)} \qquad (8.51)$$

8.5.4   Perturbation potential flows

We now assume irrotational flow. This allows eliminating the three u, v, w perturbation velocity components in terms of the single normalized perturbation potential variable ϕ, which is the usual perturbation potential φ normalized with the freestream.

$$\phi = \varphi/V_\infty \qquad (8.52)$$

$$u\,\hat{\mathbf{x}} + v\,\hat{\mathbf{y}} + w\,\hat{\mathbf{z}} = \nabla\phi \qquad (8.53)$$

$$\mathbf{V} = \mathbf{V}_\infty + V_\infty(u\,\hat{\mathbf{x}} + v\,\hat{\mathbf{y}} + w\,\hat{\mathbf{z}}) = V_\infty \left[(1+\phi_x)\,\hat{\mathbf{x}} + \phi_y\,\hat{\mathbf{y}} + \phi_z\,\hat{\mathbf{z}} \right] \qquad (8.54)$$

Note that ϕ has units of length, so that $\nabla\phi$ is dimensionless.

Second-order perturbation potential equation

Replacing u, v, w with ϕ_x, ϕ_y, ϕ_z in equations (8.49),(8.51) gives the *Second-Order Perturbation Potential* (PP2) equation and associated flow-tangency condition:

$$\left[(1-M_\infty^2)\phi_x - \tfrac{1}{2}M_\infty^2 \left(Q\phi_x^2 + \phi_y^2 + \phi_z^2 \right) \right]_x + \left[\phi_y - M_\infty^2 \phi_x\phi_y \right]_y + \left[\phi_z - M_\infty^2 \phi_x\phi_z \right]_z = 0 \qquad (8.55)$$

$$(1+\phi_x)\,n_x + \phi_y\,n_y + \phi_z\,n_z = 0 \qquad \text{(Body BC)} \qquad (8.56)$$

Transonic small-disturbance equation

We now note that for a small-disturbance flow, most of the quadratic terms in (8.55) can be dropped, except when the freestream flow is close to sonic, $M_\infty \simeq 1$. In this case we can approximate $Q \simeq \gamma+1$, and we also note that $Q\,\phi_x^2 \simeq (\gamma+1)\,\phi_x^2$ may not be small compared to $(1-M_\infty^2)\,\phi_x$. Furthermore, for slender bodies we have

$$n_x \;\ll\; n_y\,,\, n_z$$

so that the product $\phi_x n_x$ in (8.56) is a higher-order quantity compared to $\phi_y n_y$ and $\phi_z n_z$. Hence we drop all quadratic terms except for ϕ_x^2, which results in the following nonlinear *transonic small-disturbance* (TSD) equation, and a first-order flow-tangency condition.

$$\left[(1-M_\infty^2)\,\phi_x - \tfrac{\gamma+1}{2}M_\infty^2\,\phi_x^2 \right]_x + \left[\phi_y \right]_y + \left[\phi_z \right]_z \;=\; 0 \tag{8.57}$$

$$n_x + \phi_y\,n_y + \phi_z\,n_z \;=\; 0 \qquad \text{(Body BC)} \tag{8.58}$$

An alternative equivalent form of the TSD equation (8.57) is

$$\left[(1-M_\infty^2) - (\gamma+1)M_\infty^2\,\phi_x \right]\phi_{xx} + \phi_{yy} + \phi_{zz} \;=\; 0 \tag{8.59}$$

which looks like a Laplace equation except for the ϕ_x-dependent coefficient multiplying the ϕ_{xx} term.

Strictly speaking, the quadratic terms $\phi_y^2 + \phi_z^2$ in (8.56) should also have been retained in the TSD equation (8.57). However, because of the strong lateral dilation effect shown in Figure 8.5 they are typically much smaller than $Q\phi_x^2$ and hence can be dropped. One possible exception is in cases with strongly swept shock waves, in which these may need to be retained.

Prandtl-Glauert equation

Provided the freestream flow is sufficiently far from sonic, we can in addition drop the quadratic term from the TSD equation (8.57) or (8.59) to give the *Prandtl-Glauert* (PG) equation.

$$(1-M_\infty^2)\,\phi_{xx} + \phi_{yy} + \phi_{zz} \;=\; 0 \tag{8.60}$$

The first-order flow-tangency condition (8.58) remains the same here. The most significant change from the TSD equation is that the PG equation is now <u>linear</u>, which is an enormous simplification which will be extensively exploited in the subsequent sections.

Laplace equation

As a final step, if we assume low speed flow, with $M_\infty^2 \ll 1$, the PG equation (8.60) simplifies to the *Laplace* equation.

$$\phi_{xx} + \phi_{yy} + \phi_{zz} \;=\; 0 \tag{8.61}$$

Although this equation appears to be subject to the same small-disturbance approximations as its PG, TSD, and PP2 predecessors, it is in fact completely general for any low-speed flow. The reason is that all the higher-order terms which were dropped were also multiplied by M_∞^2 or higher powers, so that with $M_\infty^2 \simeq 0$ all these dropped terms were already negligible anyway. Alternatively, the Laplace equation could also have been obtained directly from the starting continuity equation (8.47) by a priori assuming that ρ is constant in the low speed case.
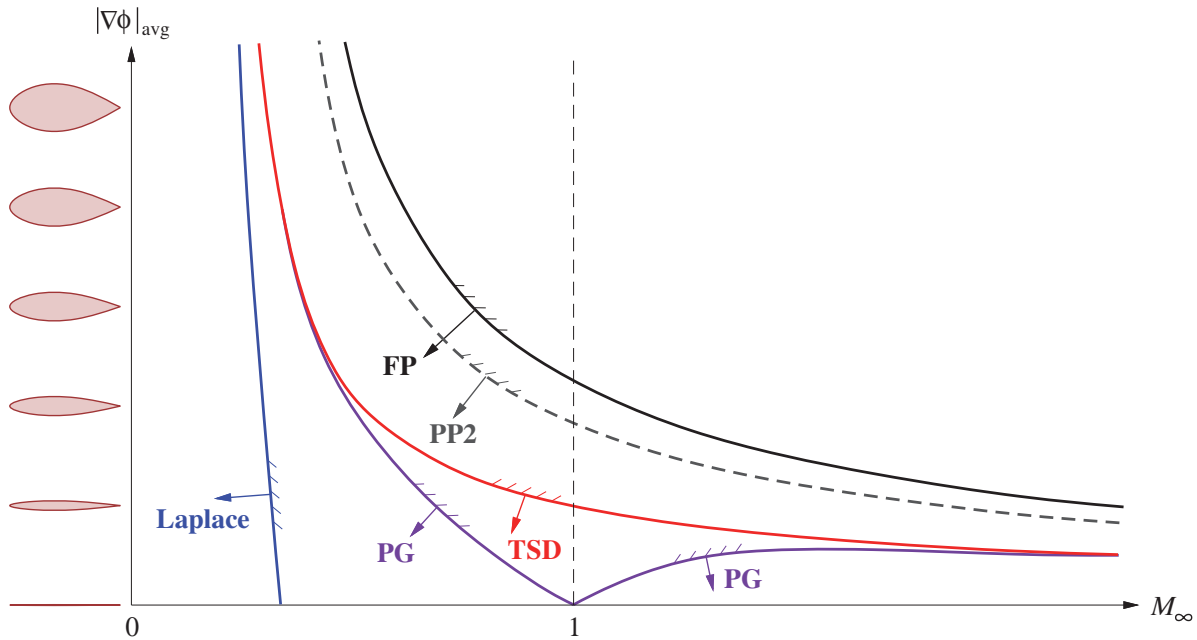
Figure 8.11: Qualitative ranges of validity of various general and small-disturbance potential-flow equations, versus freestream Mach, and versus body slenderness as measured by the perturbation velocity averaged over the flow-field.

8.5.5   Ranges of validity

Figure 8.11 diagrams the range of validity of the five potential equations considered here, versus $|\nabla\phi|_{\mathrm{avg}}$ which is a measure of "non-slenderness," and versus the freestream Mach number M_∞.

The following observations can be made:

- At low speeds where $M_\infty^2 \ll 1$, all five equations are equally valid, even for non-slender bodies (viscous effects are not being considered here). The simplest Laplace equation is then the logical choice to use here.

- For low-subsonic Mach numbers, above $M_\infty > 0.3$ or so, compressibility effects become progressively more pronounced, in which case the PG equation becomes the logical choice to use.

- For flows sufficiently close to sonic, $M_\infty \simeq 1$, specifically transonic flows, the PG equation becomes unsuitable because it cannot represent normal shock waves. In this case the simplest possible equation which can be used is TSD, since it can capture normal shock waves and their associated wave drag.

- For supersonic flows sufficiently far past $M_\infty = 1$, the PG equation again becomes valid. In this situation it becomes a form of the *wave equation*, and can represent weak oblique shocks for which the flow remains everywhere locally supersonic.

- For all but very low freestream Mach numbers, the PG or TSD equations become increasingly restricted to smaller body thicknesses and/or small angles of attack as M_∞ increases. The reason is that the leading terms which were dropped in the PG and TSD derivations were of the form $M_\infty^2 \phi_x \phi_y$, etc. Hence, for a fixed error from these terms, the upper limit on the tolerable $|\nabla\phi|_{\mathrm{avg}}$ must decrease as M_∞ increases.

- For a sufficiently fat body, at some point depending on M_∞, it is necessary to switch to the PP2 or FP

equations for adequate accuracy. Solving PP2 is not any easier or less expensive than solving the FP equation, so PP2 is not used in practice (here it was only a stepping stone to TSD and PG).

- For all but low-speed flows, FP also has an upper limit on body slenderness, even though no small-disturbance approximations were used in its derivation. The reason is that high-speed non-slender flows will have strong shock waves and large shock-wake velocity defects, which invalidate the isentropy and irrotationality assumptions underlying the FP equation.

8.6 Prandtl-Glauert Analysis

8.6.1 Prandtl-Glauert interpretation

The significance of the M_∞^2 term in the PG equation (8.60) can be explained as follows. Starting with the velocity $\mathbf{V}$ written in terms of the perturbation potential (8.54) we have

$$V_\infty \left(\phi_{xx} + \phi_{yy} + \phi_{zz} \right) \;=\; \nabla \cdot \mathbf{V} \;\equiv\; \sigma \;=\; \frac{1}{2} \frac{\nabla(V^2) \cdot \mathbf{V}}{a^2} \tag{8.62}$$

where the last term is the field source σ as given by the compressible continuity equation (8.1). For small-disturbance flows where $|\nabla\phi| \ll 1$ we can now make the following approximations to the quantities above.

$$\nabla(V^2) \;\simeq\; 2V_\infty^2 \left(\phi_{xx}\,\hat{\mathbf{x}} + \phi_{xy}\,\hat{\mathbf{y}} + \phi_{xz}\,\hat{\mathbf{z}} \right)$$
$$\mathbf{V} \;\simeq\; V_\infty\,\hat{\mathbf{x}}$$
$$a^2 \;\simeq\; a_\infty^2$$
$$\sigma \;=\; \frac{1}{2} \frac{\nabla(V^2) \cdot \mathbf{V}}{a^2} \;\simeq\; \frac{V_\infty^3}{a_\infty^2}\phi_{xx} \;=\; M_\infty^2 \left(V_\infty\,\phi_{xx} \right)$$

Equation (8.62) then simplifies to

$$\phi_{xx} + \phi_{yy} + \phi_{zz} \;\simeq\; M_\infty^2 \phi_{xx} \tag{8.63}$$

which is equivalent to the PG equation (8.60). Hence, the extra $M_\infty^2\phi_{xx}$ term in the PG equation is nothing more than an approximation to the field source distribution $\sigma(\mathbf{r})$. The great simplification here is that this approximate field source is now linearly related (i.e. proportional) to the unknown $\phi(\mathbf{r})$ perturbation potential's derivatives, and as a result can be eliminated through a linear variable transformation as follows.

8.6.2 Prandtl-Glauert transformation

The *Prandtl-Glauert transformation* applies to the overall flow problem, including the boundary conditions. It has a single scaling parameter

$$\beta \;\equiv\; \sqrt{1 - M_\infty^2} \tag{8.64}$$

called the *Prandtl-Glauert factor* (not to be confused with the sideslip angle). The transformation of the flow problem has the form $\phi_{(x,y,z;M_\infty)} \rightarrow \bar{\phi}_{(\bar{x},\bar{y},\bar{z})}$ where the PG variables denoted by the overbar are defined as follows.

$$\left\{ \begin{array}{c} \bar{x} \\ \bar{y} \\ \bar{z} \end{array} \right\} = \left\{ \begin{array}{c} x \\ \beta y \\ \beta z \end{array} \right\} \qquad , \qquad \bar{\phi} = \beta^2 \phi \tag{8.65}$$

As sketched in Figure 8.12, the geometry is shrunk in y, z by the β factor. This reduces all the geometric angles, aspect ratios, and also the x components of all normal vectors $\mathbf{n} \equiv \{n_x\ n_y\ n_z\}^T$ by the same factor.

$$\bar{\alpha} = \beta\,\alpha \quad , \qquad \bar{A\!R} = \beta\,A\!R \quad , \qquad \bar{\mathbf{n}} \equiv \left\{ \begin{array}{c} \bar{n}_x \\ \bar{n}_y \\ \bar{n}_z \end{array} \right\} = \left\{ \begin{array}{c} \beta n_x \\ n_y \\ n_z \end{array} \right\} \tag{8.66}$$

It also gives the following relations between the various derivatives.

$$()_x = ()_{\bar{x}} \qquad ()_y = \beta()_{\bar{y}} \qquad ()_z = \beta()_{\bar{z}}$$
$$()_{xx} = ()_{\bar{x}\bar{x}} \qquad ()_{yy} = \beta^2()_{\bar{y}\bar{y}} \qquad ()_{zz} = \beta^2()_{\bar{z}\bar{z}} \tag{8.67}$$

Using the above transformation relations converts the PG equation and wall BC in physical space into the Laplace equation and wall BC in the transformed space.

$$\bar{\phi}_{\bar{x}\bar{x}} + \bar{\phi}_{\bar{y}\bar{y}} + \bar{\phi}_{\bar{z}\bar{z}} = 0 \tag{8.68}$$

$$\text{Wall BC:} \qquad \bar{\phi}_{\bar{y}}\bar{n}_y + \bar{\phi}_{\bar{z}}\bar{n}_z = -\bar{n}_x \tag{8.69}$$

$$\text{or:} \qquad \bar{\phi}_{\bar{z}} = \bar{Z}'(\bar{x}) - \bar{\alpha} \quad \text{(in 2D)} \tag{8.70}$$
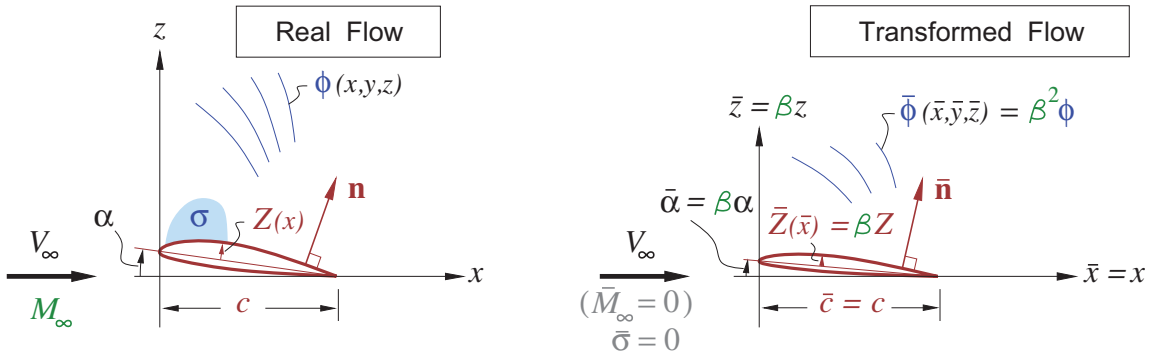
Figure 8.12: Prandtl-Glauert transformation from physical variables (left) to PG variables (right).

The fact that a compressible flow looks incompressible after the PG transformation can be explained or interpreted in a number of ways. One explanation is that the perturbation velocity field in the transformed space has zero divergence and zero curl,

$$\bar{\sigma} \equiv \bar{\nabla} \cdot (\bar{\nabla}\bar{\phi}) = 0 \qquad \text{(equation (8.68))}$$
$$\bar{\omega} \equiv \bar{\nabla} \times (\bar{\nabla}\bar{\phi}) = \mathbf{0} \qquad \text{(identity)}$$

and hence is an incompressible and irrotational flow. Another useful although less rigorous explanation is associated with the thickening effect, which reduces percentage-wise streamtube area variations in the real flow. A low speed flow over a more slender body also has smaller streamtube area variations, so the y, z-scaled incompressible flow mimics the real compressible flow's more uniform streamtube area distributions.

8.6.3   Prandtl-Glauert equation solution procedure

The great practical importance of the PG transformation is that it allows small-disturbance subsonic compressible flow problems which are not transonic (not too close to $M_\infty = 1$) to be solved by incompressible potential flow methods. This is accomplished by the following systematic procedure.

1. The real flow problem has geometry defined in x, y, z, with given $M_\infty > 0$

2. Scale all y, z dimensions by the PG factor $\beta = \sqrt{1 - M_\infty^2}$. This gives a transformed geometry in the PG space $\bar{x}, \bar{y}, \bar{z}$, with $\bar{\alpha}, \bar{n}_x, \bar{A\!R}\ldots$ all reduced by the same factor of β.

3. Calculate the flow over the transformed geometry using an incompressible flow method and related flow models. These include thin airfoil theory, vortex-lattice, panel, far-field approximations, images, etc. This gives the transformed perturbation potential $\bar{\phi}_{(\bar{x},\bar{y},\bar{z})}$, and/or the transformed perturbation velocities $\bar{\phi}_{\bar{x}}, \bar{\phi}_{\bar{y}}, \bar{\phi}_{\bar{z}}$, pressures $\bar{C}_p$, forces $\bar{C}_L$, etc.

4. Calculate the physical perturbation potential and/or velocities using the reverse PG transformations.

$$\phi \;=\; \frac{1}{\beta^2}\,\bar\phi \tag{8.71}$$

$$\phi_x \;=\; \frac{\partial(\bar\phi/\beta^2)}{\partial\,\bar x} \;=\; \frac{1}{\beta^2}\,\bar\phi_{\bar x}$$

$$\phi_y \;=\; \frac{\partial(\bar\phi/\beta^2)}{\partial(\bar y/\beta)} \;=\; \frac{1}{\beta}\,\bar\phi_{\bar y} \tag{8.72}$$

$$\phi_z \;=\; \frac{\partial(\bar\phi/\beta^2)}{\partial(\bar z/\beta)} \;=\; \frac{1}{\beta}\,\bar\phi_{\bar z}$$

With the velocities available, the physical pressure coefficient can now be calculated directly from its exact definition (8.12). But since the small-disturbance approximation is assumed to be valid here, it's useful to consider an alternative simplified small-disturbance form based on the asymptotic pressure expression (8.43).

$$\frac{p}{p_\infty} \;=\; 1 \;-\; \gamma M_\infty^2 \phi_x \;+\; \ldots \tag{8.73}$$

$$C_p \;\equiv\; \frac{p-p_\infty}{\frac{\gamma}{2}M_\infty^2\,p_\infty} \;\simeq\; -2\,\phi_x \;=\; \frac{1}{\beta^2}\left(-2\,\bar\phi_{\bar x}\right) \;=\; \frac{1}{\beta^2}\,\bar C_p \tag{8.74}$$

$$C_L \;=\; \frac{1}{S_{\text{ref}}}\iint \Delta C_p \,\mathrm{d}x\,\mathrm{d}y \;=\; \frac{1}{\beta^2}\left(\frac{1}{\bar S_{\text{ref}}}\iint \Delta \bar C_p \,\mathrm{d}\bar x\,\mathrm{d}\bar y\right) \;=\; \frac{1}{\beta^2}\,\bar C_L \tag{8.75}$$

The advantage here is that if the incompressible solution method directly reports the pressures $\bar C_p$, forces $\bar C_L$, etc., then the corresponding physical quantities can be obtained immediately. Relations (8.74) and (8.75) are collectively known as *Göthert's Rule* [58].

5. To calculate the induced drag coefficient the Trefftz plane wake integral (5.47) can be used, since this only requires that the Trefftz plane's perturbation flow be incompressible.

$$|\mathbf{V}-\mathbf{V}_\infty|^2/a_\infty^2 \;=\; |\nabla\phi|^2 M_\infty^2 \;\ll\; 1$$

This is certainly valid even if M_∞^2 itself is not small. Applying the reverse PG transformation to the Trefftz plane wake integral gives the required induced drag transformation rule.

$$C_{D_i} \;=\; -\frac{1}{S_{\text{ref}}}\int \Delta\phi\,\frac{\partial\phi}{\partial n}\,\mathrm{d}s \;=\; \frac{1}{\beta^3}\left(-\frac{1}{\bar S_{\text{ref}}}\int \Delta\bar\phi\,\frac{\partial\bar\phi}{\partial\bar n}\,\mathrm{d}\bar s\right) \;=\; \frac{1}{\beta^3}\,\bar C_{D_i} \tag{8.76}$$

Compressible 2D airfoil

Consider the 2D airfoil problem for compressible flow, shown in Figure 8.12. Assuming the airfoil is very thin for simplicity, its geometry is defined entirely by its $Z(x)$ camberline shape. As discussed in the previous unsteady-flow Chapter 7, and sketched in Figure 8.13, the vortex sheet strength representing the transformed incompressible flow will have the form

$$\bar\gamma(\bar x) \;=\; \gamma_\alpha\,\bar\alpha \;+\; \gamma_Z\,\bar\varepsilon \tag{8.77}$$

where $\gamma_\alpha(x)$ and $\gamma_Z(x)$ are sheet strength distributions for a unit α and a unit camber shape $Z(x)/\varepsilon$, respectively, with ε being the maximum camber value. These unit distributions can be computed a priori. For example, first-order thin airfoil theory as derived in Appendix D gives

$$\gamma_\alpha(x) \;=\; 2V_\infty\sqrt{\frac{c}{x}-1}$$

and $\gamma_Z(x)$ depends in a more complicated manner on the particular unit camber shape. The circulation and lift coefficient will then also have two corresponding independent components.

$$\bar{c}_\ell = c_{\ell_\alpha} \bar{\alpha} + c_{\ell_Z} \bar{\varepsilon} \tag{8.78}$$

$$\text{where} \quad c_{\ell_\alpha} \equiv \int_0^1 2\frac{\gamma_\alpha}{V_\infty} \, \mathrm{d}(x/c) = 2\pi \tag{8.79}$$

$$c_{\ell_Z} \equiv \int_0^1 2\frac{\gamma_Z}{V_\infty} \, \mathrm{d}(x/c) \tag{8.80}$$
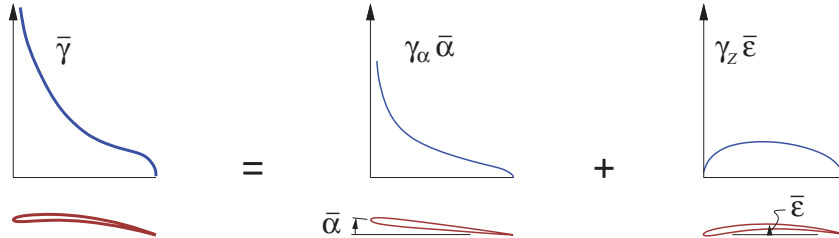
Figure 8.13: Thin airfoil vortex sheet strength and corresponding loading have independent components proportional to angle of attack $\bar{\alpha}$ and maximum camber $\bar{\varepsilon}$.

The compressible c_ℓ is computed by applying the reverse transformations to the solution (8.78).

$$c_\ell = \frac{1}{\beta^2}\bar{c}_\ell = \frac{1}{\beta^2}\left[c_{\ell_\alpha}(\beta\alpha) + c_{\ell_Z}(\beta\varepsilon)\right] = \frac{1}{\beta}\left[c_{\ell_\alpha}\alpha + c_{\ell_Z}\varepsilon\right] \tag{8.81}$$

$$c_\ell = \frac{1}{\beta}(c_\ell)_{\text{inc}} \tag{8.82}$$

The final relation (8.82), called *Prandtl's Rule*, states that the 2D lift coefficient for the compressible case increases by the factor of $1/\beta$ over the incompressible value $(c_\ell)_{\text{inc}}$ for that same airfoil. This can be considered a "shortcut method" for 2D cases, since $(c_\ell)_{\text{inc}}$ is the incompressible value for the physical (not transformed) airfoil shape and angle of attack. It also applies to calculation of C_p, c_m, etc. However, Prandtl's Rule does <u>not</u> hold for 3D cases, where it is necessary to perform the PG geometry transformation and then use Göthert's Rule to obtain the correct compressible solution.

Compressible 3D finite wing

Consider a simple, flat rectangular wing with aspect ratio $A\!R$ and an uncambered airfoil. The objective is to determine its C_L and C_{D_i} for a given angle of attack α and freestream Mach M_∞. Following the PG solution procedure we transform this to $\bar{x}, \bar{y}, \bar{z}$ space where the corresponding transformed wing has

$$\bar{A\!R} = \beta\,A\!R \tag{8.83}$$

$$\bar{\alpha} = \beta\,\alpha \tag{8.84}$$

and its flow-field is governed by the Laplace equation for $\bar{\phi}$. For a high aspect ratio wing this is approximately solved by classical lifting line theory given in Appendix E. The final results for the lift coefficient (E.37) and induced drag coefficient (E.23) can then be directly applied to the transformed problem,

$$\bar{C}_L \simeq \frac{c_{\ell_\alpha}}{1 + c_{\ell_\alpha}/(\pi\bar{A\!R})}\,\bar{\alpha} \tag{8.85}$$

$$\bar{C}_{D_i} = \frac{\bar{C}_L^2}{\pi\,\bar{A\!R}\,\bar{e}} \tag{8.86}$$

where $c_{\ell_\alpha} \simeq 2\pi$ is the wing airfoil's 2D lift-curve slope. An offset to $\bar{\alpha}$ from the wing airfoil camber has been omitted from (8.85), so that $\bar{\alpha}$ is in effect measured from the transformed wing airfoil's zero-lift line. The span efficiency $\bar{e}(\bar{A\!R})$ depends on the transformed wing's aspect ratio, as shown in Figure 8.14.
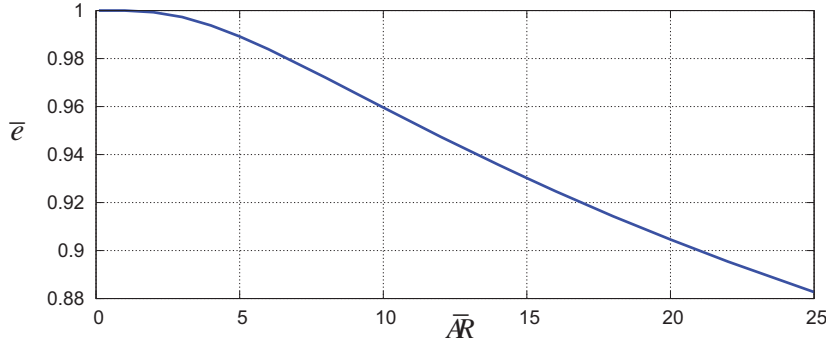
Figure 8.14: Span efficiency versus aspect ratio for simple rectangular wing in incompressible flow, calculated with a Vortex-Lattice method.

We now apply the reverse transformation to the incompressible results (8.85), (8.86).

$$C_L = \frac{1}{\beta^2}\bar{C}_L = \frac{1}{\beta^2}\frac{c_{\ell_\alpha}}{1 + c_{\ell_\alpha}/(\pi\,\beta\,A\!R)}(\beta\alpha) = \frac{c_{\ell_\alpha}}{\beta + c_{\ell_\alpha}/(\pi A\!R)}\alpha \tag{8.87}$$

$$C_{D_i} = \frac{1}{\beta^3}\bar{C}_{D_i} = \frac{1}{\beta^3}\frac{(\beta^2 C_L)^2}{\pi\,(\beta A\!R)\,\bar{e}} = \frac{C_L^2}{\pi\,A\!R\,\bar{e}} \tag{8.88}$$

The 3D lift-curve slope of the wing $\partial C_L/\partial\alpha$ is now seen to depend on β as well as $A\!R$, as plotted in Figure 8.18. Two limiting cases or interest are

$$\frac{\partial C_L}{\partial\alpha} \simeq \pi A\!R \quad , \qquad A\!R \to 0$$

$$\frac{\partial C_L}{\partial\alpha} \simeq \frac{c_{\ell_\alpha}}{\beta} \quad , \qquad A\!R \to \infty \quad (2D)$$

so that small aspect ratio wing flows are independent of compressibility effects. This can be seen in the coalescence of the incompressible and compressible curves in Figure 8.15.
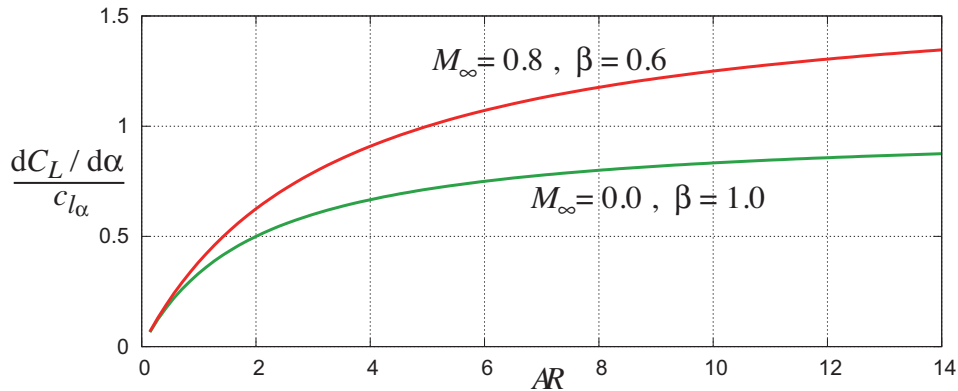

Figure 8.15: Lift-curve slope of simple rectangular wing versus aspect ratio, for two freestream Mach numbers.

For a given C_L, the C_{D_i} is seen to be mostly unaffected by compressibility, except via the small effect of the span efficiency $\bar{e}$ which decreases slightly with $\bar{A\!R}$. For a near-elliptical planform we would have $\bar{e} \simeq 1$,

in which case C_{D_i} would be essentially independent of M_∞. This insensitivity of C_{D_i} to the aircraft flight Mach is consistent with Trefftz-plane theory, in which the lift and the induced drag are implicitly related to each other via the aircraft's trailing vorticity distribution. The aircraft's compressible near-field has no bearing on this lift and induced drag relation.

Low-speed infinite swept wing

We will now investigate the lift characteristics of an infinite swept wing. The incompressible case will be considered first, followed by the compressible case treated via the PG transformation in the next section.

An infinite wing with sweep angle Λ and streamwise chord c is shown in Figure 8.16. The angle of attack α is defined along the x-axis as usual, and hence it also appears in the streamwise section.
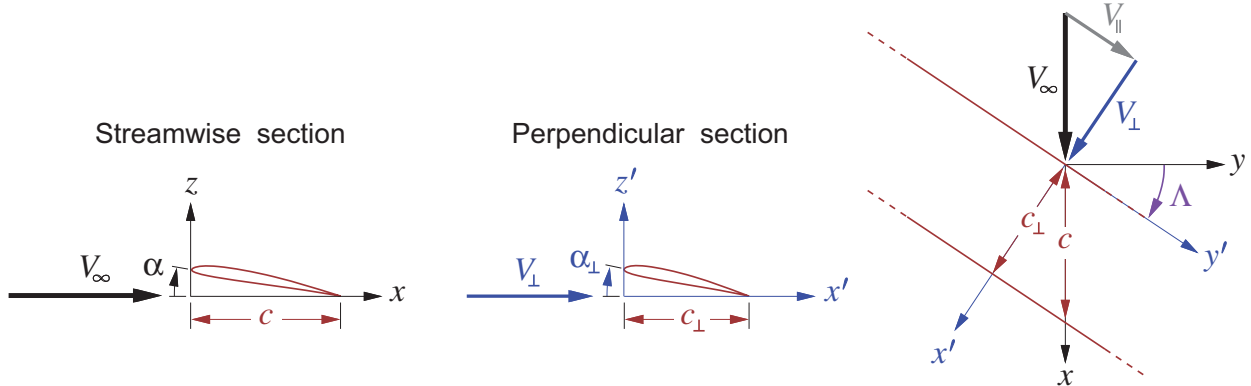
Figure 8.16: Lift of infinite swept wing is determined entirely by geometry and velocity in perpendicular $x'z'$-plane section.

Consider the flow as described in the rotated x', y', z' coordinates where y' is along the wing, and the $x'z'$-plane is perpendicular to the wing. Since each y' location is the same, we must have $\partial()/\partial y' = 0$ for all flow-field quantities. The inviscid y'-momentum equation is then

$$\rho u' \frac{\partial v'}{\partial x'} + \rho w' \frac{\partial v'}{\partial z'} = -\frac{\partial p}{\partial y'} = 0 \tag{8.89}$$

which implies that v' is everywhere constant, and equal to the wing-parallel freestream component

$$v'(\mathbf{r}) = V_\infty \sin \Lambda \equiv V_\| \tag{8.90}$$

so as to match the freestream. The continuity and remaining x', z'-momentum equations are

$$\begin{aligned}
\frac{\partial \rho u'}{\partial x'} + \frac{\partial \rho w'}{\partial z'} &= 0 \\
\rho u' \frac{\partial u'}{\partial x'} + \rho w' \frac{\partial u'}{\partial z'} &= -\frac{\partial p}{\partial x'} \\
\rho u' \frac{\partial w'}{\partial x'} + \rho w' \frac{\partial w'}{\partial z'} &= -\frac{\partial p}{\partial z'}
\end{aligned} \tag{8.91}$$

which describe potential 2D flow in the perpendicular $x'z'$-plane. Specifically, the velocities and pressure fields have the form $u', w', p'(x',z')$, and depend only on the projected airfoil shape, chord, freestream velocity, and angle of attack, all denoted by the $()_\perp$ subscript.

$$c_\perp = c \cos \Lambda \tag{8.92}$$
$$V_\perp = V_\infty \cos \Lambda \tag{8.93}$$
$$\alpha_\perp = \alpha / \cos \Lambda \tag{8.94}$$

And since the pressure field depends only on these parameters, the lift must also, with the spanwise $V_\parallel$ velocity being irrelevant.

Assuming $\alpha_\perp$ is defined from the airfoil's zero-lift line, the incompressible 2D-section lift is

$$\mathrm{d}L \;=\; \tfrac{1}{2}\rho V_\perp^2\, c_{\ell_\alpha}\, \alpha_\perp\, \mathrm{d}S \tag{8.95}$$

where $c_{\ell_\alpha} \simeq 2\pi$ is the 2D lift-curve slope, and $\mathrm{d}S = c_\perp\, \mathrm{d}y' = c\, \mathrm{d}y$ is an element of wing area on which the element of lift $\mathrm{d}L$ acts. The total lift is then

$$
\begin{aligned}
L \;=\; \int \mathrm{d}L \;&=\; \tfrac{1}{2}\rho V_\perp^2\, c_{\ell_\alpha}\, \alpha_\perp\, S \\
&=\; \tfrac{1}{2}\rho(V_\infty \cos \Lambda)^2\, c_{\ell_\alpha}\, (\alpha/\cos \Lambda)\, S
\end{aligned} \tag{8.96}
$$

$$C_L \;\equiv\; \frac{L}{\tfrac{1}{2}\rho V_\infty^2 S} \;=\; c_{\ell_\alpha}\, \alpha \cos \Lambda \tag{8.97}$$

$$\frac{\partial C_L}{\partial \alpha} \;=\; c_{\ell_\alpha} \cos \Lambda \tag{8.98}$$

so that sweep reduces the lift by the factor $\cos \Lambda$ relative to an unswept wing at the same α.

Compressible infinite swept wing

For the compressible infinite swept wing, the PG transformation gives the following modified geometry, also sketched in Figure 8.17.

$$\bar{\alpha} \;=\; \beta\,\alpha \tag{8.99}$$

$$\tan \bar{\Lambda} \;=\; \frac{1}{\beta}\,\tan \Lambda$$

$$\text{or equivalently} \quad \cos \bar{\Lambda} \;=\; \frac{\beta \cos \Lambda}{\sqrt{\beta^2 \cos^2\Lambda + \sin^2\Lambda}} \tag{8.100}$$
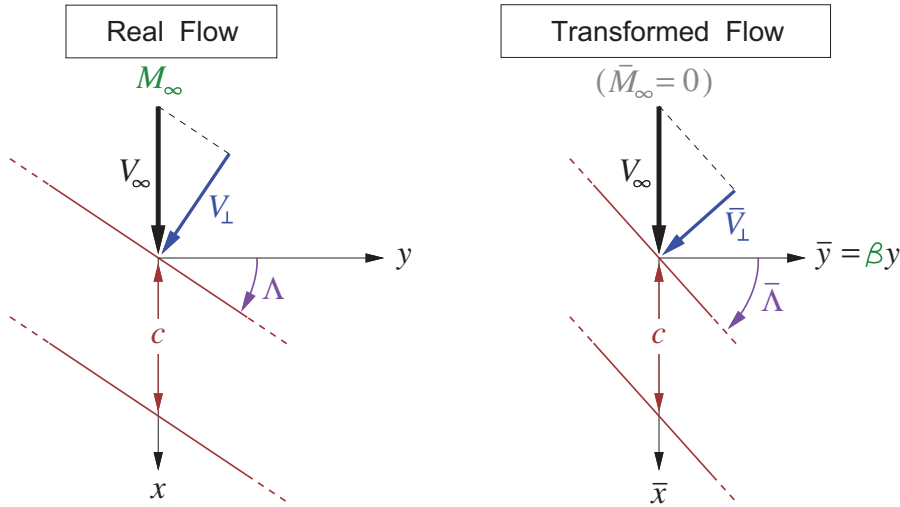
Figure 8.17: Prandtl-Glauert transformation of infinite swept wing.

Applying the previously-derived incompressible solution (8.97) we have

$$\bar{C}_L \;=\; c_{\ell_\alpha}\, \bar{\alpha} \cos \bar{\Lambda} \tag{8.101}$$

and the compressible C_L is then obtained using Göthert's Rule and the reverse PG transformations.

$$C_L = \frac{1}{\beta^2}\bar{C}_L = \frac{1}{\beta^2}c_{\ell_\alpha}\beta\,\alpha\,\frac{\beta\cos\Lambda}{\sqrt{\beta^2\cos^2\Lambda + \sin^2\Lambda}} = \frac{c_{\ell_\alpha}\cos\Lambda}{\sqrt{\beta^2\cos^2\Lambda + \sin^2\Lambda}}\,\alpha \qquad (8.102)$$

$$\frac{\partial C_L}{\partial\alpha} = \frac{c_{\ell_\alpha}\cos\Lambda}{\sqrt{\beta^2\cos^2\Lambda + \sin^2\Lambda}} \qquad (8.103)$$

The $\partial C_L/\partial\alpha$ expression above is plotted in Figure 8.18. Two limiting cases of interest are

$$\frac{\partial C_L}{\partial\alpha} \simeq \frac{c_{\ell_\alpha}}{\beta} \qquad , \qquad \Lambda\to 0° \quad (2D)$$

$$\frac{\partial C_L}{\partial\alpha} \simeq \frac{c_{\ell_\alpha}\cos\Lambda}{\sin\Lambda} \qquad , \qquad \Lambda\to 90°$$

so that large sweep angles mitigate compressibility effects, as can be seen by the coalescence of the incompressible and compressible curves in Figure 8.18.
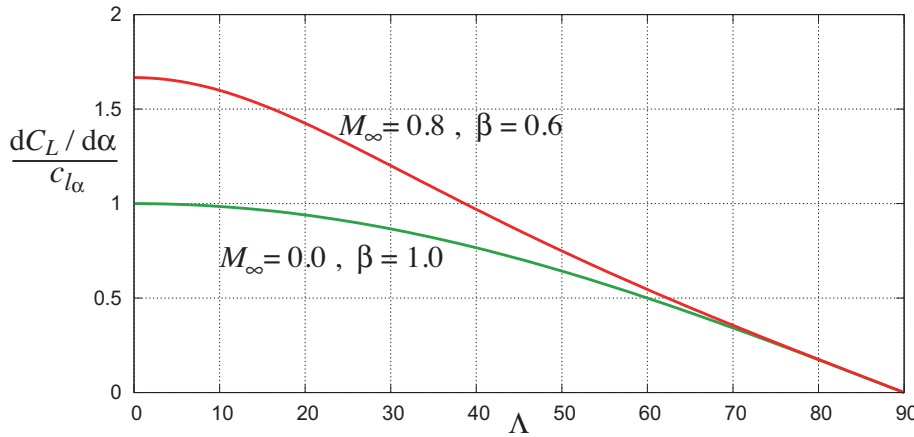
Figure 8.18: Lift-curve slope of infinite swept wing versus sweep, for two freestream Mach numbers. Sweep reduces the influence of Mach number on the wing's lift.

8.7   Subsonic Compressible Far-Fields

8.7.1   Far-field definition approaches

Two approaches can be used to define the far-field for any given compressible flow situation:

1. Define the far-field expansion in physical space. A complication now is that the integrals for the far-field coefficients must include contributions from the field sources. For example, the 2D far-field x-doublet strength of an airfoil represented by source and vortex sheets is

$$\kappa_x = \int(-\lambda x' + \gamma z')\,\mathrm{d}s' + \iint -\frac{1}{2}\frac{\nabla(\mathbf{V}\cdot\mathbf{V})\cdot\mathbf{V}}{a^2}\,x'\,\mathrm{d}x'\,\mathrm{d}z'$$

where the last integral over the field sources $\sigma(x',z')$ would be difficult or impractical to compute in practice.

2. Define the far-field expansion in Prandtl-Glauert space. Now the x-doublet strength is

$$\bar{\kappa}_x = \int(-\bar{\lambda}\bar{x}' + \bar{\gamma}\bar{z}')\,\mathrm{d}\bar{s}' \qquad (8.104)$$

in which the field source integral does not appear, since $\bar{\sigma} \simeq 0$ within the transformed flow-field. Existing incompressible-flow estimates for the coefficients can therefore be used. The resulting transformed far-field potential or velocities are then reverse-transformed to obtain the physical potential or velocities. This far-field definition approach is clearly better, and will be used here.

8.7.2 Compressible 2D far-field

Since the transformed flow problem is incompressible, we can re-use the far-field expressions for the far-field potentials and velocities which were developed in Chapter 2. For the 2D case we have

$$\bar{\phi}_{\mathrm{ff}(\bar{x},\bar{z})} = \frac{\bar{\Lambda}}{2\pi}\ln\bar{r} - \frac{\bar{\Gamma}}{2\pi}\bar{\theta} + \frac{\bar{\kappa}_x}{2\pi}\frac{\bar{x}}{\bar{r}^2} + \frac{\bar{\kappa}_z}{2\pi}\frac{\bar{z}}{\bar{r}^2} \tag{8.105}$$

$$\frac{\partial\bar{\phi}_{\mathrm{ff}}}{\partial\bar{x}}_{(\bar{x},\bar{z})} = \frac{\bar{\Lambda}}{2\pi}\frac{\bar{x}}{\bar{r}^2} + \frac{\bar{\Gamma}}{2\pi}\frac{\bar{z}}{\bar{r}^2} + \frac{\bar{\kappa}_x}{2\pi}\frac{\bar{z}^2-\bar{x}^2}{\bar{r}^4} + \frac{\bar{\kappa}_z}{2\pi}\frac{-2\bar{x}\bar{z}}{\bar{r}^4} \tag{8.106}$$

$$\frac{\partial\bar{\phi}_{\mathrm{ff}}}{\partial\bar{z}}_{(\bar{x},\bar{z})} = \frac{\bar{\Lambda}}{2\pi}\frac{\bar{z}}{\bar{r}^2} - \frac{\bar{\Gamma}}{2\pi}\frac{\bar{x}}{\bar{r}^2} + \frac{\bar{\kappa}_x}{2\pi}\frac{-2\bar{x}\bar{z}}{\bar{r}^4} + \frac{\bar{\kappa}_z}{2\pi}\frac{\bar{x}^2-\bar{z}^2}{\bar{r}^4} \tag{8.107}$$

where $\bar{r},\bar{\theta}$ are defined in the transformed space.

$$\bar{r} \equiv \sqrt{\bar{x}^2+\bar{z}^2} = \sqrt{x^2+(\beta z)^2} = \sqrt{x^2+(1-M_\infty^2)z^2} \tag{8.108}$$

$$\bar{\theta} \equiv \arctan\left(\frac{\bar{z}}{\bar{x}}\right) = \arctan\left(\frac{\beta z}{x}\right) \tag{8.109}$$

The four far-field coefficients can be defined directly from the incompressible definitions, with the reverse transformation immediately included to put them in terms of the physical parameters.

$$\bar{\Lambda} = V_\infty\bar{\delta}^*_\infty = V_\infty\delta^*_\infty\,\beta \tag{8.110}$$

$$\bar{\Gamma} = \frac{1}{2}V_\infty\bar{c}\,\bar{c}_\ell = \frac{1}{2}V_\infty c\,c_\ell\,\beta^2 \tag{8.111}$$

$$\bar{\kappa}_x = V_\infty\bar{A}\left(1+\frac{\bar{t}_{\max}}{\bar{c}}\right) = V_\infty A\,\beta\left(1+\beta\frac{t_{\max}}{c}\right) \tag{8.112}$$

$$\bar{\kappa}_z = \frac{1}{2}V_\infty\bar{c}^2\,\bar{c}_{m_0} = \frac{1}{2}V_\infty c^2\,c_{m_0}\,\beta^2 \tag{8.113}$$

A complication in relating $\bar{\Lambda}$ to the drag coefficient is that at high speeds the boundary layer and wake fluid is heated significantly via friction, which reduces its density relative to the potential flow. The reduced density increases δ^* relative to θ, as can be seen from comparing their definitions (4.4) and (4.11) for $\rho/\rho_e<1$. An approximate relation between the far-downstream thicknesses is

$$\delta^*_\infty \simeq \left(1+(\gamma-1)M_\infty^2\right)\theta_\infty \tag{8.114}$$

which follows from the assumption that the wake has a constant total enthalpy, as discussed in Section 1.6. The far-field source (8.110) can then be more conveniently given in terms of the profile drag coefficient $c_d = 2\theta_\infty/c$ as follows.

$$\bar{\Lambda} = V_\infty\theta_\infty\beta\left(1+(\gamma-1)M_\infty^2\right) = \frac{1}{2}V_\infty\,c\,c_d\,\beta\left(1+(\gamma-1)M_\infty^2\right) \tag{8.115}$$

With all the transformed far-field coefficients known, the transformed perturbation potential and velocities can be calculated from (8.105),(8.106),(8.107) at any field point of interest. The physical perturbation potential and velocities are then obtained by the usual reverse transformations:

$$\phi_{\mathrm{ff}} = \frac{1}{\beta^2}\bar{\phi}_{\mathrm{ff}} \tag{8.116}$$

$$u_{\mathrm{ff}} = \frac{\partial\phi_{\mathrm{ff}}}{\partial x} = \frac{1}{\beta^2}\frac{\partial\bar{\phi}_{\mathrm{ff}}}{\partial\bar{x}} \tag{8.117}$$

$$v_{\mathrm{ff}} = \frac{\partial\phi_{\mathrm{ff}}}{\partial y} = \frac{1}{\beta}\frac{\partial\bar{\phi}_{\mathrm{ff}}}{\partial\bar{y}} \tag{8.118}$$

$$w_{\mathrm{ff}} = \frac{\partial\phi_{\mathrm{ff}}}{\partial z} = \frac{1}{\beta}\frac{\partial\bar{\phi}_{\mathrm{ff}}}{\partial\bar{z}} \tag{8.119}$$

One complication with this treatment is the far-field contribution of the higher-order compressibility terms in the PP2 equation (8.55), which are ignored in the first-order PG equation. Specifically, the source and vortex parts of ϕ_{ff} in (8.105) have their own field-source distributions as given by (8.1), which then should be included in the $\bar{\kappa}_x$ integral (8.104) above, and the corresponding $\bar{\kappa}_z$ integral as well. This correction is treated by Cole and Cook [59]. The main effect is that an airfoil's far-field x-doublet now also depends to some extent on its lift, not just on its area.

8.7.3   Compressible 3D far-field

The 3D incompressible far-field potential and velocities, when written using the transformed variables, become applicable to the compressible case,

$$\bar{\phi}_{\text{ff}}(\bar{x},\bar{y},\bar{z}) \;=\; \frac{\bar{\Sigma}}{4\pi}\frac{-1}{\bar{r}} \;+\; \frac{\bar{\mathcal{K}}_x}{4\pi}\frac{\bar{x}}{\bar{r}^3} \;+\; \frac{\bar{\mathcal{K}}_y}{4\pi}\frac{\bar{y}}{\bar{r}^3} \;+\; \frac{\bar{\mathcal{K}}_z}{4\pi}\frac{\bar{z}}{\bar{r}^3} \tag{8.120}$$

$$\frac{\partial\bar{\phi}_{\text{ff}}}{\partial\bar{x}}(\bar{x},\bar{y},\bar{z}) \;=\; \frac{\bar{\Sigma}}{4\pi}\frac{\bar{x}}{\bar{r}^3} \;+\; \frac{\bar{\mathcal{K}}_x}{4\pi}\frac{\bar{r}^2-3\bar{x}^2}{\bar{r}^5} \;+\; \frac{\bar{\mathcal{K}}_y}{4\pi}\frac{-3\bar{x}\bar{y}}{\bar{r}^5} \;+\; \frac{\bar{\mathcal{K}}_z}{4\pi}\frac{-3\bar{x}\bar{z}}{\bar{r}^5} \tag{8.121}$$

$$\frac{\partial\bar{\phi}_{\text{ff}}}{\partial\bar{y}}(\bar{x},\bar{y},\bar{z}) \;=\; \frac{\bar{\Sigma}}{4\pi}\frac{\bar{y}}{\bar{r}^3} \;+\; \frac{\bar{\mathcal{K}}_x}{4\pi}\frac{-3\bar{x}\bar{y}}{\bar{r}^5} \;+\; \frac{\bar{\mathcal{K}}_y}{4\pi}\frac{\bar{r}^2-3\bar{y}^2}{\bar{r}^5} \;+\; \frac{\bar{\mathcal{K}}_z}{4\pi}\frac{-3\bar{y}\bar{z}}{\bar{r}^5} \tag{8.122}$$

$$\frac{\partial\bar{\phi}_{\text{ff}}}{\partial\bar{z}}(\bar{x},\bar{y},\bar{z}) \;=\; \frac{\bar{\Sigma}}{4\pi}\frac{\bar{z}}{\bar{r}^3} \;+\; \frac{\bar{\mathcal{K}}_x}{4\pi}\frac{-3\bar{x}\bar{z}}{\bar{r}^5} \;+\; \frac{\bar{\mathcal{K}}_y}{4\pi}\frac{-3\bar{y}\bar{z}}{\bar{r}^5} \;+\; \frac{\bar{\mathcal{K}}_z}{4\pi}\frac{\bar{r}^2-3\bar{z}^2}{\bar{r}^5} \tag{8.123}$$

$$\bar{r} \;\equiv\; \sqrt{\bar{x}^2+\bar{y}^2+\bar{z}^2} \;=\; \sqrt{x^2+(1-M_\infty^2)(y^2+z^2)} \tag{8.124}$$

The incompressible 3D far-field analysis of Section (2.12) gives the far-field source Σ in terms of the body's wake momentum defect and drag, and gives the far-field x–doublet $\mathcal{K}_x$ in terms of the body's volume. Noting that both the area and volume scale as β^2 in the PG transformation, the transformed strengths for the transformed far-field expansion are given in terms of the physical parameters as follows. Relation (8.114) is also applied to relate the wake displacement area to the momentum area and drag.

$$\bar{\Sigma} \;=\; V_\infty\bar{\Delta}^*_\infty \;=\; V_\infty\Delta^*_\infty\,\beta^2 \;=\; \frac{1}{2}V_\infty S_{\text{ref}}\,C_{D_p}\,\beta^2\left(1+(\gamma{-}1)M_\infty^2\right) \tag{8.125}$$

$$\bar{\mathcal{K}}_x \;=\; V_\infty\bar{\mathcal{V}} \;=\; V_\infty\,\mathcal{V}\,\beta^2 \tag{8.126}$$

8.8   Small-Disturbance Supersonic Flows

The Prandtl-Glauert equation is valid for slender supersonic flows sufficiently far beyond $M_\infty = 1$. As a minimum, the flow must be supersonic everywhere, with no locally-subsonic regions. Furthermore, the perturbation velocities must be small enough so the quadratic and higher-order terms in the mass flux expansions (8.44)–(8.46) are much less than unity. Because these also scale as M_∞^2 or M_∞^4, the validity of the PG equation becomes restricted to flows which are more and more slender as the Mach number increases. This shrinking range of validity with increasing Mach number is indicated in Figure 8.11.

8.8.1   Supersonic flow analysis problem

The linearized small-disturbance supersonic flow problem has the same governing PG equation and flow-tangency condition as the subsonic case,

$$-(M_\infty^2-1)\,\phi_{xx} \;+\; \phi_{yy} \;+\; \phi_{zz} \;=\; 0 \tag{8.127}$$

$$n_x \;+\; \phi_y\,n_y \;+\; \phi_z\,n_z \;=\; 0 \qquad \text{(Body BC)} \tag{8.128}$$

but the ϕ_{xx} term now has a negative sign. This fundamentally changes the nature of the solutions, which exhibit *waves* propagating from the body. It's also necessary to redefine β so it stays real.

$$\beta \equiv \sqrt{M_\infty^2 - 1} \qquad \text{(supersonic flows)} \qquad (8.129)$$

8.8.2 2D supersonic airfoil

The wave-like nature of supersonic PG solutions is most easily seen in the 2D thin airfoil case, where we drop ϕ_{yy} and set $(n_x, n_y, n_z) = (\alpha - Z', \, 0, \, 1)$. The PG problem (8.127), (8.128) then simplifies to

$$-\beta^2 \phi_{xx} + \phi_{zz} = 0 \qquad (8.130)$$
$$\phi_z = Z' - \alpha \qquad \text{(on } 0 \leq x \leq c, \; z = 0^\pm\text{)} \qquad (8.131)$$

which has the following solution, shown in Figure 8.19 as the separate α and $Z'(x)$ components.

$$\phi(x,z\,;M_\infty) = \begin{cases} 0 & , & \xi^\pm < 0 & \text{(upstream of wave systems)} \\ \frac{1}{\beta}\left[\, \alpha\,\xi^+ - Z_u(\xi^+)\right] & , & 0 \leq \xi^+ \leq c, \; z > 0 & \text{(inside upper wave system)} \\ \frac{1}{\beta}\left[-\alpha\,\xi^- + Z_l(\xi^-)\right] & , & 0 \leq \xi^- \leq c, \; z < 0 & \text{(inside lower wave system)} \\ \frac{1}{\beta}\left[\,\pm\alpha\,c\,\right] & , & c < \xi^\pm & \text{(downstream of wave systems)} \end{cases} \qquad (8.132)$$

$$\xi^+(x,z\,;M_\infty) = x - \beta z$$
$$\xi^-(x,z\,;M_\infty) = x + \beta z \qquad (8.133)$$
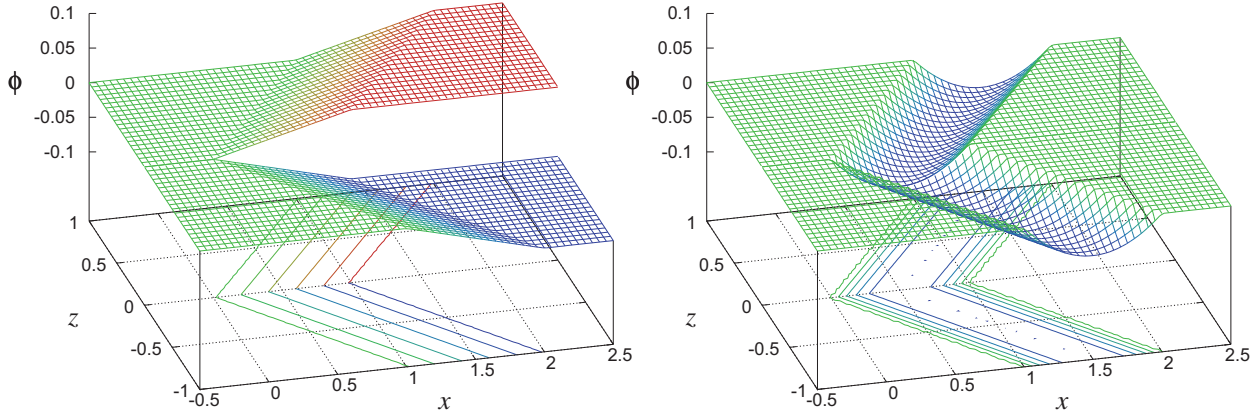
Figure 8.19: Supersonic potentials over 2D airfoil. Left: $\alpha = 0.05$. Right: $Z(x) = 0.2(x - x^2/c)$.

The ξ functions are called *characteristics*, along which the solution is constant in this case. Figure 8.20 shows the perturbation velocities and streamlines for the thickness-only case.

The perturbation x-velocities give the pressure coefficients.

$$C_{p_u} = -2\,(\phi_x)_u = -2\,\frac{\mathrm{d}\phi}{\mathrm{d}\xi^+}\frac{\partial\xi^+}{\partial x} = \frac{2}{\beta}\left[-\alpha + Z'_u(\xi^+)\right] \qquad (8.134)$$

$$C_{p_l} = -2\,(\phi_x)_l = -2\,\frac{\mathrm{d}\phi}{\mathrm{d}\xi^-}\frac{\partial\xi^-}{\partial x} = \frac{2}{\beta}\left[\,\alpha - Z'_l(\xi^-)\right] \qquad (8.135)$$

The lift coefficient can then also be computed, assuming the airfoil has $Z_u = Z_l = 0$ at $x = 0, c$.

$$c_\ell = \oint -C_p\,\hat{\mathbf{n}}\cdot\hat{\mathbf{z}}\;\mathrm{d}(x/c) = \int_0^1 (C_{p_l} - C_{p_u})_{z=0}\;\mathrm{d}(x/c) = \frac{4}{\beta}\,\alpha \qquad (8.136)$$
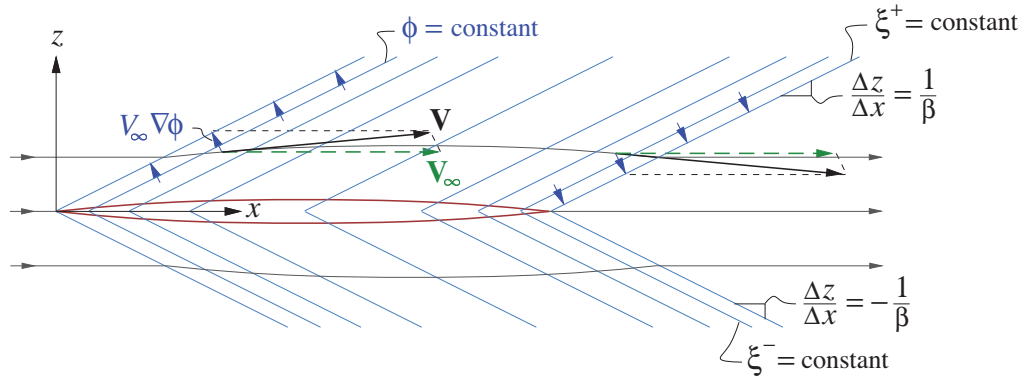
Figure 8.20: Supersonic flow over 2D airfoil with symmetric thickness only ($\alpha=0$).

Relation (8.136) is the *Ackeret equation* for 2D supersonic lift. The lift-curve slope is $\mathrm{d}c_\ell/\mathrm{d}\alpha = 4/\beta$ which can be compared with the $2\pi/\beta$ value on the subsonic side. Interestingly, the supersonic c_ℓ is independent of the airfoil shape, since it does not have the c_{ℓ_0} camber term of the subsonic case.

The lift can also be obtained from the circulation via the Kutta-Joukowski theorem, which is valid for compressible flows. The circulation is the wake potential jump given by the last form in (8.132).

$$c_\ell \;\equiv\; \frac{L'}{\tfrac{1}{2}\rho_\infty V_\infty^2 c} \;=\; \frac{\rho_\infty V_\infty \Gamma}{\tfrac{1}{2}\rho_\infty V_\infty^2 c} \;=\; \frac{2\,\Gamma}{cV_\infty} \;=\; \frac{2\,\Delta\phi_{\text{wake}}}{c} \;=\; \frac{4}{\beta}\,\alpha \tag{8.137}$$

Unlike subsonic inviscid 2D airfoils which have zero drag, supersonic inviscid 2D airfoils in general have nonzero *wave drag*. This is associated with the oblique waves which carry energy away from the airfoil, and hence is different in nature than the wave drag due to a normal shock on subsonic/transonic airfoils which dissipates energy locally. Using the integral momentum theorem on the contour around the airfoil shown in Figure 8.21, we have

$$D'_w \;=\; \oint -\rho\mathbf{V}\cdot\hat{\mathbf{n}}\,(\mathbf{V}-\mathbf{V}_\infty)\cdot\hat{\mathbf{x}}\;\mathrm{d}l \;\simeq\; -\rho_\infty V_\infty^2 \oint \phi_z\,\phi_x\,n_z\;\mathrm{d}l \tag{8.138}$$

which can in general be separated into wave drag due to lift and wave drag due to thickness.

$$c_{dw} \;\equiv\; \frac{D'_w}{\tfrac{1}{2}\rho_\infty V_\infty^2 c} \;=\; (c_{dw})_\ell \;+\; (c_{dw})_\tau \tag{8.139}$$

$$(c_{dw})_\ell \;=\; \frac{4}{\beta}\,\alpha^2 \;=\; c_\ell\,\alpha \tag{8.140}$$

$$(c_{dw})_\tau \;=\; \frac{2}{\beta}\int_0^1 \left[(Z'_u)^2 + (Z'_l)^2\right]\mathrm{d}(x/c) \tag{8.141}$$

It should be noted that all the above results are valid only for thin airfoils at small angles of attack, since the small-disturbance approximation was used to derive its governing PG equation. An alternative approach is to use *Shock-Expansion Theory* based on oblique-shock and Prandtl-Meyer expansion-fan functions (see Shapiro [60]). These do not rely on small-disturbance approximations and hence are more accurate, but they do not apply to general 3D flows. Since most practical supersonic applications have low aspect ratios which result in strongly 3D flow, we will restrict our analysis to the PG equation.
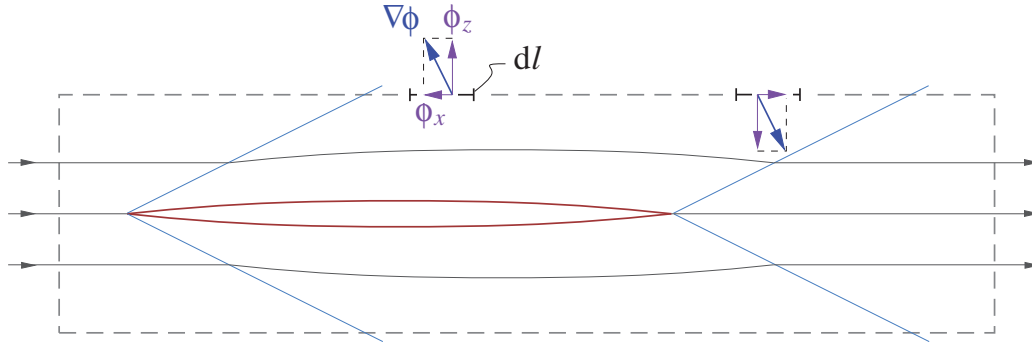
Figure 8.21: Control volume contour for calculation of supersonic wave drag via the integral momentum theorem.

8.8.3 Canonical supersonic flow

The PG transformation (8.65), (8.66) can be applied to the supersonic case if the redefined β is used. Now the PG equation (8.60) reduces to

$$- \bar{\phi}_{\bar{x}\bar{x}} + \bar{\phi}_{\bar{y}\bar{y}} + \bar{\phi}_{\bar{z}\bar{z}} = 0 \qquad (8.142)$$

which is the *wave equation*. It has an implied $\bar{M}_\infty = \sqrt{2}$, $\bar{\beta} = 1$, so that its characteristics have slopes of ± 1. This is called the *canonical* supersonic flow. This is only a minor simplification from the physical flow, since it does not provide any special advantages for solving supersonic flow problems, unlike in subsonic flow where the canonical flow is incompressible. Here its main advantage is theoretical, in that the properties of all small-disturbance supersonic flows can be investigated by considering only the canonical case.

8.8.4 Supersonic singularities

The linearity of the PG equation allows the construction of general 3D flows by superposition of *supersonic singularities*. These are analogues of the subsonic source, vortex, and doublet singularities, but have a number of important differences. One major difference is that a supersonic singularity is singular everywhere on its *Mach cone surface*, not just at a single point like in the subsonic case, and is also undefined in some regions of space. These features will require care in the construction of supersonic superposition integrals.

Hyperbolic radius

For defining supersonic-singularity kernel functions, a useful field function is the *hyperbolic radius*,

$$h_{(\mathbf{r}\,;\,M_\infty)} \equiv \sqrt{x^2 - (M_\infty^2 - 1)(y^2 + z^2)} \qquad (8.143)$$

which is the closest distance between the singularity point at the origin and the hyperboloid surface containing the field point $\mathbf{r}$, as shown in Figure 8.22. The term "radius" originates from the observation that for the incompressible case $M_\infty = 0$ it reduces to the actual distance function $h_{(\mathbf{r}\,;\,0)} = |\mathbf{r}| = \sqrt{x^2 + y^2 + z^2}$. For a singularity point located at some arbitrary location $\mathbf{r}'$ other than the origin, the hyperbolic radius is obtained by the usual shift of the function's argument, $h_{(\mathbf{r} - \mathbf{r}'\,;\,M_\infty)}$. The equation

$$h_{(\mathbf{r} - \mathbf{r}'\,;\,M_\infty)} = 0$$

therefore defines a Mach cone with its apex at location $\mathbf{r}'$.
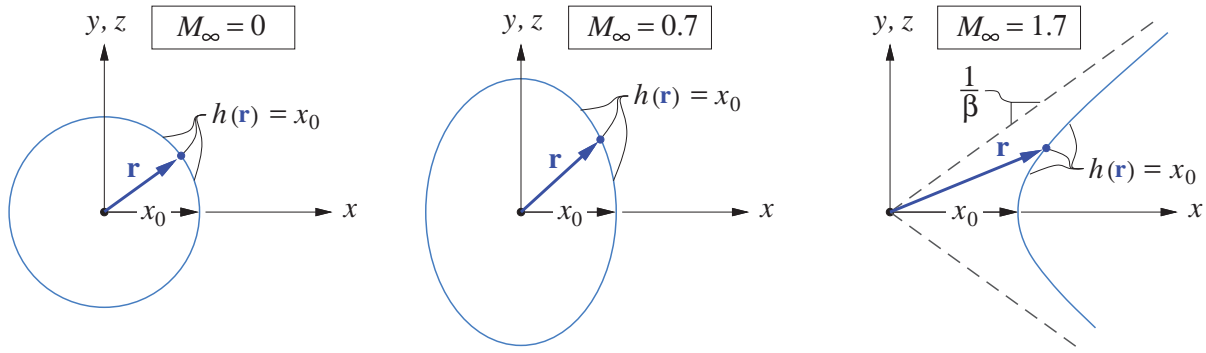
Figure 8.22: Hyperbolic radius function $h(\mathbf{r}; M_\infty)$ for the supersonic case on the right is the nearest distance x_0 between the origin and the hyperboloid containing the field point $\mathbf{r}$. For the incompressible case $M_\infty = 0$ on the left, this h function becomes the ordinary distance $h(\mathbf{r};0) = |\mathbf{r}|$.

Supersonic point source

The basic 3D singularity from which all others can be constructed is the *supersonic point source*, which has the following unit-strength potential or kernel function, plotted in Figure 8.23.

$$\hat{\phi}_\Sigma(\mathbf{r}; M_\infty) = \begin{cases} \dfrac{-1}{2\pi h} & , \quad x > \beta\sqrt{y^2+z^2} \\ 0 & , \quad x \le \beta\sqrt{y^2+z^2} \end{cases} \tag{8.144}$$
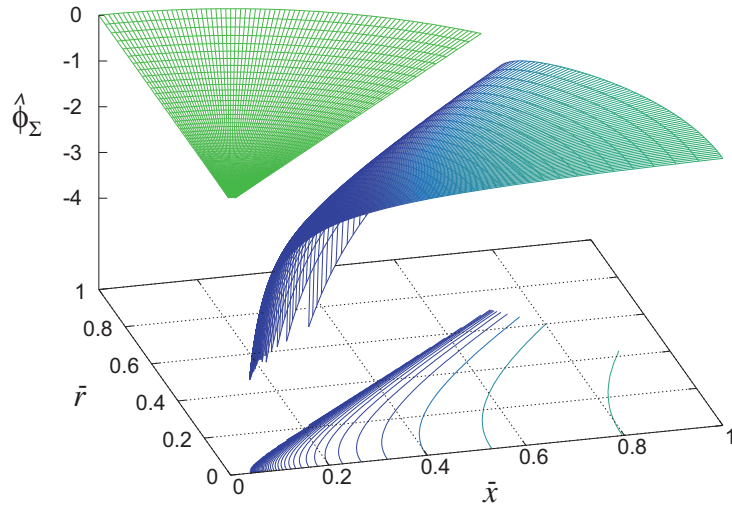
Figure 8.23: Potential of unit supersonic point source, plotted in canonical coordinates $\bar{x}$ and $\bar{r} = \sqrt{\bar{y}^2+\bar{z}^2}$. Potential is singular on Mach cone, defined by $h=0$ and emanating from the singularity point which in the plot is at the origin. A polar mesh is used in the plot to show the edge of the Mach cone.

The term "source" is a bit misleading here, since this flow-field is not just the usual point source at the origin, but also includes the field source distribution
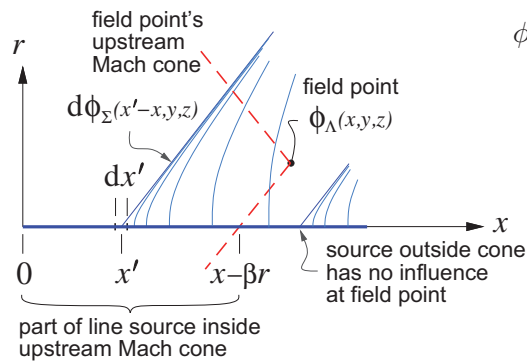
$$\sigma(\mathbf{r}) = \nabla^2 \hat{\phi}_\Sigma = M_\infty^2 \frac{\partial^2 \hat{\phi}_\Sigma}{\partial x^2}$$

which is generated by the point source. It's also important to note that an isolated supersonic source of finite strength is not physical, since its σ field has an infinite strength everywhere on its $h(\mathbf{r})=0$ Mach cone

surface. The velocity field also has a very strong $1/|\mathbf{r}-\mathbf{r}'|^2$ singularity everywhere in the vicinity of the Mach cone surface. A more physical flow-field will be obtained only after a distribution of infinitesimal point sources is superimposed, as will be considered in the following sections.

Supersonic line source

Superposition of a line of supersonic point sources (8.144) along the x-axis, from the origin downstream, creates a *supersonic line source*. This can represent supersonic flow over a body of revolution.

$$\phi_\Lambda(x,y,z\,;M_\infty) = \int_0^{x-\beta r} \Lambda(x')\,\hat{\phi}_\Sigma(x-x',y,z\,;M_\infty)\,\mathrm{d}x'$$

$$= \frac{1}{2\pi}\int_0^{x-\beta r} \frac{-\Lambda(x')}{\sqrt{(x-x')^2 - \beta^2 r^2}}\,\mathrm{d}x' \quad (8.145)$$

$$r \equiv \sqrt{y^2 + z^2} \quad (8.146)$$

The radial distance r from the x-axis will be convenient to use for axisymmetric potential distributions such as this one. Note that this is a change in notation from elsewhere in this book, where r typically denotes $|\mathbf{r}|$.

The integration range in (8.145) is restricted to only those point sources on the x-axis which can influence the field point x, y, z. This range is what lies inside the <u>upstream</u> Mach cone emanating from the field point, as sketched in the figure above.

For the case of a unit line-source density $\Lambda(x) = 1$, we can integrate (8.145) to give the unit line source potential, shown plotted in Figure 8.24.

$$\hat{\phi}_\Lambda(x,y,z\,;M_\infty) = \int_0^{x-\beta r} \hat{\phi}_\Sigma(x-x',y,z\,;M_\infty)\,\mathrm{d}x'$$

$$= \frac{1}{2\pi}\ln\left[\frac{x-h}{\beta r}\right] = \frac{1}{2\pi}\ln\left[\frac{x}{\beta r} - \sqrt{\left(\frac{x}{\beta r}\right)^2 - 1}\right] \quad (8.147)$$

$$\frac{\partial\hat{\phi}_\Lambda}{\partial x} = \frac{-1}{2\pi h} \quad (8.148)$$

$$\frac{\partial\hat{\phi}_\Lambda}{\partial r} = \frac{1}{2\pi}\left(\frac{1}{h}\frac{\beta^2 r}{x-h} - \frac{1}{r}\right) \quad (8.149)$$

Note that the highly singular nature of the point source potential has been mitigated to a weak logarithmic singularity for the line source. The strength of the perturbation velocities $\partial\hat{\phi}_\Lambda/\partial x$ and $\partial\hat{\phi}_\Lambda/\partial r$, has also been mitigated to a $1/|\mathbf{r}-\mathbf{r}'|$ singularity along the origin's Mach cone where $h=0$, and also on the x-axis where $r=0$.

The local source line strength $\Lambda(x)$ required to model a body of revolution with area and corresponding radius distributions $A(x) = \pi R(x)^2$ can be determined by same approach used in the subsonic case. Remembering that ϕ is normalized with the freestream velocity, the flow tangency condition at the body surface is

$$\left.\frac{\partial\phi}{\partial r}\right|_{r=R} = \frac{\mathrm{d}R}{\mathrm{d}x}$$
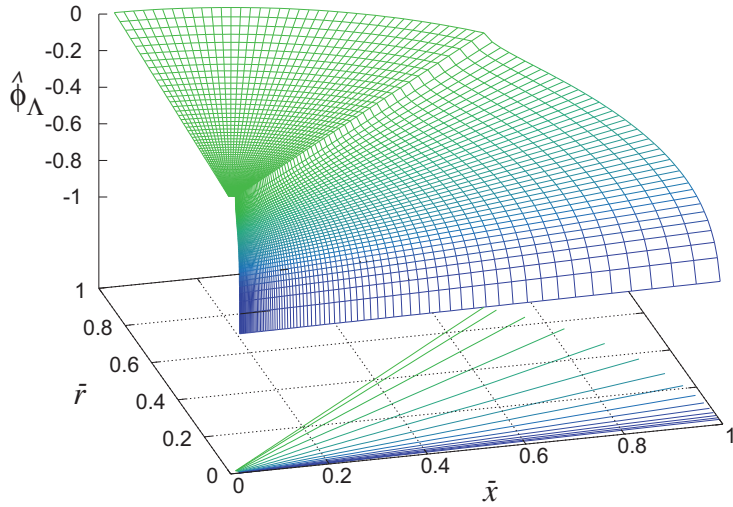
Figure 8.24: Potential of a unit supersonic line source extending from the origin downstream.

which when rewritten using the unit-strength radial velocity (8.149) gives the required line source strength Λ in terms of the body geometry.

$$\Lambda \frac{\partial \hat{\phi}_\Lambda}{\partial r}\bigg|_{r=R} = \frac{\Lambda}{2\pi}\left(\frac{1}{\sqrt{x^2-\beta^2 R^2}}\frac{\beta^2 R}{x-\sqrt{x^2-\beta^2 R^2}} - \frac{1}{R}\right) = \frac{\mathrm{d}R}{\mathrm{d}x} \tag{8.150}$$

However, for a slender body we have $R/x \ll 1$, so that we can approximate

$$\sqrt{x^2-\beta^2 R^2} = x\sqrt{1-\frac{\beta^2 R^2}{x^2}} \simeq x\left(1-\frac{1}{2}\frac{\beta^2 R^2}{x^2}\right) \simeq x$$

in which case the expression in the parentheses in (8.150) reduces to

$$\frac{1}{\sqrt{x^2-\beta^2 R^2}}\frac{\beta^2 R}{x-\sqrt{x^2-\beta^2 R^2}} - \frac{1}{R} \simeq \frac{1}{x}\frac{\beta^2 R}{x\frac{1}{2}\frac{\beta^2 R^2}{x^2}} - \frac{1}{R} = \frac{1}{x}\frac{2x}{R} - \frac{1}{R} = \frac{1}{R}$$

so that the overall expression (8.150) for Λ simplifies greatly.

$$\frac{\Lambda}{2\pi}\frac{1}{R} = \frac{\mathrm{d}R}{\mathrm{d}x}$$
$$\Lambda = 2\pi R\frac{\mathrm{d}R}{\mathrm{d}x} = \frac{\mathrm{d}A}{\mathrm{d}x} \tag{8.151}$$

Aside from a factor of V_∞ (Λ here corresponds to Λ/V_∞ as defined previously), the line source strength (8.151) is exactly the same as expression (6.72) for a slender body in incompressible flow. Since Λ here also depends only on the total cross-sectional area $A(x)$, it can be used for bodies which aren't exactly axisymmetric.

8.8.5 Wave drag of arbitrary slender bodies of revolution

The control-volume wave drag analysis of a 2D airfoil, which gave result (8.138), extends readily to the axisymmetric body of revolution. The result is

$$D_w = -\rho_\infty V_\infty^2 \iint \phi_z\, \phi_x\, \mathrm{d}\mathcal{S} \tag{8.152}$$

where the integral area element dS is on a cylindrical "pipe" surface surrounding the body and aligned with the freestream. The potential φ can be obtained by the line-source superposition integral (8.145). Ashley and Landahl [50] combine these two expressions and give after some manipulation

$$D_w = -\frac{\rho_\infty V_\infty^2}{4\pi} \int_0^\ell \int_0^\ell \frac{d\Lambda}{dx'}(x') \frac{d\Lambda}{dx''}(x'') \ln|x'-x''| \ dx' \ dx'' \tag{8.153}$$

where body extends over $x = 0 \ldots \ell$. Note that the drag depends on the square of $d\Lambda/dx = d^2A/dx^2$, so that low wave drag dictates bodies which have smooth cross-sectional area distributions. This is one example of Whitcomb's *supersonic area rule*, discussed in detail by R.T. Jones [61].

Bodies with minimum wave drag

Following Sears [62] and Haack [63], the line source model developed above will now be applied to a body of length ℓ, with some arbitrary area distribution $A(x)$. Using the trigonometric coordinate $\vartheta(x)$

$$x = \frac{\ell}{2}(1 - \cos\vartheta) \quad, \qquad dx = \frac{\ell}{2}\sin\vartheta \ d\vartheta \tag{8.154}$$

the line source strength or equivalently dA/dx is expanded in a Fourier sine series.

$$\Lambda(x) = \frac{dA}{dx} = \ell\sum_{n=2}^\infty \mathcal{B}_n \sin n\vartheta \tag{8.155}$$

The area distribution $A(x)$ and the total body volume $\mathcal{V}$ can then also be given in terms of the same series coefficients.

$$A(x) = \int_0^x \frac{dA}{dx} \ dx = \frac{\ell}{2}\int_0^\vartheta \frac{dA}{dx} \sin\vartheta \ d\vartheta = \frac{\ell^2}{2}\sum_{n=2}^\infty \mathcal{B}_n \int_0^{\vartheta(x)} \sin n\vartheta \ \sin\vartheta \ d\vartheta$$

$$= \frac{\ell^2}{4}\sum_{n=2}^\infty \mathcal{B}_n\left(\frac{\sin(n{-}1)\vartheta}{n{-}1} - \frac{\sin(n{+}1)\vartheta}{n{+}1}\right) \tag{8.156}$$

$$\mathcal{V} = \int_0^\ell A(x) \ dx = \frac{\ell}{2}\int_0^\pi A(\vartheta) \sin\vartheta \ d\vartheta = \frac{\pi\ell^3}{16}\mathcal{B}_2 \tag{8.157}$$

The $n = 1$ series term has been excluded because it gives a finite base area at $x = \ell$. In reality the large separated wake generated by the base area would make the present potential-flow model results not very realistic for that case.

Substitution of the source strength expansion (8.155) into the wave drag expression (8.153) gives the following result, obtained by Sears.

$$D_w = \frac{\pi}{8}\rho_\infty V_\infty^2 \ell^2 \sum_{n=2}^\infty n\mathcal{B}_n^2$$

$$= \frac{1}{2}\rho_\infty V_\infty^2 \frac{128}{\pi} \frac{\mathcal{V}^2}{\ell^4}\left[1 + \frac{3}{2}\left(\frac{\mathcal{B}_3}{\mathcal{B}_2}\right)^2 + \frac{4}{2}\left(\frac{\mathcal{B}_4}{\mathcal{B}_2}\right)^2 + \ldots\right] \tag{8.158}$$

Comparing the volume expression (8.157) with the wave drag expression (8.158) we see that the lowest wave drag for a given body volume $\mathcal{V}$ and length ℓ is obtained by setting $\mathcal{B}_3 = \mathcal{B}_4 \ldots = 0$ and leaving only $\mathcal{B}_2$ nonzero. The resulting shape is the *Sears-Haack body*, shown in Figure 8.25. Note that its wave drag is independent of the freestream Mach number, provided of course that M_∞ is sufficiently far into the supersonic range as required by the assumed supersonic PG flow model.

The very strong dependence of wave drag on the volume and the inverse length is the primary reason why the design of supersonic aircraft naturally favors a long and slender layout with minimal volume. These design drivers are not present in subsonic aerodynamics.
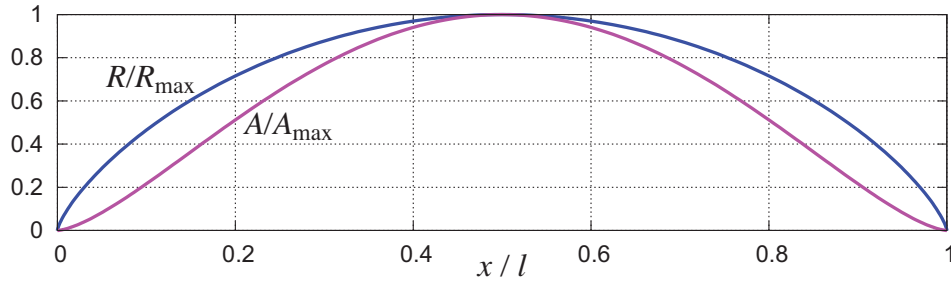
Figure 8.25: Sears-Haack body shape $R(x)$ which gives minimum supersonic wave drag for given length and volume. Corresponding body cross-sectional area $A = \pi R^2$ is also shown.

8.8.6   Supersonic lifting flows

Supersonic lift singularities

To represent the flow over lifting surfaces we need supersonic z-doublets which are derived from the source.

$$\hat{\phi}_{\mathcal{K}_z}(\mathbf{r}\,;M_\infty) \;\equiv\; \frac{\partial \hat{\phi}_\Sigma}{\partial z} \;=\; \begin{cases} \dfrac{1}{2\pi}\dfrac{-\beta^2 z}{h^3} &,\quad x > \beta\sqrt{y^2+z^2} \\[2mm] 0 &,\quad x < \beta\sqrt{y^2+z^2} \end{cases} \tag{8.159}$$

The corresponding y-doublet for modeling sideforce can also be considered. But this has exactly the same form as the z-doublet with y and z swapped, so there is no need to derive this separately.

We now define the potential of a semi-infinite z-doublet line extending downstream from the origin, which can be considered as a supersonic horseshoe vortex with an infinitesimal width $\mathrm{d}y$.

$$\begin{aligned} \hat{\phi}_{\Gamma_z}(x,y,z\,;M_\infty) \;&\equiv\; \int_0^{x-\beta\sqrt{y^2+z^2}} \hat{\phi}_{\mathcal{K}_z}(x{-}x',y,z\,;M_\infty)\;\mathrm{d}x' \\[2mm] &=\; \frac{-\beta^2 z}{2\pi} \int_0^{x-\beta\sqrt{y^2+z^2}} \frac{\mathrm{d}x'}{[(x{-}x')^2 - \beta^2(y^2{+}z^2)]^{3/2}} \\[2mm] &=\; \frac{1}{2\pi}\frac{z}{y^2{+}z^2}\frac{x}{h} \end{aligned} \tag{8.160}$$

The upper integration limit over the doublet strip is the x' point where the strip intersects the field point's upstream Mach cone. This can be determined as the x' point where the hyperbolic radius from the field point is zero.

$$\begin{aligned} h(x{-}x',y,z\,;M_\infty) \;&\equiv\; \sqrt{(x{-}x')^2 - \beta^2(y^2{+}z^2)} \;=\; 0 \\ \rightarrow\quad x' \;&=\; x - \beta\sqrt{y^2+z^2} \end{aligned}$$

The alternative positive-root solution $x' = x + \beta\sqrt{y^2+z^2}$ is not used, since this corresponds to the downstream Mach cone, and any doublet in this Mach cone has no influence on the field point.

As an example application of superposition of infinitesimal horseshoe vortices (8.160), the potential of a general unswept lifting line extending from $y = -b/2$ to $y = b/2$ is obtained by superposition of this unit solution across the span, with the appropriate y-coordinate shift.

$$\begin{aligned} \phi(x,y,z\,;M_\infty) \;&=\; \int_{y_1}^{y_2} \Gamma(y')\,\hat{\phi}_{\Gamma_z}(x,y{-}y',z\,;M_\infty)\;\mathrm{d}y' \\[2mm] &=\; \frac{1}{2\pi}\int_{y_1}^{y_2} \Gamma(y')\,\frac{z}{(y{-}y')^2{+}z^2}\,\frac{x}{\sqrt{x^2 - \beta^2[(y{-}y')^2{+}z^2]}}\;\mathrm{d}y' \end{aligned} \tag{8.161}$$
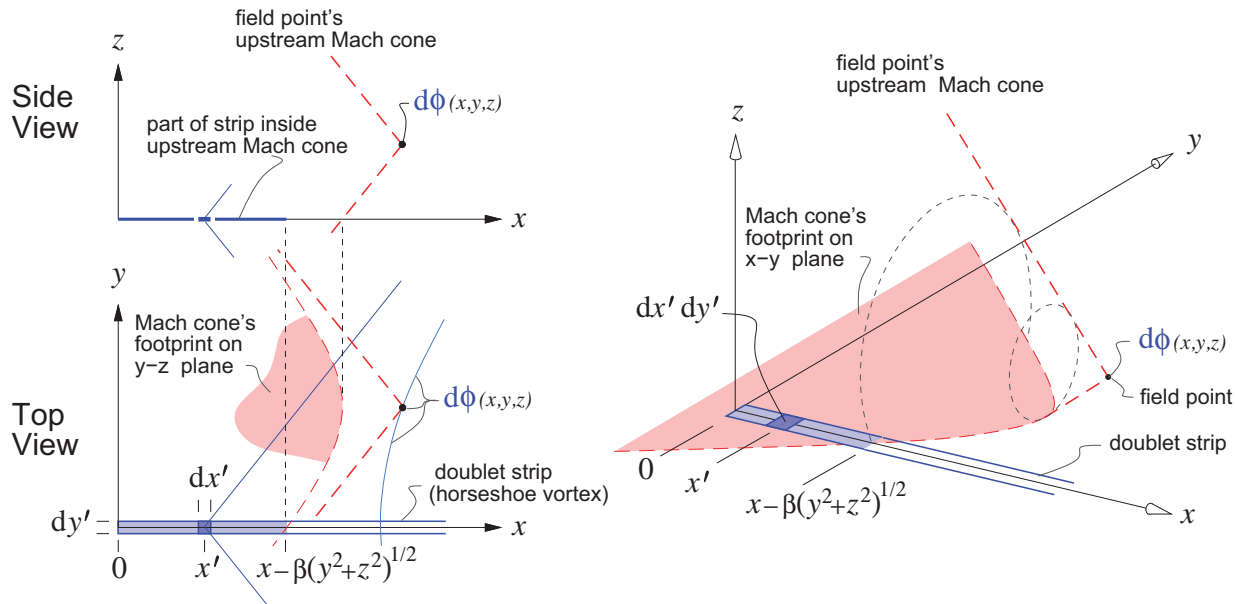
Figure 8.26: Integration over each doublet strip is restricted to region inside the field point's upstream Mach cone.

The y_1 and y_2 integration limits are obtained by first finding the Mach cone where $h(x, y-y', z\,;\, M_\infty) = 0$, which gives $y' = y^\pm$ at the Mach cone. These are then clipped to within the lifting-line tips at $\pm b/2$.

$$
\begin{aligned}
y^+ &\equiv y + \sqrt{(x/\beta)^2 - z^2} \\
y^- &\equiv y - \sqrt{(x/\beta)^2 - z^2} \\
y_{\max}(x,y,z\,;\,M_\infty) &= \max\left\{-b/2\,,\, \min[\,b/2\,,\, y^+\,]\right\} \\
y_{\min}(x,y,z\,;\,M_\infty) &= \max\left\{-b/2\,,\, \min[\,b/2\,,\, y^-\,]\right\}
\end{aligned}
\tag{8.162}
$$

For the specific case of a uniform $\Gamma_{(y)} = \text{constant}$ distribution, which corresponds to one horseshoe vortex for the whole wing, the superposition integral (8.161) evaluates to the following form.

$$
\begin{aligned}
\phi(x,y,z\,;\,M_\infty) = \frac{\Gamma}{2\pi} \frac{z}{|z|} \Bigg\{ &\arctan\left[\frac{x}{|z|} \frac{y_{\max} - y}{\sqrt{x^2 - \beta^2[(y_{\max}-y)^2 + z^2]}}\right] \\
&- \arctan\left[\frac{x}{|z|} \frac{y_{\min} - y}{\sqrt{x^2 - \beta^2[(y_{\min}-y)^2 + z^2]}}\right] \Bigg\}
\end{aligned}
\tag{8.163}
$$

This is shown in Figure 8.27 over yz planes at three downstream x locations, and compared to the subsonic version for $M_\infty = 0$.

Two limiting cases are:

- Near the lifting line, such that with $y^\pm$ inside the tips (not clipped to $\pm b/2$) and x being close to the z-axis and within the Mach lines from the vortex at the origin, we have the α solution of the 2D airfoil in the limit of zero chord.

$$
\phi(x,y,z\,;\,M_\infty) = \frac{\Gamma}{2\pi} \frac{z}{|z|} \left\{\arctan[+\infty] - \arctan[-\infty]\right\} = \frac{\Gamma}{2} \frac{z}{|z|}
\tag{8.164}
$$

This is shown in Figure 8.27 for $x = 0.5$ on the left.
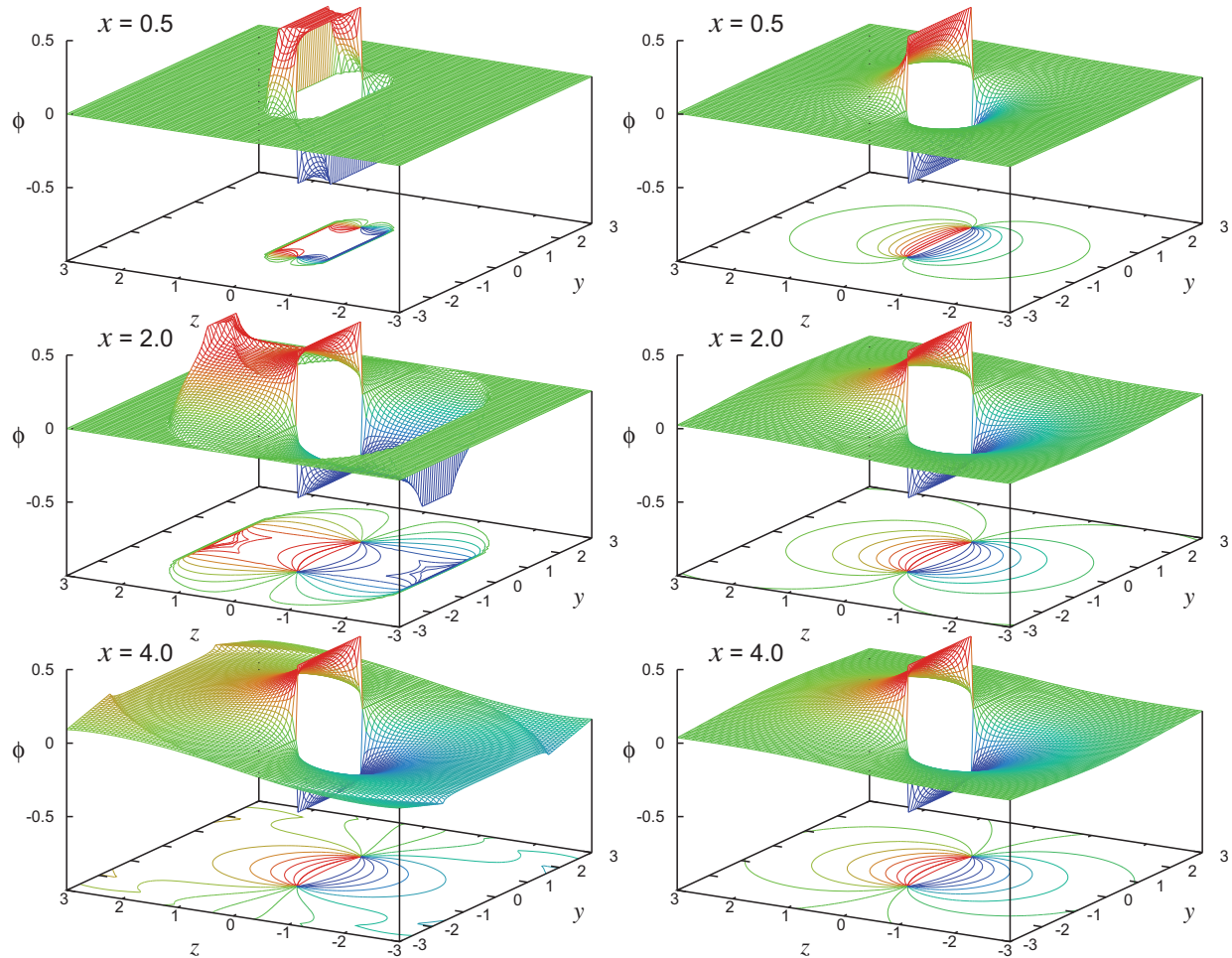
Figure 8.27: Potential field over yz planes behind a supersonic (left) and subsonic (right) horseshoe vortex. Away from the Mach cone, the two flows become the same downstream.

- Far downstream in the Trefftz plane, fairly close to the x axis so that $x^2 \gg y^2 + z^2$, we have the incompressible flow about two 2D vortices of strength $\pm\Gamma$, located at $(y,z) = (\pm b/2, 0)$.

$$\frac{x}{\sqrt{x^2 - \beta^2(y^2+z^2)}} \;\simeq\; 1$$

$$\phi(x,y,z\,;M_\infty) \;\simeq\; \frac{\Gamma}{2\pi}\left\{\arctan\left[\frac{b/2-y}{z}\right] + \arctan\left[\frac{b/2+y}{z}\right]\right\} \qquad (8.165)$$

Hence, the Trefftz plane flow here is the same as with an incompressible freestream, as shown in Figure 8.27 for $x=8$. For the intermediate downstream distance $x=2$, The Trefftz plane flow appears subsonic close to the trailing legs, but supersonic farther away near the Mach cone trace.

Wave drag of a lifting surface

The flow over a general thin supersonic lifting wing can be obtained by superposition of infinitesimal supersonic horseshoe vortices (8.160) over its surface. The integration limits of such superpositions must obey the Mach cone dependence requirements, which can become complex for general wing planforms. One approach which handles these requirements in a systematic manner is the method of Evvard and Krasilshchikova, as summarized by Ashley and Landahl [50].

The supersonic wave system created by the horseshoe vortex distribution will in general produce a *wave drag due to lift*, much like the line source representing a body produced a wave drag due to volume or thickness. Jones [64] determined the following minimum wave drag due to lift, which is obtained by a wing which has elliptical loading both in the spanwise <u>and</u> in the chordwise directions.

$$D_w = \frac{L^2}{\frac{1}{2}\rho_\infty V_\infty^2 \, \pi b^2} \left(\sqrt{1 + \frac{\pi^2}{16} A\!R^2 \beta^2} - 1 \right) \tag{8.166}$$

Combining this with the classical induced-drag relation (5.71) for the elliptical-loading case gives the total supersonic drag due to lift.

$$D_w + D_i = \frac{L^2}{\frac{1}{2}\rho_\infty V_\infty^2 \, \pi b^2} \sqrt{1 + \frac{\pi^2}{16} A\!R^2 \beta^2} \tag{8.167}$$

This can also be given in the usual non-dimensional form using the lift and drag coefficient definitions.

$$C_{D_w} + C_{D_i} = \frac{C_L^2}{\pi A\!R} \sqrt{1 + \frac{\pi^2}{16} A\!R^2 \beta^2} \tag{8.168}$$
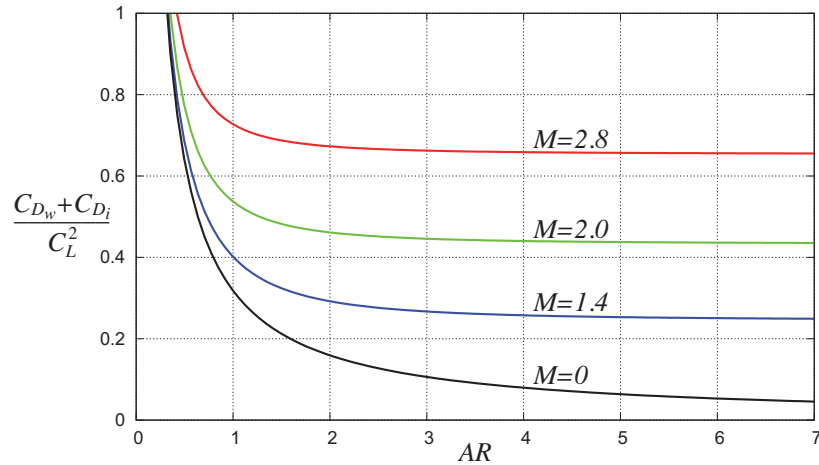
Figure 8.28: Wave+induced drag of supersonic wing with elliptical spanwise and chordwise loading.

The last term in (8.167) proportional to $A\!R^2$ favors low aspect ratios so that the lift is distributed over a large chord. This is in direct contrast to the subsonic case, where the chordwise loading distribution is immaterial to drag due to lift. One practical consequence is that efficient supersonic configurations tend to favor relatively low aspect ratios in order to spread out the lift load in the chordwise direction.

8.9 Transonic Flows

8.9.1 Onset of transonic flow

Any aerodynamic body has a maximum local velocity and local Mach number value somewhere near the surface which is greater than the freestream. Hence, as the freestream Mach number over a particular geometry at some angle of attack is gradually increased from small values, the maximum local Mach number $\max(M)$ will eventually reach and then exceed unity while the freestream is still subsonic, or $M_\infty < 1$. The freestream Mach value M_∞ when the threshold $\max(M) = 1$ is crossed is called the *critical Mach number*

for that particular geometry and angle of attack. For potential flow over the body, the local Mach number field has the functional form $M(\mathbf{r}\,;M_\infty)$, so that the defining condition for the critical Mach can be stated as

$$\max_{\mathbf{r}}\left[\,M(\mathbf{r}\,;M_{\text{crit}})\,\right] \;=\; 1$$

where in practice only the surface points $\mathbf{r}$ need to be examined for the maximum local Mach number. An equivalent criterion is in terms of the sonic pressure coefficient, shown in Figure 8.29, which is defined from the $C_p(M\,;M_\infty)$ function (8.11) with $M=1$ substituted.

$$C_p^*(M_\infty) \;\equiv\; C_p(1\,;M_\infty) \;=\; \frac{2}{\gamma M_\infty^2}\left\{\left[\frac{1+\frac{\gamma-1}{2}M_\infty^2}{1+\frac{\gamma-1}{2}}\right]^{\gamma/(\gamma-1)} - 1\right\} \qquad (8.169)$$

An alternative definition for the critical Mach number is then defined as follows.

$$\min_{\mathbf{r}}\left[\,C_p(\mathbf{r}\,;M_{\text{crit}})\,\right] \;=\; C_p^*(M_\infty)$$
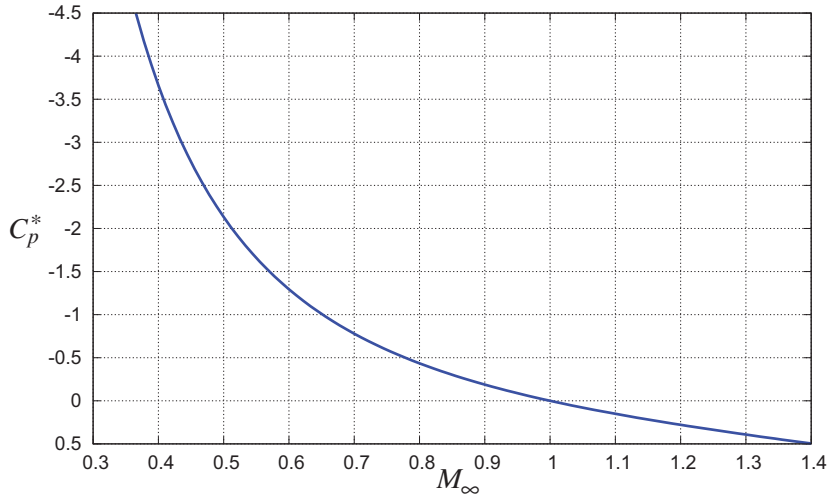
Figure 8.29: Critical pressure coefficient vs. freestream Mach, for air ($\gamma=1.4$).

At the typical flight Mach numbers $M_\infty \simeq 0.7\ldots0.85$ of jet transport aircraft, only modestly negative local C_p values of $-0.75\ldots-0.3$ are required to reach a local $M=1$. Consequently, such aircraft necessarily have transonic flow over their wings. Figure 8.30 shows computed $C_p(x)$ distributions for a typical "supercritical" airfoil designed to operate in the transonic condition, which occurs for $M_\infty > M_{\text{crit}} = 0.71$ for this airfoil at this angle of attack. Larger angles of attack make the upper-surface C_p values more negative, and hence decrease M_{crit}. In general, each airfoil will therefore have some $M_{\text{crit}}(\alpha)$ or $M_{\text{crit}}(c_\ell)$ dependency, depending on whether α or c_ℓ is being held fixed as M_∞ is varied.

The supersonic region over the airfoil which appears in transonic flow is typically terminated by a normal shock wave, as described in Section 8.3 earlier in this chapter. The shock for the RAE 2822 airfoil for the $M_\infty = 0.76$ case is shown in Figure 8.31, along with the Mach waves or characteristics (see Section 8.8.2). These characteristic lines are defined by (8.133), except that the characteristic slope β is defined using the local supersonic M values ahead of the shock rather than M_∞.

As M_∞ is increased beyond M_{crit}, the shock wave strengthens and causes a very rapid increase in the overall profile drag. This is due to the increase in the shock's own wave drag (see Section 8.3), and also due to the boundary layer being subjected to the intense adverse pressure gradient of the shock wave which increases the boundary layer's downstream momentum defect. Consequently, economical transonic operation is feasible at a freestream Mach which is only slightly beyond M_{crit}. The consequences for swept wing design will be discussed further in Section 8.9.3.
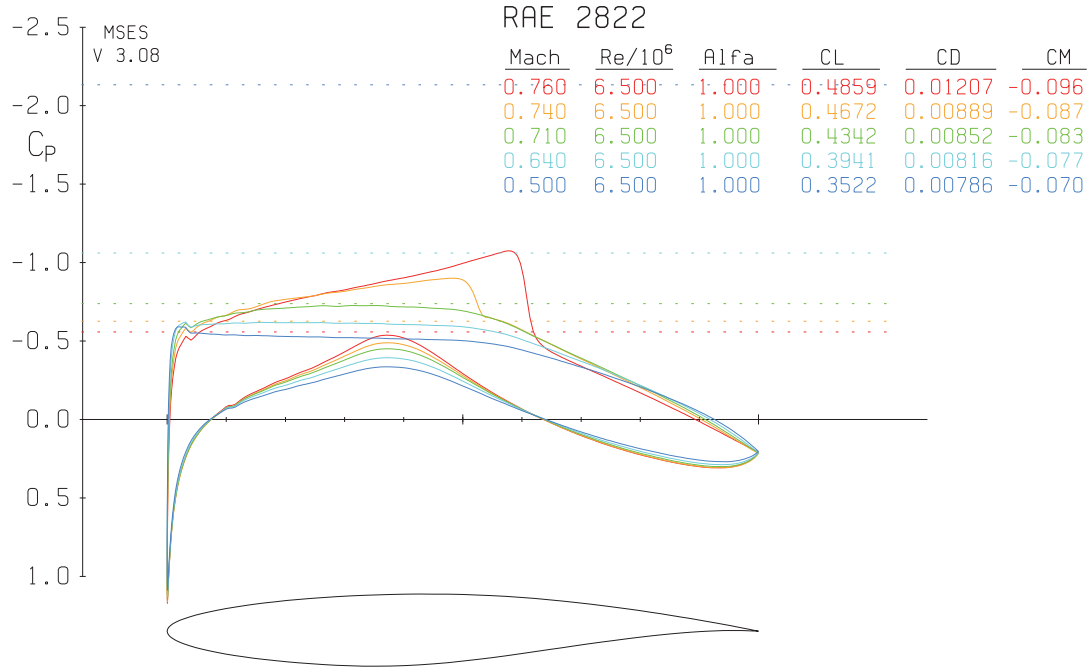
Figure 8.30: $C_p(x)$ distributions over RAE 2822 airfoil at $\alpha = 1°$, for a range of freestream Mach numbers M_∞. The C_p^* levels for each M_∞ are also shown as dotted lines. The critical Mach number is $M_{\mathrm{crit}} \simeq 0.71$, with a shock wave forming for $M_\infty > M_{\mathrm{crit}}$.
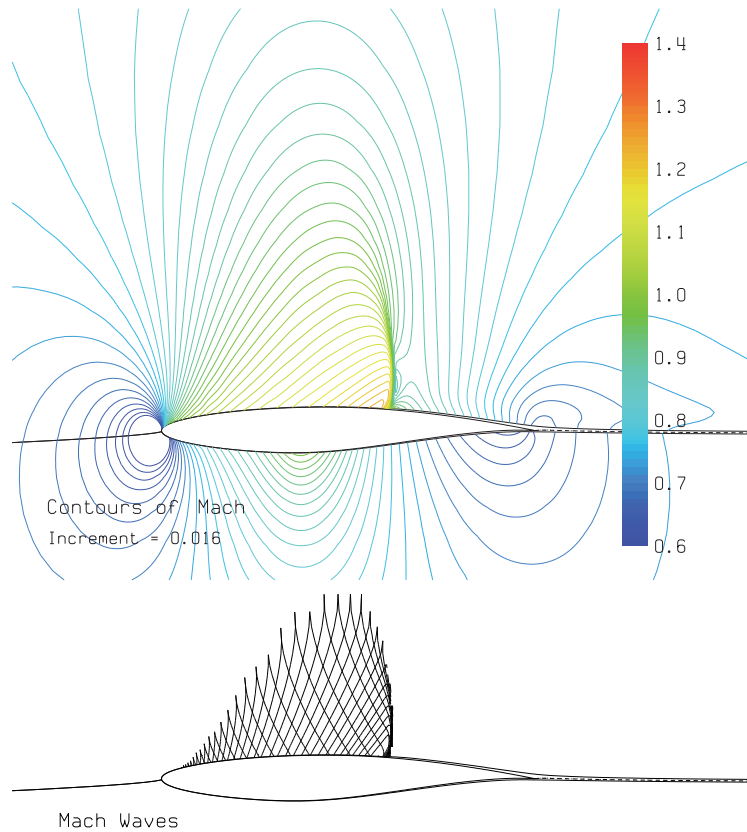
Figure 8.31: Mach isocontours and Mach waves over RAE 2822 airfoil at $\alpha = 1°$ and $M_\infty = 0.76$.

8.9.2 TSD equation analysis

The simplest description of transonic flow is provided by the TSD equation (8.59) derived earlier, which can be re-written in the following form.

$$\mathcal{S}\phi_{xx} + \phi_{yy} + \phi_{zz} = 0 \tag{8.170}$$

$$\mathcal{S}(\mathbf{r}) \equiv 1 - M_\infty^2 - (\gamma+1)M_\infty^2\,\phi_x \simeq 1 - M^2 \tag{8.171}$$

Superficially, the TSD equation has the same form as the PG equation, except the global coefficient $1-M_\infty^2$ is replaced by the local coefficient $\mathcal{S}(\mathbf{r})$. This is approximately the local $1 - M^2$ value, to first order in the perturbation x velocity ϕ_x. The assumption $M_\infty \simeq 1$ was also made to slightly further simplify the $\gamma+1$ factor in the higher-order ϕ_x term. This $\mathcal{S}$ is in effect a "sonic discriminator," since $\mathcal{S}>0$ in subsonic regions which have a Laplace-like behavior, and $\mathcal{S}<0$ in supersonic regions which have a wave-like behavior. The TSD equation in the transonic regime is therefore a PDE of *mixed type*. The *sonic line* (or *sonic surface* in 3D) which forms the boundary of the supersonic zone is the $M=1$ or $\mathcal{S}=0$ isocontour.

It's useful to see how the nonlinearity of the TSD equation is capable of representing shock waves. To examine this we consider the 2D TSD equation written in divergence form,

$$\left[(1-M_\infty^2)\phi_x - \tfrac{\gamma+1}{2}M_\infty^2\,\phi_x^2\right]_x + \left[\phi_z\right]_z = 0 \tag{8.172}$$

and integrate this over a small distance $x_0 \ldots x$, as shown in Figure 8.32.
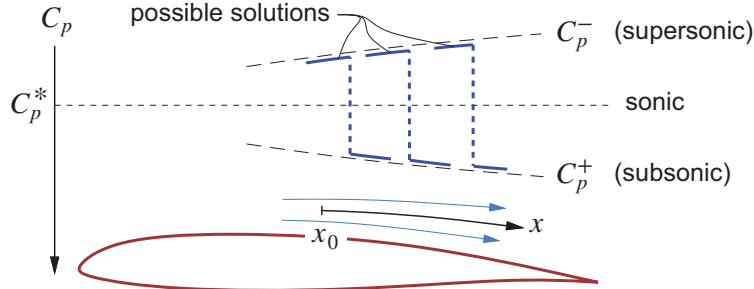
Figure 8.32: Simplified TSD solution admits a subsonic and a supersonic flow. A discontinuous jump between them at any location can be interpreted as a normal shock.

We will assume that $\phi_{zz} \simeq A$ is constant, which corresponds to the streamlines being convergent ($A < 0$) or divergent ($A > 0$).

$$\int_{x_0}^{x}\left[(1-M_\infty^2)\phi_x - \tfrac{\gamma+1}{2}M_\infty^2\,\phi_x^2\right]_x \mathrm{d}x + \int_{x_0}^{x} A\,\mathrm{d}x = 0$$

$$(1-M_\infty^2)\,\phi_x - \tfrac{\gamma+1}{2}M_\infty^2\,\phi_x^2 = B - Ax \tag{8.173}$$

The integration constant B will depend on A and also on the value of ϕ_x at the initial point x_0. The above relation (8.173) is a quadratic equation for the perturbation speed ϕ_x, or equivalently $C_p = -2\phi_x$, which has the following solution.

$$C_p(x) = C_p^* \pm \sqrt{(C_p^*)^2 + C} \tag{8.174}$$

$$\text{where} \quad C(x) = \frac{8}{\gamma+1}\frac{B - Ax}{M_\infty^2}$$

This admits two distinct solutions, $C_p^+ > C_p^*$ (subsonic) and $C_p^- < C_p^*$ (supersonic), which can be interpreted as the flows on the two sides of a normal shock. This simplified analysis does not predict where the shock will occur, which in an actual TSD solution would be implicitly determined by the freestream Mach number and the overall airfoil geometry.

8.9.3 Transonic airfoils

Airfoil performance characterization

For a compressible airfoil flow, both c_d and c_ℓ depend on the three parameters $\alpha, M_\infty, Re_\infty$. But when examining airfoil performance it's more useful to combine these into the form,

$$c_d(c_\ell, M_\infty, Re_\infty)$$

in which α is a dummy parameter. We can now consider individual *drag polars* at fixed M_∞, or alternatively individual *Mach drag-rise curves* at fixed c_ℓ. These two types of slices through the $\{c_d, c_\ell, M_\infty\}$ airfoil parameter space are sketched in Figure 8.33. To allow application to a swept wing, the c_d is actually broken down into separate friction and pressure drag components c_{d_f} and c_{d_p}, with the split either estimated or computed directly. Actual computed curves are shown in Figure 8.34.
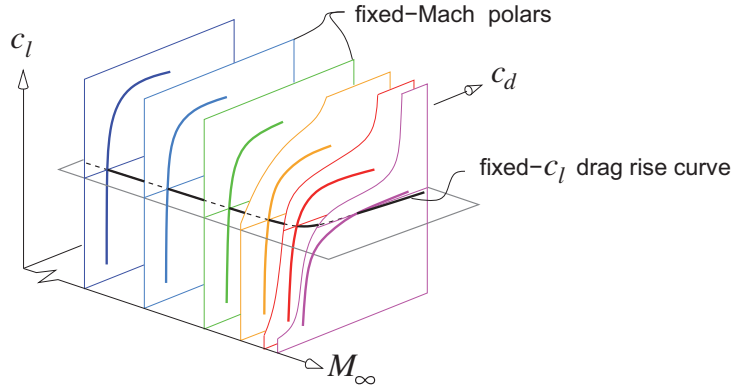
Figure 8.33: Two types of slices through the $\{c_d, c_\ell, M_\infty\}$ airfoil parameter space.
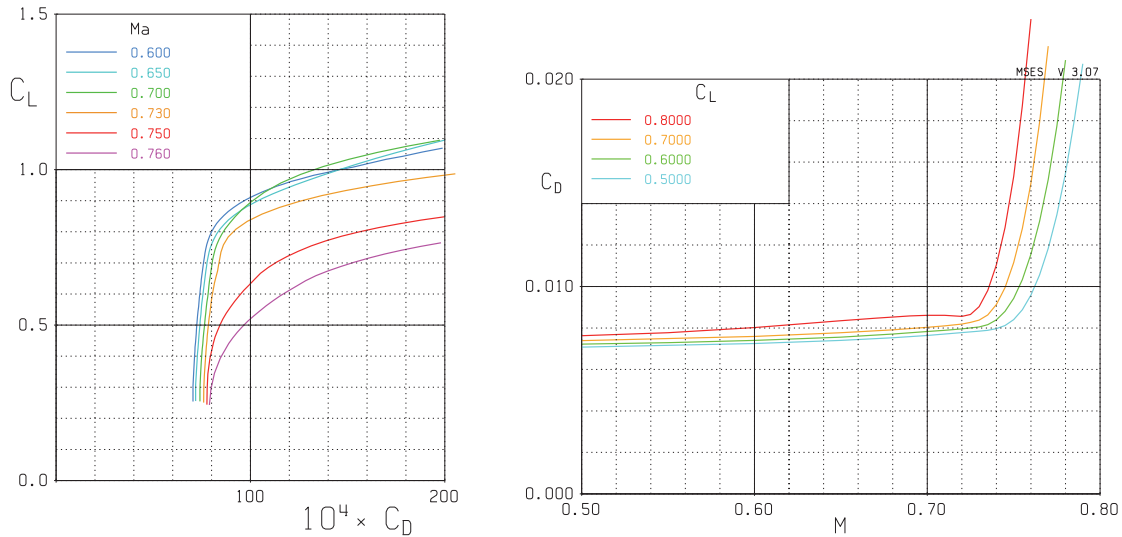
Figure 8.34: Computed polars and corresponding Mach drag-rise curves for a transonic airfoil.

Strictly speaking all these drag coefficients also depend on Re_∞, but with the fully-turbulent flows found on large jet aircraft the drag coefficient scales roughly as $c_d \sim \log(Re_\infty)^{-2}$, which is a quite weak dependence.

Airfoil performance drivers

The fuel weight required by an aircraft to fly a specified range R is given by the Breguet relation,

$$W_\mathrm{fuel} = W_\mathrm{ZF}\left[\exp\left(\frac{C_D}{M_\infty^{1/2}C_L}\,\frac{TSFC}{M_\infty^{1/2}}\,\frac{R}{a_\infty}\right) - 1\right] \tag{8.175}$$

where W_{ZF} is the zero-fuel (landing) weight, and *TSFC* is the engine thrust-specific fuel consumption. The particular grouping $TSFC/M_\infty^{1/2}$ is chosen because for modern turbofan engines this ratio is nearly independent of M_∞ (i.e. *TSFC* varies as $M_\infty^{1/2}$), so that the remaining factor $C_D/M_\infty^{1/2}C_L$ isolates and measures the aircraft's aerodynamic performance for fuel economy. It is therefore of great interest to find the best airfoil, C_L, M_∞, and wing-sweep combination which minimizes this parameter.

Optimum unswept wing

It is useful to first consider an unswept wing. We therefore assume

$$c_\ell = C_L$$
$$C_{D_{\mathrm{wing}}} = c_d(c_\ell, M_\infty)$$
$$C_D = C_{D_{\mathrm{wing}}} + \frac{C_L^2}{\pi AR} + C_{D_{\mathrm{rest}}}$$

where $C_{D_{\mathrm{wing}}}$ is the wing's profile+wave drag, and $C_{D_{\mathrm{rest}}}$ is the profile drag of the remaining fuselage, tail, and nacelle components. The objective is to find the optimum C_L, M_∞ combination which minimizes the $C_D/M_\infty^{1/2}C_L$ fuel-burn parameter. For a numerical example we can pick

$$AR = 10 \quad , \quad C_{D_{\mathrm{rest}}} = 0.025$$

which are typical for modern jet transports. Using the 2D 12%-thick airfoil c_d Mach drag-rise sweeps shown in Figure 8.34, the corresponding fuel-economy parameters are shown in Figure 8.35. The optimum combination is roughly at

$$C_L = 0.8 \quad , \quad M_\infty = 0.725 \qquad \text{(unswept-wing optimum)}$$

although this will also depend on the airfoil thickness. A larger thickness will typically optimize to a lower C_L and a lower M_∞, with a corresponding increase in the fuel-burn parameter. However, a thicker wing is structurally favorable and hence lighter, so that the W_{ZF} factor in the Breguet relation (8.175) may overcome this aerodynamic drawback and give a net benefit.
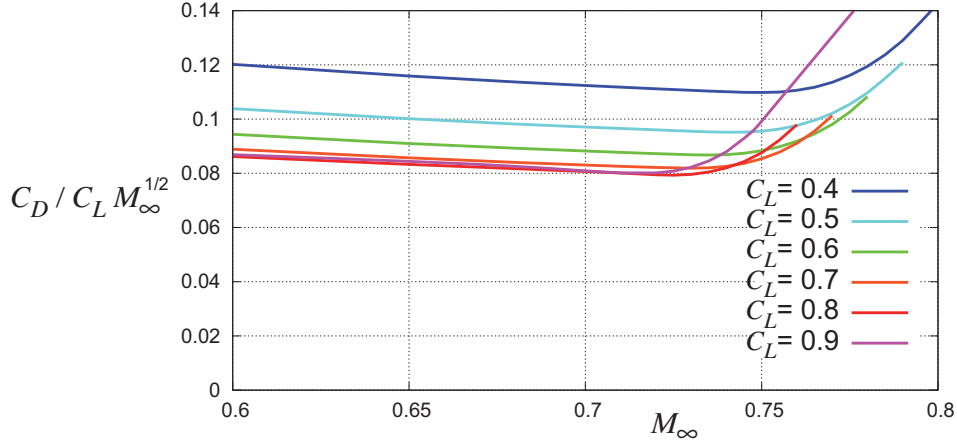
Figure 8.35: Fuel-burn parameter versus M_∞, C_L for an unswept wing.

Swept-wing airfoil characterization

The earlier analysis of an infinite swept wing in Section 8.6.3 indicated that the lift depends only on the perpendicular velocity and Mach component $V_\perp = V_\infty \cos\Lambda$ and $M_\perp = M_\infty \cos\Lambda$. The same arguments apply to the airfoil's boundary layers, provided we ignore the spanwise flow's increase of the total-velocity

Reynolds number, which is reasonable for fully-turbulent flow. Consequently, the 2D airfoil lift-coefficient characteristics shown in Figure 8.34 apply to a swept wing via the following relations.

$$M_\perp = M_\infty \cos\Lambda \tag{8.176}$$

$$c_\ell = C_{L_\perp} = C_L/\cos^2\Lambda \tag{8.177}$$

$$c_d = c_d(c_\ell\,;M_\perp) \tag{8.178}$$

To obtain the wing's profile drag coefficient $C_{D_{\text{wing}}}$ from the 2D-section c_d value we first break down the latter into the friction and pressure components,

$$c_d = c_{d_{\text{f}}} + c_{d_{\text{p}}} \tag{8.179}$$

with a roughly $\frac{2}{3}, \frac{1}{3}$ split, respectively, being typical for transonic airfoils.

The velocity within the 3D boundary layer on the wing and hence the surface skin friction vectors $\boldsymbol{\tau}_{\text{w}}$ will be mostly aligned with the outer potential flow, which is on average parallel to the freestream velocity $\mathbf{V}_\infty$ and hence the aircraft's $\hat{\mathbf{x}}$ direction, as indicated in Figure 8.36. This skin friction's magnitude must also scale with the local potential-flow dynamic pressure, which scales with the freestream dynamic pressure $\frac{1}{2}\rho_\infty V_\infty^2$. This gives the following estimate for the wing's friction drag vector.

$$D_{\text{f}}\,\hat{\mathbf{x}} = \iint \boldsymbol{\tau}_{\text{w}}\,\mathrm{d}S \simeq \tfrac{1}{2}\rho_\infty V_\infty^2\,S\,c_{d_{\text{f}}}\,\hat{\mathbf{x}} \tag{8.180}$$

In contrast, the pressure forces act along the wing surface normal vectors $\hat{\mathbf{n}}$ which lie in the plane perpendicular to the wing, so the pressure drag vector must be along the local chordwise vector $\hat{\mathbf{x}}'$ which lies in this plane. It must also scale as $\frac{1}{2}\rho_\infty V_\perp^2$, since it must vanish in the limit of purely-spanwise flow at $90°$ sweep.

$$D_{\text{p}_\perp}\,\hat{\mathbf{x}}' = \iint -p\hat{\mathbf{n}}\,\mathrm{d}S \simeq \tfrac{1}{2}\rho_\infty V_\perp^2\,S\,c_{d_{\text{p}}}\,\hat{\mathbf{x}}' = \tfrac{1}{2}\rho_\infty V_\infty^2\,S\,c_{d_{\text{p}}}\,\cos^2\Lambda\,\hat{\mathbf{x}}' \tag{8.181}$$
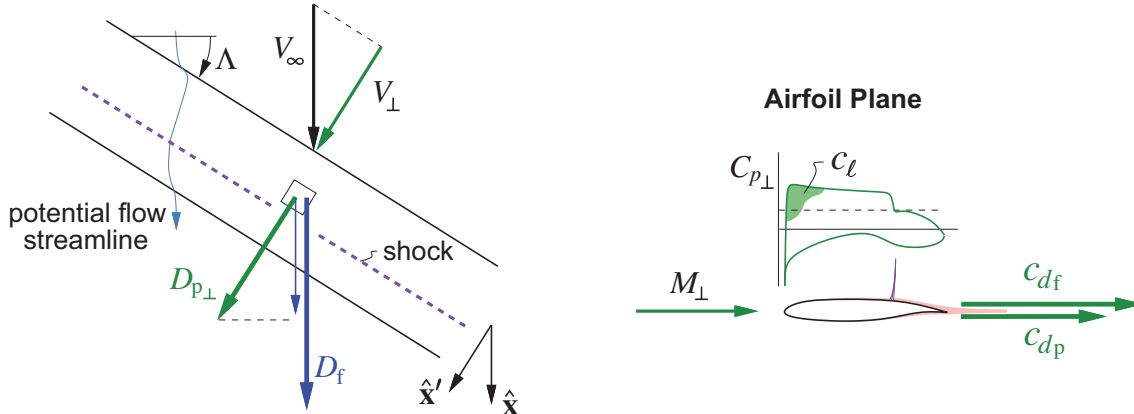
Figure 8.36: Profile drag of swept wing estimated from airfoil-plane friction and pressure-drag coefficients.

The total wing profile drag and corresponding drag coefficient are then

$$D_{\text{wing}} = \left(D_{\text{f}}\,\hat{\mathbf{x}} + D_{\text{p}_\perp}\hat{\mathbf{x}}'\right)\cdot\hat{\mathbf{x}} = D_{\text{f}} + D_{\text{p}_\perp}\cos\Lambda \tag{8.182}$$

$$C_{D_{\text{wing}}} \equiv \frac{D_{\text{wing}}}{\frac{1}{2}\rho_\infty V_\infty^2\,S} = c_{d_{\text{f}}} + c_{d_{\text{p}}}\cos^3\Lambda \tag{8.183}$$

so that the wing's overall profile-drag to lift ratio is

$$\frac{C_{D_\text{wing}}}{C_L} = \frac{c_{d_\text{f}} + c_{d_\text{p}} \cos^3\Lambda}{c_\ell \cos^2\Lambda} \tag{8.184}$$

which <u>increases</u> monotonically with sweep if $2c_{d_\text{f}} > c_{d_\text{p}}$ which is invariably the case in the absence of significant flow separation. Hence, wing sweep by itself does not improve the wing's drag/lift ratio, and in fact decreases it. The fuel-burn benefit from sweep instead originates from the speed/efficiency characteristics of jet engines, considered next.

Optimum swept wing

Sweep introduces another design parameter into the wing design space, which is now $\{C_L, M_\infty, \Lambda\}$, and also includes the airfoil thickness if different airfoils are being considered. The airfoil coefficients with the above sweep corrections give the fuel-burn parameter in the form

$$\frac{C_D}{M_\infty^{1/2} C_L} = \frac{c_{d_\text{f}} + c_{d_\text{p}} \cos^3\Lambda + (c_\ell \cos^2\Lambda)^2/(\pi AR) + C_{D_\text{rest}}}{M_\infty^{1/2} c_\ell \cos^2\Lambda} \tag{8.185}$$

which is shown in Figure 8.37. The optimum design-parameter combination is now

$$c_\ell = 0.9 \quad , \quad M_\infty = 0.825 \quad , \quad \Lambda = 30° \qquad \text{(swept-wing optimum)}$$

and the corresponding fuel-burn parameter value of about 0.078 is smaller than the 0.080 value for the unswept-wing case shown in Figure 8.35 for a typical supercritical airfoil. The reduction is modest, but perhaps more importantly it occurs at a $0.825/0.725 - 1 = 14\%$ greater speed which itself has economic benefits.

The optimum design parameters found here for the swept-wing case are quite close to what's seen on most modern jet transports, with the exception of the c_ℓ value. In practice, lower values of $c_\ell \simeq 0.75$ are used for several reasons: 1) Because of local c_ℓ reductions near the wingtips, wing root, and over the fuselage, the actual airplane C_L is necessarily smaller than the infinite swept-wing value $c_\ell \cos^2\Lambda$. 2) Structural weight considerations favor thicker airfoils than what this aerodynamic-only optimization indicates, and thicker transonic airfoils have lower optimum c_ℓ values.
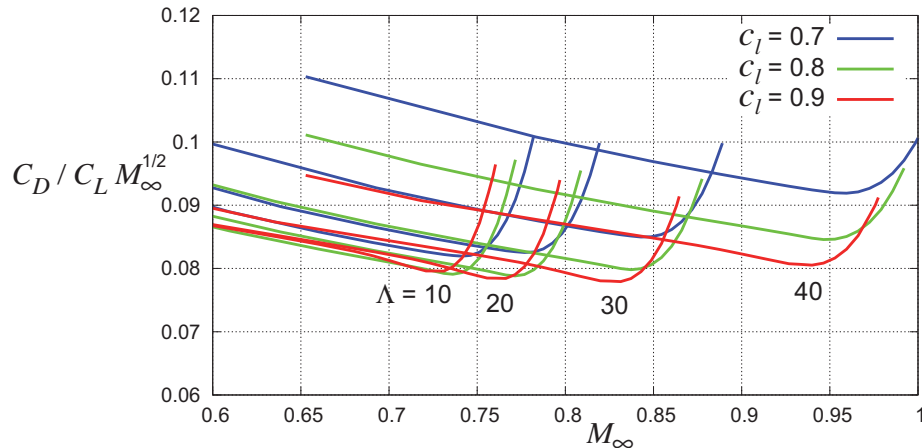
Figure 8.37: Fuel-burn parameter versus $M_\infty, c_\ell, \Lambda$.

Chapter 9

Introduction to Flight Dynamics

This chapter will treat the key concepts and formulations used in the discipline of flight dynamics and control. The primary focus here will be on the aerodynamic characterization of the aircraft, as required for flight dynamics applications. For a complete treatment of the subject, see Etkin [65] and Nelson [66].

9.1 Frames of Reference

Description of body or fluid positions, velocities, and rotation rates requires a frame of reference for these quantities. For unsteady aerodynamics and flight dynamics, two distinct frames of reference are useful:

- An inertial "Earth" frame, either fixed to the Earth or translating uniformly relative to the Earth.
- The non-inertial "body" frame, typically fixed to the aerodynamic body of interest.

Figure 9.1 illustrates the distinction between the two frames. For steady aerodynamics the body frame is most natural, although the Earth (or airmass) frame is also useful as in the case of Trefftz-plane theory treated in Chapter 5. For unsteady aerodynamics the Earth frame is more natural because it is inertial.
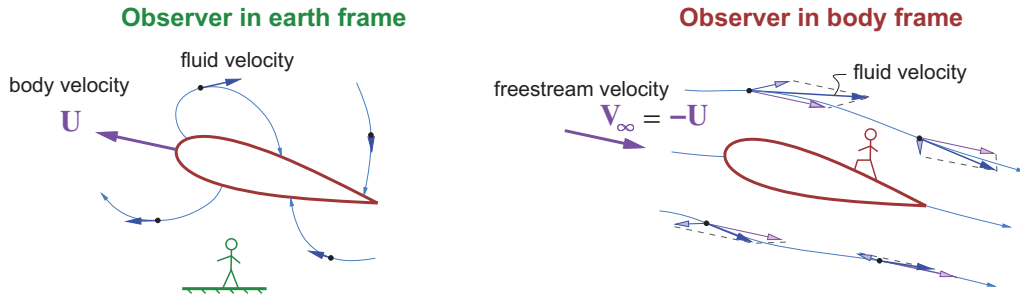
Figure 9.1: Body moving at velocity $\mathbf{U}$ through fluid, as seen in the Earth and body frames.

9.2 Axis Systems

The orientation of the axis system used to quantify any vector or tensor is arbitrary. Common choices are to align one axis (e.g. the x axis) with either a body feature such as an airfoil chordline, or with the freestream direction. If the body is only translating, a common axis system can be used for all quantities. However, if the body is rotating, then two axis systems naturally arise:

- "Earth" axes x^e, y^e, z^e fixed to the ground. These are non-rotating (the Earth's rotation is neglected).
- "Body" axes x^b, y^b, z^b fixed to the body. These rotate along with the body relative to inertial space.

Note that "frame" and "axes" are distinct concepts. For example, the aircraft position, velocity, and rotation rate $\mathbf{R}_o, \mathbf{U}, \mathbf{\Omega}$ treated in Chapter 7 were all defined in the Earth frame. But $\mathbf{R}_o$ is usually expressed via its Earth-axes x^e, y^e, z^e components, while $\mathbf{U}, \mathbf{\Omega}$ are usually expressed via the aircraft's body-axes x^b, y^b, z^b components. Relating them requires the axis transformation relations developed in Appendix F.

9.3   Body Position and Rate Parameters

Application of the equations of fluid motion in unsteady or quasi-steady flow situations requires specification of the velocity of every point on the body surface. This is parameterized by the inertial-frame quantities,

$$\mathbf{U}(t) \quad \text{velocity vector of body reference point O}$$
$$\boldsymbol{\Omega}(t) \quad \text{rotation-rate vector of body}$$

so that a point P at some location $\mathbf{r}_\mathrm{p}$ on the body relative to point O has the following velocity.

$$\mathbf{U}_\mathrm{p} \;=\; \mathbf{U} + \boldsymbol{\Omega}\times\mathbf{r}_\mathrm{p}$$

In aircraft flight dynamics applications the atmosphere is occasionally specified to have some nonuniform "gust" velocity field $\mathbf{V}_\mathrm{gust}(\mathbf{R},t)$, whose effect on the forces on the aircraft is to be determined. To evaluate this gust velocity at each point $\mathbf{r}_\mathrm{p}$ on the aircraft requires knowing that point's Earth position within the gust field. This is parameterized by

$$\mathbf{R}_\mathrm{o}(t) \qquad \text{position of body reference point O}$$
$$\phi, \theta, \psi(t) \quad \text{body roll, elevation, and heading Euler angles}$$

which are sketched in Figure 9.2.   The Earth position of point P and the gust velocity at that point can then be obtained from the $\mathbf{V}_\mathrm{gust}(\mathbf{R},t)$ field.

$$\mathbf{R}_\mathrm{p}(\mathbf{r},t) \;=\; \mathbf{R}_\mathrm{o}(t) + \mathbf{r}_\mathrm{p} \tag{9.1}$$
$$(\mathbf{V}_\mathrm{gust})_\mathrm{p} \;=\; \mathbf{V}_\mathrm{gust}(\mathbf{R}_\mathrm{p},t) \tag{9.2}$$
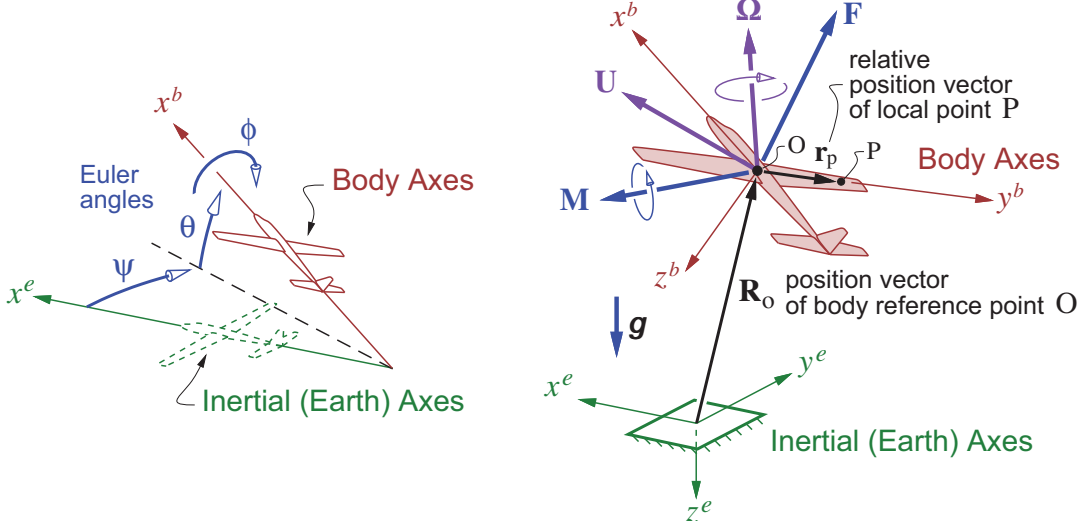
Figure 9.2: Aircraft motion parameters. Total aerodynamic force $\mathbf{F}$ and moment $\mathbf{M}$ are also shown. Euler angles define transformation matrices $\bar{\bar{\mathbf{T}}}_b^e$ or $\bar{\bar{\mathbf{T}}}_e^b$ between body and Earth axes, developed in Appendix F.

9.4   Axis Parameterization and Conventions

The body reference-point position vector $\mathbf{R}_\mathrm{o}$ is best given by its components along the inertial Earth axes, shown as x^e, y^e, z^e in Figure 9.2. In contrast, the local position vector $\mathbf{r}$, and the body velocity and rotation

rate vectors $\mathbf{U}, \boldsymbol{\Omega}$ are best given in the body axes x^b, y^b, z^b, since these are also used to describe the flow about the body, e.g. via the velocity field $\mathbf{V}_{(\mathbf{r},t)}$. To translate the individual components of any vector, such as $\mathbf{U}$, from body to Earth axes, we apply the general vector transformation (F.1) derived in Appendix F.

$$\mathbf{U}^e \equiv \begin{Bmatrix} U_x^e \\ U_y^e \\ U_z^e \end{Bmatrix} = \begin{bmatrix} & \bar{\bar{\mathbf{T}}}_b^e & \end{bmatrix} \begin{Bmatrix} U_x^b \\ U_y^b \\ U_z^b \end{Bmatrix} \equiv \bar{\bar{\mathbf{T}}}_b^e \mathbf{U}^b \tag{9.3}$$

The direction-cosine transformation matrix $\bar{\bar{\mathbf{T}}}_b^e$ is now formed as the product of three simple rotation matrices for the individual Euler angles in the standard sequence $-\phi, -\theta, -\psi$:

$$\bar{\bar{\mathbf{T}}}_b^e = \begin{bmatrix} \cos\psi & -\sin\psi & 0 \\ \sin\psi & \cos\psi & 0 \\ 0 & 0 & 1 \end{bmatrix} \begin{bmatrix} \cos\theta & 0 & \sin\theta \\ 0 & 1 & 0 \\ -\sin\theta & 0 & \cos\theta \end{bmatrix} \begin{bmatrix} 1 & 0 & 0 \\ 0 & \cos\phi & -\sin\phi \\ 0 & \sin\phi & \cos\phi \end{bmatrix}$$

$$= \begin{bmatrix} \cos\theta\cos\psi & \sin\phi\sin\theta\cos\psi - \cos\phi\sin\psi & \cos\phi\sin\theta\cos\psi + \sin\phi\sin\psi \\ \cos\theta\sin\psi & \sin\phi\sin\theta\sin\psi + \cos\phi\cos\psi & \cos\phi\sin\theta\sin\psi - \sin\phi\cos\psi \\ -\sin\theta & \sin\phi\cos\theta & \cos\phi\cos\theta \end{bmatrix} \tag{9.4}$$

The reciprocal conversion matrix $\bar{\bar{\mathbf{T}}}_e^b$ is composed of the reverse rotation sequence ψ, θ, ϕ. But this is also the inverse of $\bar{\bar{\mathbf{T}}}_b^e$, which is simply its transpose as derived in Appendix F for the general case.

$$\bar{\bar{\mathbf{T}}}_e^b = \bar{\bar{\mathbf{T}}}_b^{e^{-1}} = \bar{\bar{\mathbf{T}}}_b^{e^T} \tag{9.5}$$

As an application example, consider equations (9.1) and (9.2) used to obtain the gust velocity at an aircraft point P. The aircraft position $\mathbf{R}_o$ and the $\mathbf{V}_{\text{gust}(\mathbf{R},t)}$ function are typically provided in Earth axes, i.e. as $\mathbf{R}_o^e$ and $\mathbf{V}_{\text{gust}}^e(\mathbf{R}^e,t)$, while the point P vector $\mathbf{r}_p$ is known in body axes, as $\mathbf{r}_p^b$. Expressions (9.1) and (9.2) would therefore need to be evaluated as

$$\mathbf{R}_p^e = \mathbf{R}_o^e + \bar{\bar{\mathbf{T}}}_b^e \mathbf{r}_p^b \tag{9.6}$$

$$\mathbf{V}_{\text{gust}_p}^b = \bar{\bar{\mathbf{T}}}_e^b \mathbf{V}_{\text{gust}}^e(\mathbf{R}_p^e,t) \tag{9.7}$$

with the final result $\mathbf{V}_{\text{gust}_p}^b$ being in the body axes. This would then be usable for calculation of body forces and moments which are typically performed in the body axes.

9.5 Flow Angles

The aircraft's velocity $\mathbf{U}$ components in the body axes can be defined in terms of its magnitude V_∞ and the angles of attack α and sideslip angle β, or vice versa. In the standard convention these relations are

$$\mathbf{U}^b = \begin{Bmatrix} U_x^b \\ U_y^b \\ U_z^b \end{Bmatrix} = -\mathbf{V}_\infty^b = V_\infty \begin{Bmatrix} \cos\alpha\cos\beta \\ \sin\beta \\ \sin\alpha\cos\beta \end{Bmatrix} \tag{9.8}$$

$$V_\infty = \sqrt{(U_x^b)^2 + (U_y^b)^2 + (U_z^b)^2}$$

$$\alpha = \arctan\left(U_z^b/U_x^b\right) \tag{9.9}$$

$$\beta = \arctan\left(U_y^b/\sqrt{(U_x^b)^2 + (U_z^b)^2}\right)$$

so that $\{U_x^b, U_y^b, U_z^b\}$ and $\{V_\infty, \alpha, \beta\}$ are equivalent alternative parameter sets, related by the reciprocal relations (9.8) and (9.9).

9.6   Aircraft Kinematic Relations

This section derives the kinematic equations of aircraft motion used in flight dynamics and control. See Etkin [65] and Nelson [66] for further details.

9.6.1   Aircraft position rate

The rate of the position $\mathbf{R}_o^e$ in Earth axes equals its velocity $\mathbf{U}^e$ in Earth axes.

$$\frac{\mathrm{d}}{\mathrm{d}t}\mathbf{R}_o^e = \mathbf{U}^e \tag{9.10}$$

In practice this is expressed as

$$\boxed{\frac{\mathrm{d}}{\mathrm{d}t}\mathbf{R}_o^e = \bar{\bar{\mathbf{T}}}_b^e \mathbf{U}^b} \tag{9.11}$$

since the velocity is defined as $\mathbf{U}^b$ in the body axes. Integration of (9.11) to obtain the aircraft trajectory $\mathbf{R}_o(t)$ therefore requires not only the aircraft velocity $\mathbf{U}^b(t)$, but also the concurrent Euler angles $\phi, \theta, \psi(t)$ which are needed to compute the transformation matrix $\bar{\bar{\mathbf{T}}}_b^e(t)$ at each step in time.

9.6.2   Aircraft orientation rate

Appendix F derives the expression (F.7) for the rotation-rate matrix $\overrightarrow{\overrightarrow{\Omega}}^e$. Choosing the (3,2), (1,3), (2,1) elements of this expression and stacking them in that order as a vector gives a relation between the rotation rate's Earth-axis components and the Euler angle rates.

$$\left\{\begin{array}{c} \Omega_x^e \\ \Omega_y^e \\ \Omega_z^e \end{array}\right\} = \left[\quad \bar{\bar{\mathbf{K}}}_b^e \quad\right] \left\{\begin{array}{c} \dot{\phi} \\ \dot{\theta} \\ \dot{\psi} \end{array}\right\} \tag{9.12}$$

$$\text{where} \qquad \bar{\bar{\mathbf{K}}}_b^e = \left[\begin{array}{ccc} \cos\psi\,\cos\theta & -\sin\psi & 0 \\ \sin\psi\,\cos\theta & \cos\psi & 0 \\ -\sin\theta & 0 & 1 \end{array}\right] \tag{9.13}$$

Pre-multiplying (9.12) by $\bar{\bar{\mathbf{T}}}_e^b$ puts this result in body axes.

$$\left\{\begin{array}{c} \Omega_x^b \\ \Omega_y^b \\ \Omega_z^b \end{array}\right\} = \left[\quad \bar{\bar{\mathbf{T}}}_e^b \quad\right] \left\{\begin{array}{c} \Omega_x^e \\ \Omega_y^e \\ \Omega_z^e \end{array}\right\} = \left[\quad \bar{\bar{\mathbf{T}}}_e^b \quad\right]\left[\quad \bar{\bar{\mathbf{K}}}_b^e \quad\right] \left\{\begin{array}{c} \dot{\phi} \\ \dot{\theta} \\ \dot{\psi} \end{array}\right\} \tag{9.14}$$

Evaluating the matrix-matrix product above gives

$$\mathbf{\Omega}^b = \left\{\begin{array}{c} \Omega_x^b \\ \Omega_y^b \\ \Omega_z^b \end{array}\right\} = \left[\begin{array}{ccc} 1 & 0 & -\sin\theta \\ 0 & \cos\phi & \sin\phi\,\cos\theta \\ 0 & -\sin\phi & \cos\phi\,\cos\theta \end{array}\right] \left\{\begin{array}{c} \dot{\phi} \\ \dot{\theta} \\ \dot{\psi} \end{array}\right\} \tag{9.15}$$

which can then be inverted to give the rate equation for the Euler angles.

$$\boxed{\frac{\mathrm{d}}{\mathrm{d}t}\left\{\begin{array}{c} \phi \\ \theta \\ \psi \end{array}\right\} = \left[\begin{array}{ccc} 1 & \sin\phi\,\tan\theta & \cos\phi\,\tan\theta \\ 0 & \cos\phi & -\sin\phi \\ 0 & \sin\phi/\cos\theta & \cos\phi/\cos\theta \end{array}\right] \left\{\begin{array}{c} \Omega_x^b \\ \Omega_y^b \\ \Omega_z^b \end{array}\right\}} \tag{9.16}$$

9.7 Dynamics Relations

9.7.1 Linear momentum

The linear momentum equation (Newton's Second Law) for an aircraft, properly expressed in the inertial Earth frame and Earth axes is

$$\mathbf{F}^e + m\,\mathbf{g}^e = m\,\frac{\mathrm{d}\mathbf{U}^e}{\mathrm{d}t} \tag{9.17}$$

where the total force acting on the aircraft is the aerodynamic force $\mathbf{F}$ plus the gravity force $m\mathbf{g}$, shown in Figure 9.2. The equivalent form in the more convenient body axes is obtained using the transformation matrix, by substituting $\mathbf{F}^e = \bar{\bar{\mathbf{T}}}^e_b\mathbf{F}^b$, etc., and performing a few manipulations as follows.

$$
\begin{aligned}
\bar{\bar{\mathbf{T}}}^e_b\,\mathbf{F}^b + m\,\bar{\bar{\mathbf{T}}}^e_b\,\mathbf{g}^b &= m\,\frac{\mathrm{d}}{\mathrm{d}t}(\bar{\bar{\mathbf{T}}}^e_b\mathbf{U}^b) \\
&= m\left(\bar{\bar{\mathbf{T}}}^e_b\dot{\mathbf{U}}^b + \dot{\bar{\bar{\mathbf{T}}}}^e_b\mathbf{U}^b\right) \\
&= m\left(\bar{\bar{\mathbf{T}}}^e_b\dot{\mathbf{U}}^b + \vec{\boldsymbol{\Omega}}^e\bar{\bar{\mathbf{T}}}^e_b\mathbf{U}^b\right) \\
&= m\left(\bar{\bar{\mathbf{T}}}^e_b\dot{\mathbf{U}}^b + \vec{\boldsymbol{\Omega}}^e\mathbf{U}^e\right) \\
&= m\left(\bar{\bar{\mathbf{T}}}^e_b\dot{\mathbf{U}}^b + (\boldsymbol{\Omega}\times\mathbf{U})^e\right) \tag{9.18}
\end{aligned}
$$

Relation (F.9) has been used to replace $\dot{\bar{\bar{\mathbf{T}}}}^e_b$ in the third step above. Premultiplying the final result by $\bar{\bar{\mathbf{T}}}^b_e$ gives the linear momentum equation for the aircraft with all quantities specified in the body axes.

$$\boxed{\mathbf{F}^b + m\,\mathbf{g}^b = m\left(\dot{\mathbf{U}}^b + \boldsymbol{\Omega}^b\times\mathbf{U}^b\right)} \tag{9.19}$$

9.7.2 Angular momentum

The angular momentum equation for the aircraft is

$$\mathbf{M}^e = \frac{\mathrm{d}\mathbf{H}^e}{\mathrm{d}t} \tag{9.20}$$

$$\mathbf{H}^e = \bar{\bar{\mathbf{I}}}^e\,\boldsymbol{\Omega}^e + \mathbf{h}^e \tag{9.21}$$

where the total angular momentum vector $\mathbf{H}$ has been introduced, with $\mathbf{h}$ being any onboard angular momentum due to propellers, turbines, etc. The total aerodynamic moment $\mathbf{M}$, shown in Figure 9.2, is assumed to be taken about the center of mass, and $\bar{\bar{\mathbf{I}}}$ is the mass moment of inertia about the center of mass. To put the angular momentum equation (9.20) in the more convenient body axes, we follow the same procedure as for the linear momentum equation above, except that $\mathbf{F}$ is now replaced by $\mathbf{M}$, and $m\mathbf{U}$ is replaced by $\mathbf{H}$.

$$
\begin{aligned}
\bar{\bar{\mathbf{T}}}^e_b\,\mathbf{M}^b &= \frac{\mathrm{d}}{\mathrm{d}t}(\bar{\bar{\mathbf{T}}}^e_b\mathbf{H}^b) \\
&\;\;\vdots \\
&= \bar{\bar{\mathbf{T}}}^e_b\dot{\mathbf{H}}^b + (\boldsymbol{\Omega}\times\mathbf{H})^e \tag{9.22}
\end{aligned}
$$

Premultiplying the final result by $\bar{\bar{\mathbf{T}}}^b_e$, and then replacing $\mathbf{H}^b$ by $\bar{\bar{\mathbf{I}}}^b\boldsymbol{\Omega}^b + \mathbf{h}^b$ gives the angular momentum equation for the aircraft in body axes.

$$\boxed{\mathbf{M}^b = \bar{\bar{\mathbf{I}}}^b\dot{\boldsymbol{\Omega}}^b + \boldsymbol{\Omega}^b\times\left(\bar{\bar{\mathbf{I}}}^b\boldsymbol{\Omega}^b + \mathbf{h}^b\right)} \tag{9.23}$$

9.8 Flight Dynamics Formulation

9.8.1 Variable and vector definitions

In this section we will adopt the following simplified notation for the aircraft motion parameters and aero-dynamic forces and moments. This notation is fairly standard in the discipline of flight dynamics, stability, and control.

$$
\mathbf{R}^e = \begin{Bmatrix} x^e \\ y^e \\ z^e \end{Bmatrix} \qquad
\mathbf{U}^b = \begin{Bmatrix} u \\ v \\ w \end{Bmatrix} \qquad
\mathbf{\Omega}^b = \begin{Bmatrix} p \\ q \\ r \end{Bmatrix} \qquad
\mathbf{F}^b = \begin{Bmatrix} X \\ Y \\ Z \end{Bmatrix} \qquad
\mathbf{M}^b = \begin{Bmatrix} \mathcal{L} \\ \mathcal{M} \\ \mathcal{N} \end{Bmatrix}
$$

The components of the first three vectors above, together with the three Euler angles, are grouped in the following *state vector* with 12 components:

$$
\mathbf{x}(t) = \{ \; x^e \; y^e \; z^e \quad \phi \; \theta \; \psi \quad u \; v \; w \quad p \; q \; r \; \}^T \tag{9.24}
$$

As treated in Section 6.3, the aerodynamic forces X, Y, Z and moments $\mathcal{L}, \mathcal{M}, \mathcal{N}$ are functions of this state vector, and also of the *control vector* $\boldsymbol{\delta}$, which for a typical aircraft consists of aerodynamic control surface deflections and engine forces.

$$
\boldsymbol{\delta}(t) = \{ \; \delta_a \; \delta_e \; \delta_r \; \delta_f \; \delta_T \; \}^T \tag{9.25}
$$

The first four components correspond to aileron, elevator, rudder, and flap deflections, and the last component is an engine-thrust variable. Unconventional aircraft may have other types of control variables.

9.8.2 General equations of motion

The 12 state vector components (9.24) are governed by 12 ODEs in time. These are the six kinematic equations for the aircraft position rate (9.11) and the Euler angle rates (9.16), and the six dynamic equations for the linear momentum rate (9.19) and the angular momentum rate (9.19). Using the new simplified notation defined above, these 12 equations are written out fully as follows.

$$
\begin{aligned}
\dot{x}^e &= (\cos\theta \, \cos\psi)\, u + (\sin\phi \, \sin\theta \, \cos\psi - \cos\phi \, \sin\psi)\, v + (\cos\phi \, \sin\theta \, \cos\psi + \sin\phi \, \sin\psi)\, w \\
\dot{y}^e &= (\cos\theta \, \sin\psi)\, u + (\sin\phi \, \sin\theta \, \sin\psi + \cos\phi \, \cos\psi)\, v + (\cos\phi \, \sin\theta \, \sin\psi - \sin\phi \, \cos\psi)\, w \quad (9.26) \\
\dot{z}^e &= (-\sin\theta)\, u + (\sin\phi \, \cos\theta)\, v + (\cos\phi \, \cos\theta)\, w
\end{aligned}
$$

$$
\begin{aligned}
\dot{\phi} &= p + q \sin\phi \tan\theta + r \cos\phi \tan\theta \\
\dot{\theta} &= q \cos\phi - r \sin\phi \\
\dot{\psi} &= q \sin\phi / \cos\theta + r \cos\phi / \cos\theta
\end{aligned} \tag{9.27}
$$

$$
\begin{aligned}
X - mg \sin\theta &= m\,(\dot{u} + qw - rv) \\
Y + mg \sin\phi \cos\theta &= m\,(\dot{v} + ru - pw) \\
Z + mg \cos\phi \cos\theta &= m\,(\dot{w} + pv - qu)
\end{aligned} \tag{9.28}
$$

$$
\begin{aligned}
\mathcal{L} &= I_{xx}\,\dot{p} + I_{xy}\,\dot{q} + I_{xz}\,\dot{r} + (I_{zz} - I_{yy})\, qr + I_{yz}\,(q^2 - r^2) + I_{xz}\, pq - I_{xy}\, pr + h_z\, q - h_y\, r \\
\mathcal{M} &= I_{xy}\,\dot{p} + I_{yy}\,\dot{q} + I_{yz}\,\dot{r} + (I_{xx} - I_{zz})\, rp + I_{xz}\,(r^2 - p^2) + I_{xy}\, qr - I_{yz}\, qp + h_x\, r - h_z\, p \quad (9.29) \\
\mathcal{N} &= I_{xz}\,\dot{p} + I_{yz}\,\dot{q} + I_{zz}\,\dot{r} + (I_{zz} - I_{xx})\, pq + I_{xy}\,(p^2 - q^2) + I_{yz}\, rp - I_{xz}\, rq + h_y\, p - h_x\, q
\end{aligned}
$$

When the three linear momentum equations (9.28) are multiplied by $1/m$, and the three angular momentum equations (9.29) are multiplied by the inverse of the moment of inertia tensor, $\overline{\overline{\mathbf{I}}}^{-1}$, they become explicit expressions for the linear and angular velocity rates, $\dot{u} = \dots , \dot{p} = \dots$, etc. All the 12 equations (9.26)–(9.29) then collectively have the classical state-space evolution form with 12 equation components:

$$
\boxed{\dot{\mathbf{x}} = \mathbf{f}(\mathbf{x}, \boldsymbol{\delta})} \tag{9.30}
$$

9.8.3   Linearized equations of motion

The state-space equation system (9.30) above is nonlinear. To make stability and control problems tractable, these equations are first put into *linearized* forms. We assume some steady flight in the *trim state* $\mathbf{x}_0$, $\boldsymbol{\delta}_0$. The trim state has $\dot{\mathbf{x}}_0 = \mathbf{0}$, except for the position rate and heading rate components.

$$\dot{x}^e = u_0^e \quad , \qquad \dot{y}^e = v_0^e \quad , \qquad \dot{z}^e = w_0^e \quad , \qquad \dot{\psi} = r_0^e$$

Straight flight has a zero heading rate $r_0^e = 0$, while steady turning flight has $r_0^e \neq 0$.

In the system equation (9.30), consider small perturbations $\Delta\mathbf{x}(t)$ and $\Delta\boldsymbol{\delta}(t)$ about the trim state, as shown in Figure 9.3.

$$\mathbf{x}(t) \;=\; \mathbf{x}_0 + \Delta\mathbf{x}(t) \tag{9.31}$$

$$\boldsymbol{\delta}(t) \;=\; \boldsymbol{\delta}_0 + \Delta\boldsymbol{\delta}(t) \tag{9.32}$$

$$\dot{\mathbf{x}}_0 + \Delta\dot{\mathbf{x}} \;=\; \mathbf{f}_{(\mathbf{x}_0+\Delta\mathbf{x},\,\boldsymbol{\delta}_0+\Delta\boldsymbol{\delta})} \;\simeq\; \mathbf{f}_{(\mathbf{x}_0,\,\boldsymbol{\delta}_0)} + \left.\frac{\mathrm{d}\mathbf{f}}{\mathrm{d}\mathbf{x}}\right|_{\mathbf{x}_0,\boldsymbol{\delta}_0}\!\!\Delta\mathbf{x} + \left.\frac{\mathrm{d}\mathbf{f}}{\mathrm{d}\boldsymbol{\delta}}\right|_{\mathbf{x}_0,\boldsymbol{\delta}_0}\!\!\Delta\boldsymbol{\delta} \tag{9.33}$$

Since the trim state is physical, it must by itself obey the equations of motion.

$$\dot{\mathbf{x}}_0 \;=\; \mathbf{f}_{(\mathbf{x}_0,\,\boldsymbol{\delta}_0)} \tag{9.34}$$

Subtracting (9.34) from (9.33) gives the *linearized equations of motion* which govern the small state vector perturbations,

$$\Delta\dot{\mathbf{x}} \;=\; \bar{\bar{\mathbf{A}}}\,\Delta\mathbf{x} + \bar{\bar{\mathbf{B}}}\,\Delta\boldsymbol{\delta} \tag{9.35}$$

$$\bar{\bar{\mathbf{A}}} \equiv \left.\frac{\mathrm{d}\mathbf{f}}{\mathrm{d}\mathbf{x}}\right|_{\mathbf{x}_0,\boldsymbol{\delta}_0} \quad , \qquad \bar{\bar{\mathbf{B}}} \equiv \left.\frac{\mathrm{d}\mathbf{f}}{\mathrm{d}\boldsymbol{\delta}}\right|_{\mathbf{x}_0,\boldsymbol{\delta}_0}$$

with $\bar{\bar{\mathbf{A}}}$ and $\bar{\bar{\mathbf{B}}}$ being the *system Jacobian matrices* which depend on the trim state.

actual state
$\mathbf{x}(t) \;=\; \mathbf{x}_0 + \Delta\mathbf{x}(t)$
later perturbation
initial perturbation
$\mathbf{x}_0$ trim state
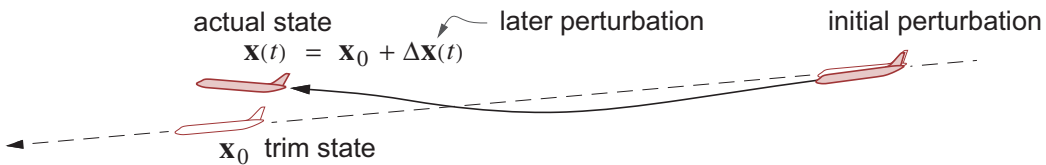
Figure 9.3: Aircraft state considered as a small perturbation from a trim state. Instability is indicated if the perturbation grows exponentially from an initial perturbation.

9.8.4   Natural response

For the *fixed-stick* case of no control inputs, $\Delta\boldsymbol{\delta} = \mathbf{0}$, the general solution of the Linear Time Invariant (LTI) ODE system (9.35) is a superposition of eight *flight-dynamics eigenmodes*,

$$\Delta\mathbf{x}(t) \;=\; \sum_{k=1}^{8} \mathbf{v}_k \, \exp(\lambda_k t) \quad , \qquad \lambda_k \;=\; \sigma_k + \mathrm{i}\,\omega_k \tag{9.36}$$

where $\lambda_{1...8}$ are the nonzero eigenvalues and $\mathbf{v}_{1...8}$ are the corresponding eigenvectors of the Jacobian matrix $\bar{\bar{\mathbf{A}}}$. Each of the remaining four zero eigenvalues corresponds to a shift in x, y, z, ψ, which has no influence on the dynamics and hence is excluded from the mode summation.

The magnitude of each ω_k and the sign and magnitude of σ_k indicate the nature of that mode. If $\omega_k = 0$ then the motion is monotonic, and if $\omega_k \neq 0$ then the motion is oscillatory. The latter actually consists of two complex-pair modes, $\lambda = \sigma \pm \mathrm{i}\omega$. If $\sigma_k > 0$ then that mode is *unstable*, meaning that the aircraft will exhibit exponential divergence from the trimmed flight state.

9.8.5 Symmetry

In the completely general case, the $\bar{\bar{\mathbf{A}}}$ and $\bar{\bar{\mathbf{B}}}$ matrices of the linearized dynamics system (9.35) are nearly full. But if we have

- geometric symmetry (the airplane is left/right symmetric), and
- aerodynamic symmetry with $v_0 = p_0 = r_0 = \phi_0 = 0$, and
- negligible onboard angular momentum, $\mathbf{h} \simeq \mathbf{0}$,

then $\bar{\bar{\mathbf{A}}}$ and $\bar{\bar{\mathbf{B}}}$ have the following form after the state vector and the equations are re-ordered as indicated. Zero or nearly zero matrix elements are shown blank.

$$
\frac{\mathrm{d}}{\mathrm{d}t}
\begin{Bmatrix}
\Delta u \\ \Delta w \\ \Delta q \\ \Delta \theta \\ \hline \Delta v \\ \Delta p \\ \Delta r \\ \Delta \phi \\ \hline \Delta x^e \\ \Delta y^e \\ \Delta z^e \\ \Delta \psi
\end{Bmatrix}
=
\begin{bmatrix}
\cdot\;\cdot\;\cdot\;\cdot & & \\
\cdot\;\cdot\;\cdot\;\cdot & & \\
\cdot\;\cdot\;\cdot\;\cdot & & \\
\cdot\;\cdot\;\cdot\;\cdot & & \\
\hline
 & \cdot\;\cdot\;\cdot\;\cdot & \\
 & \cdot\;\cdot\;\cdot\;\cdot & \\
 & \cdot\;\cdot\;\cdot\;\cdot & \\
 & \cdot\;\cdot\;\cdot\;\cdot & \\
\hline
\cdot\;\cdot\;\cdot\;\cdot & \cdot\;\cdot\;\cdot\;\cdot & \\
\cdot\;\cdot\;\cdot\;\cdot & \cdot\;\cdot\;\cdot\;\cdot & \\
\cdot\;\cdot\;\cdot\;\cdot & \cdot\;\cdot\;\cdot\;\cdot & \\
\cdot\;\cdot\;\cdot\;\cdot & \cdot\;\cdot\;\cdot\;\cdot &
\end{bmatrix}
\begin{Bmatrix}
\Delta u \\ \Delta w \\ \Delta q \\ \Delta \theta \\ \hline \Delta v \\ \Delta p \\ \Delta r \\ \Delta \phi \\ \hline \Delta x^e \\ \Delta y^e \\ \Delta z^e \\ \Delta \psi
\end{Bmatrix}
+
\begin{bmatrix}
\cdot\;\cdot\;\cdot & \\
\cdot\;\cdot\;\cdot & \\
\cdot\;\cdot\;\cdot & \\
 & \\
\hline
 & \cdot\;\cdot \\
 & \cdot\;\cdot \\
 & \cdot\;\cdot \\
 & \\
\hline
 & \\
 & \\
 & \\
 &
\end{bmatrix}
\begin{Bmatrix}
\Delta \delta_T \\ \Delta \delta_f \\ \Delta \delta_e \\ \Delta \delta_a \\ \Delta \delta_r
\end{Bmatrix}
\tag{9.37}
$$

The first four rows constitute the *Longitudinal Dynamics* subset, the middle four rows are the *Lateral Dynamics* subset, and the last four rows are the *Navigation* subset.

The last four navigation variables $\Delta x^e, \Delta y^e, \Delta z^e, \Delta \psi$ generally have zero matrix columns, even for asymmetric aircraft. This implies that the matrix will have at least four zero eigenvalues, $\lambda_{9,10,11,12} = 0$, whose corresponding eigenmodes contain only the steady displacements of the four navigation variables.

$$
\begin{aligned}
\mathbf{v}_9 \exp(0t) &= \{ \qquad\quad | \qquad\quad | \Delta x^e \qquad\quad \}^T \\
\mathbf{v}_{10} \exp(0t) &= \{ \qquad\quad | \qquad\quad | \quad \Delta y^e \qquad \}^T \\
\mathbf{v}_{11} \exp(0t) &= \{ \qquad\quad | \qquad\quad | \qquad \Delta z^e \; \}^T \\
\mathbf{v}_{12} \exp(0t) &= \{ \qquad\quad | \qquad\quad | \qquad\quad \Delta \psi \}^T
\end{aligned}
$$

This is expected from coordinate invariance – the dynamics cannot be affected if the airplane position is displaced, or if it is pointed in another direction in the plane parallel to the Earth surface. This justifies excluding these four trivial steady displacement modes from the dynamical mode summation (9.36).

One notable exception occurs if atmospheric property variation is significant over the vertical extent of the motion. In this case there will be some dependence on the Δz^e variable, and there will be only three trivial modes present in the system.

9.9 Aerodynamic Force and Moment Linearizations

Force and moment coefficients have been already defined in Section 6.3. In the most common notation used in flight dynamics these are

$$
\begin{aligned}
C_x &\equiv X/QS & C_\ell &\equiv \mathcal{L}/QSb \\
C_y &\equiv Y/QS & C_m &\equiv \mathcal{M}/QSc \\
C_z &\equiv Z/QS & C_n &\equiv \mathcal{N}/QSb
\end{aligned}
\tag{9.38}
$$

where S, b, c are the reference area, span, chord. To avoid conflict with the pitch rate q, the symbol Q is used to denote the reference freestream dynamic pressure in lieu of the alternative q_∞.

$$Q \equiv \tfrac{1}{2}\rho V^2 = \tfrac{1}{2}\rho(u^2 + v^2 + w^2) \tag{9.39}$$

Perturbations of velocity, flow angles, and normalized rates about the trim state are related to the state variable perturbations as follows.

$$\Delta\bar{u} \equiv \frac{\Delta u}{u_0} \qquad\qquad \Delta\bar{p} \equiv \Delta\left(\frac{pb}{2V}\right) \simeq \Delta p \frac{b}{2u_0}$$

$$\Delta\beta \equiv \Delta\left(\arctan\frac{v}{\sqrt{u^2+w^2}}\right) \simeq \frac{\Delta v}{u_0} \qquad \Delta\bar{q} \equiv \Delta\left(\frac{qc}{2V}\right) \simeq \Delta q \frac{c}{2u_0} \tag{9.40}$$

$$\Delta\alpha \equiv \Delta\left(\arctan\frac{w}{u}\right) \simeq \frac{\Delta w}{u_0} \qquad\qquad \Delta\bar{r} \equiv \Delta\left(\frac{rb}{2V}\right) \simeq \Delta r \frac{b}{2u_0}$$

The dynamic pressure perturbation is linearized in the same manner.

$$\Delta Q = \Delta\left[\tfrac{1}{2}\rho(u^2 + v^2 + w^2)\right] \simeq \rho\left(u_0\,\Delta u + v_0\,\Delta v + w_0\,\Delta w\right) \simeq \rho u_0\,\Delta u = 2Q\frac{\Delta u}{u_0} \tag{9.41}$$

The coefficient perturbations give the state variable and control variable perturbations via the stability and control derivatives as follows. Again, blank matrix elements indicate derivatives which are zero for a symmetric aircraft in a symmetric trim state flight condition. An asymmetric trim state would have all the elements nonzero.

$$\begin{Bmatrix} \Delta C_x \\ \Delta C_y \\ \Delta C_z \end{Bmatrix} = \begin{bmatrix} C_{x_u} & & C_{x_\alpha} \\ & C_{y_\beta} & \\ C_{z_u} & & C_{z_\alpha} \end{bmatrix} \begin{Bmatrix} \Delta\bar{u} \\ \Delta\beta \\ \Delta\alpha \end{Bmatrix} + \begin{bmatrix} & C_{x_q} & \\ C_{y_p} & & C_{y_r} \\ & C_{z_q} & \end{bmatrix} \begin{Bmatrix} \Delta\bar{p} \\ \Delta\bar{q} \\ \Delta\bar{r} \end{Bmatrix} + \begin{bmatrix} C_{x_{\delta_T}} & \\ & \\ & C_{z_{\delta_f}} \end{bmatrix} \begin{Bmatrix} \Delta\delta_T \\ \Delta\delta_f \end{Bmatrix} \tag{9.42}$$

$$\begin{Bmatrix} \Delta C_\ell \\ \Delta C_m \\ \Delta C_n \end{Bmatrix} = \begin{bmatrix} & C_{\ell_\beta} & \\ C_{m_u} & & C_{m_\alpha} \\ & C_{n_\beta} & \end{bmatrix} \begin{Bmatrix} \Delta\bar{u} \\ \Delta\beta \\ \Delta\alpha \end{Bmatrix} + \begin{bmatrix} C_{\ell_p} & & C_{\ell_r} \\ & C_{m_q} & \\ C_{n_p} & & C_{n_r} \end{bmatrix} \begin{Bmatrix} \Delta\bar{p} \\ \Delta\bar{q} \\ \Delta\bar{r} \end{Bmatrix} + \begin{bmatrix} C_{\ell_{\delta_a}} & \\ & C_{m_{\delta_e}} \\ & C_{n_{\delta_r}} \end{bmatrix} \begin{Bmatrix} \Delta\delta_a \\ \Delta\delta_e \\ \Delta\delta_r \end{Bmatrix} \tag{9.43}$$

The dimensional force and moment perturbations about the trim state are now expressed in terms of the coefficient and dynamic pressure perturbations obtained above.

$$\Delta X = \Delta(QSC_x) \simeq QS\left(2C_{x_0}\,\Delta\bar{u} + C_{x_\alpha}\Delta\alpha + C_{x_q}\Delta\bar{q} + C_{x_{\delta_T}}\Delta\delta_T\right)$$

$$\Delta Y = \Delta(QSC_y) \simeq QS\left(C_{y_\beta}\Delta\beta + C_{y_p}\Delta\bar{p} + C_{y_r}\Delta\bar{r}\right) \tag{9.44}$$

$$\Delta Z = \Delta(QSC_z) \simeq QS\left(2C_{z_0}\,\Delta\bar{u} + C_{z_\alpha}\Delta\alpha + C_{z_q}\Delta\bar{q} + C_{z_{\delta_f}}\Delta\delta_f + C_{z_{\delta_e}}\Delta\delta_e\right)$$

$$\Delta\mathcal{L} = \Delta(QSbC_\ell) \simeq QSb\left(C_{\ell_\beta}\Delta\beta + C_{\ell_p}\Delta\bar{p} + C_{\ell_r}\Delta\bar{r} + C_{\ell_{\delta_a}}\Delta\delta_a\right)$$

$$\Delta\mathcal{M} = \Delta(QScC_m) \simeq QSc\left(2C_{m_0}\,\Delta\bar{u} + C_{m_\alpha}\Delta\alpha + C_{m_q}\Delta\bar{q} + C_{m_{\delta_e}}\Delta\delta_e\right) \tag{9.45}$$

$$\Delta\mathcal{N} = \Delta(QSbC_n) \simeq QSb\left(C_{n_\beta}\Delta\beta + C_{n_p}\Delta\bar{p} + C_{n_r}\Delta\bar{r} + C_{n_{\delta_r}}\Delta\delta_r\right)$$

As discussed in Section 6.3.2, aero-lag effects also make the forces and moments depend on the angle of attack rate. This could be represented above by additional terms with the associated stability derivatives, such as $C_{z_{\dot{\alpha}}}\Delta\dot{\alpha}$, $C_{m_{\dot{\alpha}}}\Delta\dot{\alpha}$, etc. These are left out here for brevity.

9.10   Stability Derivative Specification

Aerodynamic force and moment coefficients and their derivatives are usually specified in the *stability axes* $(x^{b'}, z^{b'})$, which are rotated about $y^b = y^{b'}$ by the freestream angle of attack α, as shown in Figure 9.4. The main reason for this axis choice is that the stability derivatives in stability axes exhibit a minimal variation with the trim-state α_0 within the normal operating range. Specifically, in unstalled flight, the lateral cross-derivatives C'_{ℓ_r} and C'_{n_p} are very nearly proportional to the trim C_{L_0}, and the remaining derivatives are nearly the same for all C_{L_0} values. This considerably simplifies the stability and control specification of an aircraft for all trim conditions. The 2×2 rotation matrix $\bar{\bar{\mathbf{S}}}$ then defines the body-axis xz vector components in terms of the $x'z'$ components, shown in Figure 9.4. This is effectively the same as matrix $\bar{\bar{\mathbf{T}}}^{\mathrm{s}}$ defined by (6.4) in Section 6.2.1.

$$\bar{\bar{\mathbf{S}}}(\alpha) \equiv \begin{bmatrix} \cos\alpha & -\sin\alpha \\ \sin\alpha & \cos\alpha \end{bmatrix} \quad , \quad \frac{\mathrm{d}\bar{\bar{\mathbf{S}}}}{\mathrm{d}\alpha}(\alpha) = \begin{bmatrix} -\sin\alpha & -\cos\alpha \\ \cos\alpha & -\sin\alpha \end{bmatrix} \tag{9.46}$$

$$\begin{Bmatrix} C_x \\ C_z \end{Bmatrix} = \begin{bmatrix} \bar{\bar{\mathbf{S}}} \end{bmatrix} \begin{Bmatrix} -C_D \\ -C_L \end{Bmatrix} \quad , \quad \begin{Bmatrix} C_\ell \\ C_n \end{Bmatrix} = \begin{bmatrix} \bar{\bar{\mathbf{S}}} \end{bmatrix} \begin{Bmatrix} C'_\ell \\ C'_n \end{Bmatrix} \quad , \quad \begin{Bmatrix} \bar{p} \\ \bar{r} \end{Bmatrix} = \begin{bmatrix} \bar{\bar{\mathbf{S}}} \end{bmatrix} \begin{Bmatrix} \bar{p}' \\ \bar{r}' \end{Bmatrix} \tag{9.47}$$

The remaining y-axis components $C_y, C_m, \bar{q}$ are the same between the two axis systems.
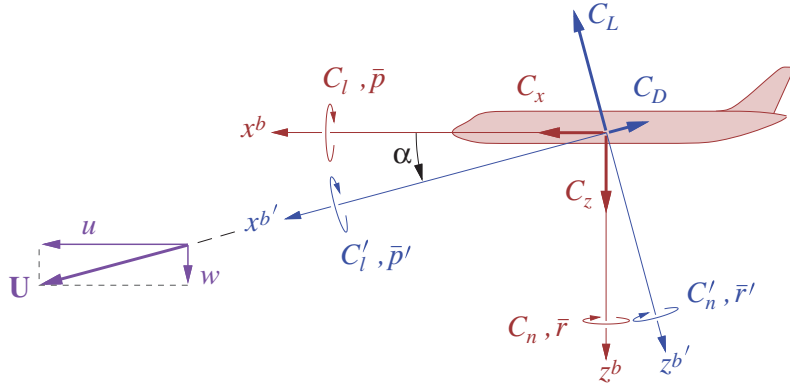
Figure 9.4: Force and moment coefficients in body and stability axes. This is the non-dimensional equivalent to Figure 6.2.

The body-axis derivatives with respect to α, all defined at the trim state, can now be computed:

$$\begin{Bmatrix} C_{x_\alpha} \\ C_{z_\alpha} \end{Bmatrix} = \begin{bmatrix} \dfrac{\mathrm{d}\bar{\bar{\mathbf{S}}}}{\mathrm{d}\alpha}\Big|_0 \end{bmatrix} \begin{Bmatrix} -C_{D_0} \\ -C_{L_0} \end{Bmatrix} + \begin{bmatrix} \bar{\bar{\mathbf{S}}}_0 \end{bmatrix} \begin{Bmatrix} -C_{D_\alpha} \\ -C_{L_\alpha} \end{Bmatrix} \simeq \begin{Bmatrix} C_{L_0} - C_{D_\alpha} \\ -C_{L_\alpha} \end{Bmatrix} \tag{9.48}$$

The body-axis moment derivatives with respect to β and control deflections are similarly computed.

$$\begin{Bmatrix} C'_{\ell_\beta} \\ C'_{n_\beta} \end{Bmatrix} = \begin{bmatrix} \bar{\bar{\mathbf{S}}}_0 \end{bmatrix} \begin{Bmatrix} C'_{\ell_\beta} \\ C'_{n_\beta} \end{Bmatrix} \simeq \begin{Bmatrix} C'_{\ell_\beta} - \alpha_0\, C'_{n_\beta} \\ C'_{n_\beta} + \alpha_0\, C'_{\ell_\beta} \end{Bmatrix} \tag{9.49}$$

$$\begin{Bmatrix} C'_{\ell_\delta} \\ C'_{n_\delta} \end{Bmatrix} = \begin{bmatrix} \bar{\bar{\mathbf{S}}}_0 \end{bmatrix} \begin{Bmatrix} C'_{\ell_\delta} \\ C'_{n_\delta} \end{Bmatrix} \simeq \begin{Bmatrix} C'_{\ell_\delta} - \alpha_0\, C'_{n_\delta} \\ C'_{n_\delta} + \alpha_0\, C'_{\ell_\delta} \end{Bmatrix} \tag{9.50}$$

The sideforce derivatives with respect to the body-axis rates are obtained with the reverse rotation by the transpose of $\bar{\bar{\mathbf{S}}}$:

$$\begin{pmatrix} C_{y_p} & C_{y_r} \end{pmatrix} = \begin{pmatrix} C'_{y_p} & C'_{y_r} \end{pmatrix} \begin{bmatrix} \bar{\bar{\mathbf{S}}}_0^T \end{bmatrix} \simeq \begin{pmatrix} C'_{y_p} - \alpha_0\, C'_{y_r} & C'_{y_r} + \alpha_0\, C'_{y_p} \end{pmatrix} \tag{9.51}$$

Converting the moment derivatives with respect to $\bar{p}, \bar{r}$ into the body axes requires two rotations, a pre-rotation by $\bar{\bar{\mathbf{S}}}$ for the moments and a reverse post-rotation by $\bar{\bar{\mathbf{S}}}^T$ for the rates.

$$\begin{bmatrix} C_{\ell_p} & C_{\ell_r} \\ C_{n_p} & C_{n_r} \end{bmatrix} = \begin{bmatrix} \bar{\bar{\mathbf{S}}}_0 \end{bmatrix} \begin{bmatrix} C'_{\ell_p} & C'_{\ell_r} \\ C'_{n_p} & C'_{n_r} \end{bmatrix} \begin{bmatrix} \bar{\bar{\mathbf{S}}}_0^T \end{bmatrix} \tag{9.52}$$

9.11 Longitudinal Dynamics Subset

The longitudinal-dynamics system is the upper 4×4 part of the overall system (9.37).

$$\begin{Bmatrix} \Delta\dot{u} \\ \Delta\dot{w} \\ \Delta\dot{q} \\ \Delta\dot{\theta} \end{Bmatrix} = \begin{bmatrix} X_u & X_w & 0 & -g \\ Z_u & Z_w & u_0 & 0 \\ M_u & M_w & M_q & 0 \\ 0 & 0 & 1 & 0 \end{bmatrix} \begin{Bmatrix} \Delta u \\ \Delta w \\ \Delta q \\ \Delta\theta \end{Bmatrix} + \begin{bmatrix} X_{\delta_T} & 0 & 0 \\ 0 & Z_{\delta_f} & 0 \\ 0 & 0 & M_{\delta_e} \\ 0 & 0 & 0 \end{bmatrix} \begin{Bmatrix} \Delta\delta_T \\ \Delta\delta_f \\ \Delta\delta_e \end{Bmatrix} \tag{9.53}$$

The matrix elements above are the following dimensional stability derivatives.

$$
\begin{aligned}
X_u &= \frac{QS}{m}\frac{1}{u_0}C_{x_u} & Z_u &= \frac{QS}{m}\frac{1}{u_0}C_{z_u} & M_u &= \frac{QSc}{I_y}\frac{1}{u_0}C_{m_u} \\
X_w &= \frac{QS}{m}\frac{1}{u_0}C_{x_\alpha} & Z_w &= \frac{QS}{m}\frac{1}{u_0}C_{z_\alpha} & M_w &= \frac{QSc}{I_y}\frac{1}{u_0}C_{m_\alpha} \\
X_q &= \frac{QS}{m}\frac{c}{2u_0}C_{x_q} & Z_q &= \frac{QS}{m}\frac{c}{2u_0}C_{z_q} & M_q &= \frac{QSc}{I_y}\frac{c}{2u_0}C_{m_q} \\
X_{\delta_T} &= \frac{QS}{m}C_{x_{\delta_T}} & Z_{\delta_f} &= \frac{QS}{m}C_{z_{\delta_f}} & M_{\delta_e} &= \frac{QSc}{I_y}C_{m_{\delta_e}}
\end{aligned}
\tag{9.54}
$$

These assume that the moment of inertia tensor $\bar{\bar{\mathbf{I}}}$ has only the single pitch inertia element $I_{yy} \equiv I_y$, with I_{xy} and I_{yz} being zero, which is consistent with the assumed left/right symmetry.

For a typical pitch-stable aircraft in fixed-stick flight with $\Delta\delta_T = \Delta\delta_f = \Delta\delta_e = 0$, the four eigenvalues of the longitudinal system (9.53) are shown in Figure 9.5, and have the following characteristics.

$\sigma_{\mathrm{ph}} \pm i\omega_{\mathrm{ph}}$ Phugoid mode (slow, weakly damped)
$\sigma_{\mathrm{SP}} \pm i\omega_{\mathrm{SP}}$ Short-Period mode (fast, well-damped)
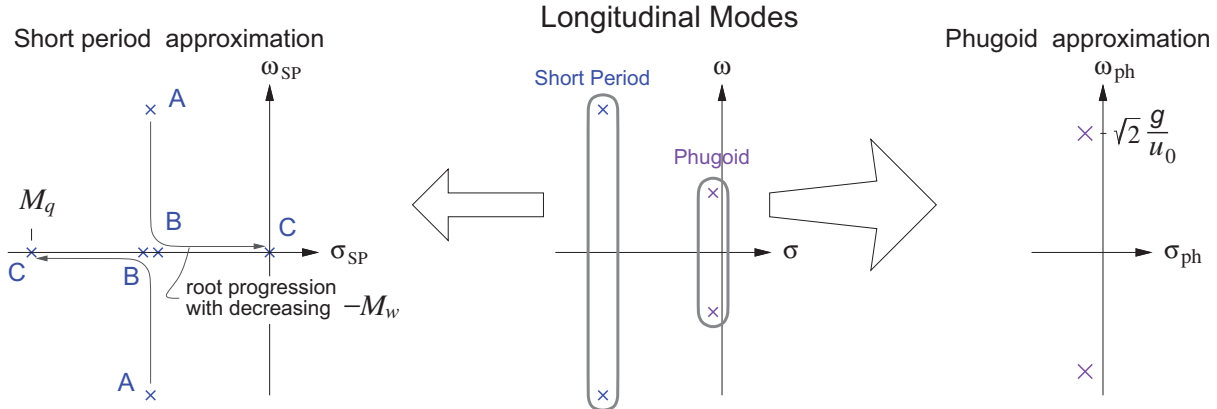
Figure 9.5: Typical longitudinal dynamics eigenvalues of a conventional aircraft. Short period and phugoid eigenvalues closely match those given by their respective approximation models.

These two eigenvalue pairs have good *spectral separation*, so that they can be estimated reasonably well in isolation by assuming that some motion components are negligible. This will give some insight into the key aircraft aerodynamic parameters which influence these eigenmodes. The assumed motions are shown in Figures 9.6 and 9.7, and are analyzed in the following sections.

9.11.1 Phugoid approximation

Here we assume pitch equilibrium, or $\Delta\mathcal{M}=0$, which implies a negligible pitch rate and pitch acceleration, $\Delta q \simeq 0$, $\Delta\dot{q} \simeq 0$. The airplane is thus assumed to remain in pitch trim, implying a fixed-α motion so that $\Delta w = u_0\,\Delta\alpha = 0$, as shown in Figure 9.6.
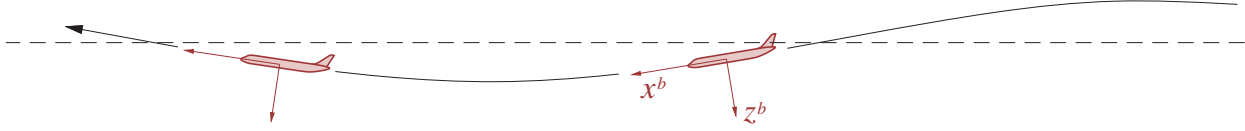
Figure 9.6: Assumed motion for the phugoid approximation.

The full longitudinal system (9.53) then simplifies to the "phugoid" system:

$$\begin{Bmatrix} \Delta\dot{u} \\ \Delta\dot{\theta} \end{Bmatrix} = \begin{bmatrix} X_u & -g \\ -Z_u/u_0 & 0 \end{bmatrix} \begin{Bmatrix} \Delta u \\ \Delta\theta \end{Bmatrix} + \begin{bmatrix} X_{\delta_T} \\ 0 \end{bmatrix} \{\Delta\delta_T\} \tag{9.55}$$

Its 2×2 matrix has the two phugoid eigenvalues

$$\lambda_{1,2} \equiv \sigma_{\mathrm{ph}} \pm \mathrm{i}\,\omega_{\mathrm{ph}} = \frac{1}{2}\left[X_u \pm \sqrt{X_u^2 + 4gZ_u/u_0}\, \right]$$

which have the following phugoid frequency and damping ratio.

$$\omega_{\mathrm{ph}} = \frac{1}{2}\sqrt{-X_u^2 - 4gZ_u/u_0} \simeq \sqrt{2}\,\frac{g}{u_0} \qquad \text{(slow)} \tag{9.56}$$

$$\zeta_{\mathrm{ph}} \equiv \frac{-\sigma_{\mathrm{ph}}}{\sqrt{\sigma_{\mathrm{ph}}^2 + \omega_{\mathrm{ph}}^2}} \simeq \frac{1}{\sqrt{2}}\frac{C_{D_0}}{C_{L_0}} \qquad \text{(weakly damped)} \tag{9.57}$$

The corresponding eigenmodes in the sum (9.36) then give the natural response of the aircraft to pitch perturbations in the uncontrolled or "fixed-stick" case with $\Delta\delta_T = 0$.

For high speed aircraft the phugoid period $2\pi/\omega_{\mathrm{ph}}$ is measured in minutes, which is a rather slow motion compared to more typical aircraft maneuvers. For clean airplanes with large lift/drag ratios $L/D = C_{L_0}/C_{D_0}$, the phugoid damping ratio is seen to be especially small. On such aircraft, adequate suppression of unwanted phugoid motions requires either an autopilot or active pitch control by the pilot.

9.11.2 Short-period approximation

Here we assume that the pitching motions are too fast for the airplane to respond significantly to the resulting lift changes, so that during the pitch oscillations it travels in a straight line at a fixed speed. The straight-line motion implies $\Delta u = 0$ and $\Delta w = u_0\,\Delta\theta$, as shown in Figure 9.7.
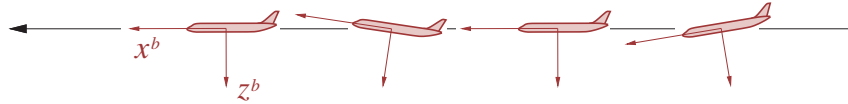
Figure 9.7: Assumed motion for the short-period approximation.

This reduces the full longitudinal system (9.53) to the smaller 2×2 "short period" system:

$$\begin{Bmatrix} \Delta\dot{q} \\ \Delta\dot{\theta} \end{Bmatrix} = \begin{bmatrix} M_q & u_0 M_w \\ 1 & 0 \end{bmatrix} \begin{Bmatrix} \Delta q \\ \Delta\theta \end{Bmatrix} + \begin{bmatrix} M_{\delta_e} \\ 0 \end{bmatrix} \{\Delta\delta_e\} \tag{9.58}$$

For the fixed-stick case $\Delta\delta_e = 0$, this has the following two short-period eigenvalues.

$$\lambda_{1,2} \equiv \sigma_{\mathrm{SP}} \pm i\omega_{\mathrm{SP}} = \frac{1}{2}\left[M_q \pm \sqrt{M_q^2 + 4u_0 M_w}\,\right]$$

These eigenvalues strongly depend on the pitch stability derivative $M_w \sim C_{m_\alpha}$, which is normally negative. As M_w increases (becomes less negative), there are three distinct limiting cases, labeled A,B,C in Figure 9.5.

A) $M_w < -M_q^2/4u_0:\quad \sigma_{\mathrm{SP}} = \frac{1}{2}M_q\;,\quad \omega_{\mathrm{SP}} = \frac{1}{2}\sqrt{-M_q^2 - 4u_0 M_w}$ (damped oscillatory)

B) $M_w = -M_q^2/4u_0:\quad \sigma_{\mathrm{SP}} = \frac{1}{2}M_q\;,\quad \frac{1}{2}M_q$ (critically damped)   (9.59)

C) $M_w = 0$ $:\quad \sigma_{\mathrm{SP}} = M_q\;,\quad 0$ (instability threshold)

The gradual increase of M_w, or equivalently of C_{m_α}, can in practice be caused by a rearward movement of the center of mass, or a gradual reduction in the horizontal tail area or moment arm. Case C indicates that instability will occur when C_{m_α} becomes positive.

In reality, case C invalidates the short-period approximations. These assumed that the short-period motion was fast compared to the phugoid's frequency, but case C shows a stationary short-period mode with a zero frequency and zero time constant. Hence, it is necessary to examine this case in more detail.

The actual behavior of the four eigenvalues of the full unsimplified longitudinal-dynamics system (9.53) is shown in the Figure 9.8. Note that it is actually one of the phugoid eigenvalues which first becomes unstable. The associated eigenmode cannot be categorized as either a short-period motion or a phugoid motion, but is instead a monotonic pitch divergence. Nevertheless, despite the weakness of the short-period approximation at the predicted onset of instability, the $C_{m_\alpha} \geq 0$ criterion obtained from this approximation predicts the instability of the full unsimplified longitudinal system quite well.
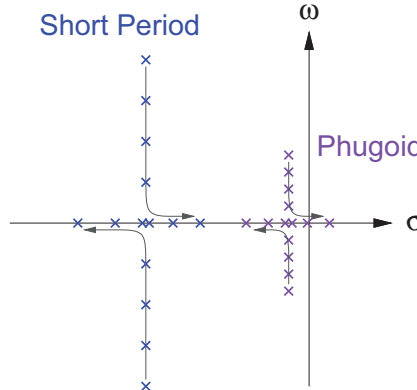
Figure 9.8: Progression of eigenvalues of complete longitudinal dynamics system as M_w (or C_{m_α}) becomes less negative and crosses zero.

9.12   Lateral Dynamics Subset

It is assumed that the aircraft has y-symmetry, so the products of inertia I_{xy} and I_{yz} vanish. Also, the xz body axes are assumed to be aligned with the inertia tensor's principal xz axes, so in these axes the I_{xz} product vanishes as well. With these assumptions the inertia tensor is then diagonal.

$$\bar{\bar{\mathbf{I}}} \equiv \begin{bmatrix} I_{xx} & I_{xy} & I_{xz} \\ I_{xy} & I_{yy} & I_{yz} \\ I_{xz} & I_{yz} & I_{zz} \end{bmatrix} = \begin{bmatrix} I_x & & \\ & I_y & \\ & & I_z \end{bmatrix}$$

The lateral-dynamics system, which is the middle 4×4 part of the overall system (9.37), then has the form

$$
\begin{Bmatrix} \Delta \dot{v} \\ \Delta \dot{p} \\ \Delta \dot{r} \\ \Delta \dot{\phi} \end{Bmatrix}
=
\begin{bmatrix}
Y_v & Y_p & Y_r - u_0 & g \cos \theta_0 \\
L_v & L_p & L_r & 0 \\
N_v & N_p & N_r & 0 \\
0 & 1 & 0 & 0
\end{bmatrix}
\begin{Bmatrix} \Delta v \\ \Delta p \\ \Delta r \\ \Delta \phi \end{Bmatrix}
+
\begin{bmatrix}
Y_{\delta_a} & Y_{\delta_r} \\
L_{\delta_a} & L_{\delta_r} \\
N_{\delta_a} & N_{\delta_r} \\
0 & 0
\end{bmatrix}
\begin{Bmatrix} \Delta \delta_a \\ \Delta \delta_r \end{Bmatrix}
\qquad (9.60)
$$

in which the matrix elements are the following dimensional stability derivatives.

$$
\begin{aligned}
Y_v &= \frac{QS}{m} \frac{1}{u_0} C_{y_\beta} & L_v &= \frac{QSb}{I_x} \frac{1}{u_0} C_{\ell_\beta} & N_v &= \frac{QSb}{I_z} \frac{1}{u_0} C_{n_\beta} \\
Y_p &= \frac{QS}{m} \frac{b}{2u_0} C_{y_p} & L_p &= \frac{QSb}{I_x} \frac{b}{2u_0} C_{\ell_p} & N_p &= \frac{QSb}{I_z} \frac{b}{2u_0} C_{n_p} \\
Y_r &= \frac{QS}{m} \frac{b}{2u_0} C_{y_r} & L_r &= \frac{QSb}{I_x} \frac{b}{2u_0} C_{\ell_r} & N_r &= \frac{QSb}{I_z} \frac{b}{2u_0} C_{n_r} \\
Y_{\delta_a} &= \frac{QS}{m} C_{y_{\delta_a}} & L_{\delta_a} &= \frac{QSb}{I_x} C_{\ell_{\delta_a}} & N_{\delta_a} &= \frac{QSb}{I_z} C_{n_{\delta_a}} \\
Y_{\delta_r} &= \frac{QS}{m} C_{y_{\delta_r}} & L_{\delta_r} &= \frac{QSb}{I_x} C_{\ell_{\delta_r}} & N_{\delta_r} &= \frac{QSb}{I_z} C_{n_{\delta_r}}
\end{aligned}
\qquad (9.61)
$$

For a typical aircraft in fixed-stick flight with $\Delta \delta_a = \Delta \delta_r = 0$, the four eigenvalues of the lateral system (9.60) are shown in Figure 9.9, and have the following characteristics.

σ_{roll}	Roll-subsidence mode	(very fast, damped)
σ_{spiral}	Spiral mode	(very slow, stable or unstable)
$\sigma_{\mathrm{DR}} \pm i\,\omega_{\mathrm{DR}}$	Dutch Roll mode	(oscillatory, moderately damped)
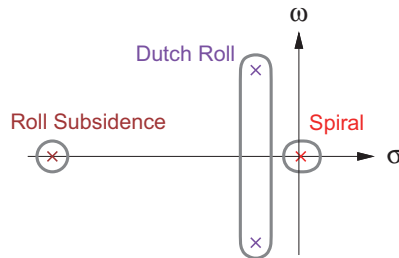
Figure 9.9: Typical lateral dynamics eigenvalues of a conventional aircraft.

As in the longitudinal-dynamics case, we will now obtain approximate expressions for these eigenvalues by assuming a simplified motion for the corresponding mode. The analysis follows that of Nelson [66].

9.12.1 Roll-subsidence approximation

For the roll-subsidence mode we assume a pure rolling motion about the x^b axis, shown in Figure 9.10.
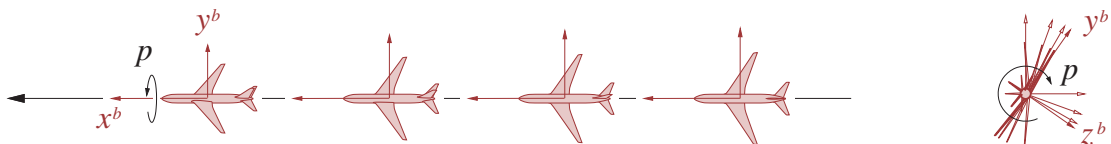
Figure 9.10: Assumed motion for the roll-subsidence approximation.

In this case only $\Delta\phi$ and $\Delta\dot{\phi} = \Delta p$ are nonzero, so the lateral-dynamics system (9.60) reduces to the following single first-order ODE.

$$\{\Delta\dot{p}\} = [\, L_p \,]\{\Delta p\} + [\, L_{\delta_a} \quad L_{\delta_r} \,]\begin{Bmatrix} \Delta\delta_a \\ \Delta\delta_r \end{Bmatrix} \tag{9.62}$$

Its eigenvalue for the fixed-stick case $\Delta\delta_a = \Delta\delta_r = 0$ follows immediately.

$$\sigma_{\mathrm{roll}} \simeq L_p = \frac{QSb^2}{2I_x u_0} C_{\ell_p} \tag{9.63}$$

Since C_{ℓ_p} is always negative, this corresponds to a monotonic decay in the roll rate. For most aircraft the characteristic damping time constant $1/\sigma_{\mathrm{roll}}$ is less than one second.

9.12.2 Spiral approximation

For this mode we assume that the roll accelerations are negligible, and only yaw motions dominate as shown in Figure 9.11. Setting $\Delta\dot{p} = 0$ in the second roll-moment line in the lateral system (9.60) then gives

$$0 = L_v\Delta v + L_r\Delta r$$
$$\text{or} \quad \Delta v = -\frac{L_r}{L_v}\Delta r. \tag{9.64}$$

Combining this with the fourth yaw-moment line gives

$$\{\Delta\dot{r}\} = \left[N_r - N_v\frac{L_r}{L_v}\right]\{\Delta r\} \tag{9.65}$$

whose eigenvalue is

$$\sigma_{\mathrm{spiral}} \simeq N_r - N_v\frac{L_r}{L_v} = \frac{QSb^2}{2I_z u_0}\left(C_{n_r} - C_{n_\beta}\frac{C_{\ell_r}}{C_{\ell_\beta}}\right) \tag{9.66}$$

which corresponds to monotonic yaw motion. In reality some roll motion (into the turn) is also present, since roll and yaw motions are always coupled to some extent in the full lateral system (9.60).
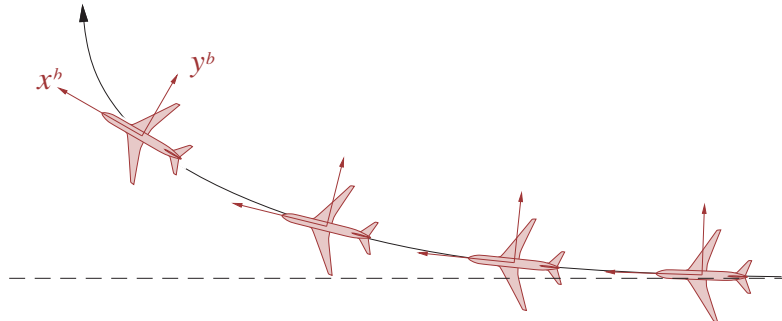
Figure 9.11: Assumed motion for the spiral-mode approximation. The tightening rate of the spiral path is shown greatly exaggerated.

The spiral mode can be either stable or unstable, depending on the values of the four stability derivatives appearing in (9.66). For conventional aircraft configurations, increasing the vertical-tail arm, increasing the dihedral, and decreasing the trim lift coefficient C_{L_0} all tend to make the spiral mode more stable. The magnitude of σ_{spiral} also scales roughly with the vertical tail area via the C_{n_r} and C_{n_β} derivatives

in (9.66). Therefore, increasing the vertical tail size will further stabilize a spirally-stable aircraft, and further destabilize a spirally-unstable aircraft.

Most aircraft are slightly spirally unstable, although the instability is slow enough to be easily controlled by a pilot who is attentive to the bank angle, either by observing the horizon or the artificial-horizon instrument. A wing-leveling autopilot can perform the same function without pilot input.

9.12.3   Dutch-roll approximation

The Dutch roll mode is an analog of the short-period mode, in that it mainly consists of relatively fast yawing motions, but which are now about the vertical axis. However, the Dutch roll mode is more complicated because it usually also involves significant roll motions. It is these secondary roll motions, which resemble those of a (Dutch) skater, which give the mode its name. Nevertheless, it is still useful to idealize the motion as shown in Figure 9.12, for which we have $\Delta v = -u_0 \, \Delta \psi$, and roll accelerations are assumed negligible. These assumptions reduce the full lateral system (9.60) to the smaller 2×2 Dutch roll system:
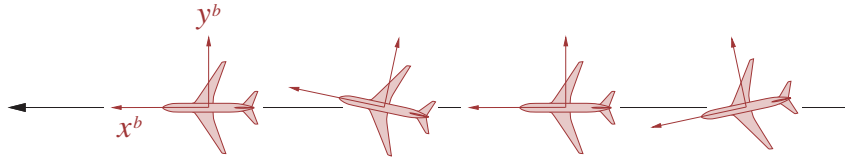
Figure 9.12: Assumed motion for the Dutch-roll approximation.

$$\left\{ \begin{matrix} \Delta \dot{v} \\ \Delta \dot{r} \end{matrix} \right\} = \left[\begin{matrix} Y_v & Y_r - u_0 \\ N_v & N_r \end{matrix} \right] \left\{ \begin{matrix} \Delta v \\ \Delta r \end{matrix} \right\} \tag{9.67}$$

This has the following two Dutch-roll eigenvalues.

$$\begin{aligned} \lambda_{1,2} &\equiv \sigma_{\mathrm{DR}} \pm \mathrm{i} \omega_{\mathrm{DR}} \\ \sigma_{\mathrm{DR}} &\simeq N_r + Y_v & = \frac{QSb^2}{2I_z u_0} \left(C_{n_r} + \frac{I_z}{mb^2} C_{y_\beta} \right) \\ \omega_{\mathrm{DR}}^2 &\simeq u_0 N_v + Y_v N_r - N_v Y_r & = \frac{QSb}{I_z} \left(C_{n_\beta} + \frac{\rho Sb}{4m} (C_{y_\beta} C_{n_r} - C_{n_\beta} C_{y_r}) \right) \end{aligned} \tag{9.68}$$

It must be pointed out that the neglect of roll in the assumed Dutch-roll motion in Figure 9.12 makes the resulting eigenvalue expressions (9.68) somewhat questionable. In particular, a large wing dihedral is known to make the Dutch-roll mode of actual aircraft less damped or even unstable, but this is not represented in the approximate results above since the associated C_{ℓ_β} derivative does not appear. However, the eigenvalues of the full 4×4 lateral system (9.60) will capture this destabilizing effect of dihedral on the Dutch-roll mode.

9.13   Stability Derivative Estimation

In modern fight dynamics practice, the stability and control derivatives are most conveniently computed numerically. The simplest and most common such approach is to employ the Vortex Lattice method developed in Chapter 6, although more advanced panel or grid methods may also be used. However, the classical derivative estimation techniques, such as those described by Etkin [65] and Nelson [66], are still very useful to gain some insight into how the geometry of a conventional aircraft influences the derivatives and hence the aircraft's dynamical behavior. The derivatives are estimated in terms of the aircraft's geometric parameters listed in Table 9.1. The reference (wing) area, span, chord will be denoted by S, b, c as before.

Table 9.1: Parameters used to estimate stability derivatives of a conventional aircraft.

AR	aspect ratio $(= b^2/S)$
S_{h}	horizontal tail area
S_{v}	vertical tail area
AR_{h}	horizontal tail's aspect ratio
AR_{v}	vertical tail's aspect ratio
λ	wing taper ratio $(= c_{\mathrm{tip}}/c_{\mathrm{root}})$
ℓ_{h}	distance from wing's aerodynamic center to horizontal tail
ℓ_{v}	distance from wing's aerodynamic center to vertical tail
ℓ_{cg}	distance from wing's aerodynamic center to mass centroid
Υ	effective wing dihedral angle (radians)
$\mathcal{V}_{\mathrm{fuse}}$	fuselage volume

9.13.1 Component derivatives

The estimation formulas are based on the lift-slope derivatives of the wing and tail surfaces, typically based on the lifting-line result (E.38) applied to each surface.

$$C_{L_\alpha} = \frac{c_{\ell_\alpha}}{1 + c_{\ell_\alpha}/(\pi AR)} \tag{9.69}$$

$$(C_{L_\alpha})_{\mathrm{h}} = \frac{(c_{\ell_\alpha})_{\mathrm{h}}}{1 + (c_{\ell_\alpha})_{\mathrm{h}}/(\pi AR_{\mathrm{h}})} \tag{9.70}$$

$$(C_{L_\alpha})_{\mathrm{v}} = \frac{(c_{\ell_\alpha})_{\mathrm{v}}}{1 + (c_{\ell_\alpha})_{\mathrm{v}}/(\pi AR_{\mathrm{v}})} \tag{9.71}$$

The lift-curve slopes c_{ℓ_α} of the wing and tail airfoils can be obtained from 2D airfoil experimental data or calculations. The thin-airfoil approximation $c_{\ell_\alpha} \simeq 2\pi$ is also commonly used. Compressibility effects can also be included here via the Prandtl-Glauert theory and sweep theory as in equations (8.87) and (8.103). It should also be noted that "endplate" effects on the vertical tail by the horizontal tail can significantly increase $(C_{L_\alpha})_{\mathrm{v}}$ from its estimate above.

The angle of attack seen by the horizontal tail is modified by its own induced downwash, and also by the downwash angle of the wing at the tail location. The latter is denoted by ε, and can be estimated as

$$\varepsilon \simeq k\frac{C_L}{\pi AR} \tag{9.72}$$

$$\frac{\mathrm{d}\varepsilon}{\mathrm{d}\alpha} \simeq k\frac{C_{L_\alpha}}{\pi AR} \tag{9.73}$$

$$k = 1 + \frac{1}{\sqrt{1+(\ell_{\mathrm{h}}/b)^2}}\left(\frac{1}{\pi\,\ell_{\mathrm{h}}/b}+1\right) \tag{9.74}$$

where the factor k is obtained from a horseshoe-vortex model of the wing and its trailing vortex system. The effect of the downwash is to reduce the horizontal tail's effective lift-curve slope with respect to the aircraft angle of attack by the factor $1-\mathrm{d}\varepsilon/\mathrm{d}\alpha$.

The drag coefficient's dependence on the angle of attack is commonly estimated assumed to be confined entirely to the induced drag component.

$$C_D = C_{D_p} + \frac{C_L^2}{\pi AR} \tag{9.75}$$

$$C_{D_\alpha} = \frac{2C_{L_0}C_{L_\alpha}}{\pi AR} \tag{9.76}$$

The fuselage's contribution to the overall lift is typically assumed to be captured by the center part of the wing "hidden" in the fuselage, which is already included in the C_{L_α} derivative. But a fuselage does typically have an additional significant pitching and yawing moment contributions. These can be estimated by the slender-body theory result (6.77), which has the following non-dimensional forms.

$$(C_{m_\alpha})_\text{fuse} = \frac{2\mathcal{V}_\text{fuse}}{Sc} \tag{9.77}$$

$$(C_{n_\beta})_\text{fuse} = \frac{-2\mathcal{V}_\text{fuse}}{Sb} \tag{9.78}$$

These contributions are destabilizing in pitch and yaw.

9.13.2 Longitudinal derivatives

The axial-force derivatives can now be estimated using the wing, horizontal-tail, and fuselage derivatives above. For the axial force we have

$$C_x = C_L \sin\alpha - C_D \cos\alpha \simeq C_L\,\alpha - C_D \tag{9.79}$$

$$C_{x_\alpha} = C_{L_0} - C_{D_\alpha} = C_{L_0}\left(1 - \frac{2C_{L_\alpha}}{\pi A\!R}\right) \tag{9.80}$$

$$C_{x_q} \simeq 0 \tag{9.81}$$

where small-angle approximations have been made. The normal force derivatives are estimated in the same manner,

$$C_z = -C_L \cos\alpha - C_D \sin\alpha \simeq -C_L - C_D\,\alpha \tag{9.82}$$

$$C_{z_\alpha} = -C_{L_\alpha} - C_{D_0} \tag{9.83}$$

$$C_{z_q} \simeq -2(C_{L_\alpha})_\text{h}\,V_\text{h} \tag{9.84}$$

$$V_\text{h} \equiv \frac{S_\text{h}\ell_\text{h}}{Sc} \tag{9.85}$$

with V_h denoting the horizontal tail volume coefficient.

The pitching moment is assumed to have wing, tail, and fuselage contributions.

$$C_{m_\alpha} = C_{L_\alpha}\frac{\ell_\text{cg}}{c} - (C_{L_\alpha})_\text{h}\,V_\text{h}\left(1 - \frac{\mathrm{d}\varepsilon}{\mathrm{d}\alpha}\right) + (C_{m_\alpha})_\text{fuse} \tag{9.86}$$

$$C_{m_q} = -2(C_{L_\alpha})_\text{h}\,V_\text{h}\,\frac{\ell_\text{h}}{c} + (C_{m_q})_\text{fuse} \tag{9.87}$$

The downwash factor $1-\mathrm{d}\varepsilon/\mathrm{d}\alpha$ is excluded from C_{m_q}. The reason is that this pitch-rate derivative dominates mainly in rapid pitching motions (e.g. in the short-period mode) where the wing's shed and trailing vorticity perturbations do not have sufficient time to convect to the tail to appreciably change the downwash there. However, the downwash factor can be added if the short-period mode is expected to be significantly slower than the wing–tail convection time. This will also give a smaller and hence more conservative estimate of pitch damping.

9.13.3 Lateral derivatives

The side force derivatives are estimated using the force derivative on the vertical tail.

$$C_{y_\beta} = -\frac{S_\text{v}}{S}(C_{L_\alpha})_\text{v} \tag{9.88}$$

$$C_{y_r} = -2V_\text{v}(C_{L_\alpha})_\text{v} \tag{9.89}$$

$$V_\text{v} \equiv \frac{S_\text{v}\ell_\text{v}}{Sb} \tag{9.90}$$

The vertical tail volume coefficient V_v naturally appears.

The rolling moment derivatives are obtained by using lifting-line theory applied to the wing sections, with the local velocities and resulting local angle of attack modified by the sideslip together with the wing dihedral, and by the roll and yaw rates. Integration of the local z-force perturbation across the span together with the local moment arm gives the rolling moment perturbation.

$$C_{\ell_\beta} = -C_{L_\alpha} \frac{\Upsilon}{6} \frac{1+2\lambda}{1+\lambda} \tag{9.91}$$

$$C_{\ell_p} = -C_{L_\alpha} \frac{1}{12} \frac{1+3\lambda}{1+\lambda} \tag{9.92}$$

$$C_{\ell_r} = \frac{C_{L_0}}{4} \tag{9.93}$$

The contributions of the tail surfaces are neglected here, but could be included with a more detailed analysis.

The yaw moment derivatives are obtained in a similar manner using the local z-force perturbations. The fuselage contribution is also included.

$$C_{n_\beta} = (C_{L_\alpha})_v V_v + (C_{n_\beta})_{\text{fuse}} \tag{9.94}$$

$$C_{n_p} = -\frac{C_{L_0}}{8} \tag{9.95}$$

$$C_{n_r} = -2(C_{L_\alpha})_v V_v \frac{\ell_v}{b} \tag{9.96}$$

Chapter 10

Flow-Field and Force Measurement

This chapter will examine the topic of aerodynamic force measurement in solid-wall and open-jet wind tunnels. Both direct force measurement (near-field) and wake survey (far-field) methods will be considered.

10.1 Wind Tunnel Methods – Overview

The two most common purposes of wind tunnel tests are:

1. To determine what the forces and moments would be on the actual object in flight. The tests can be performed either on the actual object, or more commonly on a suitable scale model.

2. To obtain data for validation or calibration of theoretical or computational methods, using some representative model geometry and flow conditions. In addition to the overall loads, ideally this data includes more detailed information such as surface pressures and flow-field velocity distributions.

If the intent is to simulate an unbounded flow-field about a 2D airfoil or a 3D aircraft in flight, then the tunnel walls or tunnel jet boundaries will have unwanted influences on the flow velocities at the model location and hence on the model aerodynamic loads. Modeling and estimation of these tunnel boundary effects to correct measured data is a major goal of this chapter. Another goal is to give a sense of the theoretical and practical challenges in wind tunnel measurements. For a much more complete treatment of wind tunnel testing methods and techniques, see Barlow et al [67].

10.2 Direct Force Measurements

This section examines the measurement of the aerodynamic forces and moments acting on a model mounted in a wind tunnel, using a load sensor.

10.2.1 Force component definitions and rotations

The angle of attack α is generally defined between the model reference line and the direction of the *tunnel freestream*, which is defined as the velocity vector which is present in the empty tunnel. It will be denoted here by $\mathbf{V}_\infty$, even though there is no flow "at infinity" in a wind tunnel. Assuming the tunnel freestream is horizontal, the axis for the lift force component L is most conveniently chosen to be vertical, along the gravity vector. The axis for the sideforce Y is then defined orthogonal to the other two.

The force vector acting on a wind tunnel model can be measured by mounting the model on a load sensor. After the model weight and other instrumentation biases (or "wind-off tares") are properly subtracted, the remaining force $\mathbf{F}$ consists of the integrated pressure and shear forces acting on the model surface, and hence is the aerodynamic near-field force as defined in Chapter 5. This force is reported as components along the sensor's *sensing axes*.

For a sensor which is solidly attached to the model and moves with it, it is most convenient to define the model's xyz geometry axes to lie along the sensor axes, so that the load sensor directly reports F_x, F_y, F_z, as shown in Figure 10.1. These forces must then be projected onto the freestream axes to give the lift L and drag D, by using the overall model angle of attack α and the stability-axis matrix relation (6.5), restated as follows.

$$
\begin{aligned}
D &= F_x \cos \alpha + F_z \sin \alpha \\
Y &= F_y \\
L &= F_z \cos \alpha - F_x \sin \alpha
\end{aligned}
\tag{10.1}
$$

If the model is also at a sideslip angle then the wind-axis matrix relation (6.6) would be used instead. This more general case will not be considered here.
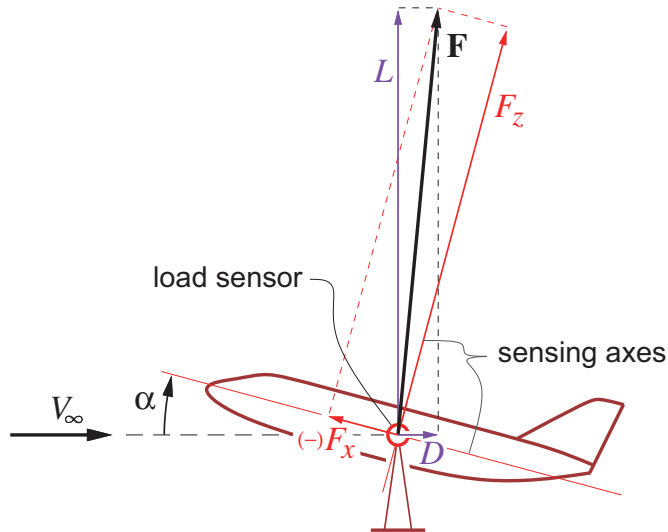
Figure 10.1: Axial and normal force components F_x, F_z along load sensor axes resolved into drag and lift components D, L along and normal to the freestream. Axial force F_x is defined positive towards the tail, opposite to direction shown.

In some wind tunnel installations the load sensor is fixed relative to the wind tunnel rather than the model, and the model then pivots on the sensor to change the angle of attack. Ideally this type of sensor is fixed with its axes aligned with the freestream so that it directly reports the D, Y, L force components, and the rotation calculations (10.1) are then skipped.

10.2.2 Drag measurement error sensitivity

The measurement of aerodynamic forces by a load sensor generally gives accurate lift and sideforce components. However, if the lift and sideforce are very large compared to the drag, as is typical for most aircraft, then measuring the drag accurately is much more difficult. A major potential source of error is misalignment of the sensor relative to its assumed orientation. This is sketched in Figure 10.2, for the case $\alpha = 0$ for simplicity. If there is a small alignment error angle θ_{err}, as in Figure 10.2 on the right, the sensor will report the following incorrect forces $L_{\mathrm{err}}, D_{\mathrm{err}}$, and corresponding fractional drag error.

$$
L_{\mathrm{err}} = L \cos \theta_{\mathrm{err}} - D \sin \theta_{\mathrm{err}} \simeq L
\tag{10.2}
$$

$$
D_{\mathrm{err}} = D \cos \theta_{\mathrm{err}} + L \sin \theta_{\mathrm{err}} \simeq D + L\,\theta_{\mathrm{err}}
\tag{10.3}
$$

$$
\frac{D_{\mathrm{err}} - D}{D} = \frac{L}{D}\,\theta_{\mathrm{err}}
\tag{10.4}
$$

Perfect sensor alignment **Sensor slightly misaligned with freestream**
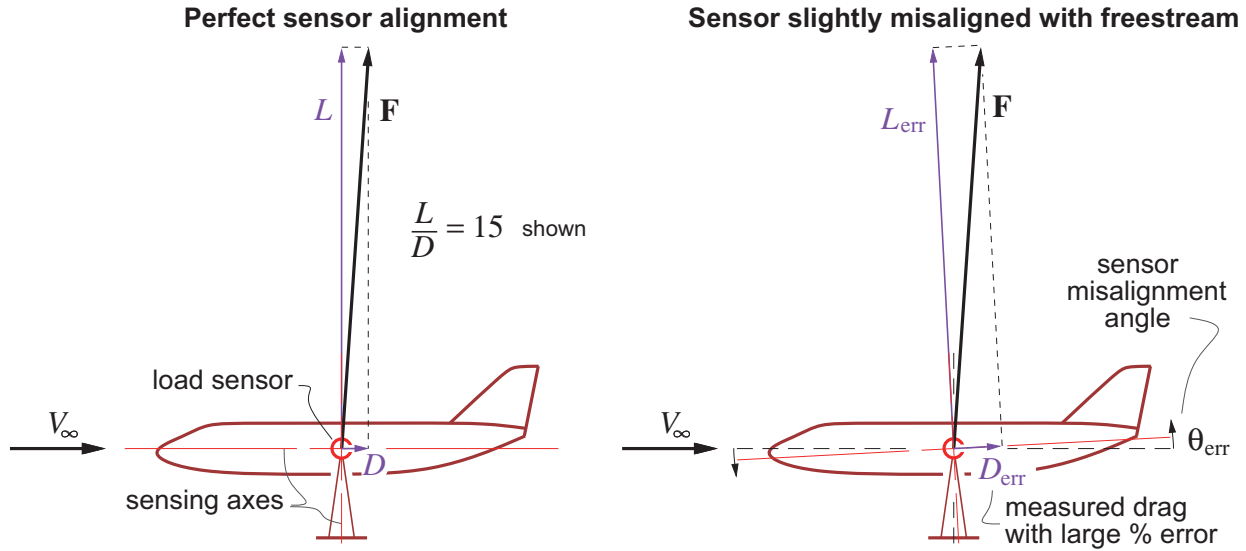
Figure 10.2: Ideal situation for measuring aerodynamic forces with a load sensor (left). In the presence of lift, a small misalignment of sensing axes from freestream direction results in a large fractional error in the measured drag (right).

In the usual situation which has $L \gg D$, the $D \sin\theta_{\mathrm{err}}$ lift term is negligible so the effect of θ_{err} on the measured lift is very small. But the $L \sin\theta_{\mathrm{err}}$ drag term is very significant and can cause large fractional measured drag errors. For example, for the case sketched in Figure 10.2 which has $L/D = 15$, an axis misalignment of $\theta_{\mathrm{err}} = 1° = 0.01745\,\mathrm{rad}$ will produce a very large 26% error in the measured drag.

The angle error can be due to either an incorrect alignment of the sensor with the model, or an incorrect measurement of the angle of attack, or possibly due to the actual tunnel freestream flow direction being misaligned with the assumed direction. Obtaining small drag measurement errors for a lifting model therefore as a minimum requires very precise geometric and aerodynamic angle measurements.

For the remainder of this chapter we will assume that sufficient care has been used with the angle measurements and load sensor alignment so that the true force and moment components on the model are correctly measured. We will also assume that the tunnel freestream dynamic pressure q_∞ corresponding to V_∞ is correctly measured, sufficiently far from the model to avoid any influence from the model's near-field flow.

10.2.3 Uncorrected coefficients

Even with perfect measurement accuracy, measured loads which are intended to represent unbounded flow are still considered to be *uncorrected* for wind tunnel wall or jet boundary effects, and are denoted by the $(\ )_{\mathrm{u}}$ subscript. However, they can still be non-dimensionalized by the freestream dynamic pressure and the chosen geometric reference quantities into their corresponding coefficients. Corrections for both 2D and 3D coefficients will be derived, but for brevity only the lift, drag, and pitching moment will be presented.

$$c_{\ell\mathrm{u}} \equiv \frac{L'_{\mathrm{u}}}{q_\infty c_{\mathrm{ref}}} \quad , \quad c_{d\mathrm{u}} \equiv \frac{D'_{\mathrm{u}}}{q_\infty c_{\mathrm{ref}}} \quad , \quad c_{m\mathrm{u}} \equiv \frac{\mathcal{M}'_{\mathrm{u}}}{q_\infty c_{\mathrm{ref}}^2} \tag{10.5}$$

$$C_{L\mathrm{u}} \equiv \frac{L_{\mathrm{u}}}{q_\infty S_{\mathrm{ref}}} \quad , \quad C_{D\mathrm{u}} \equiv \frac{D_{\mathrm{u}}}{q_\infty S_{\mathrm{ref}}} \quad , \quad C_{m\mathrm{u}} \equiv \frac{\mathcal{M}_{\mathrm{u}}}{q_\infty S_{\mathrm{ref}} c_{\mathrm{ref}}} \tag{10.6}$$

The uncorrected angle of attack α_{u} is the geometric model angle, and the uncorrected Reynolds number is $Re_{\mathrm{u}} = V_\infty c_{\mathrm{ref}}/\nu$. The subsequent sections will address the problem of how to use this uncorrected data to obtain the *corrected* coefficients which <u>would</u> be obtained from the model if it was operated in an unbounded flow at the corrected angle of attack and corrected Reynolds number.

10.3   Wind Tunnel Corrections

The topic of wind tunnel corrections is a fairly large field, which started with the work of Glauert [68]. Later work by Allen and Vincenti [69] considered compressible flows, and many other refinements have been developed since. The objective here is to formulate the wind tunnel corrections using the flow-field modeling concepts and far-field models developed in Chapter 2. This will further illustrate the effectiveness of these concepts, and will also provide readily accessible means for computing the corrections in applications.

The approach here follows the classical method of images to represent the influence of the walls or jet boundaries in the wind tunnel. After the image strengths are set by the wall or jet boundary conditions, they are then used to give velocity perturbations $\Delta u(x)$ and $\Delta w(x)$ along the tunnel axis. These velocity perturbations in turn produce changes in the model's flow-field and forces, which will be estimated using the various aerodynamics models and methods developed throughout this book. Removal of these predicted changes from the measured data and estimating their effects on the flow conditions constitutes wind tunnel corrections.

To allow focusing on the concepts rather than the details, the tunnel correction formulation and procedure will first be given for the 2D case, for both solid-wall and open-jet tunnels. The 3D solid-wall and open-jet tunnel cases will then be examined.

10.3.1   2D solid-wall boundaries

A solid-wall wind tunnel has the flow-tangency condition $w = 0$ everywhere on its top and bottom walls. This flow can be constructed by adding a cascade of +/- images to the real body's source and vortex sheets, as shown in Figure 10.3. The source sheets of the images have the same sign as the sheets representing the real model, while the vortex sheets of the images alternate in sign. In this superposition, $\mathbf{V}_\infty$ is the velocity in the tunnel with the model (and hence the images) absent, consistent with the previous definition.
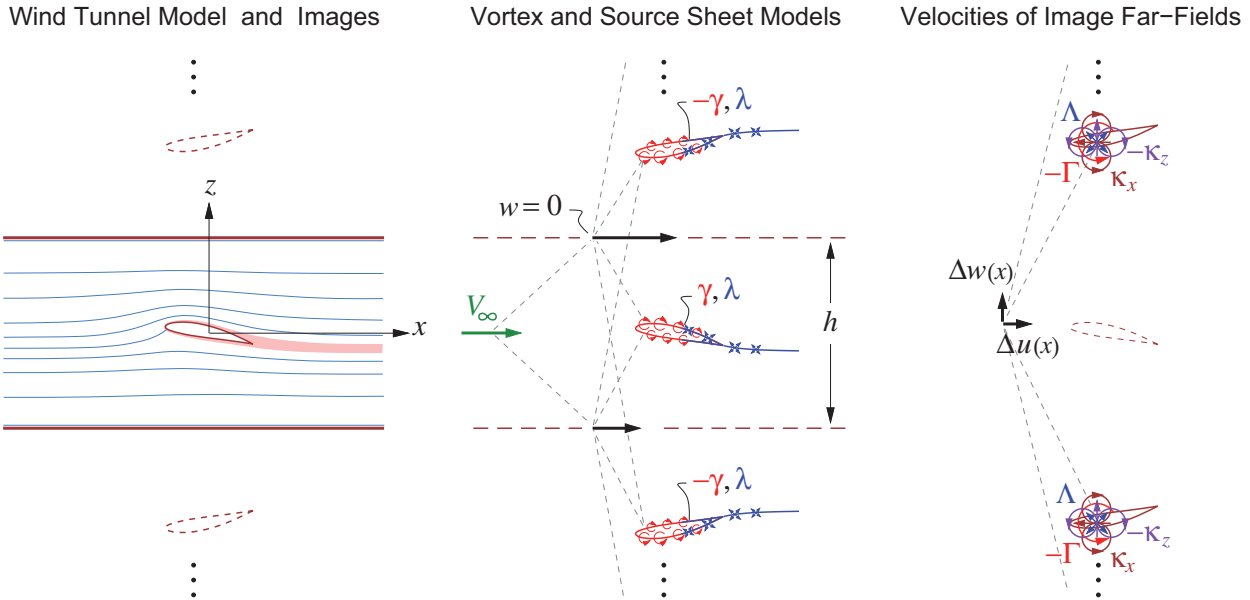
Figure 10.3: 2D airfoil model in tunnel (left) is modeled as an infinite cascade of +/- vortex-sheet and source-sheet images which give physically-correct straight streamlines at the wall locations (center). These images have equivalent lumped 2D point singularities (right). Images produce velocity changes $\Delta u(x), \Delta w(x)$ along the centerline which would be absent in unbounded flow.

Next, we sum the horizontal and vertical velocity contributions $\Delta u(x), \Delta w(x)$ of the images alone, at

some location x along the tunnel centerline. The far-field model (2.79) is used for each image, so that these velocities can be expressed in terms of independent unit-strength components (or kernel functions) $\hat{u}_\Lambda, \hat{u}_{\kappa_x}, \hat{w}_\Gamma, \hat{w}_{\kappa_z}$ which are summations over all the images' far-field sources, vortices, and doublets. The normalized tunnel coordinates X, Y, Z will be convenient here.

$$\Delta u_{(x)} \;=\; \frac{\Lambda}{h}\,\hat{u}_\Lambda \;+\; \frac{\kappa_x}{h^2}\,\hat{u}_{\kappa_x} \tag{10.7}$$

$$\Delta w_{(x)} \;=\; \frac{\Gamma}{h}\,\hat{w}_\Gamma \;+\; \frac{\kappa_z}{h^2}\,\hat{w}_{\kappa_z} \tag{10.8}$$

$$\hat{u}_\Lambda{(x)} \;=\; \frac{1}{\pi}\left[\frac{X}{1+X^2} + \frac{X}{4+X^2} + \frac{X}{9+X^2} + \dots\right] + \frac{1}{2} \qquad \text{(2D solid walls)} \tag{10.9}$$

$$\hat{w}_\Gamma{(x)} \;=\; \frac{1}{\pi}\left[\frac{X}{1+X^2} - \frac{X}{4+X^2} + \frac{X}{9+X^2} - \dots\right] \qquad \text{(2D solid walls)} \tag{10.10}$$

$$\hat{u}_{\kappa_x}{(x)} \;=\; \frac{1}{\pi}\left[\frac{1-X^2}{(1+X^2)^2} + \frac{4-X^2}{(4+X^2)^2} + \frac{9-X^2}{(9+X^2)^2} + \dots\right] \qquad \text{(2D solid walls)} \tag{10.11}$$

$$\hat{w}_{\kappa_z}{(x)} \;=\; \frac{1}{\pi}\left[\frac{1-X^2}{(1+X^2)^2} - \frac{4-X^2}{(4+X^2)^2} + \frac{9-X^2}{(9+X^2)^2} - \dots\right] \qquad \text{(2D solid walls)} \tag{10.12}$$

$$X \equiv \frac{x}{h} \quad , \qquad Y \equiv \frac{y}{h} \quad , \qquad Z \equiv \frac{z}{h} \tag{10.13}$$

Each term in the brackets is the contribution of one image pair above and below the tunnel. The added $1/2$ term in (10.9) is needed to obtain $\Delta u = 0$ for large negative X at the tunnel inflow. The additional useful relations

$$\frac{\mathrm{d}\hat{u}_\Lambda}{\mathrm{d}X} \;=\; \hat{u}_{\kappa_x} \quad , \qquad \frac{\mathrm{d}\hat{w}_\Gamma}{\mathrm{d}X} \;=\; \hat{w}_{\kappa_z} \tag{10.14}$$

will also be used to formulate pressure-gradient and flow-curvature corrections.

For any X value the summations can be performed numerically with as many terms as needed to obtain the asymptotic result to a sufficient tolerance. However, at the model location $X = 0$, the sums have the following known analytic results.

$$\hat{u}_\Lambda(0) \;=\; \frac{1}{2} \;, \quad \hat{w}_\Gamma(0) \;=\; 0 \;, \quad \hat{u}_{\kappa_x}(0) \;=\; \frac{\pi}{6} \;, \quad \hat{w}_{\kappa_z}(0) \;=\; \frac{\pi}{12} \qquad \text{(2D solid walls)} \tag{10.15}$$

The $\Delta u, \Delta w$ superpositions defined by equations (10.7)–(10.12) correspond to z locations midway between the top and bottom walls, which is where the model is assumed to be positioned. Away from the centerline Δu would also have terms with Γ and κ_z contributions, and Δw would have terms with Λ and κ_x contributions. To get some insight into the nature of wind tunnel wall effects, the complete 2D superpositions were used to compute streamline patterns of the "effective freestream" velocity field

$$\mathbf{V}_{\text{eff}}{(x,z)} \;=\; \mathbf{V}_\infty \;+\; \Delta u_{(x,z)}\,\hat{\mathbf{x}} \;+\; \Delta w_{(x,z)}\,\hat{\mathbf{z}} \tag{10.16}$$

for a number of basic wind tunnel models having only one far-field component present. The resulting streamline patterns are shown in Figures 10.4 and 10.5, one component at a time. Four basic effects can be identified. These are discussed and quantified next.

Volume and wake blockage

The model volume, or cross-sectional area A in 2D, produces a local constriction of the $\mathbf{V}_{\text{eff}}$ streamlines via the image doublets κ_x. The model's drag and associated wake displacement thickness δ_∞^* produces a further constriction via the image sources Λ. Both velocity perturbations are shown in Figure 10.6. Note that the

$$\frac{\kappa_x}{Vh^2} = 0.2$$

Speed increase from volume blockage

$$\Delta u > 0$$

$$\frac{\Lambda}{Vh} = 0.25$$

Pressure gradient from wake blockage

$$\frac{\mathrm{d}\Delta u}{\mathrm{d}x} > 0$$
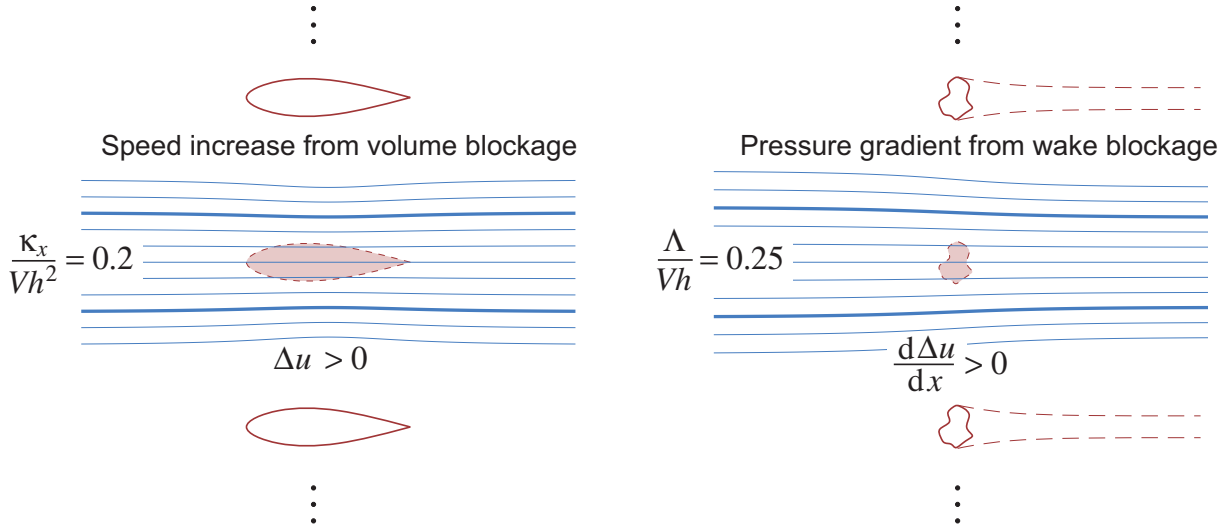
Figure 10.4: Streamlines of the effective freestream $\mathbf{V}_{\mathrm{eff}}(x,z)$ resulting from model images required to model effects of solid tunnel walls. Shown are models with only volume (left) and only profile drag (right). Images have a positive Δu and $\mathrm{d}\Delta u/\mathrm{d}x$ along the tunnel centerline at the real model location.

Flow curvature from lift

$$\frac{\Gamma}{Vh} = 0.5$$

$$\frac{\mathrm{d}\Delta w}{\mathrm{d}x} > 0$$

Flow angle from pitching moment

$$\frac{\kappa_z}{Vh^2} = 0.125$$

$$\Delta w > 0$$
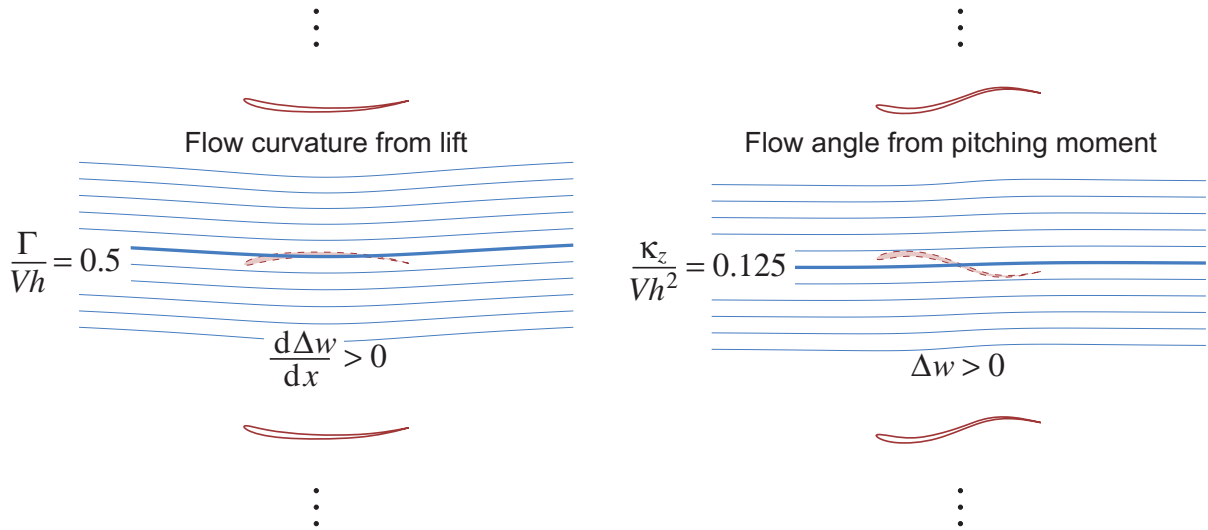
Figure 10.5: Streamlines of the effective freestream $\mathbf{V}_{\mathrm{eff}}(x,z)$ resulting from model images required to model effects of solid tunnel walls. Shown are models with only lift (left) and only pitching moment (right). Images have a positive $\mathrm{d}\Delta w/\mathrm{d}x$ and Δw along the tunnel centerline at the real model location.

doublet effect is local while the source effect persists downstream. At the model at $x=0$, these perturbations due to the volume and the wake displacement produce an increase ΔV in the effective freestream speed, known as the *blockage effect*. To first order this depends only on the streamwise velocity perturbation Δu.

$$V_{\mathrm{eff}} = V_\infty + \Delta V \tag{10.17}$$

$$\frac{\Delta V}{V_\infty} = \frac{\Delta u(0)}{V_\infty} = \frac{1}{2}\frac{\Lambda}{V_\infty h} + \frac{\pi}{6}\frac{\kappa_x}{V_\infty h^2} = \frac{1}{4}\frac{c}{h}c_d + \frac{\pi}{6}\frac{A}{h^2} \qquad \text{(2D solid walls)} \tag{10.18}$$

The far-field source and doublet relations (2.85) and (2.89) have been used to write Λ and κ_x in terms of the model's drag coefficient c_d and cross-sectional area A, with the assumption $V_{\mathrm{eff}} \simeq V_\infty$. This is justified
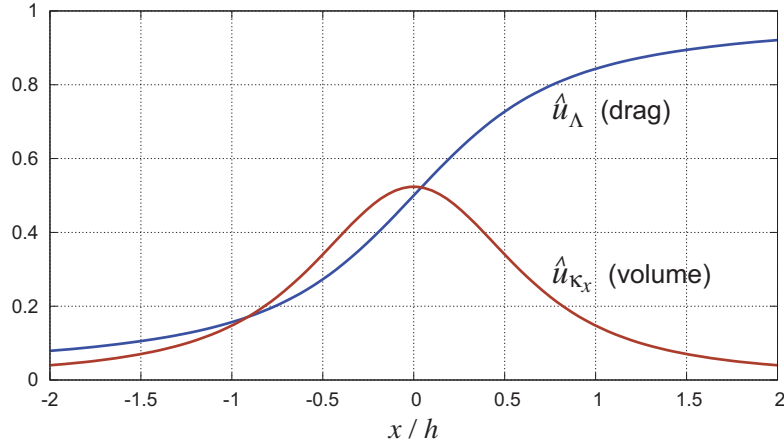
Figure 10.6: Streamwise velocity disturbances along the tunnel centerline due to solid walls, for unit-strength far-field doublet (from model volume) and far-field source (from model drag).

because $\Delta V/V_\infty$ is a small quantity, so this will incur only a second-order error which is negligible.

The small increase in the effective freestream speed also produces the following increased effective freestream dynamic pressure at the model location.

$$q_{\text{eff}} \;\equiv\; \frac{1}{2}\rho V_{\text{eff}}^2 \;=\; q_\infty\left(1+\frac{\Delta V}{V_\infty}\right)^2 \;\simeq\; q_\infty\left(1+2\frac{\Delta V}{V_\infty}\right) \;=\; q_\infty\left(1+\frac{1}{2}\frac{c}{h}c_d+\frac{\pi}{3}\frac{A}{h^2}\right) \quad (10.19)$$

It will also be useful to approximate the inverse dynamic pressure ratio

$$\frac{q_\infty}{q_{\text{eff}}} \;=\; \left(1+\frac{1}{2}\frac{c}{h}c_d+\frac{\pi}{3}\frac{A}{h^2}\right)^{-1} \;\simeq\; 1-\frac{1}{2}\frac{c}{h}c_d-\frac{\pi}{3}\frac{A}{h^2} \qquad \text{(2D solid walls)} \quad (10.20)$$

which assumes that the two correction factors are much less than unity.

Wake-induced buoyancy

An additional effect of the wake displacement is that it produces an acceleration of the effective freestream at the model location $x=0$, as can be seen from the $\hat{u}_\Lambda(x)$ curve in Figure 10.6.

$$\frac{\mathrm{d}V_{\text{eff}}}{\mathrm{d}x} \;=\; \frac{\mathrm{d}\Delta V}{\mathrm{d}x} \;=\; \frac{\mathrm{d}\Delta u}{\mathrm{d}x}(0) \;=\; \frac{\Lambda}{h^2}\frac{\mathrm{d}\hat{u}_\Lambda}{\mathrm{d}X}(0) \;=\; \frac{\pi}{6}\frac{\Lambda}{h^2} \;=\; \frac{\pi}{12}\frac{V_\infty\,c}{h^2}c_d \qquad (10.21)$$

The result is a streamwise pressure gradient

$$\frac{\mathrm{d}p_{\text{eff}}}{\mathrm{d}x} \;=\; -\rho V_\infty\frac{\mathrm{d}V_{\text{eff}}}{\mathrm{d}x} \;=\; -\frac{\pi}{12}\frac{\rho V_\infty^2\,c}{h^2}c_d \qquad (10.22)$$

which then acts on the airfoil's cross-sectional area to produce an added *buoyancy drag* which will need to be subtracted from the uncorrected drag.

$$\Delta D'_{\text{buoy}} \;=\; -\frac{\mathrm{d}p_{\text{eff}}}{\mathrm{d}x}A \;=\; \frac{\pi}{12}\rho V_\infty^2\,c\,c_d\frac{A}{h^2} \qquad (10.23)$$

$$\Delta c_{d_{\text{buoy}}} \;=\; \frac{D'_{\text{buoy}}}{\frac{1}{2}\rho V_\infty^2\,c} \;=\; \frac{\pi}{6}\frac{A}{h^2}c_d \qquad \text{(2D solid walls)} \quad (10.24)$$

Streamline curvature

The model lift and associated image circulations produce a local flow curvature χ via the streamwise derivative $\mathrm{d}\Delta w/\mathrm{d}x$,

$$\chi \;=\; \frac{1}{V_\infty}\frac{\mathrm{d}\Delta w}{\mathrm{d}x}(0) \;=\; \frac{\Gamma}{V_\infty h^2}\frac{\mathrm{d}\hat{w}_\Gamma}{\mathrm{d}X}(0) \;=\; \frac{\pi}{12}\frac{\Gamma}{V_\infty h^2} \;=\; \frac{\pi}{24}\frac{c}{h^2}\,c_{\ell\mathrm{u}} \tag{10.25}$$

where the far-field vortex relation (2.84) has been used. Again, the assumption $V_{\mathrm{eff}} \simeq V_\infty$ is made here.

This flow curvature effectively adds to the airfoil's real curvature and thus changes its lift and pitching moment. The effects can be estimated by first-order thin airfoil theory as given in Appendix D, by specifying a parabolic camberline with the specified curvature. This produces the following change in the lift and moment coefficients which will need to be subtracted from the uncorrected values.

$$\Delta c_{\ell\mathrm{curv}} \;=\; \frac{\pi}{2}\chi\,c \;=\; \frac{\pi^2}{48}\frac{c^2}{h^2}\,c_{\ell\mathrm{u}} \qquad \text{(2D solid walls)} \tag{10.26}$$

$$\Delta c_{m\mathrm{curv}} \;=\; -\frac{\pi}{8}\chi\,c \;=\; -\frac{\pi^2}{192}\frac{c^2}{h^2}\,c_{\ell\mathrm{u}} \qquad \text{(2D solid walls)} \tag{10.27}$$
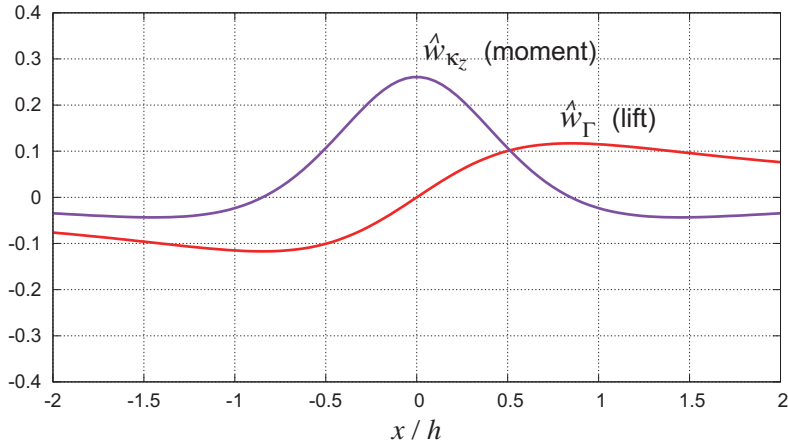
Figure 10.7: Vertical velocity disturbances along the tunnel centerline due to solid walls, for unit-strength far-field vortex (from model lift) and far-field z-doublet (from model pitching moment).

Flow angle

The far-field z-doublet is given by the pitching moment about the far-field singularity location, which is somewhat arbitrary. However, the most rational choice is to choose this location at the lift centroid, which is also the vorticity centroid. In that case the pitching moment about this location and the z-doublet are both zero, so no lift correction needs to be applied for the $\hat{w}_{\kappa_z}$ perturbation velocity component.

$$\Delta c_{d_{\mathrm{angle}}} \;=\; 0 \tag{10.28}$$

However, the flow angle perturbation represents a direct correction to the experimental angle of attack.

$$\Delta\alpha_{\mathrm{angle}} \;=\; \frac{\Delta w(0)}{V_\infty} \;=\; \frac{\kappa_z}{V_\infty h^2}\,\hat{w}_{\kappa_z}(0) \;=\; \frac{\pi}{3}\frac{c^2}{h^2}\,(c_{m\mathrm{u}})_{c/2}$$

$$\;=\; \frac{\pi}{3}\frac{c^2}{h^2}\left(c_{m\mathrm{u}} + \frac{1}{4}\,c_{\ell\mathrm{u}}\right) \qquad \text{(2D solid walls)} \tag{10.29}$$

The midchord pitching moment coefficient $(c_{m\mathrm{u}})_{c/2}$ was used to define the far-field z–doublet, since that's where the far-field vortex was assumed to be placed for the flow-curvature corrections above.

Application of 2D wall corrections

We now assume that all the velocity perturbations from the images are small, so that the resulting force perturbation from each velocity perturbation can be subtracted linearly from the uncorrected coefficients. The dynamic pressure scaling is then applied to produce the final corrected coefficients.

$$c_d = \frac{q_\infty}{q_{\text{eff}}} \left(c_{d_\text{u}} - \Delta c_{d_\text{buoy}} - \Delta c_{d_\text{angle}} \right) \tag{10.30}$$

$$c_\ell = \frac{q_\infty}{q_{\text{eff}}} \left(c_{\ell_\text{u}} - \Delta c_{\ell_\text{curv}} \right) \tag{10.31}$$

$$c_m = \frac{q_\infty}{q_{\text{eff}}} \left(c_{m_\text{u}} - \Delta c_{m_\text{curv}} \right) \tag{10.32}$$

The angle of attack and Reynolds number which the model effectively sees are also obtained by correcting for the perturbed flow angle and flow speed.

$$\alpha = \alpha_\text{u} + \Delta\alpha_\text{angle} \tag{10.33}$$

$$Re = \frac{V_{\text{eff}}}{V_\infty} Re_\text{u} \tag{10.34}$$

Substituting the various changes into the correction relations derived from the solid-wall image models and dropping the higher-order terms, gives the corrected coefficients in terms of the uncorrected values.

$$c_d = \left(1 - \frac{1}{2}\frac{c}{h} c_d - \frac{\pi}{2}\frac{A}{h^2} \right) c_{d_\text{u}} \tag{10.35}$$

$$c_\ell = \left(1 - \frac{1}{2}\frac{c}{h} c_d - \frac{\pi}{3}\frac{A}{h^2} - \frac{\pi^2}{48}\frac{c^2}{h^2} \right) c_{\ell_\text{u}} \tag{10.36}$$

$$c_m = \left(1 - \frac{1}{2}\frac{c}{h} c_d - \frac{\pi}{3}\frac{A}{h^2} \right) c_{m_\text{u}} + \frac{\pi^2}{192}\frac{c^2}{h^2} c_{\ell_\text{u}} \tag{10.37}$$

$$\alpha = \alpha_\text{u} + \frac{\pi}{24}\frac{c^2}{h^2} \left(c_{m_\text{u}} + \frac{1}{4} c_{\ell_\text{u}} \right) \tag{10.38}$$

$$Re = \left(1 + \frac{1}{4}\frac{c}{h} c_d + \frac{\pi}{6}\frac{A}{h^2} \right) Re_\text{u} \tag{10.39}$$

Equation (10.35) can be solved for c_d explicitly, or on the righthand side $c_d \simeq c_{d_\text{u}}$ can be assumed in the usual case where that term is very small.

10.3.2 2D open-jet boundaries

The 2D open-jet wind tunnel considered here still has solid sidewalls which are spanned by the model, these being necessary to obtain 2D flow. However, the top and bottom flow boundaries are free streamlines at a constant ambient pressure p_∞, which will make the overall flow-field different from what it would be in an unbounded flow. Images can again be used to model this effect, as shown in Figure 10.8, but the image signs are different from the solid-wall case. Specifically, the image vortex sheets all have the same sign as those representing the real airfoil, while the source sheets alternate in sign. This gives zero x-velocity perturbations at the jet boundary, and thus to first order makes this boundary a constant-pressure surface.

For concise results we again use the far-field of each image to compute the overall velocity contributions $\Delta u(x)$, $\Delta w(x)$ along the jet centerline, so they can be given by expressions (10.7) and (10.8) which have source, vortex, and doublet components. The kernel functions of these components are now different from

Wind Tunnel Model and Images   Vortex and Source Sheet Models   Velocities of Image Far−Fields
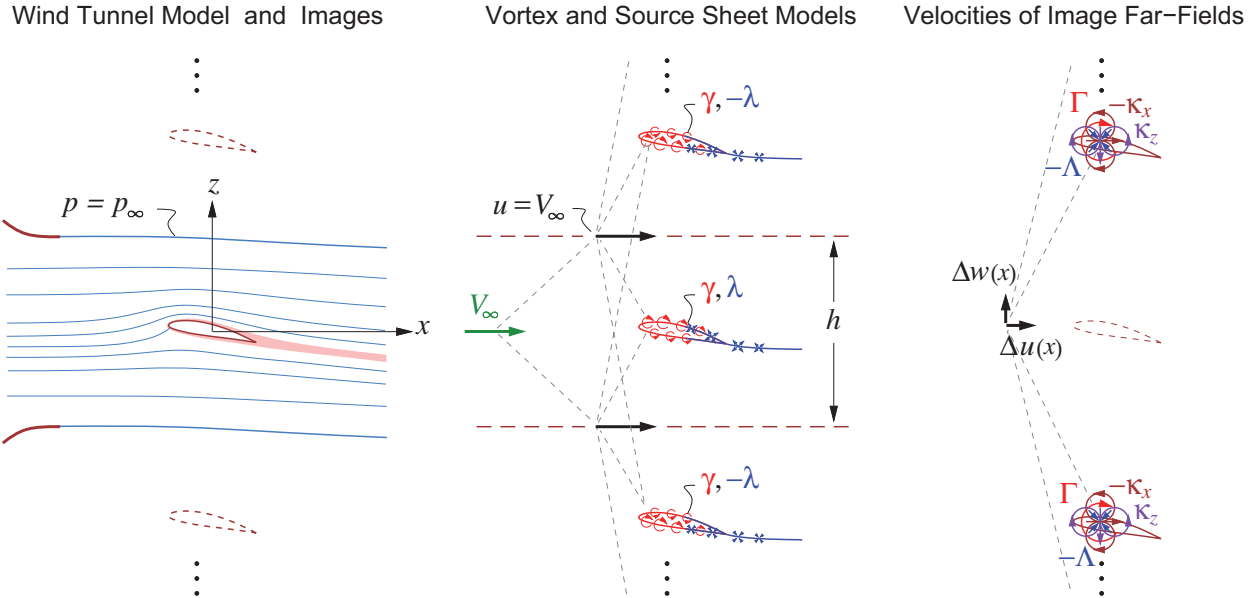
Figure 10.8: 2D airfoil in open-jet tunnel (left) is modeled as an infinite cascade of -/+ images which ensure zero streamwise velocity perturbation and hence constant pressure at the jet boundaries (center). Source, vortex, and doublet far-fields of images produce velocity changes $\Delta u(x), \Delta w(x)$ along the centerline which are absent in unbounded flow (right).

the solid-wall case, and are given as follows.

$$\hat{u}_\Lambda(x) = \frac{1}{\pi}\left[-\frac{X}{1+X^2} + \frac{X}{4+X^2} - \frac{X}{9+X^2} + \cdots\right] \qquad \text{(2D open jet)} \qquad (10.40)$$

$$\hat{w}_\Gamma(x) = \frac{1}{\pi}\left[-\frac{X}{1+X^2} - \frac{X}{4+X^2} - \frac{X}{9+X^2} - \cdots\right] - \frac{1}{2} \qquad \text{(2D open jet)} \qquad (10.41)$$

$$\hat{u}_{\kappa_x}(x) = \frac{1}{\pi}\left[-\frac{1-X^2}{(1+X^2)^2} + \frac{4-X^2}{(4+X^2)^2} - \frac{9-X^2}{(9+X^2)^2} + \cdots\right] \qquad \text{(2D open jet)} \qquad (10.42)$$

$$\hat{w}_{\kappa_z}(x) = \frac{1}{\pi}\left[-\frac{1-X^2}{(1+X^2)^2} - \frac{4-X^2}{(4+X^2)^2} - \frac{9-X^2}{(9+X^2)^2} - \cdots\right] \qquad \text{(2D open jet)} \qquad (10.43)$$

At the model location $X=0$, the sums have the following known analytic results.

$$\hat{u}_\Lambda(0) = 0 \ , \qquad \hat{w}_\Gamma(0) = -\frac{1}{2} \ , \qquad \hat{u}_{\kappa_x}(0) = -\frac{\pi}{12} \ , \qquad \hat{w}_{\kappa_z}(0) = -\frac{\pi}{6} \qquad \text{(2D open jet)} \quad (10.44)$$

Figures 10.9 and 10.10 show the streamline patterns of the resulting $\mathbf{V}_{\text{eff}}(x,z)$ field for each image singularity component. Most of the effects are reversed from the solid-wall case, and the most notable difference is the overall turning of the jet by the model lift.

Volume and wake blockage

In the open-jet wind tunnel, the model's volume (area in 2D) results in the closest images having a negative volume, which produces a local dilation of the $\mathbf{V}_{\text{eff}}$ streamlines. The model's viscous wake displacement results in images with negative displacement, which produces a further spreading. The components of the streamwise velocity perturbation $\Delta u(x)$ along the tunnel axis which are associated with these flow changes are shown in Figure 10.11, which can be compared to Figure 10.6 for the solid-wall case.
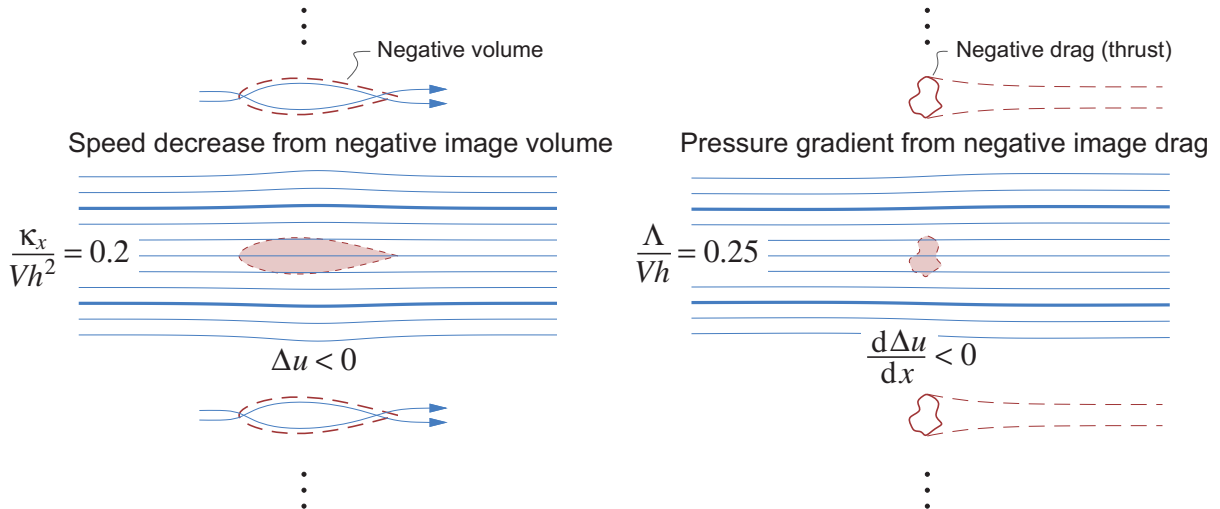
Figure 10.9: Streamlines of the effective freestream $\mathbf{V}_{\text{eff}}(x,z)$ resulting from model images required to model effects of open-jet boundaries. Shown are models with only volume (left) and only profile drag (right). Images have a negative Δu and $\mathrm{d}\Delta u/\mathrm{d}x$ along the jet centerline at the real model location.
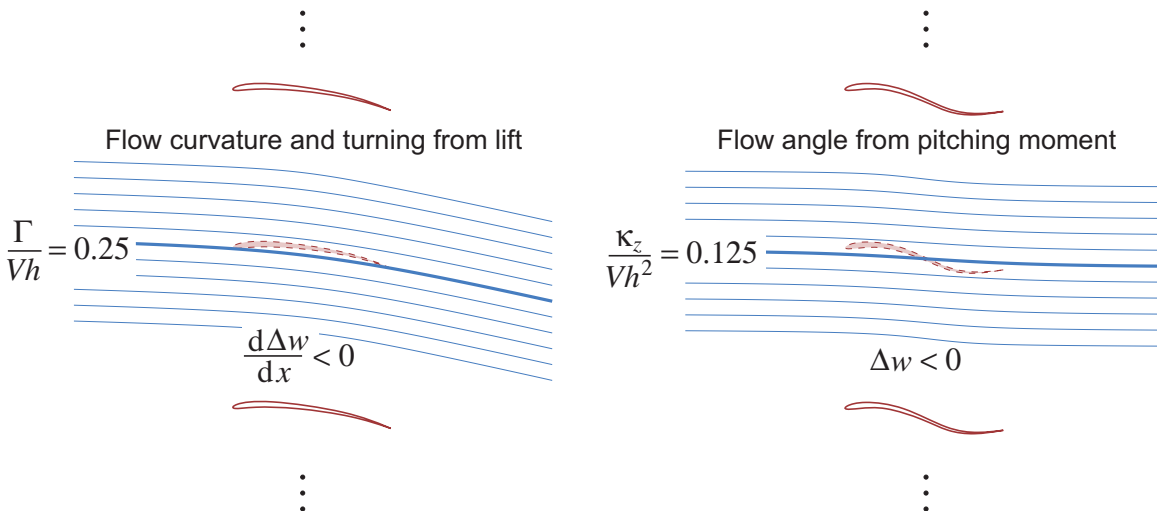
Figure 10.10: Streamlines of the effective freestream $\mathbf{V}_{\text{eff}}(x,z)$ resulting from model images required to model effects of open-jet boundaries. Shown are models with only lift (left) and only pitching moment (right). Images have a negative $\mathrm{d}\Delta w/\mathrm{d}x$ and Δw along the jet centerline at the real model location.

The open-jet boundaries produce a decrease in the velocity and effective dynamic pressure at the model via a negative volume blockage term. Since $\hat{u}_{\Lambda}(0) = 0$, the wake blockage effect is entirely absent here.

$$\frac{\Delta V}{V_{\infty}} = \frac{\Delta u(0)}{V_{\infty}} = -\frac{\pi}{12}\frac{\kappa_x}{V_{\infty}h^2} = -\frac{\pi}{12}\frac{A}{h^2} \qquad \text{(2D open jet)} \qquad (10.45)$$

$$q_{\text{eff}} \simeq q_{\infty}\left(1 + 2\frac{\Delta V}{V_{\infty}}\right) = q_{\infty}\left(1 - \frac{\pi}{6}\frac{A}{h^2}\right) \qquad\qquad (10.46)$$

$$\frac{q_{\infty}}{q_{\text{eff}}} \simeq 1 + \frac{\pi}{6}\frac{A}{h^2} \qquad\qquad \text{(2D open jet)} \qquad (10.47)$$
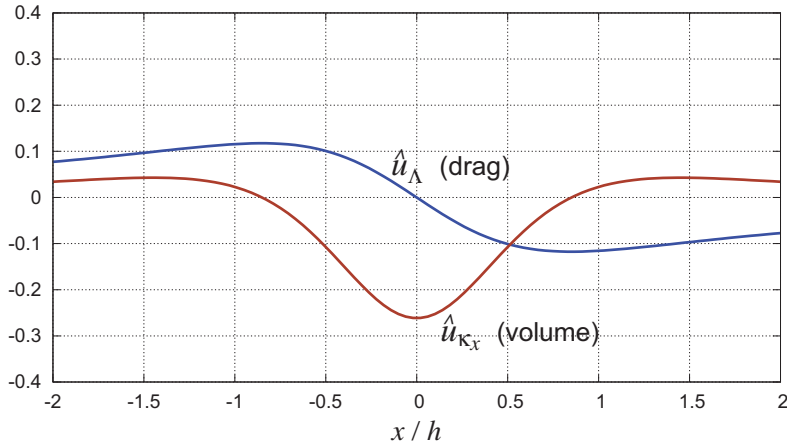
Figure 10.11: Streamwise velocity disturbances along the tunnel jet centerline due to open-jet boundaries, for unit-strength far-field doublet (from model volume) and far-field source (from model drag).

Wake-induced buoyancy

The first images of the model's far-field source are negative, which produces a decelerating effective freestream at the model, as shown in Figure 10.11. Hence the wake-induced buoyancy effect in the open-jet case is opposite in sign and half as large as in the solid-wall case. The resulting buoyancy drag change then also has the opposite sign.

$$\Delta c_{d_{\mathrm{buoy}}} \;=\; -\frac{\pi}{12}\frac{A}{h^2}\,c_d \qquad\qquad \text{(2D open jet)} \qquad (10.48)$$

Streamline curvature

Compared to the solid-wall case, the curvature effect of lift is opposite in sign, and twice in magnitude.

$$\Delta c_{\ell_{\mathrm{curv}}} \;=\; -\frac{\pi^2}{24}\frac{c^2}{h^2}\,c_{\ell\mathrm{u}} \qquad\qquad \text{(2D open jet)} \qquad (10.49)$$

$$\Delta c_{m_{\mathrm{curv}}} \;=\; \frac{\pi^2}{96}\frac{c^2}{h^2}\,c_{\ell\mathrm{u}} \qquad\qquad \text{(2D open jet)} \qquad (10.50)$$

Flow angle

The flow angle change at the model is

$$\Delta\alpha_{\mathrm{angle}} \;=\; \frac{\Delta w(0)}{V_\infty} \;=\; \frac{\Gamma}{V_\infty h}\,\hat{w}_\Gamma(0) \;+\; \frac{\kappa_z}{V_\infty h^2}\,\hat{w}_{\kappa_z}(0)$$

$$\;=\; -\frac{1}{4}\frac{c}{h}\,c_{\ell\mathrm{u}} \;-\; \frac{\pi}{12}\frac{c^2}{h^2}\,(c_{m\mathrm{u}})_{c/2} \qquad \text{(2D open jet)} \qquad (10.51)$$

where the first lift term did not appear in the solid-wall case, but it dominates here. This term will also tilt the lift vector to create an additional drag component along the tunnel freestream direction.

$$\Delta c_{d_{\mathrm{angle}}} \;=\; \frac{1}{4}\frac{c}{h}\,c_{\ell\mathrm{u}}^2 \qquad\qquad \text{(2D open jet)} \qquad (10.52)$$

This added drag scales as c_ℓ^2, and thus behaves much like induced drag. It should also be noted that for reasonable c/h ratios this correction will be very large compared to the final corrected drag coefficient. For this reason, measurement of 2D drag in the presence of lift by direct load sensing is likely to be impractical in an open-jet wind tunnel. An alternative method will be considered in Section 10.4.2.
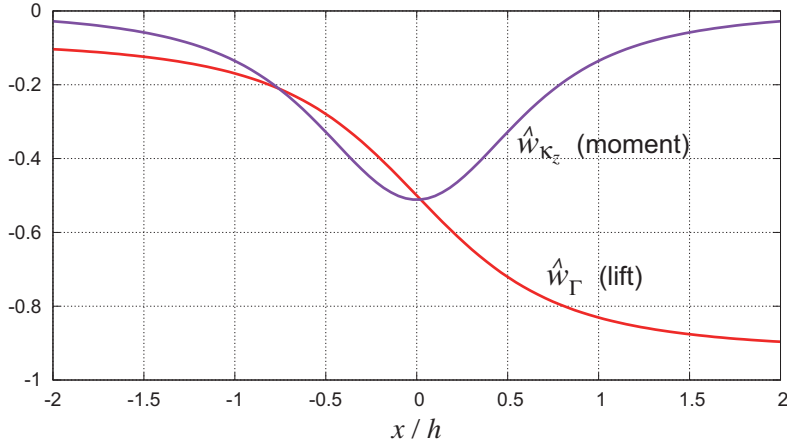
Figure 10.12: Vertical velocity disturbances along the tunnel centerline due to solid walls, for unit-strength far-field vortex (from model lift) and far-field z-doublet (from model pitching moment).

Application of 2D jet corrections

Substituting the changes for the open-jet case into the correction relations (10.30)–(10.32) gives the corrected coefficients and operating parameters in terms of the uncorrected values.

$$c_d = \left(1 + \frac{\pi}{4}\frac{A}{h^2}\right) c_{d\mathrm{u}} - \frac{1}{4}\frac{c}{h} c_{\ell\mathrm{u}}^2 \tag{10.53}$$

$$c_\ell = \left(1 + \frac{\pi}{6}\frac{A}{h^2} + \frac{\pi^2}{24}\frac{c^2}{h^2}\right) c_{\ell\mathrm{u}} \tag{10.54}$$

$$c_m = \left(1 + \frac{\pi}{6}\frac{A}{h^2}\right) c_{m\mathrm{u}} - \frac{\pi^2}{96}\frac{c^2}{h^2} c_{\ell\mathrm{u}} \tag{10.55}$$

$$\alpha = \alpha_{\mathrm{u}} - \frac{\pi}{12}\frac{c^2}{h^2}\left(c_{m\mathrm{u}} + \frac{1}{4} c_{\ell\mathrm{u}}\right) - \frac{1}{4}\frac{c}{h} c_{\ell\mathrm{u}} \tag{10.56}$$

$$Re = \left(1 - \frac{\pi}{12}\frac{A}{h^2}\right) Re_{\mathrm{u}} \tag{10.57}$$

10.3.3 3D tunnel images

Figure 10.13 shows a 3D lifting object in a wind tunnel of dimensions $Bh \times h$ (B is the cross-section's aspect ratio). Its far-field is represented by a 3D x-doublet $\mathcal{K}_x$ which models the volume $\mathcal{V}$, a 3D source Σ which models profile drag D_p. These far-field strengths were derived in Section 2.12:

$$\mathcal{K}_x = V_\infty \mathcal{V} \tag{10.58}$$

$$\Sigma = \frac{D_p}{\rho V_\infty} = \frac{1}{2}V_\infty C_{D_p} S_{\mathrm{ref}} \tag{10.59}$$

In the case of a powered model with engines which produce thrust, D_p would be the <u>net</u> streamwise force on the model excluding induced drag, or "profile drag – thrust." When this is zero, the positive momentum defect of the viscous wakes is canceled by the negative momentum defect of the propulsive jets.

The lifting object trails a vortex wake, which can be lumped into a semi-infinite 2D z-doublet line. Its strength κ_z is obtained from the far-field κ_z definition (2.83), applied to the vortex wake in the Trefftz-Plane yz coordinates by replacing $-\gamma_y x$ with $\gamma_x y$. The Trefftz-Plane vorticity relation (5.37) and final lift

result (5.65) are also used.

$$\kappa_z \;=\; \int \gamma_x\, y \, \mathrm{d}s \;=\; \int -\frac{\mathrm{d}(\Delta\varphi)}{\mathrm{d}s}\, y\, \mathrm{d}s \;=\; \int \Delta\varphi\, \mathrm{d}y \;=\; \frac{L}{\rho V_\infty} \;=\; \frac{1}{2} V_\infty\, C_L\, S_{\mathrm{ref}} \tag{10.60}$$

This doublet-line representation assumes that the model's span is small compared to the tunnel dimensions Bh or h. For larger spans it is more realistic to use a horseshoe vortex to represent the model's far-field [67]. But the model-span/tunnel-height ratio then becomes another parameter to consider, and the tunnel corrections also become more complicated. Since the focus here is illustration of the main tunnel-wall effects, the simpler doublet-line representation of the model and vortex wake will be used.
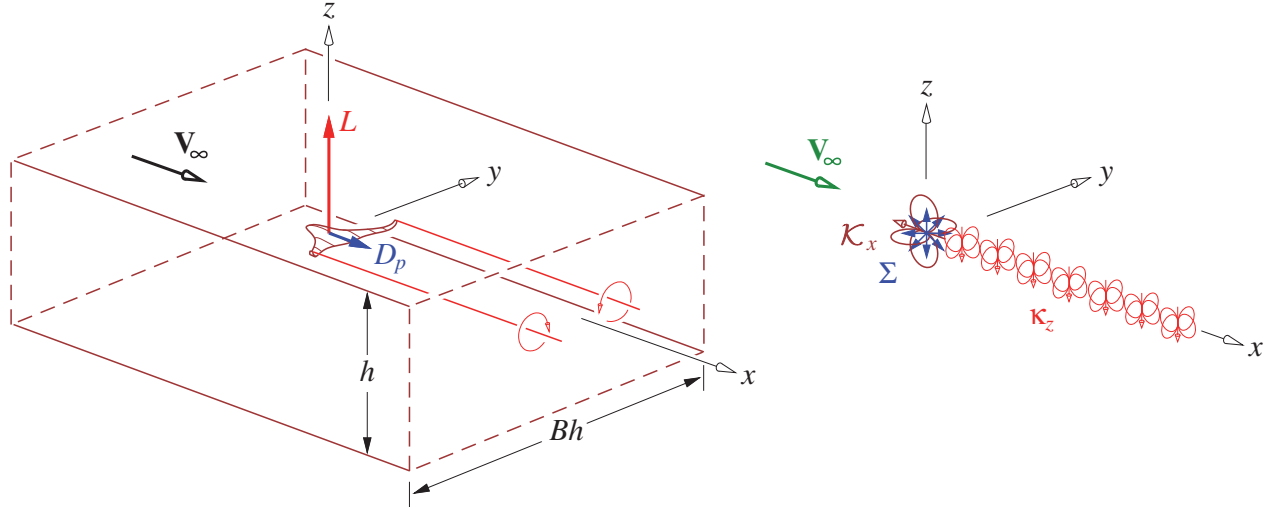
Figure 10.13: 3D lifting object in a wind tunnel of dimensions $Bh \times h$. The far-fields of the object's images are represented by the singularities $\mathcal{K}_x, \Sigma, \kappa_z$, associated by the object's volume, net profile drag, and lift, respectively.

The model's images will produce velocity perturbations along the tunnel axis which in general have the form

$$\Delta u(x\,;B) \;=\; \frac{\Sigma}{h^2}\, \hat{u}_\Sigma \;+\; \frac{\mathcal{K}_x}{h^3}\, \hat{u}_{\mathcal{K}_x} \tag{10.61}$$

$$\Delta w(x\,;B) \;=\; \frac{\kappa_z}{h^2}\, \hat{w}_{\kappa_z} \tag{10.62}$$

$$\frac{\mathrm{d}\Delta u}{\mathrm{d}x}(x\,;B) \;=\; \frac{\Sigma}{h^3}\, \frac{\mathrm{d}\hat{u}_\Sigma}{\mathrm{d}X} \;=\; \frac{\Sigma}{h^3}\, \hat{u}_{\mathcal{K}_x} \tag{10.63}$$

$$\frac{\mathrm{d}\Delta w}{\mathrm{d}x}(x\,;B) \;=\; \frac{\kappa_z}{h^3}\, \frac{\mathrm{d}\hat{w}_{\kappa_z}}{\mathrm{d}X} \tag{10.64}$$

where the unit-strength velocity kernels $\hat{u}_\Sigma, \hat{u}_{\mathcal{K}_x}, \hat{w}_{\kappa_z}$ are the sums over all the images as in the 2D case. The streamwise derivative of Δw is also summed to obtain flow curvature corrections. It's convenient to first define the unit-strength x and z velocities $\hat{U}$ and $\hat{W}$ for each image singularity.

$$\hat{U}_{\Sigma(x,y,z)} \;=\; \frac{1}{4\pi} \frac{X}{[X^2+Y^2+Z^2]^{3/2}} \tag{10.65}$$

$$\hat{U}_{\mathcal{K}_x(x,y,z)} \;=\; \frac{1}{4\pi} \frac{Y^2+Z^2-2X^2}{[X^2+Y^2+Z^2]^{5/2}} \tag{10.66}$$

$$\hat{W}_{\kappa_z(x,y,z)} \;=\; \frac{1}{4\pi} \frac{1}{Y^2+Z^2} \left\{ \frac{Y^2-Z^2}{Y^2+Z^2} \left(\frac{X}{[X^2+Y^2+Z^2]^{1/2}} +1 \right) - \frac{XZ^2}{[X^2+Y^2+Z^2]^{3/2}} \right\} \tag{10.67}$$

$$\frac{\mathrm{d}\hat{W}_{\kappa_z}}{\mathrm{d}X}(x,y,z) \;=\; \frac{1}{4\pi} \frac{1}{Y^2+Z^2} \left\{ \frac{Y^2-Z^2}{[X^2+Y^2+Z^2]^{3/2}} - Z^2 \frac{Y^2+Z^2-2X^2}{[X^2+Y^2+Z^2]^{5/2}} \right\} \tag{10.68}$$

10.3.4   3D solid-wall boundaries

For the tunnel cross-section and model shown in Figure 10.13, the flow tangency requirement on all four solid walls is imposed by the array of images shown in Figure 10.14. As in the 2D case, the images produce axial and vertical velocity perturbations along the tunnel centerline, given by summing over all the images in the yz plane. The j index sums along y, and the k index sums along z.

$$\hat{u}_{\mathcal{K}_x}(x\,;B) \;=\; \sum_{j=-\infty}^{\infty}\sum_{k=-\infty}^{\infty} \hat{U}_{\mathcal{K}_x}(X, jB, k) \qquad \text{(3D solid walls)} \quad (10.69)$$

$$\hat{u}_{\Sigma}(x\,;B) \;=\; \sum_{j=-\infty}^{\infty}\sum_{k=-\infty}^{\infty} \hat{U}_{\Sigma}(X, jB, k) \;+\; \frac{1}{2B} \qquad \text{(3D solid walls)} \quad (10.70)$$

$$\hat{w}_{\kappa_z}(x\,;B) \;=\; \sum_{j=-\infty}^{\infty}\sum_{k=-\infty}^{\infty} (-1)^k\,\hat{W}_{\kappa_z}(X, jB, k) \qquad \text{(3D solid walls)} \quad (10.71)$$

$$\frac{\mathrm{d}\hat{w}_{\kappa_z}}{\mathrm{d}X}(x\,;B) \;=\; \sum_{j=-\infty}^{\infty}\sum_{k=-\infty}^{\infty} (-1)^k\,\frac{\mathrm{d}\hat{W}_{\kappa_z}}{\mathrm{d}X}(X, jB, k) \qquad \text{(3D solid walls)} \quad (10.72)$$

The $j=0, k=0$ self-influence term is omitted from the above double sums. Along the tunnel axis, these velocity perturbations look qualitatively similar to those for the 2D case shown in Figures 10.6 and 10.7. Their values at the $x=0$ model location are plotted versus the section aspect ratio B in Figure 10.15.
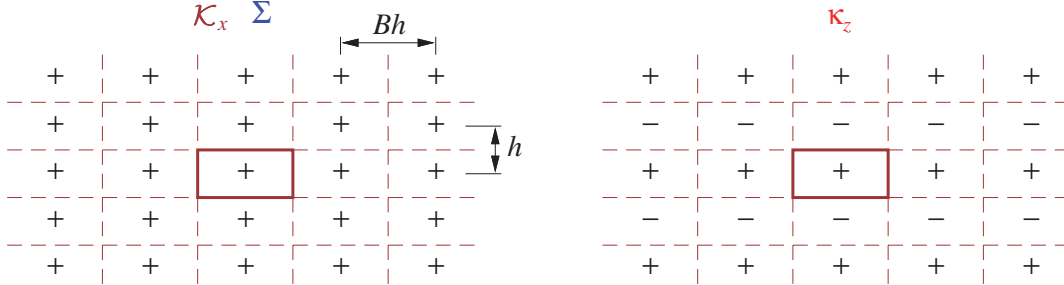
Figure 10.14: Image arrays around a 3D tunnel cross section, needed to produce zero normal velocity at the walls (solid rectangle), Left figure gives signs of the image 3D x-doublet and source strengths. Right figure gives signs of the image 2D z-doublet strengths.
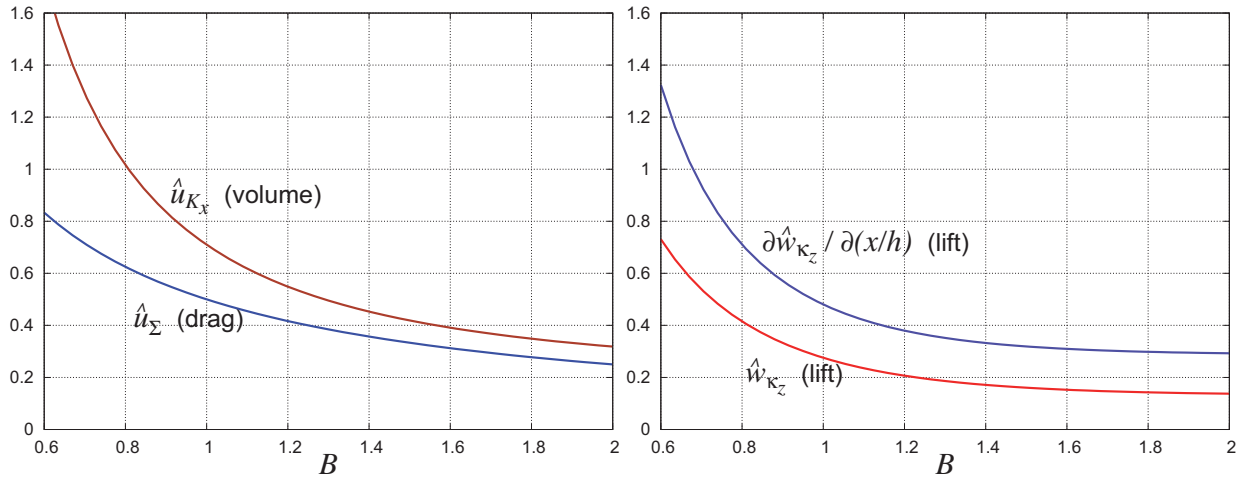
Figure 10.15: 3D velocity disturbances at the model location $x=0$ versus tunnel section aspect ratio, for a solid-wall tunnel.

10.3.5 3D open-jet boundaries

The constant pressure or $\Delta u = 0$ requirement on the open-jet boundary is obtained with the image arrays shown in Figure 10.16. The perturbation velocities are given by the following sums over the images.

$$\hat{u}_{\mathcal{K}_x}(x\,;B) \;=\; \sum_{j=-\infty}^{\infty}\sum_{k=-\infty}^{\infty}(-1)^{(j+k)}\hat{U}_{\mathcal{K}_x}(X, jB, k) \qquad \text{(3D open jet)} \quad (10.73)$$

$$\hat{u}_{\Sigma}(x\,;B) \;=\; \sum_{j=-\infty}^{\infty}\sum_{k=-\infty}^{\infty}(-1)^{(j+k)}\hat{U}_{\Sigma}(X, jB, k) \qquad \text{(3D open jet)} \quad (10.74)$$

$$\hat{w}_{\kappa_z}(x\,;B) \;=\; \sum_{j=-\infty}^{\infty}\sum_{k=-\infty}^{\infty}(-1)^{j}\hat{W}_{\kappa_z}(X, jB, k) \qquad \text{(3D open jet)} \quad (10.75)$$

$$\frac{\mathrm{d}\hat{w}_{\kappa_z}}{\mathrm{d}X}(x\,;B) \;=\; \sum_{j=-\infty}^{\infty}\sum_{k=-\infty}^{\infty}(-1)^{j}\,\frac{\mathrm{d}\hat{W}_{\kappa_z}}{\mathrm{d}X}(X, jB, k) \qquad \text{(3D open jet)} \quad (10.76)$$

Again, the $j = 0, k = 0$ self-influence term is omitted from these double sums. The velocity values at the $x = 0$ model location are plotted versus the section aspect ratio B in Figure 10.17.
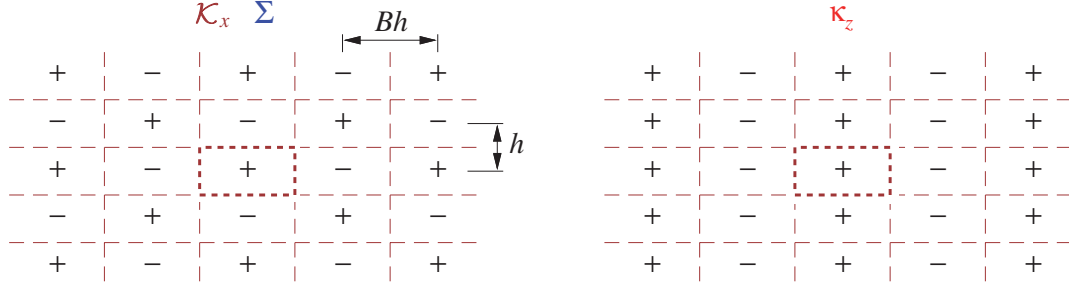
Figure 10.16: Image arrays around a 3D tunnel cross section needed to produce $\Delta u = 0$ at the jet boundary (dotted), thus representing an open jet. Left figure gives signs of the image 3D x-doublet and source strengths. Right figure gives signs of the image 2D z-doublet strengths.
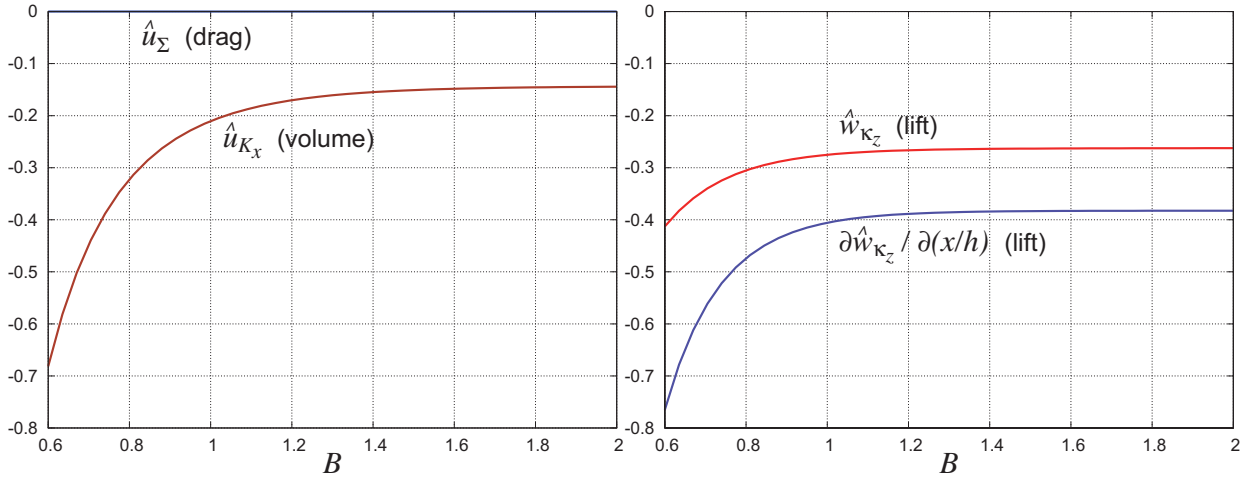
Figure 10.17: 3D velocity disturbances at the model location $x = 0$ versus tunnel section aspect ratio, for an open-jet tunnel.

The 3D image velocities derived above are the starting point for application to actual tunnel corrections as described next. The corrections for solid-wall and open-jet tunnels have the same form, except that the magnitudes and signs are different.

Volume and wake blockage

The blockage effects are essentially the same as in the 2D case, as given by (10.18) and (10.19).

$$\frac{\Delta V}{V_\infty} = \frac{\Delta u(0)}{V_\infty} = \frac{\Sigma}{V_\infty h^2}\,\hat{u}_\Sigma(0) + \frac{\mathcal{K}_x}{V_\infty h^3}\,\hat{u}_{\mathcal{K}_x}(0) = \frac{S_{\text{ref}}}{h^2}\frac{C_{D_p}}{2}\,\hat{u}_\Sigma(0) + \frac{\mathcal{V}}{h^3}\,\hat{u}_{\mathcal{K}_x}(0) \tag{10.77}$$

$$\frac{q_\infty}{q_{\text{eff}}} \simeq 1 - 2\frac{\Delta V}{V_\infty} = 1 - \frac{S_{\text{ref}}}{h^2}C_{D_p}\,\hat{u}_\Sigma(0) - 2\frac{\mathcal{V}}{h^3}\,\hat{u}_{\mathcal{K}_x}(0) \tag{10.78}$$

The 3D far-field models (2.110),(2.113) have been used to express Σ and $\mathcal{K}_x$ in term of the model's profile drag coefficient and volume. The velocity kernel factors $\hat{u}_\Sigma(0)$ and $\hat{u}_{\mathcal{K}_x}(0)$ depend on the tunnel cross-section aspect ratio B, and can be obtained from Figure 10.15 for a solid-wall tunnel, or from Figure 10.17 for an open-jet tunnel.

Wake-induced buoyancy

The streamwise acceleration from the wake displacement is also computed the same way as in 2D.

$$\frac{\mathrm{d}V_{\text{eff}}}{\mathrm{d}x} = \frac{\mathrm{d}\Delta V}{\mathrm{d}x} = \frac{\Lambda}{h^3}\,\hat{u}_{\mathcal{K}_x}(0) = \frac{V_\infty}{h}\frac{S_{\text{ref}}}{h^2}\frac{C_{D_p}}{2}\,\hat{u}_{\mathcal{K}_x}(0) \tag{10.79}$$

The resulting streamwise pressure gradient acts on the body's volume $\mathcal{V}$ to produce an additional buoyancy drag which must be removed from the measured drag.

$$\Delta C_{D_{\text{buoy}}} = \frac{1}{\frac{1}{2}\rho V_\infty^2\,S_{\text{ref}}}\,\rho V_\infty\frac{\mathrm{d}V_{\text{eff}}}{\mathrm{d}x}\,\mathcal{V} = \frac{\mathcal{V}}{h^3}\,C_{D_p}\,\hat{u}_{\mathcal{K}_x}(0) \tag{10.80}$$

Flow angle

The vertical velocity Δw at the model will produce an angle correction as in the 2D case.

$$\Delta\alpha_{\text{angle}} = \frac{\Delta w(0)}{V_\infty} = \frac{\mathcal{K}_z}{V_\infty h^2}\,\hat{w}_{\mathcal{K}_z}(0) = \frac{1}{2}\frac{S_{\text{ref}}}{h^2}C_{Lu}\,\hat{w}_{\mathcal{K}_z}(0) \tag{10.81}$$

This angle will also tilt the lift vector and produce a drag correction which must be removed from the measured drag.

$$\Delta C_{D_{\text{angle}}} = -C_{Lu}\,\Delta_{\text{angle}} = -\frac{1}{2}\frac{S_{\text{ref}}}{h^2}C_{Lu}^2\,\hat{w}_{\mathcal{K}_z}(0) \tag{10.82}$$

This drag correction scales as C_L^2 like induced drag, and is in fact equivalent to "ground effect" for the solid-wall case. For the open-jet case the correction has the opposite sign.

Streamline curvature

The flow curvature is given by the streamwise derivative of Δw as in the 2D case.

$$\chi = \frac{\mathcal{K}_z}{V_\infty h^3}\frac{\mathrm{d}\hat{w}_{\mathcal{K}_z}}{\mathrm{d}X}(0) = \frac{1}{2h}C_{Lu}\frac{S_{\text{ref}}}{h^2}\frac{\mathrm{d}\hat{w}_{\mathcal{K}_z}}{\mathrm{d}X}(0) \tag{10.83}$$

The effect on the lift and moment coefficients depends on the model configuration, since different components will see different flow angles in the presence of the curved flow. However, we note that the flow angle distribution due to the streamline curvature is the same as that generated by an equivalent pitch rate

$q_{\text{curv}} = \mathrm{d}\Delta w/\mathrm{d}x = V_\infty \chi$. Hence, it is reasonable and convenient to quantify the flow curvature effect in terms of the aircraft's pitch-rate stability derivatives C_{L_q}, C_{m_q}, treated in Chapter 6.

$$\Delta C_{L_{\text{curv}}} \;=\; C_{L_q} \frac{\Delta q\, c_{\text{ref}}}{2 V_\infty} \;=\; C_{L_q} \frac{\chi\, c_{\text{ref}}}{2} \;=\; \frac{1}{4} C_{L_u} C_{L_q} \frac{S_{\text{ref}} c_{\text{ref}}}{h^3} \frac{\mathrm{d}\hat{w}_{\kappa_z}}{\mathrm{d}X}(0) \tag{10.84}$$

$$\Delta C_{m_{\text{curv}}} \;=\; C_{m_q} \frac{\Delta q\, c_{\text{ref}}}{2 V_\infty} \;=\; C_{m_q} \frac{\chi\, c_{\text{ref}}}{2} \;=\; \frac{1}{4} C_{L_u} C_{m_q} \frac{S_{\text{ref}} c_{\text{ref}}}{h^3} \frac{\mathrm{d}\hat{w}_{\kappa_z}}{\mathrm{d}X}(0) \tag{10.85}$$

The change in lift coefficient will also produce a change in drag coefficient. Here we will assume that only the induced drag component is affected.

$$\Delta C_{D_{\text{curv}}} \;=\; \frac{\mathrm{d}C_{D_i}}{\mathrm{d}C_L} \Delta C_{L_{\text{curv}}} \;=\; \frac{2 C_{L_u}}{\pi\, A\!R\, e} \Delta C_{L_{\text{curv}}} \tag{10.86}$$

Application of 3D tunnel corrections

The force and moment coefficients are corrected for the tunnel boundary velocity perturbations in the same basic manner as in the 2D case.

$$C_D \;=\; \frac{q_\infty}{q_{\text{eff}}} \left(C_{D_u} - \Delta C_{D_{\text{curv}}} - \Delta C_{D_{\text{buoy}}} - \Delta C_{D_{\text{angle}}} \right) \tag{10.87}$$

$$C_L \;=\; \frac{q_\infty}{q_{\text{eff}}} \left(C_{L_u} - \Delta C_{L_{\text{curv}}} \right) \tag{10.88}$$

$$C_m \;=\; \frac{q_\infty}{q_{\text{eff}}} \left(C_{m_u} - \Delta C_{m_{\text{curv}}} \right) \tag{10.89}$$

The angle of attack and Reynolds number which the model effectively sees are also obtained by correcting for the perturbed flow angle and flow speed.

$$\alpha \;=\; \alpha_u + \Delta\alpha_{\text{angle}} \tag{10.90}$$

$$Re \;=\; \frac{V_{\text{eff}}}{V_\infty} Re_u \tag{10.91}$$

Substituting the various changes into the correction relations derived from the solid-wall image models and dropping the higher-order terms, gives the corrected coefficients in terms of the uncorrected values.

$$C_D \;=\; \left(1 - \frac{S_{\text{ref}}}{h^2} C_{D_p} \hat{u}_\Sigma(0) - 2\frac{\mathcal{V}}{h^3} \hat{u}_{\mathcal{K}_x}(0)\right) C_{D_u} - \frac{1}{2} \frac{S_{\text{ref}} c_{\text{ref}}}{h^3} C_{L_q} \frac{C_{L_u}^2}{\pi A\!R e} \frac{\mathrm{d}\hat{w}_{\kappa_z}}{\mathrm{d}X}(0)$$
$$- \frac{\mathcal{V}}{h^3} C_{D_p} \hat{u}_{\mathcal{K}_x}(0) + \frac{1}{2} \frac{S_{\text{ref}}}{h^2} C_{L_u}^2 \hat{w}_{\kappa_z}(0) \tag{10.92}$$

$$C_L \;=\; \left(1 - \frac{S_{\text{ref}}}{h^2} C_{D_p} \hat{u}_\Sigma(0) - 2\frac{\mathcal{V}}{h^3} \hat{u}_{\mathcal{K}_x}(0)\right) C_{L_u} - \frac{1}{4} \frac{S_{\text{ref}} c_{\text{ref}}}{h^3} C_{L_q} C_{L_u} \frac{\mathrm{d}\hat{w}_{\kappa_z}}{\mathrm{d}X}(0) \tag{10.93}$$

$$C_m \;=\; \left(1 - \frac{S_{\text{ref}}}{h^2} C_{D_p} \hat{u}_\Sigma(0) - 2\frac{\mathcal{V}}{h^3} \hat{u}_{\mathcal{K}_x}(0)\right) C_{m_u} - \frac{1}{4} \frac{S_{\text{ref}} c_{\text{ref}}}{h^3} C_{m_q} C_{L_u} \frac{\mathrm{d}\hat{w}_{\kappa_z}}{\mathrm{d}X}(0) \tag{10.94}$$

$$\alpha \;=\; \alpha_u + \frac{1}{2} \frac{S_{\text{ref}}}{h^2} C_{L_u} \hat{w}_{\kappa_z}(0) \tag{10.95}$$

$$Re \;=\; \left(1 + \frac{1}{2} \frac{S_{\text{ref}}}{h^2} C_{D_p} \hat{u}_\Sigma(0) + \frac{\mathcal{V}}{h^3} \hat{u}_{\mathcal{K}_x}(0)\right) Re_u \tag{10.96}$$

Note that application of these corrections requires knowing the profile drag and induced drag components of the total drag.

10.4   2D tunnel drag measurements

10.4.1   Flow two-dimensionality requirements

Valid 2D wind tunnel experiments, regardless of the measurement techniques used, in general require that the flow is actually two-dimensional to a sufficient accuracy. The model must span the entire test section, since any significant gaps between the model wingtips and the tunnel walls will result in the generation of trailing vorticity and unwanted induced drag. Unfortunately, the model wingtips will adversely interact with the tunnel-wall boundary layers, which will usually add spurious pressure drag to the model. The wall boundary layer fluid can also flow spanwise onto the model and disturb the model's ideally 2D boundary layers. To avoid these problems, the tunnel wall boundary layers just ahead of the model ideally should be removed with local wall suction, or energized with tangential blowing. Also, the model aspect ratio b/c can be made large to reduce the effect of the ends. Large tunnel height to model chord ratios h/c are also desirable to minimize the tunnel-wall effects and the associated corrections, which will be discussed later.

Assuming that sufficient precautions are taken to ensure good flow two-dimensionality, the drag of a 2D model with negligible lift can be satisfactorily measured with a load sensor. However, measurement of the drag of a 2D <u>lifting</u> airfoil using a load sensor is extraordinarily difficult. Because a 2D airfoil can easily have $L'/D' \simeq 100$ or more, the drag error from load-sensor misalignment as given by equation (10.4) becomes overwhelming. For example, a misalignment error of $\theta_{\mathrm{err}} = 1°$ and $L'/D' = 100$ will give 175% error in the measured drag, rendering the experimental results meaningless. Furthermore, even small drag additions from the model/wall junction interaction can overwhelm the model's small drag. In practice, the direct drag force measurement approach is simply not suitable for 2D lifting airfoils. A good alternative is the wake momentum drag measurement technique, which is described next.

10.4.2   Wake momentum drag measurement

This method seeks to measure the profile drag indirectly, via the far-field momentum defect of the airfoil's wake which is defined in terms of the wake velocity profile $u(z)$. This in turn is obtained from the wake total pressure profile $p_o(z)$ measured via a *wake rake* (or *drag rake*), which is an array of pitot tubes with spacing Δz, as shown in Figure 10.18. The local static pressure p_{e} at the rake location is also measured via a static probe. This static pressure is typically assumed to be constant across the wake.
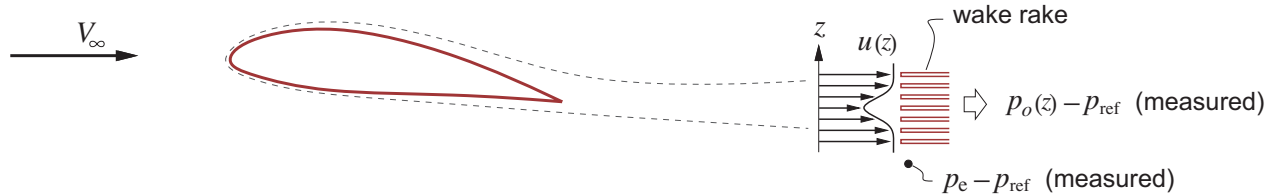
Figure 10.18: Wake measurement via a wake rake for determination of 2D profile drag.

Most pressure sensors report a <u>difference</u> between two pressures, with one of these being some convenient chosen reference pressure p_{ref} supplied to the sensor. Typically this is either p_∞ or p_{o_∞}, or some other comparable pressure. Regardless, the reported data is actually $p_o(z) - p_{\mathrm{ref}}$ and $p_{\mathrm{e}} - p_{\mathrm{ref}}$.

The wake velocity profile is computed from the rake pressure data and the definition of total pressure.

$$u(z) \;=\; \sqrt{\frac{2[p_o(z) - p_{\mathrm{e}}]}{\rho}} \;=\; \sqrt{\frac{2[(p_o(z) - p_{\mathrm{ref}}) - (p_{\mathrm{e}} - p_{\mathrm{ref}})]}{\rho}} \tag{10.97}$$

$$u_{\mathrm{e}} \;=\; u(z_{\mathrm{e}}) \tag{10.98}$$

The displacement and momentum thicknesses and corresponding shape parameter are then computed by numerical integration over the $i = 1 \ldots N$ rake tubes.

$$\delta^* = \int \left(1 - \frac{u}{u_e}\right) dz \simeq \sum_{i=1}^{N} \left(1 - \frac{u_i}{u_e}\right) \Delta z \tag{10.99}$$

$$\theta = \int \left(1 - \frac{u}{u_e}\right) \frac{u}{u_e} dz \simeq \sum_{i=1}^{N} \left(1 - \frac{u_i}{u_e}\right) \frac{u_i}{u_e} \Delta z \tag{10.100}$$

$$H = \frac{\delta^*}{\theta} \tag{10.101}$$

From the far-field force analysis given in Appendix C, the profile drag/span is the momentum defect far downstream in the wake.

$$D' = P_\infty = \rho V_\infty^2 \theta_\infty \tag{10.102}$$

$$c_d \equiv \frac{D'}{\frac{1}{2}\rho V_\infty^2 c} = 2\frac{\theta_\infty}{c} \tag{10.103}$$

The wake reaches its final value θ_∞ downstream of the airfoil's static pressure near-field, where $p_e = p_\infty$ and correspondingly $u_e = V_\infty$. Hence, the rake should ideally be placed far downstream, well away from the airfoil's near-field. One practical difficulty with this is that the wake spreads rapidly downstream, and the velocity defect profile $u_e - u_{(z)}$ becomes small and is difficult to measure accurately. So for measurement accuracy of the velocity profile it's desirable to measure the wake close behind the airfoil where $p_e \neq p_\infty$ in general.

This conflict is resolved by measuring the wake fairly close behind the airfoil, and then extrapolating the results to far-downstream conditions using the Squire-Young formula (4.118) which was derived and discussed in Section 4.13.3, and is restated as follows for convenience.

$$\theta_\infty = \theta_{(\bar{x})} \left(\frac{u_e(\bar{x})}{V_\infty}\right)^{(H_{\mathrm{avg}}+2)} \tag{10.104}$$

$$\text{where} \quad H_{\mathrm{avg}} = \frac{H_{(\bar{x})} + 1}{2} \tag{10.105}$$

Coincidentally, this relation was originally developed by Squire and Young [34] for the calculation of profile drag by extrapolation from the trailing edge quantities, thus avoiding shear layer calculations into the wake. Here, it is used to avoid the need to measure the wake too far downstream.

Appendix A

Vector Notation

This Appendix will summarize various vector symbols and operations which are convenient for formulating the equations of fluid motion. The operations will also be interpreted as vector-matrix products. A scalar will be denoted here by α, vectors by $\mathbf{u}$ and $\mathbf{v}$, and matrices by $\bar{\bar{\mathbf{A}}}$, with the following cartesian components.

$$\mathbf{u} \equiv \begin{Bmatrix} u_x \\ u_y \\ u_z \end{Bmatrix} \qquad\qquad \mathbf{v} \equiv \begin{Bmatrix} v_x \\ v_y \\ v_z \end{Bmatrix} \qquad\qquad \bar{\bar{\mathbf{A}}} \equiv \begin{bmatrix} A_{xx} & A_{xy} & A_{xz} \\ A_{yx} & A_{yy} & A_{yz} \\ A_{zx} & A_{zy} & A_{zz} \end{bmatrix}$$

A vector is assumed here to be a column vector by convention. Its transpose $()^T$ is then a row vector, which is sometimes needed to properly form vector-vector and vector-matrix products.

A.1 Vector and Matrix Multiplication

Vector Inner (Dot) Product

$$\mathbf{u} \cdot \mathbf{v} \;=\; \mathbf{u}^T \mathbf{v} \;=\; \begin{Bmatrix} \mathbf{u}^T \end{Bmatrix} \begin{Bmatrix} \mathbf{v} \end{Bmatrix} \;=\; u_x v_x + u_y v_y + u_z v_z \qquad \text{(scalar)}$$

Vector Outer Product

$$\mathbf{u} \otimes \mathbf{v} \;=\; \mathbf{u}\mathbf{v}^T \;=\; \begin{Bmatrix} \mathbf{u} \end{Bmatrix} \begin{Bmatrix} \mathbf{v}^T \end{Bmatrix} \;=\; \begin{bmatrix} u_x v_x & u_x v_y & u_x v_z \\ u_y v_x & u_y v_y & u_y v_z \\ u_z v_x & u_z v_y & u_z v_z \end{bmatrix} \qquad \text{(matrix)}$$

Matrix-Vector Product

$$\bar{\bar{\mathbf{A}}} \cdot \mathbf{v} \;=\; \bar{\bar{\mathbf{A}}}\,\mathbf{v} \;=\; \begin{bmatrix} \bar{\bar{\mathbf{A}}} \end{bmatrix} \begin{Bmatrix} \mathbf{v} \end{Bmatrix} \;=\; \begin{Bmatrix} A_{xx}v_x + A_{xy}v_y + A_{xz}v_z \\ A_{yx}v_x + A_{yy}v_y + A_{yz}v_z \\ A_{zx}v_x + A_{zy}v_y + A_{zz}v_z \end{Bmatrix} \qquad \text{(vector)}$$

Vector-Matrix-Vector Product

$$\mathbf{u} \cdot \bar{\bar{\mathbf{A}}} \cdot \mathbf{v} \;=\; \mathbf{u}^T \bar{\bar{\mathbf{A}}}\,\mathbf{v} \;=\; \begin{Bmatrix} \mathbf{u}^T \end{Bmatrix} \begin{bmatrix} \bar{\bar{\mathbf{A}}} \end{bmatrix} \begin{Bmatrix} \mathbf{v} \end{Bmatrix} \;=\; \begin{matrix} u_x(A_{xx}v_x + A_{xy}v_y + A_{xz}v_z) \\ + u_y(A_{yx}v_x + A_{yy}v_y + A_{yz}v_z) \\ + u_z(A_{zx}v_x + A_{zy}v_y + A_{zz}v_z) \end{matrix} \qquad \text{(scalar)}$$

Vector Cross Product
This is computed via the determinant, or via the antisymmetric matrix $\vec{\vec{\mathbf{u}}}$ formed from $\mathbf{u}$'s components:

$$\mathbf{u} \times \mathbf{v} \;=\; \det \begin{bmatrix} \hat{\mathbf{x}} & \hat{\mathbf{y}} & \hat{\mathbf{z}} \\ u_x & u_y & u_z \\ v_x & v_y & v_z \end{bmatrix} \;=\; \vec{\vec{\mathbf{u}}}\mathbf{v} \;=\; \begin{bmatrix} 0 & -u_z & u_y \\ u_z & 0 & -u_x \\ -u_y & u_x & 0 \end{bmatrix} \begin{Bmatrix} \mathbf{v} \end{Bmatrix} \;=\; \begin{Bmatrix} u_y v_z - u_z v_y \\ u_z v_x - u_x v_z \\ u_x v_y - u_y v_x \end{Bmatrix} \qquad \text{(vector)}$$

Vector-Matrix Cross Product

$$\mathbf{u} \times \bar{\bar{\mathbf{A}}} = \vec{\mathbf{u}}\bar{\bar{\mathbf{A}}} = \begin{bmatrix} u_y A_{zx} - u_z A_{yx} & u_y A_{zy} - u_z A_{yy} & u_y A_{zz} - u_z A_{yz} \\ u_z A_{xx} - u_x A_{zx} & u_z A_{xy} - u_x A_{zy} & u_z A_{xz} - u_x A_{zz} \\ u_x A_{yx} - u_y A_{xx} & u_x A_{yy} - u_y A_{xy} & u_x A_{yz} - u_y A_{xz} \end{bmatrix} \qquad \text{(matrix)}$$

A.2 Scalar and Vector Derivative Operations

Partial differentiation with respect to the x, y, z coordinates will be compactly denoted by $\partial_x, \partial_y, \partial_z$.

Gradient of Scalar

$$\nabla \alpha = \left\{ \begin{array}{c} \partial_x \alpha \\ \partial_y \alpha \\ \partial_z \alpha \end{array} \right\} \qquad \text{(vector)}$$

Divergence of Vector

$$\nabla \cdot \mathbf{u} = \partial_x u_x + \partial_y u_y + \partial_z u_z \qquad \text{(scalar)}$$

Curl of Vector

$$\nabla \times \mathbf{u} = \det \begin{bmatrix} \hat{\mathbf{x}} & \hat{\mathbf{y}} & \hat{\mathbf{z}} \\ \partial_x & \partial_y & \partial_z \\ u_x & u_y & u_z \end{bmatrix} = \left\{ \begin{array}{c} \partial_y u_z - \partial_z u_y \\ \partial_z u_x - \partial_x u_z \\ \partial_x u_y - \partial_y u_x \end{array} \right\} \qquad \text{(vector)}$$

Gradient of Vector

$$\nabla \mathbf{u} = \begin{bmatrix} - & (\nabla u_x)^T & - \\ - & (\nabla u_y)^T & - \\ - & (\nabla u_z)^T & - \end{bmatrix} = \begin{bmatrix} | & | & | \\ \partial_x \mathbf{u} & \partial_y \mathbf{u} & \partial_z \mathbf{u} \\ | & | & | \end{bmatrix} = \begin{bmatrix} \partial_x u_x & \partial_y u_x & \partial_z u_x \\ \partial_x u_y & \partial_y u_y & \partial_z u_y \\ \partial_x u_z & \partial_y u_z & \partial_z u_z \end{bmatrix} \qquad \text{(matrix)}$$

This $\nabla \mathbf{u}$ is not symmetric in general. It is symmetric <u>only</u> if $\mathbf{u}$ is irrotational, or $\nabla \times \mathbf{u} = \mathbf{0}$.

A.3 Matrix Derivative Operations

The divergence of a matrix is unambiguous only for a symmetric matrix, denoted here by $\bar{\bar{\mathbf{S}}}$.

$$\bar{\bar{\mathbf{S}}} = \begin{bmatrix} - & \mathbf{S}_x^T & - \\ - & \mathbf{S}_y^T & - \\ - & \mathbf{S}_z^T & - \end{bmatrix} = \begin{bmatrix} | & | & | \\ \mathbf{S}_x & \mathbf{S}_y & \mathbf{S}_z \\ | & | & | \end{bmatrix} = \begin{bmatrix} S_{xx} & S_{xy} & S_{xz} \\ S_{yx} & S_{yy} & S_{yz} \\ x_{zx} & S_{zy} & S_{zz} \end{bmatrix} , \qquad \begin{array}{l} S_{xy} = S_{yx} \\ S_{xz} = S_{zx} \\ S_{yz} = S_{zy} \end{array}$$

As indicated, $\bar{\bar{\mathbf{S}}}$ can be formed from the three vectors $\mathbf{S}_x, \mathbf{S}_y, \mathbf{S}_z$ in rows or columns. Note that these are not completely independent because of the three symmetry relations $(\mathbf{S}_x)_y = S_{xy} = S_{yx} = (\mathbf{S}_y)_x$, etc.

Divergence of Symmetric Matrix

$$\nabla \cdot \bar{\bar{\mathbf{S}}} = \left\{ \begin{array}{c} \nabla \cdot \mathbf{S}_x \\ \nabla \cdot \mathbf{S}_y \\ \nabla \cdot \mathbf{S}_z \end{array} \right\} = \left\{ \begin{array}{c} \partial_x S_{xx} + \partial_y S_{xy} + \partial_z S_{xz} \\ \partial_x S_{yx} + \partial_y S_{yy} + \partial_z S_{yz} \\ \partial_x S_{zx} + \partial_y S_{zy} + \partial_z S_{zz} \end{array} \right\} \qquad \text{(vector)}$$

Divergence of Matrix-Vector Product (expanded)

$$\nabla \cdot \left(\bar{\bar{\mathbf{S}}} \cdot \mathbf{u} \right) = \left(\nabla \cdot \bar{\bar{\mathbf{S}}} \right) \cdot \mathbf{u} + \left(\bar{\bar{\mathbf{S}}} \cdot \nabla \right) \cdot \mathbf{u} \qquad \text{(scalar)}$$

or equivalently

$$\begin{array}{lcl} \partial_x(S_{xx}u_x + S_{xy}u_y + S_{xz}u_z) & & (\partial_x S_{xx} + \partial_y S_{xy} + \partial_z S_{xz})\, u_x \quad + \quad (S_{xx}\partial_x + S_{xy}\partial_y + S_{xz}\partial_z)\, u_x \\ +\, \partial_y(S_{yx}u_x + S_{yy}u_y + S_{yz}u_z) & = & +\, (\partial_x S_{yx} + \partial_y S_{yy} + \partial_z S_{yz})\, u_y \quad + \quad (S_{yx}\partial_x + S_{yy}\partial_y + S_{yz}\partial_z)\, u_y \\ +\, \partial_z(S_{zx}u_x + S_{zy}u_y + S_{zz}u_z) & & +\, (\partial_x S_{zx} + \partial_y S_{zy} + \partial_z S_{zz})\, u_z \quad + \quad (S_{zx}\partial_x + S_{zy}\partial_y + S_{zz}\partial_z)\, u_z \end{array}$$

Appendix B

Sheet Jump Relations

This Appendix will evaluate the velocity field of infinite flat constant-strength source and vortex sheets. In the sheet's $s\ell n$ Cartesian coordinate system, the field point $\mathbf{r}$ is placed at $(0, 0, n)$, and the general integration point $\mathbf{r}'$ is at $(s, \ell, 0)$, as shown in Figure B.1.
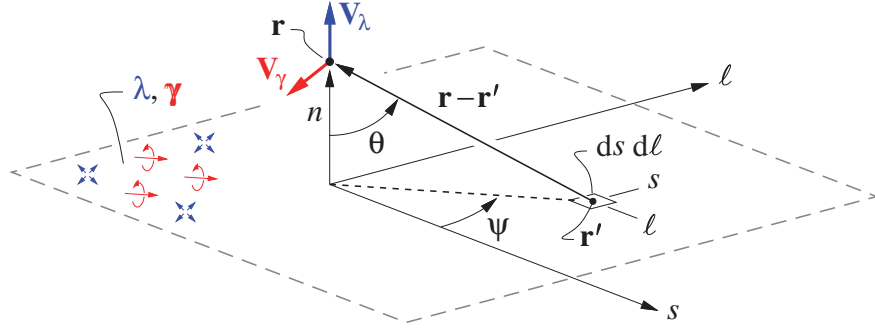
Figure B.1: Velocity calculation geometry for infinite flat source and vortex sheet.

Applying the general $\mathbf{V}_\lambda$ expression (2.15) to this case, we have $\mathbf{r} - \mathbf{r}' = (-s, -\ell, n)$, and the source-sheet part of the velocity at the field point is then

$$\mathbf{V}_{\lambda(0,0,n)} = \frac{\lambda}{4\pi} \int_{-\infty}^{\infty} \int_{-\infty}^{\infty} \frac{-s\,\hat{\mathbf{s}} - \ell\,\hat{\boldsymbol{\ell}} + n\,\hat{\mathbf{n}}}{(s^2 + \ell^2 + n^2)^{3/2}} \, \mathrm{d}s \, \mathrm{d}\ell \tag{B.1}$$

which when integrated must have zero $\hat{\mathbf{s}}$ and $\hat{\boldsymbol{\ell}}$ components because of their antisymmetric integrands. The remaining nonzero $\hat{\mathbf{n}}$ component is readily evaluated by first switching to the spherical angle coordinates θ, ψ shown in Figure B.1.

$$s = n \tan\theta \, \cos\psi \tag{B.2}$$

$$\ell = n \tan\theta \, \sin\psi \tag{B.3}$$

$$s^2 + \ell^2 + n^2 = n^2 \tan^2\theta + n^2 = \frac{n^2}{\cos^2\theta} \tag{B.4}$$

$$\mathrm{d}s \, \mathrm{d}\ell = \left(\frac{\partial s}{\partial\theta} \frac{\partial\ell}{\partial\psi} - \frac{\partial s}{\partial\psi} \frac{\partial\ell}{\partial\theta} \right) \mathrm{d}\theta \, \mathrm{d}\psi = \left(n^2 \frac{\sin\theta}{\cos^3\theta} \right) \mathrm{d}\theta \, \mathrm{d}\psi \tag{B.5}$$

$$\mathbf{V}_{\lambda(0,0,n)} = \frac{\lambda}{4\pi} \int_0^{2\pi} \left[\int_0^{\pi/2} \hat{\mathbf{n}} \, \frac{n}{|n|} \sin\theta \, \mathrm{d}\theta \right] \mathrm{d}\psi = \frac{\lambda\,\hat{\mathbf{n}}}{2} \frac{n}{|n|} \tag{B.6}$$

In (B.5), the area integration element $\mathrm{d}s \, \mathrm{d}\ell$ is related to $\mathrm{d}\theta \, \mathrm{d}\psi$ via the coordinate-transformation Jacobian factor in the parentheses.

A similar calculation gives the velocity of a uniform-strength infinite vortex sheet.

$$\mathbf{V}_{\gamma(0,0,n)} \;=\; \frac{\boldsymbol{\gamma}\times\hat{\mathbf{n}}}{2}\frac{n}{|n|} \tag{B.7}$$

The most general case has superimposed source and vortex sheets, with possibly an additional contribution from boundaries or a freestream.

$$\mathbf{V}_{(0,0,n)} \;=\; \frac{\lambda\,\hat{\mathbf{n}}}{2}\frac{n}{|n|} \;+\; \frac{\boldsymbol{\gamma}\times\hat{\mathbf{n}}}{2}\frac{n}{|n|} \;+\; \mathbf{V}_b \tag{B.8}$$

The *velocity jump* across the sheet is defined and evaluated as

$$\Delta\mathbf{V} \;\equiv\; \lim_{n\to 0}\left[\mathbf{V}_{(0,0,n)} - \mathbf{V}_{(0,0,-n)}\right]$$
$$\Delta\mathbf{V} \;=\; \lambda\,\hat{\mathbf{n}} \;+\; \boldsymbol{\gamma}\times\hat{\mathbf{n}} \tag{B.9}$$

and the reciprocal relations can be obtained by forming first $\hat{\mathbf{n}}\cdot\Delta\mathbf{V}$ and then $\hat{\mathbf{n}}\times\Delta\mathbf{V}$.

$$\lambda \;=\; \hat{\mathbf{n}}\cdot\Delta\mathbf{V} \tag{B.10}$$
$$\boldsymbol{\gamma} \;=\; \hat{\mathbf{n}}\times\Delta\mathbf{V} \tag{B.11}$$

Although the above calculations were performed for flat, infinite, constant-strength sheets, the jump relations (B.9),(B.10),(B.11) are valid for a sheet of any size or shape, provided the sheet geometry and strength distributions are smooth at the field point, without any corner or crease. The justification is that in the $n\to 0$ limit, a compensating magnification of the smooth sheet will approach the flat-sheet case shown in Figure B.1.

A relation for the doublet sheet strength μ which was used to define a divergence-free vortex-sheet strength

$$\boldsymbol{\gamma} \;=\; \hat{\mathbf{n}}\times\widetilde{\nabla}\mu \tag{B.12}$$

can be derived by first writing the velocity in terms of the surface-parallel and surface-normal components of the potential gradient,

$$\nabla\varphi \;=\; \mathbf{V} \;=\; \widetilde{\nabla}\varphi \;+\; \frac{\partial\varphi}{\partial n}\,\hat{\mathbf{n}} \tag{B.13}$$

where the in-surface gradient $\widetilde{\nabla}$ has the $\hat{\mathbf{s}}$ and $\hat{\boldsymbol{\ell}}$ components. Taking the difference across the sheet gives

$$\Delta\mathbf{V} \;=\; \widetilde{\nabla}(\Delta\varphi) \;+\; \Delta\!\left(\frac{\partial\varphi}{\partial n}\right)\hat{\mathbf{n}} \tag{B.14}$$

where the order of the Δ and $\widetilde{\nabla}$ operations has been swapped. Forming $\hat{\mathbf{n}}\times\{$equation (B.14)$\}$ gives

$$\hat{\mathbf{n}}\times\Delta\mathbf{V} \;=\; \hat{\mathbf{n}}\times\widetilde{\nabla}(\Delta\varphi) \;+\; \Delta\!\left(\frac{\partial\varphi}{\partial n}\right)\hat{\mathbf{n}}\times\hat{\mathbf{n}} \tag{B.15}$$

$$\text{or} \qquad \boldsymbol{\gamma} \;=\; \hat{\mathbf{n}}\times\widetilde{\nabla}(\Delta\varphi) \tag{B.16}$$

since $\hat{\mathbf{n}}\times\hat{\mathbf{n}} = \mathbf{0}$. Equating (B.12) and (B.16) gives

$$\hat{\mathbf{n}}\times\widetilde{\nabla}\mu \;=\; \hat{\mathbf{n}}\times\widetilde{\nabla}(\Delta\varphi) \tag{B.17}$$

and since $\widetilde{\nabla}()$ and $\hat{\mathbf{n}}$ are always orthogonal, the cross products in (B.17) are redundant and can be dropped.

$$\widetilde{\nabla}\mu \;=\; \widetilde{\nabla}(\Delta\varphi) \tag{B.18}$$

Comparing the left and right sides above we conclude that

$$\mu \;=\; \Delta\varphi \tag{B.19}$$

apart from an arbitrary additive constant. This very simple potential-jump result complements the velocity-jump relations (B.10) and (B.11).

Appendix C

2D Airfoil Far-Field Lift and Drag

This Appendix will relate the circulation and source strengths of a 2D airfoil's far-field, defined in Chapter 2, to the airfoil's lift and drag. The derivations will use the integral momentum theorem derived in Chapter 5.

C.1   Far-Field Model

The general 2D far-field expansion for the velocity (2.79) from Chapter 2 is restated here for convenience.

$$
\begin{aligned}
\mathbf{V}_{(x,z)} \; \simeq \; \mathbf{V}_{\mathrm{ff}(x,z)} \; &= \; \mathbf{V}_\infty \; + \; \nabla\varphi_{\mathrm{ff}} \\
&= \; \mathbf{V}_\infty \; + \; \frac{\Lambda}{2\pi}\,\frac{x\,\hat{\mathbf{x}} + z\,\hat{\mathbf{z}}}{r^2} \; + \; \frac{\Gamma}{2\pi}\,\frac{z\,\hat{\mathbf{x}} - x\,\hat{\mathbf{z}}}{r^2} \\
&\quad + \; \frac{\kappa_x}{2\pi}\,\frac{(z^2-x^2)\,\hat{\mathbf{x}} - 2xz\,\hat{\mathbf{z}}}{r^4} \; + \; \frac{\kappa_z}{2\pi}\,\frac{-2xz\,\hat{\mathbf{x}} + (x^2-z^2)\,\hat{\mathbf{z}}}{r^4}
\end{aligned}
\tag{C.1}
$$

The coefficients $\Lambda, \Gamma, \kappa_x, \kappa_z$ are defined by the area integrals (2.74)–(2.77) over the source and vorticity fields, or by the simpler lumped integrals (2.80)–(2.83) over the equivalent source and vortex sheets. However, these definitions are not useful in cases where the sheet strength details are unknown. This Appendix will obtain simpler alternative expressions for Γ and Λ in terms of the airfoil's lift and drag.

The x, z axis orientation will be chosen so that the x axis lies along the freestream velocity.

$$
\mathbf{V}_\infty \; = \; V_\infty\,\hat{\mathbf{x}} \; + \; 0\,\hat{\mathbf{z}}
\tag{C.2}
$$

Sufficiently far from the airfoil, the far-field velocity (C.1) is an excellent approximation to the actual flow about a real lifting 2D airfoil. However, since $\mathbf{V}_{\mathrm{ff}}$ is irrotational it cannot represent the viscous wake which trails downstream, as shown on the left side of Figure C.1. This is corrected here by adding the negative *wake defect* velocity $\Delta u_{\mathrm{wake}}(z) = u - V_\infty$, to make the modified far-field+wake velocity

$$
\mathbf{V}_{\mathrm{ffw}} \; = \; \mathbf{V}_{\mathrm{ff}} \; + \; \Delta u_{\mathrm{wake}}\,\hat{\mathbf{x}}
\tag{C.3}
$$

where it is understood that Δu_{wake} is zero everywhere far from the airfoil except in the downstream wake. It is useful to define the *wake defect volume flow rate/span*, as the integrated wake defect velocity.

$$
\dot{\mathcal{V}}'_{\mathrm{wake}} \; \equiv \; \int -\Delta u_{\mathrm{wake}}\;\mathrm{d}z
\tag{C.4}
$$

We will now apply mass and momentum conservation relations using the modified far-field velocity $\mathbf{V}_{\mathrm{ffw}}$. For simplicity, only the freestream, source, and vortex terms will be retained. A full analysis would reveal that the κ_x, κ_z doublet terms have no net mass or momentum contributions in any case.
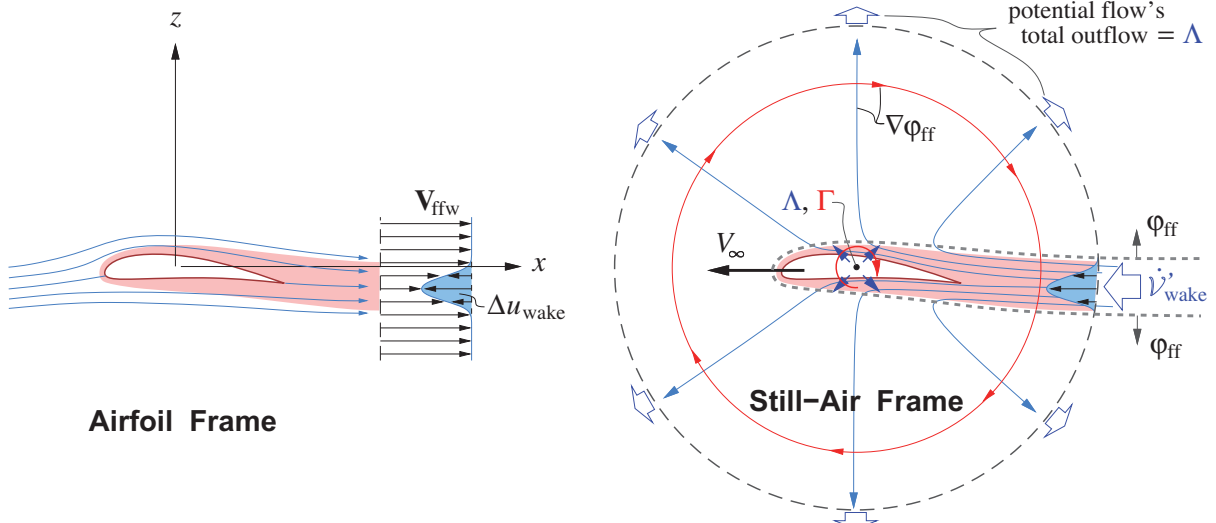
Figure C.1: Viscous wake velocity defect as seen in airfoil frame on left. In the still-air frame, the wake is a jet towards the airfoil which outflows as the apparent far-field source Λ. The velocity field of the far-field vortex Γ has no outflow component. The x, z–doublets are not shown.
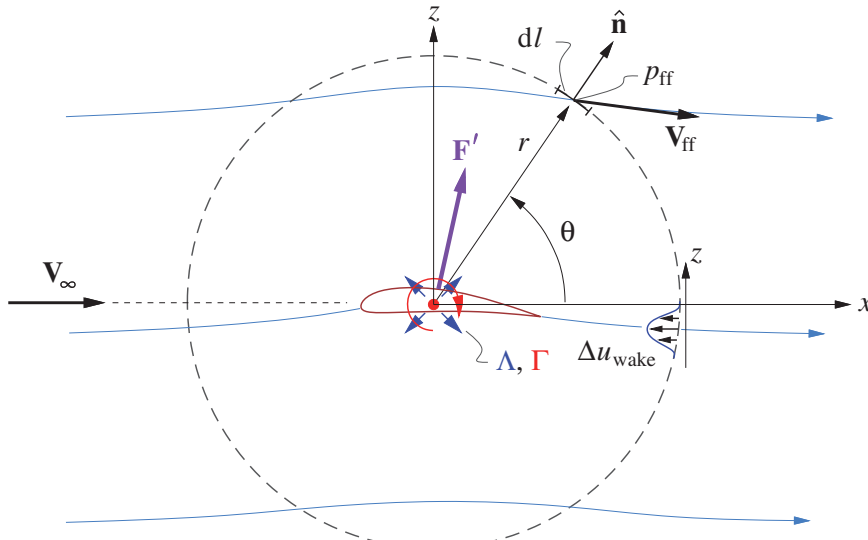
Figure C.2: Outer control volume for calculation of airfoil force. The freestream velocity V_∞ and the Λ, Γ singularities provide the far-field velocity $\mathbf{V}_{\text{ff}}$ on the contour, which then also provides the pressure p_{ff} via Bernoulli's equation. Terms with the compact wake defect Δu_{wake} will be integrated locally over z.

C.2   Outer Contour Integration

The outer control volume is defined as a circle of some radius r, shown in Figures C.1 and C.2. The control-volume integrations will then be most easily performed in polar coordinates, in which the boundary length element $\mathrm{d}l$, the unit normal vector $\hat{\mathbf{n}}$, and the far-field velocity $\mathbf{V}_{\text{ff}}$ take the following forms.

$$
\begin{aligned}
\mathrm{d}l &= r \, \mathrm{d}\theta \\
\hat{\mathbf{n}} &= \hat{\mathbf{r}} \\
\mathbf{V}_{\text{ff}(\theta)} &= V_\infty \left(\cos\theta \; \hat{\mathbf{r}} \; - \; \sin\theta \; \hat{\boldsymbol{\theta}} \right) + \frac{\Lambda}{2\pi r} \hat{\mathbf{r}} \; - \; \frac{\Gamma}{2\pi r} \hat{\boldsymbol{\theta}}
\end{aligned}
\tag{C.5}
$$

2D Airfoil Far-Field Lift and Drag

The following integrals will allow evaluation of the various control volume terms by inspection.

$$\int_0^{2\pi} \sin\theta \; d\theta \;=\; 0 \qquad \int_0^{2\pi} \sin^2\theta \; d\theta \;=\; \pi \qquad \int_0^{2\pi} d\theta \;=\; 2\pi$$
$$\int_0^{2\pi} \cos\theta \; d\theta \;=\; 0 \qquad \int_0^{2\pi} \cos^2\theta \; d\theta \;=\; \pi \qquad \int_0^{2\pi} \sin\theta \cos\theta \; d\theta \;=\; 0 \tag{C.6}$$

C.3   Mass Conservation

The integral mass conservation equation (1.27) applies to any contour surrounding the airfoil.

$$\oint \rho \left(\mathbf{V} \cdot \hat{\mathbf{n}} \right) \, dl \;=\; 0 \tag{C.7}$$

Using $\mathbf{V} = \mathbf{V}_{\text{ffw}}$ as defined by (C.3) and (C.5), forming the dot product with $\hat{\mathbf{n}}$, and evaluating the mass integral for the circular control volume gives

$$\mathbf{V}_{\text{ffw}} \cdot \hat{\mathbf{n}} \;=\; V_\infty \cos\theta \;+\; \frac{\Lambda}{2\pi r} \;+\; \Delta u_{\text{wake}}$$
$$\oint \rho \left(\mathbf{V}_{\text{ffw}} \cdot \hat{\mathbf{n}} \right) dl \;=\; \rho r \int_0^{2\pi} \left(V_\infty \cos\theta \;+\; \frac{\Lambda}{2\pi r} \right) d\theta \;+\; \rho \int \Delta u_{\text{wake}} \, dz$$
$$0 \;=\; \rho \Lambda \;-\; \rho \dot{\mathcal{V}}'_{\text{wake}}$$
$$\dot{\mathcal{V}}'_{\text{wake}} \;=\; \Lambda \tag{C.8}$$

As shown on the right side of Figure C.1, when viewed in the still-air frame, $\dot{\mathcal{V}}'_{\text{wake}}$ is the volume flow of the jet of fluid running upstream towards the airfoil. Because of mass conservation, the jet cannot simply disappear, but must flow out radially as shown. Far from the airfoil this radial outflow is precisely what is being represented by the far-field source Λ located at the airfoil. Its total outflow rate is Λ, which is the same as the wake inflow rate $\dot{\mathcal{V}}'_{\text{wake}}$ as shown by the mass conservation argument above.

C.4   Momentum Conservation

The far-field force expression (5.13) in the 2D case has the form

$$\mathbf{F}' \;=\; -\oint \rho \left(\mathbf{V} \cdot \hat{\mathbf{n}} \right) \mathbf{V} \, dl \;+\; \oint \left(p_\infty - p \right) \hat{\mathbf{n}} \, dl \tag{C.9}$$

where $\mathbf{F}'$ is the force vector/span exerted on the airfoil, shown in Figure C.2. The constant p_∞ has been included in the pressure integral, which is permitted since $\oint \hat{\mathbf{n}} \, dl = \mathbf{0}$ for any closed circuit. Dotting equation (C.9) with $\hat{\mathbf{x}}$ and $\hat{\mathbf{z}}$ gives separate equations for the drag/span and lift/span components of $\mathbf{F}'$.

$$\mathbf{F}' \cdot \hat{\mathbf{x}} \;=\; D' \;=\; -\oint \rho \left(\mathbf{V} \cdot \hat{\mathbf{n}} \right) \left(\mathbf{V} \cdot \hat{\mathbf{x}} \right) dl \;+\; \oint \left(p_\infty - p \right) \left(\hat{\mathbf{n}} \cdot \hat{\mathbf{x}} \right) dl \tag{C.10}$$

$$\mathbf{F}' \cdot \hat{\mathbf{z}} \;=\; L' \;=\; -\oint \rho \left(\mathbf{V} \cdot \hat{\mathbf{n}} \right) \left(\mathbf{V} \cdot \hat{\mathbf{z}} \right) dl \;+\; \oint \left(p_\infty - p \right) \left(\hat{\mathbf{n}} \cdot \hat{\mathbf{z}} \right) dl \tag{C.11}$$

For evaluation of the pressure integrals above, the far-field pressure is defined from the irrotational velocity

via Bernoulli's equation (1.109).

$$p_\infty - p_{\text{ff}(x,z)} = \frac{1}{2}\rho\left(V_{\text{ff}}^2 - V_\infty^2\right) \tag{C.12}$$

$$V_{\text{ff}}^2 - V_\infty^2 = \left[V_\infty\cos\theta + \frac{\Lambda}{2\pi r}\right]^2 + \left[-V_\infty\sin\theta - \frac{\Gamma}{2\pi r}\right]^2 - V_\infty^2$$

$$= 2V_\infty\frac{\Lambda}{2\pi r}\cos\theta + 2V_\infty\frac{\Gamma}{2\pi r}\sin\theta + \frac{\Lambda^2+\Gamma^2}{(2\pi r)^2} \tag{C.13}$$

Note that Δu_{wake} is not included in V_{ff}^2 for the pressure, since it is the potential flow which determines the pressure which is imposed on the thin wake. However, Δu_{wake} is included in the velocity dot products appearing in the momentum-flux terms in (C.10) and (C.11), which are computed as follows.

$$\hat{\mathbf{x}} = \cos\theta\,\hat{\mathbf{r}} - \sin\theta\,\hat{\boldsymbol{\theta}}$$

$$\hat{\mathbf{z}} = \sin\theta\,\hat{\mathbf{r}} + \cos\theta\,\hat{\boldsymbol{\theta}}$$

$$\hat{\mathbf{n}}\cdot\hat{\mathbf{x}} = \cos\theta$$

$$\hat{\mathbf{n}}\cdot\hat{\mathbf{z}} = \sin\theta$$

$$\mathbf{V}_{\text{ffw}}\cdot\hat{\mathbf{x}} = \left[V_\infty\cos\theta + \frac{\Lambda}{2\pi r}\right]\cos\theta - \left[-V_\infty\sin\theta - \frac{\Gamma}{2\pi r}\right]\sin\theta + \Delta u_{\text{wake}}$$

$$= V_\infty + \frac{\Lambda}{2\pi r}\cos\theta + \frac{\Gamma}{2\pi r}\sin\theta + \Delta u_{\text{wake}} \tag{C.14}$$

$$\mathbf{V}_{\text{ffw}}\cdot\hat{\mathbf{z}} = \left[V_\infty\cos\theta + \frac{\Lambda}{2\pi r}\right]\sin\theta + \left[-V_\infty\sin\theta - \frac{\Gamma}{2\pi r}\right]\cos\theta$$

$$= \frac{\Lambda}{2\pi r}\sin\theta - \frac{\Gamma}{2\pi r}\cos\theta \tag{C.15}$$

C.5 Far-Field Lift/Span

For the first momentum-flow integral in the lift equation (C.11) we have

$$-\oint \rho\left(\mathbf{V}_{\text{ffw}}\cdot\hat{\mathbf{n}}\right)\left(\mathbf{V}_{\text{ffw}}\cdot\hat{\mathbf{z}}\right)\mathrm{d}l$$

$$= -\rho\oint\left(V_\infty\cos\theta + \frac{\Lambda}{2\pi r} + \Delta u_{\text{wake}}\right)\left(\frac{\Lambda}{2\pi r}\sin\theta - \frac{\Gamma}{2\pi r}\cos\theta\right)\mathrm{d}l \tag{C.16}$$

Before replacing $\mathrm{d}l$ with $r\,\mathrm{d}\theta$ to perform the integration, it's helpful to first to expand the integrand and separate out the terms containing Δu_{wake}, which are best integrated in the vertical wake coordinate z.

$$-\oint \rho\left(\mathbf{V}_{\text{ffw}}\cdot\hat{\mathbf{n}}\right)\left(\mathbf{V}_{\text{ffw}}\cdot\hat{\mathbf{z}}\right)\mathrm{d}l$$

$$= -\rho r\int_0^{2\pi}\left(\frac{V_\infty\Lambda}{2\pi r}\sin\theta\cos\theta - \frac{V_\infty\Gamma}{2\pi r}\cos^2\theta + \frac{\Lambda^2}{(2\pi r)^2}\sin\theta - \frac{\Lambda\Gamma}{(2\pi r)^2}\cos\theta\right)\mathrm{d}\theta$$

$$\qquad - \rho\int \Delta u_{\text{wake}}\left(\frac{\Lambda}{2\pi r}\sin\theta - \frac{\Gamma}{2\pi r}\cos\theta\right)\mathrm{d}z$$

$$= \frac{\rho V_\infty\Gamma}{2} - \frac{\rho\dot{\mathcal{V}}'_{\text{wake}}\Gamma}{2\pi r}$$

$$\simeq \frac{\rho V_\infty\Gamma}{2} \tag{C.17}$$

The second term containing $\dot{\mathcal{V}}'_{\text{wake}}$ has been dropped, since it goes to zero when the radius r of the control volume is made very large.

Using result (C.13), the pressure integral in the lift equation (C.11) evaluates as follows.

$$
\begin{aligned}
\oint (p_\infty - p_{\text{ff}}) \, (\hat{\mathbf{n}} \cdot \hat{\mathbf{z}}) \, \mathrm{d}l
&= r \int_0^{2\pi} \frac{1}{2}\rho \left(V_{\text{ff}}^2 - V_\infty^2 \right) \sin\theta \, \mathrm{d}\theta \\
&= \frac{1}{2}\rho r \int_0^{2\pi} \left(2V_\infty \frac{\Lambda}{2\pi r} \cos\theta + 2V_\infty \frac{\Gamma}{2\pi r} \sin\theta + \frac{\Lambda^2 + \Gamma^2}{(2\pi r)^2} \right) \sin\theta \, \mathrm{d}\theta \\
&= \frac{\rho V_\infty \Gamma}{2}
\end{aligned}
\tag{C.18}
$$

Adding integrals (C.17) and (C.18) gives the *Kutta-Joukowsky Theorem* relating lift and circulation.

$$
\boxed{L' = \rho V_\infty \Gamma}
\tag{C.19}
$$

Since a far-field expansion can in principle be computed for any flow by lumping its source and vorticity fields, the Kutta-Joukowsky Theorem must apply to the flow about any 2D object, not just an airfoil. The object must, however, must be in an infinite or sufficiently extensive flow, so that the far-field expansion (C.5) is valid far from the object. It is not valid if the object is very close to a solid wall, for example.

C.6 Far-Field Drag/Span

The first momentum flow integral in the drag equation (C.10) is evaluated as follows, where we again separate out the Δu_{wake} terms before integration.

$$
\begin{aligned}
-\oint \rho \, (\mathbf{V}_{\text{ffw}} \cdot \hat{\mathbf{n}})(\mathbf{V}_{\text{ffw}} \cdot \hat{\mathbf{x}}) \, \mathrm{d}l & \\
= -\rho \oint & \left(V_\infty \cos\theta + \frac{\Lambda}{2\pi r} + \Delta u_{\text{wake}} \right)\left(V_\infty + \frac{\Lambda}{2\pi r}\cos\theta + \frac{\Gamma}{2\pi r}\sin\theta + \Delta u_{\text{wake}} \right) \mathrm{d}l \tag{C.20} \\
= -\rho r \int_0^{2\pi} & \left(V_\infty^2 \cos\theta + \frac{V_\infty \Lambda}{2\pi r}(1+\cos^2\theta) + \frac{V_\infty \Gamma}{2\pi r}\cos\theta\,\sin\theta + \frac{\Lambda^2}{(2\pi r)^2}\cos\theta + \frac{\Lambda\Gamma}{(2\pi r)^2}\sin\theta \right) \mathrm{d}\theta \\
& - \rho \int \left(V_\infty \Delta u_{\text{wake}} \cos\theta + (V_\infty + \Delta u_{\text{wake}}) \, \Delta u_{\text{wake}} \right) \mathrm{d}z \\
= -\frac{3}{2}\rho V_\infty \Lambda & + \rho V_\infty \dot{\mathcal{V}}'_{\text{wake}} + P_\infty \\
= -\frac{1}{2}\rho V_\infty \Lambda & + P_\infty \tag{C.21}
\end{aligned}
$$

$$
P_\infty \equiv \rho \int_{\text{wake}} (V_\infty + \Delta u_{\text{wake}})\,(-\Delta u_{\text{wake}}) \, \mathrm{d}z = \int \rho u \,(V_\infty - u) \, \mathrm{d}z
\tag{C.22}
$$

where (C.8) has been used to replace $\dot{\mathcal{V}}'_{\text{wake}}$ with Λ, and the streamwise wake momentum defect P_∞ has been defined. Note also that the approximation $\cos\theta \simeq 1$ was made in the $\int (\ ) \, \mathrm{d}z$ integral, since $\theta \simeq 0$ at the wake location where it exits the control volume.

Again using result (C.13), the pressure integral in the drag equation (C.10) evaluates as follows.

$$
\begin{aligned}
\oint (p_\infty - p_{\text{ff}}) \, (\hat{\mathbf{n}} \cdot \hat{\mathbf{x}}) \, \mathrm{d}l
&= r \int_0^{2\pi} \frac{1}{2}\rho \left(V_{\text{ff}}^2 - V_\infty^2 \right) \cos\theta \, \mathrm{d}\theta \\
&= \frac{1}{2}\rho r \int_0^{2\pi} \left(2V_\infty \frac{\Lambda}{2\pi r} \cos\theta + 2V_\infty \frac{\Gamma}{2\pi r} \sin\theta + \frac{\Lambda^2 + \Gamma^2}{(2\pi r)^2} \right) \cos\theta \, \mathrm{d}\theta \\
&= \frac{\rho V_\infty \Lambda}{2}
\end{aligned}
\tag{C.23}
$$

Adding integrals (C.21) and (C.23) gives the drag as being equal to the streamwise wake momentum defect.

$$\boxed{D' = P_\infty}$$
(C.24)

Recall that the far-field source strength Λ is defined by (C.8) as the wake defect volume flow $\dot{\mathcal{V}}'_{\mathrm{wake}}$ at the control volume boundary. However, this changes somewhat along the wake in the manner shown in Figure C.3, so that the exact value of Λ depends on where the outer boundary is placed. However, as the wake spreads and Δu_{wake} tends to zero, $\dot{\mathcal{V}}'_{\mathrm{wake}}$ will asymptote to the value set by $D' = P_\infty$. This can be seen by restating and comparing the definitions (C.4) and (C.22),

$$\rho V_\infty \dot{\mathcal{V}}'_{\mathrm{wake}} \equiv \rho V_\infty \int_{\mathrm{wake}} -\Delta u_{\mathrm{wake}} \, \mathrm{d}z$$

$$P_\infty \equiv \rho \int_{\mathrm{wake}} (V_\infty + \Delta u_{\mathrm{wake}}) (-\Delta u_{\mathrm{wake}}) \, \mathrm{d}z$$

which become the same in the $\Delta u_{\mathrm{wake}} \to 0$ limit. Hence, if we make the logical choice of defining Λ to be the asymptotic wake defect volume flow, then we have an expression relating the profile drag and the far-field source.

$$\boxed{D' = \rho V_\infty \Lambda}$$
(C.25)

This is a drag complement to the Kutta-Joukowsky lift theorem (C.19).

The local momentum defect $P(x)$ itself varies in the wake, but asymptotes to its far-downstream value P_∞ much faster than $\dot{\mathcal{V}}'_{\mathrm{wake}}$. Its evolution is governed by the von Karman integral momentum equation (4.27), which in the wake simplifies to

$$\frac{\mathrm{d}P}{\mathrm{d}x} = \delta^* \frac{\mathrm{d}p}{\mathrm{d}x}$$
(C.26)

where p is the static pressure. The pressure directly behind the airfoil quickly asymptotes to very nearly the freestream value $p \to p_\infty$ within a fraction of the chord. Beyond this point P then stays constant regardless of the wake spreading, as indicated in Figure C.3.
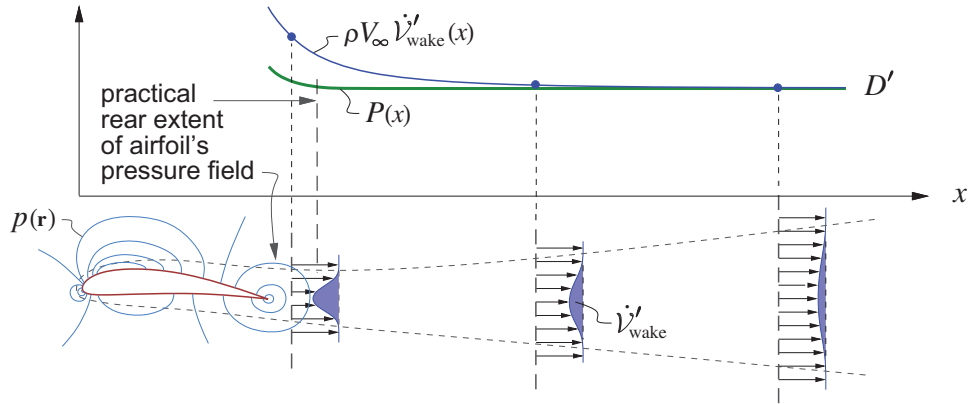
Figure C.3: Scaled wake-defect volume flow $\rho V_\infty \dot{\mathcal{V}}'_{\mathrm{wake}}$ asymptotes towards the wake momentum defect P, which is constant and equal to $P_\infty = D'$ outside of the airfoil's pressure field.

Appendix D

Extended Thin Airfoil Theory

This Appendix derives an extended version of Glauert's incompressible thin airfoil theory [8]. Although this has largely been replaced by panel methods in applications, it is still valuable as a conceptual model, and is also the basis of simple 3D flow models such as lifting-line theory. Here, the extension accounts for finite airfoil thickness by the addition of a source sheet to the usual vortex sheet. A precise definition of the various sheet velocities appearing in the theory will also be made.

D.1 Geometry and Problem Formulation

As shown in Figure D.1, the airfoil extends over $0 \leq x \leq c$, and has upper and lower surfaces defined by the camber function $Z(x)$ and the thickness function $t(x)$. Small angle approximations will be used where appropriate.

$$
\begin{aligned}
z_u(x) &= Z + \tfrac{1}{2}t & \text{(D.1)} \\
z_l(x) &= Z - \tfrac{1}{2}t & \text{(D.2)}
\end{aligned}
$$
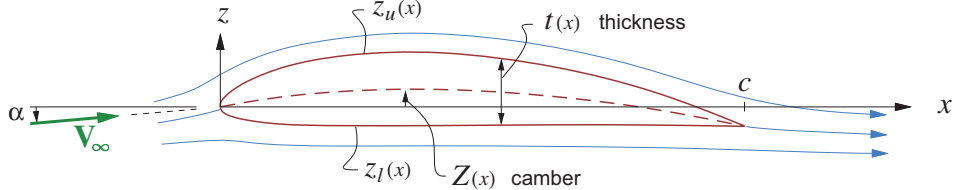
Figure D.1: Thin airfoil theory geometry definition.

The components of the freestream velocity $\mathbf{V}_\infty = u_\infty \hat{\mathbf{x}} + w_\infty \hat{\mathbf{z}}$ are defined in terms of the angle of attack α.

$$
\begin{aligned}
u_\infty &= V_\infty \cos \alpha & \text{(D.3)} \\
w_\infty &= V_\infty \sin \alpha & \text{(D.4)}
\end{aligned}
$$

It's useful to note that if the trailing edge is not required to be at $z = 0$, as shown in Figure D.1, then there is a redundancy in $Z(x)$ and α. Specifically, the substitutions $Z \to Z + \theta x$ and $\alpha \to \alpha + \theta$ simultaneously rotate the airfoil and the freestream by the same angle θ (assuming $\theta \ll 1$), so that there is no effect on the physical angle of attack and no effect on the flow and on the aerodynamic forces. This redundancy is not problematic, and is convenient in cases where the camberline is changed, such as by a flap deflection.

As diagrammed in Figure D.2, the airfoil's perturbation velocity field is represented by source and vortex sheets of strengths $\lambda(x), \gamma(x)$ placed on the x axis along the chord. This is essentially equivalent to the source-sheet transpiration model used to represent the effective displacement of a viscous wake, shown in Figure 3.4. Here, the source sheet models the physical displacement of the airfoil thickness, while the

added vortex sheet captures the nonzero loading across the airfoil. The components of the upper and lower velocities $\mathbf{V}^+, \mathbf{V}^-$ on each side of the sheet at $z = 0^+, 0^-$ can be written in terms of their average values u, w, and their jumps λ, γ.

$$\mathbf{V}^+ = u^+\hat{\mathbf{x}} + w^+\hat{\mathbf{z}} \quad , \qquad u^+(x) = u_\infty + u + \tfrac{1}{2}\gamma \quad , \qquad w^+(x) = w_\infty + w + \tfrac{1}{2}\lambda \qquad (D.5)$$
$$\mathbf{V}^- = u^-\hat{\mathbf{x}} + w^-\hat{\mathbf{z}} \quad , \qquad u^-(x) = u_\infty + u - \tfrac{1}{2}\gamma \quad , \qquad w^-(x) = w_\infty + w - \tfrac{1}{2}\lambda \qquad (D.6)$$

Note that these locally satisfy the sheet velocity jump relations (B.10),(B.11) derived in Appendix B.

$$(\mathbf{V}^+ - \mathbf{V}^-) \cdot \hat{\mathbf{x}} = \gamma \qquad (D.7)$$
$$(\mathbf{V}^+ - \mathbf{V}^-) \cdot \hat{\mathbf{z}} = \lambda \qquad (D.8)$$

The average perturbation velocities u, w along the x axis are in turn expressible in terms of λ and γ by the usual 2D superposition integrals (2.23) and (2.24), specialized here with $z = 0$.

$$\left[\tfrac{1}{2}(\mathbf{V}^+ + \mathbf{V}^-) - \mathbf{V}_\infty \right] \cdot \hat{\mathbf{x}} = u(x) = \frac{1}{2\pi} \int_0^c \lambda(x') \frac{\mathrm{d}x'}{x - x'} \qquad (D.9)$$

$$\left[\tfrac{1}{2}(\mathbf{V}^+ + \mathbf{V}^-) - \mathbf{V}_\infty \right] \cdot \hat{\mathbf{z}} = w(x) = \frac{1}{2\pi} \int_0^c -\gamma(x') \frac{\mathrm{d}x'}{x - x'} \qquad (D.10)$$
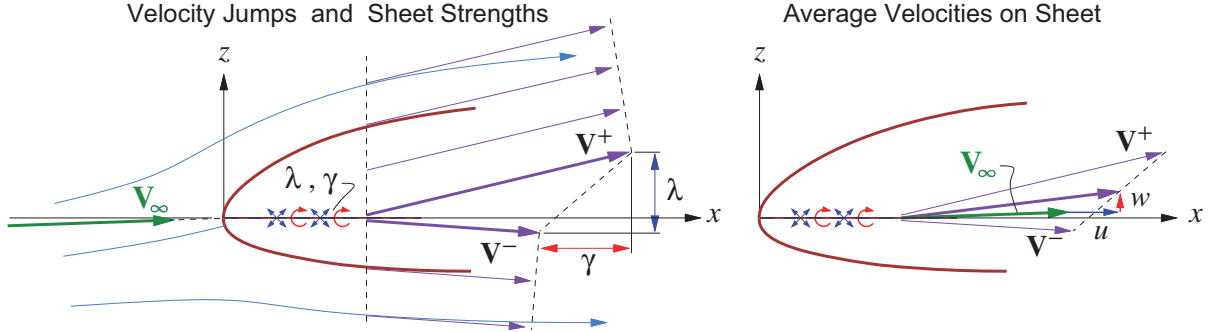
Figure D.2: Normal and tangential jumps between upper and lower sheet velocities $\mathbf{V}^+(x), \mathbf{V}^-(x)$, are represented by source and vortex sheet strengths $\lambda(x), \gamma(x)$, which then define the average perturbation velocities $u(x), w(x)$ via the superposition integrals (D.9) and (D.10).

Mass conservation is now applied to two infinitesimal $\mathrm{d}x$–wide control volumes above and below the sheets shown in Figure D.3.

$$(u^+ + \mathrm{d}u^+)(z_u + \mathrm{d}z_u) - u^+ z_u - w^+ \mathrm{d}x = 0$$
$$(u^- + \mathrm{d}u^-)(z_l + \mathrm{d}z_l) - u^- z_l - w^- \mathrm{d}x = 0$$

$$\text{or} \qquad \frac{\mathrm{d}}{\mathrm{d}x}\left[\left(u_\infty + u + \tfrac{1}{2}\gamma\right)\left(Z + \tfrac{1}{2}t\right) \right] - \left(w_\infty + w + \tfrac{1}{2}\lambda\right) = 0 \qquad (D.11)$$

$$\frac{\mathrm{d}}{\mathrm{d}x}\left[\left(u_\infty + u - \tfrac{1}{2}\gamma\right)\left(Z - \tfrac{1}{2}t\right) \right] - \left(w_\infty + w - \tfrac{1}{2}\lambda\right) = 0 \qquad (D.12)$$

Subtracting [(D.11)−(D.12)] and averaging $\tfrac{1}{2}$[(D.11)+(D.12)] produces simplified but equivalent forms.

$$\frac{\mathrm{d}}{\mathrm{d}x}\left[(u_\infty + u)\, t \; + \; \gamma\, Z \right] = \lambda \qquad (D.13)$$

$$\frac{\mathrm{d}}{\mathrm{d}x}\left[(u_\infty + u)\, Z \; + \; \tfrac{1}{4}\gamma\, t \right] = w_\infty + w \qquad (D.14)$$

Since $u(x)$ and $w(x)$ are given in terms of $\lambda(x)$ and $\gamma(x)$ by the superposition integrals (D.9) and (D.10), the mass conservation requirements (D.13) and (D.14) are two linear coupled integro-differential equations which are to be solved for the unknown sheet strengths $\lambda(x)$ and $\gamma(x)$. The inputs are the known geometry functions $t(x)$ and $Z(x)$, and the angle of attack which defines u_∞ and w_∞.
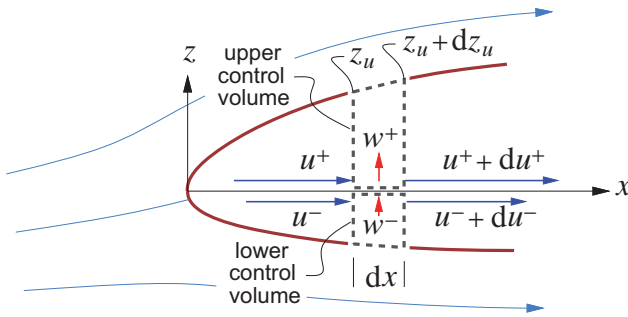
Figure D.3: Mass conservation applied to infinitesimally-wide upper and lower control volumes.

D.2 First-Order Solution

Classical thin airfoil theory assumes that the velocity perturbations and the geometric angles are small.

$$\frac{\mathrm{d}Z}{\mathrm{d}x},\ \frac{\mathrm{d}t}{\mathrm{d}x},\ \frac{u}{V_\infty},\ \frac{w}{V_\infty},\ \frac{\lambda}{V_\infty},\ \frac{\gamma}{V_\infty},\ \alpha \ll 1$$

To a first approximation we can therefore drop the quadratic products of these quantities from the control-volume equations (D.13), (D.14), giving their simplified versions

$$\frac{\mathrm{d}}{\mathrm{d}x}\left(u_\infty t\right) = \lambda \tag{D.15}$$

$$\frac{\mathrm{d}}{\mathrm{d}x}\left(u_\infty Z\right) = w + w_\infty \tag{D.16}$$

which are now decoupled. Also, the streamwise perturbation velocity u is not involved in their solution.

D.2.1 Source-sheet solution

Using the first-order approximation $\cos\alpha \simeq 1$, or equivalently $u_\infty \simeq V_\infty$, equation (D.15) is an explicit expression for the source sheet strength independent of the airfoil camber and freestream angle of attack.
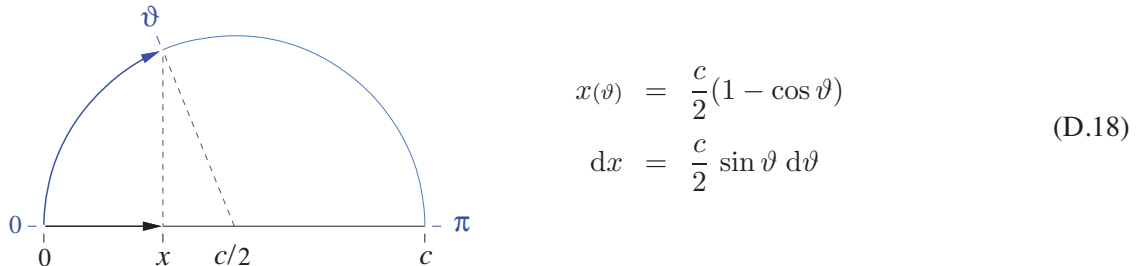
$$\boxed{\lambda(x) = V_\infty\,\frac{\mathrm{d}t}{\mathrm{d}x}} \tag{D.17}$$

This is the same as relation (2.86) derived via the same type of control volume analysis as used here.

D.2.2 Vortex-sheet solution

The solution of equation (D.16) for γ is more involved. One possible numerical solution approach is the Vortex Lattice method described in Chapter 6. Here, we will instead use Glauert's semi-analytical Fourier series solution method. This relies on a change in the independent variable $x \to \vartheta$, with $\vartheta = 0...\pi$.

$$x(\vartheta) = \frac{c}{2}(1-\cos\vartheta)$$

$$\mathrm{d}x = \frac{c}{2}\sin\vartheta\,\mathrm{d}\vartheta \tag{D.18}$$

With these substitutions, the superposition integrals (D.9) and (D.10) take on the following equivalent forms.

$$u(\vartheta) = \frac{1}{2\pi} \int_0^\pi \lambda(\vartheta') \frac{\sin \vartheta' \, d\vartheta'}{\cos \vartheta' - \cos \vartheta} \tag{D.19}$$

$$w(\vartheta) = \frac{1}{2\pi} \int_0^\pi -\gamma(\vartheta') \frac{\sin \vartheta' \, d\vartheta'}{\cos \vartheta' - \cos \vartheta} \tag{D.20}$$

Substituting (D.20) for w in equation (D.16), approximating $\sin \alpha \simeq \alpha$, and dividing by V_∞ produces the following integral equation for the unknown vortex sheet strength $\gamma(\vartheta)$.

$$\frac{1}{2\pi} \int_0^\pi \frac{\gamma(\vartheta')}{V_\infty} \frac{\sin \vartheta' \, d\vartheta'}{\cos \vartheta' - \cos \vartheta} = \alpha - \frac{dZ}{dx}(\vartheta) \qquad (0 < \vartheta < \pi) \tag{D.21}$$

We must also impose a *Kutta condition* to ensure physically-correct smooth flow at the trailing edge.

$$\gamma = 0 \qquad (\vartheta = \pi) \tag{D.22}$$

The driving function $\alpha - dZ/dx$ in (D.21) is now assumed to be represented by a *Fourier cosine series*,

$$\alpha - \frac{dZ}{dx}(\vartheta) = \mathcal{A}_0 - \sum_{n=1}^\infty \mathcal{A}_n \cos n\vartheta \tag{D.23}$$

illustrated in Figure D.4. The negative sign in front of the sum could be absorbed into all the $\mathcal{A}_n$ coefficients, but is left outside for later algebraic simplicity.
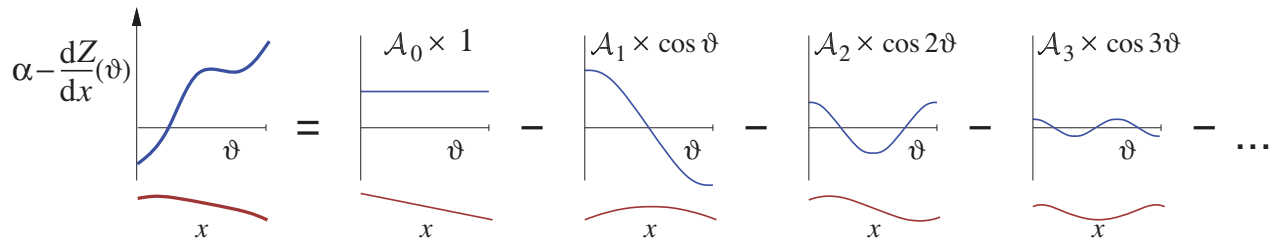
Figure D.4: Cosine series used to represent the net slope of the airfoil's camberline, which drives the flow-tangency integral equation (D.21).

The required coefficients $\mathcal{A}_0, \mathcal{A}_1, \mathcal{A}_2 \ldots$ are computed one by one by multiplying (D.23) by $1, \cos \vartheta, \cos 2\vartheta \ldots$ and integrating over $0 \ldots \pi$.

$$\boxed{\mathcal{A}_0 = \alpha - \frac{1}{\pi} \int_0^\pi \frac{dZ}{dx} \, d\vartheta \quad , \quad \mathcal{A}_n = \frac{2}{\pi} \int_0^\pi \frac{dZ}{dx} \cos n\vartheta \, d\vartheta} \tag{D.24}$$

The *orthogonality property* of the cosine functions is also used.

$$\int_0^\pi \cos n\vartheta \, \cos m\vartheta \, d\vartheta = \begin{cases} \pi & (\text{if } n = m = 0) \\ \pi/2 & (\text{if } n = m \neq 0) \\ 0 & (\text{if } n \neq m) \end{cases} \tag{D.25}$$

The integrals in (D.24) can be evaluated either analytically or numerically. If dZ/dx is smooth, then the higher $\mathcal{A}_n$ coefficients will rapidly decrease and the infinite series can be safely truncated.

Replacing $\alpha - dZ/dx$ in equation (D.21) by its Fourier series (D.23) gives the integral equation

$$\frac{1}{2\pi} \int_0^\pi \frac{\gamma(\vartheta')}{V_\infty} \frac{\sin \vartheta' \, d\vartheta'}{\cos \vartheta' - \cos \vartheta} = \mathcal{A}_0 - \sum_{n=1}^\infty \mathcal{A}_n \cos n\vartheta \tag{D.26}$$

which is to be solved for the unknown $\gamma(\vartheta)$ distribution. The solution is

$$\boxed{\frac{\gamma(\vartheta)}{V_\infty} = 2\left(\mathcal{A}_0 \frac{1+\cos\vartheta}{\sin\vartheta} + \sum_{n=1}^{\infty} \mathcal{A}_n \sin n\vartheta\right)} \tag{D.27}$$

which can be confirmed by substituting it into (D.26), using the trigonometric identity

$$\sin n\vartheta \sin\vartheta = \tfrac{1}{2}\left[\cos(n-1)\vartheta - \cos(n+1)\vartheta\right],$$

evaluating the integrals using the known *Glauert Integral*

$$\int_0^\pi \frac{\cos n\vartheta'\, \mathrm{d}\vartheta'}{\cos\vartheta' - \cos\vartheta} = \pi \frac{\sin n\vartheta}{\sin\vartheta}, \tag{D.28}$$

and verifying that the terms for each $\mathcal{A}_0, \mathcal{A}_1 \ldots$ coefficient match on left and right.

The leading coefficient $\mathcal{A}_0$ in the series (D.27) entirely contains the effect of the angle of attack α, plus the ϑ–averaged value of the negative camberline slope $-\mathrm{d}Z/\mathrm{d}x$. The remaining coefficients $\mathcal{A}_1, \mathcal{A}_2 \ldots$ depend only on the shape of the camberline, and in particular are independent of α. Figure D.5 shows the γ contributions of the individual camberline Fourier terms, all plotted versus the physical x coordinate rather than versus ϑ.
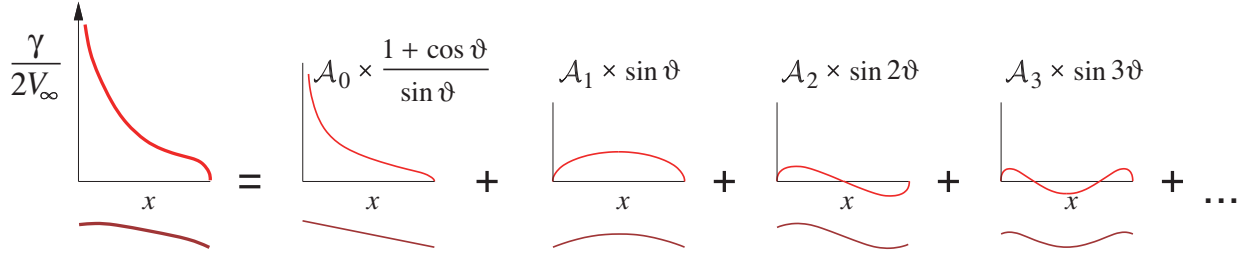
Figure D.5: Vortex sheet strength series components. Each component is associated with a specific camberline geometry mode sketched below it.

D.3 First-Order Force and Moment Calculation

Computation of the lift and moment consists of chordwise integrations of the pressure loading $p_l - p_u$ across the airfoil. In non-dimensional form this is

$$\Delta C_p \equiv \frac{p_l - p_u}{\frac{1}{2}\rho V_\infty^2} = \frac{|\mathbf{V}_u|^2 - |\mathbf{V}_l|^2}{V_\infty^2} \simeq 2\frac{\gamma}{V_\infty} \tag{D.29}$$

where the approximation is the result of dropping all quadratic quantities in accordance with the first-order thin airfoil approximations. The lift coefficient is given by

$$c_\ell = \int_0^1 \Delta C_p\, \mathrm{d}\!\left(\frac{x}{c}\right) \simeq \int_0^1 2\frac{\gamma}{V_\infty}\, \mathrm{d}\!\left(\frac{x}{c}\right) = \int_0^\pi \frac{\gamma}{V_\infty} \sin\vartheta\, \mathrm{d}\vartheta \tag{D.30}$$

in which γ is now substituted by its series (D.27).

$$c_\ell = \int_0^\pi 2\left(\mathcal{A}_0 \frac{1+\cos\vartheta}{\sin\vartheta} + \sum_{n=1}^{\infty} \mathcal{A}_n \sin n\vartheta\right) \sin\vartheta\, \mathrm{d}\vartheta \tag{D.31}$$

The integrations inside the summation can be evaluated by using the *orthogonality property* of the sine functions.

$$\int_0^\pi \sin n\vartheta \, \sin m\vartheta \, \mathrm{d}\vartheta \;=\; \begin{cases} \pi/2 & (\text{if } n = m) \\ 0 & (\text{if } n \neq m) \end{cases} \tag{D.32}$$

We see that only the $n = 1$ integral inside the summation is nonzero. The final result is

$$c_\ell \;=\; \pi\,(2\mathcal{A}_0 + \mathcal{A}_1) \;=\; 2\pi\alpha + c_{\ell_0} \tag{D.33}$$

$$c_{\ell_0} \;=\; 2\int_0^\pi \frac{\mathrm{d}Z}{\mathrm{d}x}\,(\cos\vartheta - 1)\,\mathrm{d}\vartheta \tag{D.34}$$

where the zero-angle lift coefficient c_{ℓ_0} depends only on the camberline shape. Note that the lift slope

$$\frac{\mathrm{d}c_\ell}{\mathrm{d}\alpha} \;=\; 2\pi \tag{D.35}$$

is therefore independent of the airfoil camber shape. The lift coefficient can alternatively be given by

$$c_\ell \;=\; 2\pi\,(\alpha - \alpha_{L=0}) \qquad , \qquad \alpha_{L=0} = -c_{\ell_0}/2\pi \tag{D.36}$$

where $\alpha_{L=0}$ is the *zero-lift angle* .

The moment coefficient about the quarter-chord reference point $x_\mathrm{ref}/c = 1/4$ is computed by again using the trigonometric coordinate ϑ.

$$c_{m,c/4} \;\equiv\; \frac{M'_{c/4}}{\frac{1}{2}\rho V_\infty^2\, c^2} \;=\; \frac{1}{\frac{1}{2}\rho V_\infty^2\, c^2} \int_0^c -(p_l - p_u)(x - c/4)\,\mathrm{d}x \tag{D.37}$$

$$= \int_0^1 -\Delta C_p \left(\frac{x}{c} - \frac{1}{4}\right)\,\mathrm{d}\!\left(\frac{x}{c}\right)$$

$$= \frac{\pi}{4}(\mathcal{A}_2 - \mathcal{A}_1) \;=\; \frac{1}{2}\int_0^\pi \frac{\mathrm{d}Z}{\mathrm{d}x}\,(\cos^2\vartheta - \cos\vartheta)\,\mathrm{d}\vartheta \tag{D.38}$$

The influence of camber on the airfoil $c_\ell(\alpha)$ and $c_{m,c/4}(\alpha)$ curves is illustrated in Figure D.6 An important result is that this $c_{m,c/4}$ depends only on the camberline shape, but not on the angle of attack. Therefore, the quarter-chord location is the *aerodynamic center* for any airfoil, defined as the location about which the moment is independent of α, or equivalently where

$$\frac{\mathrm{d}c_{m,c/4}}{\mathrm{d}\alpha} \;=\; 0. \tag{D.39}$$

These results are subject to the assumptions of thin airfoil theory. In practice, they are surprisingly accurate even for relatively thick or highly-cambered airfoils, especially for predicting trends (with camber, α, etc) than absolute numbers. When used merely as a conceptual framework for understanding airfoil behavior rather than for quantitative predictions, thin airfoil theory is highly applicable to almost any airfoil.

D.4   Second-Order Solution

D.4.1   General case

An improved solution for the vortex sheet strength $\gamma(x)$ can be obtained by using the first-order solution to estimate the higher-order terms which were dropped from the governing equation (D.14). These involve the
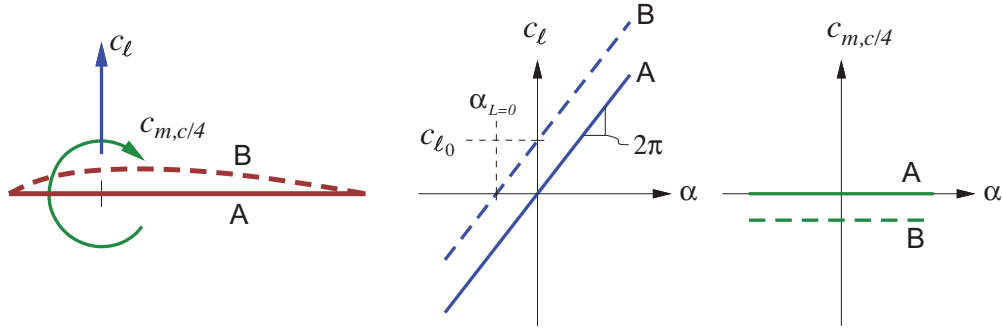
Figure D.6: Lift and moment coefficients for a flat airfoil A, and a cambered airfoil B. Camber produces only a shift in the coefficients, with no effect on the function slopes. The pitching moment about the quarter-chord has zero slope for any camber.

airfoil thickness distribution $t(x)$, which can be expanded in a Fourier sine series in the ϑ coordinate,

$$t(\vartheta) = c \sum_{n=1}^{\infty} \mathcal{B}_n \sin n\vartheta \tag{D.40}$$

$$\text{where} \quad \mathcal{B}_n = \frac{2}{\pi} \int_0^\pi \frac{t}{c} \sin n\vartheta \, \mathrm{d}\vartheta \tag{D.41}$$

The airfoil cross-sectional area is seen to depend only on the first Fourier coefficient.

$$A = \int_0^c t \, \mathrm{d}x = \frac{c}{2} \int_0^\pi t \, \sin\vartheta \, \mathrm{d}\vartheta = \frac{\pi}{4} c^2 \mathcal{B}_1 \tag{D.42}$$

The source sheet strength (D.17) can also be given in terms of the airfoil thickness series coefficients.

$$\lambda(\vartheta) = V_\infty \frac{\mathrm{d}t}{\mathrm{d}x} = V_\infty \frac{\mathrm{d}t/\mathrm{d}\vartheta}{\mathrm{d}x/\mathrm{d}\vartheta} = \frac{2V_\infty}{\sin\vartheta} \sum_{n=1}^{\infty} n\mathcal{B}_n \, \cos n\vartheta \tag{D.43}$$

Substituting this into (D.9) and evaluating the superposition integral gives the streamwise perturbation velocity u in terms of the thickness series coefficients.

$$u(\vartheta) = \frac{1}{2\pi} \sum_{n=1}^{\infty} 2V_\infty \, n\mathcal{B}_n \int_0^\pi \frac{\cos\vartheta' \, \mathrm{d}\vartheta'}{\cos\vartheta' - \cos\vartheta} = V_\infty \sum_{n=1}^{\infty} n\mathcal{B}_n \frac{\sin n\vartheta}{\sin\vartheta} \tag{D.44}$$

D.4.2 Flat elliptical-thickness airfoil

For the simple case of a "flat" airfoil with $Z=0$, the governing equation (D.14) simplifies as follows.

$$\frac{\mathrm{d}}{\mathrm{d}x} \left[\tfrac{1}{4}\gamma t \right] = w_\infty + w \tag{D.45}$$

Consider an additional simplification of an elliptical thickness distribution, which has $\mathcal{B}_2 = \mathcal{B}_3 = \ldots = 0$. Using this to simplify the lefthand side of (D.45), and replacing w on the righthand side with the superposition integral (D.10) produces the following higher-order version of equation (D.21).

$$\frac{\mathcal{B}_1}{2} \frac{1}{\sin\vartheta} \frac{\mathrm{d}}{\mathrm{d}\vartheta} \left[\frac{\gamma(\vartheta)}{V_\infty} \sin\vartheta \right] + \frac{1}{2\pi} \int_0^\pi \frac{\gamma(\vartheta')}{V_\infty} \frac{\sin\vartheta' \, \mathrm{d}\vartheta'}{\cos\vartheta' - \cos\vartheta} = \alpha \quad (\, 0 < \vartheta < \pi \,) \tag{D.46}$$

This is an integro-differential equation for the unknown $\gamma(\vartheta)$ distribution. The solution is

$$\frac{\gamma(\vartheta)}{V_\infty} = \frac{2\alpha}{1-\mathcal{B}_1} \frac{1 + \cos\vartheta}{\sin\vartheta} \tag{D.47}$$

which has exactly the same form as the leading term in the first-order solution (D.27), except it is increased by the factor $1/(1-\mathcal{B}_1)$. The lift and the lift-curve slope are therefore increased by this same factor.

For general (non-elliptical) airfoils, it is reasonable to replace $\mathcal{B}_1$ with the more easily computed airfoil area A using relation (D.42). Hence the lift-curve slope of finite-thickness airfoils is predicted to be

$$\frac{dc_\ell}{d\alpha} = \frac{2\pi}{1-(4/\pi)\,A/c^2} \tag{D.48}$$

which matches effectively-exact inviscid panel calculations reasonably well, as listed in Table D.1.

Table D.1: Lift-curve slopes $(dc_\ell/d\alpha)/(2\pi)$ predicted by higher-order thin airfoil theory, compared with effectively-exact values from a panel method in the bottom row.

	Flat plate	10% Ellipse	NACA 0006	NACA 0012
A/c^2	0	0.0785	0.0411	0.0822
equation (D.48)	1	1.111	1.055	1.117
panel method	1	1.100	1.051	1.102

Appendix E

Prandtl Lifting-Line Wing Theory

This Appendix will summarize Prandtl's lifting-line wing theory, which predicts the lift and induced drag on a planar unswept high aspect ratio wing. The physical lifting-line model was already presented in Section 5.5, and is illustrated in Figure 5.6. The focus here will be on the mathematical and computational treatment of this model. Given some wing geometry $c(y)$, $\alpha_{\mathrm{aero}}(y)$ and a freestream V_∞, α, the objective here is to determine the spanwise circulation $\Gamma(y)$ and subsequently the wing lift and induced drag L, D_i.

Although the method presented here is largely superseded by the more general lifting-surface theory and the associated vortex-lattice method treated in Chapter 6, it does serve as a useful reference case and provides a simple analytical result for the minimum induced drag of a planar wing of given span.

E.1   Lifting-Line Formulation

Since vortex lines cannot end within a fluid, a change in the wing circulation $\mathrm{d}\Gamma$ across a spanwise interval $\mathrm{d}y$ must be accompanied by an equal an opposite streamwise wake vortex filament $\gamma\,\mathrm{d}y = \mathrm{d}\Gamma_{\mathrm{wake}} = -\mathrm{d}\Gamma$, as shown in Figure E.1. This relates the wake vortex sheet strength $\gamma(y)$ to the wing circulation $\Gamma(y)$.

$$\gamma(y) \;=\; \frac{\mathrm{d}\Gamma_{\mathrm{wake}}}{\mathrm{d}y} \;=\; -\frac{\mathrm{d}\Gamma}{\mathrm{d}y} \tag{E.1}$$
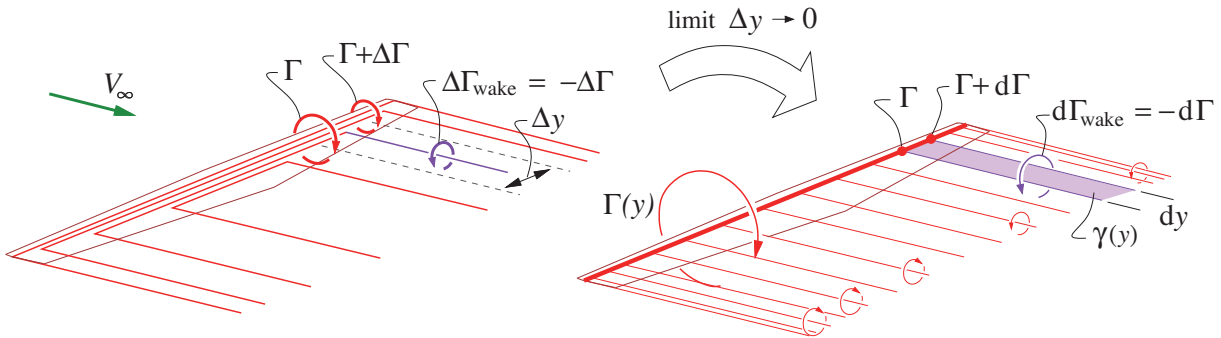
Figure E.1: Wake sheet strength related to wing's spanwise circulation gradient.

The downwash velocity and resulting induced angle at any station y are given by (5.19), (5.18), are related to $\gamma(y)$ and hence to the wing circulation gradient everywhere.

$$w_{\mathrm{wake}}(y) \;=\; \frac{1}{4\pi}\int_{-b/2}^{b/2}\frac{\mathrm{d}\Gamma}{\mathrm{d}y'}\frac{\mathrm{d}y'}{y'-y} \tag{E.2}$$

$$\alpha_i(y) \;=\; \frac{-w_{\mathrm{wake}}}{V_\infty} \tag{E.3}$$

Another feature of lifting-line theory is the assumption that each wing section behaves as a 2D airfoil flow, but with an effective angle of attack α_{eff} which includes the local induced angle of attack correction, as given by (5.22). It is convenient (but not essential) to also assume that the local 2D airfoil has a linear $c_\ell(\alpha)$ dependence based on the thin airfoil theory result (D.36).

$$c_\ell \;=\; c_{\ell_\alpha} \, \alpha_{\text{eff}} \;=\; c_{\ell_\alpha} \left(\alpha + \alpha_{\text{aero}} - \alpha_i\right) \tag{E.4}$$

$$\alpha_{\text{aero}}(y) \;=\; \alpha_{\text{geom}} - \alpha_{L=0} \tag{E.5}$$

Here $\alpha_{\text{aero}}(y)$ is the *aerodynamic twist*, which is the angle of the local zero-lift line above the wing's reference axis, and includes both the geometric twist $\alpha_{\text{geom}}(y)$ and the zero-lift angle $\alpha_{L=0}$ pictured in Figure D.6. The overall angle of attack α is the angle of the wing's reference axis relative to the freestream direction.

The lift-curve slope is $c_{\ell_\alpha} = 2\pi$ for thin airfoils in inviscid flow, but will be slightly different for thick airfoils and for viscous flow. The assumed linear $c_\ell(\alpha)$ function (E.4) restricts the subsequent results to unstalled wings. A more general $c_\ell(\alpha)$ function could be used, at the cost of some increase in complexity. This generalization will not be treated here.
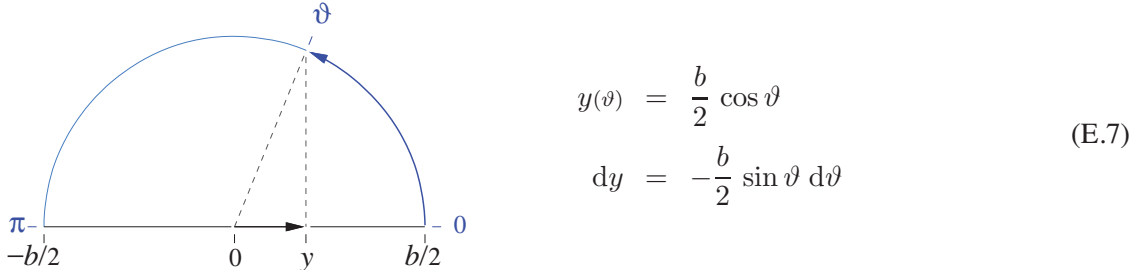
Substituting the assumed c_ℓ function (E.4) into the 2D-flow Γ–c_ℓ relation (2.84) gives the following relation between Γ and α_i.

$$\Gamma \;=\; \tfrac{1}{2} V_\infty \, c \, c_{\ell_\alpha} \left(\alpha + \alpha_{\text{aero}} - \alpha_i\right) \tag{E.6}$$

This is in effect an integral equation for the unknown $\Gamma(y)$, since α_i depends on w_{wake}, which itself depends on the overall $\Gamma(y)$ distribution via the superposition integral (E.2). This integral equation will be solved next.

E.2   Fourier Solution

The unknown $\Gamma(y)$ is expanded as a Fourier sine series in the angle coordinate $\vartheta = 0...\pi$.

$$y(\vartheta) \;=\; \frac{b}{2} \, \cos\vartheta$$

$$\mathrm{d}y \;=\; -\frac{b}{2} \, \sin\vartheta \, \mathrm{d}\vartheta \tag{E.7}$$

$$\Gamma(\vartheta) \;=\; \Gamma(y(\vartheta)) \;=\; 2bV_\infty \sum_{n=1}^{\infty} A_n \, \sin(n\vartheta) \tag{E.8}$$

$$\frac{\mathrm{d}\Gamma}{\mathrm{d}y} \, \mathrm{d}y \;=\; \frac{\mathrm{d}\Gamma}{\mathrm{d}\vartheta} \, \mathrm{d}\vartheta \;=\; 2bV_\infty \sum_{n=1}^{\infty} n A_n \, \cos(n\vartheta) \, \mathrm{d}\vartheta \tag{E.9}$$

The integral in the downwash velocity expression (E.2) can then be evaluated for each Fourier term using the Glauert integral (D.28).

$$w_{\text{wake}}(\vartheta) \;=\; \frac{V_\infty}{\pi} \sum_{n=1}^{\infty} n A_n \int_{\pi}^{0} \frac{\cos(n\vartheta')}{\cos\vartheta' - \cos\vartheta} \, \mathrm{d}\vartheta'$$

$$\;=\; -V_\infty \sum_{n=1}^{\infty} n A_n \, \frac{\sin(n\vartheta)}{\sin\vartheta} \tag{E.10}$$
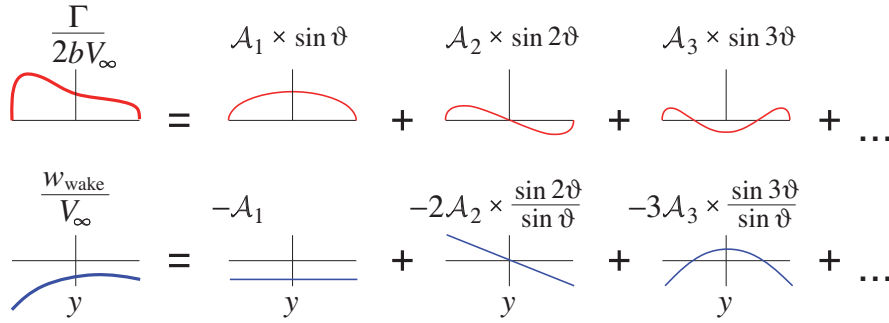
Figure E.2: Fourier terms of spanwise circulation distribution Γ, and of the resulting terms of downwash w_{wake}. All term shape functions are plotted versus the physical coordinate y.

The series terms of the circulation (E.8) and resulting downwash (E.10) are diagrammed in Figure E.2.

Combining (E.3), (E.4), (E.6), and substituting the Fourier series (E.8) and (E.10) for Γ and w_{wake} gives the following algebraic relation between all the unknown $\mathcal{A}_n$ coefficients.

$$\sum_{n=1}^{\infty} \mathcal{A}_n \left(\sin(n\vartheta) + \frac{c(\vartheta)}{4b} c_{\ell_\alpha} n \frac{\sin(n\vartheta)}{\sin \vartheta} \right) = \frac{c(\vartheta)}{4b} c_{\ell_\alpha} (\alpha - \alpha_{\text{aero}}(\vartheta)) \tag{E.11}$$

This is in effect a flow-tangency condition which states that the total freestream + downwash velocity is tangent to the airfoil zero-lift line at each spanwise point ϑ. It therefore represents infinitely many equations for the infinitely many Fourier coefficients $\mathcal{A}_n$.

In practice the series must be truncated to N terms, and the necessary N equations for the unknown $\mathcal{A}_1, \mathcal{A}_2 \ldots \mathcal{A}_N$ coefficients are obtained by performing N separate weighted integrations of equation (E.11) using suitable $W_m(\vartheta)$ weighting functions.

$$\int_0^\pi \Big\{ \text{equation (E.11)} \Big\} W_m(\vartheta) \, d\vartheta \quad ; \quad m = 1, 2 \ldots N$$

This produces the following $N \times N$ linear system for the unknown coefficients.

$$\left[\; a_{mn} \; \right] \left\{ \mathcal{A}_n \right\} = \left\{ r_m \right\} \tag{E.12}$$

where
$$a_{mn} = \int_0^\pi \left(\sin(n\vartheta) + \frac{c(\vartheta)}{4b} c_{\ell_\alpha} n \frac{\sin(n\vartheta)}{\sin \vartheta} \right) W_m(\vartheta) \, d\vartheta \tag{E.13}$$

$$r_m = \int_0^\pi \frac{c(\vartheta)}{4b} c_{\ell_\alpha} (\alpha + \alpha_{\text{aero}}(\vartheta)) W_m(\vartheta) \, d\vartheta \tag{E.14}$$

Picking W_m to be unit-impulse functions equally spaced across the $0 \ldots \pi$ interval

$$W_m = \delta(\vartheta_m) \quad ; \quad \vartheta_m = \pi \frac{m}{N+1} \tag{E.15}$$

gives a collocation-type method where the matrix and righthand side elements can be evaluated immediately.

$$a_{mn} = \sin(n\vartheta_m) + \frac{c(\vartheta_m)}{4b} c_{\ell_\alpha} n \frac{\sin(n\vartheta_m)}{\sin \vartheta_m} \tag{E.16}$$

$$r_m = \frac{c(\vartheta_m)}{4b} c_{\ell_\alpha} (\alpha + \alpha_{\text{aero}}(\vartheta)) \tag{E.17}$$

Picking W_m to be the Fourier mode functions

$$W_m = \sin m\vartheta \tag{E.18}$$

gives an alternative Galerkin-type method. For arbitrary chord and overall aerodynamic twist distributions $c(\vartheta), \alpha_{\mathrm{aero}}(\vartheta)$, this requires numerical integration of (E.13) and (E.14) for each matrix element a_{mn} and righthand side element r_m. Both W_m choices still require solution of the resulting linear system (E.12).

E.3 Force Calculation

After the $\mathcal{A}_n$ coefficients are determined by solving the linear system (E.12), the lift is obtained by the spanwise integral of the local sectional lift obtained from the Kutta-Joukowsky relation (5.23).

$$L = \rho V_\infty \int_{-b/2}^{b/2} \Gamma \, \mathrm{d}y = \rho V_\infty \int_0^\pi 2bV_\infty \sum_{n=1}^\infty \mathcal{A}_n \sin(n\vartheta) \, \frac{b}{2} \sin\vartheta \, \mathrm{d}\vartheta = \pi \frac{1}{2}\rho V_\infty^2 \, b^2 \, \mathcal{A}_1 \tag{E.19}$$

By orthogonality of the sine functions (D.32), only the first $\mathcal{A}_1$ coefficient contributes to lift.

The lifting-line induced drag integral (5.24) can also be evaluated explicitly.

$$D_i = -\rho \int_{-b/2}^{b/2} \Gamma \, w_{\mathrm{wake}} \, \mathrm{d}y = \rho \int_0^\pi \left[2bV_\infty \sum_{n=1}^\infty \mathcal{A}_n \sin(n\vartheta) \right] \left[V_\infty \sum_{n=1}^\infty n \mathcal{A}_n \frac{\sin(n\vartheta)}{\sin\vartheta} \right] \frac{b}{2} \sin\vartheta \, \mathrm{d}\vartheta$$

$$D_i = \pi b^2 \frac{1}{2} \rho V_\infty^2 \sum_{n=1}^\infty n \mathcal{A}_n^2 = \frac{(L/b)^2}{\frac{1}{2}\rho V_\infty^2 \, \pi} (1+\delta) = \frac{(L/b)^2}{\frac{1}{2}\rho V_\infty^2 \, \pi \, e} \tag{E.20}$$

$$\delta \equiv 2\left(\frac{\mathcal{A}_2}{\mathcal{A}_1}\right)^2 + 3\left(\frac{\mathcal{A}_3}{\mathcal{A}_1}\right)^2 + \ldots = \sum_{n=2}^\infty n\left(\frac{\mathcal{A}_n}{\mathcal{A}_1}\right)^2 \tag{E.21}$$

The induced drag factor $1+\delta$ is sometimes replaced by the inverse of the *span efficiency*, $1/e$, as indicated.

By choosing some suitable reference area S_{ref}, with corresponding aspect ratio $A\!R \equiv b^2/S_{\mathrm{ref}}$, the above lift and induced drag can be put into convenient dimensionless forms.

$$C_L \equiv \frac{L}{\frac{1}{2}\rho V_\infty^2 \, S_{\mathrm{ref}}} = \mathcal{A}_1 \, \pi A\!R \tag{E.22}$$

$$C_{D_i} \equiv \frac{D_i}{\frac{1}{2}\rho V_\infty^2 \, S_{\mathrm{ref}}} = \frac{\pi}{A\!R} \sum_{n=1}^\infty n \mathcal{A}_n^2 = \frac{C_L^2}{\pi \, A\!R} (1+\delta) = \frac{C_L^2}{\pi \, A\!R \, e} \tag{E.23}$$

For a given specified lift and span, the above results show that the minimum induced drag is obtained if $\delta = 0$, or $e = 1$, or equivalently $\mathcal{A}_2 = \mathcal{A}_3 \ldots = 0$, and the wing has an elliptical circulation distribution. For this case the downwash velocity and the induced angle are also constant everywhere across the wing.

$$\Gamma(y) = 2bV_\infty \mathcal{A}_1 \sin\vartheta = 2bV_\infty \frac{C_L}{\pi \, A\!R} \sqrt{1 - (2y/b)^2} \tag{E.24}$$

$$w_{\mathrm{wake}} = -V_\infty \mathcal{A}_1 = -V_\infty \frac{C_L}{\pi \, A\!R} \tag{E.25}$$

$$\alpha_i = \frac{C_L}{\pi \, A\!R} \tag{E.26}$$

Although the uniform downwash and induced-angle relations (E.25) and (E.26) are strictly correct only for an elliptical loading, they are useful as average-value estimates for a general planar wing.

E.4 Elliptical Planform Case

E.4.1 Twisted elliptical wing

For the special case of a wing with an *elliptical planform* we have

$$c(\vartheta) \;=\; c_0 \, \sin\vartheta \tag{E.27}$$

$$S_{\text{ref}} \;=\; \frac{\pi}{4} \, b\,c_0 \tag{E.28}$$

$$A\!R \;=\; \frac{4}{\pi}\frac{b}{c_0} \tag{E.29}$$

where c_0 is the center wing chord at $y=0$. In this case, with the Fourier mode weight functions (E.18), the a_{mn} coefficient matrix (E.13) becomes diagonal.

$$a_{mn} \;=\; \begin{cases} \frac{\pi}{2}\left(1 \,+\, m\,\frac{c_{\ell_\alpha}}{\pi A\!R}\right) & , \quad m=n \\ 0 & , \quad m\neq n \end{cases} \tag{E.30}$$

This then gives an explicit expression for each circulation Fourier coefficient in terms of the overall effective twist distribution $\alpha + \alpha_{\text{aero}}(\vartheta)$, via each righthand side vector element r_m.

$$r_m \;=\; \int_0^\pi \frac{c_{\ell_\alpha}}{\pi A\!R}\,(\alpha + \alpha_{\text{aero}}(\vartheta))\,\sin\vartheta\,\sin m\vartheta\;\mathrm{d}\vartheta \tag{E.31}$$

$$\mathcal{A}_m \;=\; \frac{r_m}{a_{mm}} \;=\; \frac{2}{\pi}\frac{r_m}{1 + m\,c_{\ell_\alpha}/(\pi A\!R)} \tag{E.32}$$

E.4.2 Flat elliptical wing

For the case of an *aerodynamically-flat elliptical wing*, we in addition have

$$\alpha_{\text{aero}} \;=\; \text{constant} \tag{E.33}$$

so that now only the first righthand side vector element and the first Fourier coefficient are nonzero.

$$r_m \;=\; \begin{cases} \dfrac{\pi}{2}\dfrac{c_{\ell_\alpha}}{\pi A\!R}\,(\alpha + \alpha_{\text{aero}}) & , \quad m=1 \\ 0 & , \quad m\neq 1 \end{cases} \tag{E.34}$$

$$\mathcal{A}_1 \;=\; \frac{r_1}{a_{11}} \;=\; \frac{c_{\ell_\alpha}/(\pi A\!R)}{1 + c_{\ell_\alpha}/(\pi A\!R)}\,(\alpha + \alpha_{\text{aero}}) \tag{E.35}$$

$$\mathcal{A}_2 = \mathcal{A}_3 = \ldots \;=\; 0 \tag{E.36}$$

Consequently, a flat elliptical wing has an elliptical loading at any overall angle of attack α away from stall. From (E.22) its lift coefficient is

$$C_L \;=\; \frac{c_{\ell_\alpha}}{1 + c_{\ell_\alpha}/(\pi A\!R)}\,(\alpha + \alpha_{\text{aero}}) \tag{E.37}$$

so that the wing's lift-curve slope is

$$\frac{\mathrm{d}C_L}{\mathrm{d}\alpha} \;=\; \frac{c_{\ell_\alpha}}{1 + c_{\ell_\alpha}/(\pi A\!R)} \;\simeq\; \frac{c_{\ell_\alpha}}{1 + 2/A\!R} \tag{E.38}$$

which is reduced from the 2D value c_{ℓ_α} by the factor in the denominator. Although relation (E.38) is strictly correct only for the flat elliptical wing, it is frequently used to estimate the lift-curve slope of wings with more general planforms.

Appendix F

Axis Transformations and Rotations

F.1 Axis Transformations

Any vector $\mathbf{v}$ can be given via its Earth-axes or body-axes components, denoted by superscripts $\mathbf{v}^e$ or $\mathbf{v}^b$.

$$\mathbf{v}^e \equiv \left\{ \begin{array}{c} \mathrm{v}_x^e \\ \mathrm{v}_y^e \\ \mathrm{v}_z^e \end{array} \right\} \qquad\qquad \mathbf{v}^b \equiv \left\{ \begin{array}{c} \mathrm{v}_x^b \\ \mathrm{v}_y^b \\ \mathrm{v}_z^b \end{array} \right\}$$

Transformation between the two sets of components consists of dot products with axis unit vectors. This is equivalent to the matrix-vector products,

$$\mathbf{v}^b = \bar{\bar{\mathbf{T}}}_e^b \mathbf{v}^e \qquad\qquad \mathbf{v}^e = \bar{\bar{\mathbf{T}}}_b^e \mathbf{v}^b \qquad\qquad (\text{F.1})$$

where the direction-cosine transformation matrices are composed of the unit vectors by rows.

$$\bar{\bar{\mathbf{T}}}_e^b = \begin{bmatrix} - & \hat{\mathbf{x}}_b^e & - \\ - & \hat{\mathbf{y}}_b^e & - \\ - & \hat{\mathbf{z}}_b^e & - \end{bmatrix} \qquad\qquad \bar{\bar{\mathbf{T}}}_b^e = \begin{bmatrix} - & \hat{\mathbf{x}}_e^b & - \\ - & \hat{\mathbf{y}}_e^b & - \\ - & \hat{\mathbf{z}}_e^b & - \end{bmatrix} \qquad\qquad (\text{F.2})$$

Figure F.1 illustrates relations (F.1), with $\mathbf{v}$ being an aircraft's velocity as an example.
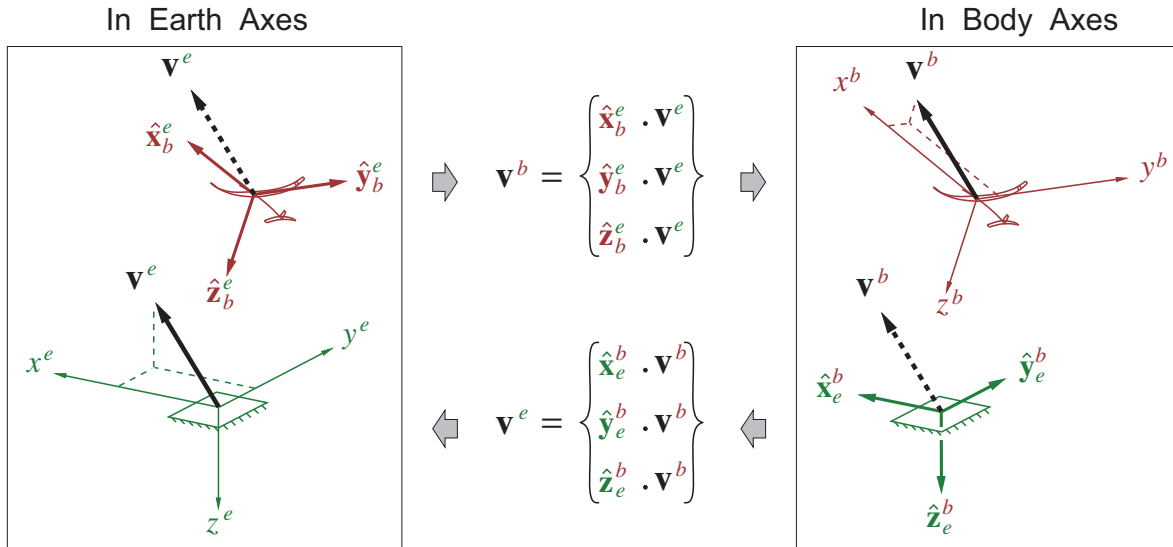
Figure F.1: Transformations of an airplane's velocity vector $\mathbf{v}$ components from Earth to body axes, and vice versa, via dot products with axis unit vectors.

Each matrix undoes the action of the other, so they must be inverses.

$$\mathbf{v}^b = \bar{\bar{\mathbf{T}}}_e^b \mathbf{v}^e = \bar{\bar{\mathbf{T}}}_e^b \left[\bar{\bar{\mathbf{T}}}_b^e \mathbf{v}^b \right] = \left[\bar{\bar{\mathbf{T}}}_e^b \bar{\bar{\mathbf{T}}}_b^e \right] \mathbf{v}^b$$

$$\rightarrow \quad \bar{\bar{\mathbf{T}}}_e^b \bar{\bar{\mathbf{T}}}_b^e = \bar{\bar{\mathbf{I}}}$$

$$\bar{\bar{\mathbf{T}}}_e^b = \bar{\bar{\mathbf{T}}}_b^{e^{-1}} \tag{F.3}$$

This implies that they can also be composed of the opposing unit vectors by columns,

$$\bar{\bar{\mathbf{T}}}_e^b = \begin{bmatrix} | & | & | \\ \hat{\mathbf{x}}_e^b & \hat{\mathbf{y}}_e^b & \hat{\mathbf{z}}_e^b \\ | & | & | \end{bmatrix} \qquad\qquad \bar{\bar{\mathbf{T}}}_b^e = \begin{bmatrix} | & | & | \\ \hat{\mathbf{x}}_b^e & \hat{\mathbf{y}}_b^e & \hat{\mathbf{z}}_b^e \\ | & | & | \end{bmatrix} \tag{F.4}$$

and also that the inverse of any cartesian transformation matrix is equal to its transpose.

$$\bar{\bar{\mathbf{T}}}^{-1} = \bar{\bar{\mathbf{T}}}^T \tag{F.5}$$

Any vector operation must be performed in common axes. For example, the operations $\mathbf{u}^e \cdot \mathbf{v}^e$ or $\mathbf{u}^e \times \mathbf{v}^e$ are valid, while evaluating $\mathbf{u}^e \cdot \mathbf{v}^b$ or $\mathbf{u}^e \times \mathbf{v}^b$ gives nonsensical results. The latter two operations would need to be reformulated as $\mathbf{u}^e \cdot (\bar{\bar{\mathbf{T}}}_b^e \mathbf{v}^b)$ and $\mathbf{u}^e \times (\bar{\bar{\mathbf{T}}}_b^e \mathbf{v}^b)$ to be valid.

F.2 Axis Rotation Relations

A unit vector can change only its direction (not magnitude) via rotation. This is illustrated in Figure F.2 which shows the rates of change of the body-axis unit vectors as a result of the body rotation rate $\mathbf{\Omega}$, where each unit-vector rate is orthogonal to that same unit vector. Using the convenient dot notation for the time derivative, $\dot{(\,)} \equiv \mathrm{d}(\,)/\mathrm{d}t$, the unit vector rates (in some frame) are explicitly given by

$$\begin{aligned} \dot{\hat{\mathbf{x}}}_b &= \mathbf{\Omega} \times \hat{\mathbf{x}}_b \\ \dot{\hat{\mathbf{y}}}_b &= \mathbf{\Omega} \times \hat{\mathbf{y}}_b \\ \dot{\hat{\mathbf{z}}}_b &= \mathbf{\Omega} \times \hat{\mathbf{z}}_b \end{aligned} \tag{F.6}$$

where $\mathbf{\Omega}$ is the rotation rate of the $\hat{\mathbf{x}}_b, \hat{\mathbf{y}}_b, \hat{\mathbf{z}}_b$ vector triplet in that same frame.
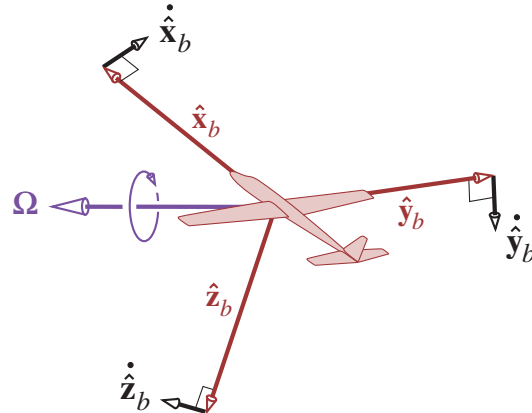
Figure F.2: Body rotation rate $\mathbf{\Omega}$ gives rates of change of its body-axis unit vectors, all seen in some arbitrary frame.

An alternative way to write any cross product is as a matrix-vector product,

$$\mathbf{\Omega} \times \mathbf{v} = \vec{\vec{\Omega}}\, \mathbf{v}$$

where the three components of the first vector $\mathbf{\Omega}$ are arranged in the antisymmetric matrix $\vec{\vec{\Omega}}$:

$$\mathbf{\Omega} = \begin{Bmatrix} \Omega_x \\ \Omega_y \\ \Omega_z \end{Bmatrix} \qquad \rightarrow \qquad \vec{\vec{\Omega}} = \begin{bmatrix} 0 & -\Omega_z & \Omega_y \\ \Omega_z & 0 & -\Omega_x \\ -\Omega_y & \Omega_x & 0 \end{bmatrix} \tag{F.7}$$

The rate definitions (F.6) can therefore be given alternatively as follows.

$$\begin{aligned} \dot{\hat{\mathbf{x}}}_b &= \vec{\vec{\Omega}}\, \hat{\mathbf{x}}_b \\ \dot{\hat{\mathbf{y}}}_b &= \vec{\vec{\Omega}}\, \hat{\mathbf{y}}_b \\ \dot{\hat{\mathbf{z}}}_b &= \vec{\vec{\Omega}}\, \hat{\mathbf{z}}_b \end{aligned} \tag{F.8}$$

When these are assembled by columns into a single matrix equation and expressed in Earth axes,

$$\begin{bmatrix} | & | & | \\ \dot{\hat{\mathbf{x}}}_b^e & \dot{\hat{\mathbf{y}}}_b^e & \dot{\hat{\mathbf{z}}}_b^e \\ | & | & | \end{bmatrix} = \begin{bmatrix} & \vec{\vec{\Omega}}^e & \end{bmatrix} \begin{bmatrix} | & | & | \\ \hat{\mathbf{x}}_b^e & \hat{\mathbf{y}}_b^e & \hat{\mathbf{z}}_b^e \\ | & | & | \end{bmatrix}$$

they become an expression for the rate of change of the transformation matrix $\bar{\bar{\mathbf{T}}}_b^e$.

$$\dot{\bar{\bar{\mathbf{T}}}}_b^e = \vec{\vec{\Omega}}^e\, \bar{\bar{\mathbf{T}}}_b^e \tag{F.9}$$

Post-multiplying this relation by $\bar{\bar{\mathbf{T}}}_e^b$ gives the rotation rate matrix in terms of the transformation matrix and its time rate.

$$\dot{\bar{\bar{\mathbf{T}}}}_b^e\, \bar{\bar{\mathbf{T}}}_e^b \tag{F.10}$$

This $\vec{\vec{\Omega}}^e$ must be antisymmetric as required by its definition (F.7). Its three independent elements (3,2), (1,3), (2,1) are the respective $\Omega_x^e, \Omega_y^e, \Omega_z^e$ components of the rotation rate vector $\mathbf{\Omega}^e$.

Relations (F.9) and (F.10) are used in Section 9.6.2 for deriving the equations of motion of a maneuvering aircraft.

Bibliography

[1] COESA Working Group. US standard atmosphere, 1976. Technical Report NAOO-S/T 76-1562, NOAA, Oct 1976.

[2] G.K. Batchelor. *An Introduction to Fluid Dynamics*. Cambridge University Press, Cambridge, 1979.

[3] M. Gad-el Hak. Stokes' Hypothesis for a Newtonian, isotropic fluid. *Journal of Fluids Engineering*, 117(1):3–5, 1995.

[4] J. Katz and A. Plotkin. *Low-Speed Aerodynamics, 2nd Edition*. Cambridge University Press, Cambridge, U.K., 2001.

[5] M. Drela. XFOIL: An analysis and design system for low Reynolds number airfoils. In T.J. Mueller, editor, *Low Reynolds Number Aerodynamics*. Springer-Verlag, Jun 1989. Lecture Notes in Engineering, No. 54, http://web.mit.edu/drela/Public/web/xfoil.

[6] M. Drela and M.B. Giles. Viscous-inviscid analysis of transonic and low Reynolds number airfoils. *AIAA Journal*, 25(10):1347–1355, Oct 1987.

[7] R.J. McGhee and W.D. Beasley. Low-speed aerodynamic characteristics of a 17-percent thick airfoil section designed for general aviation applications. Technical Note D-7428, NASA, Dec 1973.

[8] H. Glauert. *The Elements of Aerofoil and Airscrew Theory, 2nd Edition*. Cambridge University Press, Cambridge, U.K., 1959.

[9] R.C. Lock and B.R. Williams. Viscous-inviscid interactions in external aerodynamics. *Progress in Aerospace Sciences*, 24:51–171, 1987.

[10] W.C. Reynolds. Fundamentals of turbulence for turbulence modeling and simulation. In *AGARD Lecture Series*, pages 1–66, Apr 1987. AGARD-LS-86.

[11] L. (Ed.) Rosenhead. *Laminar Boundary Layers*. Dover, New York, 1963.

[12] H. Schlichting. *Boundary-Layer Theory*. McGraw-Hill, New York, 1979.

[13] S. Sato. *The Power Balance Method for Aerodynamic Performance Assessment*. PhD thesis, MIT, June 2012.

[14] F.H. Clauser. Turbulent boundary layers in adverse pressure gradients. *Journal of the Aeronautical Sciences*, 21(2):91–108, Feb 1954.

[15] D.E. Coles. The law of the wake in the turbulent boundary layer. *Journal of Fluid Mechanics*, 1:193–226, 1956.

[16] R.L. Simpson, Y.T. Chew, and B.G. Shivaprasad. The structure of a separating turbulent boundary layer. Part 1. Mean flow and Reynolds stresses. *Journal of Fluid Mechanics*, 113:23–51, 1981.

[17] R.H. Liebeck. A class of airfoils designed for high lift in incompressible flow. *Journal of Aircraft*, 10:610–617, Oct 1973.

[18] J.D. McLean. *Understanding Aerodynamics*. John Wiley and Sons, West Sussex, UK, 2013. ISBN 978-1-119-96751-4.

[19] T. Cebeci and A.M.O. Smith. *Analysis of Turbulent Boundary Layers*. Academic Press, New York, 1974.

[20] T. Cebeci and P. Bradshaw. *Momentum Transfer in Boundary Layers*. McGraw-Hill, New York, 1977.

[21] B. Thwaites. Approximate calculation of the laminar boundary layer. *Aero. Quart.*, 1:245, 1949.

[22] F.M. White. *Viscous Fluid Flow*. McGraw-Hill, New York, 1974.

[23] J.C. Le Balleur. Strong matching method for computing transonic viscous flows including wakes and separations. *La Recherche Aerospatiale*, 1981-3:21–45, 1981. English Edition.

[24] D.L. Whitfield, T.W. Swafford, and J.L. Jacocks. Calculation of turbulent boundary layers with separation and viscous-inviscid interaction. *AIAA Journal*, 19(10):1315–1322, Oct 1981.

[25] M.R. Head. Entrainment in the turbulent boundary layer. R & M Report 3152, Aeronautical Research Council, HMSO, London, 1958.

[26] J.E. Green, D.J. Weeks, and J.W.F. Brooman. Prediction of turbulent boundary layers and wakes in compressible flow by a lag-entrainment method. R & M Report 3791, Aeronautical Research Council, HMSO, London, 1977.

[27] J.H. McMasters, J.P. Crowder, and P.E. Robertson. Recent applications of vortex generators to wind turbine airfoils. AIAA-85-5014, Jun 1985.

[28] S. Goldstein. On laminar boundary layer flow near a position of separation. *Quart. J. or Mech. and Appl. Math.*, pages 1–43, 1948.

[29] L.B. Wigton and M. Holt. Viscous-inviscid interaction in transonic flow. AIAA-81-1003, 1981.

[30] A.E.P. Veldman. The calculation of incompressible boundary layers with strong viscous-inviscid interaction. In *Conference on Computation of Viscous-Inviscid Interactions*, 1980. AGARD-CP-291.

[31] M.B. Bieterman, R.G. Melvin, F.T. Johnson, J.E. Bussoletti, D.P. Young, W.P. Huffman, C.L. Hilmes, and M. Drela. Boundary layer coupling in a general configuration full potential code. Technical Report BCSTECH-94-032, Boeing, Aug 1994.

[32] Jens Osterlund. Experimental studies of zero pressure-gradient turbulent boundary-layer flow. Technical report, KTH, Stockholm, Sweden, Dec 1999. http://www.mech.kth.se/ jens/zpg/ .

[33] S.F. Hoerner. *Fluid-Dynamic Drag*. Hoerner Fluid Dynamics, Vancouver, WA, 1965.

[34] L.C. Squire and A.D. Young. The calculation of profile drag of aerofoils. R & M Report 1838, Aeronautical Research Council, HMSO, London, 1938.

[35] H.L. Reed and D. Saric, W.S.and Arnal. Linear stability theory applied to boundary layers. *Annual Reviews of Fluid Mechanics*, 28, 1996.

[36] W.S. Saric, H.L. Reed, and E.J. Kerschen. Boundary layer receptivity. *Annual Reviews of Fluid Mechanics*, 34, 2002.

[37] A.M.O. Smith and N. Gamberoni. Transition, pressure gradient, and stability theory. Report ES 26388, Douglas Aircraft Co., 1956.

[38] J.L. van Ingen. A suggested semi-empirical method for the calculation of the boundary layer transition region. Report VTH-74, Delft University of Technology, Dept. of Aerospace Engineering, the Netherlands, 1956.

[39] B.J. Abu-Ghannam and R. Shaw. Natural transition of boundary layers — The effects of turbulence, pressure gradient, and flow history. *Journal of Mechanical Engineering Science*, 22(5):213–228, 1980.

[40] I. Tani. Low speed flows involving bubble separations. *Progress in Aeronautical Sciences*, 5:70–103, 1964.

[41] M. Gaster. The structure and behavior of laminar separation bubbles. In *Separated Flows, AGARD CP 4*, 1969.

[42] R.J. McGhee, B.S. Walker, and B.F. Millard. Experimental results for the Eppler 387 airfoils at low Reynolds numbers in the Langley Low-Turbulence Pressure Tunnel. Technical Memorandum 4062, NASA, Oct 1988.

[43] M. Drela. Low-Reynolds number airfoil design for the MIT Daedalus prototype: A case study. *Journal of Aircraft*, 25(8):724–732, Aug 1988.

[44] R.H. Liebeck. Laminar separation bubbles and airfoil design at low Reynolds numbers. AIAA-92-2735-CP, June 1992.

[45] M.S. Selig. Low Reynolds number airfoil design lecture notes. In *VKI Lecture Series – Applied Vehicle Technology Panel*. NATO Research and Technology Organization, Nov 2003.

[46] A. Gopalarathnam, B.A. Broughton, B.D. McGranahan, and M.S. Selig. Design of low Reynolds number airfoils with trips. *Journal of Aircraft*, 40(4):768–775, Jul-Aug 2003.

[47] I. Kroo. Drag due to lift: Concepts for prediction and reduction. *Annual Reviews of Fluid Mechanics*, 33:587–617, 2001.

[48] A.A. Nikolski. On lift properties and induced drag of wing-fuselage combination. Technical Report NASA RE-5-1-59W, NASA, 1959.

[49] R.T. Whitcomb. A design approach and selected wind-tunnel results at high subsonic speeds for wing-tip mounted winglets. Technical Note D-8260, NASA, Jul 1976.

[50] H. Ashley and M.T. Landahl. *Aerodynamics of Wings and Bodies*. Dover, New York, 1965.

[51] E.C. Polhamus. A concept of the vortex lift of sharp-edge delta wings based on a leading-edge-suction analogy. Technical Note D-3767, NASA, Dec 1966.

[52] E.C. Polhamus. Application of the leading-edge-suction analogy of vortex lift to the drag due to lift of sharp-edge delta wings. Technical Note D-4739, NASA, Aug 1968.

[53] R.L. Bisplinghoff, H. Ashley, and R.L. Halfman. *Aeroelasticity*. Dover, New York, 1996.

[54] H. Wagner. Dynamischer auftrieb von tragflügeln. *Zeitschr. f. Angew. Math. und Mech.*, 5:17, 1925.

[55] H.G. Küssner. Zusammenfassender bericht über den instationären auftrieb von flügeln. *Luftfahrt-forschung*, 13(12):410–424, 1936.

[56] T. Theodorsen. General theory of aerodynamic instability and the mechanism of flutter. TR 490, NACA, 1935.

[57] M.M. Hafez, J.C. South, and Murman E.M. Artificial compressibility methods for numerical solution of transonic full potential equation. *AIAA Journal*, 17(8):838–844, Sep 1979.

[58] B.H. Göthert. Plane and three-dimensional flow at high subsonic speeds (extension of the Prandtl rule). TM 1105, NACA, 1946.

[59] J.D. Cole and L.P. Cook. *Transonic Aerodynamics*, volume 30 of *New-Holland Series in Applied Mathematics and Mechanics*. New-Holland, Amsterdam, New York, 1986.

[60] A.H. Shapiro. *Compressible Fluid Flow I*. Wiley, New York, 1953.

[61] R.T. Jones. Theoretical determination of the minimum drag of airfoils at supersonic speeds. *Journal of the Aeronautical Sciences*, 19(12):75–81, 1956.

[62] W.R. Sears. On projectiles of minimum wave drag. *Quart. Appl. Math.*, IV(4):361–366, Jan 1947.

[63] W. Haack. Geshossformen kleinsten wellenwiderstandes. In *Lilienthal-Gesellschaft für Lüftfahrtforschung*, volume 139, pages 14–28, Oct 9–10 1941.

[64] R.T. Jones. Theory of wing-body drag at supersonic speeds. TR 1284, NACA, 1952.

[65] B. Etkin. *Dynamics of Flight — Aircraft Stability and Control*. John Wiley and Sons, New York, 1972.

[66] R.C. Nelson. *Flight Stability and Automatic Control*. John Wiley and Sons, McGraw Hill, 1998.

[67] J.B. Barlow, W.H. Rae Jr., and A. Pope. *Low-Speed Wind Tunnel Testing, Third Edition*. John Wiley & Sons, Inc., New York, 1999.

[68] H. Glauert. Wind tunnel interference on wings, bodies and airscrews in a two-dimensional wind tunnel with consideration of the effect of compressibility. R & M Report 1566, Aeronautical Research Council, HMSO, London, 1938.

[69] J.A. Allen and W.G. Vincenti. Wall interference in a two-dimensional-flow wind tunnel with consideration of the effect of compressibility. TR 782, NACA, 1944.

Index